Cascade Conversion of Biomass Platform Chemicals with Multifunctional Zeolitic Materials

SAMUEL JOHN RAYNES

Cascade Conversion of Biomass Platform Chemicals with Multifunctional Zeolitic Materials

This thesis is submitted in partial fulfilment for the degree of PhD at the University of Durham

RAYNES, SAMUEL J.

Supervisor: Dr. Russell Taylor

12/07/2021

Statement of Originality

This thesis is based on work conducted by the author, in the Department of Chemistry at Durham University, during the period October 2016 to December 2019. All the work described in this thesis is original, unless otherwise acknowledged in the text or in the references. None of this work has been submitted for any another degree at this or any other University.

Signed: Samuel Raynes

Date: 12/07/21

Abstract

With supply beginning to outweigh demand, bioethanol is predicted to become a major platform chemical within the coming decades. Zeolites are speculated to be robust, versatile and efficient catalysts for the conversion of biomass derived platform molecules through cascade reactions. This project aims to understand and improve multifunctional zeolite catalysts for cascade conversions by exploring the ability to control the nature and location of disparate catalytic sites.

In Chapter 4, zinc oxide supported on alkali cation-exchanged mordenite (ZnO/M–MOR) prepared by a simple wetness impregnation method, is shown to be a selective and stable catalyst for the direct dehydrogenation of ethanol to acetaldehyde at 400 °C under continuous flow conditions. Through variation of the ZnO loading and the zeolite counter-cation (Na, K, Rb, Cs), an optimum catalyst material was identified, ZnO/Rb–MOR loaded at 3.5 wt% Zn. Detailed analysis of the optimized system reveals excellent selectivity and stability beyond 120 h time on stream, resulting in an average acetaldehyde productivity of 16 mmol $g_{cat}^{-1}\,h^{-1}$ and overall acetaldehyde selectivity of 90% whilst operating at an ethanol conversion level of 40 %.

In Chapter 5, the synthesis and characterization of a series of heteroatomically substituted M^{4+}–MFI type materials (where M = Si, Sn, Ti, Zr or Hf) alongside their catalytic activity for the transformation of ethanol to 1,3–butadiene with and without ZnO doping is reported. The optimum material tested, ZnO/Zr–MFI, produced 3.7 mmol $g_{cat}^{-1}\,h^{-1}$ of 1,3–butadiene at 80% ethanol conversion at the onset of reaction. A long-term stability test revealed that a significant change in product distribution from 1,3–butadiene to acetaldehyde is observed at increasing time on stream, suggesting deactivation of tetrahedral Zr centres. This deactivation is investigated and found to be largely resultant from catalyst coking and it was proven possible for the catalyst to be regenerated by thermal treatment. Additionally, optimization of ZnO/Zr–MFI by variation of hydrothermal synthesis conditions was able to improve 1,3–butadiene productivity to 4.5 mmol $g_{cat}^{-1}\,h^{-1}$.

In Chapter 6, the synthesis and characterization of heteroatomically substituted M^{2+}–MFI type materials (where M = Mg, Zn) alongside their catalytic activity for the transformation of ethanol to 1,3-butadiene with and without ZnO doping is reported. Zn–MFI is found to be able to catalyse the complete cascade reaction without additional doping of ZnO, achieving a 10% selectivity to 1,3–butadiene at 50% ethanol conversion. It is predicted that framework Zn–

O bonds in open tetrahedral sites can mimic the ethanol dehydrogenation activity of bulk ZnO. Additional doping of ZnO onto Zn–MFI is shown to increase 1,3–butadiene selectivity to 17% at 70% ethanol conversion. Doping of excess ZnO as a dedicated dehydrogenation site is also seen to reduce ethylene selectivity by up to 50%. This work lays the foundations for further investigation into the Zn–MFI system for ethanol conversion by hydrothermal synthesis variations and extended optimisation.

In Chapter 7, an attempt to marry the beneficial features of the MOR framework with Lewis acidic framework substitution is undertaken with a target of direct production of 1,3–butadiene from ethanol. Further, the effect of the tetrahedral position in which the framework is substituted with a Lewis acidic metal centre is explored. Analysis of MOR materials that were dealuminated to various extents by ^{133}Cs NMR spectroscopy would appear to demonstrate that aluminium in the T_1 position is first to be removed followed by all other positions in equal proportions. Catalytic testing of the dealuminated materials in ZnO/Rb–deAl–MOR form for reaction of ethanol showed increased Brønsted acidic activity, consistent with the presence of acidic silanol nests resulting from dealumination. Sn atoms were successfully grafted into the newly formed silanol nests by reaction with $SnCl_4$ as evidenced by solid-state ^{119}Sn NMR spectroscopy. Catalytic testing of ZnO/Rb–SnAl–MOR materials revealed retention of Brønsted acidic activity but achieved no notable productivity of 1,3–butadiene from ethanol.

Preface: An Introduction to the Bio-derived Chemicals Industry.

The Reliance of Industrial Chemistry on Fossil Fuels.

With revenue valued at approximately 5.2 trillion U.S. dollars in 2016, the global chemicals industry is a true behemoth that plays a significant role in the day to day lives of the vast majority of the population around the globe.[1] It is not too far removed to suggest that nearly every synthetic item used in the modern world contains some component that began its lifecycle travelling towards a refinery *via* a pipeline. From polymers to gasoline and solvents to plastics, the products of the petrochemical industry are nearly all encompassing.

Petrochemicals, by their very definition, are compounds traditionally obtained from the refining and processing of crude oil (petroleum) and natural gas. Within a standard refinery, the petroleum will typically undergo two major processes in varying order depending upon the desired final product. For chemical conversion, thermal cracking, be it either fluidised catalytic cracking (FCC) or hydrocracking (HC), is a chemical process in which large, less useful hydrocarbons are broken down into lighter, more valuable products. For refinement, fractional distillation is utilised to purify a feed or effluent stream by physically separating a mixture of products by their differences in boiling point and vapour pressure. When utilized in tandem, a vast array of platform chemicals is obtained that, upon further transformations, produces many thousands of varied organic compounds. Ethylene, the simplest member of the olefin family, is produced on the scale of over 150 million tonnes per annum from petroleum and natural gas and is used as an intermediate in the production of ethanol, polyethylene, polyester and polyvinyl chloride (PVC) alongside many other products.[2, 3]

Oil and natural gas, however, fall into the category of finite, non-renewable resources meaning that, at some point, these crucial pipelines will begin to run dry. The timing of this depletion is not known for sure and is often the subject of strong debate within the associated communities, but an estimate within the century is not unreasonable to most. A 2020 report from BP suggests that there is currently around 50 years of available oil reserves if production continues at 2019 levels.[4] Without action, the effect of this predicted shortage will be two-fold; not only will there be a reduction in the volume of petroleum products available, but their prices will almost certainly increase rapidly unless a suitable alternative is found. The combination of these factors will likely result in many traditional petrochemical supply routes becoming economically non-viable. As a result, great scientific effort is being applied to discover

substitutes for fossil fuels and the volume of research in the development of renewable energy sources (solar, wind and nuclear) and renewable carbon sources (biomass and fermentation) is ever increasing.

The Rise of Biomass for Production of Chemicals and Fuels.

Within recent decades, the use of biomass for energy and chemical production has increased dramatically owing to the concerns about fossil fuel supplies.[5-8] Biomass has attracted attention in petrochemical production as it is renewable and the chemicals it produces should theoretically possess a net low carbon footprint. A renewable resource is one that is classed as being non-finite or that can be readily replaced by new growth. Biomass comfortably fits within this definition as many new crops can be easily planted wherever there is space to allow them. Biomass may also be sourced from waste from other industries, such as tree bark from logging, pulp from the paper industry and even solid municipal waste. Additionally, biomass sources are seen as possessing a low carbon footprint as, throughout their lifetime, biomass crops absorb and consume CO_2 from the environment *via* photosynthesis in order to grow. As a result, much of the carbon in their tissues that is released to the atmosphere upon their combustion or usage can be considered to have been removed from the atmosphere during the lifetime of the crop, resulting in only a small net increase of atmospheric CO_2 compared with the burning of fossil fuels. Whilst this does not account for energy put into crop growth from modern intensive farming methods, any reductions in carbon footprint and steps towards carbon neutrality are typically welcomed by the scientific and environmental community. Additionally, the transformation of biomass, particularly waste streams, is a relatively accessible research area as the resources required are typically readily available and utilisation of such streams is highly desirable with possibility for rapid implementation if sufficient capital could result.

Biomass, however, is not a perfect solution and is not without its potential drawbacks. Compared to petroleum, the carbon content of biomass is considerably lower due to the much higher oxygen content of biological tissues. This poses a significant problem for biofuel production due to concerns about fuel economy and classical combustion engine damage.[9] Additionally, many modern chemical plants will require either significant process development to accept different natured feedstocks or the construction of additional infrastructure for conversion of biomass resources into more typical petroleum feed streams. Furthermore, a large portion of current biomass products are produced *via* fermentation of sugars that are

routinely sourced from edible biomass or require land that could elsewise be used for agriculture. The result of this is the contentious effect of chemical and fuel production competing with food production and further increasing fresh water usage, despite a requirement to feed an ever expanding global population.[10] Substantial effort is therefore being focused into the conversion of cellulose, non-edible biomass and particularly waste streams, such as lignocellulose and pulp, into more usable carbon sources. Finally, whilst biomass is considered renewable, its products are not always recyclable, despite the two terms being commonly conflated. Polyethylene produced from bio-derived ethanol is no different chemically to polyethylene produced from fossil fuels and no more amenable to recycling or reusability.

Therefore, whilst not a perfect solution, production of chemicals and fuels from biomass could provide a much more sustainable and renewable route to many carbon containing products typically produced from fossil fuel sources. Whilst short term hurdles, such as development of new processes or modification of existing infrastructure, will require substantive effort to overcome, a large volume of research effort is being, and should continue to be, invested into biomass conversion and technologies to overcome these potential drawbacks as the long-term benefits considerably outweigh the short-term disadvantages.

References.

1. Total revenue of the global chemical industry from 2002 to 2016 (in billion U.S. dollars). , https://www.statista.com/statistics/302081/revenue-of-global-chemical-industry/. , (accessed 12/04/18).
2. The Ethylene Technology Report 2016, https://www.researchandmarkets.com/research/2xl4dr/the_ethylene, (accessed 12/04/18).
3. H. Zimmermann and R. Walzl, in *Ullmann's Encyclopedia of Industrial Chemistry*, 2009, DOI: 10.1002/14356007.a10_045.pub3.
4. BP Statistical Review of World Energy - 69th edition, https://www.bp.com/content/dam/bp/business-sites/en/global/corporate/pdfs/energy-economics/statistical-review/bp-stats-review-2020-oil.pdf, (accessed 24/05/21).
5. BP Energy Outlook 2018 edition, https://www.bp.com/content/dam/bp/en/corporate/pdf/energy-economics/energy-outlook/bp-energy-outlook-2018.pdf, (accessed 14/06/18).
6. Á. Galán-Martín, V. Tulus, I. Díaz, C. Pozo, J. Pérez-Ramírez and G. Guillén-Gosálbez, *One Earth*, 2021, **4**, 565-583.
7. J. A. Posada, A. D. Patel, A. Roes, K. Blok, A. P. C. Faaij and M. K. Patel, *Bioresour. Technol.*, 2013, **135**, 490–499.
8. Y. Liao, S.-F. Koelewijn, G. Van den Bossche, J. Van Aelst, S. Van den Bosch, T. Renders, K. Navare, T. Nicolaï, K. Van Aelst, M. Maesen, H. Matsushima, J. M. Thevelein, K. Van Acker, B. Lagrain, D. Verboekend and B. F. Sels, *Science*, 2020, **367**, 1385–1390.
9. J. Sun and Y. Wang, *ACS Catal*, 2014, **4**, 1078–1090.

10. Avoiding Bioenergy Competition for Food Crops and Land, https://www.wri.org/sites/default/files/avoiding_bioenergy_competition_food_crops_land.pdf, (accessed 14/06/18).

Acknowledgments

First and foremost, I would like to thank Dr. Russell Taylor for his excellent supervision and support. I feel there are very few supervisors that could have made my time during my PhD as enjoyable as it has been. My thanks are extended to all members of the Taylor group whom I've had the pleasure to work with. In particular, Meera, who welcomed me from day one and who has been one of the best lab partners, housemates and friends imaginable.

I would further like to thank all members of Durham University who have helped in collecting data that has made this work possible.

Finally, I would like to thank my family and my darling Sally for their constant and unwavering love and support. They have been with me every step of the way.

Funding from Durham University for a Doctoral Training Grant is gratefully acknowledged.

Publications

The following publications are resultant from work undertaken within this thesis and are attached to the back matter in the form of appendices.

S. Raynes, M. A. Shah, and R. A. Taylor, Direct conversion of methane to methanol with zeolites: towards understanding the role of extra-framework d-block metal and zeolite framework type, *Dalton Transactions*, 2019, **48**, 10364-10384. (Appendix 4)

S. J. Raynes and R A. Taylor, Zinc oxide-modified mordenite as an effective catalyst for the dehydrogenation of (bio)ethanol to acetaldehyde, *Sustainable Energy Fuels*, 2021, **5**, 2136–2148. (Appendix 5)

Table of Contents

Glossary of Abbreviations

AA	Acetaldehyde
AlPO	Aluminophosphate
APGC	Atmospheric Pressure Gas Chromatography
ASAP-MS	Atmospheric Solids Analysis Probe-Mass Spectrometry
BAS	Brønsted Acid Site
BET	Brunauer–Emmett–Teller
BID	Barrier Ionisation Discharge (Detector)
BTX	Benzene, Toluene and Xylenes
CA	Crotonaldehyde
CHN	Carbon, Hydrogen, Nitrogen Elemental Microanalysis
CHN	Carbon, Hydrogen and Nitrogen (Elemental Microanalysis)
CP	Cross Polarisation
CPMG	Carr-Purcell-Meiboom-Gill
CTAB	Cetyl Trimethylammonium Bromide
DCM	Dichloromethane
DEE	Diethyl Ether
DFT	Density Functional Theory
DI	Deionised Water
DME	Dimethyl Ether
DR	Diffuse Reflectance
DR-UV-Vis	Diffuse Reflectance-Ultraviolet-Visible
ECD	Electron Capture Detector
EDX	Energy Dispersive X-Ray (Spectroscopy)
ED-XRF	Energy Dispersive X-Ray Fluorescence
EI	Electron Ionisation
EI	Electron Ionisation
ETBE	Ethyl *tert*-Butyl Ether
EXAFS	Extended X-Ray Absorption Fine Structure
Ex-FW	Extra-Framework
FCC	Fluidised Catalytic Cracking
FID	Flame Ionisation Detector
FW	Framework

GC-MS	Gas Chromatography-Mass Spectrometry
GC-MS-BID	Gas Chromatography-Mass Spectrometry-Barrier Ionisation Discharge Detector
GDP	Gross Domestic Product
GSHV	Gas Hourly Space Velocity
HAP	Hydroxyapatite
HC	Hydrocracking
HOMO	Highest Occupied Molecular Orbital
hpdec	High-Power Decoupling
HPLC	High Performance Liquid Chromatography
I.D.	Internal Diameter
ICP-OES	Inductively Coupled Plasma-Optical Emission Spectroscopy
IE	Ion Exchange
IR	Infrared
IWI	Incipient Wetness Impregnation
IZA	International Zeolite Association
IZA	International Zeolite Association
LAS	Lewis Acid Site
LUMO	Lowest Unoccupied Molecular Orbital
MAS	Magic Angle Spinning
MM	Molecular Mechanical
MO	Molecular Orbital
MPV	Meerwein-Ponndorf-Verley (reduction)
MPVO	Meerwein−Ponndorf−Verley−Oppenauer
MS	Mass Spectrometry
MTBE	Methyl *tert*-Butyl Ether
NMR	Nuclear Magnetic Resonance
PAH	Polycyclic Aromatic Hydrocarbons
ppm	Parts per Million
PTFE	Polytetrafluoroethylen
pXRD	Powder X-Ray Diffraction
QM	Quantum Mechanical
QP	Quadrupole

RF	Radio Frequency
SAPO	Silicoaluminophosphate
SDA	Structure Directing Agents
SEM	Scanning Electron Microscopy
SEM-EDX / SEM-EDS	Scanning Electron Microscopy-Energy Dispersive X-Ray Spectroscopy
ssNMR	Solid-State Nuclear Magnetic Resonance
TCD	Thermal Conductivity Detector
TEM	Transmission Electron Microscopy
TEOS	Tetraethyl Orthosilicate
TGA	Thermogravimetric Analysis
TMPO	Trimethyl Phosphine Oxide
TMS	Tetramethylsilane
TOS	Time on Stream
TPA	Tetrapropylammonium
TPD	Temperature Programmed Desorption
TPO	Temperature Programmed Oxidation
TPO-MS	Temperature Programmed Oxidation-Mass Spectrometry
USD	United States Dollar
USY	Ultra-Stable Y
UV-Vis	Ultraviolet-Visible
WD-XRF	Wavelength Dispersive X-Ray Fluorescence
WHSV	Weight Hourly Space Velocity
WSHV	Weight Hourly Space Velocity
XANES	X-Ray Absorption Near-Edge Spectroscopy
XAS	X-Ray Absorption Spectroscopy
XRD	X-Ray Diffraction
XRF	X-Ray Fluorescence

Introduction

1. Introduction.

1.1. Principles of Multifunctional Zeolite Catalysis.

First reported by Cronstedt in 1756, zeolites are unique minerals found naturally within the earth's crust.[1] The etymology of the term *zeolite* derives from the greek "to boil" [ζέω (*zéō*)] and "stones" [λίθος (*líthos*)] referring to Cronstedt's initial observations: upon heating the materials, water was seen to bubble from them giving rise to the description of "boiling stones", an early indication of their microporosity.

Zeolites are classified as either natural or synthetic depending upon their method of production. Natural zeolites are mined from the Earth's crust on an estimated scale of approximately 1.1 million tonnes in 2017 whilst synthetic zeolites are, as the name suggests, synthesised for a specific purpose, typically in a hydrothermal manner.[2] [3, 4] Zeolites, both natural and synthetic, find widespread commercial use owing mainly to their desirable ion-exchange properties, favourable catalytic activity, price, and robustness.[5] The largest chemical use of zeolites by volume is as a builder for detergents in which their affinity for Ca^{2+} and Mg^{2+} is exploited as a water softener.[6] The ion-exchange properties of zeolites also find use in nuclear decontamination to remove the radioactive isotopes of Sr^{2+} (^{90}Sr) and Cs^{+} (^{137}Cs).[7] In terms of catalytic activity, zeolites find use as solid acid catalysts in several crucial industrial processes such as the aforementioned fluidised catalytic cracking (FCC) and hydrocracking (HC) due to their strong Brønsted acid sites that are capable of protonating long-chain alkanes, allowing them to be broken down, or cracked, into shorter chains. Whilst development of sorption materials and cracking catalysts continues, state of the art zeolite research focusses around the transformations of bio-derived platform molecules,[8] small molecule activation[9] and greenhouse gas adsorption.[10, 11]

1.1.1. Definition and Characteristic Features of a Zeolite.

A zeolite is classified as a microporous aluminosilicate material that possesses channels and cages of molecular dimensions. The prototypical zeolite is built from $[SiO_{4/2}]$ and $[AlO_{4/2}]^{-}$ tetrahedra with the aluminium sites dispersed intermittently throughout the framework (see Figure 1.1). As alumina tetrahedra contain an Al^{3+} centre as opposed to a Si^{4+}, each aluminium site confers a formal negative charge upon the zeolite framework as a whole. As a result, exchangeable counter cations are present within the zeolite structure to preserve overall charge neutrality. These counter cations can be either organic (e.g. quaternary ammonium cations) or

inorganic (e.g. alkali metal cations) depending upon the desired purpose of the zeolite. It is important to note, however, that no two alumina tetrahedra may reside beside one another owing to Löwenstein's rule that forbids Al–O–Al bond formation. Although current density functional theory (DFT) studies predict that this rule may be overcome under certain circumstances, there is currently no experimental evidence of this prediction.[12]

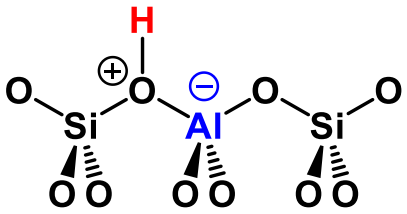

Figure 1.1: A schematic zeolite structure, counter cations are highlighted in red, aluminium atoms are highlighted in blue.

There are currently 253 known framework types that are recognized by the International Zeolite Association (IZA), each denoted by a specific three letter framework code.[13] The many frameworks differ by a wide variety of factors including: size and shape of channels (defined by the number of tetrahedral atoms in the pore ring), dimensionality, connectivity of channels and whether the channels meet to form large cavities, known as super-cages. The key structural features of five industrially relevant frameworks are outlined in Table 1.1.

Table 1.1: Selected properties of five industrially relevant zeolite framework types. All data sourced from the IZA database of zeolite structures.[13]

Framework Code	Example	Channel sizes /# T atoms	Pore Size (largest channel) / Å × Å	Channel dimensionality
BEA	Beta	12	7.3 × 7.1	3-Dimensional
FAU	Zeolite Y	12	7.4 × 7.4	3-Dimensional
FER	Ferrierite	10, 8	5.4 × 4.2	2-Dimensional
MFI	ZSM–5	10	5.6 × 5.3	3-Dimensional
MOR	Mordenite	12, 8	7.0 × 6.5	1-Dimensional[1]

[1] Although officially recognised as a 2-dimensional structure, the kinetic diameter of the 8-membered ring channel of MOR is only around the size of a He atom, hence in this project it will be treated as a pseudo 1-dimensional framework type.

Further to the standard aluminosilicate zeolite frameworks, a classification of synthetic materials known as “zeotypes” also exists. Regarded broadly as any of a family of artificial materials based on the structure of zeolites, these materials typically share many framework types with zeolites but differ by their composition; in a zeotype the tetrahedral atoms are not solely Si or Al but can be varied through a wide range of elements during the synthesis procedure. Within this term, several broad classifications of zeotypes can be made. One major classification is that of metal silicates in which the aluminium centres of the zeolite framework are substituted by various heteroatomic metal cations resulting in materials such as zincosilicates,[14] gallosilicates,[15, 16] ferrisilicates,[16] and titanosilicates in which Al has been replaced with Zn, Ga, Fe and Ti respectively.[17] A second and third major zeotype classification results from partial or total substitution of framework silicon with phosphorus, resulting in silicoaluminophosphates (SAPOs) and aluminophosphates (AlPOs) respectively.

1.1.2. Synthesis of Zeolite and Zeotype Materials.

As mentioned at the beginning of this chapter, zeolites may either be extracted from natural sources or produced synthetically, with the former being utilised primarily for high volume and low-cost applications such as sorption and exchange media. Catalytic processes, however, will more often make use of synthetic zeolites owing to the beneficial characteristics and specificity that can be introduced within the zeolite synthesis process. By and large, batch process hydrothermal synthesis is most routinely employed for the production of synthetic zeolite materials. This technique centres around the preparation of a so-called *synthesis gel* containing the zeolite precursors in their desired ratios which is then treated under heating and pressure, resulting in the crystallisation of the crystalline zeolite material. For a typical aluminosilicate synthesis gel, several components should be present: an aluminium source, a silicon source, a mineraliser, and water as a solvent. Additionally, an optional structure directing agent may be included in order to direct the growth of specific zeolite frameworks.

Perhaps the most self-explanatory components, the silicon and aluminium sources and their respective proportions within the synthesis gel help to guide the overall content of both metals and the Si/Al ratio of the synthesised zeolite. A wide variety of both Si and Al sources are routinely employed, including silicas, colloidal silicas and alkoxides of silicon, alongside aluminium salts and oxides, respectively.[18, 19] Additionally, the total or partial substitution of either aluminium or silicon sources with those of other metals, such as Sn, Zn, Ti, or others, can allow one to access heteroatomically substituted zeolite materials at the synthesis stage. At the laboratory scale, choice of metal source is limited only by their synthesis efficiency and

application safety, whereas at industrial scale, choices must be made much more carefully in terms of practicality and economics. As an example, tetraethyl orthosilicate (TEOS), a commonly employed silicon alkoxide at laboratory scale, is generally undesirable for use in industry owing to its high relative cost and the resultant production of large volumes of ethanol by hydrolysis that must be safely removed. In order to combat the non-compatibility of many laboratory scale metal sources with industrial production, many research groups dedicate substantive effort to production of known zeolite materials utilising more amenable and less expensive metal sources, especially if such sources can be acquired cheaply from other industrial waste streams.[20] A prime example of current research is the replacement of silicon alkoxides and colloidal silicas with silicon sourced from waste clays,[21, 22] coal ash[23] and rice husks.[20, 24]

Owing to the relative insolubility of many common silicon precursors in aqueous media, a *mineraliser* must also be introduced into the zeolite synthesis gel to aid precursor dissolution. The role of this mineraliser is to increase the transport and accessibility of metal precursors, typically those of silicon, in the zeolite synthesis gel. To this end, oligomeric silica species are broken down *via* formally reversible chemical reactions by the mineraliser into their monomeric components which may then repolymerise during zeolite synthesis. This mineraliser employed is almost exclusively either hydroxide (OH^-) or fluoride (F^-) and is typically introduced as either an alkali metal or quaternary ammonium salt; alkali metal bases, such as NaOH and KOH, being the most commonly employed. It must be noted that the choice of mineraliser may be crucial in zeolite synthesis gel preparation and may have sizeable effects on this final zeolitic product.[20] One major effect of mineraliser choice is on the pH of the zeolite synthesis gel, with use of basic mineralisers resulting in increased gel pH which can affect the final Si/Al ratio of the synthesised zeolite. Additionally, it is notable that use of fluoride as a mineraliser, although typically requiring longer crystallisation times, may even allow crystallisation from acidic and non-aqueous synthesis gels.[25]

Despite examples of non-aqueous synthesis gels,[25-27] water is effectively the sole solvent media used in zeolite preparation owing to it being affordable, available and easily scrubbed and recycled, making it the economic and environmental synthesis medium of choice.[18] The relative proportion of water in the prepared synthesis gel, however, may also present an effect on zeolite synthesis itself. Specifically, water content is known to influence pore diameter due to its role in void filling during hydrothermal synthesis alongside determining precursor concentrations and saturation points.[20] Additionally, the water within

the synthesis gel is the primary component responsible for generating the required autogenous pressure within the autoclave.[20]

Finally, certain additives such as structure directing agents and seeds may be introduced to the zeolite synthesis gel in order to promote formation of desired frameworks and other structural features. Commonly, structure directing agents (SDAs) are introduced to the zeolite synthesis gel in the form of quaternary ammonium cations. Upon crystallisation, the zeolite framework is built around these SDAs and their relative size can help to govern the resulting size and shape of zeolitic channels and cages. One common example relevant to this project is the use of tetrapropylammonium cations (TPA^+) to direct the formation of 10 MR channels in MFI zeolites.[28] Additionally, the use of certain SDAs can direct the location and distribution of aluminium sites within the zeolite framework as each formally negatively charged framework aluminium site must be associated with a cation. As an example, use of SDAs with two potential cationic sites may be used to locate two aluminium sites near to one another, forming paired aluminium sites at predictable distances from one another.[29, 30] Further, the use of several different template molecules, a multi-template approach, may be employed in order to direct multiple channel sizes within a zeolite material, such as formation of dual micro/mesoporosity.[31-33] Seed crystals, often obtained from previous batches of zeolite synthesis, serve a comparatively simpler purpose by acting as nucleation sites for framework growth and can act to decrease crystallisation time.

Beyond the chemical factors introduced in the form of the zeolite synthesis gel, a range of physical parameters during the hydrothermal crystallisation step may also invoke changes in the structure and characteristics of the final zeolitic product. Time and temperature are the major components of note here. Hydrothermal synthesis temperature is known to affect not only the viscosity and subsequent transport properties of the synthesis gel, but also the rate of nucleation of zeolite crystals.[20] Synthesis time on the other hand, is also important owing to different frameworks having different crystallisation rates.[20] As zeolites are thermodynamically metastable materials, excess synthesis time or temperature can often cause collapse into more stable and denser silicate phases, such as quartz. Furthermore, agitation of the system may have a considerable effect on crystallisation owing to improved precursor mobility, although it may also result in redissolution of formed zeolite phases. For further details, an excellent description of the thermodynamics and mechanism of hydrothermal zeolite synthesis, alongside the influences of synthetic parameters can be found in Lima, Bieseki, Melguizo and Pergher's "*Environmentally Friendly Zeolites: Synthesis and Source*

Materials".[20] Additionally, Casci of Johnson Matthey offers further insight into the industrial concerns regarding zeolite synthesis.[19]

Hitherto, a description of traditional hydrothermal zeolite synthesis, typical of that performed within this project, has been given. It must be noted, however, that further development into zeolite synthesis has been undertaken in order to tackle certain difficulties, often with reference to industrial production. Many of these developments come in the form of sustainability, such as the aforementioned desire to utilise waste silica and alumina sources from other industry or to minimise water consumption.[20] Additionally, investigations into both rapid and continuous zeolite crystallisation process have been ongoing in the zeolite literature.[34, 35]

1.1.3. Zeolite Modification Techniques.

In addition to variations introduced at the hydrothermal synthesis stage, zeolites can undergo a wide range of post-synthetic modifications, including inclusion of new species within the micropore network, mesopore formation, and modification of the framework composition by desilication and dealumination followed by remetallation.[36] Further, very commonly and (in principle) easily employed is ion-exchange of the counter cations. The following sections will outline common modifications techniques for improving the characteristics of zeolite materials.

1.1.3.1 Ion-Exchanges.

Widely used both commercially and in research, ion-exchange (IE) is an incredibly powerful tool in zeolite modification owing to the simplicity and effectiveness of the method. During an ion-exchange, the counter cations residing within the zeolite pores are exchanged for another cation (see Scheme 1.1). Experimentally, a solution containing the desired cation is contacted with the zeolite framework allowing solvated ions to migrate in and out of the framework until equilibrium is reached. It is possible to increase exchange levels and further push this equilibrium by performing multiple successive exchanges with fresh solutions of the desired cation. The level of exchange achievable will depend on many factors, such as the affinity of the zeolite for a particular cation (size and charge dependent), the contact time, number of treatments, pH of exchange solution, pK_a of aqueous cations, exchange temperature and hydration state of the cations.[37, 38] For example, a Li^+ ion with a strongly bound hydration sphere is unlikely to be an efficient ion to exchange into a zeolite owing to the need to break down its strong coordination sphere. Additionally, multivalent cations, such as Zn^{2+}, will likely

not undergo complete exchange into zeolite materials with high Si/Al ratios as multiple aluminium centres must be located near to one another to balance multiple cationic charges.

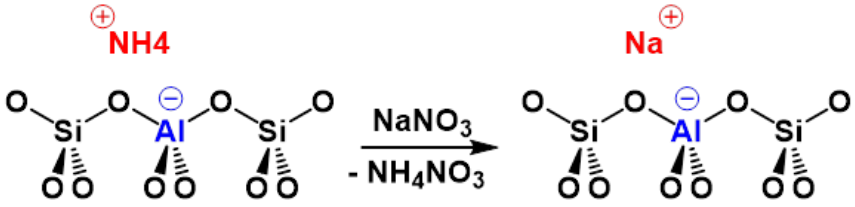

Scheme 1.1: A basic schematic of a monovalent-monovalent ion-exchange process in which ammonium cations (NH_4^+) are exchanged for incoming sodium cations (Na^+) .

1.1.3.2 Metal Impregnation.

Oft times, zeolite materials are used primarily as a support material for catalytic sites rather than their framework components undertaking catalytic reactions. In such cases, introduction of metals and metal oxide species *via* impregnation strategies is frequently employed. In contrast to the diffusion limited processes associated with ion-exchanges, it is possible to introduce metal sites directly into a zeolite *via* capillary action, known as incipient wetness impregnation (IWI) or dry-impregnation.[39] In this method, a metal precursor is solvated in a volume of solvent equal to that of the micropore volume of the zeolite, resulting in the uptake of the entire solution volume by capillary action. Typically, metal salts are solvated in water and organometallics in organic solvents owing to their high respective solubilities. Following this, the zeolite may be dried and calcined to remove solvent and precursor residues, whilst depositing the metal upon the zeolite surface in either a metallic or metal oxide form depending upon whether the subsequent heat treatment was reductive or oxidative in nature.[39] Alternatively, wetness impregnation may be employed in which a metal precursor is solvated in a volume greater than that of the zeolite micropores and the solutions thoroughly mixed before removal of the solvent *via* evacuation or heating. This method may be used to deposit more substantive quantities of metal precursor onto the zeolite materials as it is not limited by precursor solvation into a small volume of liquid. A potential downside to this method, however, is lack of control over where metal sites are deposited and potential loss of framework selectivity effects if a large volume of the metal precursor is deposited on the outer surface of the zeolite material. Additionally, in all impregnation methods (particularly wetness impregnation) it must be considered that a degree of ion-exchange is often unavoidable owing to establishment of thermodynamic equilibrium in the ion-exchange process. Attempts to minimize this effect could be made by curtailing solution contact times and avoiding

unnecessary heating steps, however considerations regarding metal distribution throughout the framework must be retained.

1.1.3.3 Reactive Grafting.

Reactive grafting is a relatively recent development in the toolbox of zeolite modification techniques. The principle is such that a highly reactive molecule, such as an organometallic, is brought into contact with the zeolite framework in order to react with either the Brønsted acid sites or framework inherent silanol defects, causing the liberation of a small molecule such as CH_4, NH_3, HCl or H_2O (see Scheme 1.2).[40] This type of grafting can typically results in distinctive and controllable placement of metal fragments throughout the framework. There are several examples of this technique being used throughout the literature utilising a wide variety of organometallic precursors, namely $ZnMe_2$, $GaMe_3$, $Ga(^iBu)_3$ and $AlMe_3$.[40-43] Further to this, Pérez-Ramírez *et al.* have shown that it is possible to use metal hydroxides (MOH, where M = Li, Na, K, Rb, Cs) in alcoholic media to deprotonate and introduce alkali metal cations onto framework silanol defects.[44] It is also possible to use a reactive grafting approach to achieve surface silylation, typically for the purpose of pore-blocking and silanol passivation, by utilisation of bulky disilazane reagents (see Scheme 1.3).[45] These reagents generally react with the silanol groups of the zeolite, forming surface bound silyl ethers and liberating ammonia.

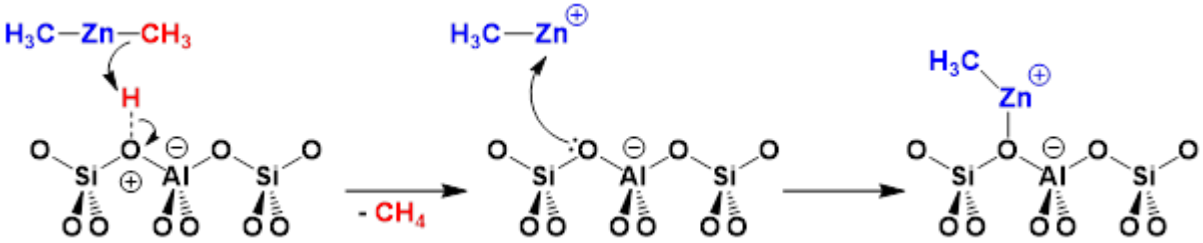

Scheme 1.2: The reactive grafting of dimethyzinc onto a zeolitic Brønsted acid site resulting in production of a framework bound zinc methyl fragment and liberation of methane.[46]

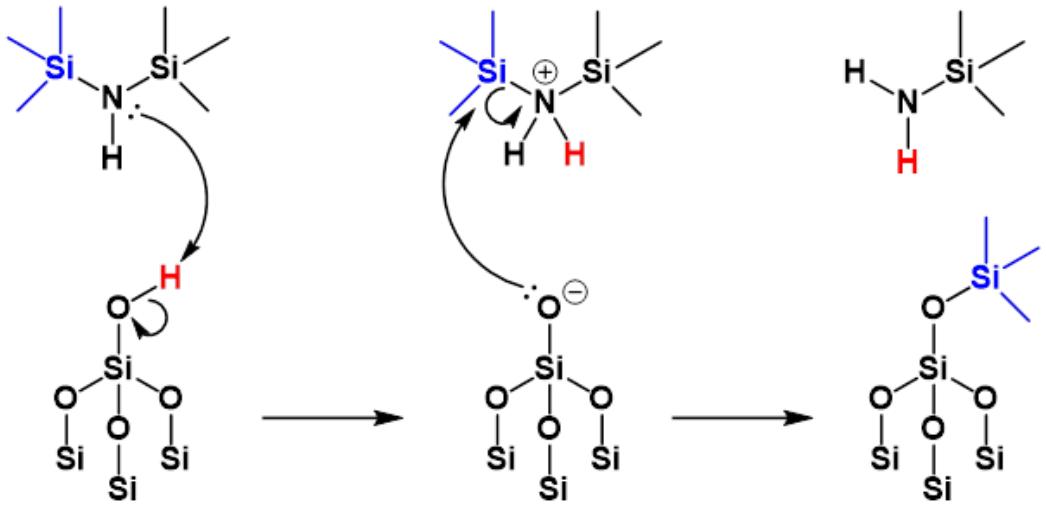

Scheme 1.3: The reactive grafting of hexamethyldisilazane onto a terminal silanol group inherent to the zeolite framework. The resulting trimethylsilanamine product may react once more with the zeolite framework, depositing a further trimethylsilyl group and liberating ammonia as a final product.[45]

1.1.3.4 Framework Modification Techniques.

Typically, the conversion of large or highly functionalised molecules requires transition states and reaction volumes larger than many standard zeolite pores can accommodate. Zeolite pores may also often be too small to accommodate given reagents (size-exclusion) or greatly restrict the rate at which they can enter and move about the channel system (diffusion limitation). In order to overcome these limitations, removal of zeolite framework atoms *via* demetallation is often employed to introduce varying degrees of mesoporosity and even macroporosity into zeolite structures, referred to as *hierarchical* structures.[47] Typically, silicon framework atoms are removed in basic media whilst aluminium framework atoms are removed by treatment in strong acids or hydrothermal steam treatment, as in the case of zeolite Ultra-Stable Y (USY).[48-52] Alternatively, mesoporosity may be established in the zeolite framework at the hydrothermal synthesis stage or *via* recrystallisation methods by introduction of mesoporogens such as surfactants which act as a secondary template for the framework to be built around; cetyl trimethylammonium bromide (CTAB) is a classic example for introduction of mesopores to MFI *via* both methods.[53-55] Regardless of the introduction method, a positive side effect of mesoporosity generation is the improvement of mass transport within the zeolite networking, with many research groups choosing to introduce the characteristic to materials that catalyse non-size restricted reactions solely to improve their catalytic performance *via* improved access to active sites.

Following demetallation, it is also possible to re-introduce a wide variety of alternative metal ions into the vacancies created. Commonly, Al^{3+} framework atoms are replaced with

similarly sized and charged species, such as Ag^{+}, Ga^{3+}, Ta^{5+}, Sn^{4+}, Ti^{4+}, Y^{3+}, Zn^{2+} and Zr^{4+} (see Scheme 1.4).[15, 49, 56-62] These framework substitutions typically provide electronic modification to the charge of the framework and modulate the strength of associated Brønsted acid sites. In the case of substitution of Al^{3+} with M^{4+}, the framework becomes charge neutral overall, and the presence of counter cations is no longer required. This process differs from zeotype synthesis as the unique atoms are introduced into an already existent framework as opposed to being present when the framework is first synthesised.

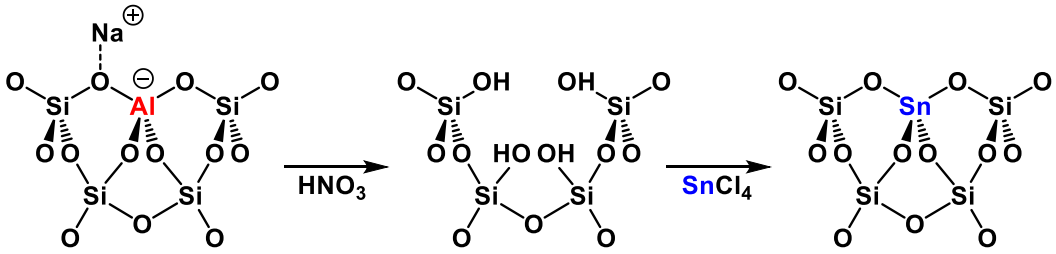

Scheme 1.4: A schematic representation of sequential acid dealumination and tin insertion into a zeolite using HNO_3 and $SnCl_4$ as reagents and precursors respectively.[63]

1.1.4. The Concept of Multifunctional Zeolite Catalysis.

Typically, it is assumed that a sole catalytic reaction step will occur over a single active site. Two examples relevant to this project are the promotion of alcohol dehydrogenation reactions and aldol condensations over metal oxide species and acid sites, respectively. The concept of a multifunctional catalyst is one that combines several disparate catalytic sites to produce a single catalytic entity that can promote a complex series of reactions without requiring multiple reactors with multiple different catalysts or conditions. The preparation of such a catalyst is significantly more feasible when utilising heterogeneous or supported catalysts when compared to homogenous catalysts as, in homogeneous systems, it is possible that any disparate catalytic sites may come together and neutralize one another. Regarding the previous example, both metal oxide species and acidic sites would need to be introduced onto the same support material. The type of process in which one reaction occurs and the products then react themselves over the same catalyst material to further progress through the synthetic pathway, is generally referred to as a cascade-style reaction.

Zeolites are ideal supports for this cascade style catalysis due to their ability to host various disparate catalytic species owing to the wide array of modification techniques available (see Section 1.1.3). It is possible to use different modification techniques in tandem to produce catalysts with several unique functionalities — a recent and relevant literature example being a BEA zeolite in which framework Al is substituted for Zr as a Lewis acidic site with

subsequent doping of Ag as a dehydrogenation promoter in order to achieve cascade ethanol to butadiene synthesis.[61] The channel system of zeolites further enhances this unique characteristic as it leads to the ability to target particular functionalities at specific locations by virtue of steric effects. In theory, reactive grafting (see Section 1.1.3.3) has the potential to introduce metal species to specific topological sites (such as targeting a specific channel size) if the steric demand of the precursor is carefully considered. $Ga(^{i}Bu)_3$, for example, should be too large to enter the micropore network of certain zeolites such as the 8MR of chabazite (CHA framework type), hence only the surface would be functionalised whilst leaving any pre-existing functionality within the channels unaffected.[42]

The concept of multifunctional zeolite materials as catalysts is not entirely new as several multifunctional systems are now commonplace in large-scale industrial processes. One major example of such systems is the mixed noble metal/zeolite system used for industrial hydrocracking.[64, 65] Therein, a platinum group metal, most typically Pt or Pd, provides a hydrogenation function whilst a zeolite, most notably zeolite Y (FAU), provides the strong acidic function required for cracking. The combination of both functionalities allows the use of a single reactor in which alkenes resulting from cracking are rapidly hydrogenated. Classically, a two-stage process in which the feed is first cracked then hydrogenated would be required. A further example of industrially relevant multifunctional zeolite catalysis is the use of Pt/MOR in $C_{5–6}$ hydro-isomerization.[64] In this system, Pt acts as a (de)hydrogenation site whilst the zeolite once again provides the strong acid functionality required to isomerise the resulting alkenes. Additionally within this system, the zeolite may confer a degree of shape-selectivity to the final isomerised product to allow targeting of specific fractions.

As a result of their myriad modification techniques and wide variety of framework topologies, zeolites materials offer an ideal and unique toolbox for the realisation of highly selective multifunctional catalysts. Although further research is needed in order to understand exactly how multiple active sites will work cooperatively and their effects on one another, the concept of multifunctional zeolites performing cascade style reactions is indeed a promising one.

1.2. Fundamentals of Heterogeneous Catalysis and Catalytic Testing.

The importance of catalysis, particularly heterogeneous catalysis, in the production of chemicals cannot be understated. Recent reports suggest up to 30% of Europe's gross domestic product (GDP) is heavily influenced by catalysis with over 80% of manufactured products produced *via* a catalysed route.[66] In this section, the fundamental concepts behind catalysis are briefly revisited and further intricacies regarding use and testing of heterogeneous systems are explored. Subsequently, the common modes of deactivation of heterogeneous catalysts, particularly zeolites, and how to assess and account for them are discussed.

1.2.1. Basic Concepts of Catalysis.

Broadly, a catalyst is defined as a substance that increases the rate of a chemical reaction without itself undergoing any permanent chemical change. This effect is most often achieved by provision of a reaction pathway that possesses lower activation energies than the uncatalysed reaction, making catalysis a purely kinetic phenomenon. In other words, the total free energy difference between reactant and product does not change regardless of whether the reaction is catalysed or not, however the free energies of transitions states may decrease with use of a catalyst. Upon application of the Arrhenius equation (Equation 1.1), these lower activation energies manifest in increased rate of reaction, the desired outcome of catalysis. It must be remembered, however, that the position of thermodynamic equilibrium is unaffected in catalysis as activation energies for both forward and backward reactions are modified by catalysis. Figure 1.2 shows a schematic representation of catalysis in a single-step reaction comprising a single transition state.

$$k = Ae^{\frac{-E_a}{RT}}$$

Equation 1.1: Arrhenius equation. k = rate constant; A = pre-exponential factor; E_a = activation energy; R = universal gas constant; T = absolute temperature.

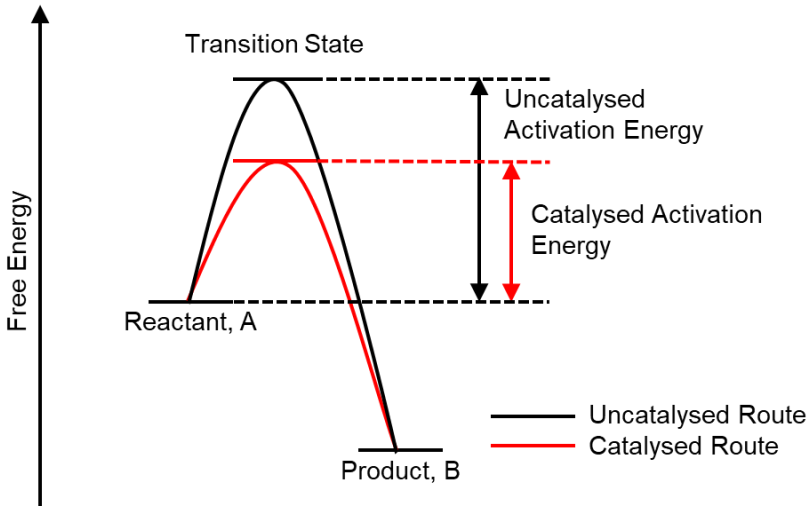

Figure 1.2: Energy diagram of a single-step exothermic reaction comprising a single transition state. Shown are the energy pathways for the uncatalysed (black) and catalysed (red) routes.

Although the position of thermodynamic equilibrium may not be altered for a given reaction, alternate reaction pathways to less thermodynamically stable products may be accessed by application of catalysis. Figure 1.3 shows two competing reaction pathways in which two different products, B and C, may form. At this point, the presence and effect of the Boltzmann distribution must be noted, but its effects are omitted to increase clarity of the example. Without a catalyst and given enough time in the thermodynamic limit, solely product B would be expected to be observed as it possesses the lowest free energy of A, B and C. Application of a suitable catalyst, however, significantly reduces the activation barrier to form product C and, working in a kinetic regime, one would expect to see an excess of product C formed (red trace in Figure 1.3). It must be noted that, given sufficient time to enter a thermodynamic regime, product B will still emerge as the major thermodynamic product (in accordance to the Boltzmann distribution) in a reversible system.

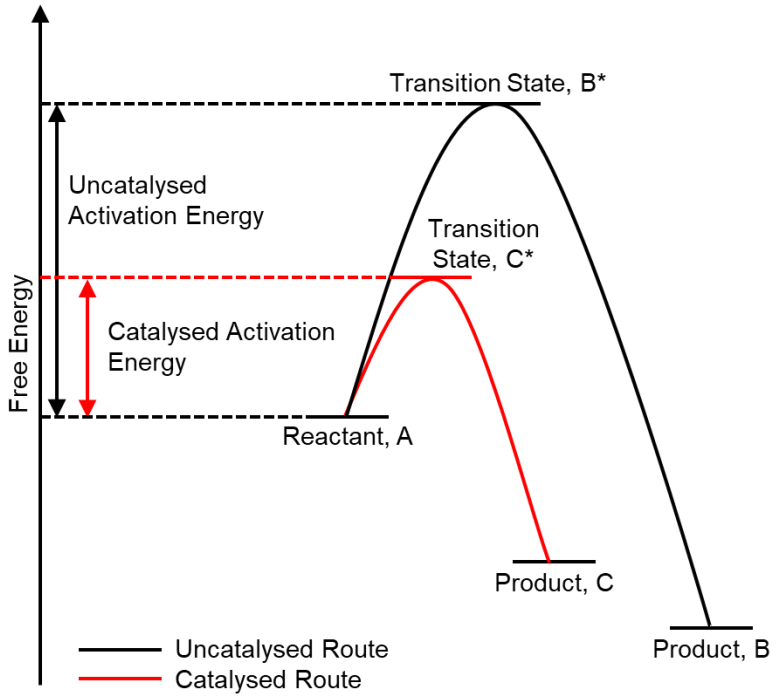

Figure 1.3: Energy diagram of a single-step exothermic reaction comprising two potential products and two respective transition states. Shown are the energy pathways for the uncatalysed (black) and catalysed (red) routes.

1.2.2. Intricacies of Heterogenous Catalysts, Their Deactivation and Precautions in Their Testing.

A heterogeneous catalyst is regarded as one which exists as a different phase to the reactants, typically a solid catalyst in a gas or liquid phase reaction. As alluded to previously, the vast majority, by volume, of industrial chemicals are produced *via* a heterogeneously catalysed route, owing to their large range of available reaction conditions, amenability to continuous processing and ease of separation from product feed streams. Despite these advantages, heterogeneous systems suffer from a relative difficulty of characterisation alongside a lesser ability to be fine-tuned for high selectivity in comparison to homogeneous systems. In particular, the former factor makes reactions intermediates difficult to probe and reaction methods hard to elucidate. Additionally, heterogeneously catalysed reactions, particularly those undertaken over fixed bed reactors, require consideration of many physical phenomena in order to maximise catalytic efficiency and yield. The following sections will aim to outline such intricacies that must be considered when designing heterogeneous catalysts, especially when use in industry is the desired endpoint. Predominantly, the concerns of using a solid zeolite catalyst affecting a gas-phase reaction in a fixed-bed continuous flow reactor are considered, as this is the dominant system employed within the original research of this thesis.

1.2.2.1. Challenges in Heterogenous Catalyst Characterisation and Mechanism Determination.

Before discussing the challenges of implementing heterogeneous catalysis successfully, the difficulties in characterising and understanding the exact nature of the chemical system in question must first be considered. Very broadly speaking, many homogenous catalysts may be well characterised by a combination of simple NMR spectroscopy, mass spectrometry and elemental analysis experiments, with single-crystal XRD acting as a "magic bullet" for molecular catalyst structure determination, providing crystallisation is possible. Heterogeneous catalyst materials, however, tend to offer a much higher degree of complexity and require a wider library of more complex techniques to characterise fully, with the exact suite of analytical techniques required heavily dependent upon the nature of the material in question. Additional complications come from the concept that the surface of many catalytic materials is often very different to the bulk material and can often exhibit different reactivity. Many spectroscopic techniques frequently employed in heterogenous catalyst characterization struggle to distinguish between the surface and bulk of the material or can only probe one or the other; hence specific care must be taken in experimental design in order to deconvolute the bulk and surface contributions. As a simple example, ICP-OES analysis of a metal impregnated zeolite may reveal that the samples contains 3.0 wt% of a given catalytically active metal, but whether this is distributed evenly throughout the material or solely deposited upon the surface (and therefore to what degree the micropore network has an effect on catalysis) is more difficult to discern.

Furthermore, determination of mechanism and reaction intermediates is particularly difficult for heterogenous systems owing to an overall lack of accessible *in-situ* and *operando* characterization and a relative inability to quench reactions in a traditional manner. Classically, heterogenous catalysts are characterised both before and after their use in a reaction and any differences interpreted as the effect of catalysis. In order to better understand behaviour of catalyst materials and to probe intermediates during reaction, both *in-situ* and *operando* characterisation studies must be further employed.[67, 68] Although frequently conflated, *in-situ* and *operando* techniques aim to achieve different objectives. *In-situ* studies are excellent for developing understanding of the catalyst material under mimic reaction conditions and what transformations result following pre-treatments, especially in combination with powerful spectroscopic handles provided by a wide array of probe molecules. *Operando* studies, however, are undertaken during the process of the desired reaction, using the reactants,

intermediates, and products themselves as probes and allowing great insight into reaction mechanism. Whilst advantageous, the implementation of *operando* studies is often difficult owing to the requirement of specialist hardware and the potential limitations of probing the reactants and products themselves. Regardless of their respective difficulties, both *in-situ* and *operando* studies are frequently employed and have been used to probe otherwise difficult observations, such as framework transformations of zeolites under reaction conditions,[69] intricacies of coke formation[70] and elucidations of reaction mechanism.[71]

1.2.2.2. Effects of Diffusion Limitation and Catalyst Morphology.

Unlike homogenous systems in which the reactant mixture and catalyst are often assumed to be in intimate contact, the rate of reaction over heterogeneous zeolite systems may be limited by transport phenomena within the system.[72] Before catalysis may occur, reagents must first come into contact with the catalytic surface which, if situated within a micropore network, may be limited by the rate of diffusion of reagents both through the interparticle space and throughout the zeolite network. In this case, although the rate of the catalytic reaction is rapid, an insufficient reagent flux may reach the catalytic sites, meaning that sites in certain geometries may often be sitting idle and the macroscopic rate of reaction is decreased. The rate of diffusion of reagents throughout a zeolite network may be affected by many factors, such as channel size and dimensionality, reaction temperature, and reactant kinetic volumes. Diffusion throughout zeolite networks may be maximised by employment of hierarchical zeolites or those with larger channel dimension and higher channel dimensionalities, although the former suggestion may affect the shape selectivity of the zeolite catalyst. In lab and industrial scale catalysis, additional considerations must be made to the macro-scale morphology of the catalyst pellets, with pellet size and shaping playing an important role in determining the rate at which reagents may reach catalytic sites alongside other important macroscopic phenomena such as heat transfer and reactor pressure drop.[73]

1.2.2.3. Deactivation of Zeolite Catalysts and Appropriate Testing Regimes.

As with most catalysts, the lifetime of heterogeneous catalysts is (often) not infinite. Similar to homogeneous systems, chemical and thermal deactivation is prevalent although heterogeneous catalysts, particularly those that are supported or shaped, may also suffer from mechanical degradation such as attrition and crushing.[74] Zeolites in particular may suffer from a range of deactivation methods such as coking, structure degradation, active site poisoning and sintering of supported species, each of which will be described briefly, alongside several other important considerations. As a further reference, C. Bartholemew's article entitled

"Mechanisms of Catalyst Deactivation" gives a more detailed overview of the following deactivation modes.[74]

Structure degradation

Structural degradation of zeolites occurs by direct attack on the zeolite framework, causing the structure to disintegrate and collapse. The effects of this degradation are twofold. Firstly, structural collapse often results in a decrease of zeolite surface area and a subsequent decrease in availability of active sites. Collapse of the micropore system may also leave active sites permanently blocked, resulting in lower catalytic activities. Additionally, loss of the micropore structure may also have effects on catalyst selectivity, particularly if the desired products were directed by shape-selectivity.

Sintering

Sintering is the process by which particles, most often reduced metal particles, agglomerate to form larger aggregates owing to the Ostwald ripening process. The effect of sintering is to effectively reduce the surface area to volume ratio of the deposited metal species. As the quantity of deposited metal is constant, the overall surface area reduces, and fewer isolated active sites are available to undertake catalysis.

Poisoning

Catalyst poisoning is a chemical phenomenon by which species either reversibly or irreversibly bind to active sites, blocking them and preventing them from participating in catalysis; hence reducing catalytic activity. It is sometimes possible to scrub poisons from a catalyst material with appropriate regeneration treatments, such as application of acid, base or heat.[75]

Coking

Formation of coke, or more generally carbon laydown, is especially prevalent in zeolite catalysts and has significant effects on their catalytic activity. Coking predominantly deactivates zeolite catalysts by two effects: blocking of the micropore network and blocking of active sites themselves, both of which limit access to active sites and reduce catalytic activity. The mechanism and products of coke formation depend strongly on reaction temperature, with higher temperatures resulting in higher degrees of polyaromatic and graphitic coke formation.[76]

Intricacies of continuous flow reaction and deactivation analysis

Additionally, on the macro-scale, the employment of zeolite catalysts in continuous flow fixed-bed reactors adds further complexity when attempting to understand their deactivation and lifetime.[77, 78] Notably, reactions in continuous flow reactors are often not spread evenly across the catalyst bed and therefore the catalyst charge is not commonly seen to deactivate at the same rate across the entire fixed bed. In such conditions, the upper part of the fixed bed where the reagent contacts first will typically perform more catalysis than the lower bed and deactivate more rapidly. This active portion is seen to move down the length of the fixed bed until the entire catalyst charge is depleted and catalysis ceases. Misinterpretations of activity and deactivation data from such phenomena manifest themselves particularly prevalently in catalyst recyclability tests. Primarily, if trying to assess catalyst deactivation rate, operating at 100% conversion is generally undesirable. When operating at 100% conversion, it is likely that only an upper segment of the catalyst bed is participating in the reaction, so, despite the upper bed deactivating, conversion is not seen to drop below 100% as the lower bed takes over. Instead, if trying to discern deactivation rates, it is better to operate at so called *differential conversion* which is where conversion is kept very low so that the entirety of the reactor bed is exposed to very similar concentrations of both reagents and products. Hence, catalyst deactivation is reflected in as close to real time as possible. Additionally, if a reaction is run at 100% conversion, ceased and the catalyst subsequently "regenerated", it may be possible that the upper part of the bed was instead irreversibly deactivated. Upon recommencement of the reaction, conversion may return to 100% as the fresh parts of the catalyst bed are utilised, giving the illusion that the catalyst was successfully regenerated to full working condition. Operation at differential conversion would allow this deactivation to be more accurately reflected upon recommencement of the catalytic reaction.

1.3. Bioethanol: A Key Bio-derived Platform Chemical.

1.3.1. Production and Current Uses of Bio-derived Ethanol.

In the preface to this thesis, the merits of biomass as a carbon source were discussed owing to both its renewable nature and net low CO_2 emissions as a fuel. Accounting for over 90% of global bio-derived fuel production and being produced on the scale of over 27 billion gallons in 2017, bio-derived ethanol is by far the largest product of biomass refining at present.[79, 80]

Traditionally, ethanol has been produced industrially *via* the acid-catalysed hydration of ethylene, the latter sourced primarily from fossil fuels.[81] In a typical bio-derived ethanol plant, however, the alcohol is produced by microbial fermentation of sugars sourced from a wide range of biomass feedstocks, including sucrose, starch, lignocellulosic and algal based biomass.[82] At present, most simple sugars can be fermented into bio-derived ethanol directly using yeasts such as *Saccharomyces cerevisiae* in a not too dissimilar approach to brewing. Slightly more complex biomass feeds, such as starch (a carbohydrate), can be broken down into fermentable sugars by a precursor hydrolysis step. Unfortunately, cellulosic and lignocellulosic feedstocks are not as amenable to traditional hydrolysis pre-treatments; hence thermochemical pre-treatment methods coupled with enzymatic digestion are being developed to extract easily fermented sugars from these more desirable sources (see Figure 1.4).[83-85]

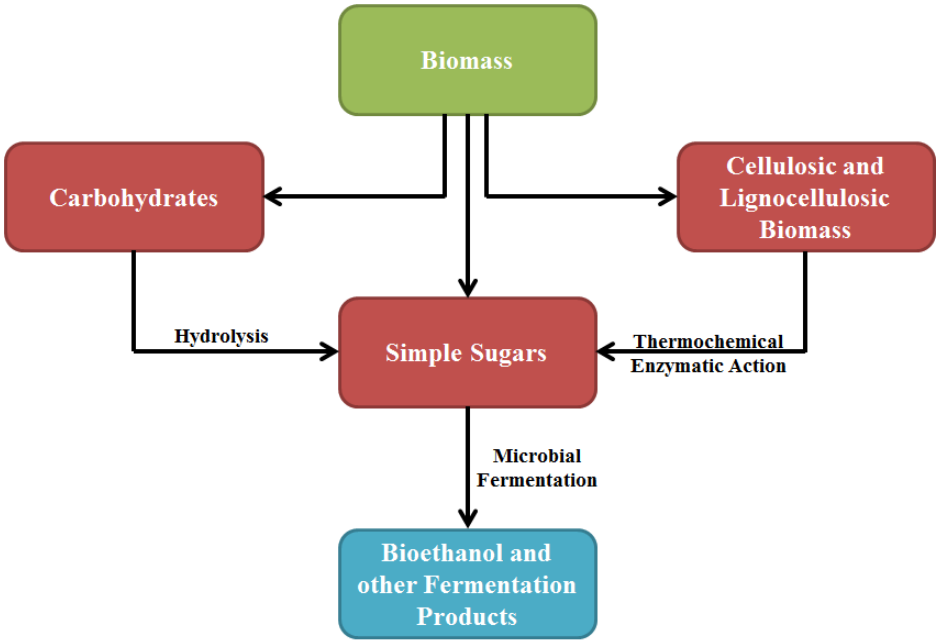

Figure 1.4: A simple flow schematic for the conversion of biomass into bio-derived ethanol.

Currently, bio-derived ethanol is consumed in a wide range of applications such as cosmetics, household products and as a food additive; however, the major use of bio-derived ethanol in many countries is for gasoline blending. The volume percentage of ethanol in gasoline can be widely varied depending upon many factors (temperature, season, adhering to a designated Reid vapour pressure), but is typically limited to around 5–10% (E5–E10).[79] Blending ratios higher than this are often met with concerns regarding fuel economy and potential negative effects on combustion engines, however slightly higher ratios (10–12%) can commonly be seen in use across the United States.[79, 86]

Regardless, as of early 2017, more bio-derived ethanol is produced in the United States than demand for E10 and exports exists, hence excess bio-derived ethanol has the potential to be a cheap, convenient and renewable carbon source from which to produce high value chemicals that are typically derived from fossil fuels.[87]

1.3.2. Current Technologies for Cascade Conversion of Bio-Derived Ethanol to Higher Value Chemicals.

Due to the wide array of reaction schemes that are accessible, ethanol (**1**) is an extremely versatile platform molecule. Utilising relatively accessible conditions, ethanol can undergo many simple transformations to widely used and industrially important chemicals. Common processes are oxidation to acetaldehyde (**2**) and acetic acid, dehydration to ethylene (**3**) and etherification reactions, namely self-etherification to form diethyl ether (**4**). From these simple products, more complex and higher value products are then accessible from bio-derived ethanol *via* subsequent reactions; often involving multistage transformations (see Scheme 1.5). ^{n}Butanol (**5**), 1,3-butadiene (**6**) and isobutylene (**7**) are all industrially important chemicals derived primarily from fossil sources. The following sections will outline the general synthesis routes of ^{n}Butanol, 1,3-butadiene and isobutylene from bioethanol and review current catalysts for their transformation from ethanol.

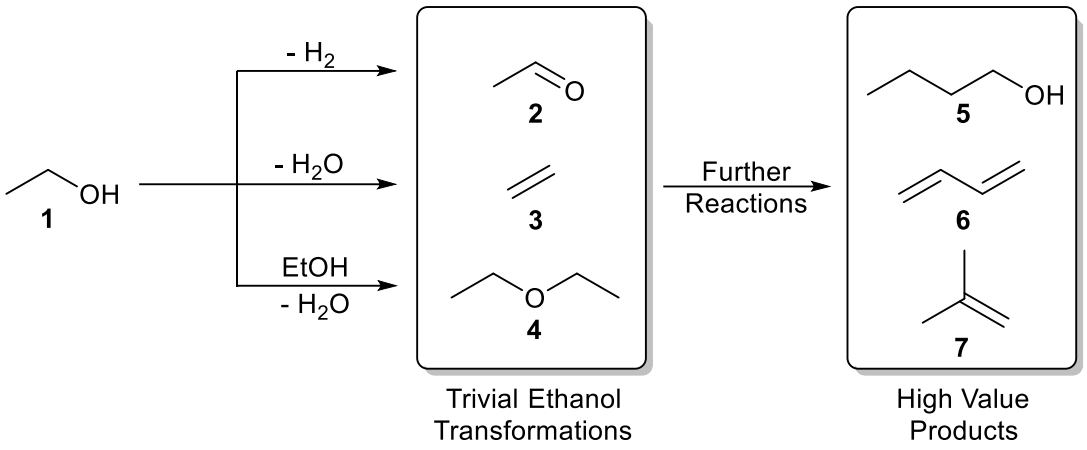

Scheme 1.5: Generalised trivial ethanol transformations and potential higher-value end products.

1.3.2.1. Bio-derived Ethanol to ^{n}Butanol.

^{n}Butanol is an industrially relevant chemical finding use as a solvent in paints, a plasticizer and as a crucial building block in the synthesis of butyl acrylate, which represents the largest industrial demand for ^{n}butanol (**8**, see Figure 1.5).[88, 89] The polymerisation of butyl acrylate forms polybutylacrylate and various copolymers, which are used in paints, sealants, coatings, adhesives, fuel, textiles, plastics, and caulk.[89] ^{n}Butanol is also seen as an advanced bio-derived fuel being more suited as a gasoline additive than ethanol owing to its higher gasoline miscibility, greater energy density and lower vapour pressure.[79, 88, 90] An additional benefit of ^{n}butanol is its lower hydrophilicity in comparison to ethanol, reducing the amount of water entrained within the blended gasoline. Further to this, ^{n}butanol is suggested as being more combustion engine friendly with no modifications to current car engines thought to be required when ^{n}butanol is used as a primary fuel or an additive.[91, 92]

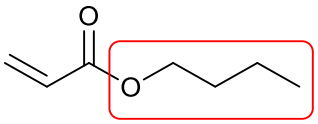

8

Figure 1.5: The important monomer: butyl acrylate. The section of the carbon chain arising from ^{n}butanol is highlighted in red.

Unlike ethanol, the vast majority of ^{n}butanol is currently produced from fossil fuels, typically through the oxo process, otherwise known as hydroformylation.[93] The oxo process to produce ^{n}butanol typically utilises a homogeneous cobalt or rhodium catalyst in order to couple propylene (**9**) and carbon monoxide to form various butanals (**10** - ^{n}butanal, **11** - isobutanal) and subsequently a nickel catalyst to produce butanols (**5**- ^{n}butanol, **12** - isobutanol) using hydrogen as a reductant in both steps (see Scheme 1.6).[90]

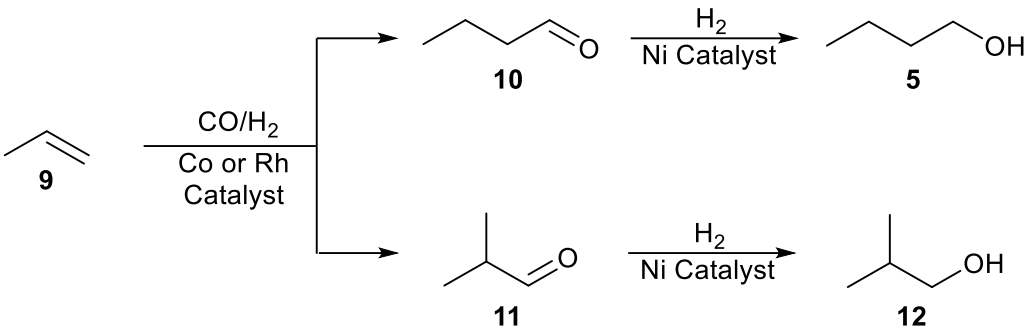

Scheme 1.6: The general oxo (hydroformylation) process for butanol production.

Recently, interest has also been sparked in the fermentative production of butanol from sugars in a similar manner to that of bioethanol production.[94, 95] Although promising, this fermentative route is often plagued by low ^{n}butanol production, toxicity of produced solvents (acetone, butanol, ethanol) to the *Clostridium* bacteria and difficult product separation.[88, 90, 96] Taking the flaws of both hydroformylation and fermentation into account, it makes commercial sense for the conversion of excess available and renewable bio-derived ethanol to ^{n}butanol to be investigated and developed.

Within the scientific literature, two proposed mechanisms for the production of ^{n}butanol from ethanol exist. The first and more widely accepted mechanism is the Guerbet coupling of ethanol, adapted from a mechanism discovered by its namesake, Marcel Guerbet, in 1909.[97] Within this mechanism, ethanol is first dehydrogenated to acetaldehyde (**2**), which then undergoes an aldol addition to form acetaldol (3–hydroxybutanal, **13**) and is subsequently dehydrated to form crotonaldehyde (**14**). At sufficiently high temperature, the conversion of acetaldehyde (**2**) to crotonaldehyde (**14**) is possible directly *via* an aldol condensation. Crotonaldehyde (**14**) may then be reduced in the presence of hydrogen to form intermediate butyraldehyde (**15**) and finally ^{n}butanol (**5**, see Scheme 1.7). Owing to the differing nature of the chemical reactions in each step of the Guerbet mechanism, multiple active sites are often employed to work in tandem to affect the total ethanol to ^{n}butanol transformation.

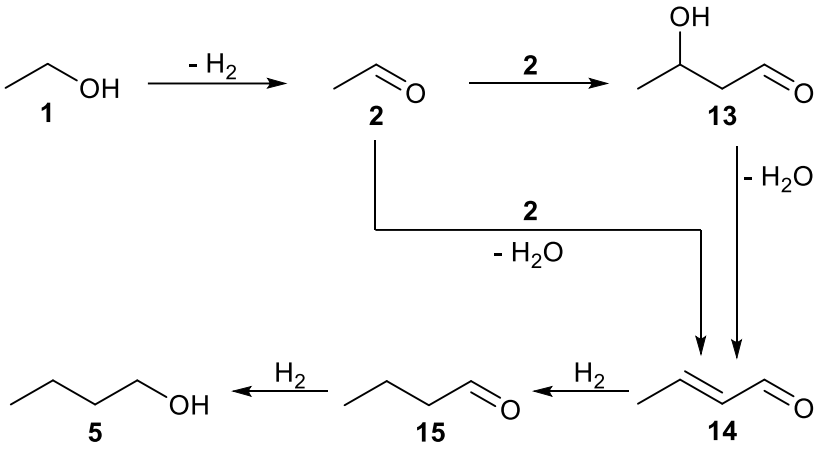

Scheme 1.7: Guebert mechanism for coupling of ethanol to form ^{n}butanol.

The second proposed mechanism of ethanol to ^{n}butanol synthesis is a direct condensation of ethanol first proposed by Yang and Meng in 1993.[98] The mechanism is more simplistic in nature than that of the Guerbet mechanism; the authors suggest that a β–position C–H bond of one ethanol molecule is activated by a strong Lewis basic site. This allows the associated hydrogen to condense with the hydroxyl group of another molecule of ethanol, resulting in a single direct step producing ^{n}butanol and an equivalent of water (see Scheme 1.8). This proposed mechanism is interesting as it can, in theory, be performed over one unique catalytic site as it proceeds directly with no intermediates. The variety of side products is theoretically also limited to only higher alcohols extended or branched by two carbon units, although in practice this may not necessarily be the case.

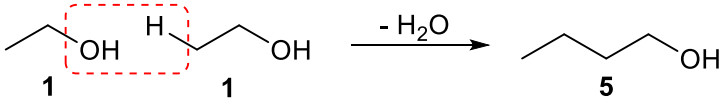

Scheme 1.8: The bimolecular direct condensation of ethanol to produce ^{n}butanol. Highlighted in red are the moieties that condense to form water.

Yang and Meng's work studies direct ethanol conversion over a series of exchanged and impregnated alkali cation zeolites, finding a rubidium and lithium exchanged sample of zeolite X (Rb–LiX) to be the most efficient for direct ^{n}butanol production at 420 °C. The authors justify their proposed mechanism (Scheme 1.8) by observing the effect of typical Guerbet intermediates on product distributions when introduced to the reactant feed. It was shown that crotonaldehyde (**14**) was not consumed under their reaction conditions; hence hydrogenation reactions and the Guerbet pathway are proposed to not be active. It is also interesting to note that monometallic ion-exchanged zeolites (Li–X, Na–X, K–X) show almost

full selectivity to gaseous dehydration products, whereas bimetallic modified zeolites (Rb/Li–X, Rb/Na–X, Rb/K–X, where $RbNO_3$ has been impregnated into the exchanged zeolite and calcined to form Rb_2O) show higher selectivity towards condensation products. The authors attribute this to the stronger Lewis basic sites resulting from impregnated Rb_2O in the bimetallic systems being more able to activate the β–hydrogen of ethanol.

Direct condensation of ethanol over strong Lewis basic sites is further suported by the work of Ndou *et al.* in which MgO is shown to act as a relatively efficient catalyst for ^{n}butanol production *via* a direct condensation route, attaining yields of up to 18%.[99] The authors also feed common Guerbet intermediates over MgO and produce only minor amounts of ^{n}butanol, further supporting the presence of the mechanism in Scheme 1.8 over solid strong basic catalysts.

Typically, catalysts that perform ethanol coupling *via* the Guerbet mechanism require a combination of active sites, predominately mixed acid/base or mixed metal/base pairs. Hydroxyapatites (HAPs, $Ca_{10-z}(HPO_4)_z(PO_4)_{6-z}(OH)_{2-z}$; $0 < z \leq 1$) are a naturally occurring mineral with a variable Ca/P molar ratio that can affect acid and base properties. At Ca/P = 1.50 and Ca/P = 1.67, HAPs are considered as acidic and basic catalysts respectively with intermediate values being associated with mixed acid/base species. Tsuchida *et al*. demonstrate in an initial report that non-stoichiometric HAP ($Ca/P \neq 1.67$) may be used to directly produce ^{n}butanol from ethanol with relatively high selectivity (selectivity = 76%, Ca/P = 1.64, 300 °C).[100] In a subsequent report the group compare several HAPs with variable Ca/P ratios for the conversion of ethanol to ^{n}butanol, finding that more basic HAPs with a higher Ca/P ratio produce the highest yields of ^{n}butanol (Ca/P = 1.67, yield = 69.8%, 25 °C).[101] Meanwhile, at lower Ca/P ratios, large yields of ethylene and diethyl ether are recorded, an observation that is consistent with the presence of acidic sites. Ho *et al.* use *in situ* titration experiments coupled with FTIR spectroscopic studies to deduce the mechanism of ethanol coupling over HAP catalysts and specific active sites.[102] It is found that strongly basic Ca–O species are responsible for dehydrogenation activity whilst phosphate/calcium oxide acid/base pairs are attributed to catalysing the aldol condensation of acetaldehyde (**2**).

Investigations of HAP–type catalysts have been extended by Ogo *et al*. to Sr–substituted HAPs.[103] In this study, Sr–HAP is shown to achieve an ^{n}butanol selectivity of 81.2% *via* a Guerbet type mechanism. This is moderately higher than that of Ca–HAP, which was recorded at 74.5%. The higher selectivity is attributed to high crotonaldehyde (**14**) selectivity

in the base catalysed aldol condensation step and reduced coke formation. The authors extend their study in a subsequent contribution in which Sr–HAPs with varying Sr/P ratio are compared.[104] Similar to the observations of Tsuchida *et al.*, it is found that an increase in Sr/P ratio leads to an increased ^{n}butanol selectivity (Sr/P = 1.70, yield = 86.4%, 300 °C), most likely resulting from an increased density of strong basic sites.[101]

Hanspal *et al*. provide an interesting contribution in which they study the effects of basic site strength on ^{n}butanol yield from ethanol.[105] Using CO_2 microcalorimetry they observe that HAPs actually possess basic sites of intermediate strength when compared to the strong basic sites of MgO. Ethanol conversion experiments demonstrated that the intermediate basic sites of HAP are much more efficient in conversion than the strong basic sites of MgO, achieving ^{n}butanol selectivities of 72% and 33% respectively. It is suggested that water dissociatively adsorbs onto the MgO whereas interactions of water with the HAP surface are more reversible. As water is a by-product of the Guerbet coupling, it is thought that this may act as a deactivator for the strong basic sites of MgO. Further work comparing the basicity of HAP and MgO confirms this basicity difference, finding that rapid H_2–D_2 exchange may occur over MgO, but not HAP.[106]

Mixed Mg/Al oxides derived from decomposition of hydrotalcites have also showed promise in the direct conversion of ethanol to ^{n}butanol.[107, 108] It is thought that the presence of Mg promotes dehydrogenation steps whereas the medium strength basic sites are active for aldol condensation. In order to efficiently catalyse the entire cascade reaction from ethanol to ^{n}butanol, it is suggested that the two sites must be proximal, resulting in a reactive acid/base pair. Based upon this observation, a range of d– and f–block metals were supported on Mg–Al mixed oxides and screened for their catalytic activity by Marcu *et al*.[109] Pd was found to be the most efficient metal screened, achieving an ^{n}butanol selectivity of 72.7% at 200 °C albeit at low ethanol conversion. Consistent with many other contributions in this review, a correlation between the density of strong/medium basic sites and ^{n}butanol selectivity was observed. In a separate report, the group doped a Mg–Al mixed oxide with Cu to varying degrees.[109] It was observed that an increase of metal content resulted in a decrease of medium and strong basic site density and hence resulted in lower ^{n}butanol selectivities.

Several other metal oxide supports doped with metal species have been tested for their efficiency in the production of ^{n}butanol. Riittonen *et al*. tested a variety of metals supported on alumina and found Ni species to be the most selective towards ^{n}butanol (selectivity = 80%, 250

°C).[110] The authors present a general series of selectivity within their work as follows: Ni > Pt > Au~Rh > Ru >> Ag. Wu *et al.* perform a similar study in which various metals are impregnated into ceria and supported on activated carbon.[91] It is observed that Pd–CeO_2 is the most selective towards ^{n}butanol whilst Cu–CeO_2 was suggested to be the highest yielding catalyst overall, achieving a selectivity of 41.3% at moderate ethanol conversion (conversion = 46.2%, 250 °C). It is suggested that a bimetallic system that combines Cu (as an ethanol dehydrogenation promoter) and Pd (as a hydrogenation promoter) supported over ceria (which provides basic sites for aldol condensation steps) may prove to be a promising catalyst in future studies.

As a result of many concordant observations within the literature reviewed in this sub-section, it is possible to draw the following important conclusions:

- Ethanol coupling to ^{n}butanol may occur *via* a multistep Guerbet coupling or a single step direct condensation.
- The Guerbet route may proceed over intermediately basic catalysts but yields and selectivities are improved dramatically upon inclusion of dedicated (de)hydrogenation sites. Relatively soft reaction conditions may be employed if this is the case.
- Direct condensation routes may proceed over strong basic sites but require high reaction temperatures to promote C–H bond activation and subsequent condensation.

1.3.2.2. Bio-derived ethanol to 1,3–Butadiene.

Another desirable product from conversion of bio-derived ethanol is 1,3–butadiene (**6**, henceforth to be referred to as "butadiene"). Owing to its pair of unsaturated bonds, butadiene is a highly functionalisable small molecule with a broad variety of synthetic applications and high commercial interest. Butadiene finds widespread use as a chemical intermediate within Diels-Alder reactions and as an important monomer in the production of synthetic rubbers, such as styrene-butadiene rubber, polybutadiene rubber, Neoprene and nitrile rubber.[111, 112]

As with ^{n}butanol in section 1.3.2.1, butadiene is sourced primarily from fossil fuels, typically being extracted from C_4 olefin streams as a by-product of steam cracking to produce ethylene (**3**). Butadiene, however, can be produced from ethanol *via* the Lebedev process (see Scheme 1.9),[113] a process developed in 1933 that is still carried out in small-scale plants in South America, Eastern Europe, China, and India.

The mechanism initially proceeds in a similar fashion to the Guerbet coupling (see Section 1.3.2.1) with ethanol (**1**) being dehydrogenated to acetaldehyde (**2**) which then undergoes an aldol addition to form acetaldol (3–Hydroxybutanal, **13**) and is subsequently dehydrated to form crotonaldehyde (**14**). As before, at sufficiently high temperature, the conversion of acetaldehyde (**2**) to crotonaldehyde (**14**) is possible directly *via* an aldol condensation. The mechanism then deviates from the Guerbet coupling as crotonaldehyde (**14**) undergoes a Meerwein-Ponndorf-Verley (MPV) reduction to form crotyl alcohol (**16**) before being subsequently dehydrated to form butadiene (**6**).[114] The MPV reduction requires the use of a sacrificial alcohol which, in the case of the Lebedev process, is a molecule of ethanol that is converted to acetaldehyde. In this case the carbonyl product may be fed back into the reactor for usage in the earlier stages of the mechanism.

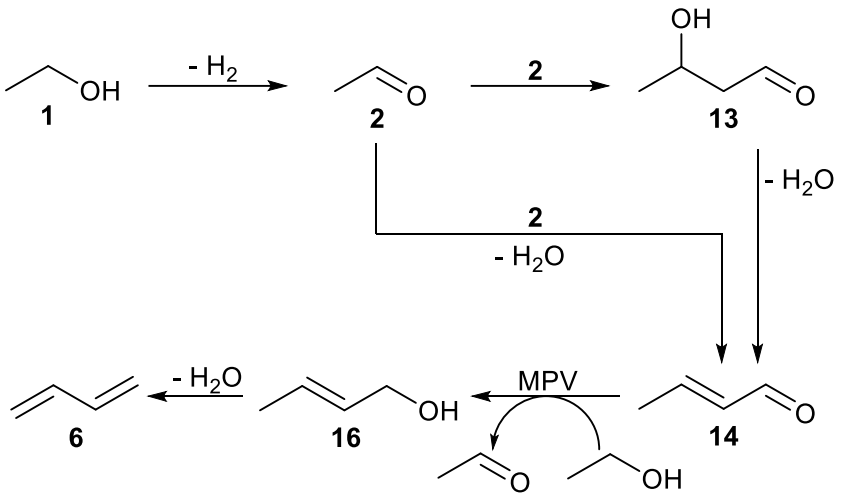

Scheme 1.9: The Lebedev mechanism for production of butadiene from ethanol.

Current catalysts for the direct conversion of ethanol to butadiene may be broadly categorised into modified silica-magnesia catalysts and zeotype materials, each of which exhibit bifunctional acid/base properties.

Zhu *et al*. performed fundamental work on their exploration of feed mixtures and reaction conditions on the conversion of ethanol (and acetaldehyde) to butadiene over the traditional Lebedev catalyst, unmodified $MgO–SiO_2$.[115] They found that a 1:3 ratio of acetaldehyde to ethanol greatly improved butadiene selectivity from 22.8 % with no acetaldehyde to 75.9%. Addition of 10 wt% water into the feed (final feed composition: 22.5:67.5:10, acetaldehyde:ethanol:water) can further increase this selectivity to 80.7% whilst retaining an ethanol/acetaldehyde conversion of approximately 30%. The authors also explored the effects of reaction temperature and Mg to Si ratio, finding an optimum temperature of 350

°C and optimum ratio of 1:1. It was also suggested that the presence of predominantly amorphous magnesium silicates (as opposed to crystalline) may be correlated with production of butadiene.

Although this report looks promising, the introduction of dehydrogenation promoting dopants is crucial if a single step ethanol to butadiene reaction is desired in order to negate the requirement of an acetaldehyde co-feed. Hence, several investigations into the effect of doping of silica-magnesia catalysts have been reported. Ohnishi *et al*. show in an early contribution that Na_2O and K_2O doping of 1:1 $MgO–SiO_2$ effectively promotes the production of butadiene from ethanol, resulting in selectivities up to 87% and yields of 87% and 70% for Na_2O and K_2O doped materials respectively.[116] However, despite its impressive results, this report of alkali metal cations is relatively isolated as the vast majority of research focusses around well-established d-block metal systems as dehydrogenation promoters. For example, Angelici *et al.* have demonstrated that CuO species are efficient dehydrogenation promoters for the conversion of ethanol to butadiene over $MgO–SiO_2$, resulting in butadiene yields and selectivities of 40% and 53% respectively.[117, 118] The authors suggest that the presence of CuO modifies the acid/base properties of the support, improving the catalyst dehydrogenation activity and increasing conversion to intermediate acetaldehyde. Additionally, Makshina *et al*. screened a wide range of transition metal oxides supported on $MgO–SiO_2$, highlighting Cu and Ag with butadiene yields of 58.2% and 56.3% and butadiene selectivities of 60% and 58% respectively at approximately 97% ethanol conversion.[119] Further catalytic tests suggest that it is not the metal loading, but rather the metal species and Mg:Si ratio that affect overall butadiene yield and selectivity. The work of Lewandowski *et al*. supports this conclusion as they observe increasing butadiene selectivity with increasing Mg:Si ratio across a series of ZrO_2/ZnO impregnated $MgO–SiO_2$ materials.[120] The authors show in two distinct series that both increasing the Mg:Si ratio and the presence of ZrO_2/ZnO dopants improve butadiene selectivity. A maximum of 68.7% butadiene selectivity at 30% ethanol conversion is recorded for a ZrO_2/ZnO impregnated 95:5 $MgO:SiO_2$ material. This catalyst that combines both of the prior observations and presents the highest selectivity reported thus far for a transition metal modified silica-magnesia based catalyst feeding ethanol alone.

Zeotypes are an emerging category of active catalyst supports for butadiene production from ethanol. Zeotypes are often synthesised by dealumination of a parent zeolite

(aluminosilicate) followed by remetallation with a Lewis acidic metal ion[2]. The work of Sushkevich *et al*. highlights the effect of the nature of active sites in Zr substituted BEA zeolites. FTIR measurements of CO adsorption and supplementary DFT calculations are used to distinguish what they define as the "open" and "closed" tetrahedral Zr sites (See Figure 1.6) as well as their relative site densities within the zeotype.[60] The authors conclude that the "open" sites are more active in the production of butadiene and promote selectivity to the desired product, rationalised by the higher acid strength and improved steric accessibility of these sites. It is also shown that the proportion of "open" sites, and hence catalytic activity, decreases with increasing Zr content. Hence, using a pre-optimised Ag loading as a dehydrogenation promoter, a Ag/ZrSiBEA with Si:Zr = 850 was shown to achieve a butadiene selectivity of 68% at 30% ethanol conversion when operated at 320 °C.

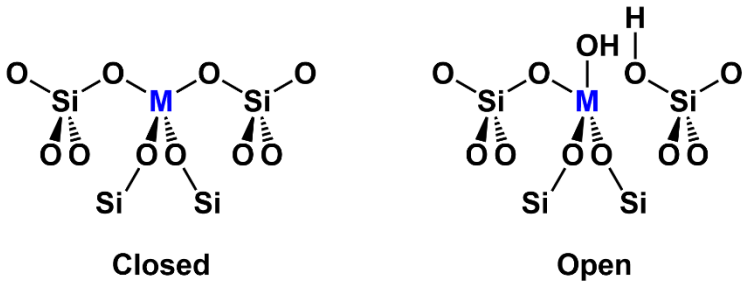

Figure 1.6: Schematic representation of closed (left) and open (right) sites in M–BEA.

Moderate improvements are offered by transition metal exchanged TaSiBEA zeotypes, with Kyriienko *et al.* reporting butadiene selectivities of 72.6% at an ethanol conversion of 87.9% over Cu/TaSiBEA at 320 °C.[57] The groups also take steps to elucidate the effect of active site proximity in the zeotype by comparison of Ag-incorporated TaSiBEA (Ag/TaSiBEA) and mechanically mixed Ag/SiBEA and TaSiBEA. The former shows much higher butadiene selectivity with the authors suggesting that this is the result of the closer proximity of dehydrogenation and condensation active sites.

At present, the highest reported selectivity to butadiene over a zeotype is reported by Dai *et al*. over bicomponent Zn–Y modified SiBEA. In this system, Zn and Y are incorporated in tandem into fully dealuminated BEA zeolite, yielding localised clusters of Zn (II) and Y(III) centres within the micropore network.[121] At low weight hourly space velocities (WHSV), butadiene selectivities of 81% at 90% ethanol conversion are observed when operated at 330 °C for a 2%Zn–8%Y/SiBEA. At higher temperature (400 °C) and WHSV, selectivity can be

[2] Zeotype nomenclature for this report is as follow: M/XY[FWC] where: [FWC] is the relevant framework code, X and Y are the non-oxygen elements composing the framework and M is any extra metal species introduced into the zeotype by ion-exchange or impregnation.

sacrificed (63%) to raise productivity from 0.11 to 2.33 $g_{butadiene}\ g_{catalyst}^{-1}\ h^{-1}$. Further work by the group elucidates the mechanism of this bifunctional active site, concluding that Zn species are more active in dehydrogenation, while Y species are more active for subsequent coupling reactions; however, both are required to work in a synergistic fashion to effectively produce butadiene directly from ethanol.[59] A similar system to Zn–Y/Si–BEA is reported by Pomalaza *et al*. in which Zn and Ta are supported in a similar fashion on Si–BEA and TUD–1, a mesoporous silica.[122] Therein a maximum butadiene selectivity of 73% is observed for Zn–Ta/TUD–1, corresponding to a butadiene productivity of 2.13 $g_{butadiene}\ g_{catalyst}^{-1}\ h^{-1}$ at a $WHSV_{EtOH}$ of 5.3 h^{-1}. However, if the $WHSV_{EtOH}$ is raised to 8.0 h^{-1}, a butadiene productivity of 2.45 $g_{butadiene}\ g_{catalyst}^{-1}\ h^{-1}$ is recorded: the highest reported value at the time of writing.

All previous highlighted literature has referred to the use of conventional 3−dimensional bulk zeolite materials. However, the benefits of structural change can be seen within the report of Wang *et al.* who report the production of MFI nanosheets and their beneficial effects on ethanol conversion and butadiene selectivity.[123] Whilst the ethanol conversion and butadiene selectivity values are reported to be 21.3 % and 36.4% for a conventional mesoporous material, 1.7LiZnHf–MFI(M), these values increase to 64.6 % and 73.0 % following adoption of a 2–dimensional nanosheet structure, 1.7LiZnHf–MFI(NS). This report relevantly highlights the effect of catalyst structure on catalytic activity and provides a basis for further investigation of structural effects on previously highlighted materials in order to attempt to further improve butadiene selectivity and productivity values.

1.3.2.3. Bioethanol to Isobutylene.

Isobutylene (**7**), another industrially important chemical sourced primarily from fossil fuels, typically finds use as a chemical intermediate in the synthesis pathway to a variety of fuel oxygenates, specifically methyl *tert*-butyl ether (MTBE) and ethyl *tert*-butyl ether (ETBE). The polymer of isobutylene, butyl rubber, finds wide use as a binder and as a chemically resistant material for use in decontamination and high chemical resistance gloves.

In order to produce isobutylene (**7**), ethanol (**1**) is first oxidised past acetaldehyde (**2**) to acetic acid (**17**). The ketonisation of acetic acid (**17**) then produces acetone (**18**) which undergoes an aldol addition or condensation to form diacetone alcohol (**19**) or mesityl oxide (**20**), respectively. Diacetone alcohol (**19**) and mesityl oxide (**20**) can exist in an equilibrium before diacetone alcohol (**19**) is subsequently decomposed to yield isobutylene (**7**) and acetic

acid (**17**), which may be fed back into the reactor (see Scheme 1.10).[124, 125] Mesityl oxide (**20**) may also be directly cracked to form isobutylene (**7**).[125]

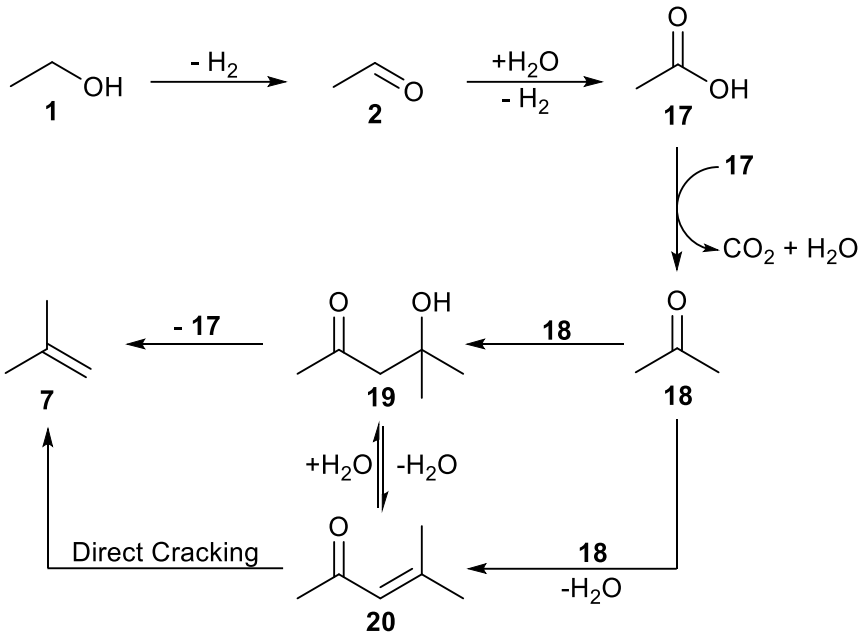

Scheme 1.10: A general mechanism for the production of isobutylene from ethanol.

Relative to ^{n}butanol and butadiene, reports of materials known to catalyse the direct synthesis of isobutylene from ethanol are scarce. Pioneered by Sun *et al.*, Zn/Zr mixed oxides ($Zn_xZr_yO_z$) emerged as the only major family of heterogeneous materials for the direct conversion of ethanol to isobutylene, recording 83% isobutylene yield over $ZnZr_{10}O_z$ in their first report.[126] The group suggests that loading ZnO weakens the inherent acidity of ZrO_2, suppressing ethanol dehydration, isobutylene isomerisation and acetone polymerisation side reactions. As a result, the newly weakened Brønsted acid sites are proposed to promote selectivity in the conversion of intermediate acetone to isobutylene. It is further suggested that the newly introduced ZnO basic sites promote dehydrogenation and acetone production.

Further work by the group supports their hypotheses regarding site activity and works to optimise the system for industrial conditions.[127] It is proposed that $ZnZr_8O_{17}$ calcined at 550 °C is an optimum catalyst for isobutylene formation in this category achieving a yield of 79% at 475 °C. Durability and regeneration tests were also performed, demonstrating isobutylene yields still in excess of 75% even after 10 h time on stream for regenerated catalysts. The suggestion that a regenerated catalyst performs better than a freshly prepared one is curious but is well rationalised; the group concludes that regenerated catalysts contain a larger proportion

of beneficial weak Brønsted acid sites as opposed to detrimental strong Brønsted acid sites, evidenced by pyridine absorption IR spectroscopy measurements.

Sun *et al*. developed their theory further with the preparation of several $Zn_xZr_yO_z$ materials which possesses purely Lewis acidic and basic sites in an attempt to curtail the undesirable side reactions associated with Brønsted acid sites.[125] These new catalysts are suggested to achieve a theoretical isobutylene selectivity of 88.9% from acetone. Selectivity to isobutylene from ethanol directly is shown to be slightly greater than 80% whilst being exceptionally resistant to coke formation, resulting in a loss of only 3% selectivity after 200 h time on stream.

Similarly, Feng *et al*. introduced strongly Lewis acidic and redox active Cr species to $Zn_xZr_yO_z$ mixed oxides to form a series of $Cr_nZn_xZr_yO_x$ catalysts with modified Lewis acid/base strength and redox potential.[128] They found that a 1:1 Cr:Zn ratio was optimal for selectivity to isobutylene with $CrZnZr_8O_z$ demonstrating an increase of isobutylene yield of 38% when compared to $ZnZr_8O_z$. From a volcano plot of their tested catalysts, it becomes clear that, although acidity and basicity have been near-optimised, the introduction of redox species may lend itself to produce mixed oxides with further increased isobutylene selectivity.

It is clear that if zeolites were to be used for isobutylene production, their natural Brønsted acid properties would need to be heavily modified to avoid undesirable side reactions. To this end, Tago *et al*. screen a series of alkali metal modified M–BEA (M = H, Na, K, Rb, Cs) zeolites produced *via* ion-exchange for the conversion of acetone into isobutylene.[129] They confirm that as acidity decreases (as measured by NH_3 TPD) isobutylene selectivity increases significantly, with Cs–BEA demonstrating selectivity of around 90% albeit at low acetone conversion. K–BEA is deemed the most promising catalyst as it combines reasonable selectivity (75%) at good conversion (approx. 70%) whilst also being relatively resistant to coke formation.

1.3. Outlook on the Use of Bio-derived Ethanol as a Carbon Source to Manufacture Higher Value Chemicals.

As discussed previously, ^{n}butanol, 1,3–butadiene and isobutylene are not the sole desirable products obtainable from bio-derived ethanol. In particular, products and fuels such as BTX (benzene, toluene, xylene)[130-132] may be sourced directly from ethanol with myriad others (including pyridine,[133] pentaetrythrol,[134] propylene[135, 136]) being sourced from ethanol and other, potentially bio-derived, co-feeds. Therefore, it is reasonable to conclude that bio-

derived ethanol has the potential to assume the position of a key platform molecule in near-future chemical industries, especially whilst its relative price and availability are particularly agreeable. To highlight this, a recent sustainability assessment of eastern European countries (Czech Republic, Hungary, Poland, and Slovakia) concluded that "*the switch of the chemical industry from crude oil to bioethanol would be theoretically feasible*" albeit provided sufficient bio-derived ethanol were available, such as that which could be feasibly be exported from the United States.[137] It is likely that a key factor that will determine the uptake of processes requiring the use of bio-derived ethanol is the ease of their implementation and operation. In this regard, development of multifunctional heterogeneous catalysts, such as those discussed within this chapter, will no doubt aid the uptake of such processes by virtue of simplifying process and plant design, regardless of catalyst complexity. It is the authors opinion that development of heterogenous catalysts, such as zeolites, that can offer single-step bioethanol transformation into higher value products, whilst maintaining long lifetimes and simple process designs will be the key to global uptake of this crucial and accessible resource.

1.4. References.

1. A. F. Cronstedt, *Kongl Vetenskaps Academiens Handlingar Stockholm*, 1756, **17**, 120.
2. C. S. Cundy and P. A. Cox, *Chem. Rev.*, 2003, **103**, 663–702.
3. Mineral Commodity Summaries - Zeolites (Natural), https://minerals.usgs.gov/minerals/pubs/commodity/zeolites/mcs-2018-zeoli.pdf, (accessed 25/04/2018).
4. E. T. C. Vogt, G. T. Whiting, A. Dutta Chowdhury and B. M. Weckhuysen, Zeolites and Zeotypes for Oil and Gas Conversion in *Advances in Catalysis*, ed. F. C. Jentoft, Academic Press, 2015, vol. 58, pp. 143–314.
5. R. W. Broach, D.-Y. Jan, D. A. Lesch, S. Kulprathipanja, E. Roland and P. Kleinschmit, Zeolites in *Ullmann's Encyclopedia of Industrial Chemistry*, DOI: https://doi.org/10.1002/14356007.a28_475.pub2.
6. 2015 Minerals Yearbook - Zeolites [Advance Release], https://minerals.usgs.gov/minerals/pubs/commodity/zeolites/myb1-2015-zeoli.pdf, (accessed 14/06/18).
7. M. W. Munthali, E. Johan, H. Aono and N. Matsue, *J. Asian Ceram. Soc.*, 2015, **3**, 245–250.
8. T. Ennaert, J. Van Aelst, J. Dijkmans, R. De Clercq, W. Schutyser, M. Dusselier, D. Verboekend and B. F. Sels, *Chem. Soc. Rev.*, 2016, **45**, 584–611.
9. P. Tomkins, M. Ranocchiari and J. A. van Bokhoven, *Acc. Chem. Res.*, 2017, **50**, 418–425.
10. R. V. Siriwardane, M.-S. Shen, E. P. Fisher and J. Losch, *Energ. Fuel.*, 2005, **19**, 1153–1159.
11. S. Abate, K. Barbera, G. Centi, P. Lanzafame and S. Perathoner, *Catal. Sci. Technol.*, 2016, **6**, 2485–2501.
12. R. E. Fletcher, S. Ling and B. Slater, *Chem. Sci.*, 2017, **8**, 7483–7491.
13. Database of Zeolite Structures, http://www.iza-structure.org/databases/, (accessed 25/04/2018).
14. T. Takewaki, L. W. Beck and M. E. Davis, *J. Phys. Chem. B*, 1999, **103**, 2674–2679.
15. R. Fricke, H. Kosslick, G. Lischke and M. Richter, *Chem. Rev.*, 2000, **100**, 2303–2406.
16. M. Sasidharan and R. Kumar, *Catal. Lett.*, 1996, **38**, 245–249.
17. L. Gómez-Hortigüela and J. Pérez-Pariente, Synthesis and Properties of Zeolite Materials Guided by Periodic Considerations in *The Periodic Table II: Catalytic, Materials, Biological and Medical Applications*, ed. D. M. P. Mingos, Springer International Publishing, Cham, 2019, pp. 53–88.
18. S. Kulprathipanja, *Zeolites in Industrial Separation and Catalysis*, Wiley, 2010.
19. J. L. Casci, *Micro. Meso. Mater.*, 2005, **82**, 217–226.
20. R. C. Lima, L. Bieseki, P. V. Melguizo and S. B. C. Pergher, *Environmentally Friendly Zeolites: Synthesis and Source Materials*, Springer International Publishing, 2019.
21. X.-Y. Li, Y. Jiang, X.-Q. Liu, L.-Y. Shi, D.-Y. Zhang and L.-B. Sun, *ACS Sustain. Chem. Eng.*, 2017, **5**, 6124–6130.
22. V. Garshasbi, M. Jahangiri and M. Anbia, *Appl. Surf. Sci.*, 2017, **393**, 225–233.
23. X. Querol, N. Moreno, J. C. Umaña, A. Alastuey, E. Hernández, A. López-Soler and F. Plana, *Int. J. Coal Geol.*, 2002, **50**, 413–423.
24. R. M. Mohamed, I. A. Mkhalid and M. A. Barakat, *Arab. J. Chem.*, 2015, **8**, 48–53.
25. A. Kuperman, S. Nadimi, S. Oliver, G. A. Ozin, J. M. Garcés and M. M. Olken, *Nature*, 1993, **365**, 239–242.
26. A. Deneyer, Q. Ke, J. Devos and M. Dusselier, *Chem. Mater.*, 2020, **32**, 4884–4919.
27. R. E. Morris and S. J. Weigel, *Chem. Soc. Rev.*, 1997, **26**, 309–317.

28. H. Van Koningsveld, H. Van Bekkum and J. C. Jansen, *Acta Crystallographica Section B*, 1987, **43**, 127–132.
29. J. R. Di Iorio and R. Gounder, *Chem. Mater.*, 2016, **28**, 2236–2247.
30. P. Rani, R. Srivastava and B. Satpati, *Cryst. Growth Des.*, 2016, **16**, 3323–3333.
31. L. Wu, V. Degirmenci, P. C. M. M. Magusin, B. M. Szyja and E. J. M. Hensen, *Chem. Commun.*, 2012, **48**, 9492–9494.
32. L. Emdadi, Y. Wu, G. Zhu, C.-C. Chang, W. Fan, T. Pham, R. F. Lobo and D. Liu, *Chem. Mater.*, 2014, **26**, 1345–1355.
33. R. Bai, Y. Song, Y. Li and J. Yu, *Trends Chem.*, 2019, **1**, 601–611.
34. Z. Liu, J. Zhu, T. Wakihara and T. Okubo, *Inorg. Chem. Front.*, 2019, **6**, 14–31.
35. Z. Liu, K. Okabe, C. Anand, Y. Yonezawa, J. Zhu, H. Yamada, A. Endo, Y. Yanaba, T. Yoshikawa, K. Ohara, T. Okubo and T. Wakihara, *Proc. Natl. Acad. Sci.*, 2016, **113**, 14267.
36. V. Valtchev, M. Gerardo, S. Mintova and J. Perez-Ramirez, *Chem. Soc. Rev.*, 2013, **42**, 263–290.
37. A. Dyer, in *Stud. Surf. Sci. Catal.*, 2007, vol. 168, pp. 525–553.
38. D. T. Richens, *The chemistry of aqua ions : synthesis, structure, and reactivity : a tour through the periodic table of the elements*, J. Wiley, Chichester ; New York, 1997.
39. P. Munnik, P. E. de Jongh and K. P. de Jong, *Chem. Rev.*, 2015, **115**, 6687–6718.
40. K. Wang, G. Cao, G. J. Kennedy, M. Afeworki, R. E. Bare and R. B. Hall, *J. Phys. Chem. C*, 2011, **115**, 18611–18617.
41. M. Garcia-Sanchez, P. C. M. M. Magusin, E. J. M. Hensen, P. C. Thune, X. Rozanska and R. A. van Santen, *J. Catal.*, 2003, **219**, 352–361.
42. K. C. Szeto, A. Gallo, S. Hernandez-Morejudo, U. Olsbye, A. De Mallmann, F. Lefebvre, R. M. Gauvin, L. Deevoye, S. L. Scott and M. Taoufik, *J. Phys. Chem. C*, 2015, **119**, 26611–26619.
43. E. A. Pidko, S. M. T. Almutairi, B. Mezari, P. C. M. M. Magusin and E. J. M. Hensen, *ACS Catal.*, 2013, **3**, 1504–1517.
44. T. C. Keller, K. Desai, S. Mitchell and J. Perez-Ramirez, *ACS Catal.*, 2015, **5**, 5388–5396.
45. R. Anwander, I. Nagl, M. Widenmeyer, G. Engelhardt, O. Groeger, C. Palm and T. Röser, *J. Phys. Chem. B*, 2000, **104**, 3532–3544.
46. S. M. T. Almutairi, B. Mezari, P. C. M. M. Magusin, E. A. Pidko and E. J. M. Hensen, *ACS Catal.*, 2012, **2**, 71–83.
47. K. Moller and T. Bein, *Chem. Soc. Rev.*, 2013, **42**, 3689–3707.
48. J. C. Groen, L. A. A. Peffer, J. A. Moulijn and R. Pérez, J., *Micro. Meso. Mater.*, 2004, **69**, 29–34.
49. B. Tang, W. Dai, G. Wu, N. Guan, L. Li and M. Hunger, *ACS Catal.*, 2014, **4**, 2801–2810.
50. R. Dutartre, L. C. de Ménorval, F. Di Renzo, D. McQueen, F. Fajula and P. Schulz, *Micropor. Mater.*, 1996, **6**, 311–320.
51. A. Klein and R. Palkovits, *Catal. Commun.*, 2017, **91**, 72–75.
52. J. C. Groen, L. A. A. Peffer, J. A. Moulijn and J. Pérez-Ramírez, *Colloids Surf. A: Physicochem. Eng. Asp.*, 2004, **241**, 53–58.
53. J. Mielby, J. O. Abildstrøm, F. Wang, T. Kasama, C. Weidenthaler and S. Kegnæs, *Angew. Chemie*, 2014, **126**, 12721–12724.
54. D. Xu, J. Feng and S. Che, *Dalton Trans.*, 2014, **43**, 3612–3617.
55. H. Chen, Y. Wang, C. Sun, X. Wang and C. Wang, *Catal. Commun.*, 2018, **112**, 10–14.

56. S. Dzwigaj, Y. Millot, J. M. Krafft, N. Popovych and P. Kyriienko, *J. Phys. Chem. C*, 2013, **117**, 12552–12559.
57. P. I. Kyriienko, O. V. Larina, S. O. Soloviev, S. M. Orlyk, C. Calers and S. Dzwigaj, *ACS Sustain. Chem. Eng.*, 2017, **5**, 2075–2083.
58. P. Wolf, C. Hammond, S. Conrad and I. Hermans, *Dalton Trans.*, 2014, **43**, 4514–4519.
59. T. Yan, W. Dai, G. Wu, S. Lang, M. Hunger, N. Guan and L. Li, *ACS Catal.*, 2018, DOI: 10.1021/acscatal.8b00014, 2760–2773.
60. V. L. Sushkevich, D. Palagin and I. I. Ivanova, *ACS Catal.*, 2015, **5**, 4833–4836.
61. V. L. Sushkevich and I. I. Ivanova, *ChemSusChem*, 2016, **9**, 2216–2225.
62. L. Qi, Y. Zhang, M. A. Conrad, C. Russell, J. T. Miller and A. T. Bell, *J. Am. Chem. Soc.*, 2020, **142**, 14674–14687.
63. W. N. P. van der Graaff, G. Li, B. Mezari, E. A. Pidko and E. J. M. Hensen, *ChemCatChem*, 2015, **7**, 1152–1160.
64. W. Vermeiren and J.-P. Gilson, *Top. Catal.*, 2009, **52**, 1131–1161.
65. P. Blauwhoff, J. Gosselink, E. Kieffer, S. Sie and W. Stork, Zeolites as catalysts in industrial processes in *Catalysis and Zeolites*, Springer, 1999, pp. 437–538.
66. C. R. Catlow, M. Davidson, C. Hardacre and G. J. Hutchings, *Philos. Trans. Royal Soc. A*, 2016, **374**, 20150089.
67. H. Topsøe, *J. Catal.*, 2003, **216**, 155–164.
68. L. Lukashuk and K. Foettinger, *Johnson Matthey Technology Review*, 2018, **62**, 316–331.
69. J. Goetze, I. Yarulina, J. Gascon, F. Kapteijn and B. M. Weckhuysen, *ACS Catal.*, 2018, **8**, 2060–2070.
70. J. Goetze and B. M. Weckhuysen, *Catal. Sci. Technol.*, 2018, **8**, 1632–1644.
71. S. A. Kadam and M. V. Shamzhy, *Catal. Today*, 2018, **304**, 51–57.
72. F. Kapteijn and J. A. Moulijn, Laboratory Testing of Solid Catalysts in *Handbook of Heterogeneous Catalysis, 2nd ed*, eds. G. Ertl, H. Knözinger, F. Schüth and J. Weitkamp, Wiley, Weinheim, 2008, pp. 2019–2045.
73. S. Mitchell, N.-L. Michels and J. Pérez-Ramírez, *Chem. Soc. Rev.*, 2013, **42**, 6094–6112.
74. C. H. Bartholomew, *Appl. Catal. A*, 2001, **212**, 17–60.
75. M. D. Argyle and C. H. Bartholomew, *Catalysts*, 2015, **5**, 145–269.
76. M. Guisnet and P. Magnoux, *Appl. Catal. A*, 2001, **212**, 83–96.
77. F. Schüth, M. D. Ward and J. M. Buriak, *Chem. Mater.*, 2018, **30**, 3599–3600.
78. S. L. Scott, *ACS Catal.*, 2018, **8**, 8597–8599.
79. J. Sun and Y. Wang, *ACS Catal.*, 2014, **4**, 1078–1090.
80. Industry Statistics: World Fuel Ethanol Production, http://www.ethanolrfa.org/resources/industry/statistics/#1454099788442-e48b2782-ea53).
81. N. Kosaric, Z. Duvnjak, A. Farkas, H. Sahm, S. Bringer-Meyer, O. Goebel and D. Mayer, Ethanol in *Ullmann's Encyclopedia of Industrial Chemistry*, 2011, DOI: 10.1002/14356007.a09_587.pub2, pp. 1–72.
82. S. H. Mohd Azhar, R. Abdulla, S. A. Jambo, H. Marbawi, J. A. Gansau, A. A. Mohd Faik and K. F. Rodrigues, *Biochem. Biophys. Rep.*, 2017, **10**, 52–61.
83. C. E. Wyman, B. E. Dale, R. T. Elander, M. Holtzapple, M. R. Ladisch and Y. Y. Lee, *Bioresour. Technol.*, 2005, **96**, 1959–1966.
84. K. A. Gray, L. Zhao and M. Emptage, *Curr. Opin. Chem. Biol.*, 2006, **10**, 141–146.
85. L. T. Mika, E. Cséfalvay and Á. Németh, *Chem. Rev.*, 2018, **118**, 505–613.

86. RFA: 31 states broke through so-called 'blend wall' in 2016, http://ethanolproducer.com/articles/15016/rfa-31-states-broke-through-so-called-undefinedblend-wallundefined-in-2016, (accessed 12/04/18).
87. U.S. fuel ethanol production continues to grow in 2017, https://www.eia.gov/todayinenergy/detail.php?id=32152).
88. C. Jin, M. F. Yao, H. F. Liu, C. F. F. Lee and J. Ji, *Renew. Sust. Energ. Rev.*, 2011, **15**, 4080–4106.
89. n-Butanol Market by Application (Butyl Acrylate, Butyl Acetate, Glycol Ethers, Direct Solvents, Plasticizers), and Region (APAC, North America, Europe, Middle East & Africa, South America) - Global Forecast to 2025, https://www.marketsandmarkets.com/Market-Reports/n-butanol-market-1089.html, (accessed 24/05/21).
90. X. Y. Wu, G. Q. Fang, Y. Q. Tong, D. H. Jiang, Z. Liang, W. H. Leng, L. Liu, P. X. Tu, H. J. Wang, J. Ni and X. N. Li, *Chemsuschem*, 2018, **11**, 71–85.
91. X. Y. Wu, G. Q. Fang, Z. Liang, W. H. Leng, K. Y. Xu, D. H. Jiang, J. Ni and X. N. Li, *Catal. Commun.*, 2017, **100**, 15–18.
92. P. Dürre, *Biotechnol. J.*, 2007, **2**, 1525–1534.
93. E. Billig and D. R. Bryant, Oxo Process in *Kirk-Othmer Encyclopedia of Chemical Technology*, DOI: doi:10.1002/0471238961.15241502091212.a01.
94. P. Dürre, *Ann. NY Acad. Sci.*, 2008, **1125**, 353–362.
95. S. B. Bankar, S. A. Survase, H. Ojamo and T. Granstrom, *RSC Adv.*, 2013, **3**, 24734–24757.
96. D. T. Jones and D. R. Woods, *Microbiol. Rev.*, 1986, **50**, 484–524.
97. M. Guerbet, *Comptes Rendus*, 1909, **149**, 129–132.
98. C. Yang and Z. Y. Meng, *J. Catal.*, 1993, **142**, 37–44.
99. A. S. Ndou, N. Plint and N. J. Coville, *Appl. Catal. A*, 2003, **251**, 337–345.
100. T. Tsuchida, S. Sakuma, T. Takeguchi and W. Ueda, *Ind. Eng. Chem. Res.*, 2006, **45**, 8634–8642.
101. T. Tsuchida, J. Kubo, T. Yoshioka, S. Sakuma, T. Takeguchi and W. Ueda, *J. Catal.*, 2008, **259**, 183–189.
102. C. R. Ho, S. Shylesh and A. T. Bell, *ACS Catal.*, 2016, **6**, 939–948.
103. S. Ogo, A. Onda and K. Yanagisawa, *Appl. Catal. A*, 2011, **402**, 188–195.
104. S. Ogo, A. Onda, Y. Iwasa, K. Hara, A. Fukuoka and K. Yanagisawa, *J. Catal.*, 2012, **296**, 24–30.
105. S. Hanspal, Z. D. Young, J. T. Prillaman and R. J. Davis, *J. Catal.*, 2017, **352**, 182–190.
106. Z. D. Young and R. J. Davis, *Catal. Sci. Technol.*, 2018, **8**, 1722–1729.
107. M. León, E. Díaz and S. Ordóñez, *Catal. Today*, 2011, **164**, 436–442.
108. D. L. Carvalho, R. R. de Avillez, M. T. Rodrigues, L. E. P. Borges and L. G. Appel, *Appl. Catal. A*, 2012, **415-416**, 96–100.
109. I.-C. Marcu, N. Tanchoux, F. Fajula and D. Tichit, *Catal. Lett.*, 2013, **143**, 23–30.
110. T. Riittonen, E. Toukoniitty, D. K. Madnani, A.-R. Leino, K. Kordas, M. Szabo, A. Sapi, K. Arve, J. Wärnå and J.-P. Mikkola, *Catalysts*, 2012, **2**, 68.
111. Butadiene Product Summary, https://www.americanchemistry.com/ProductsTechnology/Olefins/Butadiene-Product-Summarypdf.pdf, (accessed 18/04/18).
112. J. Grub and E. Löser, Butadiene in *Ullmann's Encyclopedia of Industrial Chemistry*, 2011, DOI: 10.1002/14356007.a04_431.pub2.
113. S. V. Lebedev, *Zhurnal Obshchei Khimii*, 1933, **3**, 698.

114. A. L. Wilds, The Meerwein-Ponndorf-Verley Reduction in *Organic Reactions*, 2011, DOI: doi:10.1002/0471264180.or002.05.
115. Q. Zhu, B. Wang and T. Tan, *ACS Sustain. Chem. Eng.*, 2017, **5**, 722–733.
116. R. Ohnishi, T. Akimoto and K. Tanabe, *J. Chem. Soc., Chem. Commun.*, 1985, 1613–1614.
117. C. Angelici, M. E. Z. Velthoen, B. M. Weckhuysen and P. C. A. Bruijnincx, *ChemSusChem*, 2014, **7**, 2505–2515.
118. C. Angelici, M. E. Z. Velthoen, B. M. Weckhuysen and P. C. A. Bruijnincx, *Catal. Sci. Technol.*, 2015, **5**, 2869–2879.
119. E. V. Makshina, W. Janssens, B. F. Sels and P. A. Jacobs, *Cataly. Today*, 2012, **198**, 338–344.
120. M. Lewandowski, G. S. Babu, M. Vezzoli, M. D. Jones, R. E. Owen, D. Mattia, P. Plucinski, E. Mikolajska, A. Ochenduszko and D. C. Apperley, *Catal. Commun.*, 2014, **49**, 25–28.
121. W. L. Dai, S. S. Zhang, Z. Y. Yu, T. T. Yan, G. J. Wu, N. J. Guan and L. D. Li, *ACS Catal.*, 2017, **7**, 3703–3706.
122. G. Pomalaza, G. Vofo, M. Capron and F. Dumeignil, *Green Chem.*, 2018, **20**, 3203–3209.
123. C. Wang, M. Zheng, X. Li, X. Li and T. Zhang, *Green Chem.*, 2019, **21**, 1006–1010.
124. T. N. Pham, T. Sooknoi, S. P. Crossley and D. E. Resasco, *ACS Catal.*, 2013, **3**, 2456–2473.
125. J. M. Sun, R. A. L. Baylon, C. J. Liu, D. H. Mei, K. J. Martin, P. Venkitasubramanian and Y. Wang, *J. Am. Chem. Soc.*, 2016, **138**, 507–517.
126. J. M. Sun, K. K. Zhu, F. Gao, C. M. Wang, J. Liu, C. H. F. Peden and Y. Wang, *J. Am. Chem. Soc.*, 2011, **133**, 11096–11099.
127. C. Liu, J. Sun, C. Smith and Y. Wang, *Appl. Catal. A*, 2013, **467**, 91–97.
128. L. Feng, M. Yong, W. Jinguo, H. Xiaoxiong, W. Yuanqiang and A. Wei, *ChemCatChem*, 2017, **9**, 1758–1764.
129. T. Tago, H. Konno, S. Ikeda, S. Yamazaki, W. Ninomiya, Y. Nakasaka and T. Masuda, *Catal. Today*, 2011, **164**, 158–162.
130. M. Inaba, K. Murata, M. Saito and I. Takahara, *React. Kinet. Catal. Lett.*, 2006, **88**, 135–142.
131. Z. Li, A. Lepore, B. H. Davison and C. K. Narula, *Energ. Fuel.*, 2016, **30**, 10611–10617.
132. Z. Li, A. W. Lepore, M. F. Salazar, G. S. Foo, B. H. Davison, Z. Wu and C. K. Narula, *Green Chem.*, 2017, **19**, 4344–4352.
133. A. Y. Chichibábin, *J. Prakt. Chem.*, 1924, **107**, 122–128.
134. B. Tollens and P. Wigand, *Justus Liebigs Ann. Chem.*, 1891, **265**, 316–340.
135. *Jp. Pat.*, JP 2011105613, 2011.
136. M. Inaba, K. Murata, I. Takahara and K. Inoue, *Adv. Mater. Sci. Eng.*, 2012, DOI: Artn 29348510.1155/2012/293485.
137. E. Cséfalvay, T. Hajas and L. T. Mika, *Chem. Pap.*, 2020, **74**, 3067–3076.

2. Technical Descriptions of Analytical Techniques Utilised Within This Thesis.

This chapter aims to give the reader an overview of the theoretical basis of the myriad analytical techniques utilised within this thesis for materials characterization and product analysis. Each section intends to give a brief technical description of the technique followed by an outline of its uses within this thesis and the area of zeolite science in general. Appropriate examples have been selected in order to best demonstrate the descriptions within each section.

2.1. Solid-State Nuclear Magnetic Resonance (NMR) Spectroscopy.

Solid-state nuclear magnetic resonance (ssNMR) spectroscopy is a powerful analytical technique in zeolite science which can probe solid materials and guest species on the molecular scale. ssNMR spectroscopy across different nuclei can provide insight into many interesting aspects of zeolite materials, particularly framework connectivity and constituents,[1-4] location of extra-framework cations,[5, 6] and speciation of guest molecules and fragments.[7-10]

2.1.1 Principles of NMR spectroscopy.

NMR spectroscopy is a spectroscopic technique that probes energy transitions between nuclear spin states under the effect of an external magnetic field. All nuclei are charged, and many possess a nuclear spin quantum number (I) resulting in a small nuclear magnetic moment. In the absence of an external magnetic field these nuclei will orientate randomly, and their energy levels will be degenerate. However, upon application of an external magnetic field, it is possible that these nuclear magnetic moments may align in several ways with respect to the external field, resulting in a splitting of energy levels known as the *Zeeman effect*. As an example, a spin ½ (I = ½) nucleus, such as ^{1}H, will be considered. Upon application of the external magnetic field, it is possible that the nuclear moment of ^{1}H will either align with the field or against it, resulting in a lower and higher energy state respectively (see Figure 2.1). Nuclei possessing higher spin quantum numbers (I > ½) are known as quadrupolar and possess a total of 2I+1 nuclear spin states leading to an increased number of available NMR transitions.[11]

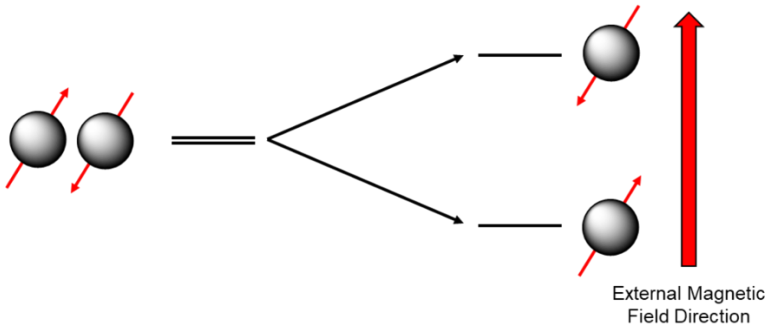

Figure 2.1: Energy level splitting of the nuclear spins of a spin-½ nucleus as a result of the Zeeman interaction upon application of a directional external magnetic field.

Naturally, the populations of these nuclear spin states are governed by a Boltzmann distribution and most nuclei exist in the low energy state. Upon application of electromagnetic energy, typically in the radio frequency (RF) range, it is possible for the nuclei to undergo a spin transition and promote a small proportion of nuclei to the higher energy state, known as excitation. Following excitation, the high energy nuclei can decay back to a lower energy state (typically the ground state) by emission of a photon with energy that can be detected and measured. Local information of nuclei may be obtained due to subtle shifts in their resonance frequency and hence energy of the emitted photon. Typically, only small numbers of nuclei are excited, and this (alongside the relatively low energies of the released photons) gives rise to the general insensitivity of NMR spectroscopy.[11]

2.1.1.1 Factors affecting NMR spectroscopy of various nuclei.

When it comes to NMR spectroscopy, not all nuclei are created (or behave) equally. Several inherent properties of the nuclei in question will affect both the inherent sensitivity of the NMR nucleus and characteristics of the required NMR experiment. Namely, these properties are the nuclei's isotopic abundance (*A*), nuclear spin (*I*) and magnetogyric ratio (γ_n); selected data for nuclei relevant to this thesis are shown in Table 2.. The isotopic abundance of a nucleus is the relative proportion of the NMR active isotope within the sample, the natural abundance being that which occurs naturally for the element without enrichment. If a desired NMR nucleus has a low isotopic abundance, a dilution effect is observed, and experiments will typically require more repetitions resulting in longer experimental times. As mentioned previously, the nuclear spin will affect NMR experiments by way of increased numbers of allowed transitions and possible quadrupolar effects, leading to more complex spectra. Finally, the magnetogyric ratio is the ratio of nucleus' magnetic moment to its angular momentum and determines both the rate and sense (clockwise or anticlockwise for positive and negative values respectively) of a nucleus' precession.[11]

Table 2.1: Selected data for NMR active nuclei relevant to this thesis.

Nucleus	Natural Abundance / %	Nuclear Spin (*I*)	Magnetogyric Ratio / 10^6 rad s^{-1} T^{-1}	Relative Sensitivity to ^1H	Ref
^{1}H	99.98	1/2	267.5	1.0000	12, 13
^{13}C	1.11	1/2	67.3	0.0002	12, 13
^{27}Al	100	5/2	69.7	0.2060	13, 14
^{29}Si	4.70	1/2	−53.1	0.0004	13
^{31}P	100	1/2	108.3	0.0066	12, 13
^{119}Sn	8.59	1/2	−99.7	0.0044	13
^{133}Cs	100	7/2	35.1	0.0474	13

2.1.1.2. NMR spectroscopy in the solid-state.

In the solution phase, many of the orientation dependent factors, specifically dipolar couplings (the direct interaction between two magnetic dipoles), which affect NMR spectra are averaged out due to rapid molecular tumbling and Brownian motion, resulting in sharp and narrow line shapes. In the solid-state, however, these motions are not as prevalent and hence can allow large dipolar coupling values and shielding anisotropies that results in broad and complex line shapes in the resulting NMR spectrum.[15]

Fortunately, magic angle spinning (MAS) may be used to average (or partially average) many of these orientation dependent factors, resulting in narrower linewidths and sharper line shapes.[15] Equations 2.1–2.4 show an expression that describes the orientation dependence of these interactions and, by setting the expression equal to zero, can be used to produce an angle value (θ) at which they will be averaged. This angle is known as the magic angle ($\theta = 54.74°$). When a sample is rotated around the magic angle with respect to the external magnetic field at a sufficiently high frequency (3–30 kHz), the measured spectrum should display greatly improved resolution (see Figure 2.2) as the shielding anisotropies are averaged.[15] Dipolar couplings may also be averaged in this way but typically require especially high rotation rates.[15]

$$3\cos^2\theta - 1 = 0 \tag{2.1}$$

$$3\cos^2\theta = 1 \tag{2.2}$$

$$\cos^2\theta = \frac{1}{3} \tag{2.3}$$

$$\theta = 54.74° \tag{2.4}$$

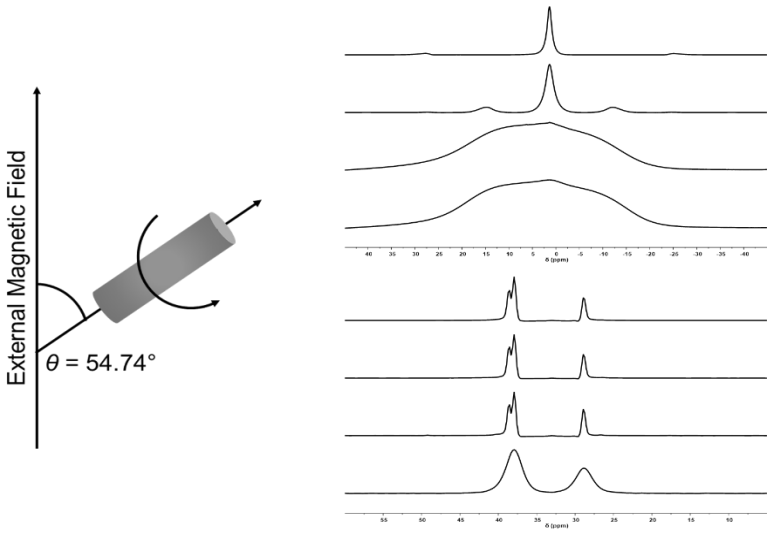

Figure 2.2: Diagram showing the concept of magic angle spinning (left) alongside example ssNMR spectra of its effect (right). Spectra show results from ^{1}H (top) and ^{13}C (bottom) direct excitation experiments of adamantane at MAS rates of 0, 1, 5, and 10 kHz (bottom to top within each stack). ^{1}H spectra averaged over 64 scans with a 5.0 s recycle delay, ^{13}C spectra averaged over 1000 scans with a 2.0 s recycle delay. All spectra acquired on a Varian VNMRS 400 MHz spectrometer using a 4 mm zirconia rotor. Spectrometer frequncies: ^{1}H = 399.88 MHz, ^{13}C = 100.55 MHz.

2.1.2 NMR experiments and pulse sequences relevant to this thesis.

Typically, the first stage of many NMR experiments is to perform a single pulse (or direct excitation) experiment. The single pulse sequence is very simple in nature and hence typically acts as a rapid probing experiment, although often it can be sufficient to gather all desired information. In a single pulse experiment, nuclei are first excited using a π/2 pulse (90°) in order to provide maximum signal strength which is then followed by signal acquisition. Following this, the nuclei are allowed to relax fully to equilibrium during what is known as the recycle delay (see Figure 2.3). Due to the low sensitivity of NMR experiments, this sequence is repeated a number of times (n) until a satisfactory signal to noise (*S/N*) ratio is obtained.[15]

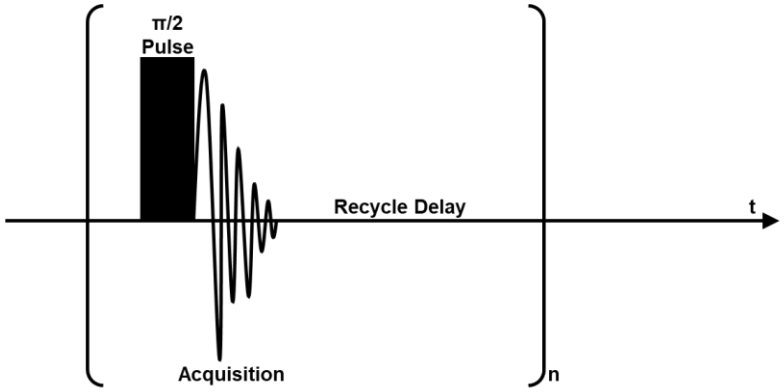

Figure 2.3: Schematic pulse sequence of a basic single pulse NMR experiment.

Many other pulse sequences are available that are able to improve sensitivity or provide additional information above that which is available from a single pulse experiment. The following sections will outline those pulse sequences which are commonly used within this thesis.

2.1.2.1 Hartman-Hahn cross-polarisation sequence.

Cross-polarisation (CP) is a valuable technique in ssNMR that can allow for dramatic signal enhancement of low abundance or low sensitivity nuclei alongside potential for reduced experimental time.[15] Typically, CP is performed on, but not limited to, two spin–½ nuclei. As an illustration, the pulse sequence for a ^{1}H–^{13}C CP experiment will be described and is shown in Figure 2.4. Initially, a π/2 pulse is applied to ^{1}H followed by a second pulse to "spin-lock" the nuclei. At this time, a second pulse is applied to ^{13}C during the cross-polarisation period in which magnetisation is transferred from ^{1}H to ^{13}C. The period of these simultaneous pulses is referred to as the contact time. Following magnetisation transfer, a high power decoupling pulse is applied to the ^{1}H channel whilst signal is acquired from the ^{13}C channel.[15] The ability to transfer magnetisation is governed by Hartman-Hahn matching, and is achieved by carful modulation of the nuclei's RF fields so that the equality in Equation 2.5 is satisfied (where X is the nucleus of interest and ^{1}H is the nuclei providing polarisation).[15]

$$\gamma^{H} B_1^{H} = \gamma^{X} B_1^{X} \tag{2.5}$$

In addition to the enhancement of signal from low sensitivity nuclei or those with long relaxation times, the CP sequence may also be used to probe the local environments of nuclei. As a high sensitivity nucleus (^{1}H or ^{19}F) local to the nucleus of interest is a requirement for the experiment to be successful, observation of signal (or lack of) therefore grants the user information regarding which resonances result from nuclei that are spatially proximate to these high sensitivity nuclei.

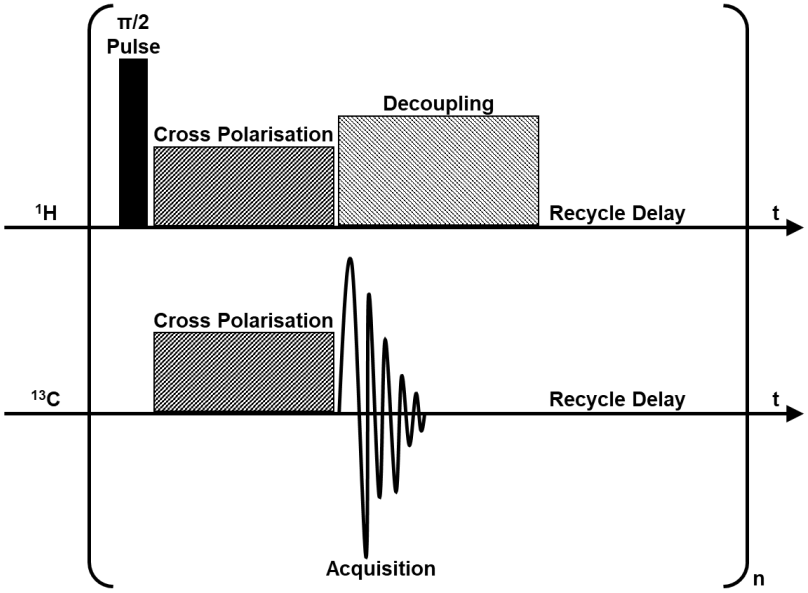

Figure 2.4: Schematic pulse sequence of a Hartman-Hahn cross-polarisation NMR experiment in which magnetisation is passed from ^{1}H nuclei to the relatively insensitive ^{13}C nuclei.

2.1.2.2 Hahn echo and Carr-Purcell-Meiboom-Gill (CPMG) echo-train sequences.

Before introducing the Carr-Purcell-Meiboom-Gill (CPMG) echo-train experiment, it is first crucial to outline the principles of the Hahn echo sequence. In the Hahn echo (or spin echo) sequence, a $\pi/2$ pulse is initially applied. Following this, the nuclear spins begin to dephase before a π pulse is applied and the spins are flipped and begin to rephase; the time between pulses is often synchronized with the rotor period τ_r. After another period of τ_r the nuclear spins coalesce and a measurable signal, an echo, is detected.[16] A schematic representation of a Hahn echo NMR experiment is shown in Figure 2.5.

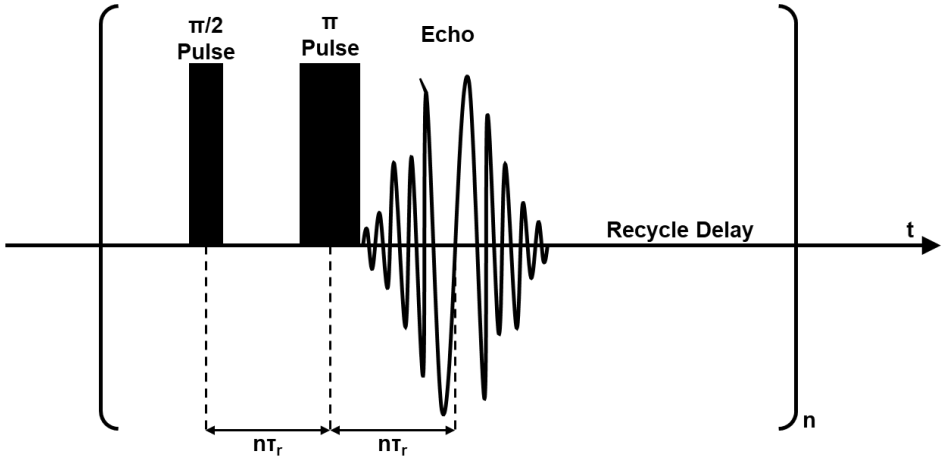

Figure 2.5: Schematic pulse sequence of a Hahn echo NMR experiment.

The CPMG sequence is similar in nature and can be thought of as a series of Hahn echo experiments (see Figure 2.6). In effect, a train of echo pulses (N) is used to constantly refocus the nuclear spins resulting in enhanced signal to noise ratio and improved experimental time. It must be noted that the echo-train may not be continued indefinitely as T_2 (spin-spin) relaxation will eventually cause dephasing and loss of signal. For this reason, the intensity of echoes is seen to decrease over time and can be used to directly correlate the value of T_2. As with the Hahn echo experiment, the time between echoes within the train is often rotor-synchronized.

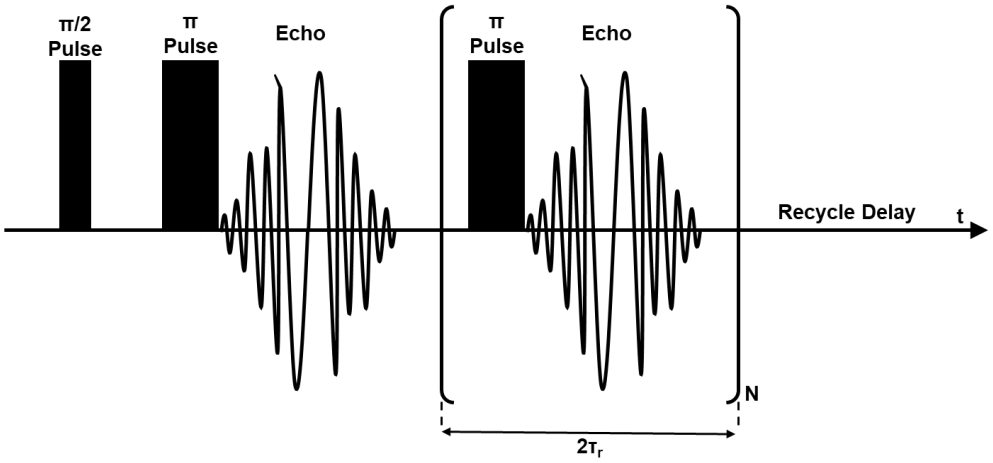

Figure 2.6: Schematic pulse sequence of a CPMG echo-train NMR experiment containing *N* echoes within the train.

2.1.3 Solid-state NMR of nuclei relevant to zeolite science.

In this section, standard NMR experiments and key observations are detailed for the major NMR nuclei relevant to this thesis and zeolite science in general.

2.1.3.1 ^{27}Al NMR spectroscopy.

Typically, ^{27}Al NMR spectroscopy of aluminosilicate zeolite materials is used to discern the quantity of aluminium that is either tetrahedrally coordinated within the zeolite framework (FW) or exists outside of the framework as small octahedral alumina clusters, referred to as extra-framework (exFW) alumina. In an ^{27}Al NMR spectrum of a zeolite, FW aluminium is typically observed to resonate around 60 ppm whilst exFW alumina is seen to resonate around 0 ppm (Figure 2.7). From integration of these peaks, it is possible to discern the proportion of framework aluminium species by use of Equation 2.6.

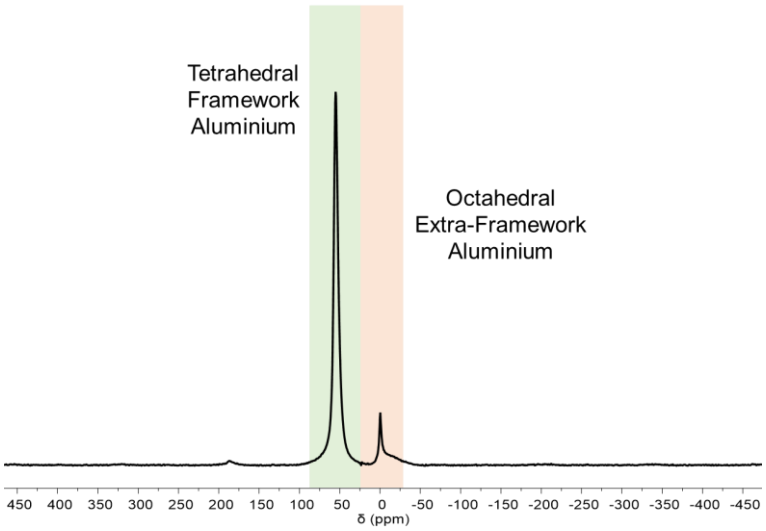

Figure 2.7: ^{27}Al ssNMR spectrum of a partially dealuminated MFI sample showing contributions from both tetrahedrally co-ordinated framework aluminium (≈ 60 ppm) and octahedrally coordinated extra-framework alumina (≈ 0 ppm). Green and orange bands represent the general resonance areas of FW and exFW aluminium respectively. Spectrum was averaged over 10000 scans with a 0.2 s recycle delay. Spectrum was acquired on a Varian VNMRS 400 MHz spectrometer using a 4 mm zirconia rotor. Spectrometer frequency: ^{27}Al = 104.20 MHz. MAS spin rate ≈ 14000 Hz.

$$Al_{FW} = Al_{Total} \times \frac{\int 60\ ppm}{(\int 60\ ppm + \int 0\ ppm)} \tag{2.6}$$

In-depth investigations into the dynamics of aluminium co-ordination in zeolites, however, show that this assignment of purely FW tetrahedral aluminium and exFW octahedral alumina species may not be as sharply defined as two different resonances. Several literature reports describe the reversible transformation of tetrahedral framework aluminium to octahedral framework aluminium within protic-form zeolites at ambient temperature.[17-21] It is shown in these reports that a small partial pressure of water at ambient temperature allows framework aluminium atoms to adopt an octahedral geometry. It is argued that these species are unstable at elevated temperature (>100 °C) at which point the speciation is reverted back to a tetrahedral geometry.[17, 18] Additionally, adsorption of a probe molecule, such as NH_3, CH_3OH or pyridine can restore the population of tetrahedral aluminium sites.[17, 19]

Further to the reported flexibility between tetrahedral and octahedral aluminium sites, tri-coordinate Lewis acidic aluminium sites have been reported, although are said to be "invisible" in regular ssNMR experiments.[18, 20, 22] Despite this, sophisticated 2D ssNMR spectroscopy with Lewis basic probe molecules[22] and XANES[18, 20] have helped to identify and characterise this highly energetic tri-coordinated species.

2.1.3.2 ^{29}Si NMR spectroscopy.

Being the major constituent of many zeolite frameworks, analysis of silicon environments can provide valuable insight into many aspects of zeolite science. ^{29}Si ssNMR spectroscopy of zeolites is typically performed as either a direct excitation or cross-polarisation experiment and can be used to qualitatively and semi-quantitatively elucidate information about factors such as framework connectivity, number and position of defect sites and can aid in surface characterization.

Although often time-consuming owing to the low relative sensitivity of the ^{29}Si nucleus, direct excitation ^{29}Si NMR experiments are frequently employed to determine the silicon atom environments of bulk zeolite materials. Assuming an aluminosilicate material, the silicon contained within it will exist in one of five different coordination environments dependent upon the number of aluminium atoms within the second coordination sphere. Typical nomenclature is represented by $Q^n(nM)$ where *n* is the number of tetrahedral atoms in the second coordination sphere and M is the tetrahedral element in the second coordination sphere. For example, $Q^4(4Al)$ represents a silicon atom in which each atom in its second coordination sphere is aluminium. For aluminosilicates, the following environments are therefore possible: $Q^1(1Al)(0Al)$, $Q^2(2Al)(1Al)(0Al)$, $Q^3(3Al)(2Al)(1Al)(0Al)$, and $Q^4(4Al)(3Al)(2Al)(1Al)(0Al)$. Each environment is shown to produce a differing resonance frequency in the range of −80 to −115 ppm as can be seen in Figure 2.8.[23, 24] A $Q^0(0Al)$ environment represents a silicon atom not included within the zeolite framework, for example as $Si(OH)_4$. In an idealized model of an aluminosilicate zeolite, the relative intensities of each NMR spectrum band can be predicted statistically when the Si/Al ratio of the material is considered but **only** if Al is randomly distributed (the presence of SDAs within zeolite synthesis will normally lead to a non-random distribution of Al within the framework).

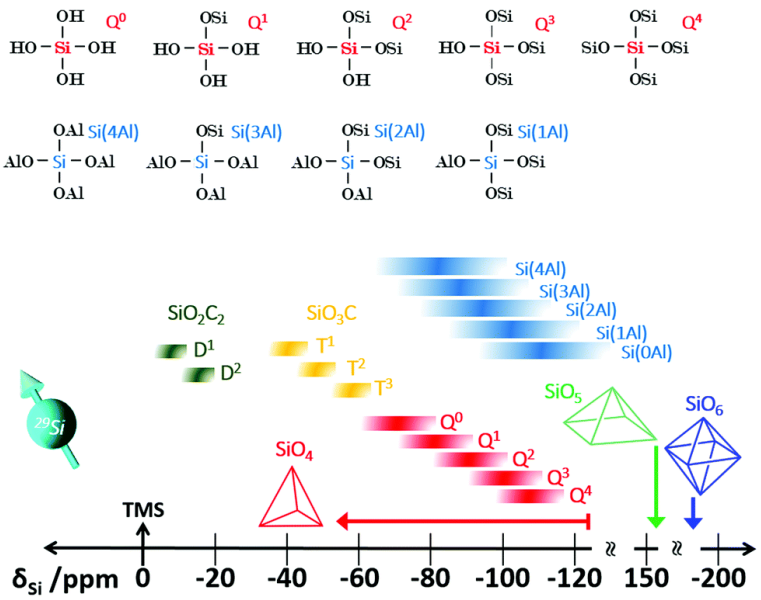

Figure 2.8: ^{29}Si chemical shift range of various Si Q^n(nM) species.[24] Reproduced by permission of The Royal Society of Chemistry.

Additionally, ^{1}H–^{29}Si CP-NMR experiments are frequently employed in order to analyse zeolite surfaces and defect sites. Due to the nature of the CP experiment, ^{29}Si nuclei proximal to ^{1}H exhibit greatly enhanced signal strength, hence any Si environments possessing terminal hydroxyl (–OH) groups feature predominantly in CP spectra. Additionally, relaxation and acquisition times are typically much too rapid for ^{29}Si environments without proximal ^{1}H species to be detected, meaning that Q^4 Si environments are not readily detected or quantified. As an example of the use of CP-NMR, the process of dealumination is easily followed by ^{1}H–^{29}Si CP-NMR experiments. Assuming an ideal zeolite crystal, the initial ^{1}H–^{29}Si CP-NMR spectrum should show no significant contributions if the terminal silanol groups of the crystal are disregarded (approx. −100 ppm). Following dealumination in which Al atoms are removed from the zeolite crystal, the surrounding Si atoms are left bearing terminal silanol groups forming a so-called "silanol nest".[25, 26] A second ^{1}H–^{29}Si CP-NMR spectrum following the dealumination procedure now shows a significant contribution from the newly formed Q^3 and Q^2 environments at around −100 ppm and −90 ppm respectively (see Figure 2.9). ^{29}Si CP-NMR spectroscopy is also frequently employed to monitor zeolite surface reactions by observation of the transformation of signals related to terminal silanol groups.

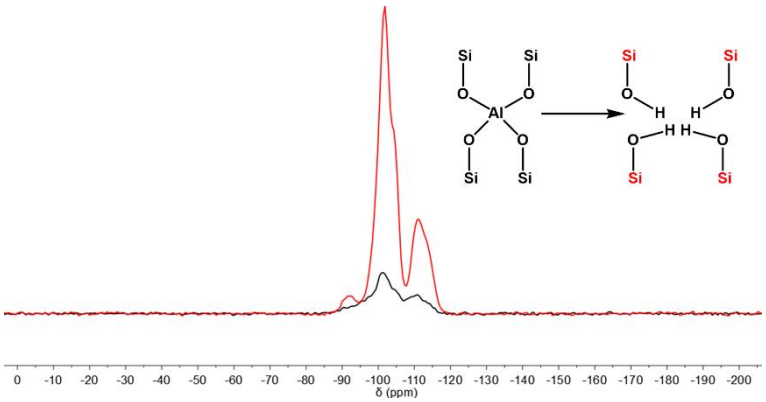

Figure 2.9: Normalised ^{1}H–^{29}Si CP-spectra of H–BEA–(12.5) (black line) and deAl– H–BEA–(12.5) (red line) averaged over 3600 and 1800 scans respectively with a 1.0 s recycle delay and a 5 ms contact time. All spectra acquired on a Varian VNMRS 400 MHz spectrometer using a 6 mm zirconia rotor. Spectrometer frequncies: ^{1}H = 399.88 MHz, ^{29}Si = 79.44 MHz. MAS spin rate ≈ 6000 Hz. Inset: schematic representation of the dealumination process and resulting silanol nest

2.1.3.3 ^{31}P NMR spectroscopy.

The use of probe molecules for characterization of acidity has become increasingly popular in zeolite science with many techniques such as NH_3 temperature-programmed desorption (NH_3-TPD) and pyridine adsorption FTIR spectroscopy becoming commonplace within zeolite characterization.[24, 27, 28] Additionally, the use of probe molecules detected by ssNMR spectroscopy has become more widespread with many NMR active nuclei being utilized, such as ^{1}H for adsorbed acetonitrile-d^3, ^{13}C for adsorbed 2-^{13}C-acetone and ^{15}N for adsorbed pyridine and other amines.[29-35] Compared to ^{1}H, ^{13}C and ^{15}N however, ^{31}P is a more preferable probe nucleus due to being a spin-½ nucleus which has 100% natural abundance and a large chemical shift range ($\Delta\delta_P$ > 650 ppm) and hence acts as a sensitive probe for acidic sites in zeolites. Owing to this enhanced sensitivity, Brønsted and Lewis acid sites of various strengths and their location within zeolite materials are able to be easily discerned and reactivity differences can be correlated.[36, 37]

In this thesis, ^{31}P ssNMR spectroscopy is predominantly used to distinguish the Brønsted or Lewis acidic nature of newly synthesised zeolite materials. To this end, trimethylphosphine oxide (Me_3P, TMPO) was dosed onto the zeolite materials under inert conditions following a dehydrative pre-treatment. Owing to its basic nature, TMPO is strongly bound to available Brønsted or Lewis acid sites through its [P=O] bond (Figure 2.10). When binding to a stronger acid site, an increased amount of electron density is donated from the [P=O] bond to the acid site, resulting in deshielding of the ^{31}P nucleus and a resulting increase in chemical shift detectable in the ^{31}P ssNMR spectrum. This affords the ability to distinguish

acid sites of different strengths in high resolution ^{31}P NMR spectra. Typically, protonation of the [P=O] bond of TMPO by Brønsted acid sites results in higher resonance frequencies and higher chemical shifts than those observed for binding of TMPO to a Lewis acidic centre, typically around δ = 86–53 ppm and δ = 60–55 ppm respectively.[38] It must be noted, however, that ^{31}P chemical shifts are only directly comparable within similar systems as the confinement effects of the zeolite framework can readily affect the stereoelectronics of the probe molecules and therefore the resulting chemical shifts. The loading volume of phosphine oxide probe molecules has also recently been shown to be able to affect the resultant chemical shift.[39]

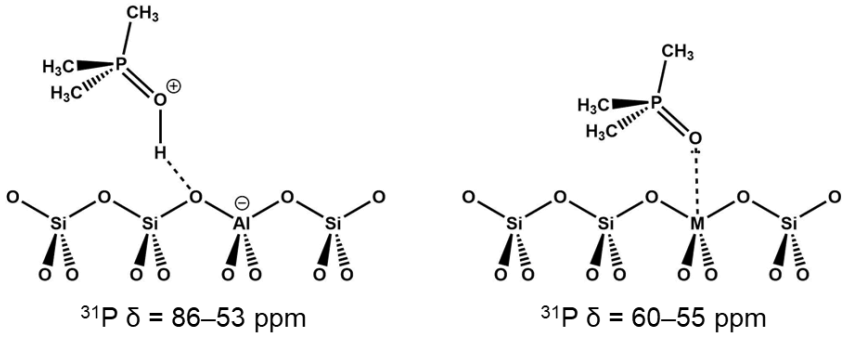

Figure 2.10: Binding modes of TMPO to Brønsted (left) and Lewis (right) acidic zeolite centers with standard ^{31}P chemical shift ranges shown below.

Additionally, utilisation of phosphines and phosphine oxides of different kinetic diameters affords the ability to selectively probe acid sites on the external surface of the zeolite crystal. Previous literature reports have shown the use of tributylphosphine oxide (Bu_3PO) and triphenylphosphine (PPh_3) as reliable probes of the external surface of MFI and MWW frameworks respectively owing to their inability to diffuse into the respective micropore networks.[32, 40, 41] Unfortunately, owing to the low acid site density of the external zeolite crystal, the resulting ^{31}P ssNMR spectra are typically of lower resolution unless large sample masses or extended experimental times are utilised.

2.1.3.4 ^{119}Sn NMR spectroscopy.

Following the increased popularity of the incorporation of Sn atoms into zeolite frameworks as Lewis acidic centres, ^{119}Sn ssNMR spectroscopy has been utilised predominantly to probe the local environment of the newly introduced Sn sites and attempt to form structure activity correlations.[2] In a similar fashion to ^{27}Al, typical ^{119}Sn ssNMR spectra show up to two relatively distinct resonances associated with octahedrally coordinated framework-included Sn species (−700 ppm) and extra-framework Sn species in the form of SnO_2 (−600 ppm), allowing the user to relatively easily distinguish Sn in either coordination environment.[1] Additionally, thoroughly dehydrated samples exhibit a resonance around (−400

ppm) owing to tetrahedrally coordinated framework Sn species.[1, 42] In order to enhance resolution and decrease experimental time, acquisition using a CP-CPMG pulse sequence is often employed (see Section 2.1.2.2).[1] In this thesis, ^{119}Sn ssNMR spectroscopy has predominantly been used to confirm the location of Sn species that have been incorporated into zeolite materials by reactive grafting of $SnCl_4$.

2.1.3.5 ^{133}Cs NMR spectroscopy.

The ability to probe cation locations of zeolite materials is of high importance in understanding the location of counter-balancing Al atoms and their locations effect on catalytic reactivity and selectivity. Whilst ^{27}Al is excellent at discerning the local environment around the Al nucleus from a framework and connectivity perspective, it offers little in the way of deducing channel size or location. Counter-cations, however, sit within the zeolite channel and are hence amenable to surrounding confinement effects from channels of various diameters. There are several NMR active nuclei available to the user that can fill this role, namely $^{6/7}$Li, ^{23}Na and ^{15}N (as $^{15}NH_3$ or similar), however ^{133}Cs is highly preferable owing to its 100% natural abundance and relatively low quadrupolar moment. ^{133}Cs ssNMR spectroscopy has been successfully used to discern Cs^+ cations in two different cation environments in MOR, resonating at 0 and −70 ppm in the example below (Figure 2.11).[6] In order to observe location specific resolution, it is critical that samples are thoroughly dehydrated prior to and during the acquisition of the ^{133}Cs ssNMR spectrum. If samples are not dehydrated, water molecules within the channels of the zeolite will act to hydrate the cation by coordination, resulting in a species akin to a solution phase Cs^+ ion and removing much of the environmental resolution.[6]

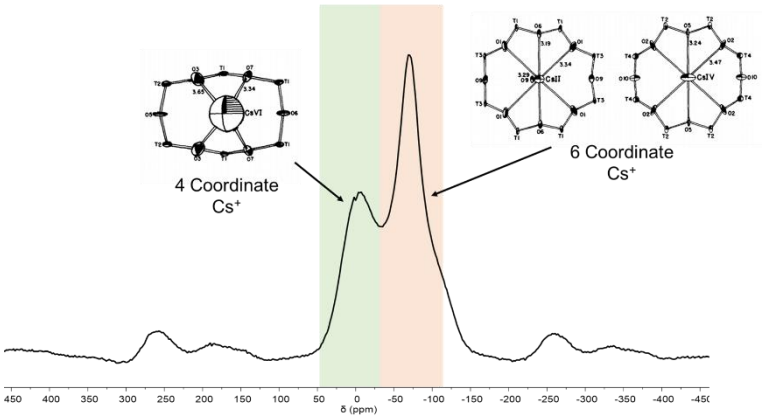

Figure 2.11: ^{133}Cs ssNMR spectrum of a Cs–MOR–(7) showing contributions from Cs^+ cations in both the 4 and 6 coordinate positions in MOR. Green and orange bands represent the general resonance areas of 4 coordinate and 6 coordinate species respectively. Spectrum was averaged over 10000 scans with a 0.2 s recycle delay. Spectrum was acquired on a Varian VNMRS 400 MHz spectrometer using a 4 mm zirconia rotor. Spectrometer frequncy: ^{133}Cs = 52.45 MHz. MAS spin rate ≈ 10000 Hz.

2.2. Diffuse Reflectance Ultraviolet-Visible Spectroscopy.

Crucial to understanding the catalytic performance of zeolite materials is the knowledge of where and in what state heteroatoms exists within the zeolite structure. Within Section X.1, ssNMR spectroscopy was discussed as a powerful technique for understanding both the location and state of NMR active nuclei such as ^{27}Al, ^{29}Si and ^{119}Sn. ssNMR spectroscopy, however, is limited by two major factors. Firstly, nuclei of interest must be NMR active and possess NMR properties (I, γ_n, A) sufficient that acquisition of an NMR spectrum is experimentally feasible. Secondly, due to being a low sensitivity technique, the concentration of the probe nucleus must be sufficiently high to afford a spectrum with an acceptable signal-to-noise (*S/N*) ratio. Within this project, many synthesised zeolite-type materials contain nuclei that are not highly amenable to ssNMR (Ti, Zr, Hf) and are also present in sufficiently low quantities that *S/N* ratio becomes a problem (0.5 – 1.0 wt%), hence making the use of ssNMR impractical. As a result, the use of diffuse reflectance ultraviolet-visible (DR-UV-Vis) spectroscopy, which is both more sensitive and element independent, can be employed to identify both framework heteroatoms and transition metal species.[43-48]

2.2.1 Principles of DR-UV-Vis Spectroscopy.

Standard practice in the liquid phase sees ultraviolet-visible (UV-Vis) spectroscopy performed in transmission mode in which a beam of light is passed through both a cell containing a solution of the desired sample and a blank reference cell, recording either absorption or transmittance as a function of incident wavelength. Solid-state samples, however,

render this approach less practical owing to their increased effect of light scattering and reflection at phase boundaries.[49-51] As a result, instead of utilising transmission spectra, measurement of solid-state samples instead utilise reflection, specifically diffuse reflection, to extract absorption properties at a given wavelength. Diffuse reflection arises from a mixture of multiple reflection, refraction and diffraction phenomena within a solid sample resulting in multiple low intensity reflections that are independent of incident angle (Figure 2.12).[49, 50] In practice, a light source is focused onto the sample by use of an ellipsoidal mirror before diffusely reflected light is collected by a second ellipsoidal mirror and focused towards a detector.[49, 50] As with solution phase UV-Vis, a reference cell is required. In the solid-state, this is typically a "white standard" such as $BaSO_4$ or MgO that produces a high degree of reflection across the entire UV-Vis window.[49, 50]

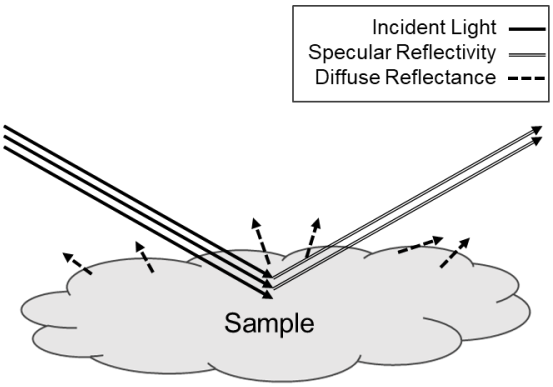

Figure 2.12: Schematic representation of specular reflectivity and diffuse reflectance phenomena.

2.2.2. DR-UV-Vis Spectroscopy of Zeolite Materials.

Within the project, DR-UV-Vis spectroscopy was predominantly used to discern whether newly introduced heteroatoms (Sn, Ti, Zr, Hf) resided within the tetrahedral zeolite framework sites, or as extra-framework metal oxide type phases. Typically, the DR-UV-Vis spectra of zeolite samples exhibit a strong absorption band centred around 220 nm ascribed to the charge transfer transition between O^{2-} and M^{4+} which is indicative of tetrahedrally coordinated framework metal atoms.[44-46] Any heteroatoms that have been unsuccessfully introduced into the zeolite tetrahedral sites will instead typically exhibit the characteristic absorbance profile of their respective metal oxide due to the different coordination environments of the native oxide versus the zeolite.

As an example, Figure 2.13 shows the normalised DR-UV-Vis spectra of a Sn–MFI material synthesised within the project, alongside two commons oxides of Sn: SnO_2 and SnO. Here it is seen that the Sn–MFI spectrum contains a single strong absorption band centred at 215 nm with no major contributions matching those of either SnO_2 or SnO, strongly suggesting

that the Sn species within Sn–MFI reside predominantly in tetrahedral zeolite framework positions.

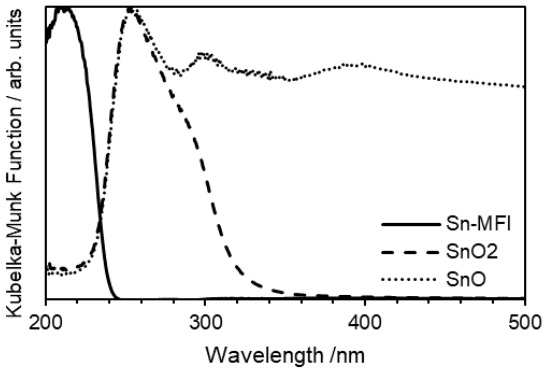

Figure 2.13: Normalised DR-UV-Vis spectra of a Sn–MFI material (solid line), SnO_2 (dashed line) and SnO (dotted line).

2.3. Structural X-Ray Diffraction (XRD).

One of the key features of zeolite materials is their unique crystal structures that result in the formation of channels and cages of molecular dimensions. Owing to the large role that these features can play in catalysis, characterisation and understanding of zeolite crystal structures is essential. To this end, X-ray diffraction (XRD) has proved an invaluable technique in zeolite science.

2.3.1. Principles of X-ray Diffraction.

Owing to their crystalline nature, zeolites and related materials contain periodic arrays of atoms, with the smallest repeat unit being labelled the *unit cell*. X-ray radiation possesses a standard wavelength of around 1 Å (10^{-10} m) and is therefore of a similar magnitude to the interatomic distances of the zeolite lattice. As electrons coherently scatter X-rays, atoms within the lattice act as single point elastic scatterers with the strength of scattering being proportional to the number of electrons possessed by the atom.[52] As a result, X-rays applied to crystalline zeolite materials can satisfy the diffraction condition and will therefore produce a regular array of diffracted waves. A large number of these diffraction waves will not be in phase with one another and will undergo destructive interference, however in a few directions the waves will align in phase and cause constructive interference. These angles may be determined by the Bragg Law shown in Equation X.7, where d is the inter-planar spacing, n is any integer, θ is the incident angle and λ is the wavelength of the incident X-ray (Figure 2.14).[52] In a typical experimental setup, λ and θ are known due to the use of a monochromatic X-ray source and the knowledge of both the incident X-ray and detector angles, hence values of d are easily obtained. For many crystalline materials, the range of d-values observed is characteristic and hence

structure identification of known materials is trivial. When applied to sufficiently sized single crystals (single crystal X-ray diffraction, scXRD) and paired with chemical information, novel structure determination by refinement is possible.

$$n\lambda = 2d \sin\theta \qquad \text{(X.7)}$$

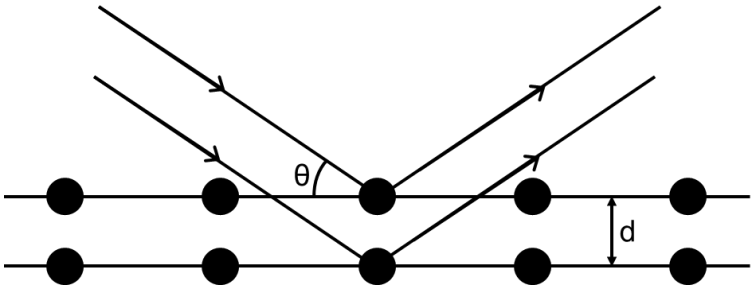

Figure 2.14: Schematic representation of the Bragg law with major quantities labelled.

2.3.2. Powder X-Ray Diffraction.

As zeolites are typically microcrystalline materials, the growth of single crystals sufficiently large for XRD structure solution is difficult and non-routine, hence powder X-ray diffraction (pXRD) has become prevalent for zeolite structure determination.[53] Whereas in scXRD the sample is assumed to be completely anisotropic (all crystal domains ordered in a single direction), pXRD assumes that the sample is instead completely isotropic, with a sufficient distribution of crystalline domains in all orientations and all reflection planes statistically represented. In practice, the incident X-ray source and detector are scanned across a desired range of 2θ values, typically whilst the sample is rotated to enhance the random orientation. Ideally for zeolites, this process will produce a diffractogram exhibiting sharp peaks corresponding to the major reflections of the zeolite samples, allowing comparison to previous data and subsequent identification of framework structure. Figure 2.15 shows a typically obtained diffraction pattern of a sample of silicalite-1 (MFI topology) synthesised within this thesis in comparison to a measured and calculated pattern available from the International Zeolite Association (IZA) zeolite structural database.[54]

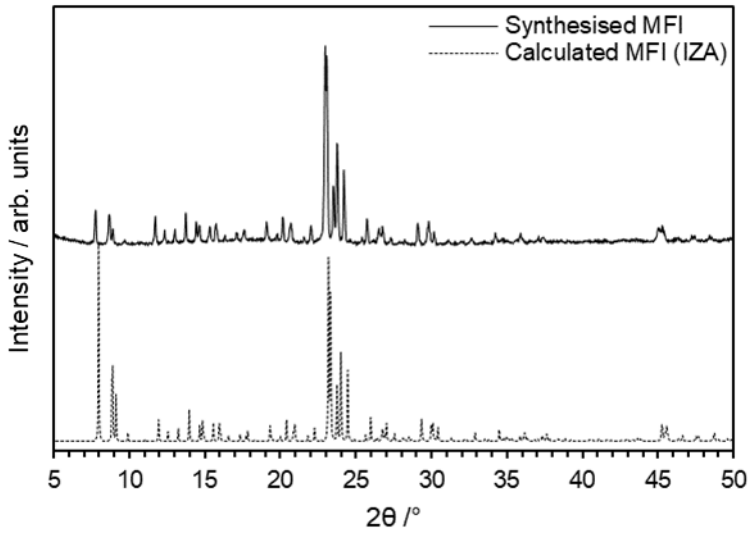

Figure 2.15: pXRD patterns within the 2θ = 5–50° range of a MFI material synthesised within this project (solid line) alongside the calculated powder pattern of MFI obtained from the IZA structural database.[54]

In addition to identifying zeolite framework type, pXRD may also be used to determine the overall crystallinity of zeolite samples. Whereas periodic and crystalline arrays of atoms scatter X-rays only in defined directions and result in typically narrow and high intensity diffractogram peaks, amorphous materials scatter weakly in all directions and result in the observation of broad low-intensity bands within the pXRD diffractogram. By comparison of the intensity of crystalline domains with a standard or reference material, a relative degree of crystallinity can be calculated.[55] Additionally, the average crystallite size of zeolites may be estimated by application of the Scherrer equation if the X-ray wavelength, line broadening (full-width at half maximum) and Bragg angle are known.[56]

2.4. X-Ray Absorption Spectroscopy (XAS).

X-Ray Absorption Spectroscopy (XAS) is a technique that monitors the absorption of X-rays by atoms of a desired metal as a function of X-ray energy. As the X-ray energy is scanned throughout the core-binding region, sudden jumps in absorption intensity, termed edges, are detected when an electron absorbs an X-ray photon with energy equal to, or greater than, the binding energy. These edges correspond to absorption of X-rays by specific core-level electrons and are named as such, i.e. absorption by 1s electrons is termed the *K-edge*.[57, 58] Following the edge jump, absorption remains high as electrons are continually excited into the continuum. Owing to the requirement of high intensity and tuneable monochromatic X-rays, synchrotron light sources are commonly employed for X-ray generation.[58] The following sections will outline the information that can be interpreted from various regions of the XAS and its application to zeolite materials.

2.4.1. X-Ray Absorption Near Edge Spectroscopy (XANES).

As the name suggests, X-Ray Absorption Near Edge Spectroscopy (XANES) is the probing of X-ray interactions close to the adsorption edge of a given metal atom. For this thesis, only the K-edge spectra, absorptions from the 1s level, are considered as no other edges were recorded within the experimental work. The *rising edge* is the strongly absorbing main interaction resulting from the dipole allowed transition between 1s and np levels ($l = \pm 1$).[57] The shape of the rising edge and position of the edge maximum allow insight into the metal oxidation state, spin state and co-ordination number. These observations result from the variation of relative orbital energies of the metal atom in question.[59] Additionally, for the K-edge spectra of many transition metal compounds, a weaker *pre-edge* feature is also observed which corresponds to the quadrupole allowed, but dipole forbidden, 1s–nd transition ($l = \pm 2$). The intensity of this feature grows as the transition becomes more allowed and typically reflects disturbances from centro-symmetry owing to nd and (n+1)p orbital mixing.[59]

2.4.2. Extended X-Ray Near Absorption Fine Structure (EXAFS).

Extended X-Ray Near Absorption Fine Structure (EXAFS) refers to the analysis of the XAS spectrum at incident X-ray energies greater than that of the edge energy. In this region, ejected photoelectrons are scattered by local backscattering atoms resulting in positive and negative absorption oscillations caused by constructive and destructive interference respectively. As the effect is heavily related to the nature and position of neighbouring atoms, analysis of these oscillation allows chemical identification of neighbouring atoms alongside interatomic distances and suggestion of bonding modes.

2.4.3. Application of XAS to Zeolite Materials.

The application of XAS to zeolite materials is widespread but is most frequently used to discern characteristics regarding guest transition metal species with the materials, be it ion-exchanged, impregnated or as a heteroatomic framework substitution. XANES is frequently applied in order to discern the active oxidation state and charge of catalytic metal species within zeolites and to offer insight into their co-ordination geometry. Additionally, *in-situ* and *operando* XANES allow changes in these qualities to be monitored as a function of time during catalytic activity to give insight into catalyst induction, transformation and deactivation.[60, 61] Further, EXAFS is frequently employed in zeolite science to evaluate bond lengths and co-ordination spheres of metal species of interest.[62] EXAFS finds particular use in discerning whether a heteroatom is included into the zeolite framework or excluded as an oxide by

comparison of M–O bond lengths and determination of whether Si is responsible for second sphere scattering.[63]

2.5. Elemental Analysis Techniques.

2.5.1. Inductively Coupled Plasma Optical Emission Spectrometry (ICP-OES).

Inductively coupled plasma optical emission spectrometry (ICP-OES) is frequently used in zeolite science for determination of metal contents of a zeolite material, examples including aluminium content in aluminosilicate frameworks and extra-framework metal species introduced to the material.

As samples must be introduced into the ICP-OES instrument in a liquid form, solid samples that are not easily dissolved, such as zeolites, must first undergo acid digestion to bring them into the liquid phase. Due to the high levels of siliceous material in zeolites, this digestion is typically performed by use of HF. Upon complete digestion of a known quantity of solid material, excess HF is boiled off and the sample is subsequently re-dispersed in a nitric acid solution of known concentration. During this stage, the resulting gaseous SiF_4 that is formed from HF digestion of siliceous zeolite is also boiled away (b.p. −86 °C)[64], hence the accurate measurement of Si values using this method is not possible. Following this digestion process, a nitric acid solution of all other metal ions from the zeolite material of interest is obtained and can be introduced directly into the ICP-OES instrument.

Upon sample introduction, the liquid is pumped into the instrument's nebulizer where it is converted to a fine mist that is introduced by argon gas flow into the ICP flame. The ICP flame here is maintained as an argon gas plasma powered by electromagnetic induction.[65] Upon entry into the ICP torch, the metals species of the sample collide with the ions and electrons of the plasma and rapidly lose and recombine with electrons of their own. The recombination of atoms and electrons releases visible light photons of characteristic wavelength for each metal species which are detected by an optical spectrometer. It is then possible to integrate the spectrum received and apply a calibration curve to produce a concentration value for each metal species detected. A full instrument schematic may be seen in Figure 2.16. Typical monochromator wavelengths for metals of interest in this thesis and listed in Section 9.2.3.

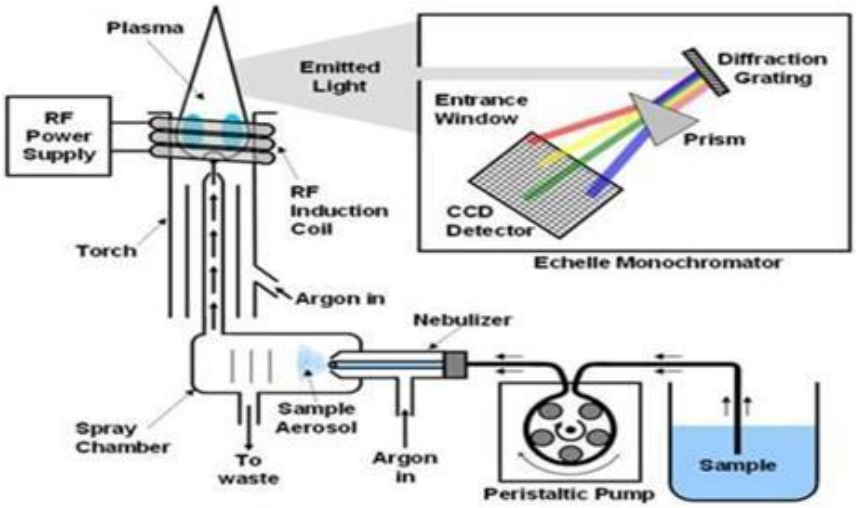

Figure 2.16: Schematic diagram of an inductively coupled plasma optical emission spectrometer. Reproduced from reference 66.[66]

2.5.2. X-Ray Fluorescence Analysis (XRF).

X-ray fluorescence (XRF) is an alternative form of elemental analysis which can provide rapid analysis of key parameters relevant to zeolite science such as silicon mass fractions and Si/Al ratios. XRF analysis is able to be performed on a wide variety of sample states from neat liquids or powders to solid pottery or metal samples. In zeolite science, samples are typically prepared *via* three major routes: analysis of loosely pressed powders, high pressure pelletization or Claisse bead fusion. Whilst lightly pressed powders and high-pressure pellets may both be quick to produce, they suffer from the risk of material inhomogeneity.[67, 68] Generally, borax bead fusion[69] is regarded as the most effective way of producing a homogeneous sample for XRF analysis.[67, 68] In this method, the sample to be analysed is mixed with an excess of borate flux before being heated beyond the melting point of the flux and agitated to form for a homogenous dispersion of analyte material. Melt phase chemical reactions of the sample within the molten flux generates glass like borates which are cast into discs of dimensions ideal for loading into the XRF spectrometer.[67, 68] In this thesis, samples of interest are diluted 10–30 fold with a flux consisting of 66.67% $Li_2B_4O_7$, 32.83% $LiBO_2$ and 0.50% LiI acting as a releasing agent and are typically treated at 1065 °C. The choice of borate cation is important, here Li^+ is chosen as the borate cation dur to Na^+ being an element of analytical interest. Claisse bead fusion is not however without its disadvantages: firstly, the method is more costly in both time and material, secondly the dilution effect on the sample has the potential to make analysis of trace metals difficult.

In order to perform analysis, the sample is first irradiated with X-rays of sufficient energy to eject an inner (K-shell) electron from the sample. Typically, these X-rays are provided from a source containing an element that is not desirable in analysis (such as Ag or Rh) so as not to obscure the obtained spectrum. Following electron ejection, outer shell electrons may drop down in energy to fill the formed vacancy, resulting in emission of an X-ray of characteristic energy for the element from which it was emitted. K←L and K←M transitions result in the ejection of K_α and K_β emission respectively (see Figure 2.17).

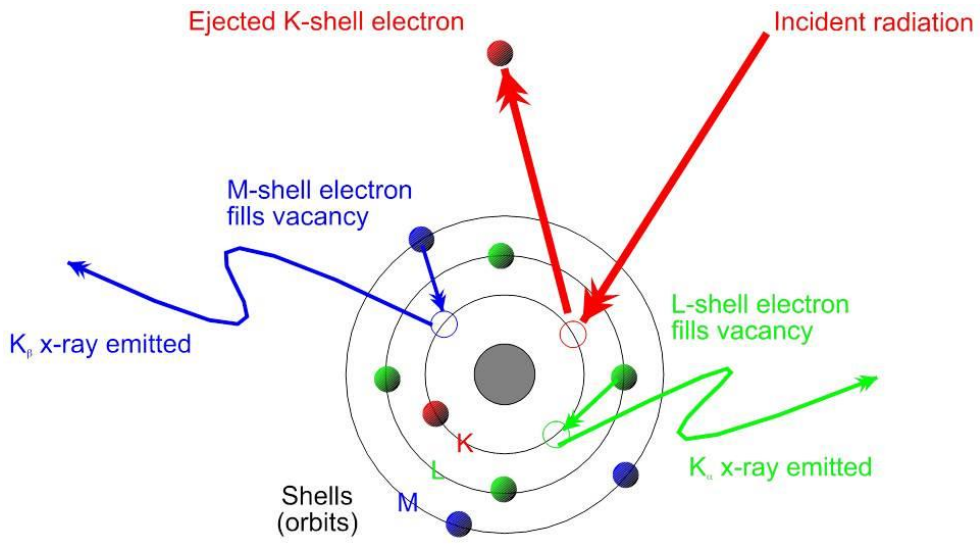

Figure 2.17: Schematic diagram of the ejection of a K-shell electron resulting in production of characteristic K_α and K_β X-rays. Image reproduced from reference 70.[70]

Whilst the principle of detection remains unchanged, there are two differing XRF detection methods used routinely, energy dispersive (ED-XRF) and wavelength dispersive (WD-XRF) detection, which both provide relative advantages and disadvantages when compared to one another. Following X-ray irradiation, ED-XRF detects the full florescence profile of the sample and uses a multi-channel analyser to separate the total radiation profile into the characteristic wavelengths of the elements present in the sample. Whilst ED-XRF systems can provide rapid and portable analysis with simple mechanics, it is typically seen to suffer from poor spectral resolution, specifically in the light to middle element range. As the characteristic X-ray wavelengths of light elements are relatively close, peak overlapping is common and subsequent energy dispersion is sometimes difficult. Additionally, high concentrations of an element may produce a spectral tail that swamps detection of more trace elements with similar wavelength energies. As a result of this, ED-XRF has a practical element range of Na and heavier.[71, 72] As opposed to detecting the full radiation profile at once, WD-XRF utilises a diffraction prism to detect single-wavelengths of characteristic radiation

sequentially. As WD-XRF detects fluorescence on a single-wavelength basis, the analysis of light to middle elements is significantly improved when compared to ED-XRF and spectral resolution is typically seen to be very high. As a result, WD-XRF systems can typically detect elements as light as Be, although the size and cost of machinery is a substantial drawback.[71, 72]

2.5.3. Carbon, Hydrogen, Nitrogen Elemental Microanalysis (CHN).

Analysis of light organic elements (carbon, hydrogen and nitrogen) within zeolite materials is of high importance in ensuring the removal of undesirable organic template molecules before reaction and for post-catalytic coke analysis. It is important to note that the measured H wt% is that associated with water and occluded species only, not that associated with the zeolite framework.[73]

CHN analysis is typically performed by measuring a small mass of sample (< 10 mg) into a tin (Sn) capsule which is loaded into the analyser and purged with He. The tin capsule containing the sample is then dropped into a quartz reactor tube maintained at approximately 900 °C at which point the He purge is temporarily enriched with O_2. The tin capsule promotes flash combustion of the sample resulting in oxidation of C, H and N containing substances to CO_2, H_2O and NO_x respectively. Even under such favourable conditions, CO is still often formed and hence passage of the gas stream over a catalyst (typically tungsten trioxide) results in quantitative production of complete oxidation products. The product stream is then passed over a copper catalyst in order to remove excess O_2 and reduce NO_x to N_2. Finally, the gas stream containing the analytically important species (CO_2 for C, H_2O for H and N_2 for N) is brought to a desired volume and pressure state before being passed over a gas chromatography column and each species detected and quantified by a thermal conductivity detector (TCD) (Figure 2.18).[74-76]

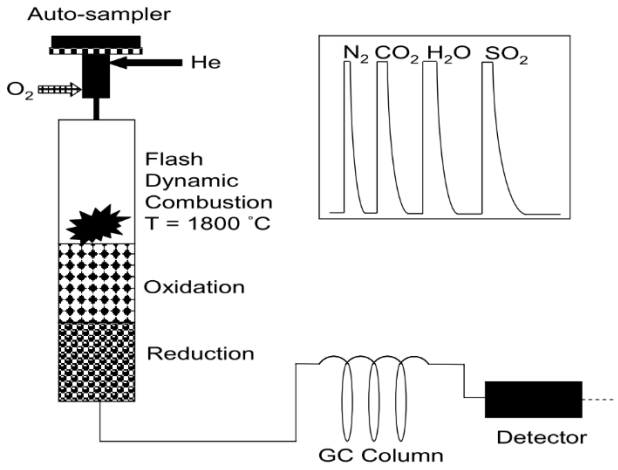

Figure 2.18: Schematic diagram of a CHN elemental analyser, adapted from reference 74.[74]

2.6. Gas Adsorption Analysis.

Gas adsorption analysis, particularly N_2 physisorption, is an important tool in understanding the catalytic properties of high surface area, porous materials such as zeolites. By use of appropriate gas adsorption models, a number of factors influential in catalysis, namely specific surface area, micropore volume and pore size distribution, can be determined.[77]

Upon exposure of a material to a gas, two common binding phenomena may be observed. These are namely *chemisorption* in which a gas molecule adheres to a surface by formation of a chemical bond and *physisorption* in which a gas molecule adheres to a surface as a result of weakly attractive Van-der Waals interactions. In a typical gas adsorption experiment, the sample is first degassed under both high vacuum and heating in order to remove all residually adsorbed species.[77] Subsequently, the analyte gas is introduced at a range of pre-determined relative pressures (p/p^0) and the quantity of gas adsorbed at each relative pressure is recorded.[77] Plotting of these data results in the production of physisorption isotherms that can be broadly classified as seen in Figure 2.19.[78] Of most relevance to this thesis are the Type I and IV isotherms. Type I(a) isotherms are typically produced by low external surface area, purely microporous solids, such as molecular sieves, with a micropore diameter of < 1 nm, whilst those containing slightly larger pores (< 2.5 nm) will exhibit Type I(b) isotherms.[78] Type IV isotherms are more typical of mesoporous materials that can undergo capillary condensation, with Type IV(a) isotherms commonly observed.[78] Additionally, it is not uncommon for hierarchical zeolite materials (those containing both micropores and mesopores) to exhibit isotherms with mixed Type I/Type IV characteristics.

Gas adsorption measurements on zeolite materials are typically taken and modelled by N_2 physisorption at −196 °C (N_2 boiling point) owing to the relatively low cost of the required consumables and reasonable understanding of the system. Use of N_2 however, does have the disadvantage of possessing a small quadrupolar moment that interacts slightly more strongly with charged species within the zeolite samples (Al^-, O^+, H^+). Hence, this results in preferential orientation of nitrogen molecules, which, owing to their non-spherical shape, produces slightly inaccurate surface coverage values. This interaction, however, is frequently taken as inherent to the technique and is often overlooked.[78, 79] Use of argon gas at −186 °C (Ar boiling point) is seen to be more accurate than N_2 for zeolite systems owing to its lack of quadrupolar interaction with charged zeolite species, but is less regularly undertaken.

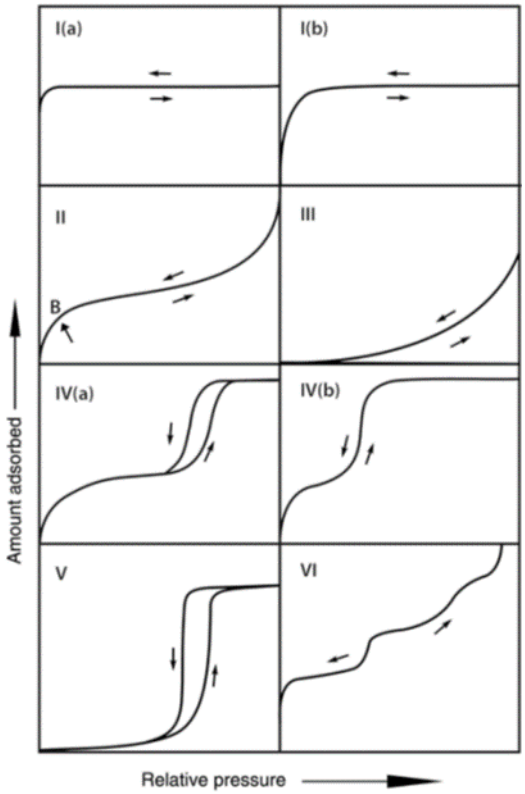

Figure 2.19: General classification of gas physisorption isotherms for porous solids, adapted from reference 78.[78]

In order to calculate the specific surface area of a material, Braunauer-Emmett-Teller (BET) theory (an extension of the Langmuir isotherm) is most commonly employed. BET theory gives the user the ability to calculate a materials specific surface by using a linear range of p/p^0 values and their respective gas adsorption quantities.[80] The application of the BET equation, however, is limited for microporous materials as the formation of an adsorption monolayer and pore-filling can become effectively indistinguishable.[81] In this thesis, gas

adsorption analysis was predominantly utilised for calculation of BET surface areas of synthesised and modified zeolite materials so as to cross-compare between samples. In order to validate the system and pressure range of BET calculation within this thesis, a measurement of a commercially available material, NH_4–FER–(10) supplied by Alfa-Aesar, was first undertaken. A specific surface area value of 372.3 ± 0.5 m^2 g^{-1} was calculated with the pressure range $p/p^0 = 0.005–0.045$ and was deemed comparable to the manufacturer quoted value of 400 m^2 g^{-1}.

2.7. Scanning Electron Microscopy (SEM).

Scanning Electron Microscopy (SEM) is a form of electron microscopy by which a surface is imaged by its interaction with a focused electron beam. When applied to zeolite materials, SEM can reveal details on crystal morphology and agglomeration in addition to elemental composition and distribution. As a result, SEM is most frequently employed to examine visual characteristics and spatial resolution of zeolite materials in order to complement bulk analysis techniques.

2.7.1. Principles of Scanning Electron Microscopy.

Principally, electron microscopy employs similar technology to that of an optical microscope by application of a series of lenses in order to expand an image sufficiently to be resolved. As the name suggest, electron microscopes utilise an electron beam owing to their smaller diffraction wavelength when compared to visible light, hence allowing high resolution on the order of nanometres as opposed to the micrometre scale allowed by optical microscopes.[82] Unlike transmission electron microscopy (TEM) which detects electrons that have passed through a sample, scanning electron microscopy (SEM) produces an image based upon detected electrons that are scattered from or close to the samples surface.[82] For SEM, the electron beam utilised is typically in the range of 5-15 keV.[83]

The major detection route for SEM is by detection of *secondary electrons* which result from inelastic collisions between the source electron beam and atoms at the sample surface.[82] These collisions result in ionisation of a valence electron which is accompanied by release of a secondary electron and an X-ray photon of characteristic wavelength (Figure 2.20).[82] As the release of secondary electrons is highly localised to the impact position of the electron beam, sub-nanometre resolution is possible.[82] Scanning of the sample surface thus allows a detailed topographical map to be produced. Additionally, electrons which are scattered elastically, termed *back scattered electrons*, may also be detected and are predominantly used to further

elucidate elemental composition as their signal intensity is proportionally related to the scattering nucleus' atomic number, *Z* (Figure 2.20).[82] As these electrons generally originate from deeper within the sample, resolution is typically lower than that observed from collection of secondary electron data.[82]

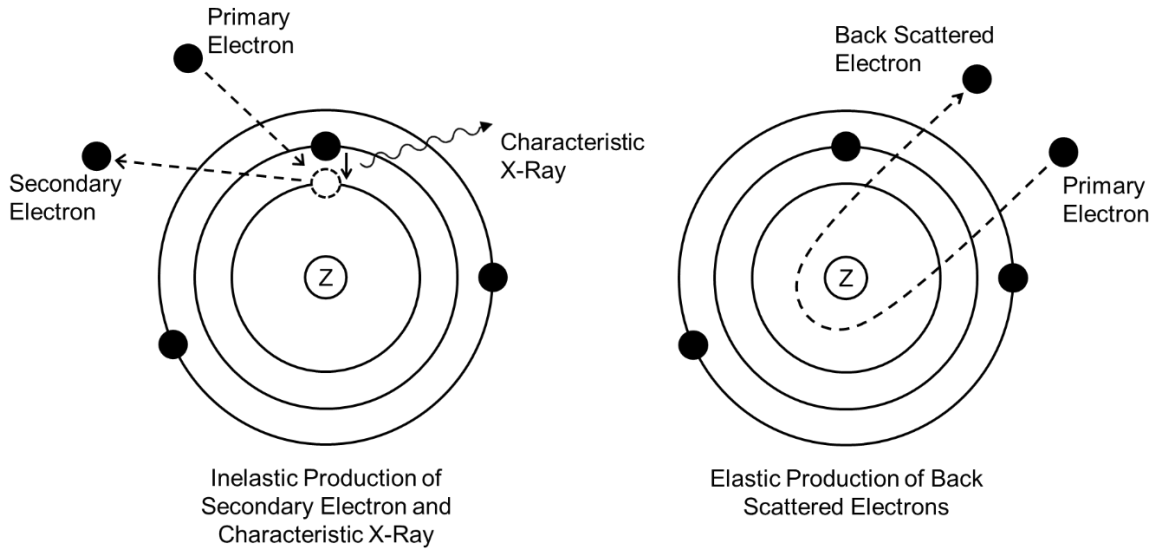

Figure 2.20: Production of species relevant to scanning electron microscopy. Left: Inelastic production of secondary electrons and characteristic X-Ray radiation. Right: Elastic production of back scattered electrons.

2.7.2. Utility of Scanning Electron Microscopy in Zeolite Catalysis.

The use of SEM in the study of zeolite materials is widespread, finding use in all aspects of the field from hydrothermal synthesis to catalytic testing. First and foremost, SEM imaging is often employed following hydrothermal synthesis in order to complement framework identification and to assess homogeneity of the produced phase. Although not a sweeping rule, many zeolite materials adopt typical structures, such as the coffin-like morphology of MFI materials.[84, 85] Additionally, following hydrothermal synthesis, presence of large agglomerates and excess reagents may be identified alongside any minor phases not detected by pXRD analysis, for example amorphous silica phases. Further, SEM imaging is used to assess the size and morphology of zeolite crystals which are characteristics of significant importance depending upon the desired end use of the zeolite. Catalysis by zeolites in particular is affected by crystal size owing to the need of reagents to diffuse into the crystal in order to come into contact with active sites within the micropore network and the need for products to diffuse out of the structure following reaction. In this sense, smaller crystals are typically seen as more desirable for catalysis, as their diffusion distance is typically lower and leads to higher rates of reaction if operating in a diffusion-controlled regime.[86] One further determination available from SEM imaging is the aspect ratio of the zeolite crystal, effectively the ratio of crystal length

to crystal width. The aspect ratio is of particular importance for zeolite catalysts with sub-3-dimensional frameworks, as the diffusion distance throughout the crystal in greatly influenced depending on the orientation of the channel system with respect to the major crystal axis.

Many modern scanning electron microscopes come equipped with an energy dispersive X-ray spectrometer (EDX) that allows determination of elemental compositions at a given target point. This combination, often abbreviated as SEM-EDX, allows elemental determination at individual points of crystals and components of a zeolite sample.[82] With this additional tool, the composition of different phases may be determined with relative ease, an endeavour not possible with most other elemental analysis techniques which merely reflect the bulk elemental composition of a sample. Further, by accumulation of sufficient EDX data points, crystals may be mapped in order to assess elemental distributions.[82] It must be acknowledged, however, that SEM and SEM-EDX are purely surface techniques and give no indication of internal or bulk compositions.

2.8. Gas Chromatography (GC) Analysis and Detectors.

2.8.1. Gas Chromatography (GC).

Gas chromatography (GC) is a common laboratory technique for separating and analysing mixtures of volatile organic compounds. The technique has found widespread use in the area of flow chemistry over fixed bed reactors in which reactions are undertaken in the gaseous phase as it allows continuous on-line monitoring.

In essence, separation of compounds by GC relies on the interaction of two phases, the *mobile phase* and the *stationary phase*. The mobile phase is the vaporised mixture of compounds to be separated, diluted into a carrier gas which is used to propel the mixture through a stationary phase, typically mounted within a GC column. Typically, the carrier gas is an inert and non-interacting gas that is selected based on its diffusivity and viscosity properties.[87] Helium is the carrier gas of choice in the vast majority of instruments, however both hydrogen and nitrogen also find use in GC applications. Hydrogen is often regarded as superior to helium for GC owing to its similar diffusivity but lower viscosity, allowing faster GC at higher inlet pressures, although safety concerns and reactivity often limit its usage.[87, 88] Nitrogen is regarded as generally poor for GC owing to its low diffusivity (approx. 0.25× that seen for hydrogen or helium) resulting in poor compound separation and requiring longer run times.[87] Unfortunately, the current decline in helium supplies may result in the need for many

GC users to switch to either hydrogen or nitrogen carriers, with many most likely choosing to opt for hydrogen.

Generally, GC columns may be subdivided into two categories of stationary phase, packed columns and capillary columns. For packed and micro-packed columns, the particles of stationary phase are packed into wide bore metal tubing, whereas for capillary GC columns the stationary phase is typically a thin layer of either liquid or polymer supported inside narrow diameter inert glass or metal tubing. The method of action for both columns is similar regardless. As the analysis mixture is swept along the column, radial diffusion allows solute molecules to interact with the stationary phase which results in individual components of the mixture moving through the column at different rates dependent upon the strength of their interaction with the stationary phase. It is possible, however, that the components may interact too frequently with the stationary phase and hence result in band broadening. Additionally, lateral diffusion within the column may also lead to broad eluent bands. Hence, there is typically an optimum gas velocity through a GC column to maximise component separation whilst minimising band broadening (see Figure 2.21). To remedy this issue, several other parameters may be varied during GC, such as temperature programming and column dimensions. Increasing temperature encourages stationary phase interactions to be briefer and hence decreases elution time. Similarly, wider columns decrease the relative amount of stationary phase surface area with respect to column volume and promote faster elution.

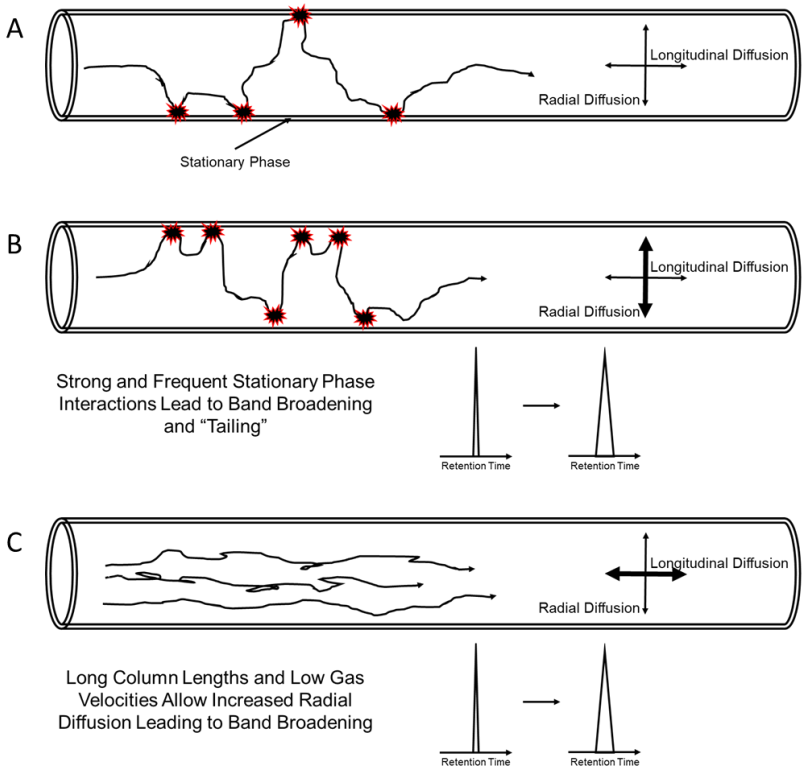

Figure 2.21: A) Interactions of the mobile phase with the stationary phase and the two possible diffusion directions of a molecule in a GC column. B) A schematic representation of how strong and frequent stationary phase interactions can induce peak broadening. C) A schematic representation of how radial diffusion can cause peak broadening in long columns or those with low gas velocity.

Following component separation, the eluents must be detected and identified as the GC itself cannot inherently do this. Several popular detectors exist, including the flame ionisation detector (FID), thermal conductivity detector (TCD) and electron capture detector (ECD). In this thesis two detectors were used, a mass spectrometer (MS) and a barrier ionisation discharge detector (BID); their respective methods of action are detailed below.

2.8.2. Mass Spectrometry (MS) Detector.

Mass spectrometry (MS) is a powerful technique often used in tandem with GC which allows not only detection of GC bands but also their identification of their components. The essence of MS is detection of ions based on their mass to charge (*m/z*) ratio. Due to many molecules producing a unique fragmentation pattern of *m/z* values, MS is frequently able to identify unknown compounds from database searching.

In this thesis, a mass spectrometer equipped with an electron ionisation (EI) ion source and quadrupole mass analyser was used. EI is an ionisation methods in which the analyte is fed into an ionisation chamber through which an electron beam is fired.[89] Interaction of the electron beam with an analyte molecules causes ionisation *via* either a dissociative or non-dissociative pathway. Dissociative ionisation occurs when the parent molecules is broken apart into a

charged fragment and neutral fragment along with loss of an electron (see Figure 2.22). For many organic molecules, the neutral loss is observed to be a single hydrogen atom or small alkyl chain such as CH_3 or CH_2CH_3. The remaining charged fragments provide substantial information on the structure and assist identification of unknown analytes. For non-dissociative ionisation, interaction with the electron beam causes the loss of a further electron from the analyte molecule but does not induce fragmentation resulting in formation of a charged molecular ion (see Figure 2.22).

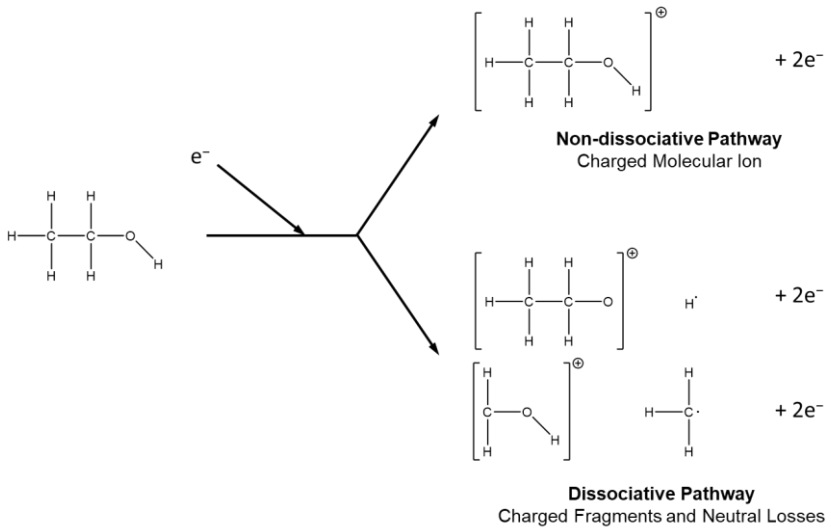

Figure 2.22: Common species resulting from electron ionisation of ethanol; shown are examples of the non-dissociative and dissociative ionisation pathways.

Following ionisation, the newly formed charged species are fed into a quadrupole mass analyser in order to separate species of varying *m/z* ratio before detection. Quadrupole systems contain four parallel rods of either cylindrical or preferably hyperbolic cross-section, with opposing rods connected electrically to one another and bearing a variable electric potential.[89] As the ions pass through the quadrupole, positive ions will be repelled and attracted to positively and negatively biased rods respectively and will hence pass through the quadrupole on an oscillatory trajectory. Additionally, the degree to which the ions are attracted or repelled and hence the curvature of the path will differ depending upon the ion's *m/z* ratio. Therefore, by careful control of the electrical potentials of the quadrupole, it is possible to produce a system in which only ions with a given *m/z* value will pass through the quadruple with a stable trajectory, whereas non-selected ions will follow an unstable trajectory and collide with the quadruple rods (see Figure 2.23). Following successful navigation of the quadrupole, the ions are detected and a signal registered. In typical operation the electrical potentials of the quadrupole rods are varied over time in order to scan a desired mass range.

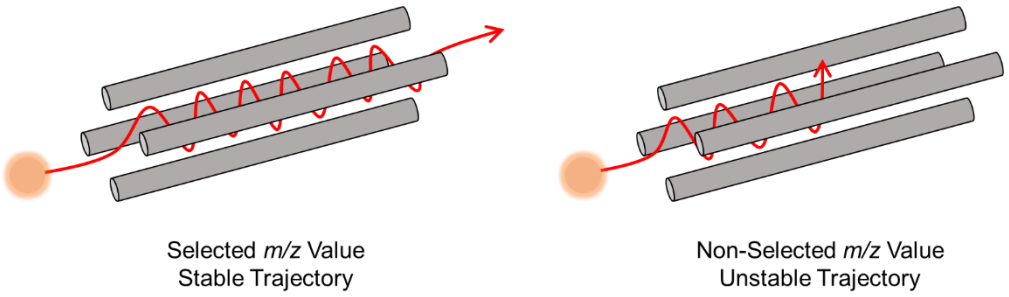

Figure 2.23: Schematics showing ion movement through a quadrupole mass analyser with selected and non-selected *m/z* ratios.

2.8.3. Barrier Ionisation Discharge Detector.

The barrier ionisation discharge (BID) detector is a plasma ionisation detector that is used predominantly in this thesis for permanent gas and light hydrocarbon analysis. Within the detector, a helium plasma is generated by applying a high voltage across a quartz dielectric chamber with a helium purge.[90, 91] Owing to the high photon energy of helium (17.7 eV), it is possible to ionise and detect all compounds except for neon and helium itself.[90, 91] Upon ionization of analytes by the helium plasma, the newly formed ions are drawn to a collector electrode where a response is generated by subtle changes in voltage reading (μV scale) and these responses are plotted as a function of time. Unfortunately, the BID detector has no inherent way of identifying compounds, hence individual peak positions must be known beforehand or calibrated for.

2.9. References.

1. Y. G. Kolyagin, A. V. Yakimov, S. Tolborg, P. N. R. Vennestrøm and I. I. Ivanova, *J. Phys. Chem. Lett.*, 2016, **7**, 1249–1253.
2. Y. G. Kolyagin, A. V. Yakimov, S. Tolborg, P. N. R. Vennestrøm and I. I. Ivanova, *J. Phys. Chem. Lett.*, 2018, **9**, 3738–3743.
3. J. A. van Bokhoven, D. C. Koningsberger, P. Kunkeler, H. van Bekkum and A. P. M. Kentgens, *J. Am. Chem. Soc.*, 2000, **122**, 12842–12847.
4. S. Greiser, M. Hunger and C. Jäger, *Solid State Nucl. Magn. Reson.*, 2016, **79**, 6–10.
5. H. Koller, B. Burger, A. M. Schneider, G. Engelhardt and J. Weitkamp, *Microporous Materials*, 1995, **5**, 219–232.
6. P. J. Chu, B. C. Gerstein, J. Nunan and K. Klier, *J. Phys. Chem.*, 1987, **91**, 3588-3592.
7. Y. G. Kolyagin, I. I. Ivanova, V. V. Ordomsky, A. Gedeon and Y. A. Pirogov, *J. Phys. Chem. C*, 2008, **112**, 20065–20069.
8. A. A. Gabrienko, S. S. Arzumanov, M. V. Luzgin, A. G. Stepanov and V. N. Parmon, *J. Phys. Chem. C*, 2015, **119**, 24910–24918.
9. J. Xu, A. Zheng, X. Wang, G. Qi, J. Su, J. Du, Z. Gan, J. Wu, W. Wang and F. Deng, *Chem. Sci.*, 2012, **3**, 2932–2940.
10. J. Xu, Q. Wang and F. Deng, *Acc. Chem. Res.*, 2019, **52**, 2179–2189.
11. P. J. Hore, *Nuclear Magnetic Resonance*, Oxford University Press, 2015.
12. T. L. James, *Online Textbook: Department of Pharmaceutical Chemistry, University of California, San Francisco*, 1998, 1–31.

13. R. K. Harris, *Chem. Soc. Rev.*, 1976, **5**, 1–22.
14. D. Grekov, T. Vancompernolle, M. Taoufik, L. Delevoye and R. M. Gauvin, *Chem. Soc. Rev.*, 2018, **47**, 2572–2590.
15. David C. Apperley, R. K. Harris and P. Hodgkinson, *Solid-State NMR: Basic Principles and Practice*, 2012.
16. E. L. Hahn, *Phys. Rev.*, 1950, **80**, 580–594.
17. A. Omegna, J. A. van Bokhoven and R. Prins, *J. Phys. Chem. B*, 2003, **107**, 8854–8860.
18. J. A. van Bokhoven, A. M. J. van der Eerden and D. C. Koningsberger, *J. Am. Chem. Soc.*, 2003, **125**, 7435–7442.
19. L. C. de Ménorval, W. Buckermann, F. Figueras and F. Fajula, *J. Phys. Chem.*, 1996, **100**, 465–467.
20. L. A. Bugaev, J. A. van Bokhoven, A. P. Sokolenko, Y. V. Latokha and L. A. Avakyan, *J. Phys. Chem. B*, 2005, **109**, 10771–10778.
21. M. Ravi, V. L. Sushkevich and J. A. van Bokhoven, *Nat. Mater.*, 2020, **19**, 1047–1056.
22. S. Xin, Q. Wang, J. Xu, Y. Chu, P. Wang, N. Feng, G. Qi, J. Trébosc, O. Lafon, W. Fan and F. Deng, *Chem. Sci.*, 2019, **10**, 10159–10169.
23. E. Lippmaa, M. Maegi, A. Samoson, M. Tarmak and G. Engelhardt, *J. Am. Chem. Soc.*, 1981, **103**, 4992–4996.
24. G. Paul, C. Bisio, I. Braschi, M. Cossi, G. Gatti, E. Gianotti and L. Marchese, *Chem. Soc. Rev.*, 2018, **47**, 5684–5739.
25. S. Dzwigaj, P. Massiani, A. Davidson and M. Che, *J. Mol. Catal. A: Chem.*, 2000, **155**, 169–182.
26. F. Yi, Y. Chen, Z. Tao, C. Hu, X. Yi, A. Zheng, X. Wen, Y. Yun, Y. Yang and Y. Li, *J. Catal.*, 2019, **380**, 204–214.
27. H. Y. Luo, J. D. Lewis and Y. Román-Leshkov, *Annu. Rev. Chem. Biomol. Eng.*, 2016, **7**, 663–692.
28. E. G. Derouane, J. C. Védrine, R. R. Pinto, P. M. Borges, L. Costa, M. A. N. D. A. Lemos, F. Lemos and F. R. Ribeiro, *Catal. Rev.*, 2013, **55**, 454–515.
29. J. Huang, Y. Jiang, V. R. Reddy Marthala, Y. S. Ooi, J. Weitkamp and M. Hunger, *Micro. Meso. Mater.*, 2007, **104**, 129–136.
30. D. H. Barich, J. B. Nicholas, T. Xu and J. F. Haw, *J. Am. Chem. Soc.*, 1998, **120**, 12342–12350.
31. H. Fang, A. Zheng, Y. Chu and F. Deng, *J. Phys. Chem. C*, 2010, **114**, 12711–12718.
32. A. Zheng, S.-B. Liu and F. Deng, *Chem. Rev. (Washington, DC, U. S.)*, 2017, **117**, 12475–12531.
33. H. M. Kao and C. P. Grey, *J. Phys. Chem.*, 1996, **100**, 5105–5117.
34. A. Zheng, S.-B. Liu and F. Deng, *Solid State Nucl. Magn. Reson.*, 2013, **55-56**, 12–27.
35. X. Yi, Y. Xiao, G. Li, Z. Liu, W. Chen, S.-B. Liu and A. Zheng, *Chem. Mater.*, 2020, **32**, 1332–1342.
36. J. D. Lewis, M. Ha, H. Luo, A. Faucher, V. K. Michaelis and Y. Román-Leshkov, *ACS Catal*, 2018, **8**, 3076–3086.
37. W. Yang, Z. Wang, J. Huang and Y. Jiang, *J. Phys. Chem. C*, 2021, **125**, 10179–10197.
38. C. Bornes, M. Sardo, Z. Lin, J. Amelse, A. Fernandes, M. F. Ribeiro, C. Geraldes, J. Rocha and L. Mafra, *Chem. Commun.*, 2019, **55**, 12635–12638.
39. Y. Wang, S. Xin, Y. Chu, J. Xu, G. Qi, Q. Wang, Q. Xia and F. Deng, *J. Phys. Chem. C*, 2021, **125**, 9497–9506.
40. Q. Zhao, W.-H. Chen, S.-J. Huang, Y.-C. Wu, H.-K. Lee and S.-B. Liu, *J. Phys. Chem. B*, 2002, **106**, 4462–4469.
41. Y. Wang, J. Zhuang, G. Yang, D. Zhou, D. Ma, X. Han and X. Bao, *J. Phys. Chem. B*, 2004, **108**, 1386–1391.

42. A. V. Yakimov, Y. G. Kolyagin, S. Tolborg, P. N. R. Vennestrøm and I. I. Ivanova, *J. Phys. Chem. C*, 2016, **120**, 28083–28092.
43. R. F. Howe, in *Stud. Surf. Sci. Catal.*, eds. H. Chon, S. I. Woo and S. E. Park, Elsevier, 1996, vol. 102, pp. 97–139.
44. N. K. Mal and A. V. Ramaswamy, *J. Mol. Catal. A: Chem.*, 1996, **105**, 149–158.
45. W. Fan, R.-G. Duan, T. Yokoi, P. Wu, Y. Kubota and T. Tatsumi, *J. Am. Chem. Soc.*, 2008, **130**, 10150–10164.
46. Y. S. Ko and W. S. Ahn, *Korean J. Chem. Eng.*, 1998, **15**, 423–428.
47. X.-H. Tang, X. Wen, S.-W. Sun and H.-Y. Jiang, in *Stud. Surf. Sci. Catal.*, eds. A. Sayari and M. Jaroniec, Elsevier, 2002, vol. 141, pp. 167–172.
48. A. Bellmann, C. Rautenberg, U. Bentrup and A. Brückner, *Catalysts*, 2020, **10**, 123.
49. Diffuse Reflectance IR and UV-vis Spectroscopy, http://www.fhi-berlin.mpg.de/acnew/department/pages/teaching/pages/teaching__wintersemester__2007_2008/jentoft_diffusereflectance_250108.pdf, (accessed 03/03/2020).
50. A. L. Ulery and L. R. Drees, in *Methods of soil analysis: Mineralogical methods. Part 5*, ASA-CSSA-SSSA, 2008, vol. 9, ch. 13.
51. F. C. Jentoft, in *Characterization of Solid Materials and Heterogeneous Catalysts*, eds. M. Che and J. C. Védrine, 2012, pp. 89–147.
52. C. Suryanarayana and M. G. Norton, *X-Ray Diffraction: A Practical Approach*, Springer US, 1998.
53. P. Wright, in *Microporous Framework Solids*, ed. P. Wright, The Royal Society of Chem., 2008, pp. 79–147.
54. Database of Zeolite Structures, http://www.iza-structure.org/databases/, (accessed 25/04/2018).
55. A. W. Burton, in *Zeolite Characterization and Catalysis: A Tutorial*, eds. A. W. Chester and E. G. Derouane, Springer Netherlands, Dordrecht, 2009, pp. 1–64.
56. A. W. Burton, K. Ong, T. Rea and I. Y. Chan, *Micro. Meso. Mater.*, 2009, **117**, 75–90.
57. J. Evans, *X-ray Absorption Spectroscopy for the Chemical and Materials Sciences*, Wiley, 2018.
58. A. Sharma, J. P. Singh, S. O. Won, K. H. Chae, S. K. Sharma and S. Kumar, in *Handbook of Materials Characterization*, ed. S. K. Sharma, Springer International Publishing, Cham, 2018, DOI: 10.1007/978-3-319-92955-2_13, pp. 497–548.
59. M. L. Baker, M. W. Mara, J. J. Yan, K. O. Hodgson, B. Hedman and E. I. Solomon, *Coord. Chem. Rev.*, 2017, **345**, 182–208.
60. D. E. Doronkin, M. Casapu, T. Günter, O. Müller, R. Frahm and J.-D. Grunwaldt, *J. Phys. Chem. C*, 2014, **118**, 10204–10212.
61. E. Borfecchia, D. K. Pappas, M. Dyballa, K. A. Lomachenko, C. Negri, M. Signorile and G. Berlier, *Catal. Today*, 2019, **333**, 17–27.
62. R. W. Joyner, A. D. Smith, M. Stockenhuber and M. W. E. van den Berg, *Phys. Chem. Chem. Phys.*, 2004, **6**, 5435–5439.
63. A. Hagen, K. H. Hallmeier, C. Hennig, R. Szargan, T. Inui and F. Roessner, in *Stud. Surf. Sci. Catal.*, eds. H. K. Beyer, H. G. Karge, I. Kiricsi and J. B. Nagy, Elsevier, 1995, vol. 94, pp. 195–202.
64. Silicon tetrafluoride safety data sheet, https://www.praxair.com/-/media/corporate/praxairus/documents/sds/silicon-tetrafluoride-sif4-safety-data-sheet-sds-p4652.pdf?la=en&rev=171ecdd721384dc5b22c1286cdbfa8ee).
65. A. Montaser and D. W. Golightly, *Inductively coupled plasmas in analytical atomic spectrometry*, VCH Publishers, 1992.
66. ICP-OES, http://www.rohs-cmet.in/content/icp-oes).

67. R. Jenkins, in *X-Ray Fluorescence Spectrometry*, John Wiley & Sons, Inc., 1999, ch. 9, pp. 141–152.
68. J. Injuk, R. Van Grieken, A. Blank, L. Eksperiandova and V. Buhrke, in *Handbook of Practical X-Ray Fluorescence Analysis*, eds. B. Beckhoff, h. B. Kanngießer, N. Langhoff, R. Wedell and H. Wolff, Springer Berlin Heidelberg, Berlin, Heidelberg, 2006, pp. 411–432.
69. R. Tertian and F. Claisse, *Principles of quantitative X-ray fluorescence analysis*, Heyden, 1982.
70. Handheld XRF: How it works, https://www.bruker.com/products/x-ray-diffraction-and-elemental-analysis/handheld-xrf/how-xrf-works.html, (accessed 02/07/2019).
71. F. Scholze, A. Longoni, C. Fiorini, L. Strüder, N. Meidinger, R. Hartmann, N. Kawahara and T. Shoji, in *Handbook of Practical X-Ray Fluorescence Analysis*, eds. B. Beckhoff, h. B. Kanngießer, N. Langhoff, R. Wedell and H. Wolff, Springer Berlin Heidelberg, Berlin, Heidelberg, 2006, pp. 199–308.
72. R. Jenkins, in *X-Ray Fluorescence Spectrometry*, John Wiley & Sons, Inc., 1999, ch. 7, pp. 111–121.
73. W. Zamechek, in *Verified Syntheses of Zeolitic Materials*, eds. H. Robson and K. P. Lillerud, Elsevier Science, Amsterdam, 2001, pp. 51–53.
74. A. M. Committee, *Analytical Methods Committee Technical Briefs*, 2008, **No. 29**.
75. CHN Elemental Microanalysis, https://www.ucl.ac.uk/pharmacy/facilities/research-services/chn-elemental-microanalysis, (accessed 03/05/2019).
76. C/H/N-Analysis, https://www.univie.ac.at/Mikrolabor/chn_eng.htm, (accessed 03/05/2019).
77. R. Bardestani, G. S. Patience and S. Kaliaguine, *Can. J. Chem. Eng.*, 2019, **97**, 2781-2791.
78. M. Thommes, K. Kaneko, A. V. Neimark, J. P. Olivier, F. Rodriguez-Reinoso, J. Rouquerol and K. S. W. Sing, *Pure Appl. Chem.*, 2015, **87**, 1051–1069.
79. J. Rouquerol, F. Rouquerol, P. Llewellyn, G. Maurin and K. S. W. Sing, *Adsorption by Powders and Porous Solids: Principles, Methodology and Applications*, Elsevier Science, 2013.
80. S. Brunauer, P. H. Emmett and E. Teller, *J. Am. Chem. Soc.*, 1938, **60**, 309–319.
81. J. Rouquerol, P. Llewellyn and F. Rouquerol, in *Stud. Surf. Sci. Catal.*, eds. P. L. Llewellyn, F. Rodriquez-Reinoso, J. Rouqerol and N. Seaton, Elsevier, 2007, vol. 160, pp. 49–56.
82. K. Akhtar, S. A. Khan, S. B. Khan and A. M. Asiri, in *Handbook of Materials Characterization*, ed. S. K. Sharma, Springer International Publishing, Cham, 2018, . pp. 113–145.
83. A. Ul-Hamid, *A Beginners' Guide to Scanning Electron Microscopy*, Springer International Publishing, 2018.
84. G. Bonilla, I. Díaz, M. Tsapatsis, H.-K. Jeong, Y. Lee and D. G. Vlachos, *Chem. Mater.*, 2004, **16**, 5697–5705.
85. M. B. J. Roeffaers, R. Ameloot, M. Baruah, H. Uji-i, M. Bulut, G. De Cremer, U. Müller, P. A. Jacobs, J. Hofkens, B. F. Sels and D. E. De Vos, *J. Am. Chem. Soc.*, 2008, **130**, 5763–5772.
86. S. Cao, F. Tao, Y. Tang, Y. Li and J. Yu, *Chem. Soc. Rev.*, 2016, **45**, 4747–4765.
87. K. Grob, *Restek Advantage*, 1997, **3**.
88. K. Grob, *Restek Advantage*, 1998, **2**.
89. E. de Hoffmann and V. Stroobant, *Mass Spectrometry: Principles and Applications*, Wiley, 2013.

90. K. Shinada, S. Horiike, S. Uchiyama, R. Takechi and T. Nishimoto, *Shimadzu Review*, 2012.
91. Z. Wang, N. Lock, R. Whitney and C. M. Taylor, *Shimadzu*, 2014.

3. Project Aims

In brief, this project aims to utilise the wide suite of available zeolite modification techniques, such as ion-exchange, impregnation and framework substitution, in order to produce a single catalyst material able to affect the cascade conversion of ethanol to a higher value product, with initial targets being ^{n}butanol and 1,3-butadiene.

In order to achieve this brief and build a catalyst with maximum efficiency, each stage of the catalytic cycle will be approached incrementally with optimisation undertaken throughout. In this sense, ethanol dehydrogenation will be targeted initially and optimised once a suitable catalytic centre is identified. Subsequently, centres active for the aldol condensation of acetaldehyde will be targeted and combined with the previous dehydrogenation centres in order to affect both catalytic steps in tandem. At this point the overall materials will be optimised and the sequence will continue. Crucially, this approach is able to account for any interplay of catalytic sites and their effect on all products throughout the cascade reaction. For example, a site designed to perform the aldol condensation of acetaldehyde may be particularly efficient for the condensation of ethanol to diethyl ether. If this is the case, then the site is unsuitable as this side reaction will limit acetaldehyde production and subsequent aldol condensation. Further, it is essential that each catalytic site is able to perform well under identical reaction conditions if a single reactor is desired. In order to best illustrate this, we may consider two catalytic sites, A and B. Catalyst A may be efficient for the dehydrogenation of ethanol to acetaldehyde at 400 °C whilst catalyst B may be efficient for the aldol condensation of acetaldehyde to crotonaldehyde at 200 °C. Whilst both of these materials are well optimised within their own regimes, it is not guaranteed that they would act efficiently together to achieve single step ethanol conversion to crotonaldehyde owing to the large temperature differences. For example, catalyst A may be inefficient in the production of acetaldehyde or even form a different product at 200 °C hence, the desired cascade reaction may not progress significantly towards crotonaldehyde.

The first aim of this project is to optimise ethanol dehydrogenation to acetaldehyde over zeolite catalysts. Initially, a range of commercially available H–form frameworks of varying dimensions (BEA, MFI, MOR) will be assessed to benchmark performance and assess size selectivity effects. The effect of reaction temperature will also be explored in the initial stages of this project. Metal oxide impregnated zeolites will be initial targets owing to their ease of production and scalability alongside ZnO being well known in the literature for ethanol

dehydrogenation reactions.[1-4] Following identification of an optimum framework and reaction conditions, a wider library of metal oxide impregnated zeolites will be produced and screened for their ability to produce acetaldehyde from ethanol *via* a direct dehydrogenation route (a direct dehydrogenation route is desirable owing to the requirement of H_2 in later stages of the ethanol to ^{n}butanol pathway). Following identification of the best performing candidate, optimisation of the material will be undertaken in order to improve acetaldehyde productivity and selectivity. Finally, the catalysts industrial applicability will be assessed by means of long-term stability, recyclability and regeneration tests with comparison to current literature and industrial materials.

Following identification of a highly selective zeolite-based catalyst for the transformation of ethanol to acetaldehyde, catalytic sites for the aldol condensation of the produced acetaldehyde will be investigated in combination with the ethanol dehydrogenation site. A likely starting point for this investigation will be Lewis acidic zeolite materials which have previously been proven to be effective for the aldol condensation of acetaldehyde and related compounds.[5-11] One such initial candidate could be Sn–BEA owing to its facile synthesis, well documented characterisation and useful ^{119}Sn ssNMR handle. Notably, Lewis acidic zeolites are also known to catalyse the MPV reduction of aldehydes, such as crotonaldehyde with ethanol, hence there may be potential to unlock the entire ethanol to butadiene pathway at this stage.[12-15] As for ethanol dehydrogenation materials, successful aldol condensation candidates will be optimised to maximise crotonaldehyde, ^{n}butanol or butadiene selectivity and productivity from ethanol. If crotonaldehyde is found to be the major product from ethanol when a dehydrogenation and Lewis acidic site are combined, further investigation into an efficacious MPV reduction or hydrogenation site will be undertaken in a similar manner to complete the ethanol to butadiene or ^{n}butanol pathways respectively.

In all, this project aims to identify a single catalytic material comprising multiple disparate active centres capable of upgrading ethanol into higher value products, such as ^{n}butanol or 1,3–butadiene. Once such a material is realized, investigations into catalyst productivities selectivites and lifetime will be undertaken, and the materials will be optimised.

3.1. References.

1. W. A. Lazier and H. Adkins, *J. Am. Chem. Soc.*, 1925, **47**, 1719–1722.
2. M. M. Rahman, S. D. Davidson, J. M. Sun and Y. Wang, *Top. Catal.*, 2016, **59**, 37–45.
3. C. Drouilly, J. M. Krafft, F. Averseng, H. Lauron-Pernot, D. Bazer-Bachi, C. Chizallet, V. Lecocq and G. Costentin, *Appl. Catal. A*, 2013, **453**, 121–129.

4. J. M. Vohs and M. A. Barteau, *Surf. Sci.*, 1989, **221**, 590–608.
5. V. L. Sushkevich, D. Palagin and I. I. Ivanova, *ACS Catal.*, 2015, **5**, 4833–4836.
6. V. L. Sushkevich and I. I. Ivanova, *ChemSusChem*, 2016, **9**, 2216–2225.
7. P. I. Kyriienko, O. V. Larina, S. O. Soloviev, S. M. Orlyk, C. Calers and S. Dzwigaj, *ACS Sustain. Chem. Eng.*, 2017, **5**, 207–-2083.
8. C. Wang, M. Zheng, X. Li, X. Li and T. Zhang, *Green Chem.*, 2019, **21**, 1006–1010.
9. V. L. Sushkevich, I. I. Ivanova and E. Taarning, *Green Chem.*, 2015, **17**, 2552–2559.
10. P. I. Kyriienko, O. V. Larina, N. O. Popovych, S. O. Soloviev, Y. Millot and S. Dzwigaj, *J. Mol. Catal. A*, 2016, **424**, 27–36.
11. M. Moliner, *Dalton Trans.*, 2014, **43**, 4197–4208.
12. D. Palagin, V. L. Sushkevich and I. I. Ivanova, *J. Phys. Chem. C*, 2016, **120**, 23566–23575.
13. V. L. Sushkevich, I. I. Ivanova, S. Tolborg and E. Taarning, *J. Catal.*, 2014, **316**, 121–129.
14. M. Boronat, A. Corma and M. Renz, *J. Phys. Chem. B*, 2006, **110**, 21168–21174.
15. A. Corma, M. E. Domine, L. Nemeth and S. Valencia, *J. Am. Chem. Soc.*, 2002, **124**, 3194–3195.

Results and Discussion

Chapter 4

Development of the Ethanol Dehydrogenation Reaction over Metal-modified Zeolite Materials.

4. Development of the Ethanol Dehydrogenation Reaction over Metal-modified Zeolite Materials.

Acetaldehyde is a versatile platform chemical that can be utilized in a variety of ways to manufacture higher value chemicals. Currently, the vast majority of acetaldehyde produced industrially is formed *via* the oxidation of ethylene by the Wacker process which utilizes a homogeneous $PdCl_2/CuCl_2$ catalyst system.[1] The process operates under moderate conditions giving 95% acetaldehyde yield for the two-stage process at 110 °C and 10 bar, although it requires substantial infrastructure investment and predominantly utilizes carbon sources that are typically produced from non-renewable feedstocks.[1-3] As the global market for acetaldehyde is predicted to grow to around USD 1.80 billion by 2022, meeting the demand through increased investment in expensive infrastructure and non-renewable carbon is undesirable.[4, 5]

Bioethanol is currently produced on a large scale (28 billion gallons in 2018) with production predominantly localized in the USA and Brazil, and produced by fermentation of corn and sugarcane, respectively.[6] In the USA, bioethanol is produced in excess and added to inventory as demands for fuel blending and exports have already largely been met.[7] The direct transformation of bioethanol into (bio)acetaldehyde and beyond could therefore prove to be a more sustainable route to many higher-value chemicals, one which utilizes an available and renewable carbon feedstock. Figure 4.1 outlines potential routes to higher value products following production of (bio)acetaldehyde from (bio)ethanol, namely the synthesis of ^{n}butanol[8] (Guerbet reaction) and butadiene[9] (Lebedev reaction), both *via* the aldol condensation,[10, 11] the synthesis of pyridine *via* acrolein with addition of ammonia (Chichibabin reaction),[12] and the synthesis of pentaerythritol by reaction with formaldehyde.[13]

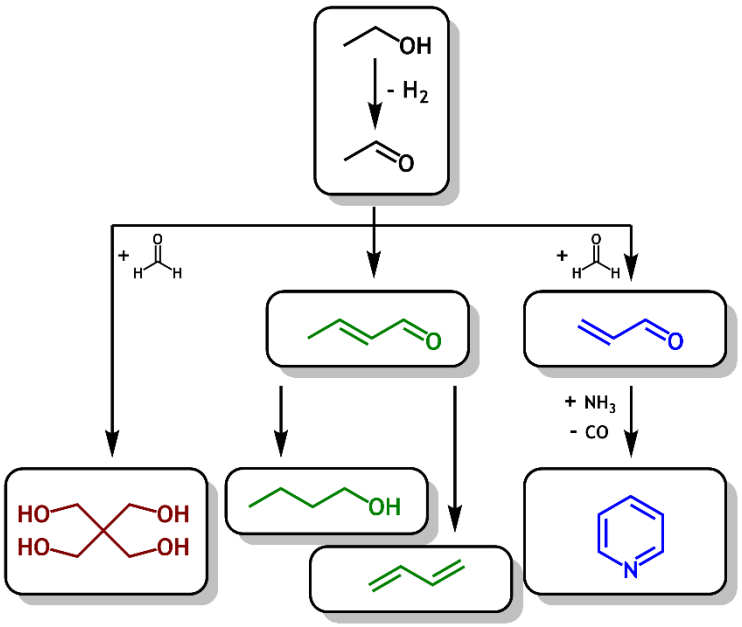

Figure 4.1: Schematic routes to higher value products available following prodcution of (bio)acetaldehyde from (bio)ethanol, such as pentaerythritol (red), butanol and butadiene (green) and pyridine (blue). Reproduced from reference 14 with permission from the Royal Society of Chemistry.[14]

Current research into the transformation of ethanol to acetaldehyde is typically practiced by two distinct methods: partial oxidation of ethanol resulting in formation of acetaldehyde and water (Equation 4.1A) and direct dehydrogenation of ethanol resulting in the formation of acetaldehyde and hydrogen (Equation 4.1B).[1]

$$A)\ CH_3CH_2OH\ (l) + \frac{1}{2}O_2(g) \rightarrow\ CH_3CHO(l) +\ H_2O\ (l)$$
$$\Delta_r H^0\ =\ -204.8\ kJ\ mol^{-1}$$
$$\Delta_r G^0\ =\ -182.4\ kJ\ mol^{-1}$$

$$B)\ CH_3CH_2OH\ (l) \rightarrow\ CH_3CHO(l) +\ H_2\ (g)$$
$$\Delta_r H^0\ =\ +81.0\ kJ\ mol^{-1}$$
$$\Delta_r G^0\ =+54.8\ \ kJ\ mol^{-1}$$

Equation 4.1: Balanced chemical equations and calculated thermodynamic quantitates for A) partial oxidation of ethanol with oxygen to form acetaldehyde and water, B) direct dehydrogenation of ethanol to form acetaldehyde and hydrogen.

Partial oxidation is an exothermic process and produces one equivalent of water as a by-product for each acetaldehyde equivalent. Owing to this, whilst lower reaction temperatures are typically utilized, an energy penalty is often incurred to separate the resultant water from the acetaldehyde product and unconverted ethanol if purified acetaldehyde or feed recycling are desired. One previous industrially practiced ethanol partial oxidation process, the Veba-Chemie process, operated at elevated temperature (500–650 °C) and utilized an elemental silver catalyst resulting in acetaldehyde yields of up to 99% at ethanol conversion values of 50–70%,

although requiring the use of fractional distillation to purify the product stream.[1, 15] Academic research into ethanol partial oxidation typically focusses on the use of supported precious metals such as Pt,[16, 17] Pd,[18] and especially Au,[19-24] at lower operating temperatures of around 200 °C. However, supported precious metal catalysts typically suffer from short lifetimes and rapid deactivation due to sintering, requiring frequent regeneration.

The direct dehydrogenation of ethanol is an endothermic process and is typically conducted at increased reaction temperatures when compared to the partial oxidation process. The reaction, however, produces a stoichiometric amount of hydrogen gas as a desirable and easily separated by-product that can be fed into the hydrogen economy, reducing reliance on the steam reforming and water-gas shift reactions for hydrogen production. Additionally, further conversion of acetaldehyde to higher-value products may require the use of hydrogen in subsequent reaction steps that can be "borrowed" from this initial dehydrogenation (such as ^{n}butanol by the Guerbet mechanism).[25] Due to the co-production of hydrogen, direct dehydrogenation of ethanol was preferred over partial oxidation in the early part of the 20th century. However, the need for frequent regeneration of the ethanol dehydrogenation catalysts (typically supported Cu based systems) pushed the partial oxidation method to be the preferred method for the production of acetaldehyde from ethanol.[1] Many current systems for direct dehydrogenation of ethanol typically focus around the use of supported metal nanoparticles and metal oxides, with related emerging technologies seeking to prevent sintering and deactivation of such supported systems.[26-30]

In particular, zeolite and porous silica materials have become an area of considerable interest as favourable supports for metal species for experimental (and computational) investigation owing to their ability to stabilize metal ions and direct metal cluster size.[24, 31-34] Traditional reduced Cu catalysts such as Cu/SiO_2, for example, are often prone to rapid deactivation through sintering in reaction times as low as 2 h TOS,[35] although careful consideration of preparation method to allow highly dispersed Cu species may allow lifetime extension of up to 500 h.[36] Cu (II) systems have also been observed to rapidly lose activity within short time frames during the ethanol dehydrogenation reaction, with the work of Yu *et al*. demonstrating complete loss of activity within 6 h TOS for bulk CuO.[31] The lifetime of Cu (II) catalysts can be extending significantly by utilising the increased dispersion effects of a zeolite support.[31, 37] Specifically, introduction of Cu^{2+} ions into the silanol nests of dealuminated BEA zeolite results in well-dispersed Cu (II) species as evidenced by XPS analysis and DR UV–VIS spectroscopy.[37] This excellent dispersion gives rise to Cu species

that are largely resistant to sintering, with Yu *et al*. demonstrating a Cu/Si–BEA system with a lifetime of over 180 h of which the first 100 h maintain a relatively stable ethanol conversion level of around 80%.[31] Additionally, throughout the reaction an acetaldehyde selectivity of >80% is maintained. The authors conclude that, throughout the course of reaction, Cu (II) species are gradually reduced to Cu (0) at which point sintering causes catalyst deactivation as evidenced by TEM and TGA analyses alongside CO-DRIFT spectroscopy. Additionally, this work by Yu *et al.* aptly demonstrates the benefits of a zeolite support in extending the lifetime of metal-based ethanol dehydrogenation systems by direct in-house comparison of Cu/Si–BEA to CuO in which an extension of stable lifetime by 100 h was achieved alongside improved acetaldehyde selectivity.[31] Additionally, Ag and Au species have been stabilised by use of a zeolite support and yielded similar results.[19, 37, 38] In particular, Ag has been supported as isolated Ag (I) species in dealuminated BEA as seen for Cu as evidenced by XPS analysis and DR–UV–Vis spectroscopy with similar reaction stabilities recorded.[37] Hence, Ag has found use as an ethanol dehydrogenation promoter for various zeolite-based ethanol transformation systems.[37-39] Zn (II) species have also been shown to be efficient dehydrogenation catalysts when incorporated into a dealuminated zeolite supports.[37, 40, 41] XPS, Py-FTIR spectroscopy and XAS analysis would appear to confirm that Zn^{2+} is readily introduced into vacant framework positions of Si–BEA,[37, 41] however, DR–UV–Vis spectroscopy performed by Kyriienko *et al*. may suggest that Zn is not fully incorporated into silanol vacancies, but instead exists partially as ZnO clusters owing to observation of an absorption band at 318 nm.[37] Work by the Li group shows that introduction of Zn into silanol nest defects of dealuminated BEA results in dehydrogenation sites which are able to achieve a stable acetaldehyde selectivity of around 45% at 70 % ethanol conversion for up to 8 h TOS.[40, 42] Qi *et al*. report an improved selectivity to acetaldehyde (60%) at lower ethanol conversion levels (40%) for a period of 7 h TOS.[41] Notably, each Zn/Si–BEA catalyst studied in this contribution exhibits an induction period of higher conversion during which ethylene is the major product. Qi *et al*. also offer a suggestion for the mechanism of ethanol dehydrogenation over framework included Zn sites (Figure 4.2). The authors state "*The process starts with dissociative adsorption of EtOH on a Zn–O atom pair to form a surface ethoxide and hydroxyl species (Steps I and II). This step is followed by abstraction of an α–H atom in what is thought to be the rate-limiting step for dehydrogenation (Step III). The α–H atom then reacts with the H atom of the hydroxyl species to form molecular hydrogen and adsorbed AcH (Step IV). The reaction cycle is completed with the desorption of H_2 and AcH (Steps V and VI).*"

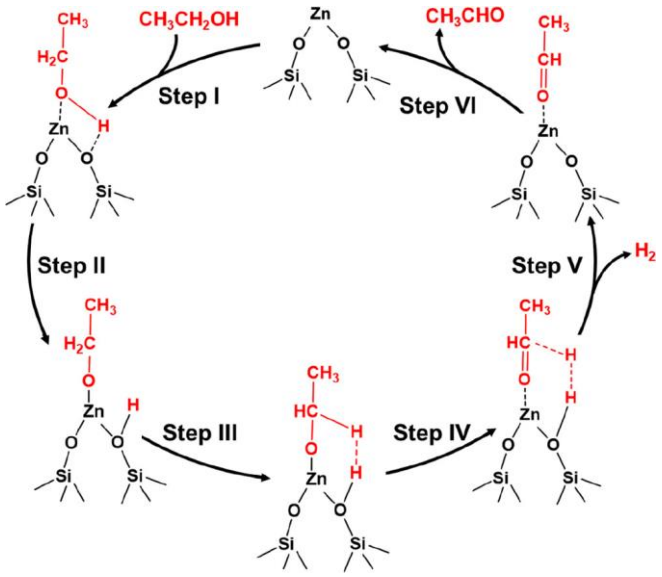

Figure 4.2: Mechanism of ethanol dehydrogenation over isolated framework Zn (II) sites as proposed by Qi *et al*. Reprinted with permission from reference 41. Copyright 2021 American Chemical Society.[41]

Additionally, some d-block metal-free zeolite systems have been realized as ethanol dehydrogenation catalysts.[15, 43] Specifically, the effect of alkaline metal activation on zeolite ultra-stable Y (USY) in the dehydrogenation of ethanol to acetaldehyde has been studied.[15, 44] Reaction of ethanol at 450 °C over USY treated with Na, K, Rb or Cs hydroxide demonstrated that treatment with NaOH was optimal in terms of both resulting ethanol conversion (14.1%) and acetaldehyde selectivity (39.4%), whilst retaining catalyst crystallinity.[15] The addition of 0.5 molar equivalents of oxygen to the ethanol feed resulted in a significant increase in both ethanol conversion (70.5%) and acetaldehyde selectivity (73.3%). Temperature-programmed surface reaction of ethanol additionally identified water as a by-product, suggesting a switch from a direct dehydrogenation to a more partial-oxidation type reaction mechanism.[15]

Further, the effect of calcination temperature on acetaldehyde selectivity for Na–ZSM–5 was explored by Bo-Qing *et al*..[43] Under relatively standard calcination conditions (550 °C), a 1% selectivity to acetaldehyde was observed at 100% ethanol conversion for reaction at 400 °C. Following an increase of calcination temperature to 1000 °C, an acetaldehyde selectivity of 77% was observed at 8.3% ethanol conversion under identical reaction conditions. A maximum acetaldehyde selectivity of 81% was observed following calcination at 1000 °C and reaction at 350 °C. The authors suggest that a higher calcination temperature changes the location of the Na^+ cation, resulting in increased basicity of the framework oxygen atoms which they predict to be active for ethanol dehydrogenation.

Overall, the production of acetaldehyde has been successfully practised industrially by a variety of methods in the past and is currently performed efficiently by the Wacker process. The future of these processes in a growing acetaldehyde market may, however, be undesirable due to the requirement for substantial infrastructure investment and the predominant utilisation of non-renewable carbon sources.[1-5] Bioethanol has been identified as a promising renewable carbon source for acetaldehyde production by either a direct dehydrogenation or partial oxidation route.[1] Many current generation catalysts, such as those based on Cu, Au and other precious metals, achieve good acetaldehyde selectivities and yields but are plagued by rapid deactivation due to sintering. Zeolites and other porous silicas have been identified as a promising class of supports for various metal-based dehydrogenation sites, exhibiting the ability to expand lifetimes significantly owing to excellent dispersion of metal particles.[19, 31, 37, 38]

In this chapter, a bottom-up approach to production of a zeolite-supported ethanol dehydrogenation catalyst is undertaken. Initially, a selection of commercially available zeolites was screened for their activity at various temperature points before the effect of zeolite counter-cation was briefly investigated. Upon identification of Na–MOR–(7) as an optimal commercial framework, a wide library of Na–MOR–(7) supported metal oxides were screened for their efficacy in the dehydrogenation of ethanol to acetaldehyde. Although a similar approach has been taken by Dai *et al.*, their investigation utilised a non-commercial dealuminated BEA support, adding an additional dealumination step that requires large scale handling of concentrated HNO_3 to undertake.[42] Following this screening exercise, ZnO/Na–MOR–(7) was identified as a promising candidate and was subject to optimisation by variation of metal-loading and zeolite counter-cation. This optimisation process was undertaken with a focus on achieving high acetaldehyde selectivity in tandem with long-term catalyst stability.

4.1. Preliminary Qualitative Investigations into the Reaction Selectivity of Ethanol Dehydrogenation over Metal-modified Zeolite Catalysts.

Initially, a wide library of zeolites with varying framework type, counter-cation and extra-framework metal species were screened in a qualitative regime in order to assess their ability to successfully catalyse the ethanol to acetaldehyde dehydrogenation reaction. The results of these screening reactions are presented in Appendix 1. All reactions were undertaken in a quartz fixed-bed flow reactor which was designed and operated in-house according to the description in Section 9.4.1.. Briefly, the catalysts were pre-treated at 150 °C before being

raised to the desired reaction temperature where ethanol was fed for a period of 2 hours. The effluent was fed *via* a −78 °C dry ice/acetone bath and the collected condensed liquid was analysed after the 2-hour TOS. Solution state ^{1}H NMR spectroscopy was used as the method of detection for liquid phase products and all NMR spectra can be seen in Appendix 1.3. It is noted that, despite ethylene not being directly detectable within the experimental set-up, the observation of water in the product effluent is strongly indicative of ethylene production from dehydration of ethanol. Another potential source of water, diethyl ether, is accounted for *via* ^{1}H NMR spectroscopy.

Although qualitative, the studies highlighted in Appendix 1 have allowed several important and project directing conclusions to be drawn. Namely, these are as follows:

- The effluent composition attained from ethanol conversion over zeolite catalysts is strongly dependent upon the zeolite framework type. In the examples given in Appendix 1, MFI and BEA materials allowed production and diffusion of aromatic products whereas the production and/or release of such products was much more limited within the MOR framework. Hence, careful selection of framework may allow the necessity for downstream product separation to be limited.
- The choice of zeolite counter-cation is paramount if reasonable degrees of ethanol dehydrogenation are desired. The use of protic (H^{+}) form zeolites promoted rapid ethanol dehydration; severely limiting acetaldehyde yield even in the presence of dehydrogenation promoters such as Zn species. Use of Na–form zeolites instead would appear to curtail the rate of ethanol dehydration, allowing higher proportions of acetaldehyde to be detected in the product effluent in all cases. Additionally, Na^{+} cations may themselves induce a small degree of ethanol dehydrogenation capability.
- The dehydrogenation of ethanol over Zn–modified zeolite systems is inefficient at 300 °C, with many systems producing no detectable acetaldehyde. Of the systems tested at the higher temperature of 400 °C, all produced a detectable quantity of acetaldehyde, implying that the dehydrogenation reaction is more favoured at higher temperatures and potentially suggesting the presence of a direct dehydrogenation mechanism.
- Of the suite of metal oxide impregnated Na–MOR materials tested, many were able to produce detectable quantities of acetaldehyde. Quantitation of these systems is required in order to elucidate the best performing materials.

4.2. Quantitative Investigations into the Reaction Selectivity of Ethanol Dehydrogenation over Metal-modified Mordenite Catalysts.

Herein, the library of metal oxides species supported on sodium-form mordenite (Na–MOR) presented in Appendix 1 are rescreened for the direct dehydrogenation of ethanol to acetaldehyde at 400 °C in a quantitative regime. Upon identification of Zn as the most promising metal species, Na–MOR, Zn–MOR and ZnO/Na–MOR were quantitatively compared in order to assess the effect of Zn speciation on catalysis, i.e. at exchange sites as Zn^{2+} cations (Zn–MOR) and as ZnO dispersed on the zeolite material (ZnO/Na–MOR). Subsequently, the effect of varying the zinc oxide loading and zeolite counter-cation for ZnO/Na–MOR is explored to arrive at the optimum catalytic material in this study, ZnO/Rb–MOR–(7) with a nominal zinc content of 3.5 Wt%. ZnO(3.5)/Rb–MOR–(7) was subjected to both a repeatability study and long-term stability test and is shown to produce repeatable performance combined with steady acetaldehyde production over 120 hours time on stream (TOS). Additionally, the ability for ZnO/Rb–MOR–(7) to resist a degree of hydration in the ethanol stream, typical of bioethanol, is explored.

4.2.1. Reassessment of various metal oxide species supported on Na–MOR–7 for the conversion of ethanol to acetaldehyde in a quantitative regime.

Appendix 1 reports a wide library of metal oxide species supported on Na–MOR were screened for their ability to produce acetaldehyde from ethanol at 400 °C. In this section, the same materials are reassessed in quantitative continuous flow regime using GC-MS with a BPX–90 detection column as detailed in Section 9.4.2 for quantification. The metal loadings of the materials as determined by ICP-OES are reiterated in Table 4.1. The resultant M_xO_y/Na–MOR–(7) materials were screened for ethanol conversion to acetaldehyde under continuous flow conditions at 400 °C. Acetaldehyde productivities normalized by catalyst mass (Figure 4.3) and molar metal content (Figure 4.4) both show ZnO/Na–MOR–(7) to be superior in terms of acetaldehyde productivity to all other supported metal oxide species tested under these reaction conditions at 1.75 h TOS. Time-resolved data is presented in Figure S4.1 and shows the same trend occurs throughout the entire reaction duration. ZnO/Na–MOR–(7) produced acetaldehyde as the major reaction product with ethylene as a minor product alongside low-intensity traces of diethyl ether and 1,3–butadiene. Most of the other metal oxide species predominantly produced ethylene as the major product as a result of preferential ethanol dehydration (Table 4.2). The major products produced from ethanol conversion over NiO/Na–

MOR–(7) and PdO/Na–MOR–(7) were CH_4 and CO suggesting that acetaldehyde was formed initially but subsequently underwent rapid decarbonylation by the catalysts, a reaction observed for several homogenous Ni and Pd catalysts,[45, 46] alongside supported Pd clusters.[26] At TOS < 0.5 h an induction period in acetaldehyde productivity is observed for some of the catalysts (ZnO/Na–MOR–(7), Co_3O_4/Na–MOR–(7) and Fe_2O_3/Na–MOR–(7)), during which period ethylene is the major product (Table 4.2 and Figure 4.5). Such induction periods have also been observed for Zn/Si–BEA by Qi *et al.*.[41]

Table 4.1: Elemental compositions of M_xO_y/Na–MOR–(7) materials obtained by ICP-OES where M = Ag, Cr, Co, Cu, Fe, Ga, Mg, Mn, Ni, Pd, Ru and Zn. Target M Wt% = 3.00. Values are averaged over multiple wavelengths where possible and appropriate. *These values were measured by ED-XRF spectroscopy as complete dissolution in HF in preparation for ICP-OES analysis could not be achieved.

Material	Al Wt%	Na Wt%	M Wt%
Ag/Na–MOR–(7)	4.88	4.21	2.92
Cr_2O_3/Na–MOR–(7)	4.80	4.15	2.69
Co_3O_4/Na–MOR–(7)	4.79	4.21	3.07
CuO/Na–MOR–(7)	5.27	4.22	4.12
Fe_2O_3/Na–MOR–(7)	5.17	4.09	3.64
Ga_2O_3/Na–MOR–(7)	4.77	4.16	1.81
MgO/Na–MOR–(7)	5.19	3.97	2.97
Mn_3O_4/Na–MOR–(7)	5.21	4.02	3.21
NiO/Na–MOR–(7)	4.81	4.27	2.91
PdO/Na–MOR–(7)	4.78	4.11	3.13*
Ru_2O_3/Na–MOR–(7)	4.77	4.14	3.64*
ZnO/Na–MOR–(7)	4.90	3.77	3.22

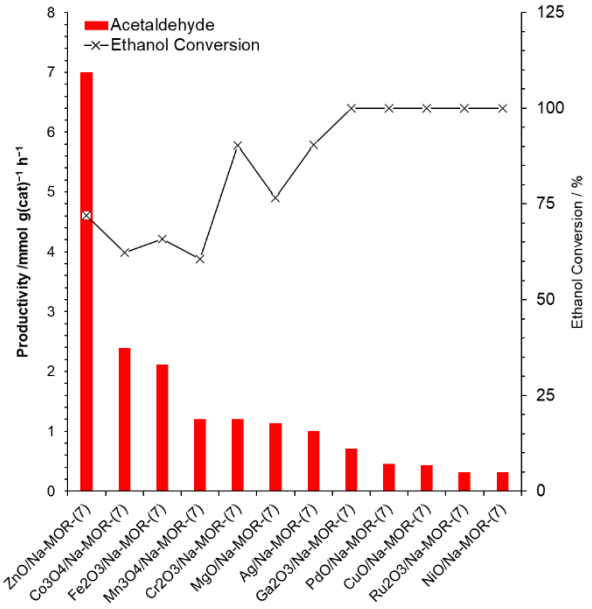

Figure 4.3: Acetaldehyde productivities normalized to catalyst mass alongside ethanol conversion values resulting from reaction of ethanol over ZnO/Na–MOR−(7), Co_3O_4/Na–MOR−(7), Fe_2O_3/Na–MOR−(7), Mn_3O_4/Na–MOR−(7), Cr_2O_3/Na–MOR−(7), Ag/Na–MOR−(7), MgO/Na–MOR−(7), Ga_2O_3/Na–MOR−(7), Ru_2O_3/Na–MOR−(7), CuO/Na–MOR−(7), PdO/Na–MOR−(7) and NiO/Na–MOR−(7) at 400 °C. Ethanol feed rate = 0.171 mmol min^{-1}, catalyst mass = 0.300 g. Detection column: BPX90. TOS = 1.75 h.

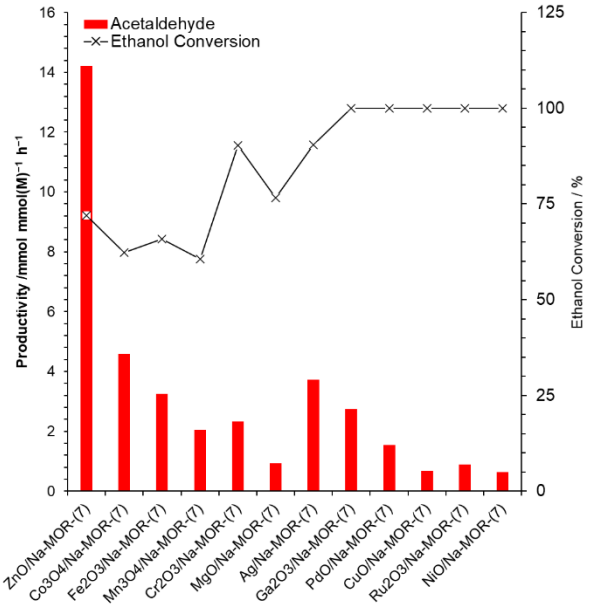

Figure 4.4: Acetaldehyde productivities normalized to metal content alongside ethanol conversion values resulting from reaction of ethanol over ZnO/Na–MOR−(7), Co_3O_4/Na–MOR−(7), Fe_2O_3/Na–MOR−(7), Mn_3O_4/Na–MOR−(7), Cr_2O_3/Na–MOR−(7), Ag/Na–MOR−(7), MgO/Na–MOR−(7), Ga_2O_3/Na–MOR−(7), Ru_2O_3/Na–MOR−(7), CuO/Na–MOR−(7), PdO/Na–MOR−(7) and NiO/Na–MOR−(7) at 400 °C. Ethanol feed rate = 0.171 mmol min^{-1}, catalyst mass = 0.300 g. Detection column: BPX90. TOS = 1.75 h.

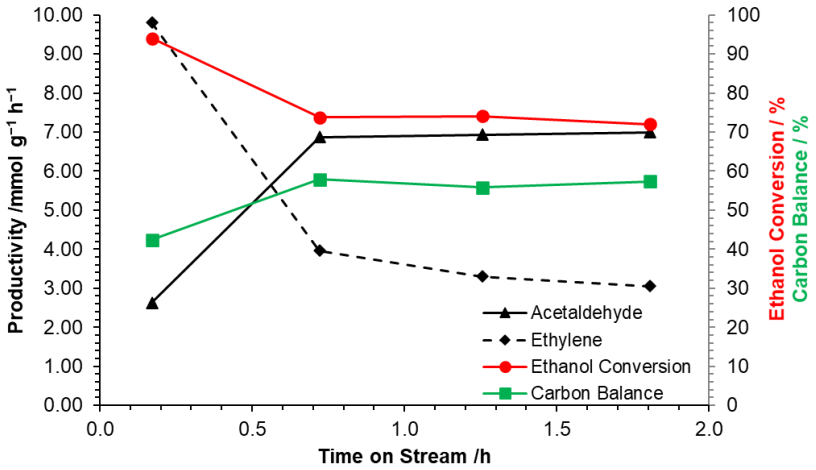

Figure 4.5: Acetaldehyde (▲) and ethylene (♦) productivities, ethanol conversion (●) and carbon balance (■, ethanol, acetaldehyde, ethylene only) resulting from reaction of ethanol over ZnO/Na–MOR–(7) for 2 hours TOS. Ethanol feed rate = 0.171 mmol min^{-1}, catalyst mass = 0.300 g. Detection column: BPX90.

Table 4.2: Acetaldehyde and ethylene productivities normalized to catalyst mass resulting from ethanol conversion over metal impregnated Na–MOR–(7) at 400 °C. Ethanol feed rate = 0.171 mmol min^{-1}, catalyst mass = 0.300 g. Detection column: BPX90.

Time on stream /h	**0.5**		**1.0**		**1.5**		**2.0**	
Productivity /mmol g_{cat}^{-1} h^{-1}	**Acetaldehyde**	**Ethylene**	**Acetaldehyde**	**Ethylene**	**Acetaldehyde**	**Ethylene**	**Acetaldehyde**	**Ethylene**
Na–MOR–(7)	0.00	2.65	1.71	3.02	1.42	3.86	1.41	4.91
Ag/Na–MOR–(7)	0.85	23.73	0.95	23.63	0.98	22.19	1.01	21.26
Cr_2O_3/Na–MOR–(7)	1.02	6.09	1.12	7.39	1.10	5.65	1.20	5.32
Co_3O_4/Na–MOR–(7)	0.58	17.78	2.25	8.32	2.48	7.05	2.40	6.21
CuO/Na–MOR–(7)	0.95	0.15	0.41	8.17	0.43	8.17	0.43	7.07
Fe_2O_3/Na–MOR–(7)	0.85	19.69	2.35	9.88	2.27	8.80	2.12	8.35
Ga_2O_3/Na–MOR–(7)	0.39	7.22	0.59	11.05	0.61	7.33	0.71	7.75
MgO/Na–MOR–(7)	0.33	4.91	1.07	3.56	1.20	3.67	1.14	3.28
Mn_3O_4/Na–MOR–(7)	1.17	13.57	1.26	10.20	1.24	9.01	1.20	8.51
NiO/Na–MOR–(7)	0.45	4.36	0.55	7.17	0.28	7.22	0.32	6.80
PdO/Na–MOR–(7)	0.26	9.58	0.39	9.56	10.36	11.17	0.45	10.24
Ru_2O_3/Na–MOR–(7)	0.63	8.81	0.65	8.81	0.67	9.24	0.32	0.53
ZnO/Na–MOR–(7)	2.63	9.80	6.87	3.96	6.93	3.30	7.00	3.05

4.2.2. The effect of zinc speciation of Zn-modified Na–MOR–7 on catalytic ethanol dehydrogenation in a quantitative regime and assessment of catalytic stability.

Following identification of ZnO/Na–MOR–(7) as a promising catalyst for the ethanol dehydrogenation reaction, Na–MOR-(7.0) materials both unmodified and modified by both zinc exchange and impregnation were tested under a quantitative regime (previously these materials had been assessed qualitatively as described in Appendix 1). Zn loadings were matched in each case to ensure that testing was more directly comparable.

Prior to catalytic testing, the materials Na–MOR-(7.0), Zn/Na–MOR-(7.0) and ZnO/Na–MOR-(7.0) were characterised using ^{27}Al solid-state NMR spectroscopy, ICP-OES elemental analysis, XRD analysis and SEM imaging. Table 4.3 contains the numerical data relevant to the catalytic tests including zinc loading and Zn/Al ratio as determined by ICP-OES.

Table 4.3: Proposed extra-framework species, zinc loadings and Zn/Al ratios determined by ICP-OES for Zn-modified Na–MOR materials. Target Zn Wt% = 3.50. Values are averaged over multiple wavelengths where possible and appropriate.

Sample	Proposed Extra-FW Species	Zn Wt%	Zn/Al Ratio
Na–MOR–(7.0)	Na^+	N/A	N/A
Zn/Na–MOR–(7.0)	Zn^{2+}, Na^+	3.70	0.31
ZnO/Na–MOR–(7.0)	ZnO, Na^+	3.71	0.32

Figure 4.6 shows the solid-state ^{27}Al NMR spectra (A), pXRD diffractograms (B) and SEM images (C) of Na–MOR-(7.0), Zn/Na–MOR-(7.0) and ZnO/Na–MOR-(7.0). All ^{27}Al NMR spectra exhibit a single resonance at approximately δ_{Al} = 55 ppm indicative of tetrahedral framework aluminium species whilst no resonances are observed at δ_{Al} = 0 ppm which would be characteristic of octahedral extra-framework alumina species (Figure 4.6A).[47, 48] It is therefore concluded that all aluminium atoms are present within the tetrahedral positions of the zeolite framework and that the effect of extra-framework alumina on the reactivity of materials is negligible. pXRD analysis strongly suggests that all materials are highly crystalline, with little amorphous character (Figure 4.6B). The noise present at diffraction angles between 2θ = 10–25 ° likely resulting from the petroleum jelly and glass slide used within sample preparation and data acquisition. All materials possess an identical diffraction pattern with no additional reflections observed; hence it may be assumed that zinc incorporation by ion-exchange and impregnation and subsequent calcination has no significant structural effect on the zeolite materials. Further, no characteristic peaks for ZnO are observed for the ZnO/Na–MOR-(7.0)

material, suggesting that the cluster size of ZnO is too small to be observable by diffraction. Finally, SEM images of the three catalysts show that all three catalysts possess very similar morphologies, seemingly unaffected by zinc incorporation method and subsequent calcination (Figure 4.6C). Again, large ZnO clusters are not observable by SEM for ZnO/Na–MOR-(7.0).

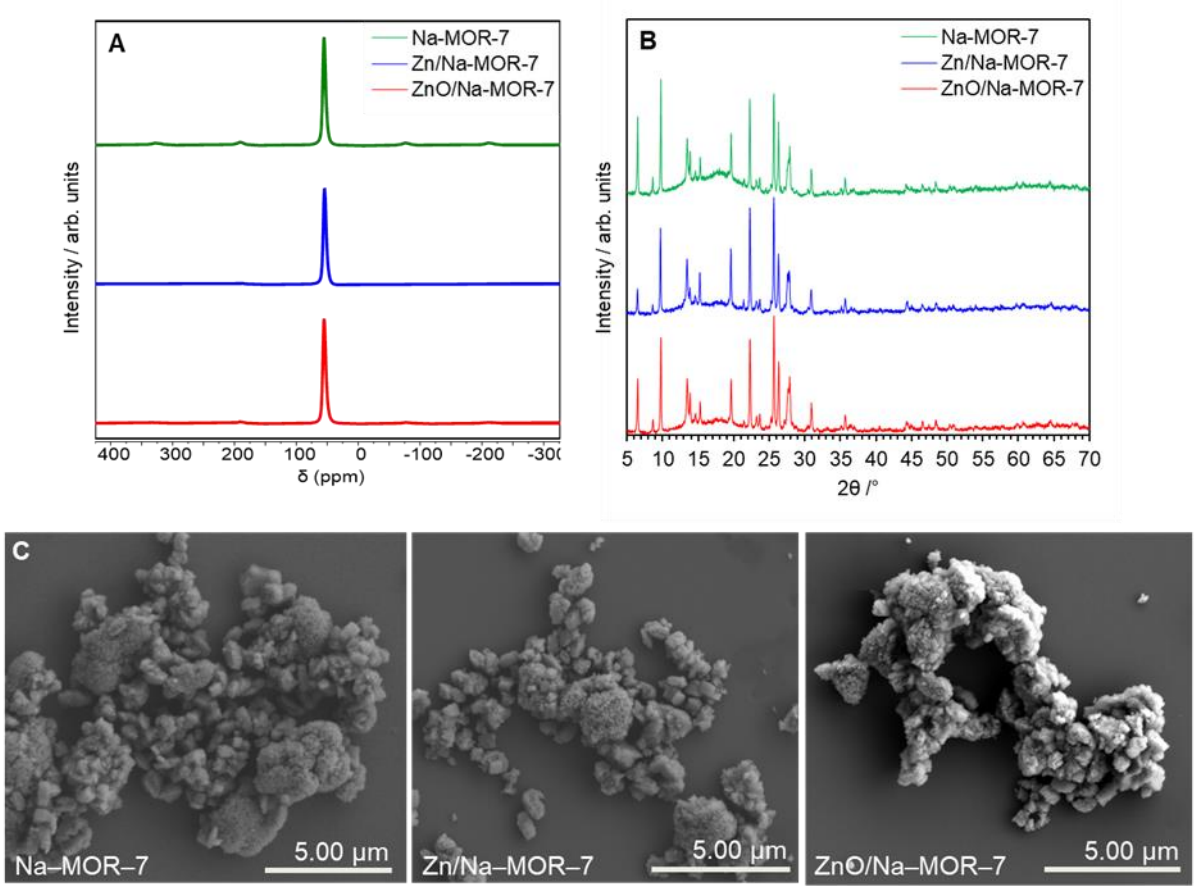

Figure 4.6: Characterisation of Na–MOR-(7.0) (green), Zn/Na–MOR-(7.0) (blue) and ZnO/Na–MOR-(7.0) (red) before reaction. A) Solid-state direct excitation ^{27}Al NMR spectra averaged over 10000 scans with a 0.2 s recycle delay. Spectrum was acquired on a Varian VNMRS 400 MHz spectrometer using a 4 mm zirconia rotor spinning at approx. 14 kHz. Spectrometer frequency: ^{27}Al = 104.20 MHz. B) pXRD diffractograms within the 2θ = 5–70° range collected at a step rate of 0.02 °. C) SEM images collected at an accelerating voltage of 5.0 kV.

Figure 4.7 shows catalytic data resulting from conversion of ethanol over Na–MOR-(7.0), Zn/Na–MOR-(7.0) and ZnO/Na–MOR-(7.0) at 400 °C. Acetaldehyde and ethylene productivities are normalised by catalyst mass. Carbon balance is calculated based on ethanol, acetaldehyde, and ethylene only as these were the only compounds calibrated for the BPX-90 column. No additional major species were detected in the mass spectra associated with these reactions, although traces of diethyl ether and 1,3–butadiene were detected. Additionally, small contributions from carbonaceous species were observed in the BID traces, namely methane, carbon monoxide, carbon dioxide, ethane, propane, and propylene.

Na–MOR-(7.0) behaves similarly to what would be expected from the qualitative screening, producing a maximum of 1.71 mmol g^{-1} h^{-1} of acetaldehyde after around 0.7 h TOS; this productivity then proceeds to decrease to around 1.41 mmol g^{-1} h^{-1} as the reaction continues (Figure 4.7A). Ethylene productivity is observed to climb from 2.65 mmol g^{-1} h^{-1} to 4.91 mmol g^{-1} h^{-1} (Figure 4.7B); an increase in ethylene productivity is concordant with a reduction in acetaldehyde productivity at a maintained conversion (approx. 60%, Figure 4.7C) and carbon balance (approx. 55%, Figure 4.7D).

Zn/Na–MOR-(7.0) exhibits perhaps the most unexpected reaction profile, producing predominantly ethylene, with very little acetaldehyde observed. This observation is in slight contradiction to that seen in the initial screening reaction, where a significant amount of acetaldehyde was seen to be produced, although only in a qualitative setup. After an induction period of around 0.7 h TOS, acetaldehyde production is seen to begin, reaching a maximum of 1.69 mmol g^{-1} h^{-1} after nearly 2 h TOS (Figure 4.7A). An ethanol conversion of 100% (Figure 4.7C) is maintained throughout the reaction, with a carbon balance in the region of 50–60% (Figure 4.7D).

ZnO/Na–MOR-(7.0) displays the highest acetaldehyde productivity following reaction of ethanol at 400 °C with a recorded maximum value of 7.00 mmol g^{-1} h^{-1} (Figure 4.7A). As is seen in Figure 4.7B, after exhibiting an initial value of 9.80 mmol g^{-1} h^{-1}, ethylene productivity is seen to rapidly decay down to 3.05 mmol g^{-1} h^{-1}. Ethanol conversion drops initially from 94% to around 72% at which point it stays constant until the end of reaction (Figure 4.7C). A carbon balance of 42% is initially recorded, however this rapidly increases and is subsequently maintained at approximately 50–60% (Figure 4.7D).

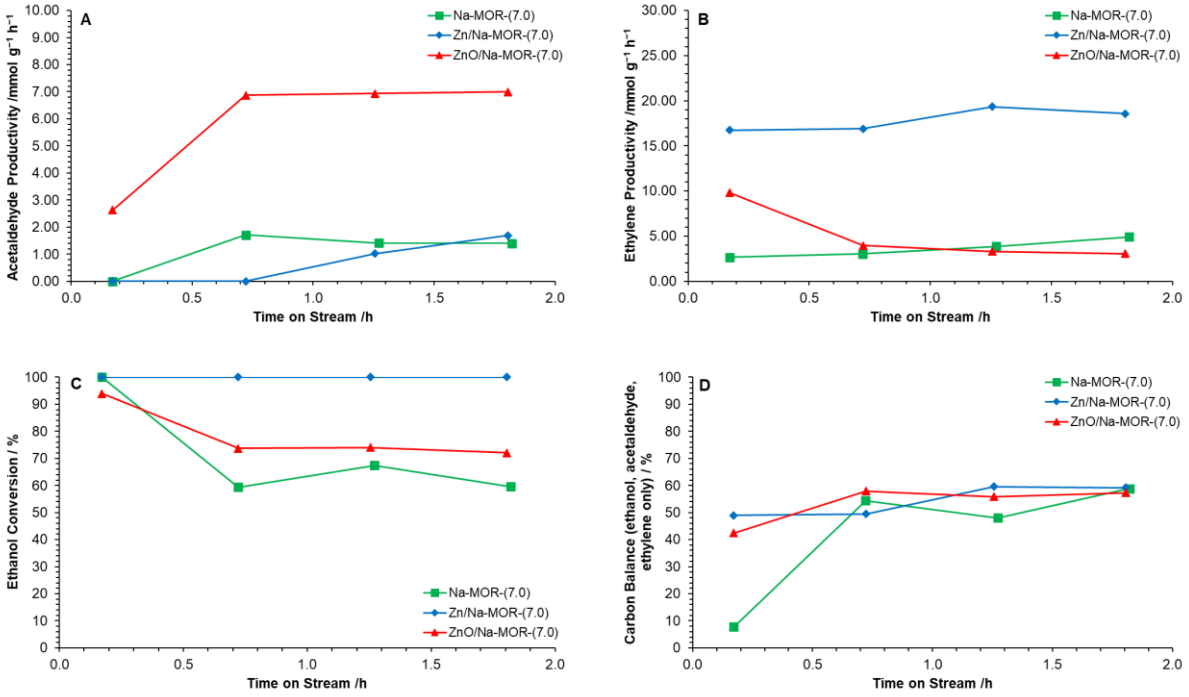

Figure 4.7: Acetaldehyde productivity (A), ethylene productivity (B), ethanol conversion (C) and carbon balance (D, ethanol, acetaldehyde, ethylene only) following reaction of ethanol over Zn modified Na–MOR materials at 400 °C for 2 h TOS. Ethanol feed rate = 0.171 mmol min^{-1}, catalyst mass = 0.300 g. Detection Column: BPX–90.

Following catalytic testing, the spent materials were analysed for their level of coke formation using CHN elemental microanalysis (Table 4.4). Additionally, post-mortem structural analysis of the catalysts was carried out using ^{27}Al solid-state NMR spectroscopy, pXRD, and SEM imaging. It is observed that carbon laydown increases in line with ethanol conversion, with Zn/Na–MOR–(7.0) producing the highest carbon value of 6.50 Wt%. Zn/Na–MOR–(7.0) is also observed to produce the highest amount of ethylene, hence has the most propensity to form large polyaromatic coke species.

Table 4.4: Catalyst coking (ΔC Wt%) of Na–MOR-(7.0), Zn/Na–MOR-(7.0) and ZnO/Na–MOR-(7.0) following ethanol dehydrogenation at 400 °C as determined by CHN microanalysis.

Sample	Catalyst Coking (ΔC Wt%)
Na–MOR–(7.0)	0.68
Zn/Na–MOR–(7.0)	6.50
ZnO/Na–MOR–(7.0)	4.03

Structural analysis of spent Na–MOR-(7.0), Zn/Na–MOR-(7.0) and ZnO/Na–MOR-(7.0) is shown in Figure 4.8 alongside the data presented previously for the as-prepared catalysts. An initial concern was that production of water at 400 °C as a side product from the undesirable ethanol dehydration reaction may result in dealumination by steaming of the zeolite

framework.[49, 50] However, the acquired solid-state ^{27}Al NMR spectra (Figure 4.8A) strongly suggest that this is not the case as no resonances indicative of octahedral extra-framework alumina species (approx. δ_{Al} = 0 ppm) are observed in any samples. Additionally, the acquired pXRD patterns show no significant loss of crystallinity following reaction, although the intensity of low-angle peaks is moderately reduced in the spent materials (Figure 4.8B). Further, SEM images of all catalysts further show no significant effect on crystal morphology following reaction with ethanol at 400 °C (Figure 4.8C). This allows the conclusion that reaction of the prepared catalysts with ethanol under the current regime affords no significant framework damage to the zeolite catalyst and that no extra-framework alumina species are created during the reaction that may serve as alternative catalytic sites. These observations strongly suggest potential for a long catalyst lifetime alongside potential regeneration and recyclability.

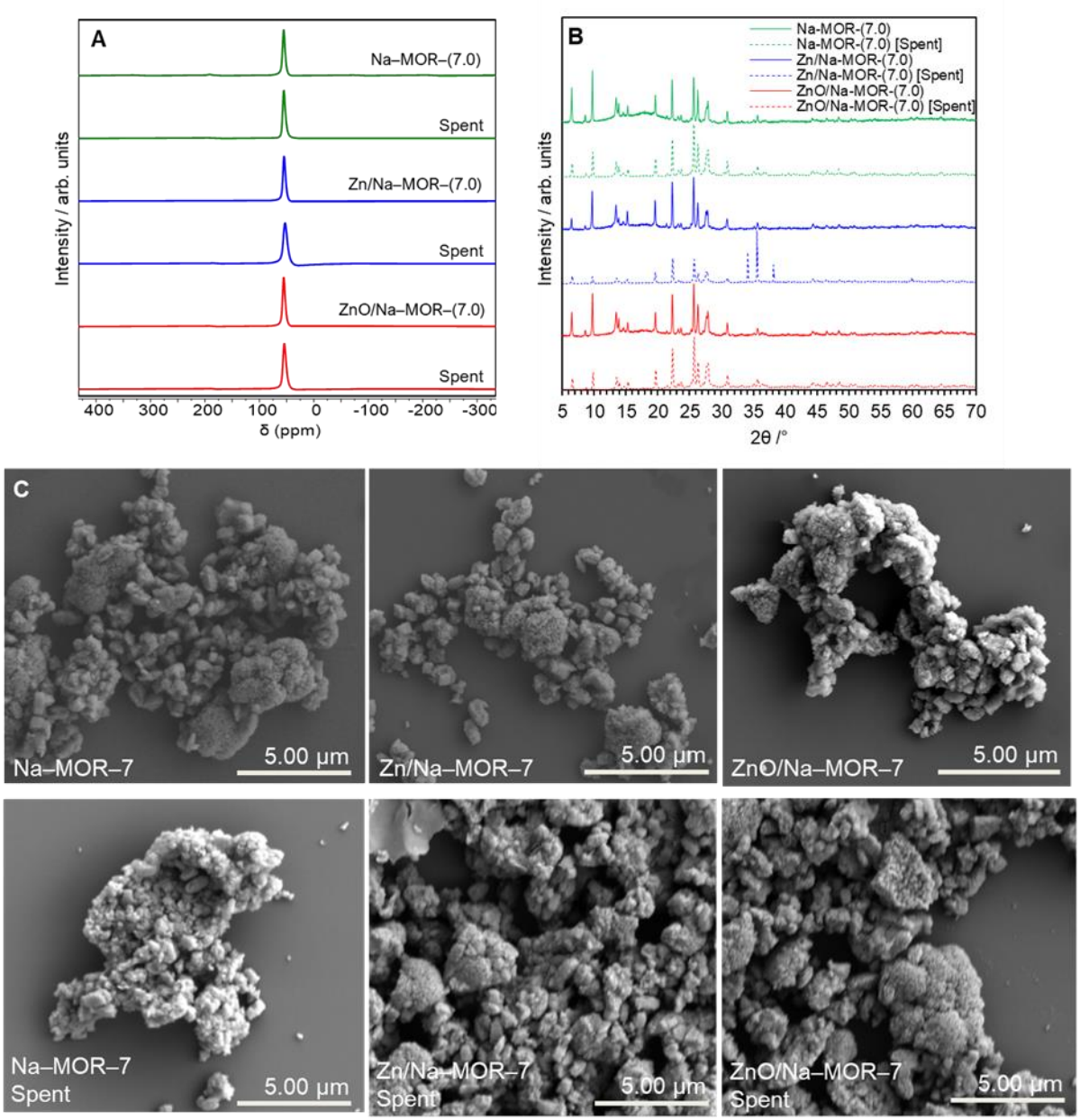

Figure 4.8: Characterisation of fresh and spent Na–MOR-(7.0) (green), Zn/Na–MOR-(7.0) (blue) and ZnO/Na–MOR-(7.0) (red) materials. A) Solid-state ^{27}Al NMR spectra averaged over 10000 scans with a 0.2 s recycle delay. Spectrum was acquired on a Varian VNMRS 400 MHz spectrometer using a 4 mm zirconia rotor spinning at approx. 14 kHz. Spectrometer frequency: ^{27}Al = 104.20 MHz. B) pXRD diffractograms within the 2θ = 5–70° range collected at a step rate of 0.02 °. C) SEM images collected at an accelerating voltage of 5.0 kV.

It can be seen, however, that the pXRD pattern for Zn/Na–MOR-(7.0) following reaction possesses new peaks at 2θ = 34.1, 35.5 and 38.2 that are not present in the as prepared material (Figure 4.8B). It was initially hypothesised that this could be resultant from reduction of Zn^{2+} cations with the H_2 liberated from ethanol dehydrogenation to form metallic Zn^0 species, or alternatively reaction of Zn^{2+} with ethanol or water to form ZnO or $Zn(OH)_2$ species. pXRD diffractograms of spent Zn/Na–MOR-(7.0), commercial Zn^0 powder, commercial ZnO and prepared $Zn(OH)_2$ are shown in Figure 4.9 alongside a sample of as-prepared Zn/Na–

MOR-(7.0) that had been reduced in pure hydrogen under reaction conditions. Whilst the sample of Zn/Na–MOR-(7.0) reduced in H_2 under reaction conditions shows development of similar peaks at 2θ = 34.1, 35.5 and 38.2 to that of spent Zn/Na–MOR-(7.0), the patterns do not seem to be an exact match of any of the proposed zinc species. This suggests that the new species are formed due to reduction of the catalyst material containing Zn^{2+} cations with H_2, so may be resultant from formation of some form of zinc aluminate species or other solid phases of the zinc materials. Preparation and characterisation of various zinc aluminate species would allow this conclusion to be further drawn. Observation of an up-field shoulder in the solid-state ^{27}Al NMR spectrum of spent Zn/Na–MOR-(7.0) (Figure 4.8A) may further support this conclusion as an up-field shoulder is normally associated with higher coordinate aluminium species.[48]

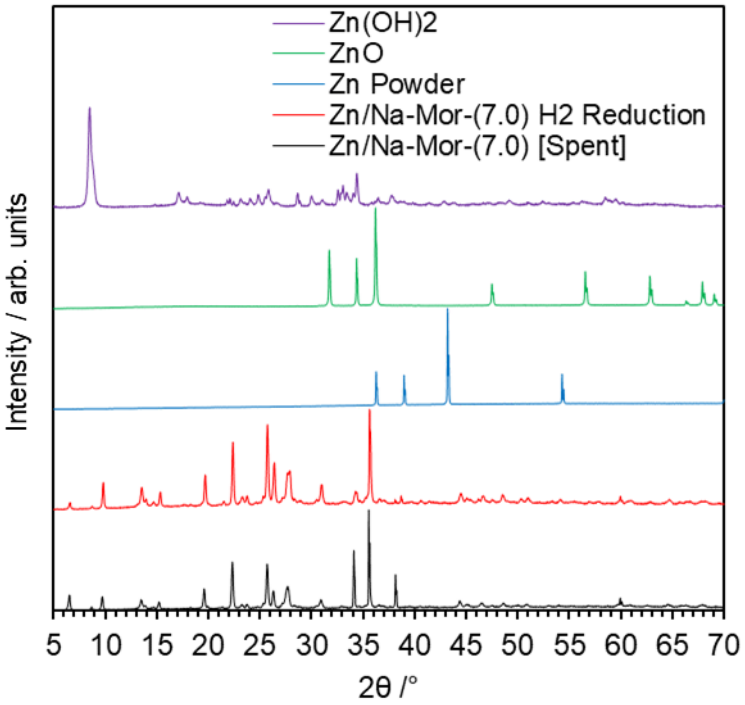

Figure 4.9: pXRD diffractograms of spent Zn/Na–MOR-(7.0), H_2 reduced Zn/Na–MOR-(7.0) and potential zinc species that could be formed during the reaction. Data collected within the 2θ = 5–70° range at a step rate of 0.02 °.

A major desirable quality of catalysts that are employed in reactions involving (bio)ethanol is their resilience towards a degree of hydration in the ethanol feedstock. Typically, (bio)ethanol can be easily purified by fractional distillation to an ethanol-water azeotrope of around 95% ethanol content by weight (89.5 mol%).[51] In order to produce anhydrous (absolute) ethanol, an entraining agent, such as benzene, cyclohexane, or heptane is added, which results in formation of a low boiling ternary azeotrope which may be removed preferentially.[51] This final azeotropic distillation step is both material and energy intensive and

it is generally desirable to be avoided if possible; hence, it is more desirable to feed ethanol of a lower grade in order to avoid this inefficient process.

In order to assess the ability of ZnO/Na-MOR-(7) to operate with more dilute, aqueous ethanol feeds, compositions of 95 mol% and 50 mol% ethanol were also fed over the catalyst at 400 °C. In each case, the liquid flow rate was kept constant (0.01 mL min^{-1}) which resulted in ethanol molar flow rates of 0.171 mmol min^{-1}, 0.162 mmol min^{-1} and 0.086 mmol min^{-1} for anhydrous (99.8%), 95% and 50% compositions respectively. Figure 4.10A, B and C show the acetaldehyde productivities for Na–MOR-(7.0), Zn/Na–MOR-(7.0) and ZnO/Na–MOR-(7.0) respectively when ethanol of anhydrous (99.8%), 95% and 50% purity are fed. As seen previously, the performance of ZnO/Na–MOR-(7.0) is superior to the other materials in terms of acetaldehyde productivity, however it is noted that the performance of all materials is improved by a degree of hydration in the ethanol feed. For each material, the highest acetaldehyde productivity is observed at a 5% hydration level (95% EtOH). Following a similar induction period, the acetaldehyde productivity for ZnO/Na–MOR– 7.0) when feeding 95% ethanol is seen to raise to 8.00 mmol g^{-1} h^{-1} compared to 7.00 mmol g^{-1} h^{-1} when feeding absolute (99.8%) ethanol. Previous literature investigation into the effect of water on ethanol conversion over bulk ZnO supports this observation, suggesting water provides a higher extent of inhibition for ethanol dehydration in comparison to dehydrogenation.[52] Additionally, in-line with the report by Rahman *et al.*, it was hypothesised that the productivity of ethylene may decrease when more water is introduced into the feed owing to equilibrium effects.[52] Figure S4.2 shows the ethylene productivity resulting from reaction of ethanol at various hydration levels over ZnO/Na–MOR-(7.0) at 400 °C and demonstrates that this hypothesis is not wholly accurate within this system, as the productivity of ethylene is relatively unchanged by introduction of 5 % water into the feed stream. The addition of 50% water, however, does have a large impact on ethylene productivity, decreasing from around 3 mmol g^{-1} h^{-1} to 2 mmol g^{-1} h^{-1} at 1.75 h TOS, although this is likely resultant from the decreased molar ethanol feed rate. The coking levels determined by the change in C Wt% (Table S4.1) are seen to decrease as hydration level increases, an observation concordant with a decrease in ethylene production. Finally, despite similar acetaldehyde and ethylene productivities at 99.8% and 95% ethanol feeds, conversion is seen to decrease from around 74% to 54% respectively, implying a reduction in formation of non-calibrated products and coke species (Figure S4.3A). This is supported by observation of an increase in carbon balance when the ethanol feed is partially hydrated (Figure S4.3B). This is a significant benefit as 95% ethanol is a typical composition

obtained following traditional fractional distillation of bio-derived ethanol and does not require the use of azeotropic distillation with entraining agents such as benzene.[44]

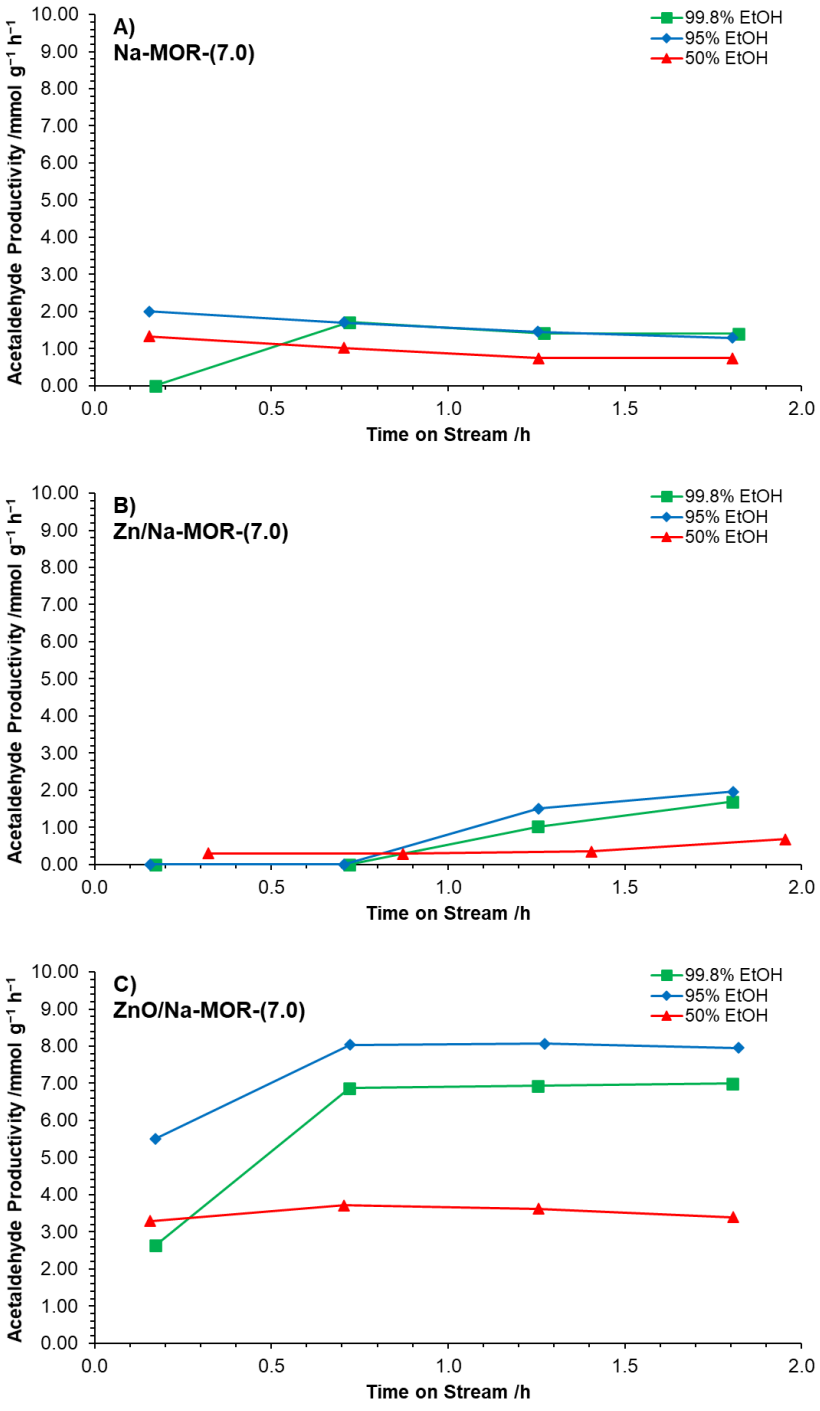

Figure 4.10: Acetaldehyde productivities for A) Na–MOR-(7.0), B) Zn/Na–MOR-(7.0) and C) ZnO/Na–MOR-(7.0) following reaction of ethanol at three different hydration levels at 400 °C for 2 h TOS. Ethanol feed rate = 0.171 mmol min^{-1}, catalyst mass = 0.300 g. Detection Column: BPX–90.

In order to assess the role of the zeolite support on the ability for ZnO to affect the dehydrogenation of ethanol to acetaldehyde at 400 °C, a comparison of catalytic results following reaction over approximately equimolar supported and non-supported ZnO was

undertaken. To this end, reaction of ethanol with a standard charge of ZnO/Na–MOR diluted in SiC was compared with an equimolar amount of bulk ZnO diluted in the same mass of SiC. Table 4.5 shows the molar Zn contents of ZnO and ZnO/Na–MOR and Figure 4.11 shows their respective acetaldehyde productivities normalised by molar Zn content. As can be seen, at equimolar Zn contents, ZnO/Na–MOR–(7.0) produces more acetaldehyde per unit Zn than unsupported ZnO. This is ascribed to a dispersion effect, with the ZnO associated with ZnO/Na–MOR–(7.0) most likely being in the form of smaller clusters, hence having a higher surface area and a higher quantity of active sites. The hypothesis of small ZnO clusters is supported by the lack of ZnO reflections in the pXRD pattern and lack of observation of ZnO particles in conventional SEM images of ZnO/Na–MOR–(7.0) (Figure 4.6B and C). In order to confirm this hypothesis, SEM-EDX mapping of ZnO/Na–MOR–(7.0) was undertaken. In order to best image the dispersion of Zn within the zeolite matrix, the sample was first set into resin before subsequent microtoming and polishing. By application of this technique some zeolite particles were able to be successfully split, allowing the crystal interior to also be imaged. As can be seen in Figure S.6, the distribution of Zn is largely homogeneous throughout the zeolite network with some larger clusters visible between zeolite particles. The observation of this largely homogenous distribution of nano-inclusions strongly supports the hypothesis that ZnO loaded onto ZnO/Na–MOR–(7.0) has a greater surface area and hence higher quantity of active sites than unsupported ZnO, leading to more efficient acetaldehyde production per molar unit of Zn.

Table 4.5: Molar Zn contents for ZnO and ZnO/Na–MOR. For ZnO/Na–MOR, Zn content was determined by ICP-OES with values averaged over multiple wavelengths where possible and appropriate.

Sample	Catalyst Mass /mg	Zn Wt%	Zn Content /mmol
ZnO	13.8	81.4	0.170
ZnO/Na–MOR–(7.0)	300	3.71	0.170

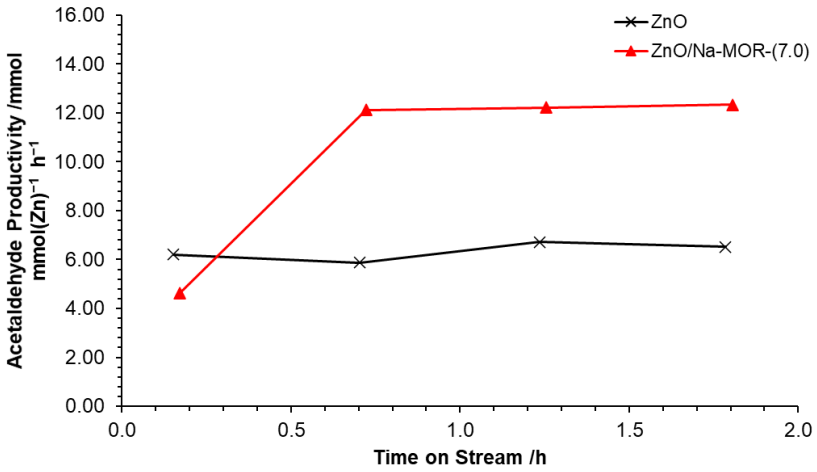

Figure 4.11: Acetaldehyde productivities normalised by Zn content for ZnO (▲) and ZnO/Na–MOR-(7.0) (×) following reaction of ethanol at 400 °C for 2 h TOS. Ethanol feed rate = 0.171 mmol min^{-1}, catalyst mass = 0.300 g. Detection Column: BPX–90.

Following identification of ZnO/Na-MOR-(7) as a promising candidate for ethanol dehydrogenation, investigation into long-term catalyst stability was undertaken. Initially, reaction of ethanol over ZnO/Na-MOR-(7) was monitored over a period of 24 h TOS at an ethanol flow rate of 0.171 mmol min^{-1}. As shown in Figure 4.12A, ethanol conversion and carbon balance remain relatively constant at 50% and 70% respectively throughout the 24-hour runtime, implying the longer-term stability of the catalyst. Additionally, it is observed that, whilst the yield of acetaldehyde remains steady at around 25% with increasing time on stream, the yield to ethylene is seen to decrease rapidly and substantially from around 15% to 3%. Plotting the productivities of acetaldehyde and ethylene over time (Figure 4.12B) confirms this observation to be ascribed to a substantial and rapid decrease in ethylene productivity whilst acetaldehyde productivity remains relatively constant. The cause of this decrease in ethylene productivity is currently under investigation but is predicted to be the result of deactivation of an acidic or basic site inherent to the zeolite material. Low-intensity traces of diethyl ether and 1,3–butadiene were also observed in the product effluent but were not calibrated for at this stage.

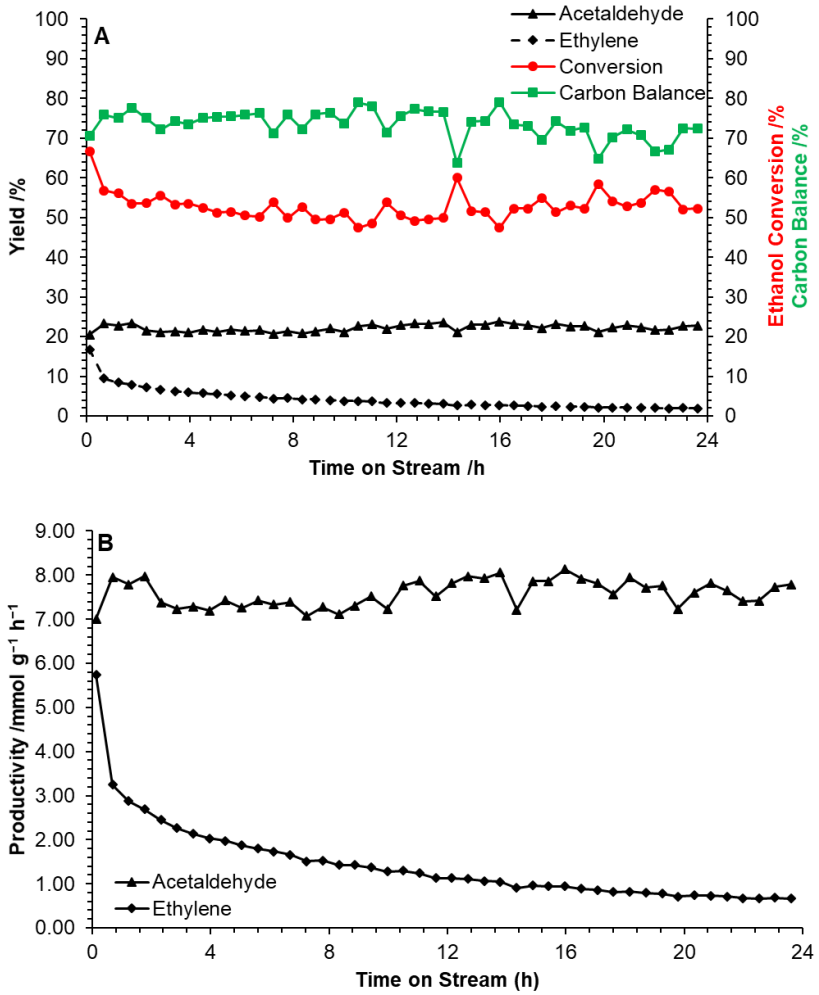

Figure 4.12: A) Acetaldehyde yield (▲), ethylene yield(♦), ethanol conversion (●) and carbon balance (■, ethanol, acetaldehyde, ethylene only) and B) Acetaldehyde productivity (▲), ethylene productivity (♦) following reaction of ethanol over ZnO/Na–MOR-(7.0) at 400 °C for 24 h TOS. Ethanol feed rate = 0.171 mmol min^{-1}, catalyst mass = 0.300 g. Detection Column: BPX–90.

Overall, it has been shown that ZnO/Na–MOR-(7.0) is the superior catalyst of those tested thus far within this report for ethanol dehydrogenation at 400 °C under flow conditions. It has been shown that introduction of zinc by a wetness impregnation method is preferable to ion-exchange for acetaldehyde production from ethanol under the given reaction conditions. Post-mortem analysis has demonstrated that ZnO/Na–MOR-(7.0), despite coking, is largely undamaged following reaction and has the potential to be oxidatively regenerated and recycled for further reaction, something which will be explored following full catalyst optimisation. Additionally, ZnO/Na–MOR-(7.0) has been shown to be able to resist a degree of hydration in the ethanol feed stream, exhibiting superior performance when 95% ethanol is fed. The benefits of the zeolite support for maximising acetaldehyde productivity have been shown. These benefits most likely arise as a result of ZnO particle dispersion, leading to a higher ZnO surface area per unit mass and a higher active site availability. ZnO/Na–MOR-(7.0) has been shown to

possess a long catalyst lifetime (24 h) with no significant deactivation observed in relation to acetaldehyde productivity.

4.2.3. Optimisation of zinc oxide loading in ZnO/Na-MOR-(7) for ethanol dehydrogenation to acetaldehyde.

In order to attempt to increase acetaldehyde productivity and selectivity of ZnO/Na–MOR-(7.0), optimisation of ZnO loading was undertaken. Initially, ZnO/Na-MOR-(7) catalysts were prepared by wetness impregnation with a targeted Zn loading of 1.0, 3.5, 5.0 and 10.0 Wt% and their catalytic performance was evaluated under flow conditions at 400 °C using the BPX-90 detection column. Upon installation of the RTX-VMS column with more extensive calibration and improved chromatography factors, the experiments were repeated to assess trend reproducibility and to obtain more accurate selectivity and carbon balance data. Additionally, during optimisation using the RTX-VMS column, the flow rate of ethanol during reactions was increased from 0.171 to 0.330 mmol min^{-1} to achieve a higher gas hourly space velocity (GHSV) and further differentiate catalyst performance at lower ethanol conversion levels.

Relevant elemental compositions of catalysts are detailed in Table 4.6, here it is seen that the zinc loadings measured by ICP-OES are close to the target value for each material. Further elemental anaysis details are shown in Table S4.2. Additionally, the Na/Al ratio of all samples is not seen to change significantly with increasing zinc loading, implying no major contribution from ion-exchange at higher loadings. In order to ensure framework retention following impregnation and calcination, pXRD analysis of the variously loaded ZnO/Na-MOR-(7) materials was undertaken. As can be seen in Figure 4.13A, all samples successfully retain a MOR framework type following the impregnation and calcination treatment. Additionally, it is observed that the sample loaded to 10.0 Wt% Zn exhibits pXRD reflections concordant with ZnO, suggesting ZnO clusters of sufficient size to produce a pXRD response are present within this material. Figure 4.13B shows the solid-state ^{27}Al NMR spectra of each ZnO/Na-MOR-(7) material and confirms that aluminium exists solely in tetrahedral framework positions ($\delta_{Al} \approx 60$ ppm) therefore ruling out any effect of extra-framework alumina on catalysis.[47] Further, conventional SEM imaging of the four catalyst variations did not show evidence of any change in catalyst morphology or large ZnO clusters on the surface of the catalyst crystals (Figure 4.13C). In order to assess the Zn distribution of each sample, SEM-EDX mapping studies were undertaken. As described in Section 9.2.5, a sample of each material was set into resin before being mechanically ground down and diamond polished. This

preparation resulted in exposure of the crystal interiors and allowed assessment of elemental distribution within the zeolite crystals. Elemental mapping of Zn within the prepared samples showed a largely homogenous distribution throughout the newly exposed surfaces of the materials with few ZnO nanoparticles present. Those ZnO particles which were present were largest and more frequently observed for samples with higher Zn loadings. (Figure S4.4–7)

Table 4.6: Nominal and measured Zn contents and Na/Al ratios for ZnO/Na–MOR–(7) materials obtained by ICP-OES. Target ZnO loading = 1.0, 3.5, 5.0, 10.0 Wt% by Zn.

Material	Nominal Zn Loading / Wt%	Measured Zn Loading / Wt%	Na/Al Ratio
ZnO/Na–MOR–(7)-1.0%	1.00	0.98	0.90
ZnO/Na–MOR–(7)-3.5%	3.50	3.22	0.90
ZnO/Na–MOR–(7)-5.0%	5.00	4.80	0.88
ZnO/Na–MOR–(7)-10%	10.00	9.79	0.91

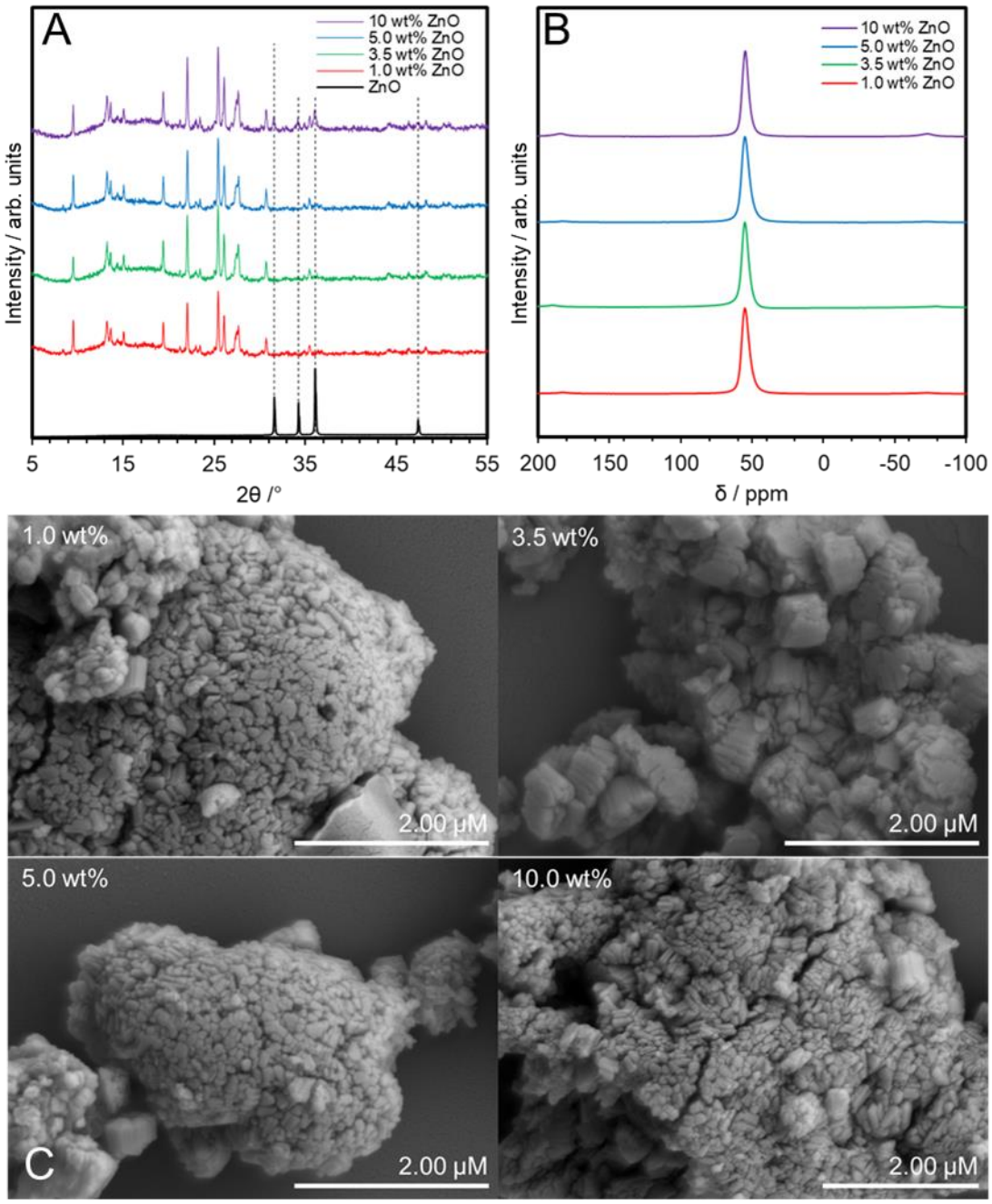

Figure 4.13: A) pXRD patterns within the 2θ = 5–55 ° range of ZnO/Na–MOR–(7) materials containing 1.0, 3.5, 5.0 and 10 Wt% ZnO by Zn. The ZnO (99.99%, Sigma-Aldrich) reference diffractogram was acquired using the same analysis conditions as those for zeolite materials; B) Solid-state ^{27}Al NMR spectra of ZnO/Na–MOR–(7) materials containing 1.0, 3.5, 5.0 and 10 Wt% ZnO by Zn; C) Conventional SEM images of ZnO/Na-MOR-(7) materials loaded at nominal 1.0, 3.5, 5.0 and 10 Wt% ZnO by Zn.

Figure 4.14 shows catalytic data resulting from reaction of ethanol over the variously loaded ZnO/Na–MOR materials at 400 °C following separation with the BPX-90 GC column. Acetaldehyde productivity normalised by catalyst mass and Zn content can be seen in Figure 4.14A and B respectively. When normalised by catalyst mass, a 10 Wt% Zn loading is seen to be superior in terms of acetaldehyde productivity, followed by 3.5 % (Figure 4.14A). Figure

4.14B shows that the productivity of the catalyst per mmol of Zn decreases as the metal loading increases, most likely resulting from larger ZnO clusters with a lesser surface area leading to fewer available active sites per unit ZnO. Interestingly, all ZnO/Na–MOR catalysts show a brief induction period in which acetaldehyde productivity increases and ethylene productivity decreases (Figure 4.14C). This feature is most pronounced for the catalysts loaded to 1.0% and 3.5% and is mirrored in the ethanol conversion rates (Figure 4.14D). This could be due to an acidic or basic site inherent to the zeolite support initially catalysing the dehydration of ethanol at a greater rate than the dehydrogenation by ZnO, leading to production of ethylene. This ethylene production may lead to coke formation which then rapidly deactivates and results in mildly higher coking values for lower Zn loaded samples (Table 4.7). Additionally, the larger amount of ZnO in the higher loaded samples may be able to better compete with, or block, the dehydration sites, resulting in a lower ethylene productivity during the induction period and lower coking.

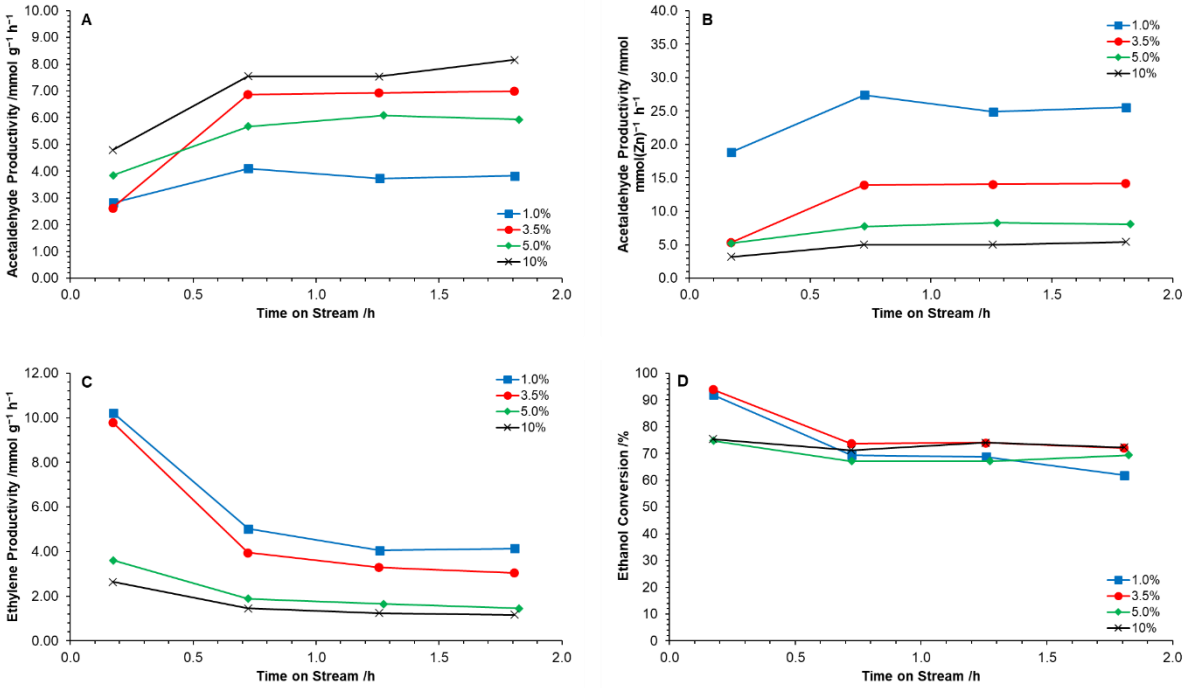

Figure 4.14: A) Acetaldehyde mass productivity, B) acetaldehyde molar productivity, C) ethylene mass productivity and D) ethanol conversion following reaction of ethanol over ZnO/Na–MOR materials at 400 °C for 4 h TOS at nominal Zn loadings of = 1.0 Wt% (■), 3.5 Wt% (●), 5.0 Wt% (♦) and 10 Wt% (▲). Ethanol feed rate = 0.171 mmol min^{-1}, catalyst mass = 0.300 g. Detection Columns: BPX-90.

Table 4.7: Catalyst coking (ΔC Wt%) of variously loaded ZnO/Na–MOR-(7.0) catalysts following ethanol dehydrogenation at 400 °C as determined by CHN microanalysis.

Sample	Catalyst Coking (ΔC Wt%)
ZnO/Na–MOR–(7.0)–1.0%	4.08
ZnO/Na–MOR–(7.0)–3.5%	4.03
ZnO/Na–MOR–(7.0)–5.0%	3.55
ZnO/Na–MOR–(7.0)–10%	2.33

Following installation of the RTX-VMS column and improved calibration, the prepared catalysts were each reassessed for ethanol dehydrogenation to acetaldehyde at 400 °C for 4 h TOS. As previously stated, the flow rate was increased from 0.171 mmol min^{-1} to 0.330 mmol min^{-1} to better differentiate performance at a higher GHSV. Figure 4.15A shows that a maximum acetaldehyde productivity is observed at 10 Wt% ZnO loading, followed by 3.5 Wt% Zn loading, when normalized by catalyst mass. The molar productivity of acetaldehyde per mole of ZnO, however, decreases with increased ZnO loading, suggesting that the catalytic efficiency of ZnO clusters decreases with increasing ZnO loading (Figure 4.15B). This is most likely resultant from the increasing size and frequency of large ZnO clusters in higher loaded samples leading to proportionally fewer available active sites. Figure 4.15D shows that ethylene selectivity decreases with increasing ZnO loading. Combined, these effects lead to the observation of a maximum acetaldehyde selectivity for ZnO/Na–MOR–(7)-3.5% (Figure 4.15C). All catalysts maintained an ethanol conversion value of around 30–50% (Figure S4.8A) at an ethanol flow rate of 0.330 mmol min^{-1}. It is noted that the induction period is not observed for these materials as the GC cycle was started after 0.5 h TOS, hence it may be concluded that the induction period is effectively complete within this time.

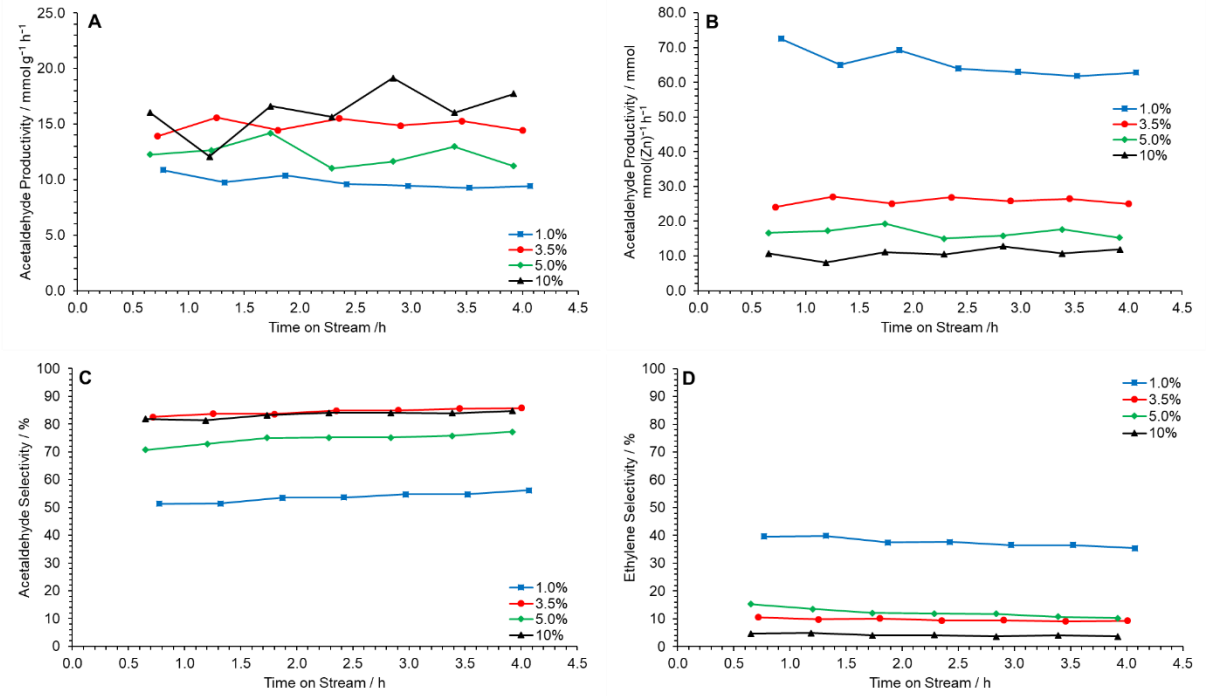

Figure 4.15: Acetaldehyde mass productivity (A), acetaldehyde molar productivity (B), acetaldehyde selectivity (C) and ethylene selectivity (D) following reaction of ethanol over ZnO/Na–MOR materials at 400 °C for 4 h TOS at nominal Zn loadings of = 1.0 Wt% (■), 3.5 Wt% (●), 5.0 Wt% (♦) and 10 Wt% (▲). Ethanol feed rate = 0.330 mmol min^{-1}, catalyst mass = 0.300 g. Detection Columns: RTX-VMS + ShinCarbon ST.

All catalysts maintained an ethanol conversion value of around 30–50% (Figure S4.8A) at an ethanol flow rate of 0.330 mmol min^{-1}. Additionally, a carbon balance of 80+% was observed for all reactions (Figure S4.8B). The yield of acetaldehyde was observed to be highest for ZnO/Na–MOR–(7)-3.5% and ZnO/Na–MOR–(7)-10.0% (Figure S4.8C). Further, elemental microanalysis of the spent catalyst charges showed the final C Wt% value of the materials following reaction decreased with increasing ZnO loading from 5.12 Wt% for ZnO/Na–MOR–(7)-1.0% to 3.02 Wt% for ZnO/Na–MOR–(7)-10% (Table 4.8). This trend correlates with a decreasing ethylene selectivity (Figure 4.15D) for more highly loaded samples and suggests that carbon laydown is likely the result of ethylene formation and subsequent aromatization as described elsewhere in the literature.[53-55]

Table 4.8: Catalyst coking (C Wt%) of variously loaded ZnO/Na–MOR-(7.0) catalysts following ethanol dehydrogenation at 400 °C as determined by CHN microanalysis.

Sample	Catalyst Coking (C Wt%)
ZnO/Na–MOR–(7.0)–1.0%	5.12
ZnO/Na–MOR–(7.0)–3.5%	4.03
ZnO/Na–MOR–(7.0)–5.0%	4.20
ZnO/Na–MOR–(7.0)–10%	3.02

Overall, these observations across both systems show ZnO/Na–MOR–(7)-3.5% to be optimal, balancing lower metal loading and high molar productivity with low ethylene selectivity. Further, decreased Zn loadings increase the efficiency of Zn usage, likely resulting from smaller cluster sizes and more available active sites as evidenced by SEM-EDX mapping. Lower Zn loadings also generally lead to increased ethylene productivity and a resulting higher carbon laydown, likely resulting from formation of aromatic coke species. Notably, the same catalysts tested under both GC regimes resulted in very similar observations, improving the validity of the above conclusions.

4.2.4. Optimisation of zeolite counter-cation in ZnO/Na-MOR-(7) for ethanol dehydrogenation to acetaldehyde.

In an attempt to further optimize the performance of zinc oxide impregnated mordenites in ethanol dehydrogenation, the effect of the zeolite counter-cation was investigated. The parent zeolite, Na–MOR–(7), was first exchanged to completion with metal nitrate solutions of K^+, Rb^+ and Cs^+ before wetness impregnation with $Zn(NO_3)_2 \cdot 6H_2O$ (3.5 Wt% by Zn) and subsequent calcination to afford ZnO(3.5)/M–MOR–(7) where M = K, Rb, or Cs. Table 4.9 shows the relevant elemental ratios and compositions for ZnO/M–MOR–(7) materials; further elemental compositions of the materials obtained by ICP-OES can be seen in Table S4.3. Whilst both K^+ and Rb^+ forms were seen to undergo complete ion-exchange, the Cs^+ exchange level was not seen to rise above 79% despite further and repeated exchange treatments. It is noted that full exchange of other large pore zeolites (BEA and FAU) with Cs^+ cations is often not observed, with many literature examples showing a maximum Cs^+ exchange level of around 80%.[56-60]

Table 4.9: Relevant elemental ratios and compositions for ZnO/M–MOR–(7) materials obtained by ICP-OES where M = Na, K, Rb, or Cs. Target ZnO loading = 3.5 Wt% by Zn.

Material	Zn / Wt%	Na/Al	K/Al	Rb/Al	Cs/Al
ZnO/Na–MOR–(7)	3.77	1.08	n.d.	n.d.	n.d.
ZnO/K–MOR–(7)	2.62	0.00	0.97	0.00	0.00
ZnO/Rb–MOR–(7)	3.12	0.00	0.00	1.00	0.00
ZnO/Cs–MOR–(7)	3.09	0.00	0.00	0.00	0.79

Figure 4.16 shows the pXRD patterns (A) and ^{27}Al solid-state NMR spectra (B) for ZnO/M–MOR–(7) materials (where M = Na, K, Rb, or Cs) indicating successful retention of both structure and tetrahedral aluminium sites following catalyst preparation.

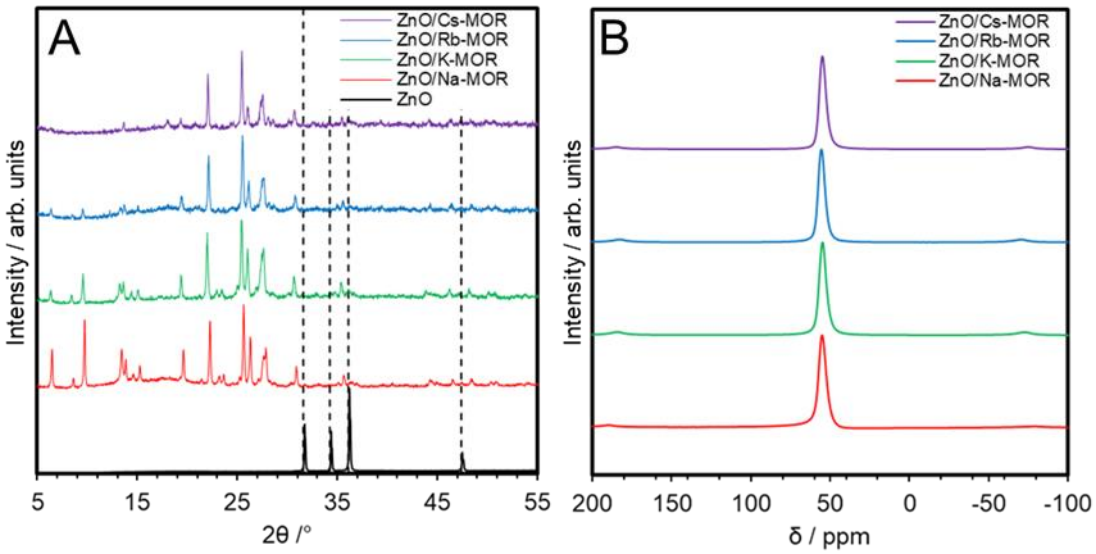

Figure 4.16: A) pXRD patterns within the 2θ = 5–55° range of ZnO/M–MOR–(7) materials where M = Na, K, Rb, or Cs. The ZnO (99.99%, Sigma-Aldrich) reference diffractogram was acquired using the same analysis conditions as those for zeolite materials; B) Solid-state ^{27}Al NMR spectra of ZnO/M–MOR–(7) materials where M = Na, K, Rb, or Cs.

Figure 4.17 shows catalytic data resulting from reaction of ethanol over the series of M–MOR and ZnO/M–MOR materials at 400 °C detected with the BPX-90 GC column at an ethanol feed rate of 0.171 mmol min^{-1}. For unmodified M–MOR catalyst, acetaldehyde production is seen to be low for all analogues, producing approximately 1.0 mmol g^{-1} h^{-1} of acetaldehyde at 60% ethanol conversion in all cases, with the exception of Na–MOR which produces a maximum of 1.7 mmol g^{-1} h^{-1} at approximately 1 h TOS (Figure 4.17A and E). The ethylene productivity of K, Rb and Cs–MOR is also similar at 1.1 mmol g^{-1} h^{-1} for Rb and Cs

analogues and a slightly higher value of 1.7 mmol g^{-1} h^{-1} for K–MOR (Figure 4.17C). Na–MOR is seen to be an outlier in terms of ethylene productivity, producing a maximum of 4.9 mmol g^{-1} h^{-1} following 2 h TOS, potentially owing to the lesser basicity of framework oxygens sites associated with Na^+ sites compared to K^+, Rb^+ or Cs^+ promoting ethanol dehydration.[15, 61]

Upon addition of ZnO to the M–MOR catalysts, the acetaldehyde productivity of the materials is seen to increase substantially, and the effect of cation choice becomes evident. Figure 4.17B and Figure 4.18A show the productivities of acetaldehyde normalised by catalyst mass and Zn content, respectively. In both cases, a trend emerged in that acetaldehyde productivity is influenced by zeolite counter cation and increases in the order of $K^+ < Cs^+ < Rb^+ < Na^+$. It is noted however that as Cs–MOR is only 80% exchanged, this may shift its relative position if total exchange were achieved. Additionally, all ZnO/M–MOR materials exhibited similar ethanol conversion levels of approximately 75%, an increase of 15% compared to the unmodified materials. Ethylene productivity (Figure 4.17D) for K, Rb and Cs analogues is seen to be similar to the unmodified catalyst, with values of approximately 1.0 mmol g^{-1} h^{-1}. Ethylene productivity for ZnO/Na–MOR is observed to be substantially higher than for Na–MOR, suggesting that an interplay of ZnO and specifically Na sites is responsible for ethanol dehydration. It is notable that this increased ethylene productivity and resultant induction period is not observed for K, Rb and Cs analogues. Additionally, the induction period of ZnO/Na–MOR is easily observed from Figure 4.17B and D, as the rapid decrease of ethylene productivity coincides with an increase in acetaldehyde productivity. As a result of limited GC calibration (BPX-90), the acetaldehyde to ethylene ratio, a pseudo measure of selectivity, was selected for materials comparison. Figure 4.18B shows that all materials exhibit an increasing selectivity to acetaldehyde as time on stream increases, most likely resulting from deactivation of the site responsible for ethanol dehydration. The general selectivity trend to acetaldehyde for zeolite counter-cation in ZnO/M–MOR catalysts observed is as follows: $Rb^+ > Cs^+ > K^+ > Na^+$.

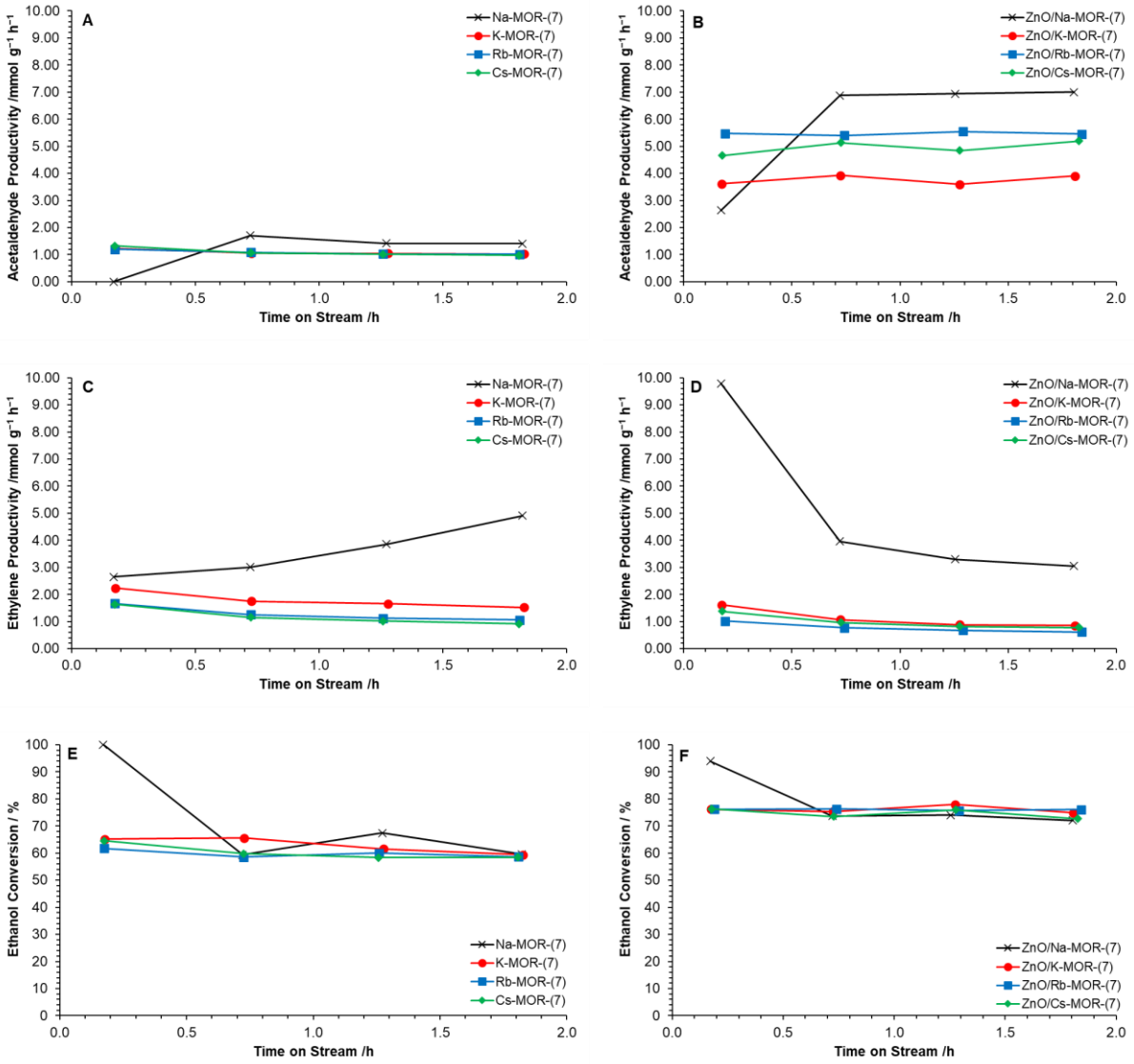

Figure 4.17: Acetaldehyde productivity (A, B), ethylene productivity (C, D) and ethanol conversion (E, F) following reaction of ethanol over M–MOR (A, C, E) and ZnO/M–MOR (B, D, E) materials at 400 °C for 4 h TOS where M = Na (▲), K (●), Rb (■) and Cs (♦). Ethanol feed rate = 0.171 mmol min^{-1}, catalyst mass = 0.300 g. Detection Column: BPX-90.

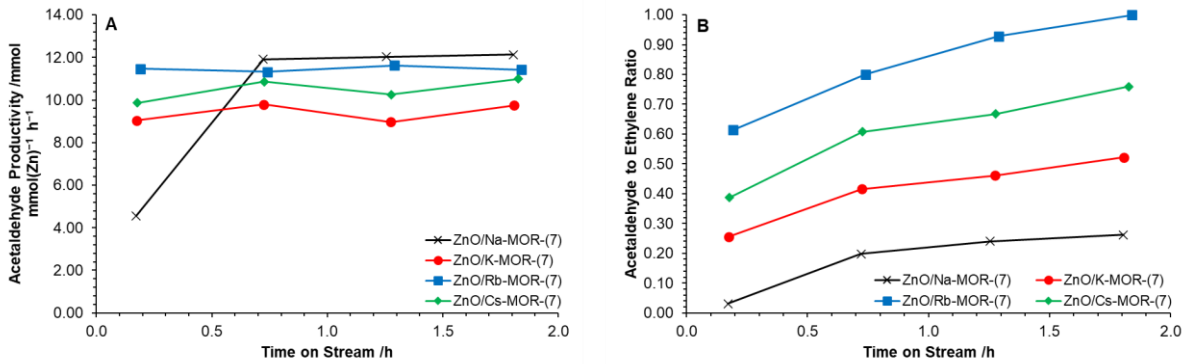

Figure 4.18: A) Acetaldehyde productivity normalised by Zn content and B) acetaldehyde to ethylene ratio for ZnO/M–MOR materials at 400 °C for 4 h TOS where M = Na (▲), K (●), Rb (■) and Cs (♦). Ethanol feed rate = 0.171 mmol min^{-1}, catalyst mass = 0.300 g. Detection Column: BPX-90.

Following installation of the RTX-VMS column and improved calibration, the prepared catalysts were each reassessed for ethanol dehydrogenation to acetaldehyde at 400 °C for 4 h TOS. As previously stated, the flow rate was increased from 0.171 mmol min^{-1} to 0.330 mmol min^{-1} to better differentiate performance at a higher GHSV. Figure 4.19 shows relevant productivity and selectivity data during the conversion of ethanol to acetaldehyde over ZnO/M–MOR–(7) (M = Na, K, Rb, or Cs) materials at 400 °C for 4 h TOS. It is observed that the zeolite extra-framework cation has a significant effect on acetaldehyde productivity and selectivity, with a general improvement in performance as follows: $Rb^+ > Cs^+ > K^+ > Na^+$. It is noted, however, that the incomplete exchange of Cs^+ ions may again have resulted in lower activity than if complete exchange were achieved. Figure 4.19A and B show that ZnO/Rb–MOR–(7) exhibits superior acetaldehyde productivity when normalized by both mass and ZnO molar content with average values of approximately 27 mmol g_{cat}^{-1} h^{-1} and 67 mmol $mmol_{ZnO}^{-1}$ h^{-1} respectively. Additionally, the selectivity to ethylene, a major side product originating from ethanol dehydration is observed to be lowest for ZnO/Rb–MOR–(7) at approximately 1% (Figure 4.19D). As a result, the selectivity to acetaldehyde for ZnO/Rb–MOR–(7) is shown to be superior to the other analogues with acetaldehyde accounting for around 95% of detected carbon containing products (Figure 4.19C). This observation is concordant with that seen for reaction in the previous GC regime, with ZnO/Rb–MOR–(7) offering the greatest acetaldehyde selectivity.

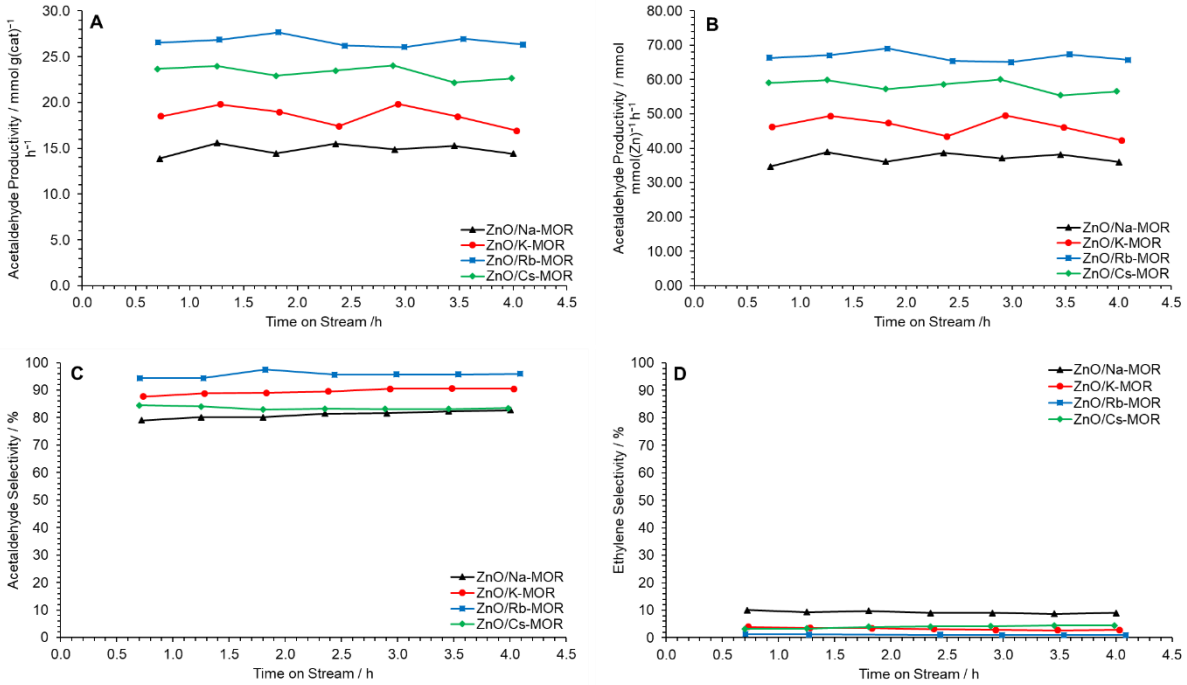

Figure 4.19: Acetaldehyde mass productivity (A), acetaldehyde molar productivity (B), acetaldehyde selectivity (C) and ethylene selectivity (D) following reaction of ethanol over ZnO/M–MOR materials at 400 °C for 4 h TOS where M = Na (▲), K (●), Rb (■) and Cs (♦). Ethanol feed rate = 0.330 mmol min^{-1}, catalyst mass = 0.300 g. Detection Columns: RTX-VMS + ShinCarbon ST.

Ethanol conversion for all reactions was around 30–50% at an ethanol flow rate of 0.330 mmol min^{-1} (Figure S4.9A). The carbon balance for all reactions was maintained at around 90% (on average) for all catalysts (Figure S4.9B). Additional carbon-containing products (CO, CO_2, CH_4) were detected but not quantified and therefore the missing carbon balance is attributed to these products and visible carbonaceous deposits. Carbon laydown values for spent catalysts as determined by CHN microanalysis are given in Table 4.10. As previously observed for ZnO/Na–MOR–(7) materials, carbon coking is generally seen to decrease with decreasing ethylene selectivity.

Table 4.10: Catalyst coking (C Wt%) of ZnO/M–MOR-(7.0) catalysts following ethanol dehydrogenation at 400 °C as determined by CHN microanalysis.

Sample	Catalyst Coking (C Wt%)
ZnO/Na–MOR–(7.0)	4.35
ZnO/K–MOR–(7.0)	4.00
ZnO/Rb–MOR–(7.0)	3.52
ZnO/Cs–MOR–(7.0)	2.34

Overall, these observations across both systems show ZnO/Rb–MOR–(7) to be optimal, maximising acetaldehyde selectivity. A general trend was observed in that $Rb^+ > Cs^+ > K^+ > Na^+$ for acetaldehyde selectivity. Lower ethylene selectivities once again decreased carbon laydown resulting from formation of aromatic coke species. Again, as the same catalysts were tested under both GC regimes and resulted in very similar observations, the validity of the above conclusions is improved. As the variable in these experiments was the zeolite counter-cation, it is proposed that modulation of the acid/base strength of their associated oxygen atoms is responsible for the observed increased acetaldehyde selectivity. As heavier alkali cations result in a less acidic/more basic associated framework oxygen atom,[62] one of two mechanisms of action are proposed. Firstly, a less acidic framework oxygen atom may result in lower rates of ethanol dehydration to ethylene, allowing increased acetaldehyde selectivity. Alternatively, the heightened base strength of the oxygen atom may interplay directly with ethanol dehydrogenation by activation of the α–hydrogen atom that is abstracted. Probing of the acid or base strength of the zeolite materials by absorption of probe molecules and subsequent analysis by DRIFTS or ssNMR could be used confirm this hypothesis. However, a mechanistic investigation, potentially by either *operando* DRIFT spectroscopy similar to that performed by Yan *et al.*,[40] or computational simulation similar to that performed by Injongkol *et al.*,[33] would likely be required to aid understanding.

4.2.5. The effect of zeolite support on acetaldehyde productivity.

Unsupported ZnO has been previously reported in the existing literature to be an efficient catalyst for the dehydrogenation of ethanol,[52, 63-65] typically achieving acetaldehyde selectivities of around 70% in a temperature range of 350–400 °C.[52, 64] The major side product of ethanol reaction over ZnO is reported to be ethylene (approximately 20–30%) with minor traces of acetone and other oxidation products. Varying catalyst pre-treatment between oxidative and inert conditions, and at different temperatures, has been shown to result in differing ethylene selectivities (38-28%) indicating the importance of the surface properties of the catalyst to the performance.[64] In addition to this finding, Morales *et al.* have reported very high acetaldehyde selectivities (88–94%) and low ethylene selectivities (1–7%) at 350 °C (6 h TOS) for a series of synthetic ZnO materials where the morphological properties of the resultant crystalline material varied, exposing different ZnO facets to different degrees.[66] In addition, ZnO supported on silica (ZnO/SiO_2, 0.5 Zn Wt%) has been shown to give 7.5% ethylene selectivity whilst achieving 62% acetaldehyde selectivity at 360 °C (10 h TOS).[67] Some of the data reported in the preceding publications is given in Table S4.4. It is clear that

due to the differing test conditions, direct comparison is challenging. However, none of the aforementioned materials were tested beyond 10 h TOS and therefore long-term performance has not been established. In addition, whilst the data reported by Morales show very good selectivities, the materials give lower calculated acetaldehyde productivities per unit zinc than those previously described in this thesis (e.g. 22.3 mmol $mmol_{Zn}^{-1}$ h^{-1} for sample ZnO–E3) showing that supporting ZnO on mordenite results in better productivities and comparable selectivities to the materials reported by Morales *et al*..[66]

The role of the newly introduced zeolite support, Rb–MOR, was assessed in-house by means of comparison between supported and unsupported ZnO alongside a physical mixture of ZnO and the zeolite support. Table 4.11 shows the catalyst compositions, Zn Wt% and molar Zn contents for each system within this study. The Zn content of ZnO/Rb–MOR–(7) was measured by ED-XRF spectroscopy to be 3.39 Wt% and its Zn content calculated to be 0.156 mmol. All ZnO systems were back calculated from this value in order to produce catalytic systems with equimolar amounts of Zn, which correlated to 12.6 mg of ZnO. Hence a 300 mg sample of ZnO/Rb–MOR–(7) was able to be compared to a 12.6 mg sample of ZnO alongside a physical mixture of 12.6 mg ZnO and 300 mg ZnO/Rb–MOR–(7), denoted as ZnO + Rb–MOR–(7.0).

Table 4.11: Molar Zn contents for ZnO/Rb–MOR–(7), a physical mixture of ZnO and Rb–MOR–(7) and ZnO. Zn content for ZnO/Rb–MOR–(7) was determined by ED-XRF with values averaged over three repeat measurements.

Sample	Catalyst Mass /mg	Zn Wt%	Zn Content /mmol
ZnO/Rb–MOR–(7)	300	3.39	0.156
ZnO + Rb–MOR–(7.0)	300 + 12.6	81.4	0.157
ZnO	12.6	81.4	0.157
ZnO	25.2	81.4	0.314

Figure 4.20 shows the selectivities to major products at 0.2 h (A) and 4.0 h (B) TOS for ZnO/Rb–MOR–(7), ZnO and a physical mixture of ZnO and Rb–MOR–(7). Acetaldehyde productivity per unit Zn and ethanol conversion levels are shown in Figure 4.20C and D. Figure 4.20B demonstrates that each catalyst achieves similar acetaldehyde selectivities of over 80% after 4 h TOS with supported ZnO/Rb–MOR–(7) achieving the highest selectivity of 89%. Figure 4.20C, however, shows the significant effect of the zeolite support in increasing acetaldehyde productivity per unit Zn. As would be expected, both unsupported ZnO (12.6 mg) and physically mixed ZnO + Rb–MOR–(7) achieve similar acetaldehyde productivities of around 20 mmol $mmol_{Zn}^{-1}$ h^{-1}, close to that reported by Morales *et al*..[66] Supported ZnO/Rb–

MOR–(7), however, is able to achieve an acetaldehyde productivity of around 48 mmol mm_{Zn}^{-1} h^{-1} marking nearly a 150% increase of productivity per unit Zn when compared to the unsupported materials. This increased acetaldehyde productivity is most likely attributed to improved Zn dispersion (as discussed in Section 4.2.3) and a resultant higher availability of active sites. The increased productivity is also due to an almost doubled ethanol conversion of around 35-40% for ZnO/Rb–MOR–(7) in comparison to around 20-25% for ZnO (12.6 mg) and ZnO + Rb–MOR–(7). In all cases, carbon balance was maintained above 80% (Figure S4.10). This result is significant as it suggests that, when correctly modified, zeolite supports are able to improve the catalytic efficiency of metal oxide materials hence allowing more effective use of diminishing metal reserves. Although zinc is not commonly regarded as a physically scarce metal, its supplies are predicted to decline within the coming century with a resultant increase in price and decrease in quality as likely outcomes.[68] Hence, awareness of how to best utilise Zn in the most sustainable manner is important, especially if applied to potential large scale industrial processes, such as the transformation of (bio)ethanol to acetaldehyde. The origin of the enhanced productivity of ZnO supported on mordenite, as well as understanding the striking influence of the extra-framework cation, will be investigated further.

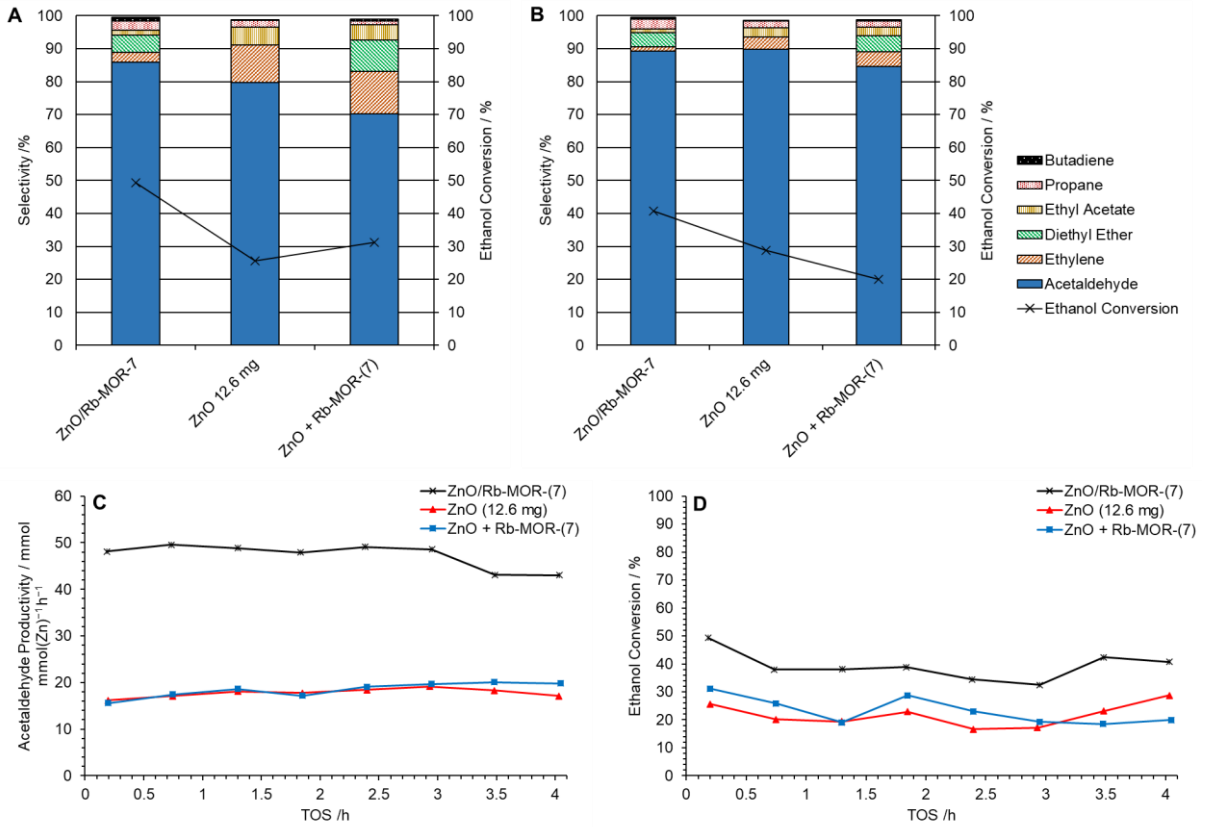

Figure 4.20: Selectivities for major products at 0.2 h TOS (A) and 4.0 h TOS (B) alongside acetaldehyde productivity per unit Zn (C) and ethanol conversion (D) for ZnO/Rb–MOR–(7) (×, 300 mg), ZnO (▲, 12.6 mg,) and a physical mixture of ZnO and Rb–MOR–(7) (■, 12.6 mg + 300 mg) at 400 °C over 4 h TOS. Ethanol feed rate = 0.399 mmol min^{-1}. Detection Columns: RTX-VMS + ShinCarbon ST.

4.2.6. Performance analysis of optimized ZnO/Rb–MOR–(7).

Upon identification of ZnO(3.5)/Rb–MOR–(7) as the optimum catalyst composition, both reproducibility studies and a long-term stability test were undertaken to assess reliability and performance over extended time scales. Figure 4.21 shows the effluent composition (A), acetaldehyde yield (B), acetaldehyde productivity (C), ethanol conversion (D) and carbon balance (E) following reaction of ethanol over ZnO(3.5)/Rb–MOR–(7) at 400 °C for 4 h TOS. The results shown are averaged over three repeat experiments with error bars denoting one standard deviation in each co-ordinate. Good reproducibility is observed across all metrics with around a 14 mmol g_{cat}^{-1} h^{-1} acetaldehyde productivity (Figure 4.21B) being observed at 50% ethanol conversion (Figure 4.21D) at an ethanol flow rate of 0.300 mmol min^{-1}. Figure 4.21C shows that the yield of acetaldehyde remains around 25%, with detected minor products including ethylene, ethane and trace amounts of diethyl ether. Figure 4.21E demonstrates that the average carbon balance is maintained above 80% across all replications, consistent with small contributions from non-calibrated carbon-containing species such as CH_4, CO and CO_2. Average coking and carbon laydown values determined by CHN microanalysis are presented

in Table 4.12. Over the three repetitions, an average carbon Wt% of the spent catalysts was determined to be 2.34% which correlates to an average coking value of 1.94 $mmol_C\ g_{cat}^{-1}$ and a carbon laydown proportion of 0.41% based on a carbon feed rate of 0.600 $mmol\ min^{-1}$.

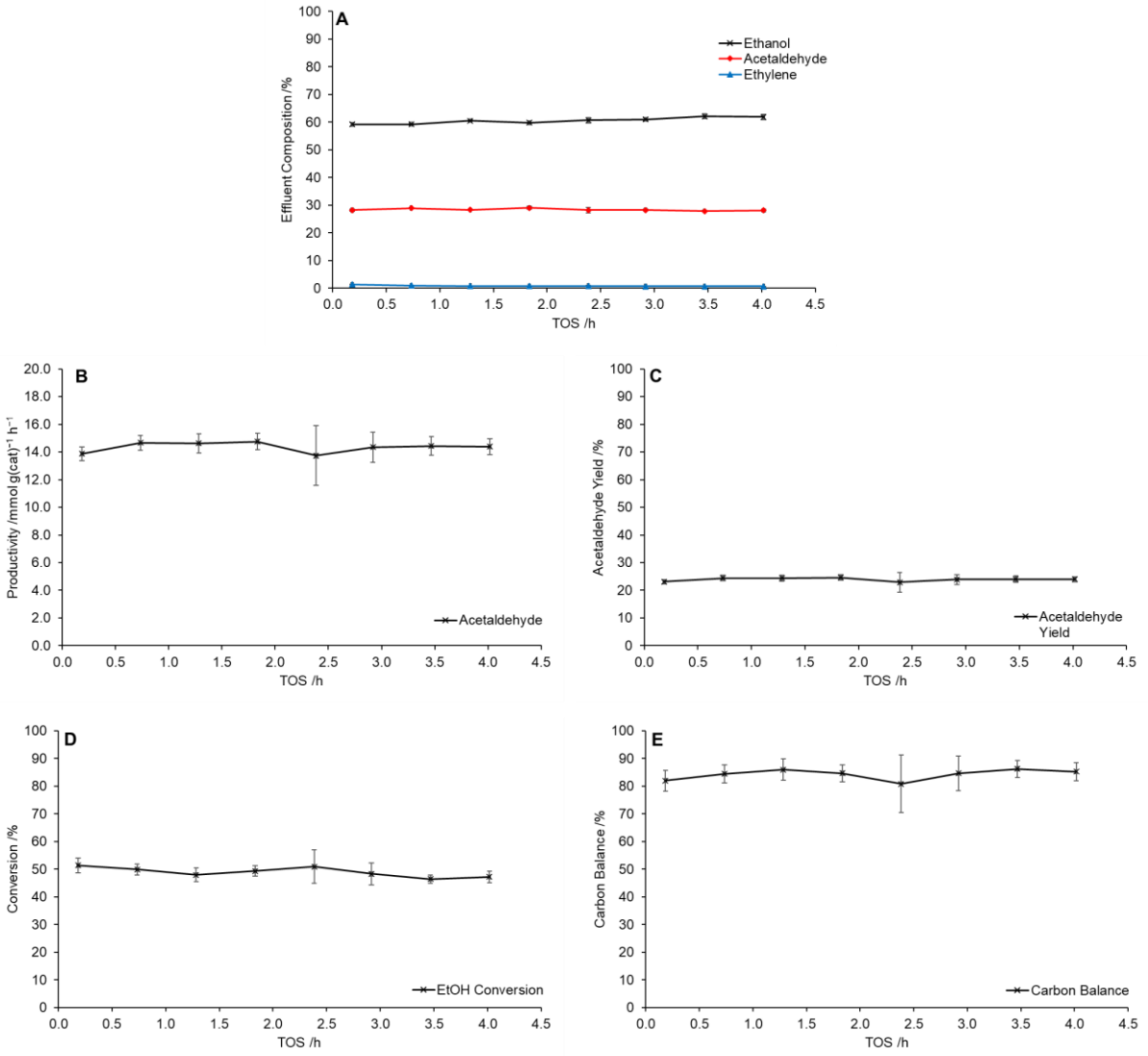

Figure 4.21: Effluent composition (A), acetaldehyde productivity (B), acetaldehyde yield (C), ethanol conversion (D) and carbon balance (E) following reaction of ethanol over ZnO(3.5)/Rb–MOR–(7) at 400 °C for 4 h TOS. Error bars are plotted as one standard deviation calculated from three experimental repeats. Effluent composition (A) depicts only major contributions from ethanol, acetaldehyde and ethylene. Ethanol feed rate = 0.300 mmol min^{-1}, catalyst mass = 0.300 g. Detection Columns: RTX-VMS + ShinCarbon ST.

Table 4.12: Catalyst coking (ΔC Wt%, $mmol_C\ g_{cat}^{-1}$) and carbon laydown for repeat runs and averages of ZnO(3.5)/Rb–MOR–(7) catalysts following ethanol dehydrogenation at 400 °C for 4 h TOS as determined by CHN microanalysis.

Run	Catalyst Coking (ΔC Wt%)	Catalyst Coking ($mmol_C\ g_{cat}^{-1}$)	Carbon Laydown (%)
1	2.36	1.97	0.41
2	2.27	1.89	0.39
3	2.33	1.94	0.40
Average	2.34	1.94	0.41

Figure 4.22 shows cumulative acetaldehyde production and acetaldehyde selectivity following reaction of ethanol at 400 °C for 120 h TOS over ZnO(3.5)/Rb–MOR–(7) at an ethanol flow rate of 0.330 mmol min^{-1}. Following an initial decrease in acetaldehyde productivity (Figure 4.23), a steady acetaldehyde productivity of around 16 mmol g^{-1} h^{-1} is achieved for the remaining 120 h TOS. Crucially, no significant deactivation is observed throughout the 120 h TOS, suggesting a long and stable catalyst lifetime. Further, throughout the course of reaction, a selectivity for acetaldehyde is maintained above 90% (Figure 4.22B). Additionally, Figure 4.23 demonstrates that an ethanol conversion of 40%, acetaldehyde yield of 25% and carbon balance of around 90% were maintained throughout the course of the reaction.

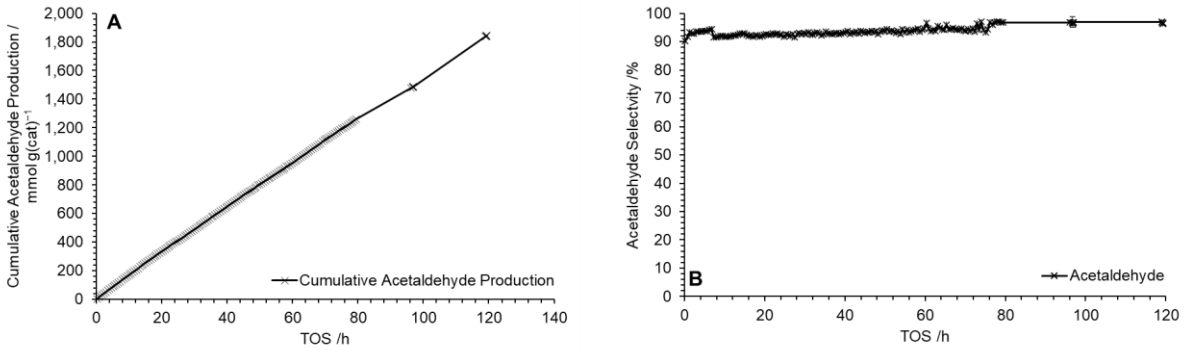

Figure 4.22: Cumulative acetaldehyde productivity (A) and acetaldehyde selectivity (B) following reaction of ethanol over ZnO(3.5)/Rb–MOR–(7) at 400 °C for 120 h TOS. Ethanol feed rate = 0.330 mmol min^{-1}, catalyst mass = 0.300 g. Detection Columns: RTX-VMS + ShinCarbon ST.

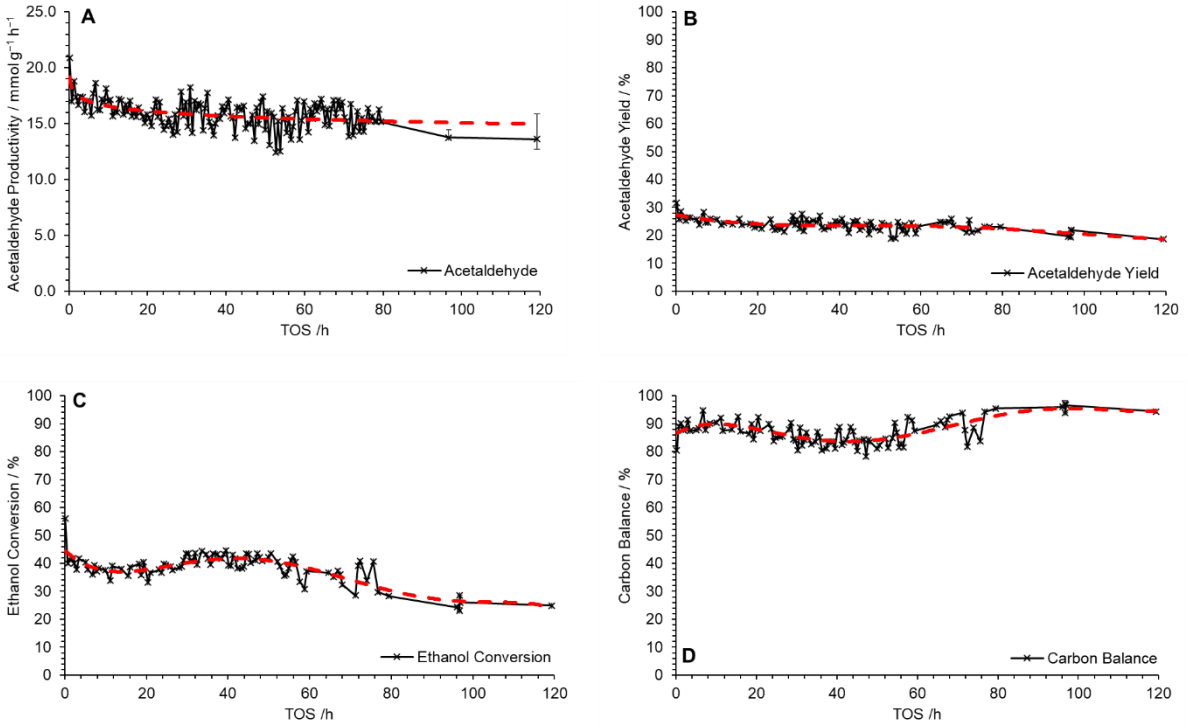

Figure 4.23: Acetaldehyde productivity (A), acetaldehyde yield (B), ethanol conversion (C) and carbon balance (D) following reaction of ethanol over ZnO(3.5)/Rb–MOR–(7) at 400 °C for 120 h TOS. Error bars dictate outliers from five subsequent averaged measurements. Ethanol feed rate = 0.330 mmol min^{-1}, catalyst mass = 0.300 g. Detection Columns: RTX-VMS + ShinCarbon ST. Red dashed lines have been added to help guide the readers' eye only.

In order to assess catalyst condition following reaction with ethanol for 120 h TOS, pXRD analysis, ^{27}Al solid-state NMR spectroscopy and CHN microanalysis were undertaken. Figure S4.11 shows the resulting pXRD diffractograms (A) and solid-state ^{27}Al spectra (B) for the fresh and spent catalysts indicating retention of both a MOR type framework and aluminium atoms exclusively in tetrahedral framework positions. Following reaction, the spent catalyst charge was found to possess a carbon content of 4.67 Wt% by CHN microanalysis, very similar to 4 h TOS (4.35 Wt%) (Table S4.5). A post-reaction carbon content of 4.67 Wt% corresponding to an average coking value of 3.89 $mmol_C\ g_{cat}^{-1}$ and an overall carbon laydown proportion of 0.02% based on a carbon feed rate of 0.660 mmol min^{-1}. Figure S4.12 demonstrates that ethylene productivity decreases significantly from 0.73 mmol $g^{-1}\ h^{-1}$ within the first two hours of reaction before levelling off to around 0.2 mmol $g^{-1}\ h^{-1}$ for the remaining reaction duration. This observation adds further credibility to the hypothesis that ethylene productivity (and subsequent aromatisation) is almost solely responsible for carbon laydown within this system and typically occurs within the initial two hours of reaction. It is proposed that through catalyst optimisation, ethylene productivity has become negligible, and deactivation through the formation of carbonaceous deposits is minimised, leading to the

extended catalyst lifetime observed. Further, it is predicted that catalyst activity may extend significantly beyond 120 h TOS, therefore further increasing industrial applicability.

4.2.6. Regeneration of ZnO(3.5)/Rb–MOR–(7) and its effects on catalyst performance.

Although no major deactivation of ZnO(3.5)/Rb–MOR–(7) was observed following reaction of ethanol for 120 h TOS, an investigation into the catalysts carbon laydown and ability to be regenerated was undertaken in the event that deactivation occurs in longer reaction timescales. To this end, a standard reaction of ethanol over ZnO(3.5)/Rb–MOR–(7) on 300 mg scale for 4 h TOS was undertaken in order to produce a coked catalyst to be regenerated. Following this reaction, the spent catalyst was treated under standard calcination conditions (550 °C for 5 h, see Section 9.3.1) in order to oxidise and remove and carbonaceous deposits. Following this, 150 mg of the regenerated catalyst was taken and subjected to a standard reaction with ethanol for 4 h TOS. In order to compare accurately, a fresh 150 mg charge of ZnO(3.5)/Rb–MOR–(7) was also subjected to a standard reaction with ethanol for 4 h TOS. Table 4.13 shows the catalyst coking values for spent and regenerated ZnO(3.5)/Rb–MOR–(7) materials in this study. Herein it can be seen that calcination is able to almost fully remove carbonaceous species from the spent ZnO(3.5)/Rb–MOR–(7) charge, with the C Wt% as measured by CHN microanalysis dropping from 2.54 to 0.10 Wt%. Figure 4.24 shows the acetaldehyde and ethylene productivities of both fresh and regenerated materials using a 150 mg catalyst charge alongside both ethanol conversion and carbon balance data. As can be seen, although the carbon content of the regenerated catalyst is effectively 0 Wt% before reaction, the reactivity is considerably different when compared to the pristine material. Notably, Figure 4.24A shows that the acetaldehyde productivity of the regenerated material (6 mmol g_{cat}^{-1} h^{-1}) is approximately half that observed for the pristine material (12 mmol g_{cat}^{-1} h^{-1}). This is likely resultant from the decreased ethanol conversion for the regenerated material (around 20%) when compared to the pristine material (around 40%) (Figure 4.24C). Further, the regenerated material is observed to produce a larger quantity of ethylene when compared to the pristine catalyst, although both show the same decreasing trend (Figure 4.24B).

Table 4.13: Catalyst coking (ΔC Wt%) for fresh, regenerated and post-run for ZnO(3.5)/Rb–MOR–(7) catalysts following ethanol dehydrogenation at 400 °C as determined by CHN microanalysis

Sample	Pre-reaction Catalyst Mass /mg	Catalyst Coking (C Wt%)
Spent ZnO(3.5)/Rb–MOR-(7.0)	300	2.54
Regenerated ZnO(3.5)/Rb–MOR-(7.0)	N/A	0.10
Spent ZnO(3.5)/Rb–MOR-(7.0)	150	2.11
Spent Regenerated ZnO(3.5)/Rb–MOR-(7.0)	150	1.36

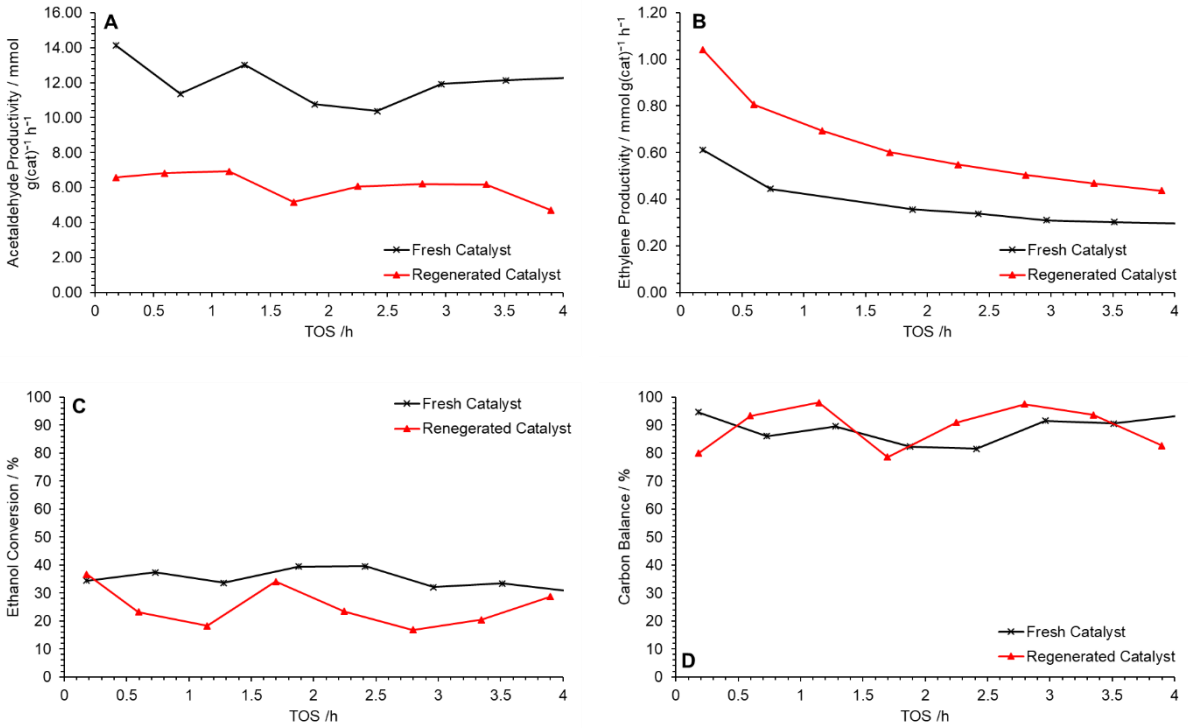

Figure 4.24: Acetaldehyde (A) and ethylene (B) productivities, ethanol conversion (C) and carbon balance (D) normalised by catalyst mass for fresh (×) and regenerated (▲) ZnO(3.5)/Rb–MOR–(7) following reaction of ethanol at 400 °C for 2 h TOS. Ethanol feed rate = 0.330 mmol min^{-1}, catalyst mass = 0.150 g. Detection Columns: RTX-VMS + ShinCarbon ST.

4.2.6. Comparison to state-of-the-art systems.

In all, ZnO(3.5)/Rb-MOR-(7) presents several advantages in comparison to other contemporary systems reported for the production of acetaldehyde from ethanol in the current literature. Primarily, ZnO(3.5)/Rb-MOR-(7) is recognised as a true direct dehydrogenation catalyst owing to the lack of O_2 co-feed required in order to produce acetaldehyde. In this regard, whilst operating at 673 K, ZnO(3.5)/Rb-MOR-(7) was able to achieve a 25% acetaldehyde yield based upon carbon fed in comparison to the 10–15 % yield reported for NaUSY-0.1 at the same temperature (Figure 5B in reference 15).[15] As a result of O_2 independence, it is highlighted that reaction of ethanol over ZnO(3.5)/Rb-MOR-(7)

additionally results in formation of hydrogen as an added-value by-product. Further, ZnO(3.5)/Rb-MOR-(7) possesses a long catalyst lifetime with little deactivation observed following 120 h TOS. It is concluded that these observations are resultant from a largely homogenous distribution of ZnO nanoparticles distributed within the zeolite micropore network that are resistant to sintering and other forms of deactivation. This long lifetime presents a considerable improvement in comparison to many contemporary catalysts that use Cu as a dehydrogenation catalyst which suffer from significant deactivation as a result of sintering within as little as 2 h TOS.[35] Other supported Cu systems, such as Cu-$ZnAl_2O_4$ also suffer from deactivation, although at slightly extended timescales (5-10 h).[69] It must be noted, however, that some modern preparation methods may lead to Cu based systems with comparable stabilities to ZnO(3.5)/Rb-MOR-(7) reported herein, e.g a Cu–BEA with a stable lifetime of 100 h,[31] a highly dispersed Cu/SiO_2 prepared by ammonia evaporation with a lifetime of 500 h,[36] and a recently reported Cu–MFI prepared by ammonia evaporation with a lifetime of 500h.[70] Additionally, copper on calcium silicate catalysts have been reported to exhibit a remarkably stable acetaldehyde production, however the longest recorded reaction duration is 20 h.[71] Finally, ZnO(3.5)/Rb-MOR-(7) may present a desirable alternative to commercial copper chromite catalysts (e.g. BASF Cu-1234-1/16-3F[72] and BASF 0203T[71]) for the synthesis of acetaldehyde from ethanol. The desire to switch from chromium containing catalysts is due to growing concern that, although active copper chromite catalysts contain Cr^{3+}, their production and disposal on an industrial scale may risk production of toxic Cr^{6+}.[71]

4.3. Conclusions.

Initially, the ability to produce acetaldehyde from ethanol at 400 °C and 300 °C was assessed for a library of H–form and Zn-modified zeolite materials (BEA, MFI, MOR). It was found that H–form zeolites did not produce any detectable quantity of acetaldehyde within this regime, rather producing large quantities of aromatic compounds and ethylene (as inferred by the detection of water). This observation is consistent with many observations within the literature of rapid ethanol dehydration to ethylene and subsequent aromatisation as catalysed by the strong Brønsted acidic sites of H–form zeolites. It is noted that H–MOR produced relatively few aromatic products when compared to H–BEA and H–MFI, potentially reducing the requirement for downstream product separation if applied on large scale. Upon modification of the H–form zeolites with Zn by both ion-exchange and impregnation, each material was observed to produce acetaldehyde at 400 °C, with only Zn-modified BEA producing acetaldehyde at 300 °C. Each system still produced considerable quantities of

aromatic products and water, likely resultant from residual Brønsted acid sites, although detection of aromatics for MOR materials was considerably lower. In order to combat ethylene production and subsequent aromatisation, Zn-modified H–MOR and Na–MOR materials were compared, with the latter showing a greatly increased acetaldehyde to ethylene ratio in the product effluent, thereby allowing conclusion that substitution of H^+ with Na^+ greatly reduces the rate of ethanol dehydration, allowing greater prevalence of the ethanol dehydrogenation reaction to acetaldehyde.

The capability of a suite of metal oxide impregnated (Ag, Cr_2O_3, Co_3O_4, CuO, Fe_2O_3, Ga_2O_3, MgO, Mn_3O_4, NiO, PdO, Ru_2O_3, ZnO) Na–MOR materials to dehydrogenate ethanol was investigated at 400 °C in both a qualitative and subsequently quantitative regime. Of the materials tested, it was concluded that ZnO/Na–MOR was superior in terms of acetaldehyde productivity both as a function of catalyst mass and of molar metal content. ZnO/Na–MOR was found to possess a lifetime of over 24 h with no appreciable decrease in acetaldehyde yield (25%).

Subsequently, ZnO/Na–MOR was optimised by both ZnO Wt% variation and alkali metal cation exchange. ZnO Wt% variation compared loadings of 1.0, 3.5, 5.0 and 10 Wt% ZnO by mass of Zn for the dehydrogenation of ethanol at 400 °C. Whilst the productivity of acetaldehyde per mol of Zn decreased substantially from 70 to 10 mmol $mmol_{Zn}$ h^{-1} when increasing ZnO loading from 1.0% to 10%, the productivity of ethylene was also seen to rise. The decreased efficiency of ethanol dehydrogenation over Zn sites was attributed to the higher prevalence of large ZnO clusters as detected by SEM-EDS. As a result of these competing factors, it was found that a ZnO loading of 3.5 Wt% by Zn was optimum in terms of acetaldehyde selectivity. Upon exchange of Na^+ cations for K^+, Rb^+ and Cs^+ analogues, acetaldehyde selectivity was seen to increase further, with the maximum acetaldehyde selectivity of 95% observed for ZnO(3.5)/Rb–MOR–(7).

Following incremental development and identification of ZnO(3.5)/Rb–MOR–(7) as the optimum catalyst material in terms of acetaldehyde selectivity, several performance analyses were undertaken to assess the materials applicability to industrial usage. First, the supported ZnO(3.5)/Rb–MOR–(7) was compared to an equimolar amount of unsupported ZnO and a physical mixture of ZnO and Rb–MOR–(7) to assess the role of the zeolite support. It was concluded that supporting ZnO onto Rb–MOR–(7) greatly benefitted the ethanol to acetaldehyde reaction, likely as a result of increased ZnO dispersion allowing a greater

proportion of active sites to be available. Further, a long-term stability test showed that ZnO(3.5)/Rb–MOR–(7) exhibited remarkable stability following 120+ h TOS, maintaining a selectivity to acetaldehyde of over 90% at an ethanol conversion value of around 40%. It was found that, whilst mild coking occurred, the framework structure of the zeolite was retained with no observation of additional phases or extra-framework alumina as evidenced by pXRD analysis or ^{27}Al ssNMR spectroscopy respectively. Unfortunately, regeneration of ZnO(3.5)/Rb–MOR–(7) was not perfect, despite a complete removal of carbon by thermal treatment the productivity of acetaldehyde decreased by around 50% from 12 to 6 mmol g_{cat}^{-1} h^{-1}. As carbon is fully removed and an increase in ethylene productivity is also observed, it is suggested that thermal treatment may alter either the phase or environment of ZnO, hence changing its reactivity.

In summary, it has been shown that ZnO impregnated MOR materials are efficient and selective catalysts for the direct dehydrogenation reaction of ethanol to form acetaldehyde at 400 °C under continuous flow conditions. ZnO/MOR catalysts may be optimized by increased ZnO loading and exchange of alkali counter-cation, with ZnO(3.5)/Rb–MOR–(7) being identified as the optimum catalyst material under the current experimental conditions. ZnO(3.5)/Rb–MOR–(7) is shown to possess a long and desirable catalyst lifetime and affords a good degree of reproducibility across a series of repeat reactions. Importantly, ethanol dehydrogenation over ZnO(3.5)/Rb–MOR–(7) would appear to progress *via* the direct dehydrogenation route as opposed to the partial oxidation route, meaning that no O_2 co-feed is required to obtain the desired acetaldehyde in good yield. The combination of high acetaldehyde selectivity and long lifetime is commercially desirable and, combined with facile and scalable catalyst preparation, make these catalyst materials interesting candidates for industrial scale-up.

4.4. References.

1. M. Eckert, G. Fleischmann, R. Jira, H. M. Bolt and K. Golka, Acetaldehyde in *Ullmann's Encyclopedia of Industrial Chemistry*, 2006, DOI: 10.1002/14356007.a01_031.pub2.
2. J. Bierhals, Carbon Monoxide in *Ullmann's Encyclopedia of Industrial Chemistry*, 2001, DOI: 10.1002/14356007.a05_203.
3. H. Zimmermann and R. Walzl, Ethylene in *Ullmann's Encyclopedia of Industrial Chemistry*, 2009, DOI: 10.1002/14356007.a10_045.pub3.
4. Acetaldehyde Market by Process (Wacker Process, Oxidation of Ethanol, Dehydrogenation of Ethanol), Derivative (Pyridine & Pyridine Bases, Pentaerythritol), Application (Food & Beverage, Chemicals, Paints & Coatings), and Region - Global Forecast to 2022, https://www.marketsandmarkets.com/Market-Reports/acetaldehyde-market-113225129.html?gclid=CjwKCAjw9vn4BRBaEiwAh0muDFXFtvmo_XxtxX3_cfMiR4GsRR61R3RrC-NFOJJ1zY6WbTRhXZGRwRoC9ZcQAvD_BwE, (accessed 27/07/20).
5. O. Rosales-Calderon and V. Arantes, *Biotechnol. for Biofuels*, 2019, **12**, 240.
6. Annual World Fuel Ethanol Production, https://ethanolrfa.org/statistics/annual-ethanol-production/, (accessed 28/01/2020).
7. U.S. fuel ethanol production continues to grow in 2017, https://www.eia.gov/todayinenergy/detail.php?id=32152).
8. M. Guerbet, *C. R. Acad. Sci.*, 1899, **128**, 511.
9. S. V. Lebedev, *Zhurnal Obshchei Khimii*, 1933, **3**, 698.
10. H. Aitchison, R. L. Wingad and D. F. Wass, *ACS Catal.*, 2016, **6**, 7125–7132.
11. E. V. Makshina, M. Dusselier, W. Janssens, J. Degreve, P. A. Jacobs and B. F. Sels, *Chem. Soc. Rev.*, 2014, **43**, 7917–7953.
12. A. Y. Chichibábin, *J. Prakt. Chem.*, 1924, **107**, 122–128.
13. B. Tollens and P. Wigand, *Justus Liebigs Ann. Chem.*, 1891, **265**, 316–340.
14. S. J. Raynes and R. A. Taylor, *Sustain. Energ. Fuel.*, 2021, **5**, 2136–2148.
15. G. M. Lari, K. Desai, C. Mondelli and J. Pérez-Ramírez, *Catal. Sci. Technol.*, 2016, **6**, 2706–2714.
16. J. J. Murcia, M. C. Hidalgo, J. A. Navío, V. Vaiano, P. Ciambelli and D. Sannino, *Catal. Today*, 2012, **196**, 101–109.
17. L. V. Mattos and F. B. Noronha, *J. Catal.*, 2005, **233**, 453–463.
18. B.-S. Jiang, R. Chang and Y.-C. Lin, *Ind. Eng. Chem. Res.*, 2013, **52**, 37–42.
19. J. Mielby, J. O. Abildstrøm, F. Wang, T. Kasama, C. Weidenthaler and S. Kegnæs, *Angew. Chem.*, 2014, **126**, 12721–12724.
20. E. Behravesh, N. Kumar, Q. Balme, J. Roine, J. Salonen, A. Schukarev, J.-P. Mikkola, M. Peurla, A. Aho, K. Eränen, D. Y. Murzin and T. Salmi, *J. Catal.*, 2017, **353**, 223–238.
21. E. A. Redina, A. A. Greish, I. V. Mishin, G. I. Kapustin, O. P. Tkachenko, O. A. Kirichenko and L. M. Kustov, *Catal. Today*, 2015, **241**, 246–254.
22. V. I. Sobolev, K. Y. Koltunov, O. A. Simakova, A.-R. Leino and D. Y. Murzin, *Appl. Catal. A*, 2012, **433-434**, 88–95.
23. T. Takei, N. Iguchi and M. Haruta, *Catal. Surv. Asia*, 2011, **15**, 80–88.
24. Y. Guan and E. J. M. Hensen, *Appl. Catal. A*, 2009, **361**, 49–56.
25. A. Corma, J. Navas and M. J. Sabater, *Chem. Rev.*, 2018, **118**, 1410–1459.
26. M. Ouyang, S. Cao, S. Yang, M. Li and M. Flytzani-Stephanopoulos, *Ind. Eng. Chem. Res.*, 2020, **59**, 2648–2656.

27. S. Hanukovich, A. Dang and P. Christopher, *ACS Catal.*, 2019, **9**, 3537–3550.
28. C. Wang, G. Garbarino, L. F. Allard, F. Wilson, G. Busca and M. Flytzani-Stephanopoulos, *ACS Catal.*, 2016, **6**, 210–218.
29. G. Garbarino, P. Riani, M. Villa García, E. Finocchio, V. Sanchez Escribano and G. Busca, *Catal. Today*, 2019, **354**, 167–175.
30. M. Almohalla, E. Gallegos-Suárez, A. Arcoya, J. Álvarez-Rodríguez, I. Rodríguez-Ramos and A. Guerrero-Ruiz, *Appl. Catal. A*, 2017, **535**, 61–68.
31. D. Yu, W. Dai, G. Wu, N. Guan and L. Li, *Chinese J. Catal.*, 2019, **40**, 1375–1384.
32. S. Tsuruya, M. Tsukamoto, M. Watanabe and M. Masai, *J. Catal.*, 1985, **93**, 303–311.
33. Y. Injongkol, T. Maihom, S. Choomwattana, B. Boekfa and J. Limtrakul, *RSC Adv.*, 2017, **7**, 38052–38058.
34. V. Markova, G. Rugg, A. Govindasamy, A. Genest and N. Rösch, *J. Phys. Chem. C*, 2018, **122**, 2783–2795.
35. Y.-J. Tu and Y.-W. Chen, *Ind. Eng. Chem. Res.*, 2001, **40**, 5889–5893.
36. H. Zhang, H.-R. Tan, S. Jaenicke and G.-K. Chuah, *J. Catal.*, 2020, **389**, 19–28.
37. P. I. Kyriienko, O. V. Larina, S. O. Soloviev, S. M. Orlyk, C. Calers and S. Dzwigaj, *ACS Sustain. Chem. Eng.*, 2017, **5**, 2075–2083.
38. V. L. Sushkevich and I. I. Ivanova, *ChemSusChem*, 2016, **9**, 2216–2225.
39. V. L. Sushkevich, I. I. Ivanova and E. Taarning, *Green Chem.*, 2015, **17**, 2552–2559.
40. T. Yan, W. Dai, G. Wu, S. Lang, M. Hunger, N. Guan and L. Li, *ACS Catal.*, 2018, **8**, 2760–2773.
41. L. Qi, Y. Zhang, M. A. Conrad, C. Russell, J. T. Miller and A. T. Bell, *J. Am. Chem. Soc.*, 2020, **142**, 14674–14687.
42. W. Dai, S. Zhang, Z. Yu, T. Yan, G. Wu, N. Guan and L. Li, *ACS Catal.*, 2017, **7**, 3703–3706.
43. X. Bo-Qing, C. Tian-Xi and L. Song, *React. Kinet. Catal. Lett.*, 1993, **49**, 223–228.
44. T. C. Keller, K. Desai, S. Mitchell and J. Perez-Ramirez, *ACS Catal.*, 2015, **5**, 5388–5396.
45. A. Modak, A. Deb, T. Patra, S. Rana, S. Maity and D. Maiti, *Chem. Commun.*, 2012, **48**, 4253–4255.
46. K. Ding, S. Xu, R. Alotaibi, K. Paudel, E. W. Reinheimer and J. Weatherly, *J. Org. Chem.*, 2017, **82**, 4924–4929.
47. J. B. Nagy and E. G. Derouane, NMR Spectroscopy and Zeolite Chemistry in *Perspectives in Molecular Sieve Science*, American Chemical Society, 1988, vol. 368, ch. 1, pp. 2–32.
48. T.-H. Chen, B. H. Wouters and P. J. Grobet, *Eur. J. Inorg. Chem.*, 2000, **2000**, 281–285.
49. A. de Lucas, P. Canizares, A. Durán and A. Carrero, *Appl. Catal. A*, 1997, **154**, 221–240.
50. M. Nielsen, A. Hafreager, R. Y. Brogaard, K. De Wispelaere, H. Falsig, P. Beato, V. Van Speybroeck and S. Svelle, *Catal. Sci. Technol.*, 2019, **9**, 3721–3725.
51. N. Kosaric, Z. Duvnjak, A. Farkas, H. Sahm, S. Bringer-Meyer, O. Goebel and D. Mayer, Ethanol in *Ullmann's Encyclopedia of Industrial Chemistry*, 2011, DOI: 10.1002/14356007.a09_587.pub2, pp. 1–72.
52. M. M. Rahman, S. D. Davidson, J. M. Sun and Y. Wang, *Top. Catal.*, 2016, **59**, 37–45.
53. V. R. Choudhary and S. D. Sansare, *Appl. Catal.*, 1984, **10**, 147–153.
54. E. A. Uslamin, H. Saito, N. Kosinov, E. Pidko, Y. Sekine and E. J. M. Hensen, *Catal. Sci. Technol.*, 2020, **10**, 2774–2785.
55. A. Devaraj, M. Vijayakumar, J. Bao, M. F. Guo, M. A. Derewinski, Z. Xu, M. J. Gray, S. Prodinger and K. K. Ramasamy, *Sci. Rep.*, 2016, **6**, 37586.

56. P. Norby, F. I. Poshni, A. F. Gualtieri, J. C. Hanson and C. P. Grey, *J. Phys. Chem. B*, 1998, **102**, 839–856.
57. M. Hunger, U. Schenk, B. Burger and J. Weitkamp, *Angew. Chem.*, 1997, **36**, 2504–2506.
58. H. Liu and C. P. Grey, *Micropor. Mesopor. Mater.*, 2002, **53**, 109–120.
59. C. Bisio, P. Massiani, K. Fajerwerg, L. Sordelli, L. Stievano, E. R. Silva, S. Coluccia and G. Martra, *Micropor. Mesopor. Mater.*, 2006, **90**, 175–187.
60. H. Tidahy, S. Siffert, J.-F. Lamonier, R. Cousin, E. Zhilinskaya, A. Aboukaïs, B.-L. Su, X. Canet, G. De Weireld and M. Frère, *Appl. Catal. B*, 2007, **70**, 377–383.
61. G. Busca, *Micropor. Mesopor. Mater.*, 2017, **254**, 3–16.
62. T. Tago, H. Konno, S. Ikeda, S. Yamazaki, W. Ninomiya, Y. Nakasaka and T. Masuda, *Catal. Today*, 2011, **164**, 158–162.
63. W. A. Lazier and H. Adkins, *J. Am. Chem. Soc.*, 1925, **47**, 1719–1722.
64. C. Drouilly, J. M. Krafft, F. Averseng, H. Lauron-Pernot, D. Bazer-Bachi, C. Chizallet, V. Lecocq and G. Costentin, *Appl. Catal. A*, 2013, **453**, 121–129.
65. J. M. Vohs and M. A. Barteau, *Surf. Sci.*, 1989, **221**, 590–608.
66. M. V. Morales, E. Asedegbega-Nieto, A. Iglesias-Juez, I. Rodríguez-Ramos and A. Guerrero-Ruiz, *ChemSusChem*, 2015, **8**, 2223–2230.
67. T. De Baerdemaeker, M. Feyen, U. Müller, B. Yilmaz, F.-S. Xiao, W. Zhang, T. Yokoi, X. Bao, H. Gies and D. E. De Vos, *ACS Catal.*, 2015, **5**, 3393–3397.
68. H. U. Sverdrup, A. H. Olafsdottir and K. V. Ragnarsdottir, *Resour. Conserv. Recycl. X*, 2019, **4**, 100007.
69. G. Pampararo, G. Garbarino, P. Riani, M. Villa García, V. Sánchez Escribano and G. Busca, *Appl. Catal. A*, 2020, **602**, 117710.
70. J. Pang, M. Zheng, C. Wang, X. Yang, H. Liu, X. Liu, J. Sun, Y. Wang and T. Zhang, *ACS Catal.*, 2020, **10**, 13624–13629.
71. A. Segawa, A. Nakashima, R. Nojima, N. Yoshida and M. Okamoto, *Ind. Eng. Chem. Res.*, 2018, **57**, 11852–11857.
72. E. Santacesaria, G. Carotenuto, R. Tesser and M. Di Serio, *Chem. Eng. J.*, 2012, **179**, 209–220.

4.5. Supplementary Information.

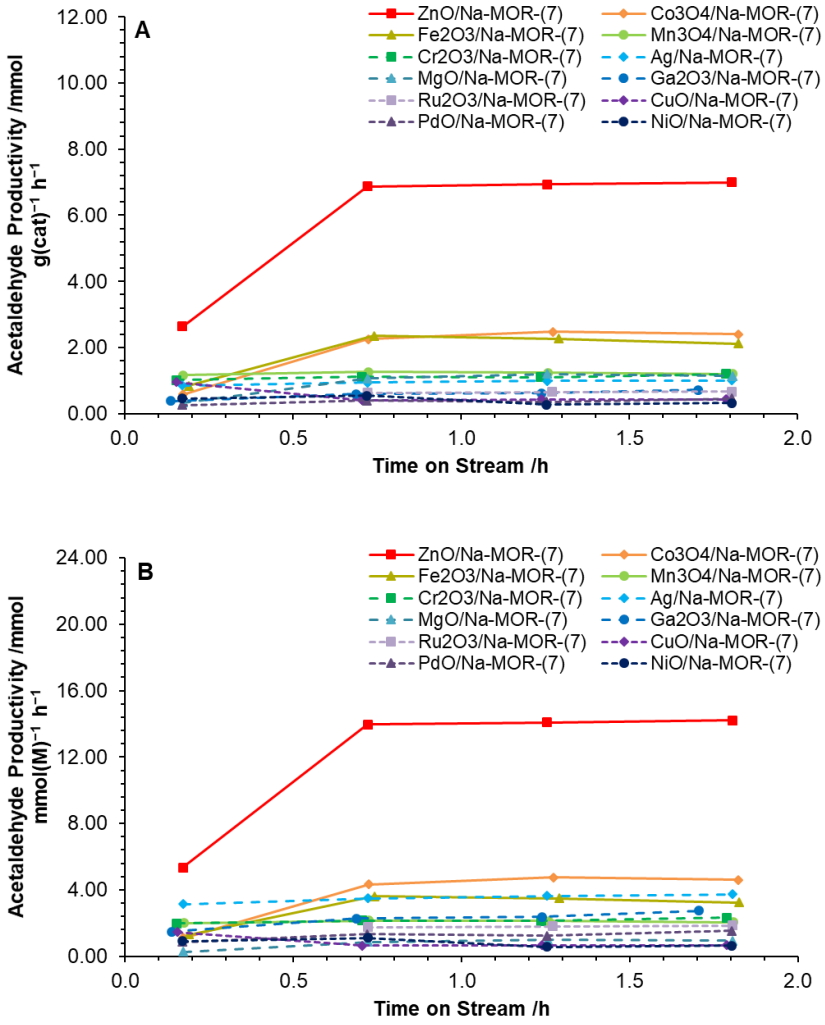

Figure S4.1: Acetaldehyde productivities normalized to A) mass of catalyst and B) mmol of extra-framework metal resulting from ethanol conversion over ZnO/Na–MOR–(7) (■), Co_3O_4/Na–MOR–(7) (♦), Fe_2O_3/Na–MOR–(7) (▲), Mn_3O_4/Na–MOR–(7) (●), Cr_2O_3/Na–MOR–(7) (■), Ag/Na–MOR–(7) (♦), MgO/Na–MOR–(7) (▲), Ga_2O_3/Na–MOR–(7) (●), Ru_2O_3/Na–MOR–(7) (■), CuO/Na–MOR–(7) (♦), PdO/Na–MOR–(7) (▲) and NiO/Na–MOR–(7) (●) at 400 °C. Ethanol feed rate = 0.171 mmol min^{-1}, catalyst mass = 0.300 g. Detection column: BPX-90.

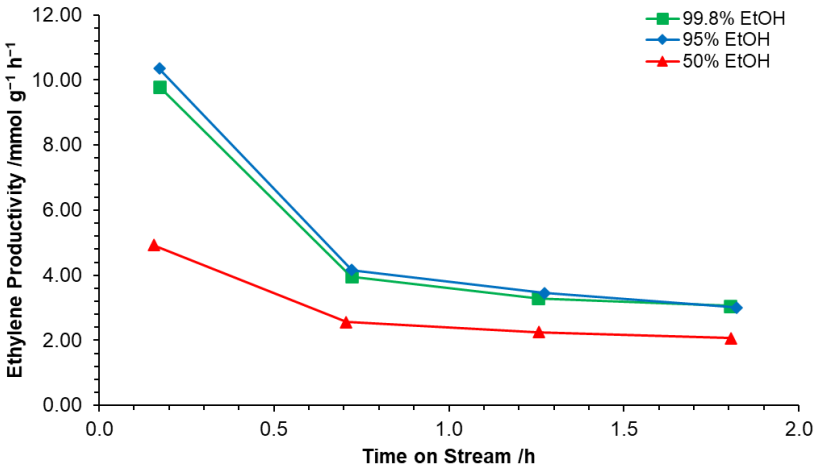

Figure S4.2: Ethylene productivities for ZnO/Na–MOR-(7.0) following reaction of ethanol at three different hydration levels at 400 °C for 2 h TOS. Ethanol feed rate = 0.171 mmol min^{-1}, catalyst mass = 0.300 g. Detection Column: BPX–90.

Table S4.1: Catalyst coking (C Wt%) of ZnO/Na–MOR-(7.0) catalysts following ethanol dehydrogenation at three different hydration levels at 400 °C for 2 h TOS as determined by CHN microanalysis.

Sample	Ethanol Grade	Catalyst Coking (C Wt%)
ZnO/Na–MOR–(7.0)	99.8	4.03
ZnO/Na–MOR–(7.0)	95	3.61
ZnO/Na–MOR–(7.0)	50	3.45

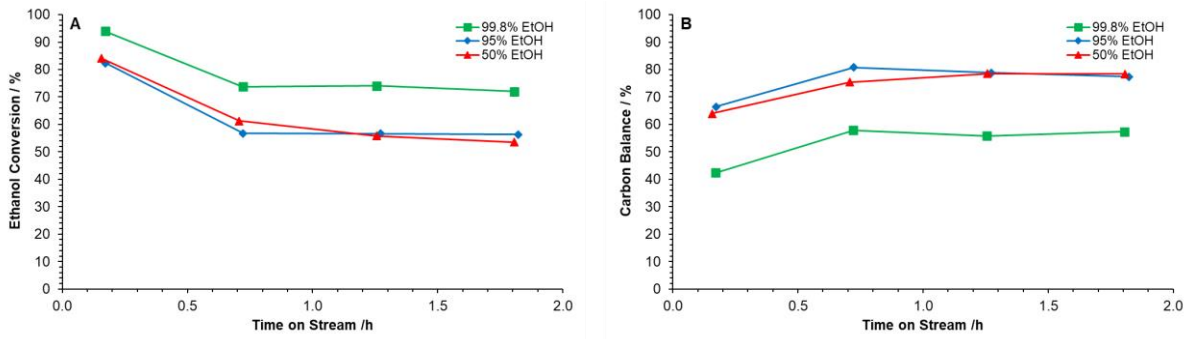

Figure S4.3: Ethanol conversion (A) and carbon balance (B) for ZnO/Na–MOR-(7.0) following reaction of ethanol at three different hydration levels at 400 °C for 2 h TOS. Ethanol feed rate = 0.171 mmol min^{-1}, catalyst mass = 0.300 g. Detection Column: BPX–90.

Table S4.2: Elemental compositions of ZnO/Na–MOR–(7) materials at varying Zn loadings obtained by ICP-OES. Values are averaged over multiple wavelengths where possible and appropriate.

Material	Al Wt%	Zn Wt%	Na Wt%
Na–MOR–(7)	4.32	0.00	3.72
ZnO/Na–MOR–(7)-1.0%	5.23	0.98	3.99
ZnO/Na–MOR–(7)-3.5%	4.90	3.77	3.22
ZnO/Na–MOR–(7)-5.0%	5.13	4.80	3.85
ZnO/Na–MOR–(7)-10%	4.85	9.79	3.76

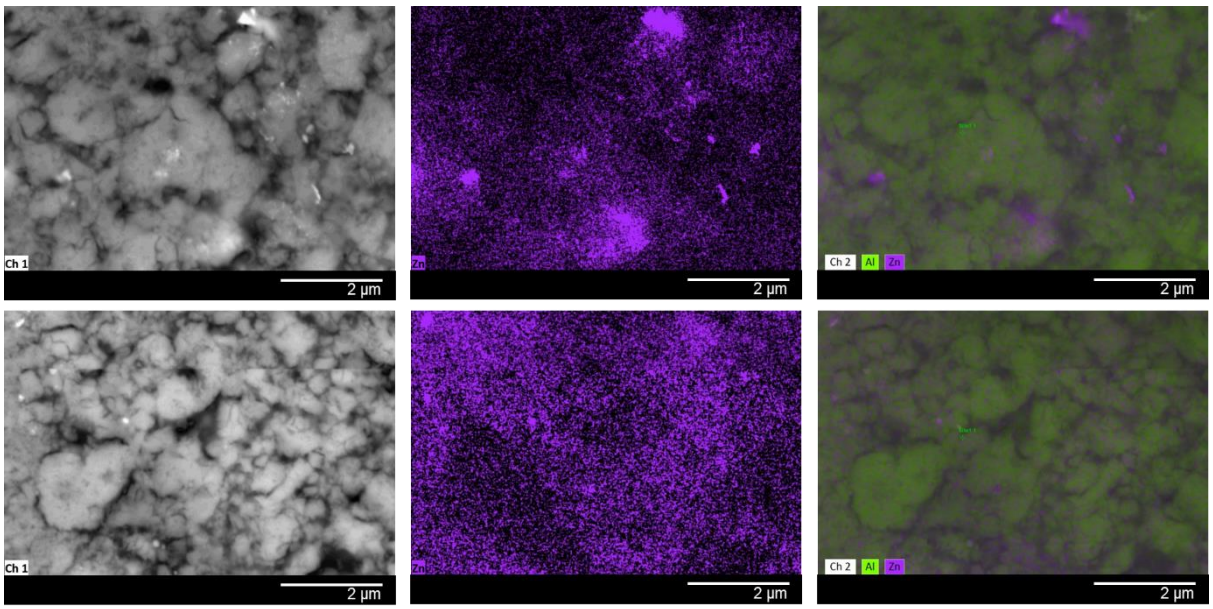

Figure S4.4: SEM image (left), Zn elemental map (centre) and Zn, Al elemental overlays (right) of ZnO/Na–MOR–(7)-10% following grinding and polishing at two different locations.

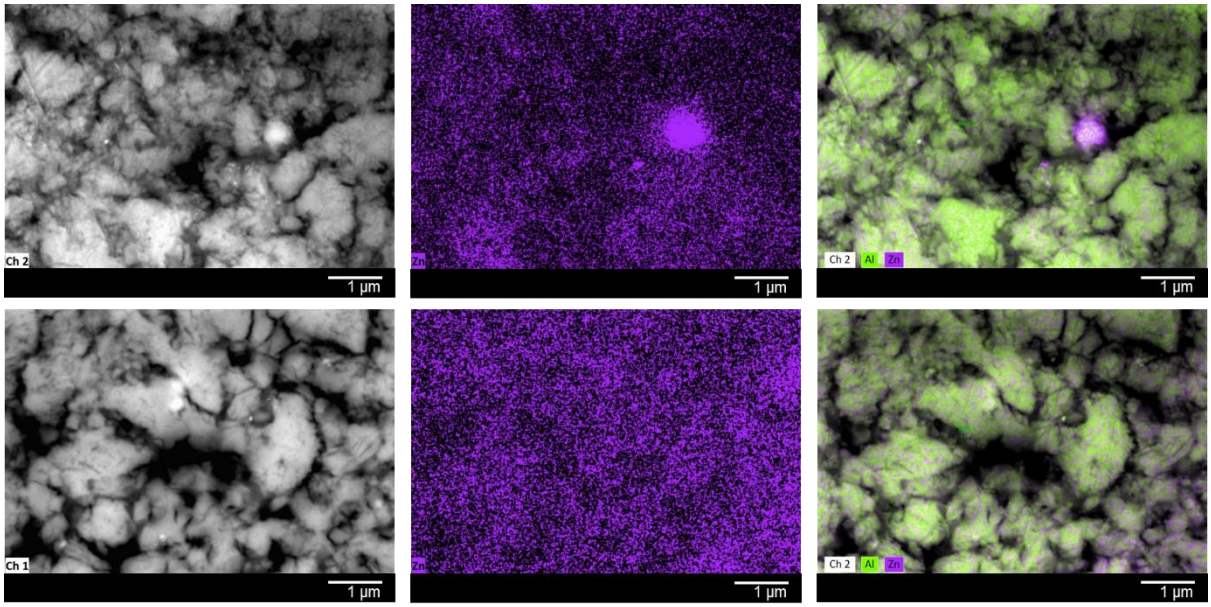

Figure S4.5: SEM image (left), Zn elemental map (centre) and Zn, Al elemental overlays (right) of ZnO/Na–MOR–(7)-5.0% following grinding and polishing at two different locations.

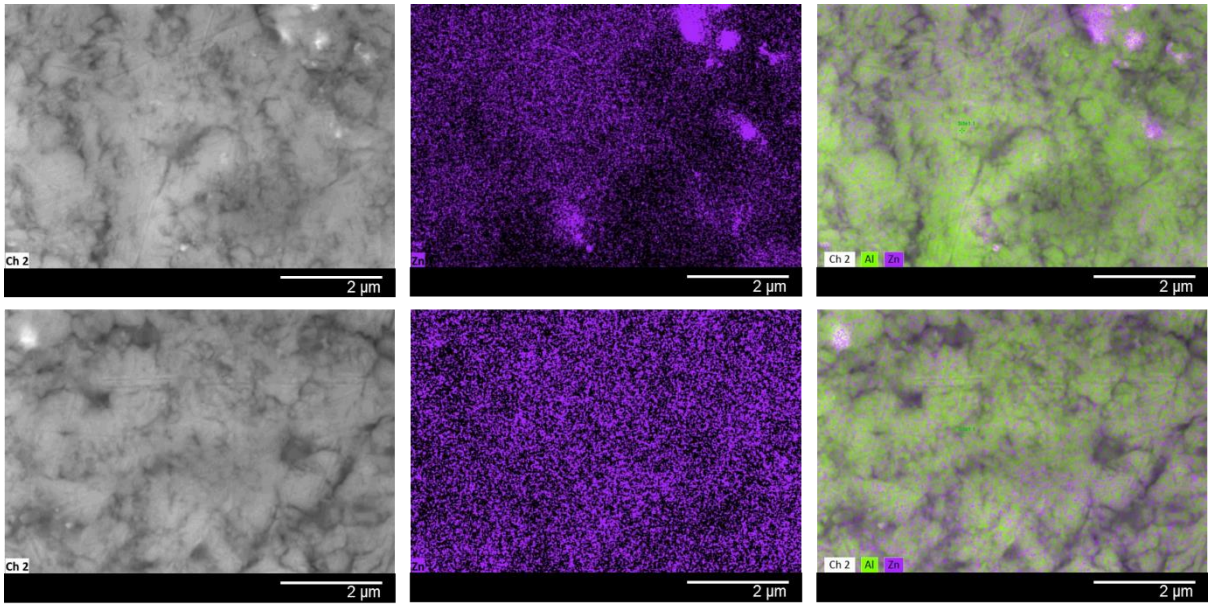

Figure S.6: SEM image (left), Zn elemental map (centre) and Zn, Al elemental overlays (right) of ZnO/Na–MOR–(7)-3.5% following grinding and polishing at two different locations.

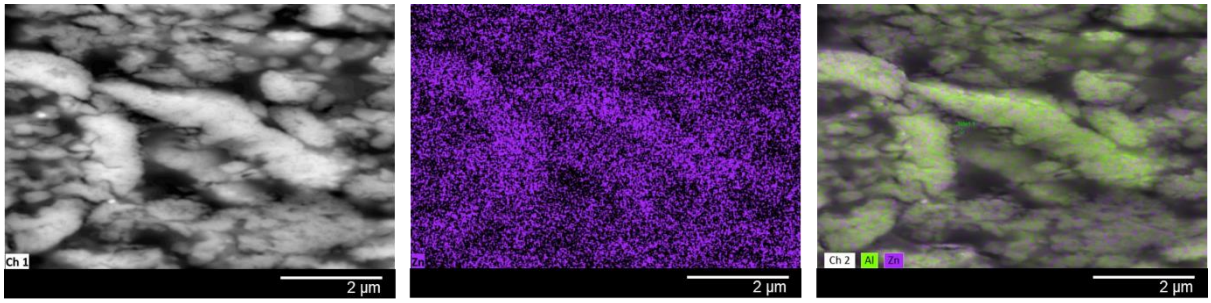

Figure S4.7: SEM image (left), Zn elemental map (centre) and Zn, Al elemental overlays (right) of ZnO/Na–MOR–(7)-1.0% following grinding and polishing.

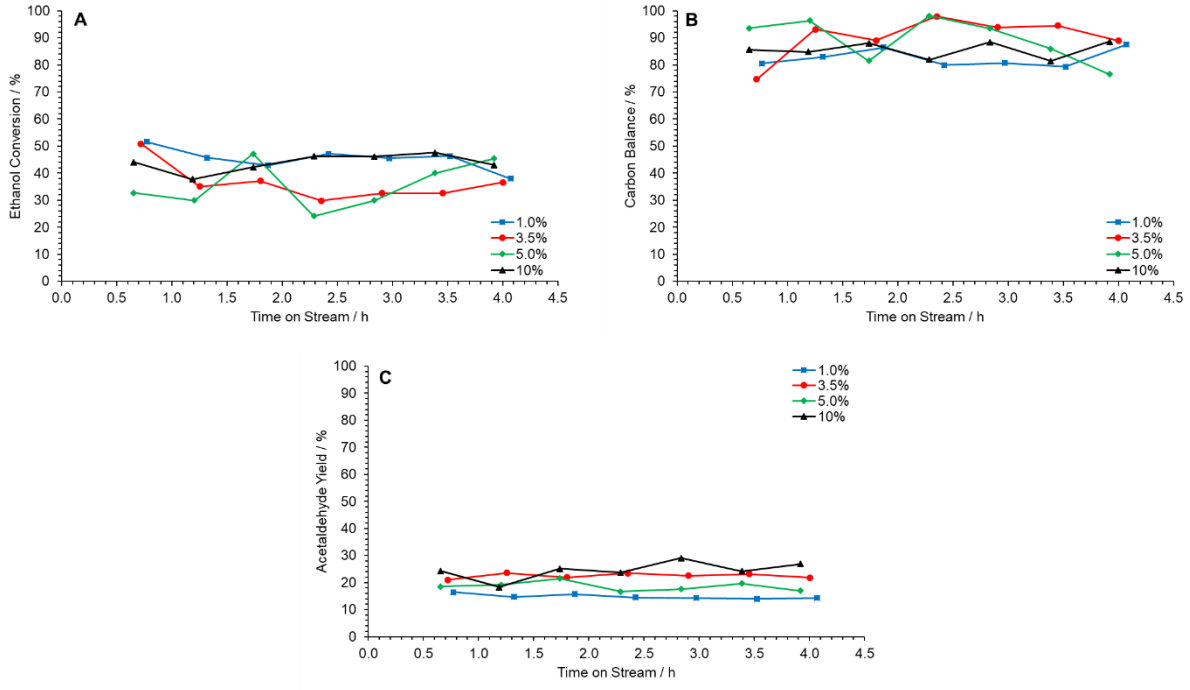

Figure S4.8: Ethanol conversion (A) and carbon balance (B) and acetaldehyde yield (C) following reaction of ethanol over ZnO/Na–MOR materials at 400 °C for 4 h TOS at nominal Zn loadings of = 1.0 Wt% (■), 3.5 Wt% (●), 5.0 Wt% (♦) and 10 Wt% (▲). Ethanol feed rate = 0.330 mmol min^{-1}, catalyst mass = 0.300 g. Detection Columns: RTX-VMS + ShinCarbon ST.

Table S4.3: Elemental compositions of ZnO/M–MOR–(7) materials obtained by ICP-OES where M = Na, K, Rb, or Cs. Target ZnO loading = 3.5 Wt% by Zn. n.d. = Not detected.

Material	Al Wt%	Zn Wt%	Na Wt%	K Wt%	Rb Wt%	Cs Wt%
ZnO/Na–MOR–(7)	4.80	3.71	4.43	n.d.	n.d.	n.d.
ZnO/K–MOR–(7)	4.87	2.62	0.00	6.83	0.00	0.00
ZnO/Rb–MOR–(7)	4.56	3.12	0.00	0.00	14.43	0.00
ZnO/Cs–MOR–(7)	4.23	3.09	0.01	0.00	0.00	16.52

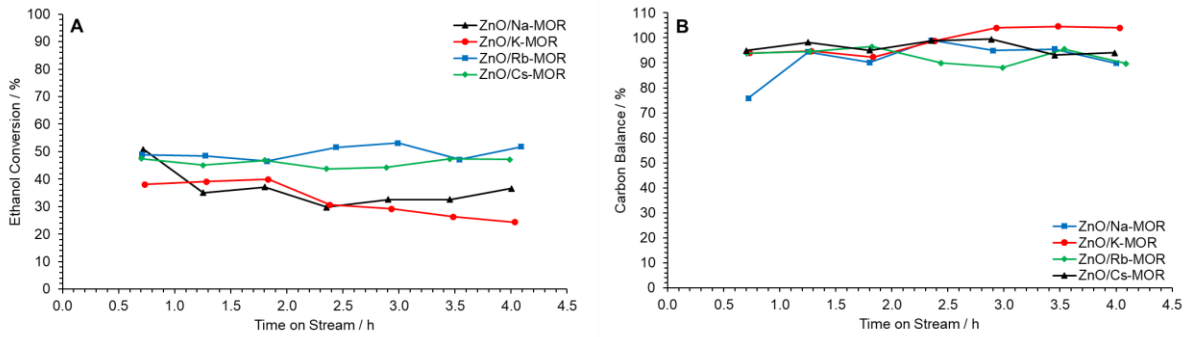

Figure S4.9: Ethanol conversion (A) and carbon balance (B) following reaction of ethanol over ZnO/M–MOR materials at 400 °C for 4 h TOS where M = Na (▲), K (●), Rb (■) and Cs (♦). Ethanol feed rate = 0.330 mmol min^{-1}, catalyst mass = 0.300 g. Detection Columns: RTX-VMS + ShinCarbon ST.

Table S4.4: Reaction conditions, conversion values and selectivites for literature ZnO materials utilized for ethanol conversion to acetaldehyde.

Entry	Catalyst	Reaction Conditions		Conversion / %	Selectivities / %		Reference
		Temperature / °C	TOS /h		Acetaldehyde	Ethylene	
1	ZnO (commercial, Sigma)	400	—	38-62	80	20	S1
2	ZnO (various syntheses plus 1 commercial)	350	6	15-20	84-94	<8	S2
3	ZnO (various syntheses)	400	—	20	80	20	S3
4	ZnO/SiO2 0.5 Wt% Zn From $Zn(NO3)_2$	360	0.5 10	66 67	57 62	10 7.5	S4
5	ZnO (1 commercial and 1 prepared)	350	—	21-32	62-72	38-28	S5
6	ZnO(3.5)/Rb–MOR–(7)	400	4 120	52 25	94 96	0.9 1.5	This paper

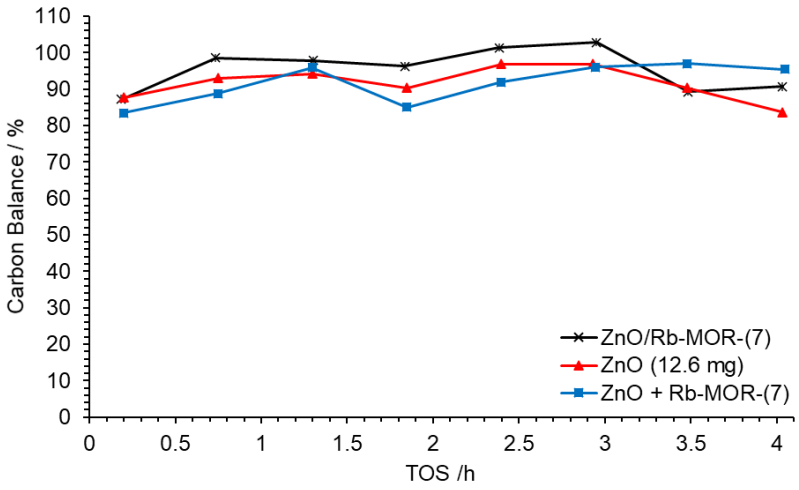

Figure S4.10: Carbon balance for ZnO/Rb–MOR–(7) (×, 300 mg), ZnO (▲, 12.6 mg,) and a physical mixture of ZnO and Rb–MOR–(7) (■, 12.6 mg + 300 mg) at 400 °C over 4 h TOS. Ethanol feed rate = 0.399 mmol min^{-1}. Detection Columns: RTX-VMS + ShinCarbon ST.

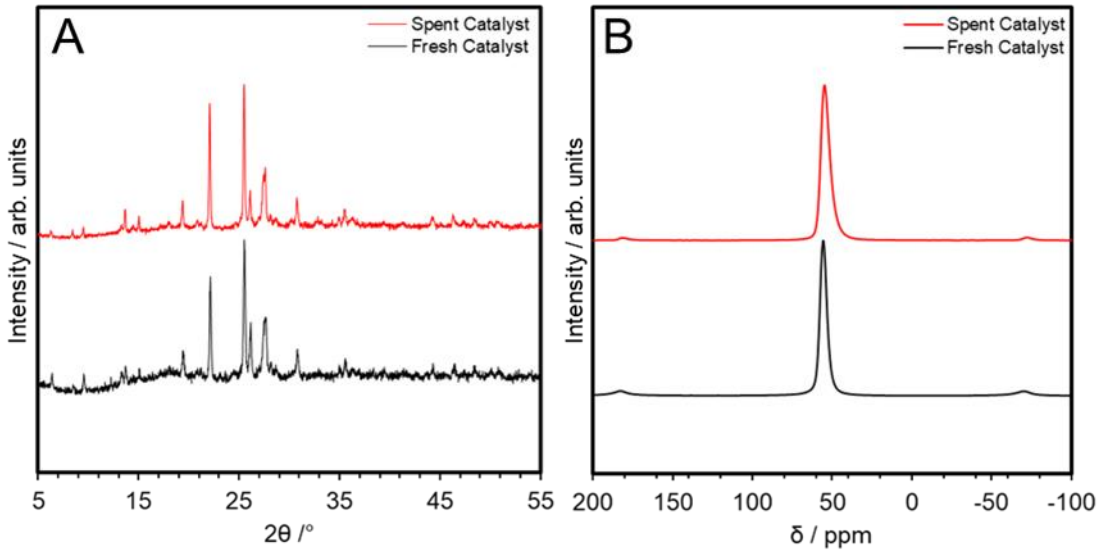

Figure S4.11: A) pXRD patterns within the 2θ = 5–55° range and B) Solid-state ^{27}Al NMR spectra for fresh ZnO(3.5)/Rb–MOR–(7) and the same material following ethanol conversion at 400 °C for 120+ h TOS.

Table S4.5: Catalyst coking (C Wt%) of ZnO/Rb–MOR-(7.0) catalysts following ethanol dehydrogenation at 400 °C at 4 and 120 h TOS as determined by CHN microanalysis.

Sample	Time on Stream / h	Catalyst Coking (C Wt%)
ZnO/Rb–MOR–(7.0)	4.0	4.35
ZnO/Rb–MOR–(7.0)	120	4.67

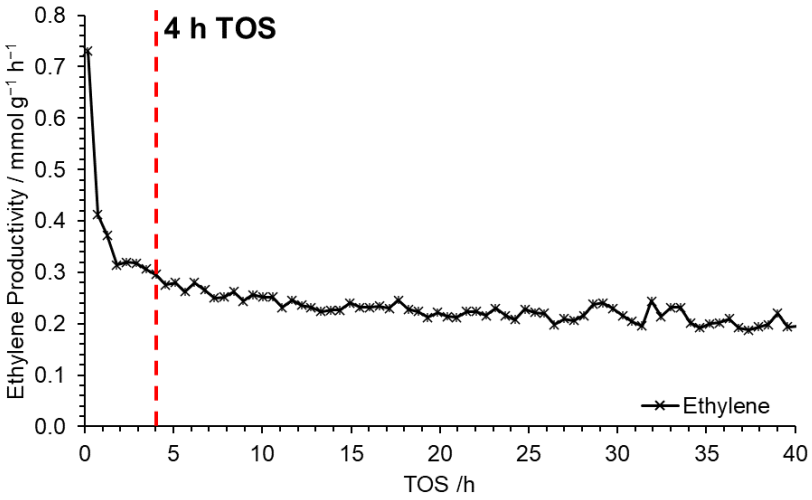

Figure S4.12: Ethylene productivity following reaction of ethanol over ZnO/Rb–MOR–(7) at 400 °C for 120 h TOS. The x-axis has been cut at 40 h TOS and a marker added at 4 h TOS to improve clarity. Ethanol feed rate = 0.330 mmol min^{-1}, catalyst mass = 0.300 g. Detection Columns: RTX-VMS + ShinCarbon ST.

References:

S1. M. M. Rahman, S. D. Davidson, J. M. Sun and Y. Wang, *Top. Catal.*, 2016, **59**, 37–45.

S2. M. V. Morales, E. Asedegbega-Nieto, A. Iglesias-Juez, I. Rodríguez-Ramos and A. Guerrero-Ruiz, *ChemSusChem*, 2015, **8**, 2223–2230.

S3. S. A. Halawy and M. A. Mohamed, *J. Mol. Catal. A Chem.*, 1995, **98**, L63–L68.

S4. T. De Baerdemaeker, M. Feyen, U. Müller, B. Yilmaz, F.-S. Xiao, W. Zhang, T. Yokoi, X. Bao, H. Gies and D. E. De Vos, *ACS Catal.*, 2015, **5**, 3393–3397.

S5. C. Drouilly, J. M. Krafft, F. Averseng, H. Lauron-Pernot, D. Bazer-Bachi, C. Chizallet, V. Lecocq and G. Costentin, *Appl. Catal. A*, 2013, **453**, 121–129.

Chapter 5

Development of Multifunctional Zeolite Materials Containing Tetravalent Metal Atoms for the Cascade Conversion of Ethanol to 1,3–Butadiene.

5. Development of Multifunctional Zeolite Materials Containing Tetravalent Metal Atoms for the Cascade Conversion of Ethanol to 1,3–Butadiene.

Following successful identification of ZnO supported on zeolite as a highly selective and stable catalyst for the dehydrogenation of ethanol to acetaldehyde in Chapter 4, efforts to identify catalytic sites for the subsequent aldol condensation and Meerwein–Ponndorf–Verley (MPV) reduction in the direct transformation of ethanol to 1,3–butadiene were undertaken. Recent zeolite literature in this field has focussed around the use of zeolite frameworks in which the trivalent aluminium atoms have been heteroatomically substituted with tetravalent and pentavalent metal species, such as Zr, Hf and Ta, resulting in a Lewis acidic rather than Brønsted acidic framework (See Section 1.1.3.4).[1-7] Within such substituted systems, the framework-incorporated Lewis acidic metal centre is found to be efficient for both the aldol condensation of acetaldehyde and MPV reduction of the resulting crotonaldehyde with ethanol.[8-11] Typically, an extra-framework noble metal or metal oxide species, such as the previously identified ZnO, is added to enhance ethanol dehydrogenation.[2, 3, 12] As a result of the successful marriage of multiple active sites, butadiene selectivites in excess of 70% resulting from the cascade conversion of ethanol have been realized over such systems.[3, 4] The reaction pathway from ethanol to butadiene is presented in Section 1.3.2.2.

Aside from the general reaction pathway presented in, it is possible that the exact reaction mechanism may change depending upon the system in question. One such relevant example is the variable mechanism of aldol condensation over metal-substituted beta zeolites.[8] Here, the nature of the Lewis acidic metal centre is shown to have a substantial effect on not only the catalytic activity of the system, but also the mechanism through which is proceeds. This effect is largely a product of two major factors. Firstly, variation of the Lewis acidic metal atom will affect the energy separation of the HOMO and LUMO of the base molecule and metal centre respectively and therefore modulate the strength of the resulting Lewis acid-base interaction.[14] Further, the nature and geometry of the LUMO is known to vary between tetravalent metal species residing within a zeolite framework.[8, 10] Secondly, the coordination environment around the Lewis acidic metal centre is not necessarily defined, hence it is possible that the metal centre may reside in either a coordinatively saturated or unsaturated site.[1, 10, 15] These differing coordination environment may results in variations to acidity type and strength alongside accessibility of the active site, hence they may have a considerable effect

on reaction rates. Finally, the polarizability of the metal centre may also play a large role in mechanistic pathway.[15]

If M^{4+} atoms substituted into zeolite tetrahedral sites are considered, two major LUMO geometries are available. For main group elements with a d^{10} configuration, such as Sn, the LUMO is calculated to be a linear combination of σ*(M–O) orbitals between the tetrahedral metal centre and framework oxygen atoms (Figure 5.1).[10, 14] For transition metal elements possessing empty d-orbital filling, such as Ti, Zr, and Hf (each element being d^0 in this case), the vacant d_{z^2} orbital acts as the acceptor instead (Figure 5.1).[14] This effect of electronic structure and orbital geometry on reaction mechanism is reported in several articles relevant to cascade ethanol conversion.[8, 10, 15-17] An important relationship reported in many of these contributions is that between metal species and basicity of the surrounding oxygen atoms. One such example is observed following DFT modelling of the Meerwein−Ponndorf−Verley (MPV) reduction of cyclohexanone with 2-butanol catalysed by Sn−beta and Zr−beta.[10] In this example, the authors, Boronat *et al.*, claim that the "*The LUMO in the Sn−beta active site is a linear combination of the four antibonding σ*(Sn−O) orbitals. When a Lewis base molecule such as cyclohexanone interacts with this site, the electron density transferred to the catalyst cannot be accepted by the tin atom, which pushes it into the orbital lobes located on the oxygen atoms. Thus, the oxygen atoms bonded to tin show a certain basic character and allow hydrogen bonding with the hydroxyl proton of 2-butanol. However, the LUMO in the Zr−beta catalyst is the* d_{z^2} *orbital on the zirconium atom, and it can accept the electron density transferred from the Lewis base molecule without increasing the basic character of the neighbouring oxygen atoms.*" DFT studies of the aldol condensation of acetaldehyde over Sn−BEA, Ti−BEA and Zr−BEA by Palagin *et al*. further supports these suggestions.[8] Therein, it is concluded that Sn−BEA is the only material of the three assessed that possesses sufficient basicity of the Sn−O−Si site following aldehyde adsorption to allow α−proton abstraction and enolization to occur. Taking the work of Boronat *et al.* and the aforementioned orbital descriptions into account, the observations of Palagin *et al.* likely result from increased basic character of the surrounding oxygen atoms owing the donation into the σ*(Sn–O) orbitals.

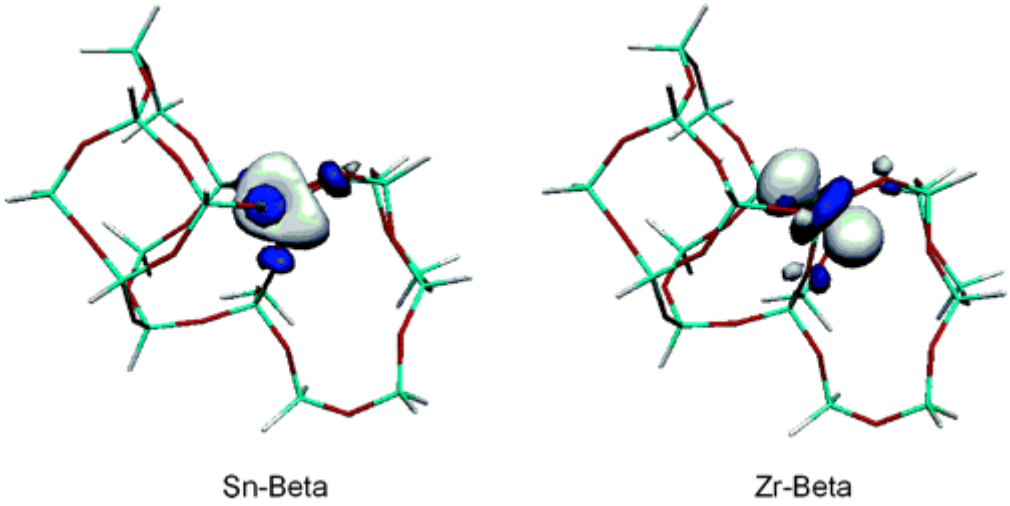

Figure 5.1: Calculated molecular orbital diagrams of tetrahedral sites containing Lewis acidic metal centres with different LUMO orbitals. Left: Sn–BEA showing a linear combination of the four antibonding σ*(Sn–O) orbitals, Right: Zr–BEA showing a d_{z^2} orbital. Reprinted with permission from reference 10. Copyright 2021 American Chemical Society.[10]

A further consideration for reactivity over M^{4+} substituted zeolites is the co-ordination environment of the Lewis acidic metal centre, namely whether the metal atom is co-coordinatively saturated or unsaturated resulting in closed and open sites, respectively. A closed site is defined as that in which a metal atom is bonded to four framework oxygen atoms, whereas an open site is one in which only three (or fewer) framework oxygen bonds are present in addition to one (or more) hydroxyl groups. Figure 5.2 shows a schematic representation of closed and open sites for M^{4+} atoms within a zeolite framework.

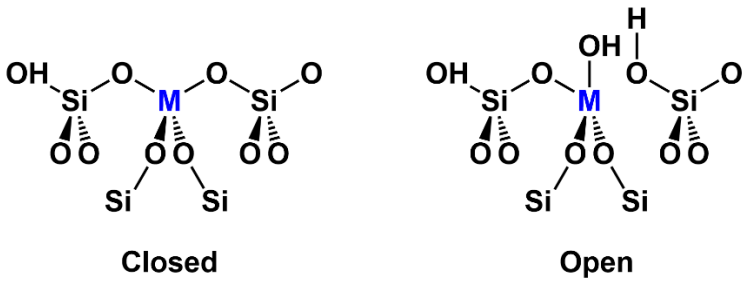

Figure 5.2: Schematic representation of closed (left) and open (right) sites in M^{4+} substituted zeolite.

Several reports have shown that open and closed sites can be identified and subsequently quantified by a range of spectroscopic techniques, the most common of which being FTIR of adsorbed probe molecules such as pyridine, acetonitrile and carbon monoxide.[1, 18-26] Within these reports, open and closed sites are typically distinguished by the use of CO absorption and the relative shifts in IR stretching frequency of the C–O bond. This may be aptly demonstrated by taking the characterisation of Zr–BEA by FTIR following CO adsorption as an example (Figure 5.3, CO adsorption is through the C atom as predicted in Figure 2 from reference 1).[1, 18] Therein, the stretching frequency of "free" pseudo-liquid CO is

recorded at 2138 cm^{-1} under the given analysis conditions. Following adsorption onto a zeolite-inherent defective silanol site, the stretching frequency is seen to increase to 2156 cm^{-1}. Upon adsorption to the hydroxyl group of an open Zr site, the stretching frequency further increases to 2163 cm^{-1}, this peak being indicative of open Zr sites. Following adsorption of CO to the Zr centre, its stretching frequency is shifted to 2176 cm^{-1} and 2185 cm^{-1} for closed and open sites respectively, allowing these two types of site to be readily distinguished and quantified.

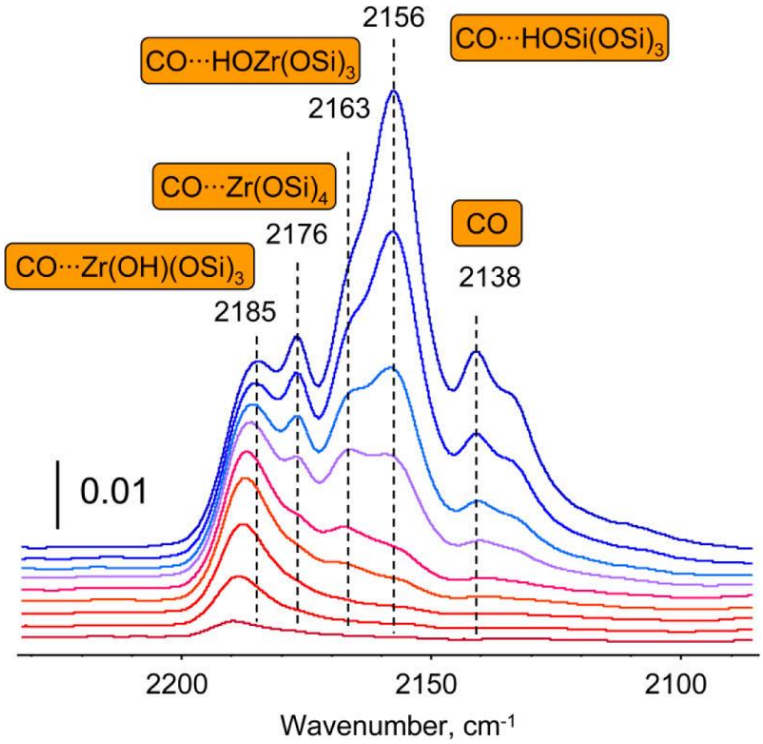

Figure 5.3: FTIR spectra of CO adsorbed on ZrBEA(130) collected with increase in the CO coverage. Coloured boxes show the configuration of adsorption sites assigned to each peak. Reprinted with permission from reference 1. Copyright 2021 American Chemical Society.[1]

Owing to the differing co-ordination environments, different reactivities may be observed for both open and closed Lewis acidic sites. One such relevant example is the improved efficiency of butadiene synthesis from ethanol over Ag/Zr–BEA reported by Sushkevich *et al.*.[1] Therein the initial rate of ethanol conversion exhibits a direct correlation with the number of open Zr sites determined by FTIR spectroscopy of adsorbed CO, whilst no direct correlation is observed with respect to closed Zr sites. This leads the authors to suggest that open Zr sites are the major active site in the transformation of ethanol to butadiene, with closed sites playing a lesser or zero role. The authors suggest that the increased activity of open Zr sites may be attributed to both a higher Lewis acid strength and steric accessibility in comparison to closed Zr sites. A further relevant example in which open and closed sites confer a noticeable reactivity difference is in the Meerwein−Ponndorf−Verley−Oppenauer (MPVO)

reduction of cyclohexanone with 2-butanol catalysed by Sn−BEA and Zr−BEA.[10] In this example, the authors conclude that partially hydrolysed open Sn sites are the predominant active sites as they better facilitate the initial alcohol deprotonation step by virtue of their increased flexibility. The enhanced MPV reductive etherification of cinnamaldehyde has also been reported by Li *et al*. in which an Al–BEA is grafted with $Zr(NO_3)_4$ in order to afford a mixed Zr–Al–BEA with Zr atoms specifically adopting an open configuration.[26] The authors cite the increased Lewis acidity as a result of open Zr sites as the main reason that both cinnamaldehyde conversion and yield of the respective products increases substantially. Furthermore, the effect of open and closed sites has also been observed for the isomerisation of glucose to fructose over Sn–BEA zeolites and the Baeyer–Villiger oxidation of cyclic ketones.[10, 15, 19, 21, 27]

Finally, the activity of Lewis acidic zeolite materials may not only be determined by their orbital geometries and relative energies, but also by the polarizability of the metal centre in question.[15] Larger metal centres typically possess a more diffuse and more polarisable electron cloud, hence resulting in a lesser energy penalty associated with the geometry change required to shift from ground state to transition state.[15] This effect of site rigidity is also a basis in the argument for and against open and closed metal sites respectively. In this case, open sites are energetically preferred as the site has a much greater flexibility and hence incurs a lower energy penalty between ground and transition states.[15]

Hence, with several factors affecting reaction over Lewis acidic centres, the prediction of relative reactivities is difficult and often a balance must be struck.[15, 17] One such study that best represents the difficulty of predicting the acidity and reactivity of Lewis acid centres is that by Yang *et al*..[28] Therein, multiple different zeolite dependent descriptors were calculated by DFT (LUMO energies, Fukui functions, absolute electronegativity, and absolute hardness) for a range of substituted MFI materials and none were found to correlate well with the experimentally observed trends in Lewis acidity.[14, 28] Instead, calculated adsorption energy of ammonia was found to better a better predicter of Lewis acid strength.[28] A further study that aptly represents the difficulty of Lewis acid strength prediction is the investigation of glucose-fructose isomerisation over metal-substituted BEA zeolites by Li *et al*..[15] Therein it is reported that, despite the considerable differences in both acid-base effects and metal polarizabilities, the apparent activation energies of reaction over Sn–BEA and Zr–BEA as calculated by a quantum mechanical/molecular mechanical (QM/MM) model are incredibly similar.

Within this chapter, the hydrothermal synthesis and characterization of a library of heteroatomically substituted Lewis acidic MFI type materials (M^{IV}–MFI, where M = Si, Sn, Ti, Zr and Hf) is reported and their inherent catalytic activity for ethanol conversion at various temperature points was explored. Subsequently, the dedicated dehydrogenation site, ZnO, identified in Chapter 4 was introduced into each catalyst material and the resulting materials were screened for their capability to affect the cascade conversion of ethanol to 1,3–butadiene by marriage of multiple disparate active sites. Upon identification of the optimum material, ZnO/Zr–MFI, a long-term stability test (72+ h) was undertaken resulting in assessment of both catalyst lifetime and deactivation profile. Further, the deactivation mode of ZnO/Zr–MFI was assessed, and a catalyst regeneration study was performed. Additionally, optimisation of the Zr–MFI by variation of hydrothermal synthesis conditions was performed in an attempt to maximise butadiene productivity.

5.1. Synthesis and Characterisation of a Library of Tetravalent Metal Containing MFI–Type Materials.

In order to identify the optimum tetravalent metal species to be used in combination with ZnO to promote direct cascade conversion of ethanol to 1,3–butadiene, a series of M–MFI (where M = Si, Sn, Ti, Zr, Hf) materials were synthesised, characterised and screened for their catalytic performance. Sn–MFI was the initial material to be synthesised as a detailed procedure was available within the literature.[29, 30] Ti, Zr, and Hf were selected as heteroatoms owing to their known Lewis acidic properties when incorporated into zeolite frameworks. Si–MFI was synthesised and tested as a reference material and benchmark.

5.1.1. Synthesis and characterisation of Sn–MFI using a known synthesis procedure.

The hydrothermal synthesis of Sn–MFI reproduces that reported by Kolyagin *et al.* and Mal *et al.* although at a temperature of 180 °C as opposed to 160 °C; the method is shown schematically in Figure 5.4.[29, 30] Briefly, a synthesis gel containing TPA–OH, TEOS, $SnCl_4 \cdot 5H_2O$ and H_2O was produced and treated under static hydrothermal conditions for 72 h at 180 °C; a more detailed method may be found in Section 9.3.6.

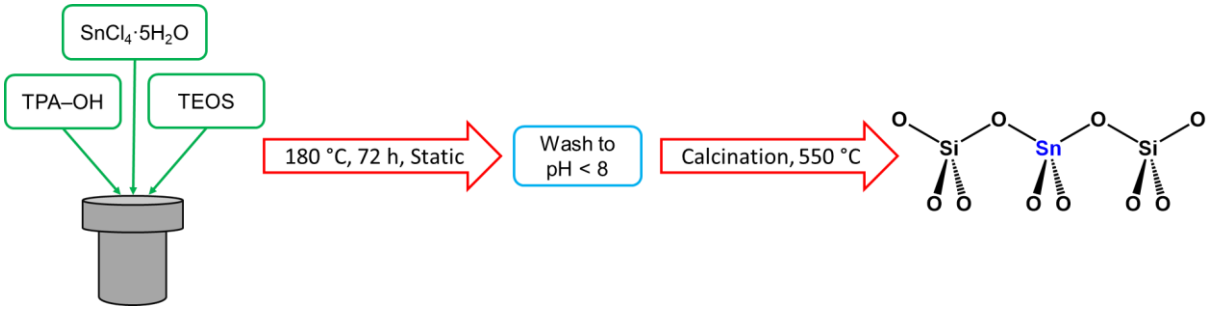

Figure 5.4: Schematic diagram of the hydrothermal synthesis procedure for Sn–MFI adapted from Kolyagin *et al.* and Mal *et al.*.[29, 30]

Following successful crystallisation, analysis of the material by pXRD, ED-XRF, DR-UV-Vis spectroscopy and ^{119}Sn ssNMR spectroscopy was undertaken to assess framework phase purity, metal incorporation and degree of framework Sn inclusion. Additionally, a second batch of Sn–MFI, denoted Sn–MFI–rep, was prepared under identical conditions and characterised to assess synthesis reproducibility.

Initially, pXRD analysis was undertaken to assess whether an MFI–type framework had been formed following hydrothermal crystallisation, and additionally whether the framework was retained following calcination to remove the organic template, TPA^+. Figure 5.5 shows the pXRD diffractograms of both Sn–MFI batches before and after calcination alongside a commercial Al–MFI as a reference material. It is observed that both batches exhibit typical features of an MFI framework and retain these features following high temperature calcination. Additionally, no presence of SnO_x phases were detected (Figure S5.1–2). Further, SEM analysis of both Sn–MFI and Sn–MFI–rep showed that a tablet-like morphology was consistently adopted, resembling that observed by Parulkar *et al.* following a similar synthesis of Sn–MFI (Figure 5.6).[31]

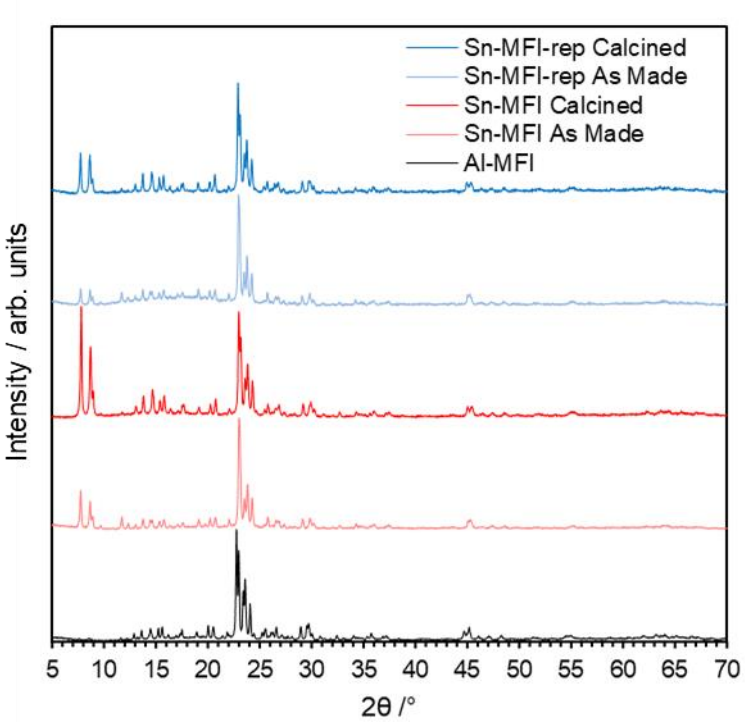

Figure 5.5: pXRD patterns in the 2θ = 5–70 ° region of synthesized Sn–MFI materials both as-made and following calcination. The diffractogram of a commercial Al–MFI material is included as an MFI framework reference.

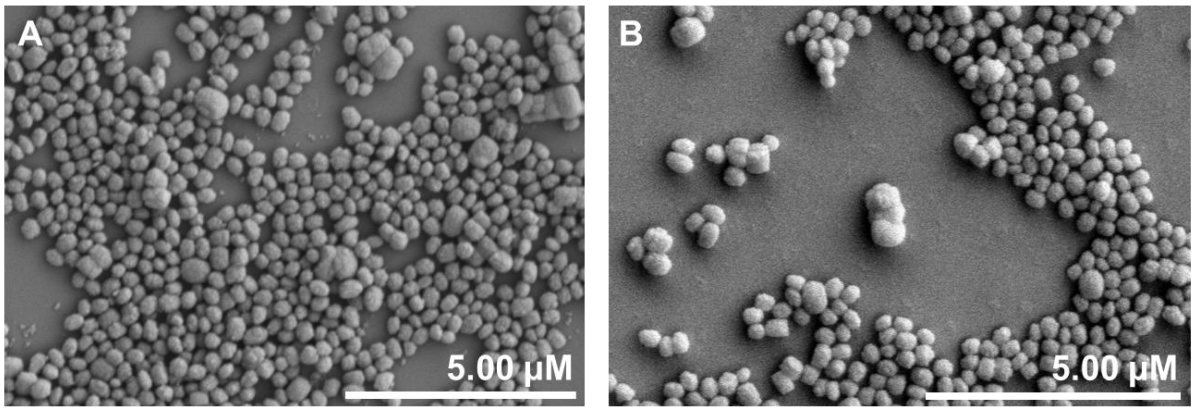

Figure 5.6: SEM images of Sn–MFI (A) and Sn–MFI–rep (B) following calcination

The Sn content from synthesised materials was assessed by means of ED-XRF analysis. Table 5.1 shows the ED-XRF elemental analysis data for both batches and shows good reproducibility between synthesis attempts in terms of Sn content and Si/Sn ratio.

Table 5.1: Elemental composition of synthesized Sn–MFI materials following calcination. ED–XRF values are averaged from three measurements and recorded as M wt%.

Material	Metal Loadings / Wt%		Elemental Ratio
	Si	Sn	Si/Sn
Sn–MFI	34.69	2.43	60.4
Sn–MFI–rep	37.16	2.32	67.6

Following elemental analysis to confirm Sn incorporation into the material, DR-UV-Vis spectroscopy and ^{119}Sn NMR spectroscopy were used to assess the degree of incorporation of Sn into the tetrahedral sites of the Sn–MFI materials. Successful framework incorporation is evidenced by DR-UV-Vis spectroscopy by exhibition of a strong absorption band centred around 220 nm ascribed to the charge transfer transition between O^{2-} and M^{4+} which is indicative of tetrahedrally coordinated framework metal atoms.[32-34] Any heteroatoms that had been unsuccessfully introduced into the zeolite tetrahedral sites would instead typically exhibit the characteristic absorbance profile for their respective metal oxide. Figure 5.7 shows the normalised DR-UV-Vis spectra of both calcined Sn–MFI materials alongside two commons oxides of Sn, $Sn^{IV}O_2$ and $Sn^{II}O$, that could be formed during the hydrothermal treatment or calcination steps. It is observed that both Sn–MFI materials exhibit a sole major absorption at around 220 nm with no significant contributions that can be correlated with either SnO or SnO_2.

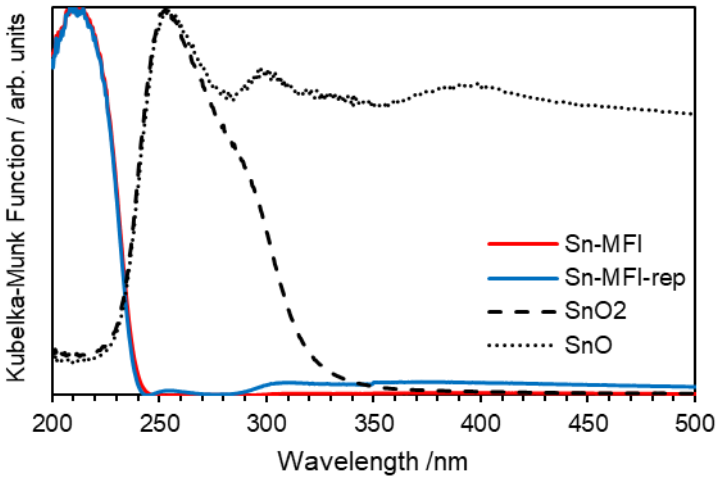

Figure 5.7: Normalised DR-UV-Vis spectra of calcined Sn–MFI materials (solid lines), SnO_2 (dashed line) and SnO (dotted line).

To further support the observations from DR-UV-Vis spectroscopy, ^{119}Sn ssNMR spectroscopic analysis was undertaken. As described in Section 2.1.3.4, typical ^{119}Sn ssNMR spectra exhibit up to two relatively distinct resonances associated with hydrated octahedrally coordinated framework-included Sn species ($\delta_{Sn} \approx -700$ ppm) and extra-framework Sn species in the form of SnO_2 ($\delta_{Sn} \approx -600$ ppm), allowing the user to relatively easily distinguish Sn in either coordination environment (Figure 5.8).[29] Additionally, thoroughly dehydrated samples exhibit a resonance around ($\delta_{Sn} \approx -400$ ppm) owing to tetrahedrally coordinated framework Sn species (Figure 5.8).[29, 35]

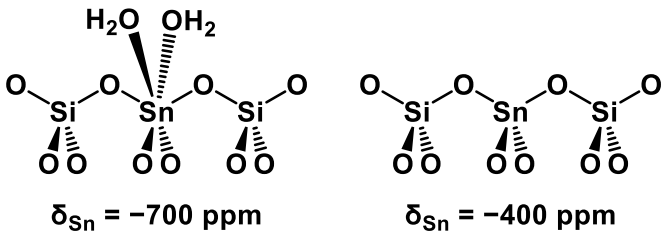

Figure 5.8: Zeolite framework included Sn species and their respective ^{119}Sn chemical shift (δ_{Sn}) regions.

Figure 5.9 shows the summed spikelet ^{1}H–^{119}Sn CP-CPMG ssNMR spectra of both pristine and calcined Sn–MFI and Sn–MFI-rep materials (raw spikelet patterns can be seen in Figure S5.3–4). Both prstine Sn–MFI materials are virtually identical, with major contributions centered at δ_{Sn} = −714 and −716 ppm, indicative of framework-included hydrated Sn species. Additionally, no contributions are observed in the region of δ_{Sn} = −600 ppm, implying a lack of extra-framework SnO_2, concordant with the observations from DR-UV-Vis spectroscopy and literature regarding Sn-containing zeolites from Kolyagin *et al.*, Mal *et al.*and Yakimov *et al.*.[29, 30, 35] Following calcination, Sn–MFI (Figure 5.9, red trace) is seen to exhibit multiple downfield resonances centered at δ_{Sn} = −501, −567, −648 and −683 ppm. These resonances could imply the presence of SnO_2 species, however this is not in agreement with the acquired DR-UV-Vis spectroscopy and may therefore instead be ascribed to partially dehydrated Sn-centres resultant from the high temperature calcination following synthesis, as dehydrated Sn-centres typically resonate downfield from hydrated octahedral Sn, at approximately δ_{Sn} = −400 ppm.[29, 35-37] The ^{1}H–^{119}Sn CP-CPMG ssNMR spectrum of Sn–MFI-rep following calcination (Figure 5.9, blue trace) is indicative of hydrated octahedral framework Sn species, with a major resonance at δ_{Sn} = −707 ppm.[29, 35-37] It is worth noting that the intensities of the spectra from calcined materials were substantially lower than those for the pristine materials, most likely owing to removal of the organic template decreasing the amount of ^{1}H nuclei available for cross-polarisation, hence a higher number of transients was acquired for each spectrum.

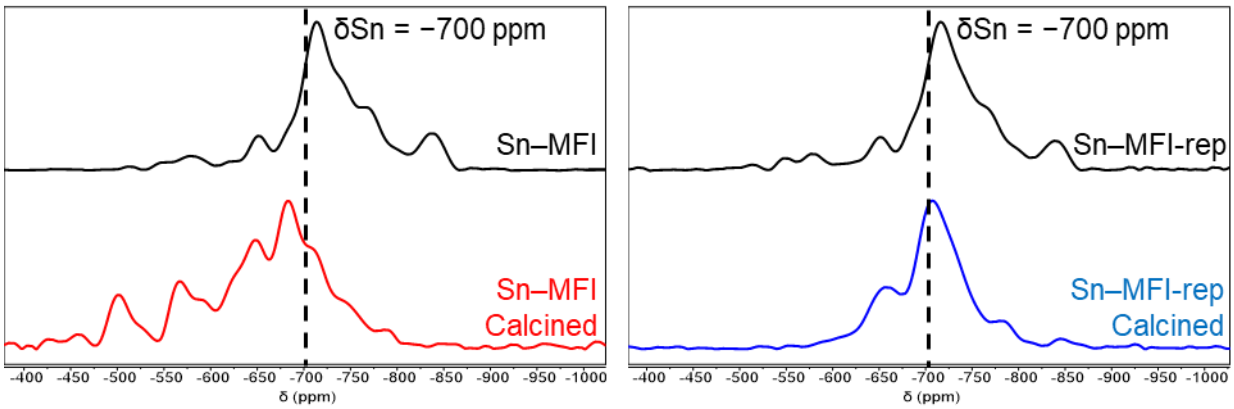

Figure 5.9: Normalised spikelet sum ^{1}H–^{119}Sn CP-CPMG ssNMR spectra of Sn–MFI materials averaged over 6400 scans for non calcined materials and 32000 and 12800 scans for calcined Sn–MFI and Sn–MFI-rep respectively with a 2.0 s recycle delay and a 5 ms contact time. All spectra acquired on a Bruker III Avance 400 MHz spectrometer using a 4 mm zirconia rotor. Spectrometer frequncies: ^{1}H = 400.17 MHz, ^{119}Sn = 149.12 MHz. MAS spin rate = 10000 Hz.

As a result of all previous characterisation of synthesised Sn–MFI materials, it is suggested that the method for Sn–MFI synthesis adapted from Kolyagin *et al.* and Mal *et al.* can reproducibly produce an MFI type material containing framework bound Sn atoms.[29, 30]

5.1.2. Synthesis and characterisation of a series of M–MFI using an adapted synthesis procedure for Sn–MFI.

As a result of the successful synthesis of Sn–MFI, the hydrothermal method was adapted by variation of the metal precursor in order to attempt to include the other desired Lewis acidic metal atoms, namely Ti, Zr and Hf, into an MFI-type framework for the purpose of ethanol conversion. A Si–MFI material was also synthesised as a reference material by omission of the metal precursor during synthesis gel formation. Figure 5.10 shows a schematic view of the synthesis procedure for M–MFI synthesis using an equimolar quantity of $SnCl_4 \cdot 5H_2O$, $Ti(^{i}OPr)_4$, $ZrOCl_2 \cdot 8H_2O$ or $HfOCl_2 \cdot 8H_2O$ for Sn, Ti, Zr and Hf analogues, respectively. Whilst other hydrothermal synthesis methods of Si,[38, 39] Ti,[40] Zr,[34, 41] and Hf[4] substituted MFI frameworks are known, a common synthesis method was used for all samples in order to maintain consistency. Elemental composition of materials collected by two orthogonal analysis techniques, ED-XRF and ICP-OES, and determined Si/M ratios are shown in Table 5.2. Despite equimolar amounts of metal precursors being used during hydrothermal synthesis, elemental compositions vary widely between different M−MFI materials but are individually within reasonable agreement across multiple elemental analysis techniques.

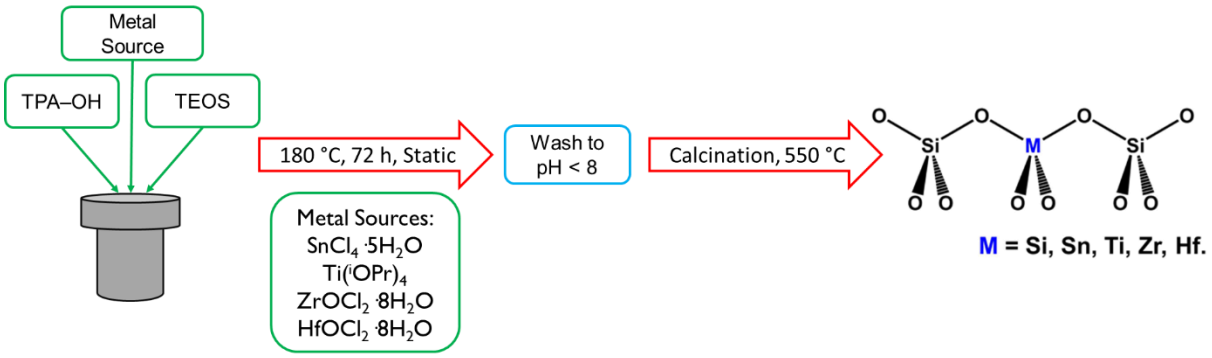

Figure 5.10: Schematic diagram of the hydrothermal synthesis procedure for M–MFI materials adapted from Kolyagin *et al.* and Mal *et al.*.[29, 30]

Table 5.2: Elemental composition and elemental ratios of synthesized M–MFI materials following calcination, where M = Si, Sn, Ti, Zr, Hf. ED–XRF values are averaged from three measurements and recorded as M wt%. ICP-OES values are measured and recorded as M wt%.

Material	Elemental Loading (ED-XRF) / Wt%					Elemental Loading (ICP-OES) / Wt%				
	Si	Sn	Ti	Zr	Hf	Si	Sn	Ti	Zr	Hf
Si-MFI	43.33	—	—	—	—	45.16	—	—	—	—
Sn-MFI	41.04	2.23	—	—	—	42.24	1.66	—	—	—
Ti-MFI	47.21	—	0.77	—	—	46.13	—	0.69	—	—
Zr-MFI	40.59	—	—	0.63	—	45.71	—	—	0.64	—
Hf-MFI	45.73	—	—	—	1.28	39.04	—	—	—	1.15
	Si/M Ratio (ED-XRF)					**Si/M Ratio (ICP-OES)**				
Si-MFI	N/A					N/A				
Sn-MFI	77.8					107.8				
Ti-MFI	104.9					113.2				
Zr-MFI	208.6					230.8				
Hf-MFI	226.3					248.5				

To ensure that an MFI-type framework was adopted by all samples, powder X-ray diffraction (pXRD) analysis was undertaken. The diffractograms for all M–MFI materials are shown in Figure 5.11 alongside a commercial Al–MFI material for reference. It is observed that all M–MFI materials adopt an MFI-type framework with no additional reflections associated with other silicate phases or extra-framework oxide species observed. It was hypothesized that inclusion of large metal ions into tetrahedral positions may result in

framework expansion and a subsequent increase in d-spacing, resulting in a decrease of 2θ values for characteristic reflections. This effect has been reported before for Sn–MFI[42] and Ti–MFI,[43] although it is normally minor ($\Delta_{2\theta}$ = 0.1°). In order to assess this, pXRD analysis was performed using LaB_6 as an internal reference for 2θ values.[44, 45] Approximately 10 wt% LaB_6 was thoroughly incorporated into the pXRD samples and resulting diffractograms were referenced to the LaB_6 (1 1 0) reflection. Figure 5.11B shows the referenced diffraction patterns in the range of 2θ = 20–30°; no substantial peak shift is evident for any M–MFI material, suggesting that no significant framework expansion was resultant from heteroatom incorporation.[42, 46] A significantly zoomed diffractogram is provided in Figure S5.7. (2θ = 7.4–9.4°) with no major peak shift evident.

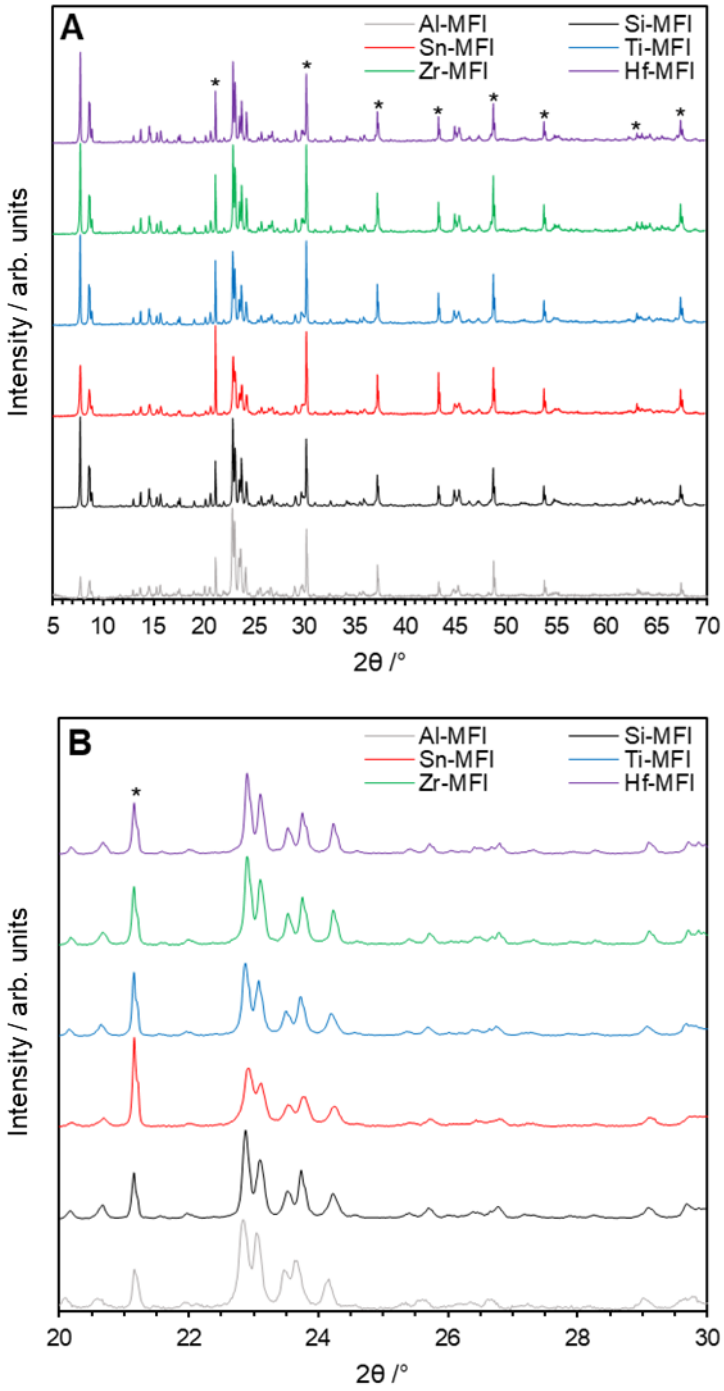

Figure 5.11: pXRD patterns in the 2θ = 5–70° (A) and 2θ = 20–30° (B) range of synthesized M–MFI materials following calcination, where M = Si, Sn, Ti, Zr, Hf. The diffractogram of a commercial Al–MFI material is included as an MFI framework reference. Asterisks (*) denote peaks corresponding to LaB_6 which was used as an internal reference for 2θ values.

Catalyst structure was further assessed by use of ^{29}Si direct excitation (Figure 5.12) and ^{1}H–^{29}Si cross-polarisation (Figure 5.13) solid-state NMR spectroscopy in order to probe the materials for silicon environments and silanol defects.[47, 48] As can be seen in Figure 5.12, for all M–MFI materials, the vast majority of silicon atoms reside in a coordinatively saturated Q_4 environment (δ_{Si} = −112 ppm), with many fewer residing in mono-unsaturated Q_3

environments ($\delta_{Si} = -103$ ppm).[47, 48] Enhancement of silanol groups by use of a ^{1}H–^{29}Si cross-polarisation sequence confirms that the large majority of defects are Q_3 in nature ($\delta_{Si} = -103$ ppm), with a minor contribution from potential Q_2 species detected for Sn–MFI (Figure 5.13).

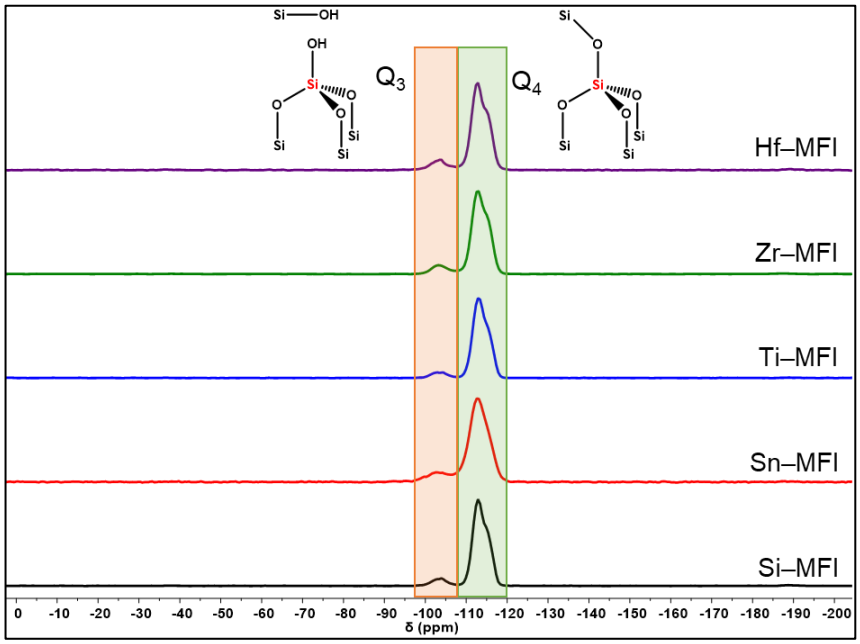

Figure 5.12: ^{29}Si direct excitation ssNMR spectra of Si–MFI, Sn–MFI, Ti–MFI, Zr–MFI and Hf–MFI following calcination. CP spectra were averaged over 376-512 transients with a 30-60 s recycle delay as optimised for each sample. Spectra were acquired on a Varian VNMRS 400 MHz spectrometer using a 6 mm zirconia rotor. Spectrometer frequency: ^{29}Si = 79.44 MHz. MAS spin rate ≈ 6000 Hz.

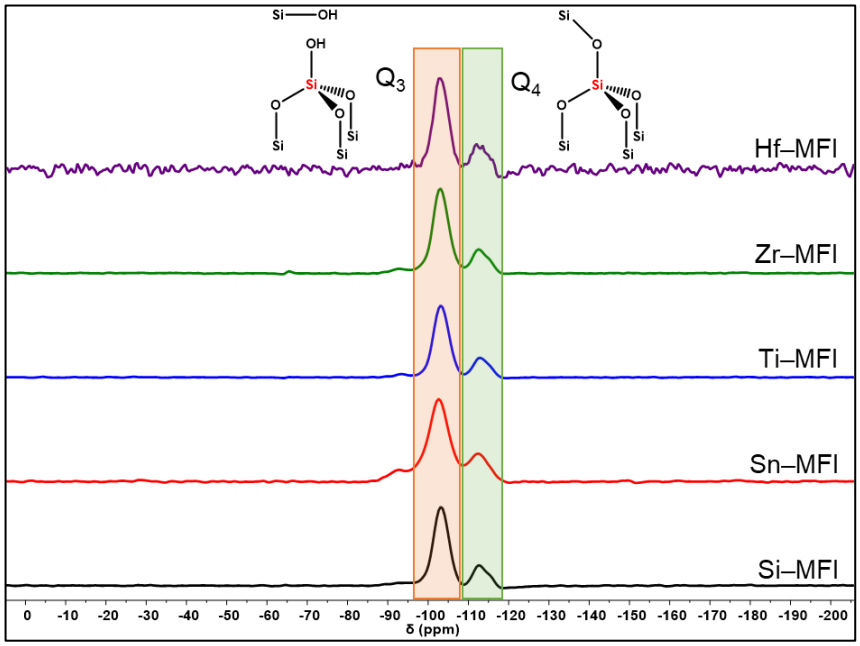

Figure 5.13: ^{1}H–^{29}Si cross polarisation ssNMR spectra of Si–MFI, Sn–MFI, Ti–MFI, Zr–MFI and Hf–MFI following calcination. CP spectra were averaged over 1800 transients with a 1-10 s recycle delay as optimised for sample. Spectra were acquired on a Varian VNMRS 400 MHz spectrometer using a 6 mm zirconia rotor. Spectrometer frequency: ^{1}H = 399.88 MHz ^{29}Si = 79.44 MHz. MAS spin rate ≈ 6000 Hz.

Catalyst morphology was assessed by means of scanning electron microscopy (SEM) imaging with traditional SEM images of M–MFI materials shown in Figure 5.14. All materials exhibit a similar morphology, being predominantly composed of small, tablet-like crystals with a diameter of around 300–400 nm. Additionally, all M–MFI materials contain larger agglomerates that adopt the "coffin-like" morphology typical of Al–MFI (ZSM–5), which are hypothesized to become more prevalent with extended synthesis times.[49, 50] The crystal morphology and size of all M–MFI materials closely resembles that seen for literature Si–MFI, Sn–MFI, Ti–MFI and Zr–MFI materials synthesized in a fluoride-free environment.[31, 38, 51-54] Further, scanning electron microscopy-energy dispersive spectroscopy (SEM-EDS) mapping of all M–MFI materials was undertaken to assess metal dispersion following synthesis and calcination. All M–MFI materials (with the exception of Si–MFI) were mapped at two distinct locations and each exhibited a homogenous distribution of heteroatomic metal atoms across the synthesized samples with no visible evidence of metal clustering (Figure 5.15–20).

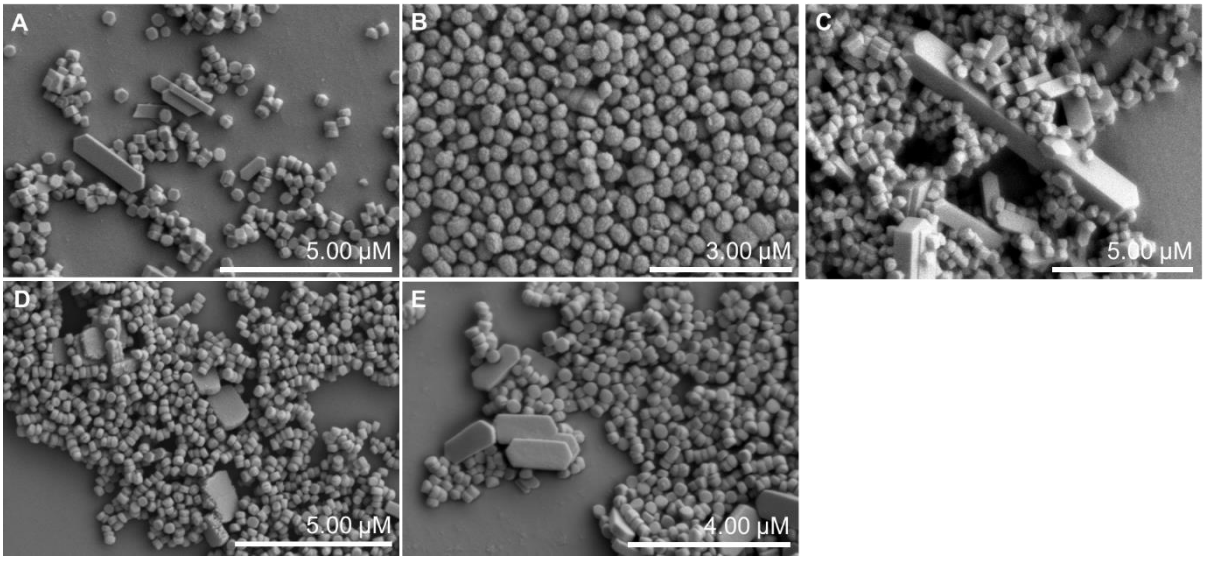

Figure 5.14: SEM images of Si–MFI (A), Sn–MFI (B), Ti–MFI (C), Zr–MFI (D) and Hf–MFI (E) following calcination.

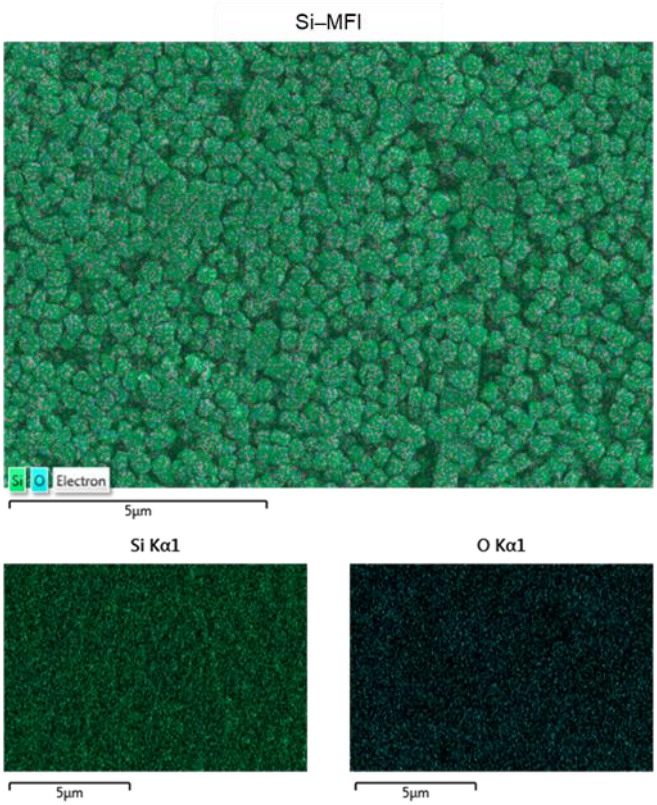

Figure 5.15: SEM-EDS mapping of Si-MFI at Si Kα_1 and O Kα_1.

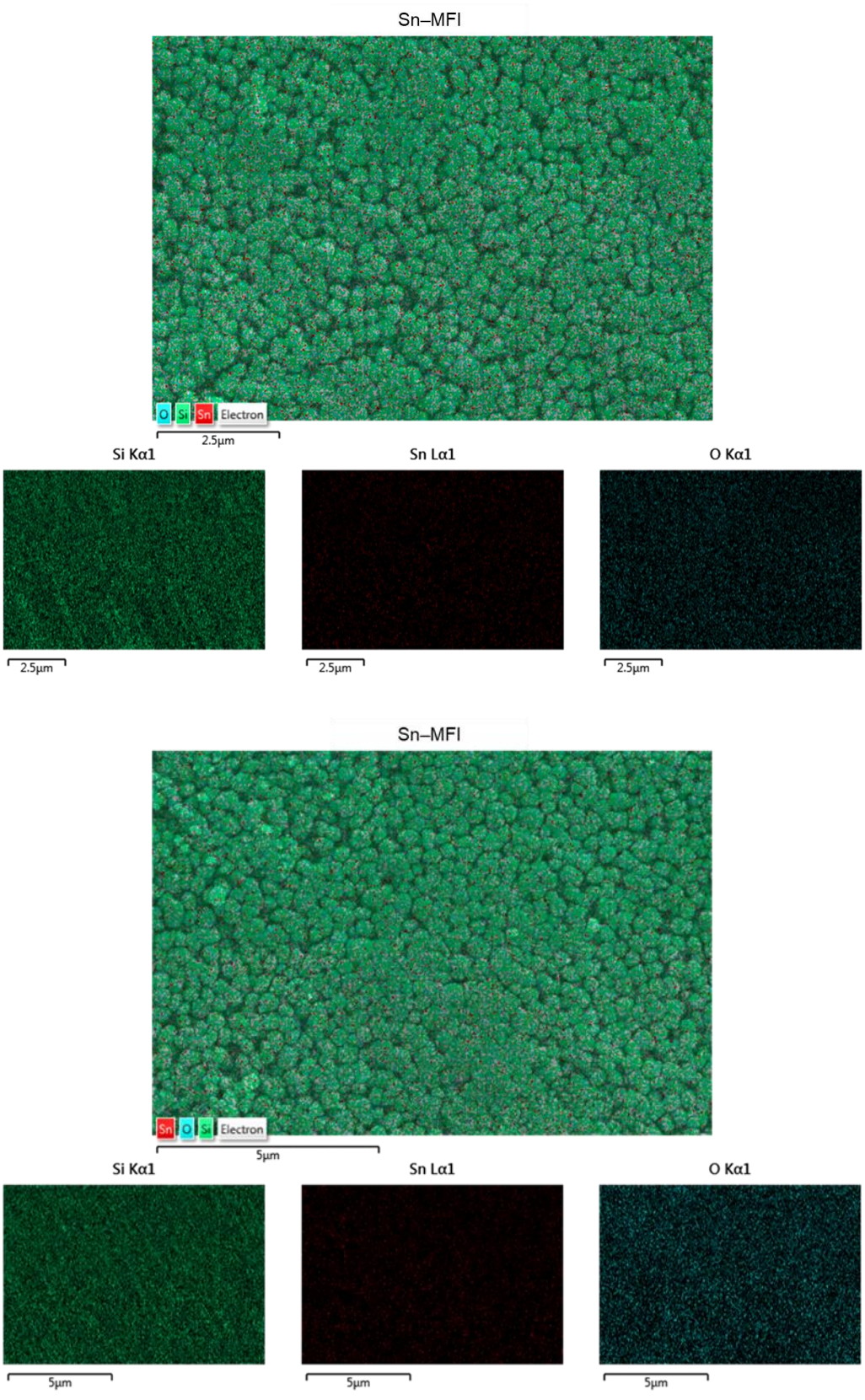

Figure 5.16: SEM-EDS mapping of Sn-MFI at Si Kα1, Sn $L\alpha_1$ and O $K\alpha_1$.

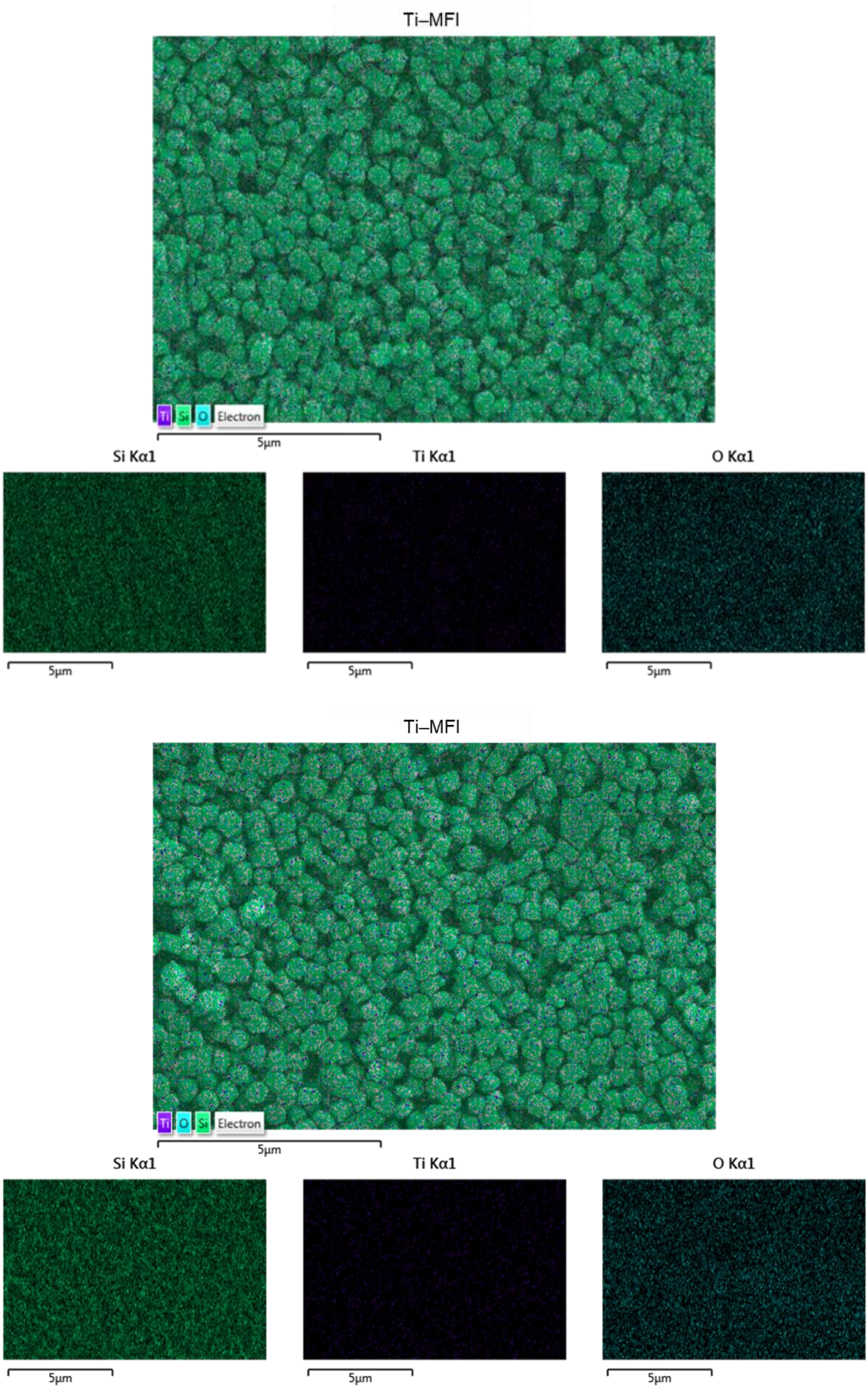

Figure 5.17: SEM-EDS mapping of Ti-MFI at Si Kα_1, Ti Kα_1 and O Kα_1.

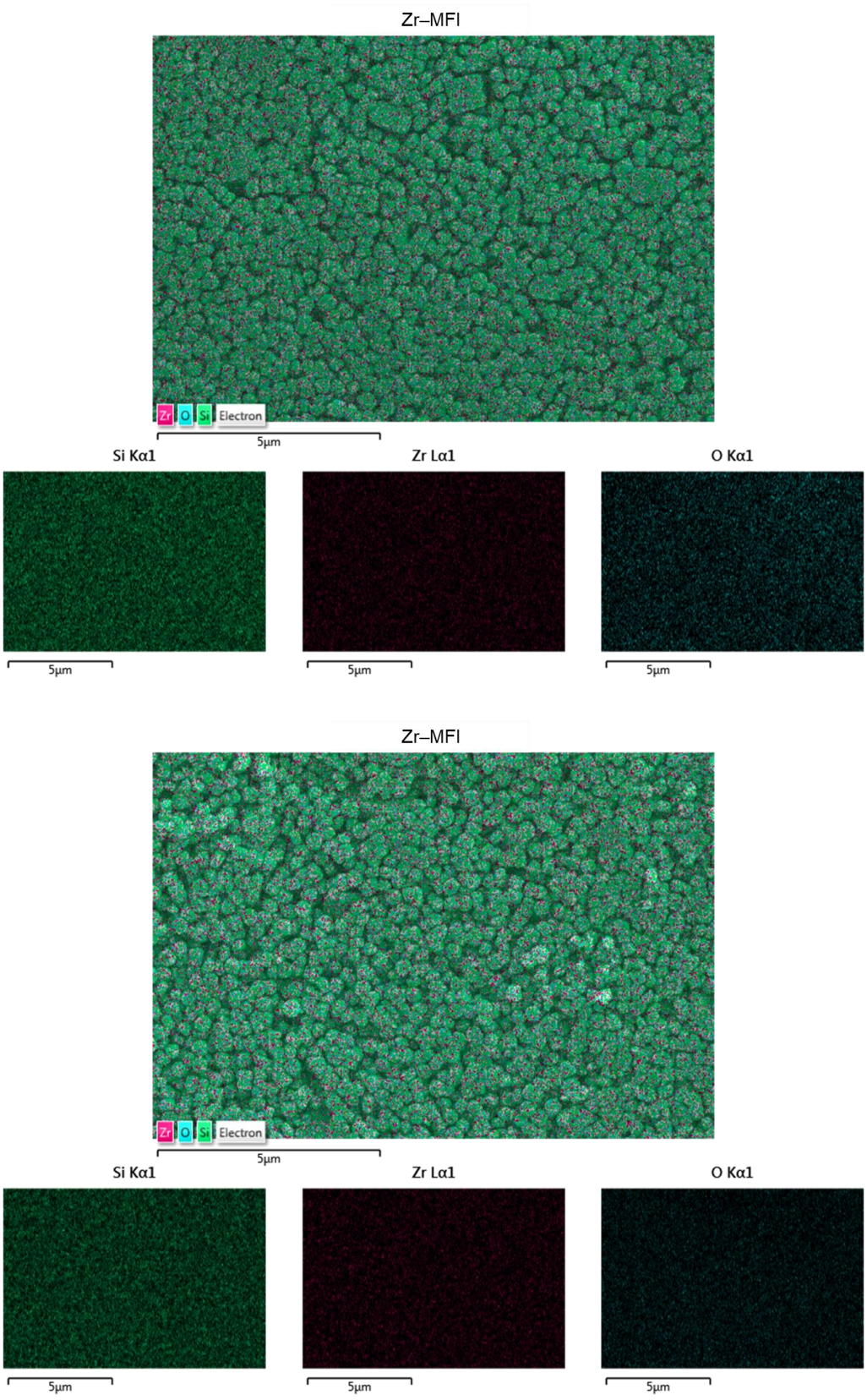

Figure 5.18: SEM-EDS mapping of Zr-MFI at Si Kα1, Zr Lα_1 and O Kα_1.

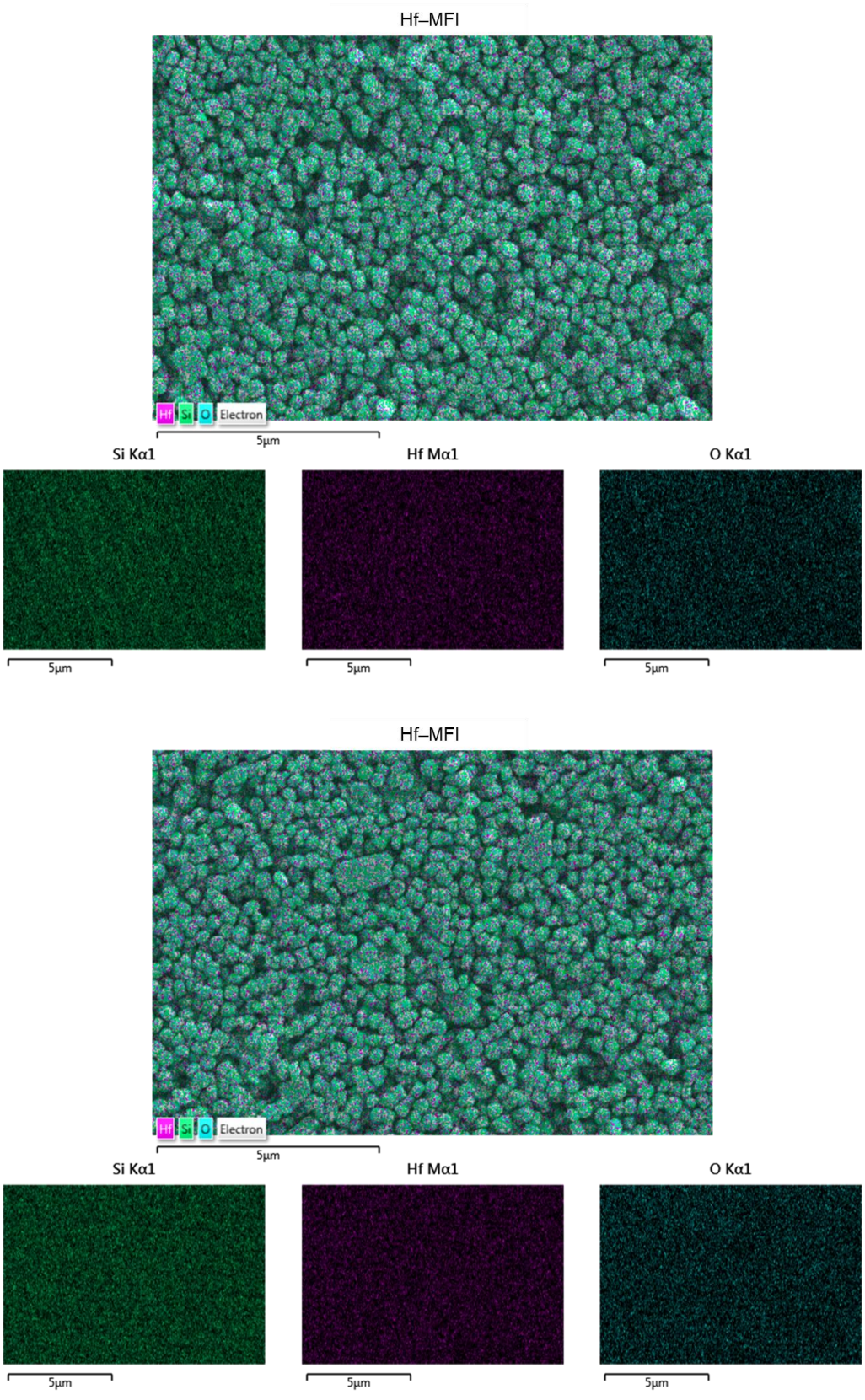

Figure 5.19: SEM-EDS mapping of Hf-MFI at Si Kα1, Hf $M\alpha_1$ and O $K\alpha_1$.

In order to assess catalyst surface area, N_2 physisorption analysis and subsequent BET surface area calculation was undertaken. All synthesized materials exhibit a similar isotherm shape (Figure 5.20), with the exception of Ti–MFI which shows a larger hysteresis loop most likely resultant from minor pore blockage owing to the presence of extra-framework titania. Calculation of the surface area of the materials using the Brunauer-Emmett-Teller (BET) equation showed that very similar surface areas were achieved, averaging around 420 $m^2\ g^{-1}$, comparable to that of a commercial Al–MFI material (Table 5.3).

Table 5.3: BET surface area values for synthesized M–MFI materials following calcination, where M = Si, Sn, Ti, Zr, Hf. A commercial Al–MFI material is included for reference.

Material	BET Surface Area / $m^2\ g^{-1}$
Si-MFI	424 ± 1.4
Sn-MFI	412 ± 2.0
Ti-MFI	430 ± 0.4
Zr-MFI	421 ± 1.6
Hf-MFI	428 ± 1.6
Commercial Al-MFI	447 ± 0.4

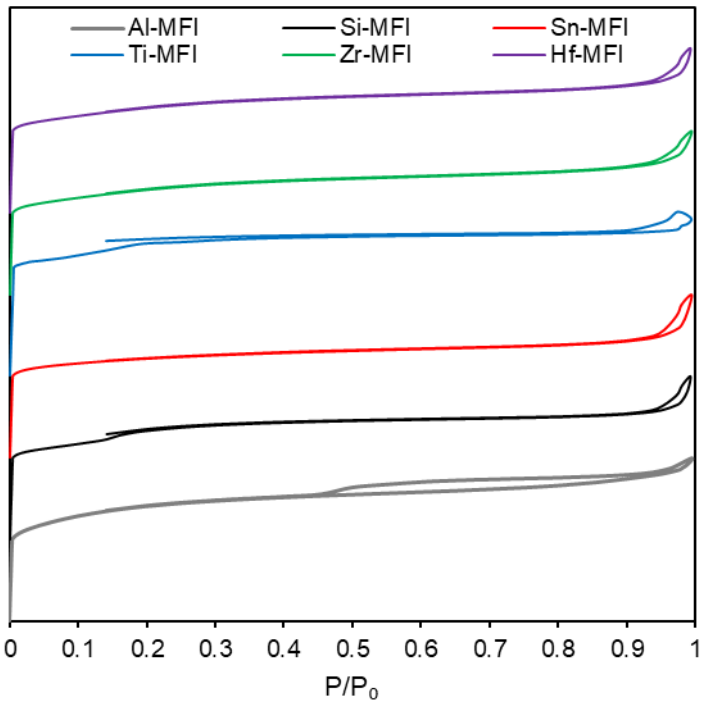

Figure 5.20: Normalised N_2 physisorption isotherm plots of synthesized M–MFI materials following calcination, where M = Si, Sn, Ti, Zr, Hf. A commercial Al–MFI material is included for reference.

Further, diffuse reflectance ultraviolet-visible (DR-UV-Vis) spectra were recorded for the calcined M–MFI samples to assess the degree of metal incorporation into the zeolite framework and to assess the presence of extra-framework metal oxide phases (Figure 5.21). All samples exhibited a strong absorption band centred around 220 nm ascribed to the charge transfer transition between O^{2-} and M^{4+}, indicative of tetrahedrally coordinated framework metal atoms.[32-34, 53, 55] The DR-UV-Vis spectra of Si, Sn, Zr and Hf–MFI do not exhibit any substantial contributions from extra-framework oxide type materials at absorption wavelengths > 250 nm, suggesting the absence of extra-framework metal oxide phases (Figure S5.8). The DR-UV-Vis spectrum of Ti–MFI does however show absorbance at around 250–300 nm arising from extra-framework titania which shows similar features to, and is therefore ascribed to, a P25 type phase (Figure S5.8). Subsequent catalytic results, however, suggest that this extra-framework material does not have any substantial effect on catalytic activity. The observation of extra-framework titania in Ti–MFI is additionally concordant with the observation of a small hysteresis loop in the N_2 physisorption isotherm Ti–MFI resultant from potential pore blockage (Figure 5.20).

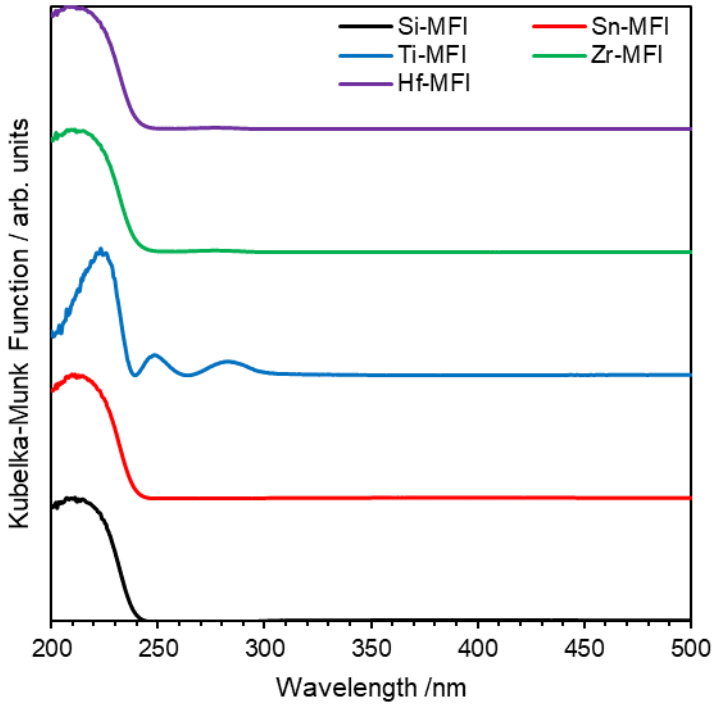

Figure 5.21: DR–UV–Vis spectra for as-synthesised M–MFI materials following calcination, where M = Si, Sn, Ti, Zr, Hf.

The combined observations from pXRD, ^{29}Si ssNMR spectroscopy, SEM-EDS mapping, N_2 physisorption analysis and DR-UV-Vis spectroscopy therefore allow the

conclusion that each synthesized M–MFI sample successfully adopts the MFI morphology and predominantly contains the desired heteroatomic metal atom within the tetrahedral positions of the MFI framework.

5.2. Variable temperature screening of M–MFI materials for ethanol to 1,3–butadiene cascade synthesis.

5.2.1. Variable temperature screening of calcined M–MFI materials.

Initially, catalytic reactions of ethanol over unmodified M–MFI materials were performed to understand their inherent catalytic capacity and product distributions resulting from ethanol conversion under flow conditions. In order to aid clarity, a nomenclature was adopted in which elemental ratios are expressed within the sample name, i.e ZnO(3.35)/Sn(108)–MFI possesses a Zn loading of 3.35 wt% and a Si/Sn ratio of 108. Figure 5.22 shows the effluent compositions at various temperature points resulting from feeding ethanol over a 300 mg charge of the pristine calcined materials. All M-MFI materials exhibit a similar behaviour under the chosen reaction conditions, with the production of diethyl ether favoured at around 300 °C and the production of ethylene favoured at ≥ 350 °C. No significant production of acetaldehyde or butadiene is observed for any of the materials tested. This behaviour is as expected of Lewis acidic type zeolitic materials, with production of diethyl ether and ethylene ascribed to Lewis acid catalysed dehydrative etherification and dehydration of ethanol respectively as seen previously and predicted computationally for Sn–BEA zeolites in the literature.[56, 57] It is predicted these observations are specifically from closed Lewis acidic metal centres as opposed to open Brønsted acidic sites as hydrolysis to form open Brønsted acidic sites has been shown to be energetically unfavourable by DFT calculations on both Sn– and Ti–MFI.[58] Although, water has been shown to induce Bronsted acid formation for Sn–BEA zeolites in the literature.[36] Interestingly, Si–MFI exhibits the ability to produce both diethyl ether and ethylene, suggesting that the presence of assumed weakly acidic silanol groups or defects are also sufficient to catalyse these reactions. Work by Della Pina *et al.* corroborates this observation of reactivity over Si–MFI alongside the temperature dependence of its selectivity, with selectivity to diethyl ether being reported at temperatures around 300–350 °C and selectivity to ethylene reported for temperatures of 400 °C and above (Table 2 in ref 59).[59] Notably, in Figure 5.22, the onset of both diethyl ether and ethylene production is observed to shift to lower temperatures as the transition down the group 4 metals from Ti(113)–MFI to Zr(231)–MFI to Hf(249)–MFI is made. Additionally, the combined effluent selectivity of acid

catalysed products is seen to increase down the group 4 metals. These observations would both suggest an increase in the relative Lewis acidity from Ti to Zr to Hf.

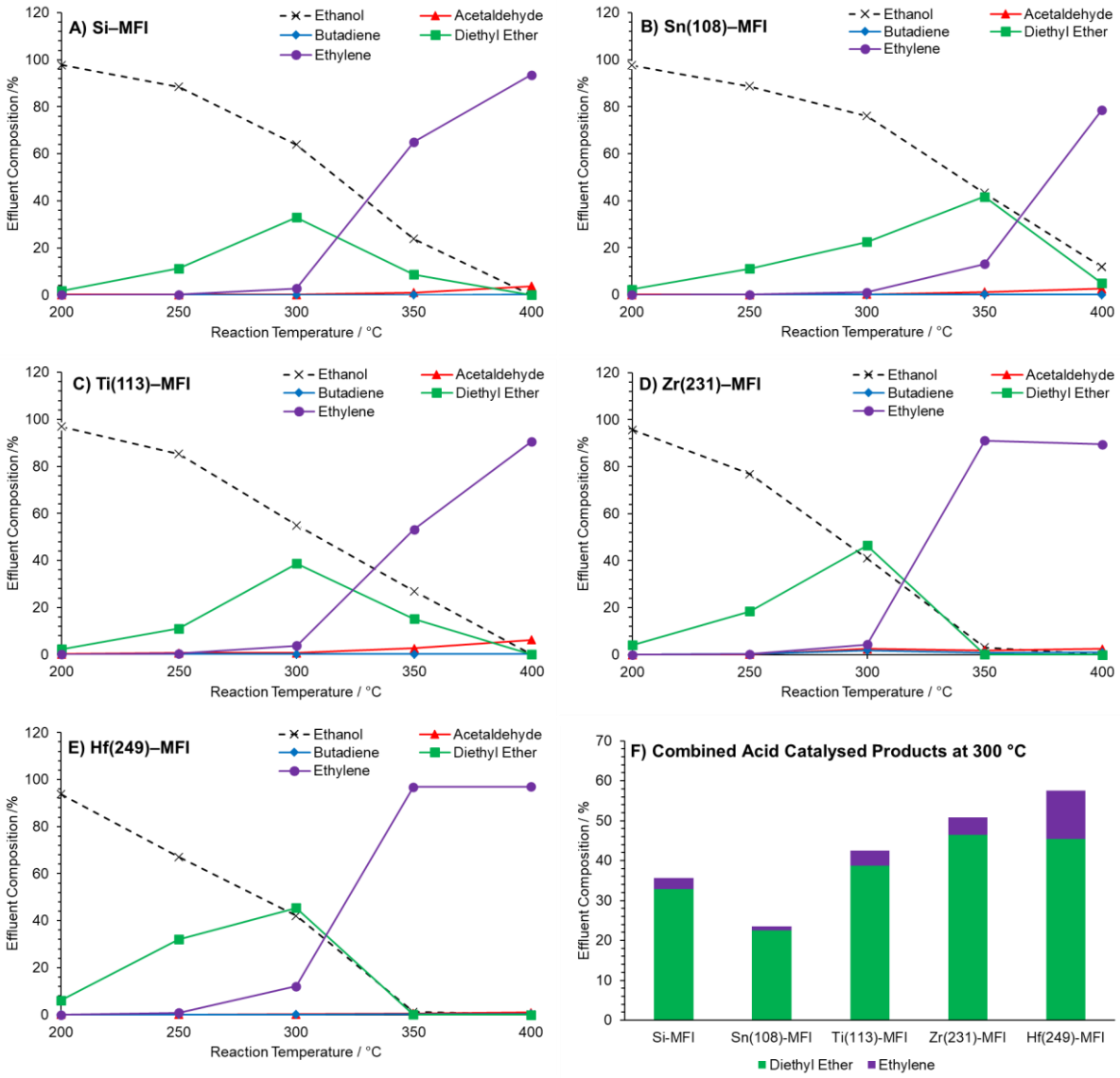

Figure 5.22: Effluent compositions resulting from reaction of ethanol at various temperatures over: Si–MFI (A), Sn(108)–MFI (B), Ti(113)–MFI (C), Zr(231)–MFI (D) and Hf(249)–MFI (E). Ethanol feed rate = 0.197 mmol min^{-1}, catalyst mass = 0.300 g. Traces for ethanol (×), acetaldehyde (▲), butadiene (♦), diethyl ether (■) and ethylene (●) are shown. Additional trace amounts of other carbon containing products were detected and accounted for but omitted for clarity. F) Combined effluent selectivity of acid catalysed products.

As discussed in the introduction to this chapter, generalised quantification of Lewis acidity (and subsequent trend matching) is difficult, as Lewis acid strength depends heavily on the system in question. In comparison to existing literature, the trend for Lewis acidity (Hf(249)–MFI > Zr(231)–MFI > Ti(113)–MFI) resulting from Figure 5.22F is concordant with DFT computational studies of the Lewis acidity of Ti- and Zr-substituted BEA zeolites, in which the adsorption energy of water onto various tetrahedral Lewis acidic centres is seen to have a greater magnitude for Zr–BEA at all framework tetrahedral positions when compared

to Ti–BEA, suggesting stronger Lewis acidity of the Zr centre.[60] Further DFT studies of NH_3 adsorption suggest that the Lewis acidity of Sn(108)–MFI is greater than that of Ti(113)–MFI, although this does not seem to be evident in the catalytic results shown in Figure 5.22. Additionally, calculated ammonia absorption energies by Yang *et al*. suggest a trend in Lewis acidity of Zr > Sn > Ti which is relatively concordant with that observed in Figure 5.22.[28] Further, investigation into the cross-aldol condensation of aromatic aldehydes with acetone over Sn–BEA, Zr–BEA and Hf–BEA by Lewis *et al*. conclude that their observed activity trend is in the order Hf ≈ Zr > Sn.[16] This reported trend is similar to that seen in Figure 5.22 and is ascribed to an electronic structure effect by the authors. The lesser observed activity of Sn in the catalytic results presented in Figure 5.22 may therefore instead be ascribed to differences in vacant acceptor orbital energy and geometry or metal polarizability as previously discussed. Hence, whilst Sn centres may possess a greater magnitude of Lewis acidity and oxygen basicity, their accepting orbital may be less available or relevant transition states may be more difficult to access.[58]

5.2.2. Zn modification of M–MFI materials and variable temperature screening of resultant ZnO/M–MFI materials.

Following successful observation of Lewis acid type behaviour from the previously synthesized M–MFI materials, it was hypothesized that addition of a dedicated dehydrogenation site to the materials would open the catalytic cycle and allow observation of direct cascade transformation of ethanol to 1,3–butadiene. This bifunctional approach has been used frequently in the literature, examples including incorporation of Ag into Zr–BEA,[2, 5] ZnO onto MgO–SiO_2,[61] and CuO onto MgO–SiO_2.[62] Work undertaken in Chapter 4 has demonstrated that wetness impregnation of ZnO onto zeolite materials is an efficient system for direct dehydrogenation of ethanol to acetaldehyde, hence all M–MFI materials were modified in this fashion resulting in a series of ZnO/M–MFI catalysts containing approximately 3.0–3.5 wt% ZnO by Zn (Table 5.4).

Table 5.4: Zn content of ZnO/M–MFI materials obtained by ICP-OES where M = Si, Sn, Ti, Zr, Hf. Target Zn wt% = 3.50. Values are averaged over multiple wavelengths where possible and appropriate.

Material	Zn Wt%
ZnO(3.15)/Si–MFI	3.15
ZnO(3.35)/Sn(108)–MFI	3.35
ZnO(3.35)/Ti(113)–MFI	3.35
ZnO(3.20)/Zr(231)–MFI	3.20
ZnO(3.13)/Hf(249)–MFI	3.13

Following preparation and subsequent calcination, catalytic reactions of ethanol over ZnO/M–MFI materials were performed to test this hypothesis. Figure 5.23 shows the effluent compositions at various temperature points resulting from feeding ethanol over the calcined ZnO/M–MFI materials (as described in Section 9.4.2). In these tests, the material was first pre-treated under N_2 flow at 400 °C for one hour before the reaction temperature was reduced to 200 °C. Ethanol flow was commenced after 15 minutes at 200 °C and lasted for one hour to allow two GC-MS-BID runs to be completed. Ethanol flow was then stopped, and the system was purged with N_2 for 15 minutes to remove excess ethanol and products, allowing clearer comparison between reactions at various temperature points. Subsequently, the temperature was raised to 250 °C and the cycle restarted. This cycle was repeated in steps of 50 °C up to a maximum temperature of 400 °C. It is observed that addition of ZnO to all M–MFI materials facilitates the production of intermediate acetaldehyde which results in observation of the hypothesized total cascade reaction of ethanol to 1,3–butadiene. Products arising from the reaction of ethanol over Lewis acidic sites, such as diethyl ether and ethylene, are still observed, albeit at lower concentrations. Figure S5.9 shows the butadiene productivities of ZnO/M–MFI materials at various reaction temperatures normalized by both catalyst mass (Figure S5.9A) and molar heteroatom content (Figure S5.9B). It is affirmed that ZnO(3.20)/Zr(231)–MFI possesses the highest butadiene productivity of all materials tested, exhibiting a maximum of 7.0 mmol g_{cat}^{-1} h^{-1} at 350 °C (Figure S5.9A). Further, the catalytic efficiency for heteroatom sites is seen to be highest for ZnO(3.20)/Zr(231)–MFI when butadiene productivity is normalized by heteroatom content (Figure 5.23F). For most ZnO/M–MFI materials a butadiene productivity peak is observed at 350 °C with the exception of ZnO(3.13)/Hf(249)–MFI which performs best at its tested maximum of 400 °C. Figure 5.23G also shows that ZnO(3.20)/Zr(231)–MFI possesses the highest proportion of effluent comprised of products on the Lebedev pathway (acetaldehyde and butadiene).

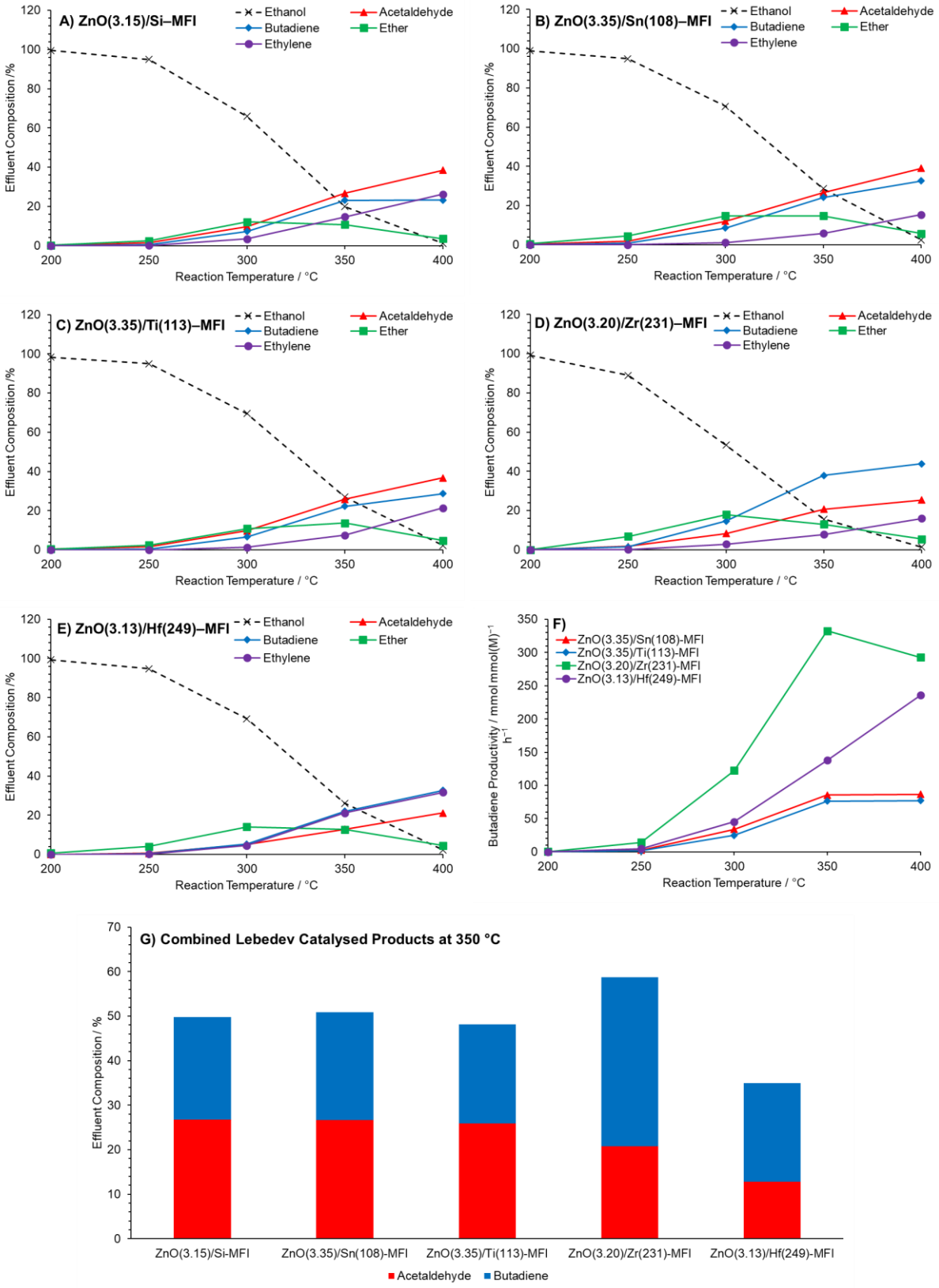

Figure 5.23: Effluent compositions resulting from reaction of ethanol at various temperatures over: ZnO(3.15)/Si–MFI (A), ZnO(3.35)/Sn(108)–MFI (B), ZnO(3.35)/Ti(113)–MFI (C), ZnO(3.20)/Zr(231)–MFI (D) and ZnO(3.13)/Hf(249)–MFI (E). Ethanol feed rate = 0.197 mmol min^{-1}, catalyst mass = 0.300 g. Traces for ethanol (×), acetaldehyde (▲), butadiene (♦), diethyl ether (■) and ethylene (●) are shown. Additional trace amounts of other carbon containing products were detected and accounted for but omitted for clarity. F) Butadiene productivities normalized by heteroatom content. G) Combined effluent selectivity of acid catalysed products.

5.3. Reproducibility, long-term stability, and deactivation of ZnO/Zr–MFI for the direct cascade synthesis of 1,3–butadiene from ethanol.

Following identification of ZnO(3.20)/Zr(231)–MFI as the optimum synthesised ZnO/M–MFI for butadiene production from ethanol in this study, a series of further time-resolved studies were undertaken. Namely, a reproducibility study was undertaken in which three reactions of ethanol over charges of ZnO(3.20)/Zr(231)–MFI from the same batch were performed and analysed for reproducibility and error margins. Additionally, a long-term stability test was undertaken in which a charge of ZnO(3.20)/Zr(231)–MFI was reacted with ethanol for over 72 h TOS in order to discern the lifetime of the catalyst. Finally, following identification of substantial deactivation within the long-term stability test, in-depth spent catalyst analysis was performed alongside a regeneration study.

5.3.1. Reproducibility study of ZnO/Zr–MFI for the direct cascade synthesis of 1,3–butadiene from ethanol.

Figure 5.24 shows effluent composition (A), selectivity (B), productivity (C) yield (D), ethanol conversion (E) and carbon balance (F) metrics resulting from three repeat reactions of ethanol at 350 °C over ZnO(3.20)/Zr(231)–MFI for 4 h TOS. For all subsequent reactions, the ethanol feed rate was increased to around 0.300 mmol min^{-1}. The results shown are averaged over three repeat experiments with error bars denoting one standard deviation in each co-ordinate. Good reproducibility is observed across all metrics with an average butadiene selectivity of around 18% observed, correlating to an average butadiene productivity and yield of 2.8 mmol g_{cat}^{-1} h^{-1} and 9.1 % respectively at an ethanol conversion value of between 50-60 %. Minor deactivation is observed in terms of ethanol conversion from an initial value of 80% dropping to around 55 % following 4 h TOS (Figure 5.24E). During this time, selectivity to diethyl ether and ethylene is seen to decrease whilst selectivity to acetaldehyde is seen to increase (Figure 5.24B). Figure 5.24F demonstrates that the average carbon balance is maintained around 90% across all replications, consistent with small contributions from non-calibrated carbon-containing species such as CH_4, CO and CO_2. Average coking and carbon laydown values determined by CHN microanalysis are presented in Table 5.5. Over the three repetitions, an average carbon wt% of the spent catalysts was determined to be 3.0% which correlates to an average coking value of 2.50 $mmol_C$ g_{cat}^{-1} and a carbon laydown proportion of 0.52% based on a carbon feed rate of 0.600 mmol min^{-1}.

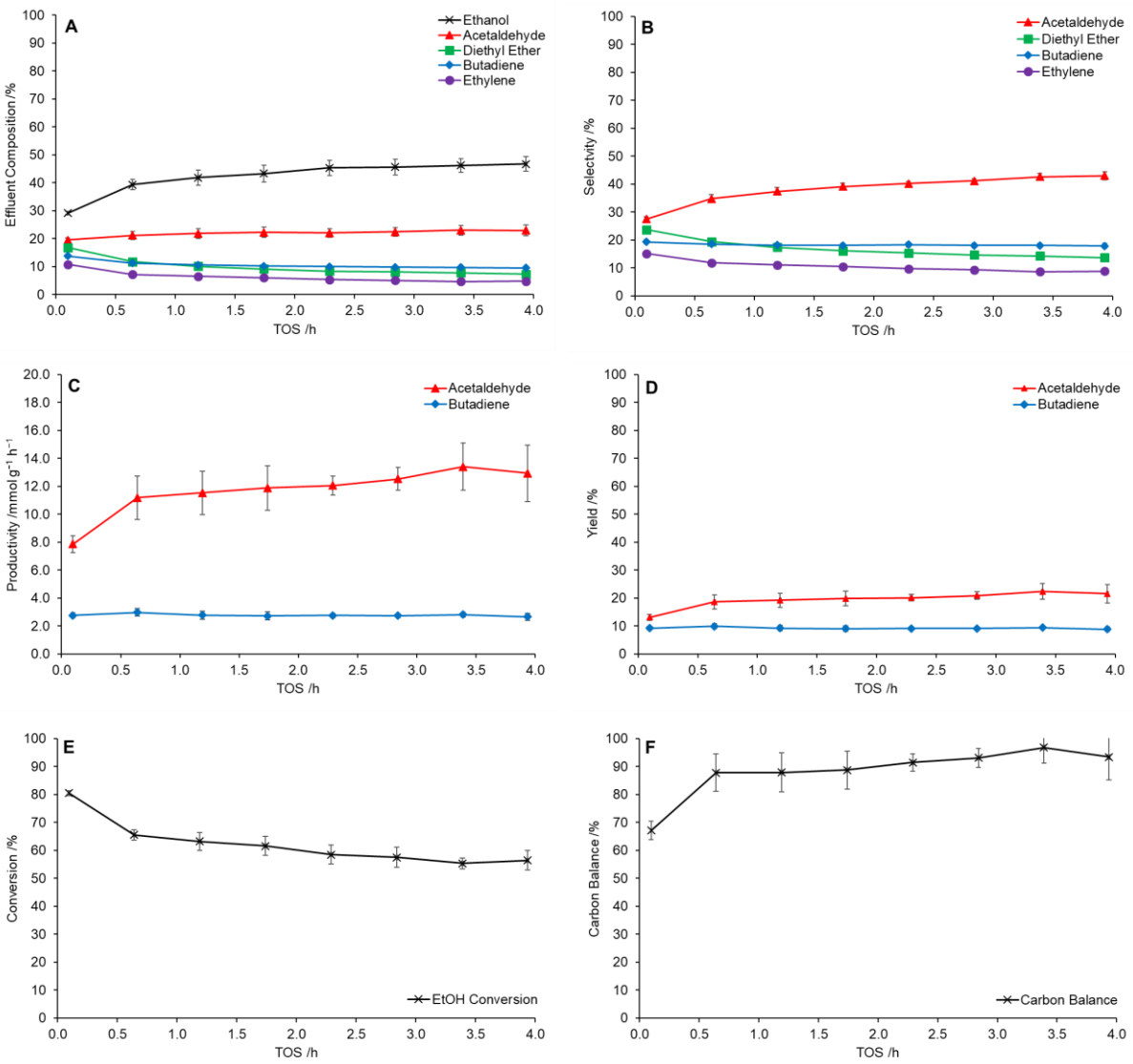

Figure 5.24: Effluent composition (A), selectivity (B), productivity (C) yield (D), ethanol conversion (E) and carbon balance (F) resulting from three repeat reactions of ethanol at 350 °C over ZnO(3.20)/Zr(231)–MFI for 4 h TOS. Ethanol feed rate = 0.300 mmol min^{-1}, catalyst mass = 0.300 g. For the effluent composition (A) and selectivity (B), traces for ethanol (×), acetaldehyde (▲), butadiene (♦), diethyl ether (■) and ethylene (●) are shown. Additional trace amounts of other carbon containing products were detected and accounted for, but were omitted for clarity. Error bars are plotted as one standard deviation calculated from three experimental repeats.

Table 5.5: Catalyst coking (ΔC wt%, mmol$_C$ g$_{cat}^{-1}$) and carbon laydown for repeat runs and averages of ZnO(3.20)/Zr(231)–MFI charges following ethanol reaction at 350 °C for 4h TOS as determined by CHN microanalysis.

Run	Catalyst Coking (ΔC Wt%)	Catalyst Coking (mmol$_C$ g$_{cat}^{-1}$)	Carbon Laydown (%)
1	3.13	2.61	0.54
2	3.03	2.52	0.53
3	2.85	2.37	0.49
Average	3.00	2.50	0.52

5.3.2. Long-term stability test of ZnO/Zr–MFI for the direct cascade synthesis of 1,3–butadiene from ethanol.

Following successful identification of ZnO(3.20)/Zr(231)–MFI as the optimum material of those tested in terms of both butadiene selectivity and productivity from ethanol, a long-term stability test (72+ h) was undertaken to monitor catalyst activity and lifetime. Figure 5.25 shows the effluent composition (A), ethanol conversion (B), butadiene productivity (C) and acetaldehyde productivity (D) resulting from reaction of ethanol at 350 °C over ZnO(3.20)/Zr(231)–MFI for 72 h TOS. From Figure 5.25A it can be seen that the output of products associated with reaction over Lewis acidic sites, namely butadiene, diethyl ether and ethylene, are seen to decrease with increasing TOS. Figure 5.25C shows that initial butadiene productivity is around 3.7 mmol g^{-1} h^{-1} but decays to around 1.0 mmol g^{-1} h^{-1} following reaction for 72 h TOS. The observation of an initial increase of acetaldehyde output before plateauing (Figure 5.25D) is ascribed instead to a steady overall production of acetaldehyde where the observed increase in acetaldehyde yield is resultant from a decrease of acetaldehyde consumption to form butadiene. This phenomenon is similar to that observed for acetaldehyde and ethylene in Chapter 4. Figure 5.25B shows that ethanol conversion initially decays from around 80% to 60% at which point it stabilizes for the remaining time on stream. Unfortunately, some oscillations ascribed to MS filament wear are observed within the data, although the general trends are still observable.

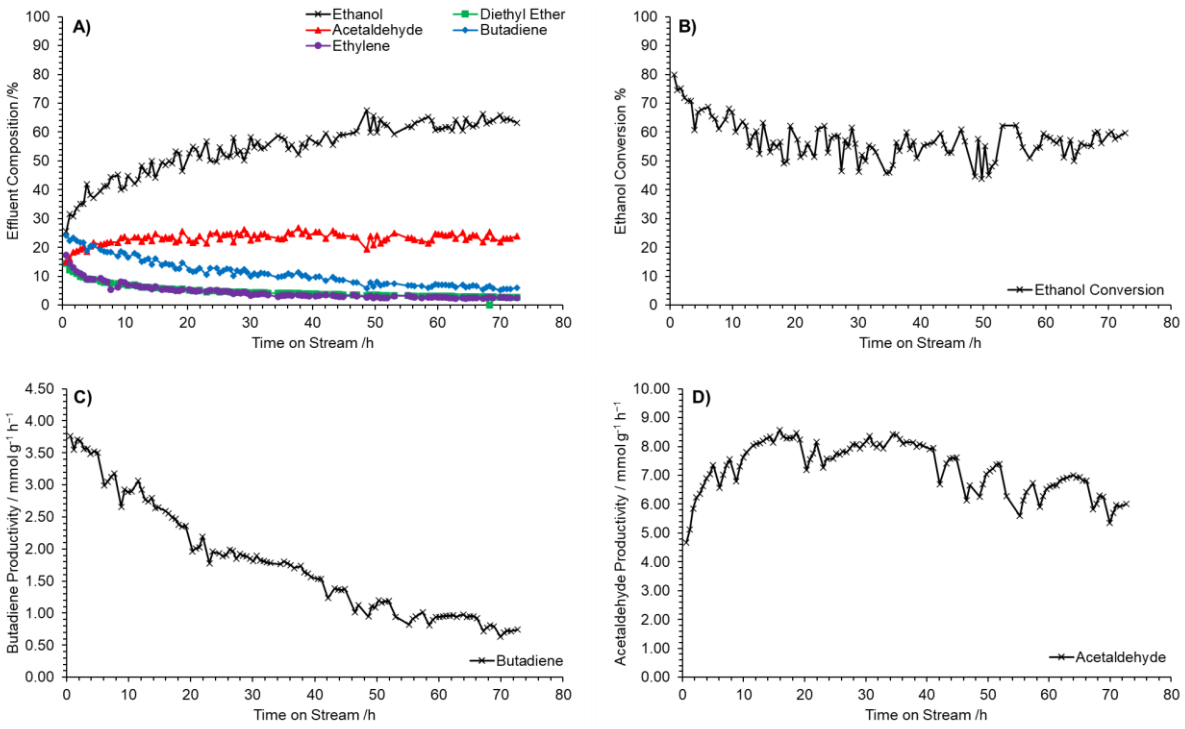

Figure 5.25: Effluent composition (A), ethanol conversion (B), butadiene productivity (C) and acetaldehyde productivity (D) resulting from reaction of ethanol at 350 °C over ZnO(3.20)/Zr(231)–MFI for 72 h TOS. Ethanol feed rate = 0.197 mmol min^{-1}, catalyst mass = 0.300 g. For the effluent composition (A), traces for ethanol (×), acetaldehyde (▲), butadiene (♦), diethyl ether (■) and ethylene (●) are shown. Additional trace amounts of other carbon containing products were detected and accounted for, but omitted for clarity.

5.3.3. Deactivation analysis of ZnO/Zr–MFI following long-term cascade synthesis of 1,3–butadiene from ethanol.

The deactivation of the catalyst for butadiene production is exhibited more prevalently in Figure 5.26 by comparison of the real cumulative butadiene production to a butadiene production extrapolated from the initial rate maximum, assuming no deactivation. Owing to the decrease in butadiene productivity (Figure 5.25C) whilst acetaldehyde productivity stays relatively constant (Figure 5.25D), it is initially suggested that the source of catalyst deactivation is Zr–centred.

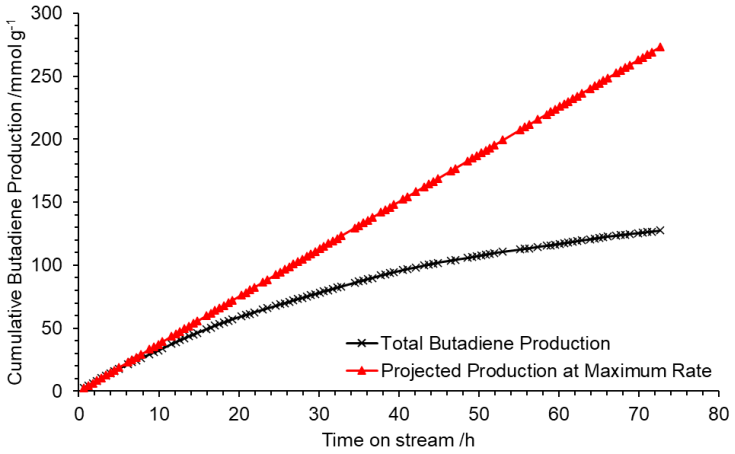

Figure 5.26: Cumulative butadiene production (×) and maximum projected butadiene production (▲) resulting from reaction of ethanol at 350 °C over ZnO(3.20)/Zr(231)–MFI for 72 h TOS. Ethanol feed rate = 0.197 mmol min^{-1}, catalyst mass = 0.300 g.

5.3.3.1. XAS analysis of Zr centres in spent ZnO/Zr-MFI materials.

In order to assess changes in the Zr coordination sphere following reaction with ethanol at 350 °C for 72 h TOS, XAS investigations were undertaken at Diamond Light Source Beamline B18. Initially, room temperature XANES-region spectra were recorded under an inert He atmosphere and their normalised plots are shown in Figure 5.27. It is observed that both spectra match those seen in literature for other Zr-substituted zeolites, namely Zr–BEA.[63] Importantly, the spectra show no major change in the shape of the XANES region of the Zr K-edge between fresh and spent catalysts, suggesting no substantial change of Zr co-ordination environment or oxidation state following reaction. It is noted that the intensity recorded for the spent catalyst charge is lower than that for the fresh charge, however this most likely relates to either sample mass or changes in relative Zr content following coking during reaction (Figure 5.27).

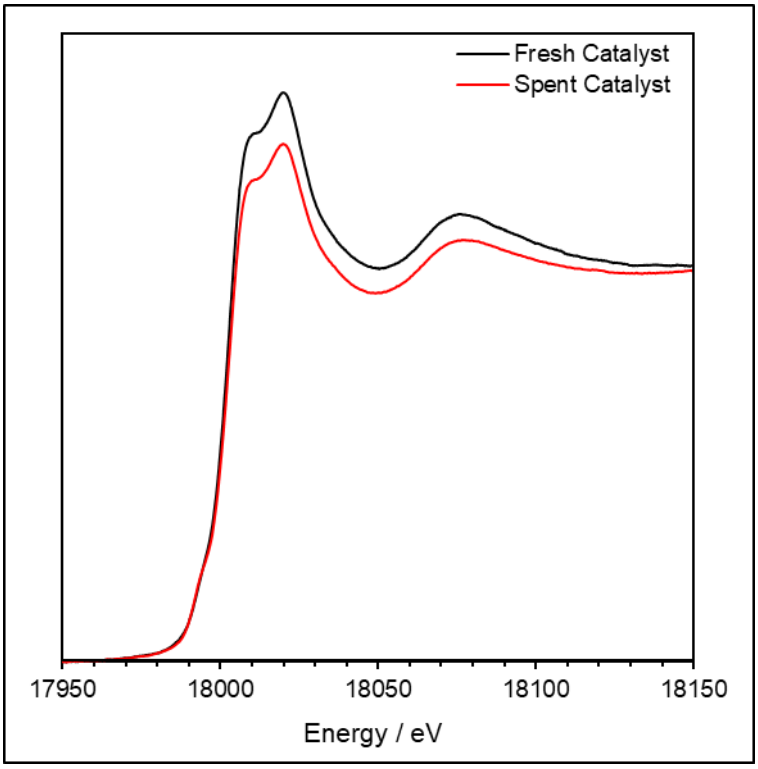

Figure 5.27: Normalized XANES data collected at the Zr K-edge for fresh and spent catalyst charges of ZnO(3.20)/Zr(231)–MFI following reaction with ethanol over 72 h TOS at 350 °C.

Additionally, the XANES spectra of fresh and spent catalyst charges were compared to both neat ZrO_2 and ZrO_2 impregnated into silicalite (ZrO_2/Sil-1) in order to assess whether oxidative deactivation had occurred. Figure 5.28 shows the room temperature XANES region of both fresh and spent catalyst charges and ZrO_2 and ZrO_2/Sil-1; no major similarities are seen between either catalyst charge or ZrO_2 species suggesting a lack of ZrO_2 within the catalyst samples.

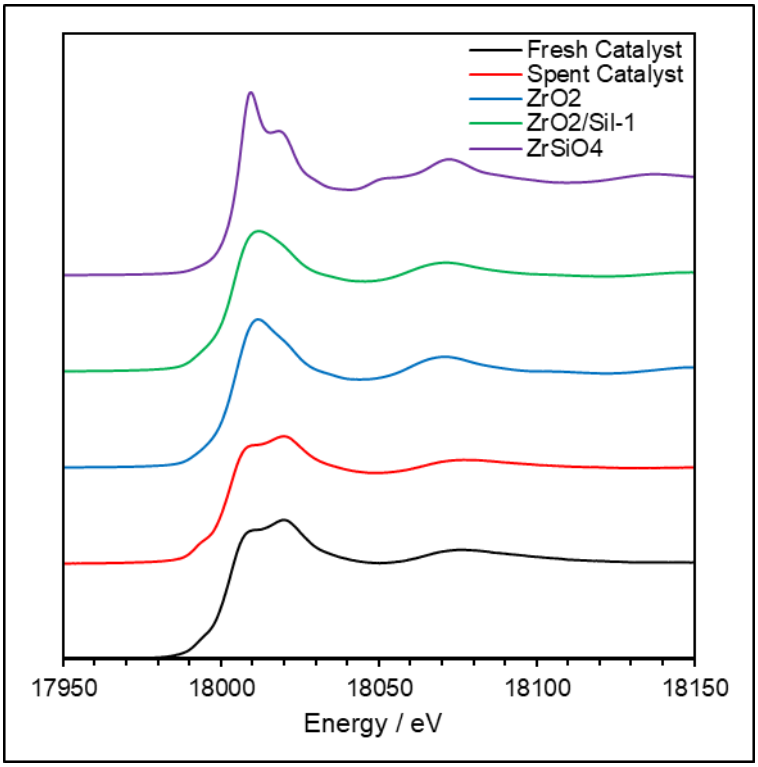

Figure 5.28: Normalized XANES data collected at the Zr K-edge for fresh and spent catalyst charges of ZnO(3.20)/Zr(231)–MFI following reaction with ethanol over 72 h TOS at 350 °C. Also shown are Zr K-ZANES spectra of ZrO_2 and ZrO_2/Sil-1.

Following initial room temperature analysis, the XANES spectra of both fresh and spent catalyst samples of ZnO(3.20)/Zr(231)–MFI from the same synthesis batch were recorded under *in-situ* conditions under flowing helium whilst ramping to 400 °C. This was performed to assess changes in Zr coordination sphere under thermal treatment akin to reaction conditions for both fresh and spent catalyst charges without ethanol flow. Figure 5.29 shows the offset and stacked XANES spectra of both fresh and spent ZnO(3.20)/Zr(231)–MFI recorded over the course of a 5 °C min^{-1} temperature ramp to 400 °C under flowing helium (40 mL min^{-1}). Both catalyst charges exhibit very similar behaviour under inert temperature ramp conditions, with effectively identical features being exhibited for both fresh and spent catalysts, suggesting no major irreversible change in Zr coordination sphere following reaction. The major observation of interest for both catalyst samples is the appearance of a pre-edge feature at approximately 17995 eV. This feature is concordant with loss of water from an octahedrally co-ordinated Zr centre and strongly supports the conclusion that Zr is within the tetrahedral positions of the zeolite framework following synthesis and is retained in these positions following reaction with ethanol at 350 °C.[63] This feature is observed as loss of water from an octahedral Zr-centre to form a penta-coordinated centre which results in a reduction of symmetry of the metal centre, allowing partial mixing of the 4d and 5p orbitals and in turn partially allowing the gerade-ungerade 1s–4p electronic transition and observation of the pre-

edge feature. This dehydration hypothesis is further supported by an observed expansion of k-space for both fresh and spent ZnO(3.20)/Zr(231)–MFI catalyst charges, concordant with an increased binding to the remaining ligands and contraction of bond lengths around the Zr-centre (Figure 5.30).

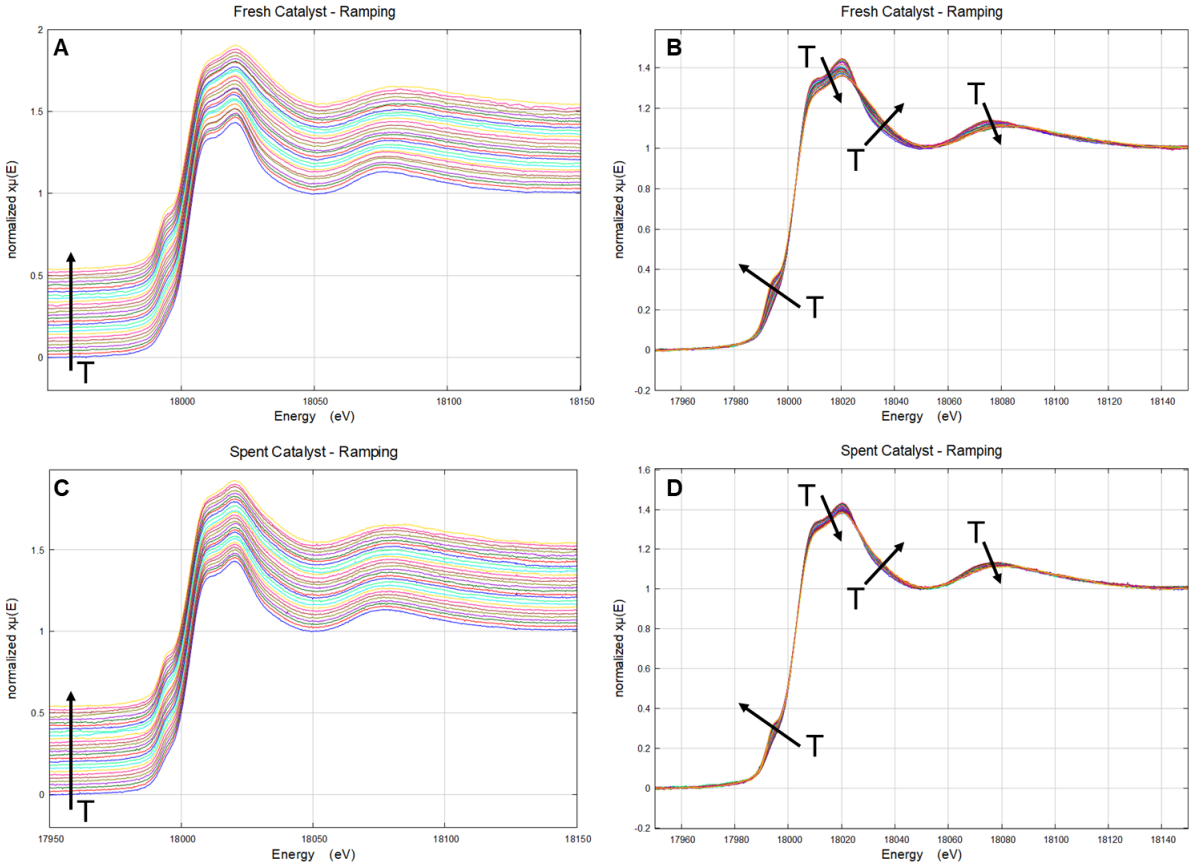

Figure 5.29: Offset and stacked XANES spectra for fresh (A + B) and spent (C + D) ZnO(3.20)/Zr(231)–MFI catalyst charges collected at the Zr K-edge and recorded over the course of a 5 °C min^{-1} temperature ramp to 400 °C under flowing helium (40 mL min^{-1}). Each line is separated by an average of 13.3 °C (approximately 2.5 min).

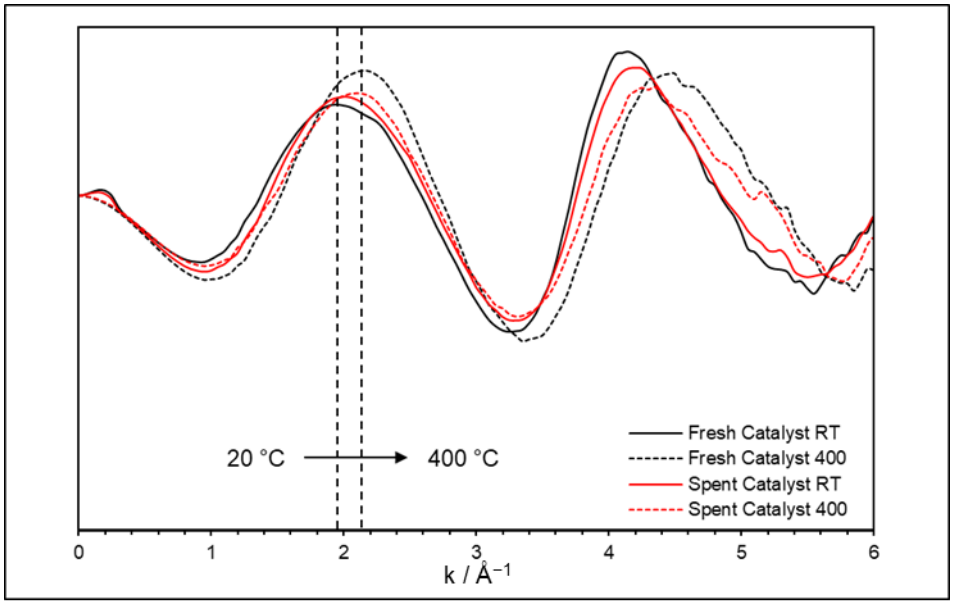

Figure 5.30: Stacked k-space plots for fresh and spent ZnO(3.20)/Zr(231)–MFI catalyst charges collected at the Zr K-edge.

Overall, across both XANES and EXAFS regions, no significant change in oxidation state or coordination geometry was observed between fresh and spent catalyst charges. Hence, it may be concluded from *in-situ* XAS analysis that deactivation of ZnO(3.20)/Zr(231)–MFI during ethanol conversion is unlikely to be due to a change of Zr speciation during reaction with ethanol at 350 °C.

5.3.3.2. Solid-state coking analysis of spent ZnO/Zr-MFI materials.

Following conclusion that a Zr coordination change was not responsible for catalyst deactivation, analysis of coking levels and speciation, alongside investigation into catalyst regeneration were undertaken. Initially, the level and nature of coke deposition following reaction was assessed by means of CHN elemental microanalysis, pXRD diffraction and solid-state ^{1}H–^{13}C cross polarization NMR spectroscopy. CHN microanalysis determined a C wt% increase of 6.39% following reaction with ethanol for 72 h at 350 °C, corresponding to 5.32 $mmol_C\ g_{cat}^{-1}$ and a coke yield of approximately 0.09%.

pXRD analysis of spent catalysts was undertaken in order to assess whether an MFI framework was maintained following reaction and if this could have had any effect on catalyst deactivation. Figure 5.31 compares the pXRD diffractograms of a fresh and spent ZnO(3.20)/Zr(231)–MFI charges and indicates that no substantial change in zeolite structure is observed, alongside no evidence of additional phases resulting from carbonaceous deposits or agglomeration of Zn or Zr oxides. The presence of large graphitic deposits is ruled out due to a lack of strong C (0 0 2) reflection at $2\theta = 26.42$ °.[64]

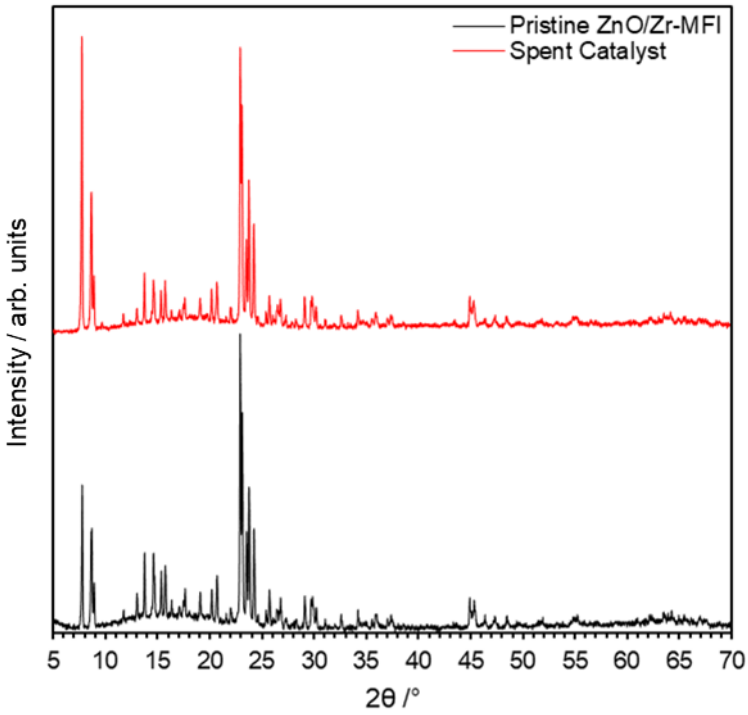

Figure 5.31: pXRD patterns for both pristine and spent ZnO(3.20)/Zr(231)–MFI following reaction with ethanol over 72 h TOS at 350 °C.

In order to identify the nature of carbon containing deposits within the spent catalyst, solid-state ^{13}C NMR spectroscopy and temperature programmed oxidation (TPO) were undertaken. Solid-state ^{1}H–^{13}C cross polarization NMR spectroscopic analysis of the spent catalyst resulted in observation of three distinct resonance bands centred around δ_C = 128, 60 and 17 ppm (Figure 5.32). The peaks centred at δ_C = 60 and 17 ppm respectively are ascribed to adsorbed ethanol species whilst the broad band spanning δ_C = 150–120 ppm is indicative of unsaturated or aromatic coke species similar to those reported in existing literature.[65-68] Temperature programmed oxidation coupled with mass spectrometry detection (TPO-MS) conducted under a 10% O_2/He atmosphere was used to identify the temperature at which the carbonaceous deposits within the spent catalyst were decomposed to H_2O, CO and CO_2. The material was first heated (*via* a 10 °C min^{-1} ramp rate) to 150 °C at which it was held for 1 h to remove any adsorbed water. Following this pre-treatment, the sample was then heated from 150–800 °C at a ramp rate of 10 °C min^{-1}. Mass spectrometry data for m/z values of 18 (H_2O), 28 (CO) and 44 (CO_2) were collected throughout and are shown in Figure 5.33. It is observed that, following the initial 150 °C pre-treatment, CO_2 (m/z = 44) is produced within the temperature window of 360–680 °C, a temperature range indicative of the presence of polycyclic aromatic hydrocarbons (PAH) and graphitic carbon being decomposed to CO_2.[69, 70] The observation of PAH and graphitic carbon is concordant with the observations from solid-

state ^{13}C NMR spectroscopy presented in Figure 5.32, although it is assumed these deposits are small in size or encapsulated within the zeolite pore network owing to lack of a graphitic pXRD response in Figure 5.31. Additionally, atmospheric solids analysis probe mass spectrometry (ASAP-MS) analysis of the spent catalyst materials was undertaken but no identifiable coke species could be discerned.

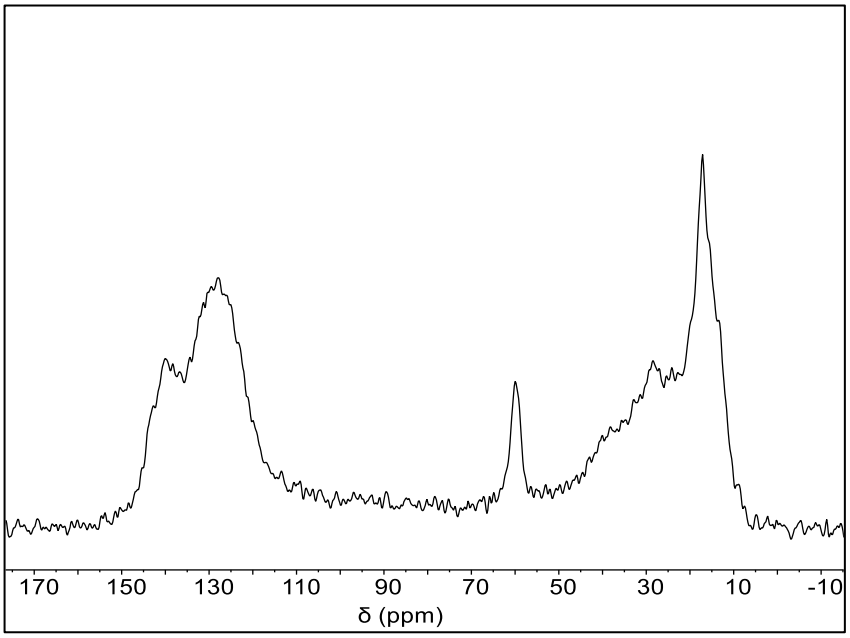

Figure 5.32: Solid-state $^{1}H–^{13}C$ cross-polarization NMR spectrum of spent ZnO(3.20)/Zr(231)–MFI material following reaction with ethanol over 72 h TOS at 350 °C. $^{1}H–^{13}C$ spectrum averaged over 10000 transients with a 1.0 s recycle delay. Spectrum acquired on a Varian VNMRS 400 MHz spectrometer using a 4 mm zirconia rotor. Spectrometer frequncies: ^{1}H = 399.88 MHz, ^{13}C = 100.55 MHz. Spin rate ≈ 10000 Hz.

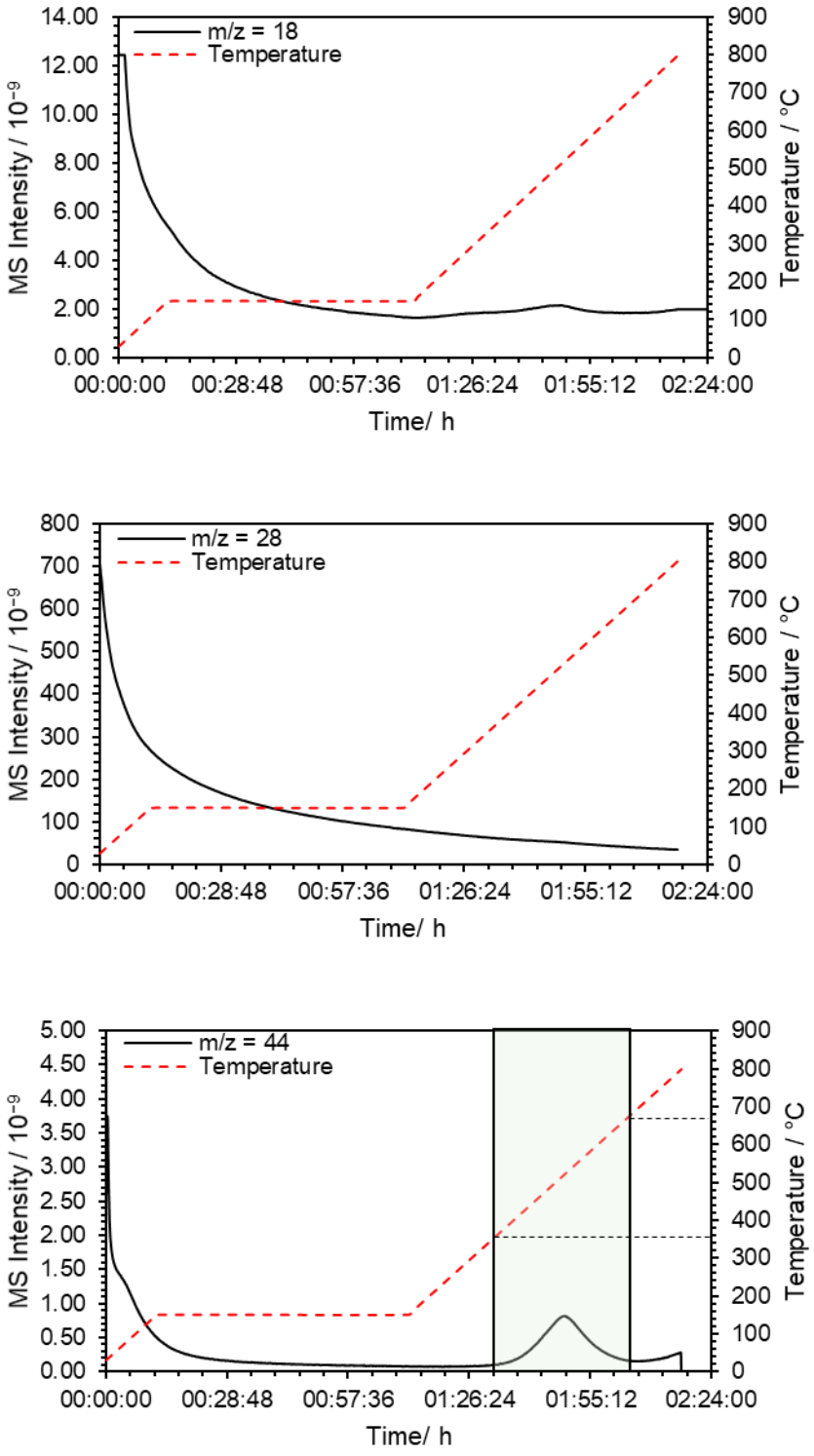

Figure 5.33: Mass spectrometry (MS) intensity traces for m/z = 18 (H_2O, top), 28 (CO, middle) and 44 (CO_2, bottom) following TPO of spent ZnO(3.20)/Zr(231)–MFI under a 10% O_2/He atmosphere. Heating program: ramp 10 °C min^{-1} to 150 °C, dwell at 150 °C for 1 h, ramp 10 °C min^{-1} to 800 °C.

5.3.3.3. Solution-state coking analysis of extracted spent ZnO/Zr-MFI materials.

In order to further assess the nature of carbonaceous deposits within post-run ZnO(3.20)/Zr(231)–MFI, the zeolite framework was digested and soluble carbon containing

species were extracted for analysis in a method similar to that reported by Bleken *et al.* and practised widely in the zeolite literature.[71-77] Briefly, two 20 mg samples of the spent catalyst were suspended in 200 μL of deionised water (DI) each before addition of 1 mL of pre-diluted Inorganic Ventures acid dissolution reagent to each sample (UA-1, HF containing reagent, 1:1 dilution with DI).[78] The samples were left to dissolve for a few minutes, although total dissolution was not achieved for either sample. Following this, 5 mL of dichloromethane (CH_2Cl_2, DCM) was added to one sample and 4 mL chloroform-d ($CDCl_3$) was added to the other. Both samples were shaken briefly to extract any dissolved carbon containing species and were allowed to separate from the aqueous layer. Finally, 2-4 mL of each organic solution was pipetted off and used for analysis.

The sample extracted into $CDCl_3$ was analysed using solution-state ^1H and ^{13}C NMR spectroscopy and the ^1H spectrum is shown in Figure 5.34. Unfortunately, the intensities of the spectra are low, likely owing to the relatively low coke loading within the spent catalyst and resulting low coke content of the NMR sample. It is however possible to observe some low intensity signals associated with aromatic protons in the ^1H NMR spectrum, concordant with previous observation from TPO-MS and solid-state ^{13}C NMR spectroscopy (Figure 5.34 - inset).

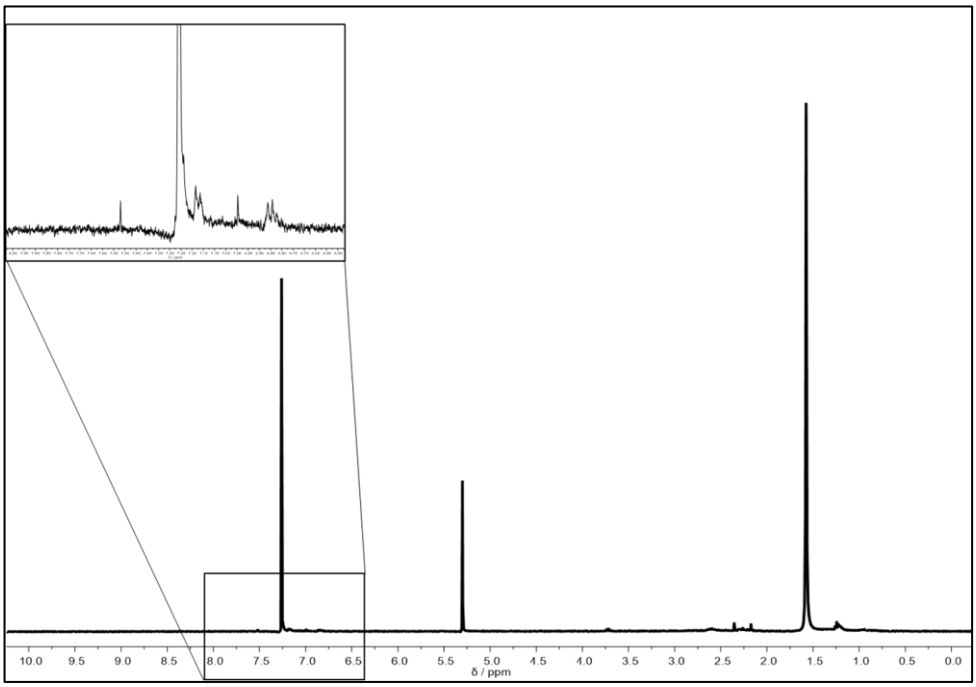

Figure 5.34: Solution state ^1H NMR spectrum of extracted coke species from ZnO(3.20)/Zr(231)–MFI following HF digestion. Spectrum was averaged over 8 scans with a 1.0 s recycle delay. Spectrum was acquired on a Bruker Avance III-HD-400 MHz spectrometer using a 4 mm borosilicate NMR tube. Spectrometer frequncy: ^1H = 399.95 MHz. Solvent: $CDCl_3$. Inset: Aromatic region of ^1H NMR spectrum (δ_H = 8.0–6.5 ppm).

The sample extracted into DCM was analysed using ASAP-MS, GC-MS and FTIR spectroscopy. Analysis of the extracted carbon containing products in DCM by ASAP-MS showed a large range of mass values when compared to a reference compound of DCM (Figure 5.35). Notably, Gaussian-like response distributions centred at m/z values of 251, 301 and 359 were detected which likely correspond to polycyclic aromatic hydrocarbon compounds and their derivatives, potentially derivatives of pyrene (*m/z* = 202+ Da) and higher fused aromatics of five (*m/z* = 240+ Da) or seven (*m/z* = 314+ Da) benzene rings.[76] Alternatively, linear derivatives, such as picene, may instead be formed owing to potential confinement effects of the zeolite support. Each distribution contains a range of responses separated by 14 Da, indicative of additional methyl groups. The observation of polycyclic aromatic hydrocarbons again correlates with previous observations from TPO-MS.

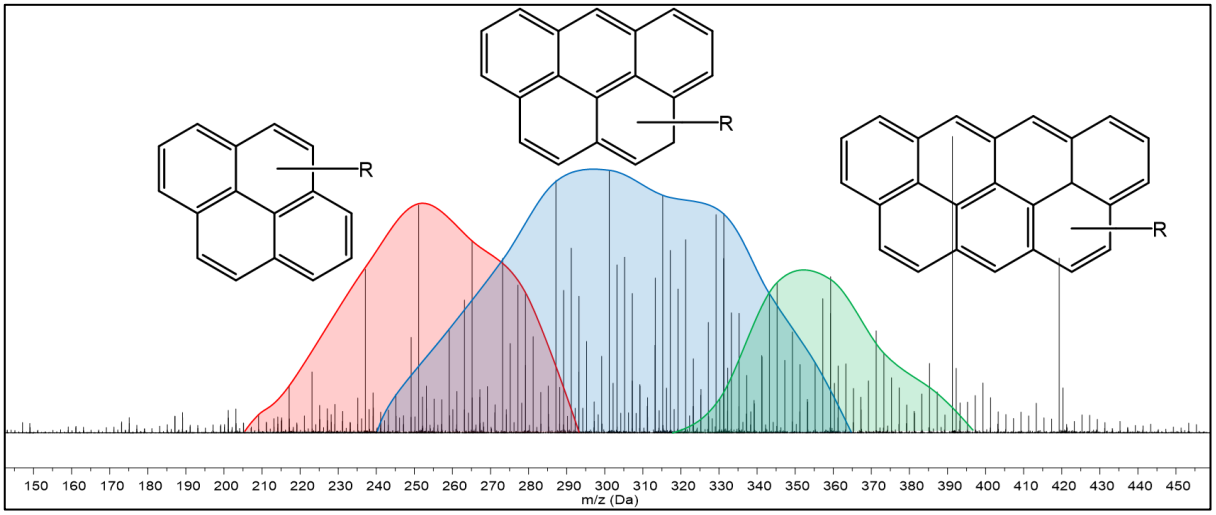

Figure 5.35: ASAP-MS mass spectra for extracted coke species in DCM solution from ZnO(3.20)/Zr(231)–MFI following HF digestion. Three major distributions corresponding to pyrene (*m/z* = 202+ Da) and higher fused aromatics of five (*m/z* = 240+ Da) or seven (*m/z* = 314+ Da) benzene rings are highlighted.

Further, GC-MS of extracted species in DCM exhibited two additional peaks at retention times of 3.41 and 3.79 min when compared to a DCM reference sample (Figure 5.36). Analysis of the mass spectra collected at these retention times indicates presence of methyl substituted benzene materials with the general formula $C_6H_{6-n}Me_n$ and *m/z* = 78 + 15n, where n = 0–6.[76] Namely, benzene (*m/z* = 78), toluene (*m/z* = 91), xylene (*m/z* = 106) and each subsequent methyl substituted benzene derivate up to hexamethylbenzene (*m/z* = 162) were detected (Figure 5.37). No additional aliphatic coke species were detected; hence results were concordant with those previously acquired by TPO-MS and ^{13}C ssNMR spectroscopy of solid catalytic materials (Figure 5.32 and Figure 5.33).

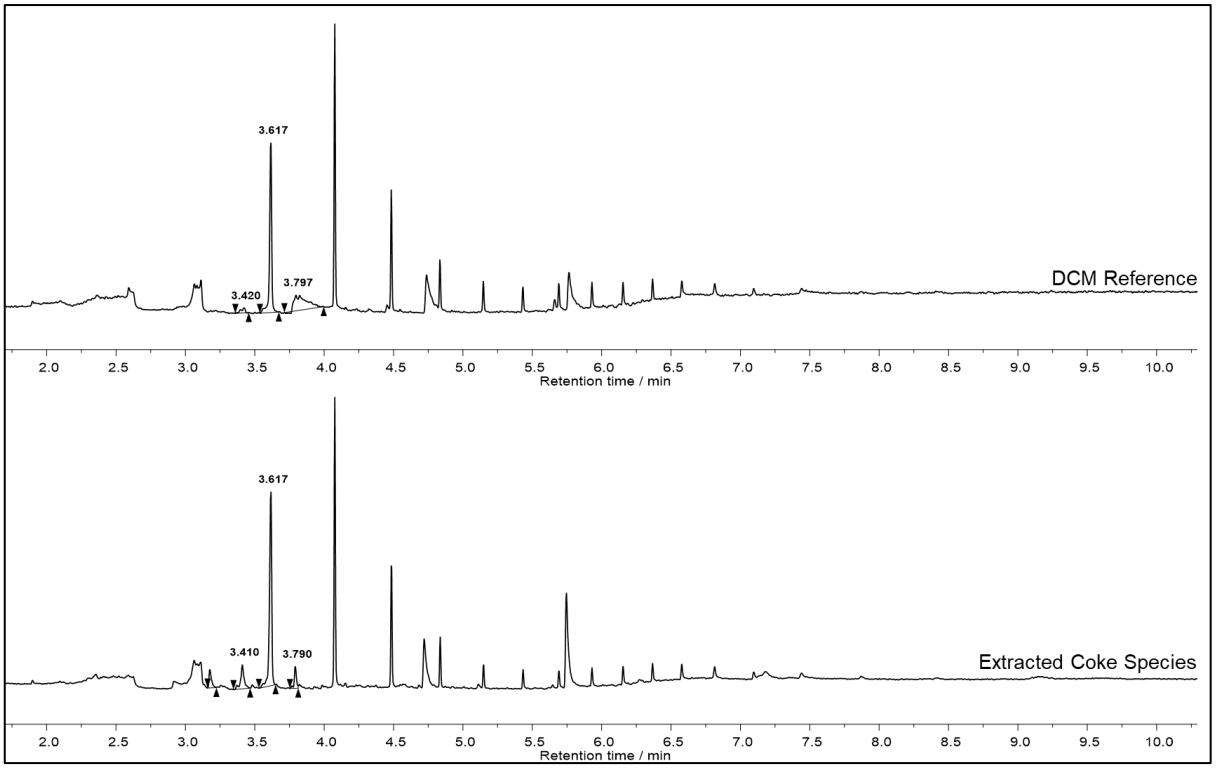

Figure 5.36: GC-MS response traces for extracted coke species from ZnO(3.20)/Zr(231)–MFI following HF digestion (bottom) alongside a DCM reference sample (top).

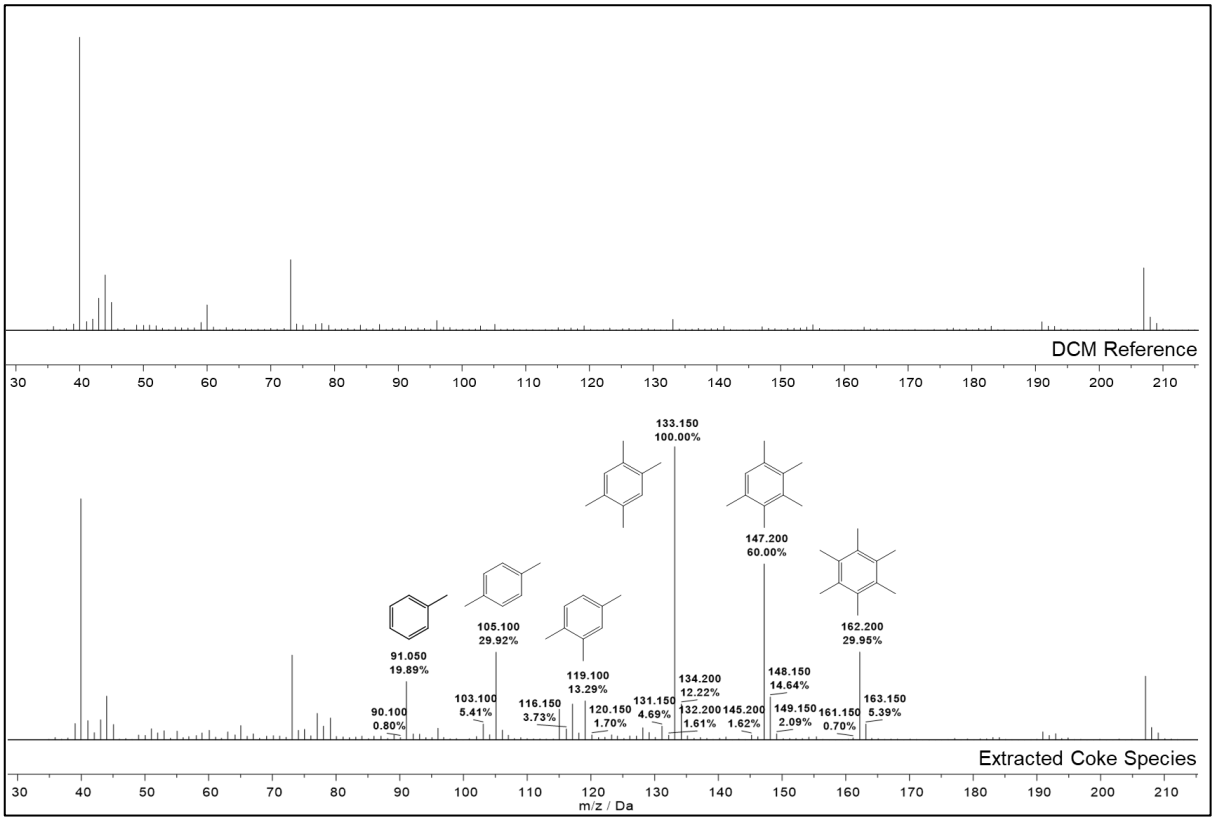

Figure 5.37: GC-MS mass spectra for extracted coke species in DCM solution from ZnO(3.20)/Zr(231)–MFI following HF digestion (bottom) alongside a DCM reference sample (top). Retention time = 3.410 min.

Finally, FTIR analysis of the carbon containing DCM solution was performed and compared to a DCM reference. FTIR spectra were collected in transmission mode between 4000–400 cm^{-1} at a step rate of 1 cm^{-1}. Figure 5.38 shows the raw full spectrum of both extracted carbon species and DCM reference (top) alongside normalised transmissions between 3500–2500 cm^{-1} (bottom left) and 1700–1400 cm^{-1} (bottom right). Despite low transmission intensities owing to low coke concentrations as described previously, bands of interest can still be identified. Namely, absorptions between 3100–3000 cm^{-1} and around 2925 cm^{-1} for the solution containing extracted coke species are suggestive of the presence of aromatic and alkyl C–H stretching respectively.[79] Further, absorptions between 1600–1400 cm^{-1}, as seen in for the DCM solution containing extracted coke species, are typical of in-ring C–C stretches for aromatic compounds.[79] The combination of these observations is suggestive of the presence of substituted benzenes as observed previously by GC-MS analysis and various other substituted aromatic species. The observations above are in good agreement with previous analysis suggesting the presence of polyaromatic and substituted aromatic coke species.

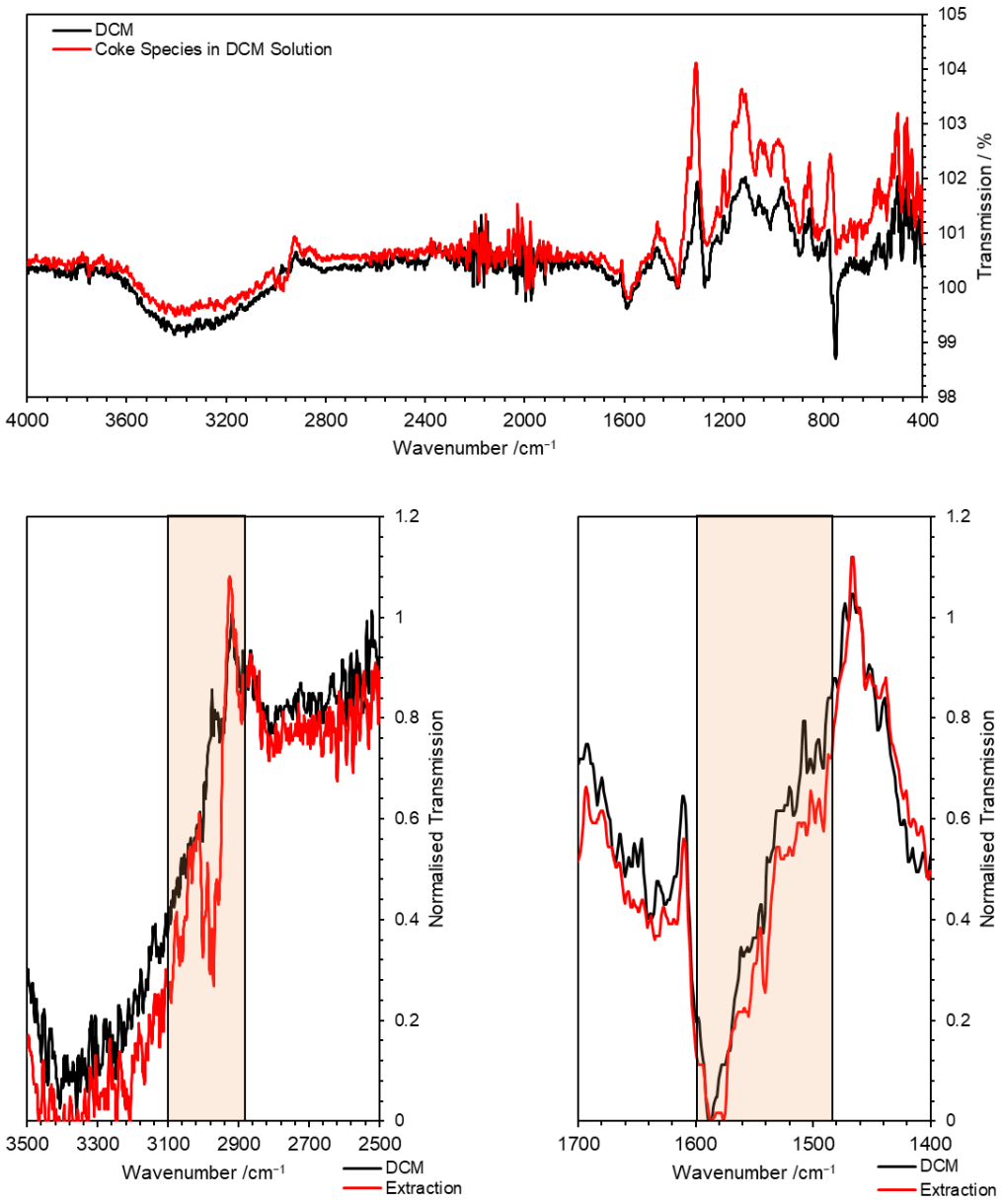

Figure 5.38: FTIR spectra of extracted coke species from ZnO(3.20)/Zr(231)–MFI in DCM and a DCM reference collected in transmission mode between 4000–400 cm^{-1} at a step rate of 1 cm^{-1} (top). Normalised transmissions between 3500–2500 cm^{-1} (bottom left) and 1600–1400 cm^{-1} (bottom right) are highlighted.

5.3.3.4. Conclusions from coking analysis of spent ZnO/Zr-MFI materials and catalyst regeneration studies.

Following in-depth coke analysis of both solid spent catalysts and extracted carbonaceous species, it can be concluded that significant laydown of aromatic, polyaromatic and potentially graphitic carbon species occurs during reaction of ethanol over ZnO/Zr-MFI at 350 °C. In order to assess the effect of carbon laydown on catalytic activity, a regeneration study of ZnO(3.20)/Zr(231)–MFI was undertaken. In this study, a spent catalyst charge was thermally treated under an oxidising atmosphere in order to decompose carbonaceous species and remove them from the zeolite framework, thus rendering active sites accessible again.[80] If

carbon laydown were the predominant deactivation mode of ZnO(3.20)/Zr(231)–MFI it would be expected that regeneration of the catalyst would restore activity to its initial values, providing removal of carbon was complete.[80]

In this study, a 300 mg catalyst charge of ZnO/Zr-MFI (calcined ZnO(3.20)/Zr(231)–MFI) underwent reaction with ethanol at 350 °C for 4 h TOS to yield spent ZnO/Zr-MFI. The spent ZnO/Zr-MFI was separated from the SiC diluent, pre-bed and post-bed and thermally treated at 550 °C for 5 h under static air in a muffle furnace (ramp rate: 5 °C min^{-1}) to yield "regenerated ZnO/Zr-MFI". A 150 mg charge of regenerated ZnO/Zr-MFI was then reacted with ethanol at 350 °C for 4 h TOS in order to assess its performance following carbon removal. The resulting material following catalysis is denoted "spent-regenerated ZnO/Zr-MFI". For comparison, a 150 mg charge of calcined ZnO/Zr-MFI was also reacted with ethanol under identical conditions. The resulting material is denoted "spent-fresh ZnO/Zr-MFI".

Table 5.6 shows the recorded carbon wt% values for each ZnO/Zr-MFI material within the regeneration study as determined by CHN microanalysis. Following initial calcination, calcined ZnO/Zr-MFI exhibits a C wt% of close to zero (0.05 %) which rises to 3.21 % following reaction with ethanol and is in the typical range expected (Table 5.5). Following regeneration, the C wt% is seen to drop back to around zero (0.10 %), indicative of near total carbon removal by the thermal treatment. Following reaction of 150 mg charges of fresh and regenerated ZnO/Zr-MFI, C wt% values of 2.87 and 2.36 were obtained respectively. Whilst the coking value of the fresh catalyst is within the expected range (Table 5.5), the coking value of the regenerated catalyst is lower than previously observed for ZnO/Zr-MFI and lies below the standard range, likely resulting from decreased ethylene production and lower ensuing aromatic production.

Table 5.6: Catalyst coking (C wt%) for fresh, spent, regenerated, spent-fresh and spent-regenerated ZnO/Zr–MFI catalysts following ethanol reaction at 350 °C for 4h TOS as determined by CHN microanalysis.

Material	Catalyst Mass / mg	Catalyst Coking (C wt%)
Calcined ZnO/Zr–MFI	300	0.05
Spent ZnO/Zr–MFI	300	3.21
Regenerated ZnO/Zr–MFI	150	0.10
Spent-Fresh ZnO/Zr–MFI	150	2.87
Spent-Regenerated ZnO/Zr–MFI	150	2.36

Figure 5.39 shows key metrics for 150 mg charges of fresh and regenerated ZnO(3.20)/Zr(231)–MFI following reaction with ethanol at 350 °C for 4 h TOS. Herein it is observed that, whilst butadiene and diethyl ether selectivities are recovered to a similar level for the regenerated material as the fresh catalyst (around 15% each), ethanol conversion is around 10% lower and carbon balance is around 10% higher throughout the run. As a result, it can be concluded that the catalytic activity of Zr is recovered to normal levels following regeneration, owing to the near identical butadiene and diethyl ether selectivities observed for both fresh and regenerated catalysts, both of which are associated with reaction over Lewis acidic Zr centres. Notably, the acetaldehyde selectivity of the regenerated catalyst is around 5% higher than for the fresh material throughout the course of the run. Further, the selectivity to ethylene is lower for the regenerated catalyst throughout the run, likely resulting in the lower coking value presented in Table 5.6.

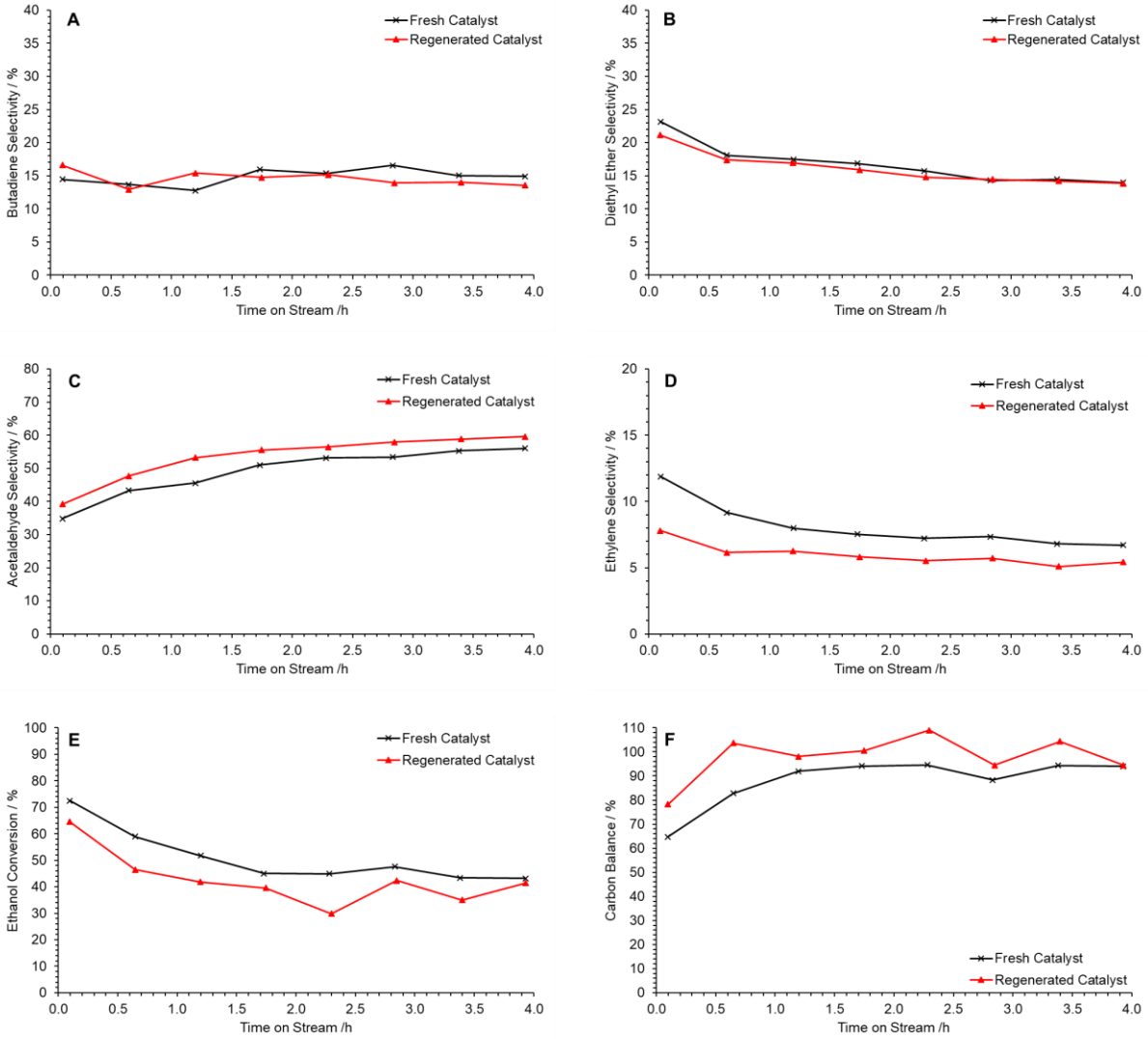

Figure 5.39: Butadiene selectivity (A) diethyl ether selectivity (B), acetaldehyde selectivity (C), ethylene selectivity (D), ethanol conversion (E) and carbon balance (F) resulting from reaction of ethanol at 350 °C over fresh (×) and regenerated (▲) ZnO(3.20)/Zr(231)–MFI for 4 h TOS. Ethanol feed rate = 0.330 mmol min^{-1}, catalyst mass = 0.150 g.

Despite conclusions that coking is the major deactivator of ZnO(3.20)/Zr(231)–MFI as a result of in-depth post-mortem analysis and successfully regeneration, it is still uncertain as to why deactivation due to coking is predominantly Zr centred, with Zn centred dehydrogenation remaining relatively unaffected (Figure 5.25). One explanation may be that, whilst Zr is largely homogenously distributed throughout the MFI framework in tetrahedral sites (Figure 5.18), ZnO is instead not homogeneously distributed as it was in Chapter 4, but rather it could be largely localised on the external surface of the zeolite crystals. If this were the case, it would be expected that Zr centred reactions (such as those that produce butadiene and diethyl ether) would be directly affected by coking of the zeolite micropore volume and the resultant blockage of active sites. However, ZnO localised on the crystal exteriors would not be affected by such coking and would therefore continue to produce acetaldehyde at a

relatively constant rate, similar to that seen in Chapter 4. In order to assess this hypothesis, SEM-EDS mapping of microtomed samples was undertaken to assess the Zn and Zr distributions within the catalyst particles. Unfortunately, the internal and external surfaces of the crystals could not be sufficiently resolved to form a meaningful conclusion for this hypothesis. Analysis using a higher resolution technique, such as TEM, could be instead used to further this investigation.

5.4. Optimisation of Zr loading in ZnO/Zr–MFI materials for the direct cascade synthesis of 1,3–butadiene from ethanol.

In order to attempt to optimise the loading of Zr within ZnO/Zr–MFI and increase butadiene productivity, several parameters affecting the hydrothermal synthesis of Zr–MFI were varied, and the resulting materials were assessed for catalytic activity. Initially, hydrothermal synthesis time and temperature were varied to assess the effect of these variables on Zr incorporation from the initial synthesis gel, alongside any differences in zeolite crystal size and morphology. Subsequently, modulation of Zr precursor concentration in the synthesis gel to attempt to directly affect the Zr loading and Si/Zr ratio of Zr–MFI was undertaken. Table 5.7 shows the synthesis conditions, resulting Zr loadings and Si/Zr ratios as determined by ED-XRF spectroscopy for a range of Zr–MFI materials prepared by variation of Zr precursor loading, synthesis time and synthesis temperature. Unless stated, all other synthesis conditions were unchanged from the general method described in Section 9.3.6. It is acknowledged that BET surface area values for each material would greatly benefit subsequent conclusions, however these could not be acquired at the time.

Table 5.7: Synthesis parameters, resultant Zr loadings and Si/Zr ratios as determined by ED-XRF spectroscopy for a range of hydrothermal synthesis variations on Zr–MFI. ED-XRF values averaged over three measurements following sample rotation.

Sample Name	Autoclave Size	$ZrOCl_2 \cdot 8H_2O$ Used / wt%	Synthesis Time /days	Synthesis Temperature / °C	Zr Loading / wt%	Si/Zr Ratio
Zr–MFI	Large	0.52	3	180	0.63	209
Zr–MFI-rep	Large	0.52	3	180	0.72	205
Zr–MFI-rep2	Large	0.52	3	180	0.76	185
Zr–MFI-S3	Small	0.52	3	180	0.79	180
Zr–MFI-S4	Small	0.52	4	180	0.80	183
Zr–MFI-S5	Small	0.52	5	180	0.83	171
Zr–MFI-150C	Small	0.52	3	150	0.71	176
Zr–MFI-200C	Small	0.52	3	200	0.67	252
Zr–MFI-1.03	Small	1.03	3	180	1.06	143
Zr–MFI-0.26	Small	0.26	3	180	0.79	197

Initially, the synthesis of Zr–MFI was repeated a further two times under identical conditions in order to establish a benchmark range for Zr incorporation for future comparison and to ensure the reproducibly of the hydrothermal synthesis procedure. Acquired ED-XRF spectroscopy data and subsequent calculation of Si/Zr ratio shows that all three materials incorporated Zr into the material to a similar degree. The Zr loading of the materials ranged from 0.63−0.76 wt%, corresponding to a Si/Zr ratio range of 185−209 (Table 5.7). Figure 5.40 shows the pXRD diffractograms of repeat hydrothermal syntheses of Zr–MFI following calcination. In each case, the resulting diffractogram clearly shows that an MFI-type framework with no undesired reflections was attained following each synthesis attempt.

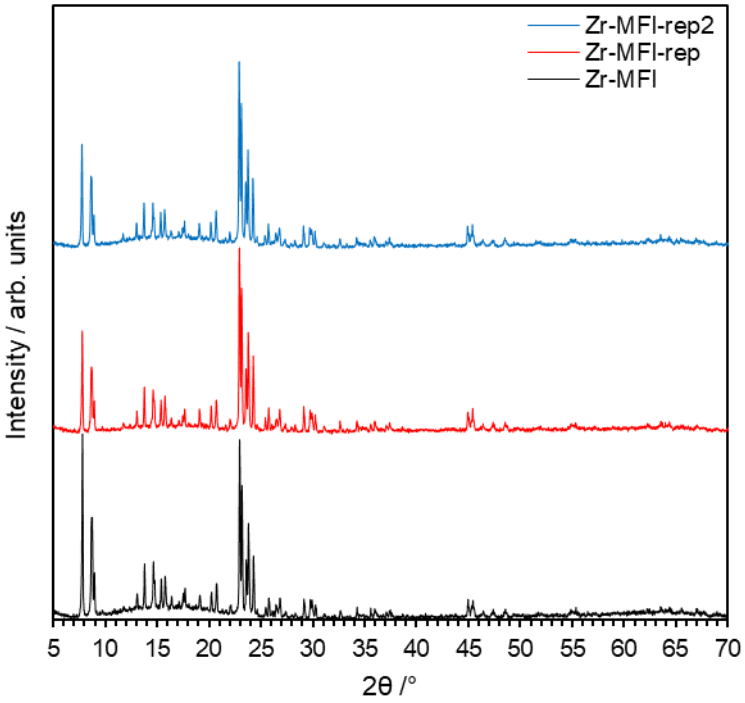

Figure 5.40: pXRD patterns in the 2θ = 5–70° range for repeat syntheses of Zr–MFI following calcination.

5.4.1. Effect of hydrothermal synthesis duration on Zr–MFI preparation and catalytic activity.

In order to maximise time efficiency and reproducibility, it was deemed more desirable to perform variations to the Zr–MFI synthesis in multiple small autoclaves at the same time, rather than repeated use of a large single autoclave. Hence, a Zr–MFI synthesis was undertaken under standard conditions is a small volume (28 mL) autoclave as a control reaction. The sample, denoted Zr–MFI-S3, was prepared from the same batch of synthesis gel prepared for Zr–MFI-rep2 and was crystallised at the same time to maximise reproducibility. Additionally, two further syntheses were prepared from the same synthesis gel batch, denoted Zr–MFI-S4

and Zr–MFI-S5, which were introduced into the synthesis oven at the same time as Zr–MFI-rep2 and Zr–MFI-S3 but were crystallised for a total of 4 and 5 days respectively.

Figure 5.41 shows the pXRD patterns for Zr–MFI-rep2, Zr–MFI-S3, Zr–MFI-S4 and Zr–MFI-S5 and it is confirmed that all materials exhibit an MFI-type framework. Further, no additional reflections from denser phases are observed regardless of increasing synthesis time, suggesting that an MFI framework is the stable phase within this synthesis regime. Elemental analyses for these materials determined by ED-XRF are shown in Table 5.7. Upon changing from a large to a small autoclave, Zr loading increase marginally to 0.79 wt% from 0.76 wt%, resulting in a decrease of Si/Zr from 185 to 180. This difference is minor but could be potentially be resultant from faster heating of the lower volume small autoclaves owing to a larger surface area to volume ratio. Alternatively, natural variation in each autoclave (as seen in Table 5.7 may also be responsible for minor differences. As synthesis time increased from 3 to 4 to 5 days at 180 °C, Zr incorporation is seen to slightly increase from 0.79 to 0.80 to 0.83 wt%, potentially resulting from increasing synthesis time improving Zr incorporation. This increased Zr loading resulted in calculated Si/Zr ratios of 180, 183 and 171 respectively, suggesting a minor increase in Zr density within the Zr–MFI materials.

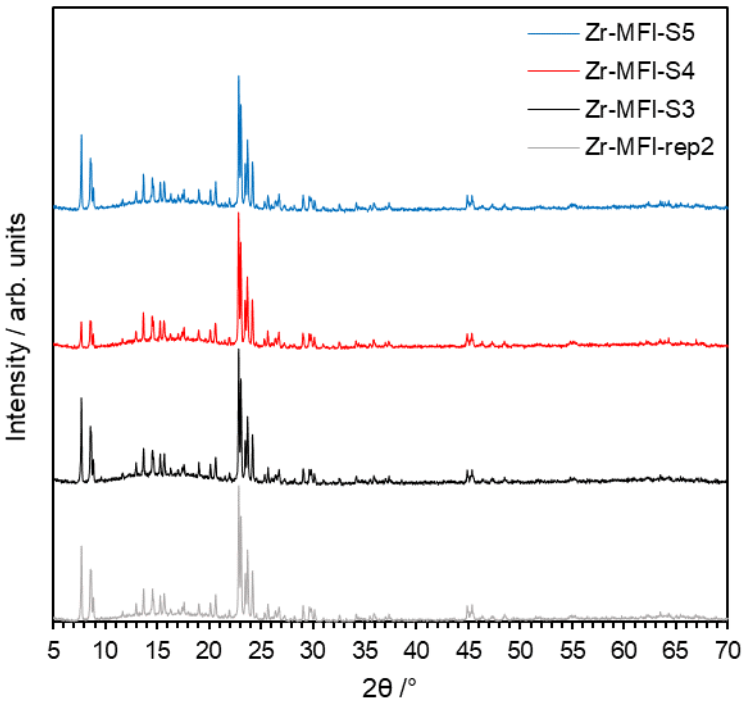

Figure 5.41: pXRD patterns in the 2θ = 5–70° range for syntheses of Zr–MFI materials in which synthesis time was varied from 3–5 days. Included is the pXRD pattern of Zr–MFI-rep2 which serves as a comparison with Zr–MFI-S3 for large and small autoclaves, respectively.

In order to further assess the effect of synthesis time on crystal morphology, SEM imaging and particle size analysis of each material was undertaken. Briefly, each image was loaded into ImageJ software and diameters of 100 tablet-like particles were measured manually. SEM images of the materials are shown in Figure 5.42 and particles size distributions are shown in Figure 5.44–47. All samples are observed to possess a similar morphology, predominantly composed of small tablet-like crystals with some larger coffin shaped agglomerates typical of MFI. All samples synthesised in the small autoclaves have a similar particle size distribution with a larger mean particle size, approximately 400 nm, than those seen for previous Zr–MFI materials synthesised in the large autoclave, approximately 325 nm. (Figure X.43).

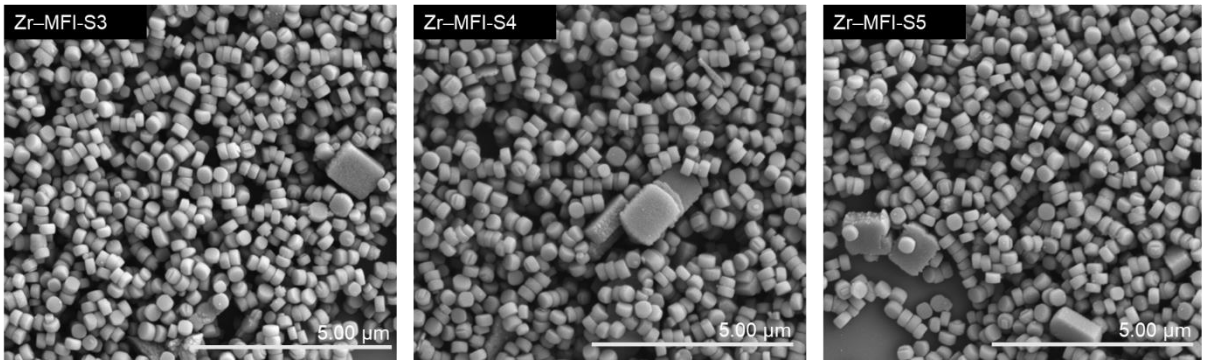

Figure 5.42: SEM images of Zr–MFI-S3 (left), Zr–MFI-S4 (centre), and Zr–MFI-S5 (right).

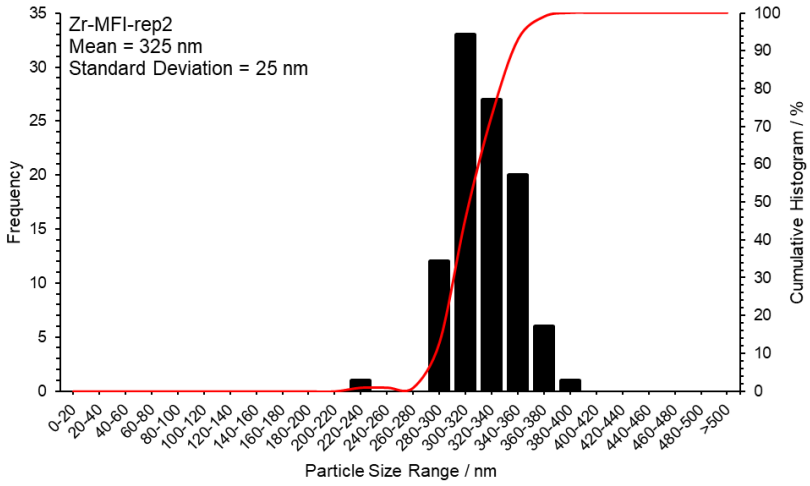

Figure X.43: Particle size distribution for Zr–MFI-rep2 shown for 100 particles. Measurements taken as the diameter of tablet-like crystals. Bin width = 20 nm.

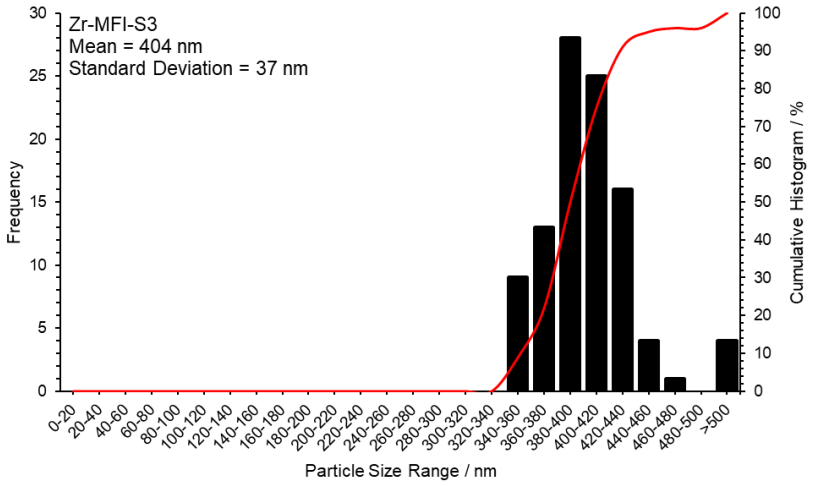

Figure 5.44: Particle size distribution for Zr–MFI-S3 shown for 100 particles. Measurements taken as the diameter of tablet-like crystals. Bin width = 20 nm.

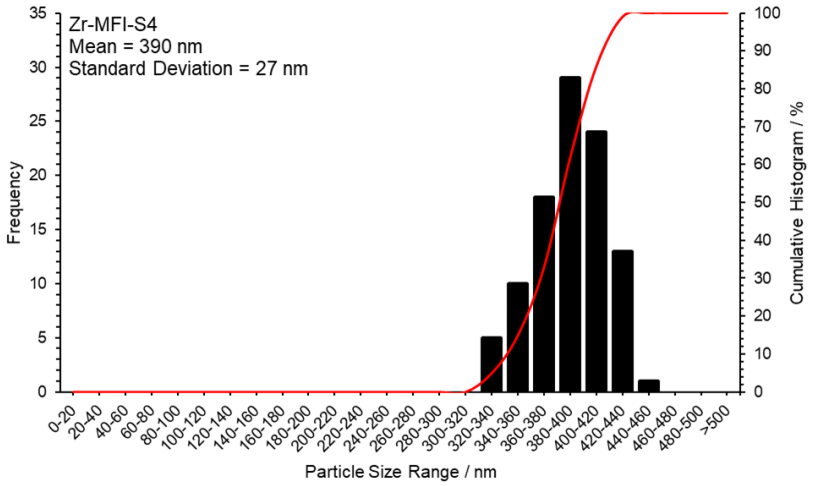

Figure 5.45: Particle size distribution for Zr–MFI-S4 shown for 100 particles. Measurements taken as the diameter of tablet-like crystals. Bin width = 20 nm.

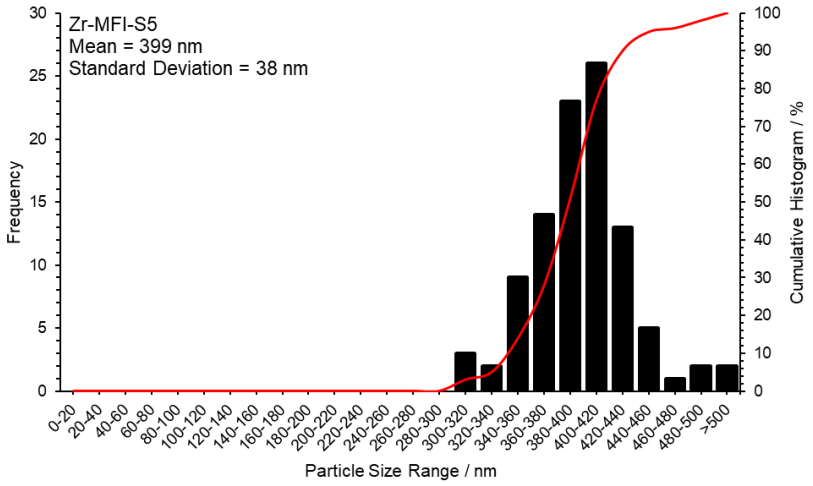

Figure 5.46: Particle size distribution for Zr–MFI-S5 shown for 100 particles. Measurements taken as the diameter of tablet-like crystals. Bin width = 20 nm.

In order to assess the effect of autoclave size and synthesis time on Zr–MFI, catalytic tests of each material in the synthesis of butadiene from ethanol at 350 °C were undertaken. Prior to catalytic tests, each material was doped with a nominal 3.5 wt% ZnO by Zn *via* the standard wetness impregnation method described in Section 9.3.3.; Zn loadings, Zr loadings, Si/Zr ratios and Zn/Zr ratios measured by ED-XRF are presented in Table 5.8. Relevant results from catalytic testing are shown in Figure 5.47. Herein it is observed that each material exhibits similar productivities of butadiene (2.5 mmol g^{-1} h^{-1}), acetaldehyde (10 mmol g^{-1} h^{-1}) and ethylene (4.0 mmol g^{-1} h^{-1}) regardless of synthesis time and autoclave size. Additionally, ethanol conversion was observed to be remarkably similar for all synthesis variations (Figure 5.47D). Although synthesis in a smaller volume autoclave resulted in a larger mean particle size and slightly decreased Si/Zr ratio, both Zr–MFI–rep2 and Zr–MFI–S3 did not display any major differences in catalytic productivities, therefore allowing conclusions that autoclave size does not play a significant part in determining catalyst morphology and activity. Additionally, it may be concluded that the effect of extended synthesis time on catalyst morphology and performance is also minimal. Following an increase in synthesis time from three to four and five days, no significant change in mean particle size was observed alongside no major differences in catalytic activity. Therefore, for all further synthesis variations, a three-day synthesis in a small volume autoclave was utilised in order to maximise synthesis efficiency.

Table 5.8: Zn loadings, Zr loadings, Si/Zr ratios and Zn/Zr ratios as determined by ED-XRF spectroscopy for a range of hydrothermal synthesis variations on ZnO/Zr–MFI. ED-XRF values averaged over three measurements following sample rotation.

Sample	Zn Content / Wt%	Zr Content / Wt%	Si/Zr Ratio	Zn/Zr Ratio
ZnO/Zr–MFI-B3	3.10	0.70	160	6.16
ZnO/Zr–MFI-S3	3.45	0.76	165	6.37
ZnO/Zr–MFI-S4	3.43	0.75	164	6.35
ZnO/Zr–MFI-S5	2.91	0.75	146	5.39

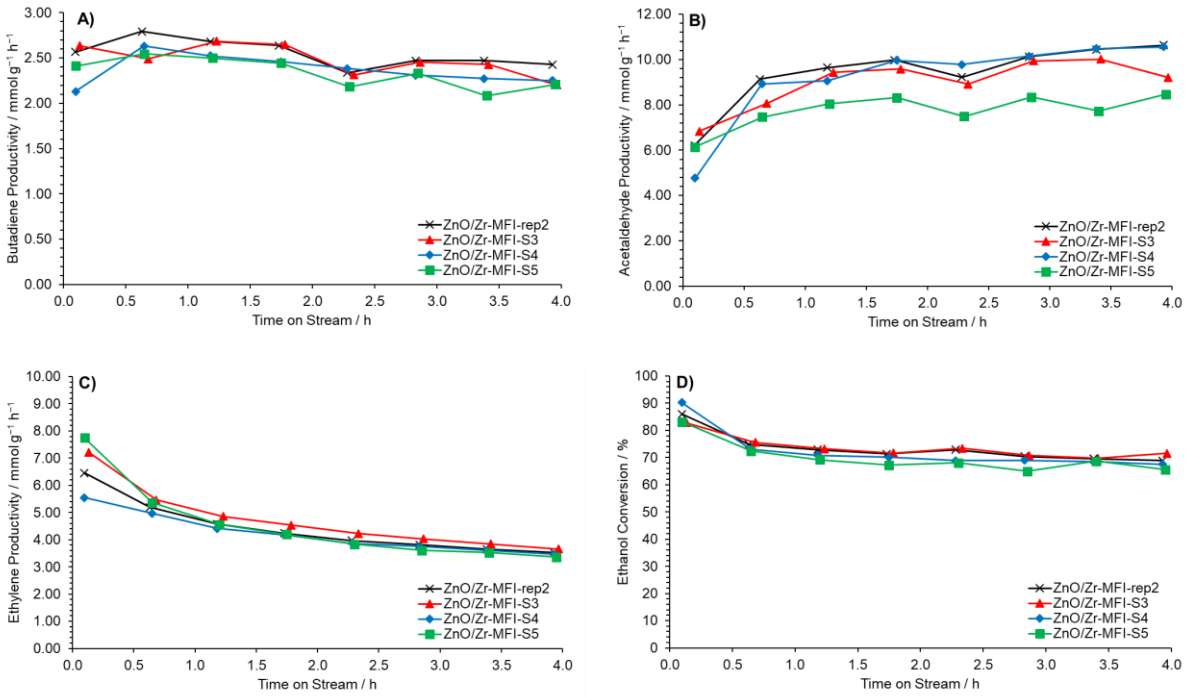

Figure 5.47: Butadiene productivity (A), acetaldehyde productivity (B), ethylene productivity (C) and ethanol conversion (D) following reaction of ethanol over ZnO/Zr–MFI materials at 350 °C for 4 h TOS following various synthesis durations of 3 days (large autoclave, ×), 3 days (small autoclave, ▲), 4 days (small autoclave, ♦) and 5 days (small autoclave, ■). Ethanol feed rate = 0.300 mmol min^{-1}, catalyst mass = 0.300 g. Detection Columns: RTX-VMS + ShinCarbon ST.

5.4.2. Effect of hydrothermal synthesis temperature on Zr–MFI preparation and catalytic activity.

Following exploration of the effect of synthesis time on the catalytic performance of Zr–MFI, the effect of hydrothermal synthesis temperature was also investigated. To this end, two materials were prepared from the same batch of synthesis gel and were treated at 150 °C and 200 °C for 72 h to afford Zr–MFI-150C and Zr–MFI-200C. These materials were additionally compared to Zr–MFI-S3 which was prepared at the standard synthesis temperature of 180 °C. An initial noticeable difference between the three syntheses was the amount of

zeolite mass recovered from each autoclave. Notably, whilst the samples treated at 180 °C and 200 °C afforded over 900 mg of material following calcination, the sample treated at 150 °C afforded only around 300 mg, with a further 160 mg able to be isolated following extended centrifuge time (Table 5.9); the sample also qualitatively exhibited a much finer texture. Despite the lower mass recovery and finer texture of Zr–MFI-150C, all samples exhibited a pXRD diffractogram as expected for an MFI material, with no additional reflections or higher degrees of amorphous material observed (Figure 5.48). ED-XRF spectroscopy of Zr–MFI-150C and Zr–MFI-200C showed a similar amount of Zr incorporation at 0.64 and 0.67 wt% respectively (Table 5.7). Interestingly, the Si/Zr ratios of Zr–MFI-150C and Zr–MFI-200C were widely different despite having similar Zr contents and being formed from the same bath of synthesis gel. Zr–MFI-150C and Zr–MFI-200C possessed final Si/Zr ratios of 176 and 252 respectively, leading to the conclusion that increased synthesis temperatures may increase Si content and result in higher Si/Zr, potentially resulting in a method to more easily achieve a targeted Si/Zr ratio. In order to confirm the degree of Zr incorporation into the zeolite framework, DR-UV-Vis spectroscopic analysis should be undertaken.[iii] One potential explanation for this observation may be that Zr is rapidly incorporated into the crystals during the early stages of synthesis, with subsequent crystal growth comprising mainly SiO_2. This would result in Zr-zoned within the crystal centres and could be investigated by means of SEM-EDX analysis.

Table 5.9: Mass recovery following calcination from variable temperature syntheses of Zr–MFI.

Sample	Synthesis Temperature / °C	Mass Recovered /mg	Average Particle Diameter / nm
Zr–MFI-150C	150	288 (+161)	362
Zr–MFI-S3	180	909	404
Zr–MFI-200C	200	934	438

[iii] Unfortunately, DR-UV-Vis spectra for Zr–MFI-S3, Zr–MFI-150C and Zr–MFI-200C were not able to be acquired. These data were typically acquired at Cardiff University and following the events of 2020/21, the remaining DR-UV-Vis spectra were not able to be obtained before thesis submission.

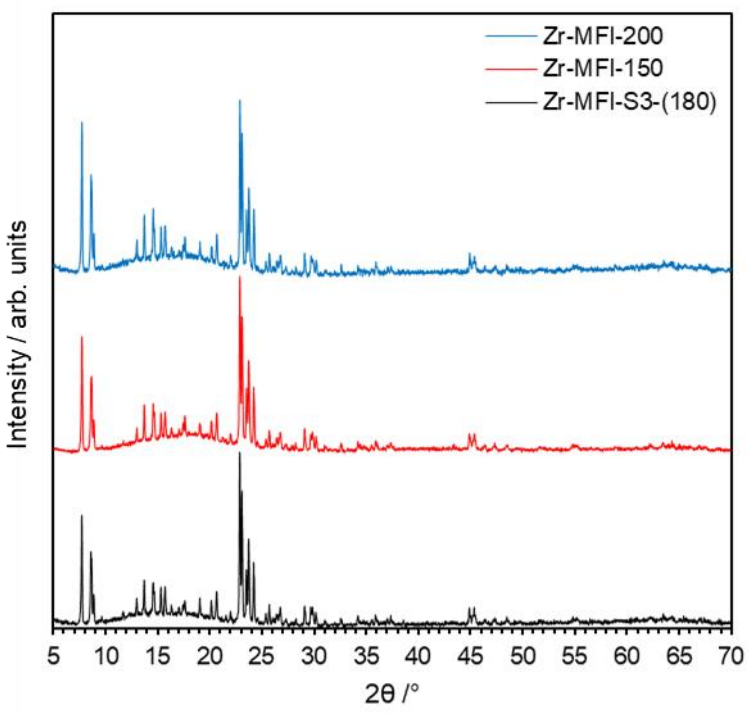

Figure 5.48: pXRD patterns in the 2θ = 5–70° range for syntheses of Zr–MFI materials in which hydrothermal synthesis temperature was set to 150 °C (Zr–MFI-150), 180 °C (Zr–MFI-S3) and 200 °C (Zr–MFI-200).

SEM analysis was undertaken in order to compare crystal morphology and particle size following variations in hydrothermal synthesis temperature; SEM images are shown in Figure 5.49. In a purely qualitative observation, the sample treated at 200 °C looked to contain a greater proportion of large coffin-like crystals in addition to larger tablet-like crystals when compared to the samples treated at 150 °C and 180 °C, potentially resulting from a higher synthesis temperature favouring larger crystal formation (possibly by increased SiO_2 incorporation). This is supported by comparison of the particle size distributions for samples synthesised at 150 °C (Figure 5.50), 180 °C (Figure 5.44) and 200°C (Figure 5.51) in which the mean particle diameter is seen to increase from 362 nm to 404 nm and 438 nm respectively for the small tablet-like crystals (Table 5.9). Careful modulation of Zr–MFI synthesis temperature may therefore allow control over zeolite textural properties, with lower synthesis temperatures allowing targeting of smaller, high surface area materials albeit at the loss of mass yield. Increased particle size at higher synthesis temperatures may also add credibility to the suggestion that excess SiO_2 grows on the crystal following initial zoning of Zr.

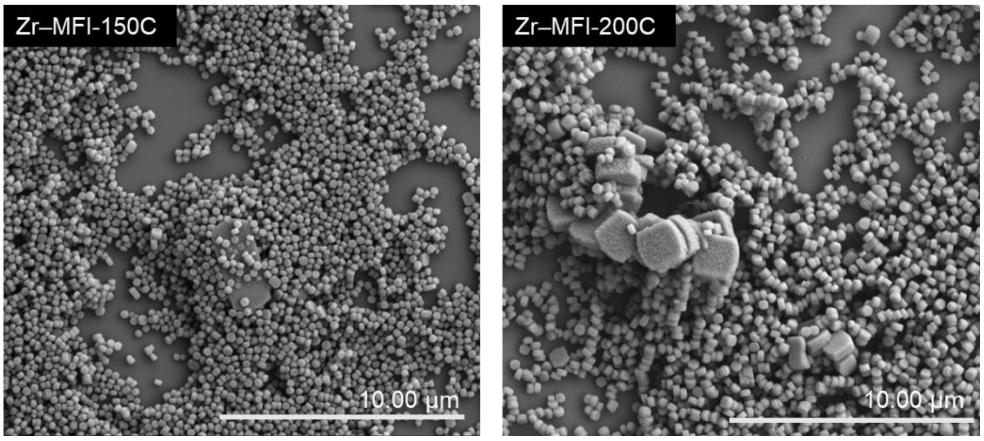

Figure 5.49: SEM images of Zr–MFI-150C (left) and Zr–MFI-200C (right).

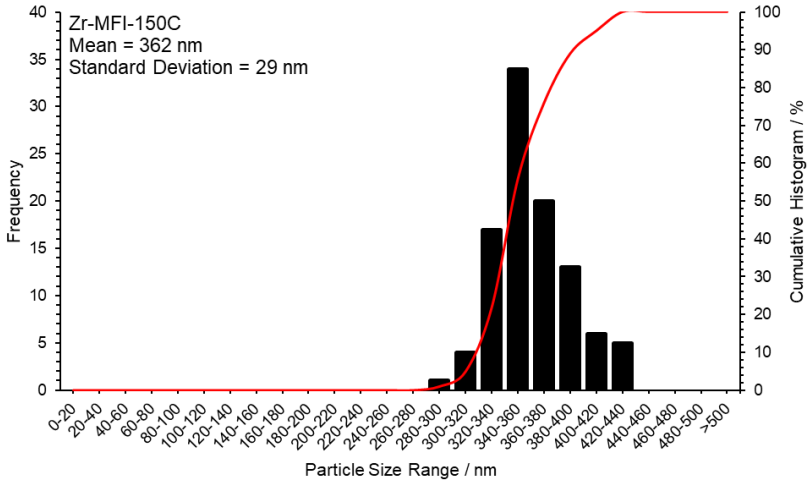

Figure 5.50: Particle size distribution for Zr–MFI-150C shown for 100 particles. Measurements taken as the diameter of tablet-like crystals. Bin width = 20 nm.

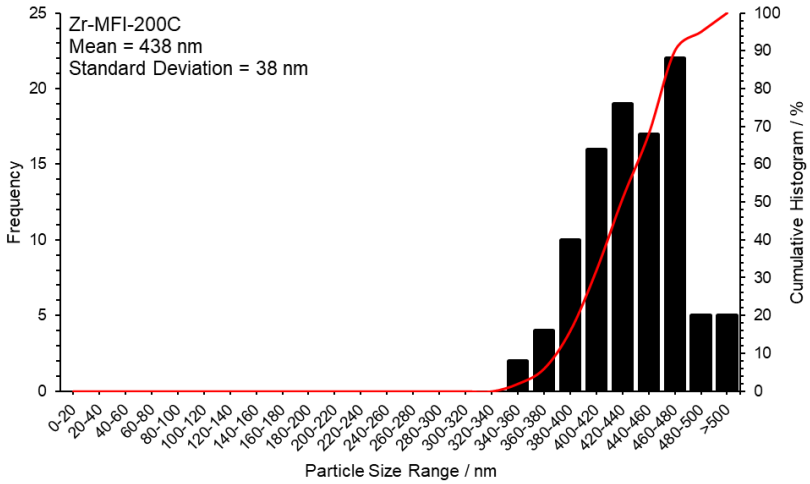

Figure 5.51: Particle size distribution for Zr–MFI-200C shown for 100 particles. Measurements taken as the diameter of tablet-like crystals. Bin width = 20 nm.

Following successful synthesis of Zr–MFI materials over a range of temperatures and subsequent analysis, the materials were doped with a nominal 3.5 wt% Zn and were tested for activity in the ethanol to butadiene cascade reaction at 350 °C for 4h TOS. Zn loadings, Zr loadings, Si/Zr ratios and Zn/Zr ratios measured by ED-XRF are presented in Table 5.10. Figure 5.52 shows butadiene productivity and ethanol conversion for ZnO/Zr–MFI-S3, ZnO/Zr–MFI-150C and ZnO/Zr–MFI-200C. Despite similar ethanol conversion trends, butadiene productivity per gram of catalyst is around 40% higher for ZnO/Zr–MFI-150C (3.5–4.0 mmol g_{cat}^{-1} h^{-1}) when compared to ZnO/Zr–MFI-S3 and ZnO/Zr–MFI-200C (2.5 mmol g_{cat}^{-1} h^{-1}). As the Si/Zr ratio for ZnO/Zr–MFI-150C (Si/Zr = 176) is similar to that for ZnO/Zr–MFI-S3 (Si/Zr = 180), it is unlikely that a decreased Si/Zr ratio is the major cause of increased butadiene productivity. This is further supported by ZnO/Zr–MFI-200C (Si/Zr = 252) exhibiting a similar butadiene productivity to ZnO/Zr–MFI-S3 (Si/Zr = 180) despite a largely different Si/Zr ratio. Instead, the major difference between ZnO/Zr–MFI-S3, ZnO/Zr–MFI-150C and ZnO/Zr–MFI-200C is their mean particle sizes, with ZnO/Zr–MFI-150C being the lowest at 362 nm. However, comparison of ZnO/Zr–MFI-rep2 and ZnO/Zr–MFI—S3 in Figure 5.47 showed that similar activities were observed regardless of substantially different particle sizes. Furthermore, comparison in Figure 5.52 shows that ZnO/Zr–MFI-200C and ZnO/Zr–MFI-S3 perform similarly despite differing mean particle sizes of the small tablet-like crystals. One potential suggestion as to the differing reactivity of ZnO/Zr–MFI-150C compared with ZnO/Zr–MFI-S3 and ZnO/Zr–MFI-200C could be the proportion of open and closed Zr sites, similar to the trends reported by Sushkevich *et al.*.[1] It may be that varying hydrothermal synthesis temperatures could affect the thermodynamics of Zr site closing, however FTIR measurements would be required to confirm this hypothesis. Additionally, initial Zr incorporation and internal zoning of Zr could lead to less accessible Zr in ZnO/Zr–MFI-S3 and ZnO/Zr–MFI-200C and lower butadiene productivity than for ZnO/Zr–MFI-150C.

Table 5.10: Zn loadings, Zr loadings, Si/Zr ratios and Zn/Zr ratios as determined by ED-XRF spectroscopy for a range of hydrothermal synthesis variations on ZnO/Zr–MFI. ED-XRF values averaged over three measurements following sample rotation

Sample	Zn Content / Wt%	Zr Content / Wt%	Si/Zr Ratio	Zn/Zr Ratio
ZnO/Zr–MFI-S3	3.45	0.76	165	6.37
ZnO/Zr–MFI-150C	3.11	0.65	176	6.72
ZnO/Zr–MFI-200C	3.94	0.58	221	9.57

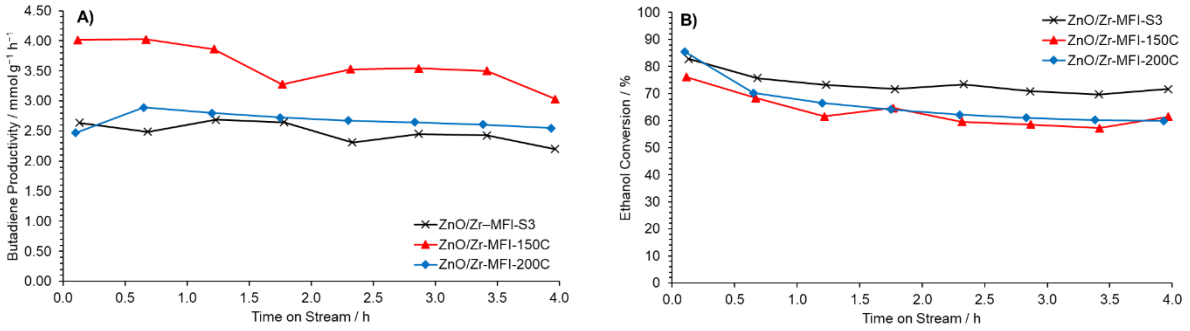

Figure 5.52: Butadiene productivity (A) and ethanol conversion (B) following reaction of ethanol over ZnO/Zr–MFI materials at 350 °C for 4 h TOS following various synthesis temperatures of 180 °C (ZnO/Zr–MFI-S3, ×), 150 °C (ZnO/Zr–MFI-150C, ▲) and 200 °C (ZnO/Zr–MFI-200C, ♦). Ethanol feed rate = 0.330 mmol min^{-1}, catalyst mass = 0.300 g. Detection Columns: RTX-VMS + ShinCarbon ST.

5.4.3. Effect of Zr-precursor concentration in the synthesis gel on Zr–MFI preparation and catalytic activity.

Modulation of Zr precursor concentration in the zeolite synthesis gel was also undertaken to observe its effect on Zr incorporation and Si/Zr ratio for Zr–MFI materials. Two samples of zeolite synthesis gel in which the mass of $ZrOCl_2 \cdot 8H_2O$ added was doubled to 1.03 wt% and halved to 0.26 wt% were prepared. Following hydrothermal synthesis and subsequent calcination, materials denoted Zr–MFI-1.03 and Zr–MFI-0.26 were produced. ED-XRF analysis of the synthesised materials showed that increasing Zr precursor proportion to 1.03 wt% did indeed increase final Zr loading to 1.06 wt% when compared to 0.79 wt% for Zr–MFI-S3 which in turn led to a decrease of Si/Zr ratio from 180 to 143 (Table 5.7). Additionally, reducing the initial Zr concentration in the zeolite synthesis gel to 0.26 wt% from 0.52% wt% resulted in no difference of Zr loading, with both samples measuring a Zr loading of 0.79 wt% and corresponding to a minor Si/Zr decrease from 180 to 197 (Table 5.7). This disproportionally high Zr loading could be attributed to the previously proposed Zr zoning mechanism. pXRD analysis of the materials was undertaken, with each synthesis variation exhibiting a standard MFI topology with no additional peaks observed from either ZrO_2 or other silicate phases (Figure 5.53). Additionally, DR-UV-Vis spectroscopic analysis could be undertaken to confirm that all additional Zr was incorporated into the zeolite tetrahedral sites.[iv]

[iv] Unfortunately, DR-UV-Vis spectra for Zr–MFI-1.03 and Zr–MFI-0.26 were not able to be acquired. These data were typically acquired at Cardiff University and following the events of 2020/21, the remaining DR-UV-Vis spectra were not able to be obtained before thesis submission.

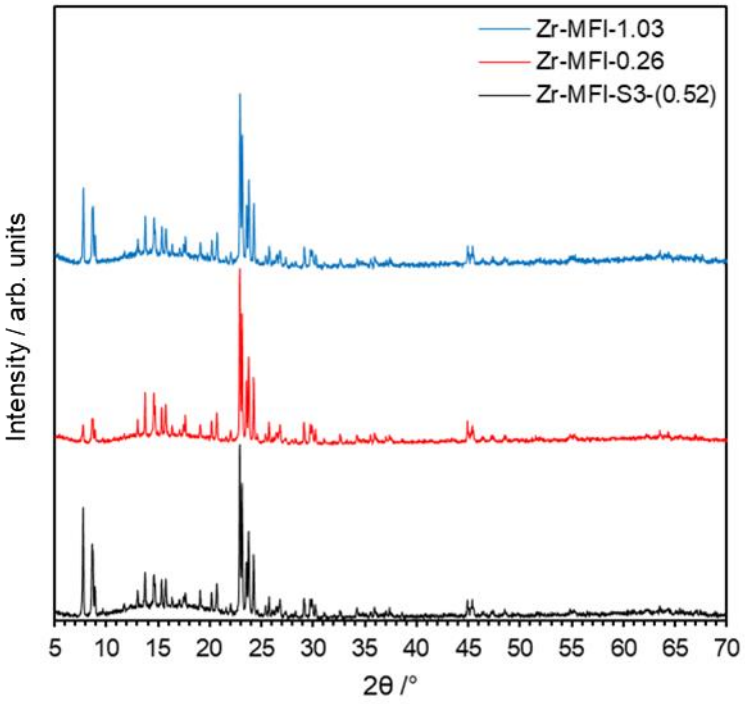

Figure 5.53: pXRD patterns in the 2θ = 5–70° range for syntheses of Zr–MFI materials in which the Zr-precurosr proportion in the zeolite synthesis gel was 0.26 wt% (Zr–MFI-0.26), 0.52 wt% (Zr–MFI-S3) and 1.03 wt% (Zr–MFI-1.03).

SEM analysis was undertaken in order to compare crystal morphology and size following variations in Zr precursor concentration and to also assess presence of any non-zeolite phases such as ZrO_2; SEM images are shown in Figure 5.54. Both materials exhibit morphology typical of that seen for Zr–MFI within this project, a majority of small tablet shaped crystals with larger coffin-shape agglomerates. Additionally, it is observed that Zr–MFI-1.03 exhibits multiple bright white spots across all crystals which are likely particles of ZrO_2. In order to confirm this suggestion, SEM-EDX analysis of the spots in combination with DR-UV-Vis spectroscopic observation could be undertaken.

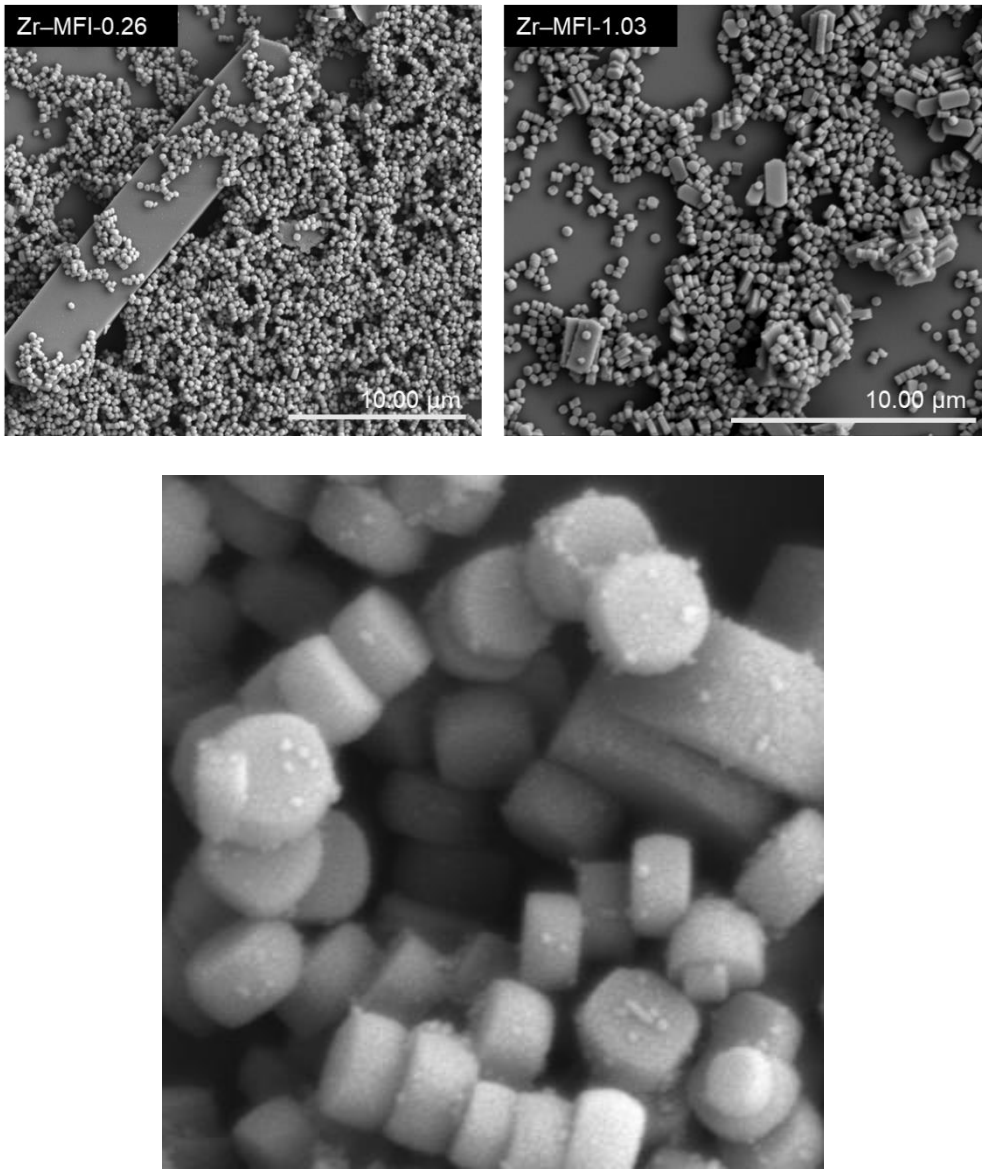

Figure 5.54: Top: SEM images of Zr–MFI-0.26 (left) and Zr–MFI-1.03 (right). Bottom: A close-up image of Zr–MFI-1.03 exhibiting bright white nanoparticles.

Figure 5.55 shows butadiene productivity and ethanol conversion for ZnO/Zr–MFI-1.03 and ZnO/Zr–MFI-0.26. Unfortunately, due to the necessity to retune the GC-MS-BID system following a repair, the recorded MS values were minorly different to those recorded in previous experiments hence, ZnO/Zr–MFI-S3 was not included for comparison to prevent erroneous conclusions. Despite similar ethanol conversion trends, butadiene productivity per gram of catalyst is around 40% higher for ZnO/Zr–MFI-1.03 (4.3 mmol g_{cat}^{-1} h^{-1}) when compared to ZnO/Zr–MFI-0.26 (3.1 mmol g_{cat}^{-1} h^{-1}). This is likely attributed to the lower Si/Zr ratio for ZnO/Zr–MFI-1.03 allowing higher conversion of produced acetaldehyde to butadiene.

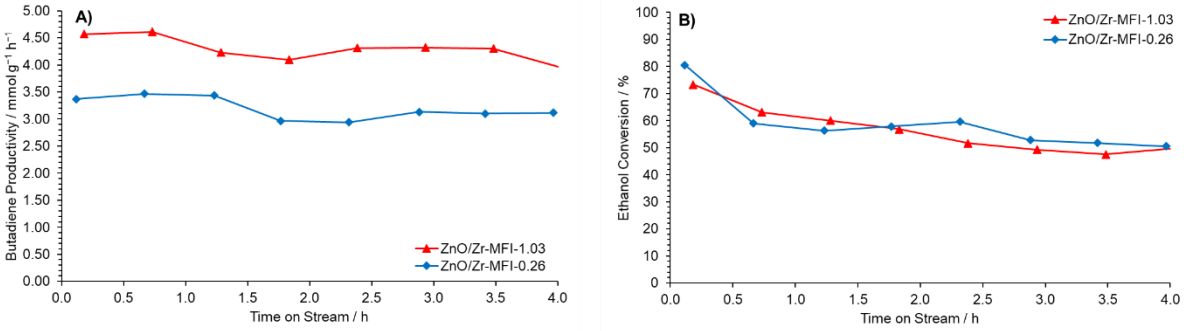

Figure 5.55: Butadiene productivity (A) and ethanol conversion (B) following reaction of ethanol over ZnO/Zr–MFI materials at 350 °C for 4 h TOS with various Zr loadings in the synthesis gel: Zr loading = 1.03% (ZnO/Zr–MFI-1.03, ▲) and 0.26% (ZnO/Zr–MFI-0.26, ♦). Ethanol feed rate = 0.390 mmol min^{-1}, catalyst mass = 0.300 g. Detection Columns: RTX-VMS + ShinCarbon ST.

5.5. Conclusions

The synthesis of Sn–MFI adapted from the reports from Kolyagin *et al.* and Mal *et al.* has been successfully reproduced yielding an MFI type material containing framework bound Sn atoms as evidenced by pXRD, SEM, DR-UV-Vis and ^{119}Sn ssNMR spectroscopy.[29, 30] Following successful synthesis of Sn–MFI, several other M^{IV} heteroatomically substituted MFI type materials containing Si, Ti, Zr and Hf in tetrahedral positions were also successfully synthesised as evidenced by pXRD, BET, SEM, and ^{29}Si ssNMR spectroscopic analysis, with isolated framework sites in all materials confirmed by DR-UV-Vis spectroscopy and SEM-EDX mapping.

Each M–MFI materials was subsequently assessed for their performance in the cascade reaction from ethanol to butadiene at varying temperature points. In each case, a product distribution composed predominantly of diethyl ether and ethylene was obtained, indicative of Lewis acidity. Each M–MFI material was then doped with ZnO which had previously been identified as a highly selective dedicated dehydrogenation site in Chapter 4. Following introduction of ZnO, the product distribution of each ZnO/M–MFI material shifted to include a large proportion of Lebedev products (acetaldehyde and butadiene), with maximum selectivites to Lebedev products observed at a reaction temperature of 350 °C. Comparison of the materials resulted in ZnO/Zr–MFI being identified as the optimum catalyst materials of those assessed. ZnO/Zr–MFI was shown to exhibit highly reproducible performance, achieving an average butadiene selectivity of around 18% observed at an ethanol conversion value of between 50-60 % after 4h TOS. Unfortunately, when subjected to a catalytic test for 24 h TOS, ZnO/Zr–MFI showed a significant loss of butadiene productivity, with deactivation proposed to be Zr centred.

The deactivation of Zr centres was assessed by means of *in-situ* XAS analysis. However, the resulting spectra showed no major change in the shape of the XANES region of the Zr K-edge between fresh and spent catalysts, suggesting no substantial change of Zr co-ordination environment or oxidation state following reaction. Subsequently, in-depth coking analysis was undertaken by means of ^{13}C ssNMR spectroscopy and TPO-MS of the spent catalyst charges, alongside FTIR, ASAP-MS and GC-MS analysis of carbonaceous species following framework dissolution. Following assessment, the presence of large, polyaromatic hydrocarbon species was identified within spent catalyst charges. Regeneration of spent ZnO/Zr–MFI by thermal treatment resulted in recovery of the catalysts activity, hence, coking was proposed to be the predominant cause of the observed deactivation.

Finally, several variations were made to the hydrothermal synthesis method of Zr–MFI in an attempt to improve butadiene productivity. Namely, synthesis time, synthesis temperature and synthesis gel Zr loading were all varied independently. Each resulting material was tested catalytically for the conversion of ethanol to butadiene at 350 °C following ZnO impregnation and compared to an in-house standard ZnO/Zr–MFI material. Hydrothermal synthesis time was varied between 3-5 days and was found to have little effect on Zr inclusion, particle size or catalytic activity of resulting ZnO/Zr–MFI materials. Hydrothermal synthesis temperature was varied between 150-200 °C and it was found that materials synthesised at a lower temperature (150 °C) exhibited a smaller mean particle size with higher Zr incorporation which resulted in greater butadiene productivity. As may be expected, increasing the Zr content within the synthesis gel resulted in increased Zr loading of Zr–MFI and higher butadiene productivity. Interestingly, significantly reducing the Zr content within the synthesis gel resulted in disproportionally high Zr loading of the resultant Zr–MFI material. As a result of these observations, it was proposed that Zr may be incorporated rapidly into the zeolite during the early phases of crystallisation, resulting in central Zr zoning within Zr–MFI materials. This proposition would favour butadiene productivity over ZnO/Zr–MFI materials with small particle diameters and increased Zr loading.

5.6. References.

1. V. L. Sushkevich, D. Palagin and I. I. Ivanova, *ACS Catal.*, 2015, **5**, 4833–4836.
2. V. L. Sushkevich and I. I. Ivanova, *ChemSusChem*, 2016, **9**, 2216–2225.
3. P. I. Kyriienko, O. V. Larina, S. O. Soloviev, S. M. Orlyk, C. Calers and S. Dzwigaj, *ACS Sustain. Chem. Eng.*, 2017, **5**, 2075–2083.
4. C. Wang, M. Zheng, X. Li, X. Li and T. Zhang, *Green Chem.*, 2019, **21**, 2006–2010.
5. V. L. Sushkevich, I. I. Ivanova and E. Taarning, *Green Chem.*, 2015, **17**, 2552–2559.
6. P. I. Kyriienko, O. V. Larina, N. O. Popovych, S. O. Soloviev, Y. Millot and S. Dzwigaj, *J. Mol. Catal. A*, 2016, **424**, 27–36.
7. M. Moliner, *Dalton Trans.*, 2014, **43**, 4197–4208.
8. D. Palagin, V. L. Sushkevich and I. I. Ivanova, *J. Phys. Chem. C*, 2016, **120**, 23566–23575.
9. V. L. Sushkevich, I. I. Ivanova, S. Tolborg and E. Taarning, *J. Catal.*, 2014, **316**, 121–129.
10. M. Boronat, A. Corma and M. Renz, *J. Phys. Chem. B*, 2006, **110**, 21168–21174.
11. A. Corma, M. E. Domine, L. Nemeth and S. Valencia, *J. Am. Chem. Soc.*, 2002, **124**, 3194–3195.
12. T. Yan, W. Dai, G. Wu, S. Lang, M. Hunger, N. Guan and L. Li, *ACS Catal.*, 2018, **8**, 2760-2773.
13. E. V. Makshina, M. Dusselier, W. Janssens, J. Degreve, P. A. Jacobs and B. F. Sels, *Chem. Soc. Rev.*, 2014, **43**, 7917–7953.
14. M. Shamzhy, M. Opanasenko, P. Concepción and A. Martínez, *Chem. Soc. Rev.*, 2019,**48**, 1095–1149.
15. Y.-P. Li, M. Head-Gordon and A. T. Bell, *ACS Catal.*, 2014, **4**, 1537–1545.
16. J. D. Lewis, S. Van de Vyver and Y. Román-Leshkov, *Angew. Chem.*, 2015, **54**, 9835–9838.
17. H. Y. Luo, D. F. Consoli, W. R. Gunther and Y. Román-Leshkov, *J. Catal.*, 2014, **320**, 198–207.
18. V. L. Sushkevich, A. Vimont, A. Travert and I. I. Ivanova, *J. Phys. Chem. C*, 2015, **119**, 17633–17639.
19. M. Boronat, P. Concepción, A. Corma, M. Renz and S. Valencia, *J. Catal.*, 2005, **234**, 111–118.
20. M. Boronat, P. Concepción, A. Corma, M. T. Navarro, M. Renz and S. Valencia, *Phys. Chem. Chem. Phys.*, 2009, **11**, 2876–2884.
21. J. W. Harris, M. J. Cordon, J. R. Di Iorio, J. C. Vega-Vila, F. H. Ribeiro and R. Gounder, *J. Catal.*, 2016, **335**, 141–154.
22. T. R. Josephson, G. R. Jenness, D. G. Vlachos and S. Caratzoulas, *Micropor. Mesopor. Mater.*, 2017, **245**, 45–50.
23. R. Bermejo-Deval, R. S. Assary, E. Nikolla, M. Moliner, Y. Román-Leshkov, S.-J. Hwang, A. Palsdottir, D. Silverman, R. F. Lobo, L. A. Curtiss and M. E. Davis, *Proc. Nat. Acad. Sci.*, 2012, **109**, 9727–9732.
24. R. Bermejo-Deval, M. Orazov, R. Gounder, S.-J. Hwang and M. E. Davis, *ACS Catal.*, 2014, **4**, 2288–2297.
25. S. Bordiga, F. Bonino, A. Damin and C. Lamberti, *Phys. Chem. Chem. Phys.*, 2007, **9**, 4854–4878.
26. G. Li, L. Gao, Z. Sheng, Y. Zhan, C. Zhang, J. Ju, Y. Zhang and Y. Tang, *Catal. Sci. Technol.*, 2019, **9**, 4055–4065.
27. J. C. Vega-Vila, J. W. Harris and R. Gounder, *J. Catal.*, 2016, **344**, 108–120.
28. G. Yang, L. Zhou and X. Han, *J. Mol. Catal. A*, 2012, **363-364**, 371–379.

29. Y. G. Kolyagin, A. V. Yakimov, S. Tolborg, P. N. R. Vennestrøm and I. I. Ivanova, *J. Phys. Chem. Lett.*, 2016, **7**, 1249–1253.
30. N. K. Mal, V. Ramaswamy, P. R. Rajamohanan and A. V. Ramaswamy, *Micropor. Mater.*, 1997, **12**, 331–340.
31. A. Parulkar, R. Joshi, N. Deshpande and N. A. Brunelli, *Appl. Catal. A*, 2018, **566**, 25–32.
32. N. K. Mal and A. V. Ramaswamy, *J. Molec. Catal. A*, 1996, **105**, 149–158.
33. W. Fan, R.-G. Duan, T. Yokoi, P. Wu, Y. Kubota and T. Tatsumi, *J. Am. Chem. Soc.*, 2008, **130**, 10150–10164.
34. Y. S. Ko and W. S. Ahn, *Korean J. Chem. Eng.*, 1998, **15**, 423–428.
35. A. V. Yakimov, Y. G. Kolyagin, S. Tolborg, P. N. R. Vennestrøm and I. I. Ivanova, *J. Phys. Chem. C*, 2016, **120**, 28083–28092.
36. V. L. Sushkevich, P. A. Kots, Y. G. Kolyagin, A. V. Yakimov, A. V. Marikutsa and I. I. Ivanova, *J. Phys. Chem. C*, 2019, **123**, 5540–5548.
37. P. Wolf, W.-C. Liao, T.-C. Ong, M. Valla, J. W. Harris, R. Gounder, W. N. P. van der Graaff, E. A. Pidko, E. J. M. Hensen, P. Ferrini, J. Dijkmans, B. Sels, I. Hermans and C. Copéret, *Helv. Chim. Acta*, 2016, **99**, 916–927.
38. P. Arudra, T. I. Bhuiyan, M. N. Akhtar, A. M. Aitani, S. S. Al-Khattaf and H. Hattori, *ACS Catal.*, 2014, **4**, 4205–4214.
39. C. A. Fyfe, D. H. Brouwer, A. R. Lewis and J. M. Chezeau, *J. Am. Chem. Soc.*, 2001, **123**, 6882–6891.
40. *US Pat.*, US4410501A, 1983.
41. M. K. Dongare, P. Singh, P. P. Moghe and P. Ratnasamy, *Zeolites*, 1991, **11**, 690–693.
42. C. Xia, Y. Liu, M. Lin, X. Peng, B. Zhu and X. Shu, *Catal. Today*, 2018, **316**, 193–198.
43. A. Thangaraj, R. Kumar, S. P. Mirajkar and P. Ratnasamy, *J. Catal.*, 1991, **130**, 1–8.
44. D. R. Black, D. Windover and A. Henins, *National Institute of Standards and Technology*, 2010.
45. C. T. Chantler, C. Q. Tran and D. J. Cookson, *Phys. Rev. A*, 2004, **69**, 042101.
46. J. Goetze, I. Yarulina, J. Gascon, F. Kapteijn and B. M. Weckhuysen, *ACS Catal.*, 2018, **8**, 2060–2070.
47. I. Grosskreuz, H. Gies and B. Marler, *Micropor. Mesopor. Mater.*, 2020, **291**, 109683.
48. K. Iyoki, K. Kikumasa, T. Onishi, Y. Yonezawa, A. Chokkalingam, Y. Yanaba, T. Matsumoto, R. Osuga, S. P. Elangovan, J. N. Kondo, A. Endo, T. Okubo and T. Wakihara, *J. Am. Chem. Soc.*, 2020, **142**, 3931–3938.
49. Z. Qin, L. Lakiss, J. P. Gilson, K. Thomas, J. M. Goupil, C. Fernandez and V. Valtchev, *Chem. Mater.*, 2013, **25**, 2759–2766.
50. J. Zhang, X. Li, J. Liu and C. Wang, *Catalysts*, 2019, **9**, 13.
51. C. A. Fyfe, R. J. Darton, H. Mowatt and Z. S. Lin, *Micropor. Mesopor. Mater.*, 2011, **144**, 57–66.
52. Z. Han, Y. Shen, F. Wang and X. Zhang, *J. Mater. Sci.*, 2018, **53**, 12837–12849.
53. Y. K. Hwang, T. Jin, J. M. Kim, Y. U. Kwon, S. E. Park and J. S. Chang, *J. Nanosci. Nanotechnol.*, 2006, **6**, 1786–1791.
54. X. Li, F. Rezaei, D. K. Ludlow and A. A. Rownaghi, *Ind. Eng. Chem. Res.*, 2018, **57**, 1446–1453.
55. T. Iida, K. Ohara, Y. Román-Leshkov and T. Wakihara, *Phys. Chem. Chem. Phys.*, 2018, **20**, 7914–7919.
56. B. C. Bukowski, J. S. Bates, R. Gounder and J. Greeley, *J. Catal.*, 2018, **365**, 261–276.
57. J. S. Bates and R. Gounder, *J. Catal.*, 2018, **365**, 213–226.

58. B. D. Montejo-Valencia, J. L. Salcedo-Pérez and M. C. Curet-Arana, *J. Phys. Chem. C*, 2016, **120**, 2176–2186.
59. C. Della Pina, E. Falletta, A. Gervasini, J. H. Teles and M. Rossi, *ChemCatChem*, 2010, **2**, 1587–1593.
60. G. Yang, E. A. Pidko and E. J. M. Hensen, *J. Phys. Chem. C*, 2013, **117**, 3976–3986.
61. O. V. Larina, P. I. Kyriienko and S. O. Soloviev, *Catal. Lett.*, 2015, **145**, 1162–1168.
62. C. Angelici, M. E. Z. Velthoen, B. M. Weckhuysen and P. C. A. Bruijnincx, *ChemSusChem*, 2014, **7**, 2505–2515.
63. P. A. Kots, A. V. Zabilska, E. V. Khramov, Y. V. Grigoriev, Y. V. Zubavichus and I. I. Ivanova, *Inorg. Chem.*, 2018, **57**, 11978–11985.
64. J. Wang, M. Yi, Z. Shen, L. Liu, X. Zhang and S. Ma, *J. Macromol. Sci. A*, 2019, **56**, 733–740.
65. A. Devaraj, M. Vijayakumar, J. Bao, M. F. Guo, M. A. Derewinski, Z. Xu, M. J. Gray, S. Prodinger and K. K. Ramasamy, *Sci. Rep.*, 2016, **6**, 37586.
66. X. Zhou, C. Wang, Y. Chu, J. Xu, Q. Wang, G. Qi, X. Zhao, N. Feng and F. Deng, *Nat. Commun.*, 2019, **10**, 1961.
67. S. Radhakrishnan, P.-J. Goossens, P. C. M. M. Magusin, S. P. Sree, C. Detavernier, E. Breynaert, C. Martineau, F. Taulelle and J. A. Martens, *J. Am. Chem. Soc.*, 2016, **138**, 2802–2808.
68. G. M. Cabello González, R. Murciano, A. L. Villanueva Perales, A. Martínez, F. Vidal-Barrero and M. Campoy, *Appl. Catal. A*, 2019, **570**, 96–106.
69. B. S. Liu, Y. Zhang, J. F. Liu, M. Tian, F. M. Zhang, C. T. Au and A. S. C. Cheung, *J. Phys. Chem. C*, 2011, **115**, 16954–16962.
70. Q. Li, W. Dai, B. S. Liu, P. J. Sarre, M. H. Xie and A. S. C. Cheung, *Mol. Astrophys.*, 2018, **13**, 22–29.
71. N. Kosinov, E. A. Uslamin, F. J. A. G. Coumans, A. S. G. Wijpkema, R. Y. Rohling and E. J. M. Hensen, *ACS Catal.*, 2018, **8**, 8459–8467.
72. F. Bleken, W. Skistad, K. Barbera, M. Kustova, S. Bordiga, P. Beato, K. P. Lillerud, S. Svelle and U. Olsbye, *Phys. Chem. Chem. Phys.*, 2011, **13**, 2539–2549.
73. P. Magnoux, P. Roger, C. Canaff, V. Fouche, N. S. Gnep and M. Guisnet, in *Stud. Surf. Sci. Catal.*, eds. B. Delmon and G. F. Froment, Elsevier, 1987, vol. 34, pp. 317–330.
74. J. Goetze, F. Meirer, I. Yarulina, J. Gascon, F. Kapteijn, J. Ruiz-Martínez and B. M. Weckhuysen, *ACS Catal.*, 2017, **7**, 4033–4046.
75. K. Ben Tayeb, S. Hamieh, C. Canaff, H. Nguyen, H. Vezin and L. Pinard, *Micropor. Mesopor. Mater.*, 2019, **289**, 109617.
76. L. Pinard, S. Hamieh, C. Canaff, F. Ferreira Madeira, I. Batonneau-Gener, S. Maury, O. Delpoux, K. Ben Tayeb, Y. Pouilloux and H. Vezin, *J. Catal.*, 2013, **299**, 284–297.
77. M. Guisnet and P. Magnoux, *Appl. Catal.*, 1989, **54**, 1–27.
78. Elemental Analysis of Zeolites, https://www.inorganicventures.com/guides-and-papers/elemental-analysis-of-zeolites, (accessed 29/10/20).
79. J. Coates, *Encyclopedia of analytical chemistry: applications, theory and instrumentation*, 2006.
80. M. Guisnet and P. Magnoux, *Appl. Catal. A*, 2001, **212**, 83–96.

5.7. Supplementary Information.

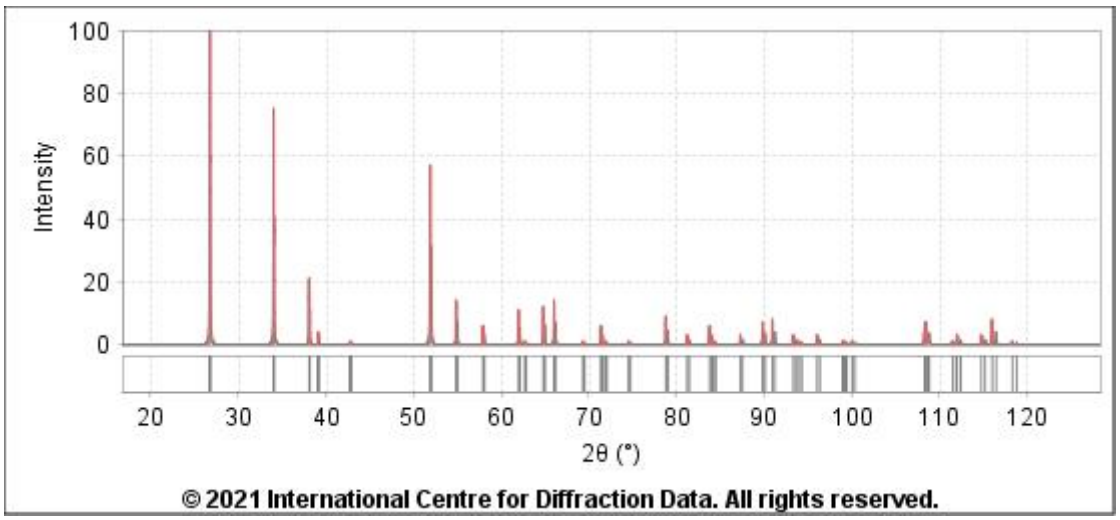

Figure S5.1: pXRD pattern for SnO_2 acquired from the ICDD database.

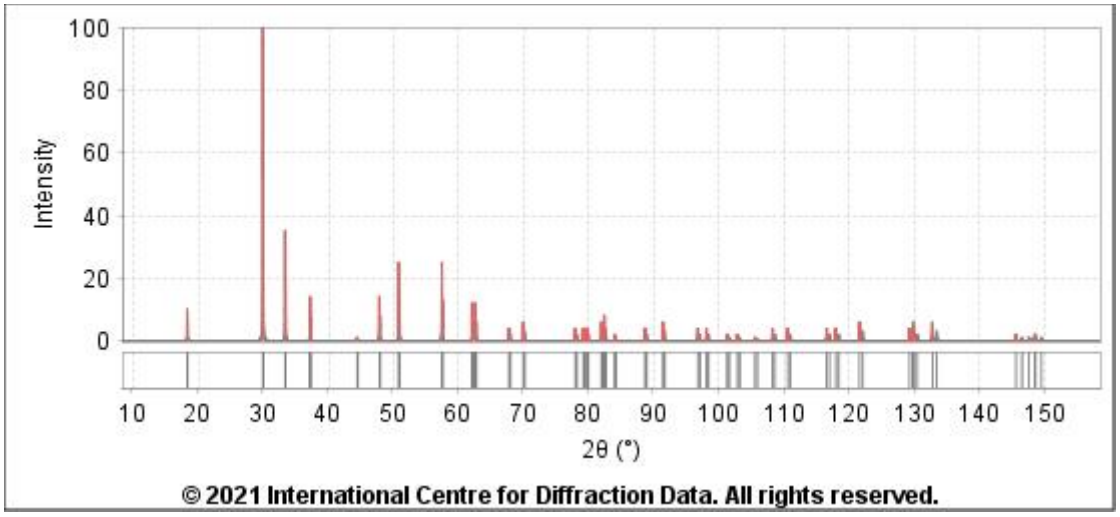

Figure S5.2: pXRD pattern for SnO acquired from the ICDD database.

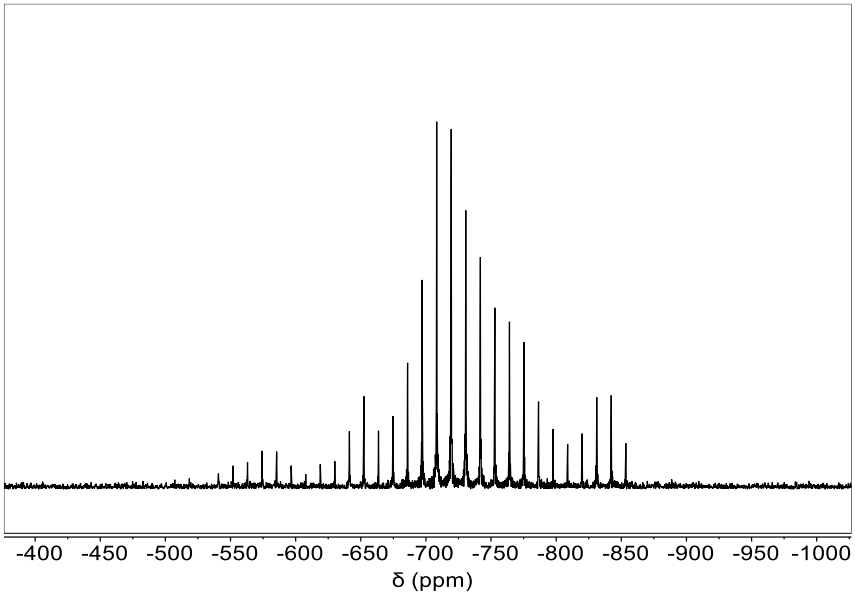

Figure S5.3: Spikelet ^{1}H–^{119}Sn CP-CPMG ssNMR spectra of as-prepared Sn–MFI averaged over 6400 scans with a 2.0 s recycle delay and a 5 ms contact time. Spectrum acquired on a Bruker III Avance 400 MHz spectrometer using a 4 mm zirconia rotor. Spectrometer frequncies: ^{1}H = 400.17 MHz, ^{119}Sn = 149.12 MHz. MAS spin rate = 10000 Hz.

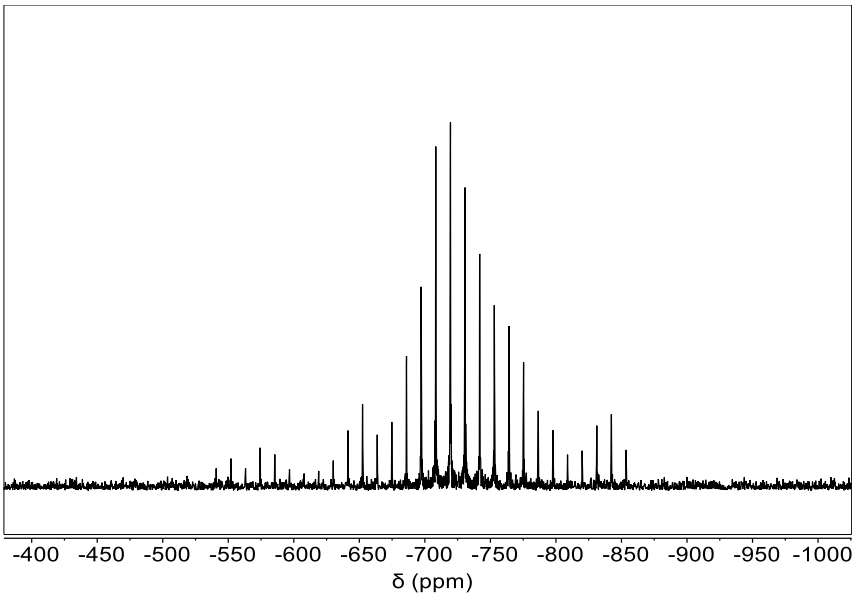

Figure S5.4: Spikelet ^{1}H–^{119}Sn CP-CPMG ssNMR spectra of as-prepared Sn–MFI–rep averaged over 6400 scans with a 2.0 s recycle delay and a 5 ms contact time. Spectrum acquired on a Bruker III Avance 400 MHz spectrometer using a 4 mm zirconia rotor. Spectrometer frequncies: ^{1}H = 400.17 MHz, ^{119}Sn = 149.12 MHz. MAS spin rate = 10000 Hz.

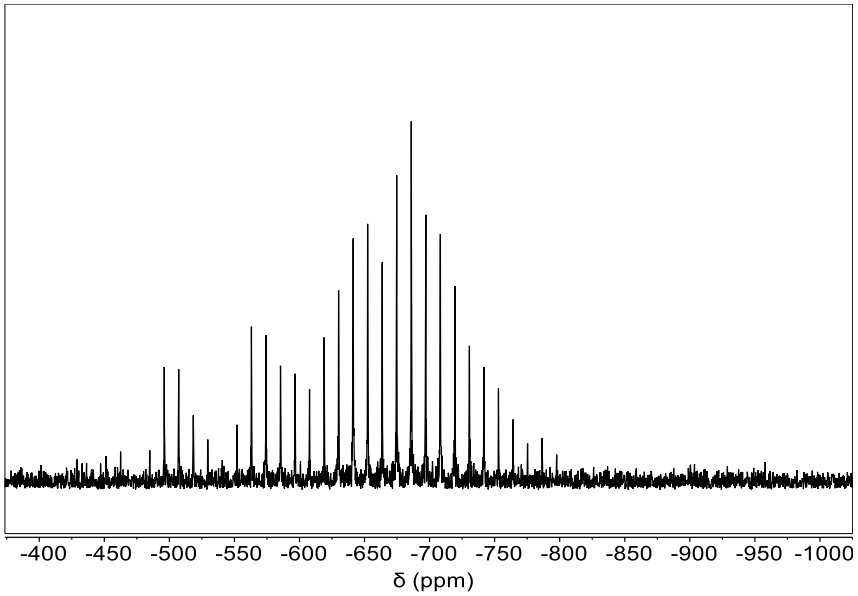

Figure S5.5: Spikelet $^{1}H–^{119}Sn$ CP-CPMG ssNMR spectra of calcined Sn–MFI averaged over 32000 scans with a 2.0 s recycle delay and a 5 ms contact time. Spectrum acquired on a Bruker III Avance 400 MHz spectrometer using a 4 mm zirconia rotor. Spectrometer frequncies: ^{1}H = 400.17 MHz, ^{119}Sn = 149.12 MHz. MAS spin rate = 10000 Hz.

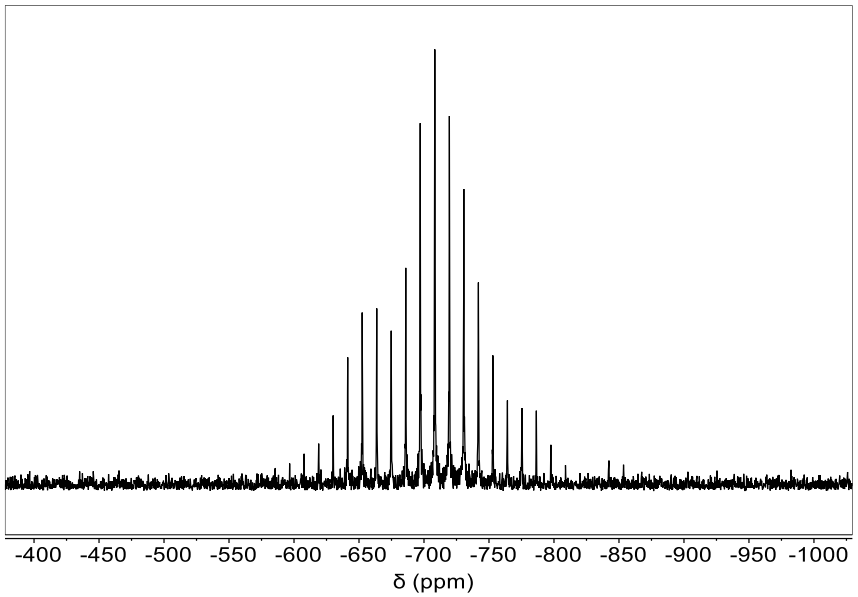

Figure S5.6: Spikelet $^{1}H–^{119}Sn$ CP-CPMG ssNMR spectra of calcined Sn–MFI–rep averaged over 12800 scans with a 2.0 s recycle delay and a 5 ms contact time. Spectrum acquired on a Bruker III Avance 400 MHz spectrometer using a 4 mm zirconia rotor. Spectrometer frequncies: ^{1}H = 400.17 MHz, ^{119}Sn = 149.12 MHz. MAS spin rate = 10000 Hz.

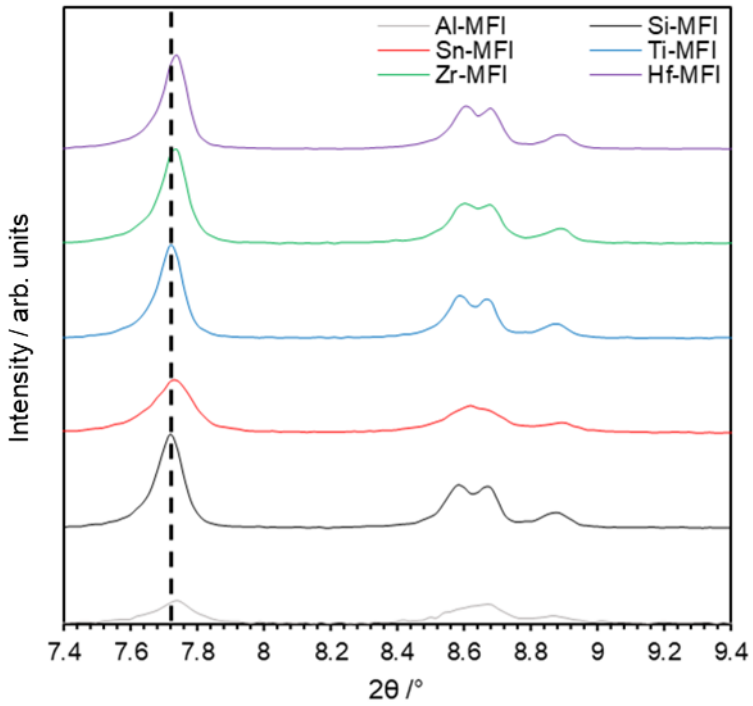

Figure S5.7: pXRD patterns in the 2θ = 5–70° (A) and 2θ = 20–30° (B) range of synthesized M–MFI materials following calcination, where M = Si, Sn, Ti, Zr, Hf. The diffractogram of a commercial Al–MFI material is included as an MFI framework reference.

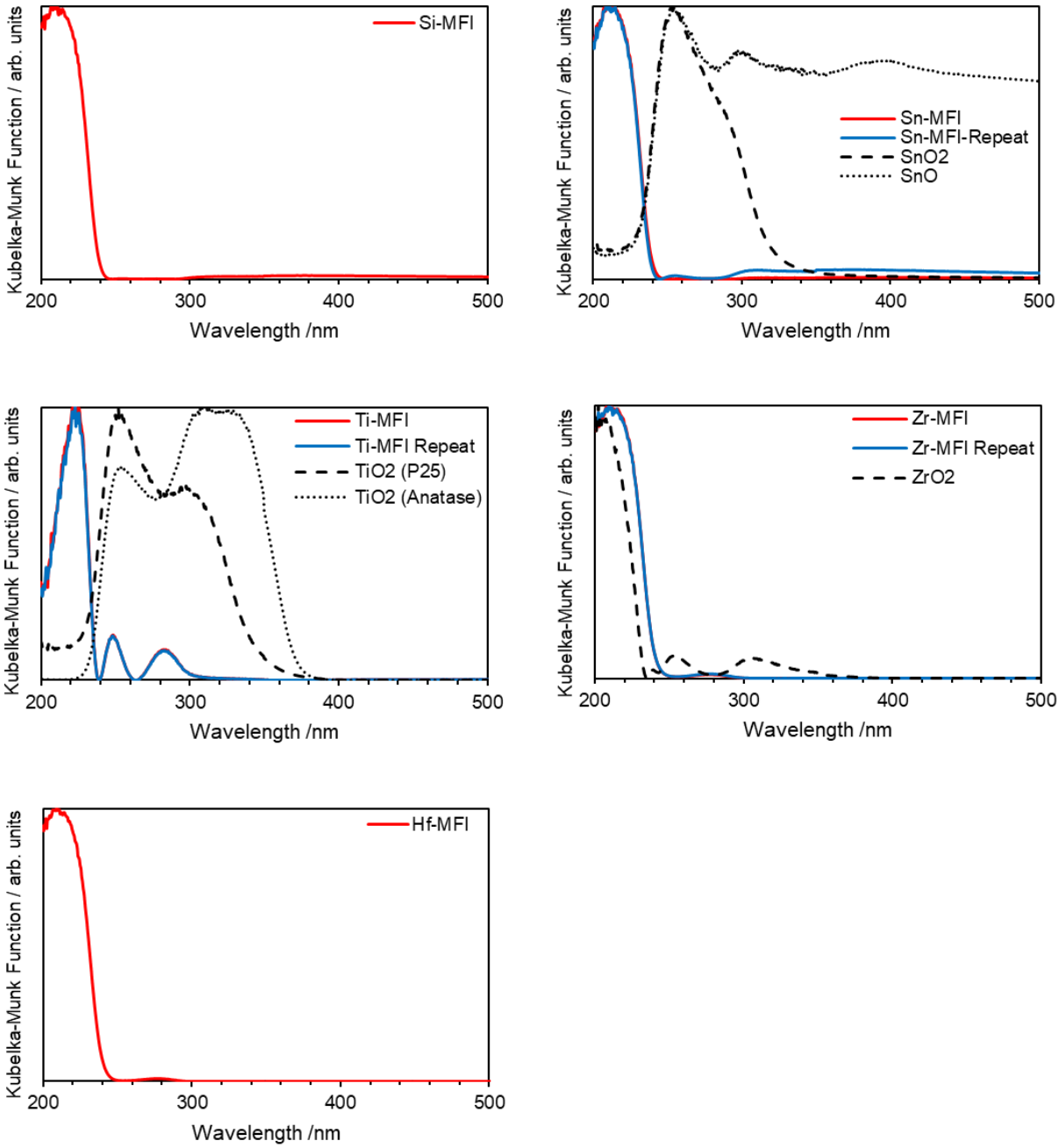

Figure S5.8: DR–UV–Vis spectra for as-synthesised M–MFI materials following calcination, where M = Si, Sn, Ti, Zr, Hf. Included for comparison are spectra of potential extra-framework oxide materials that could form during hydrothermal synthesis.

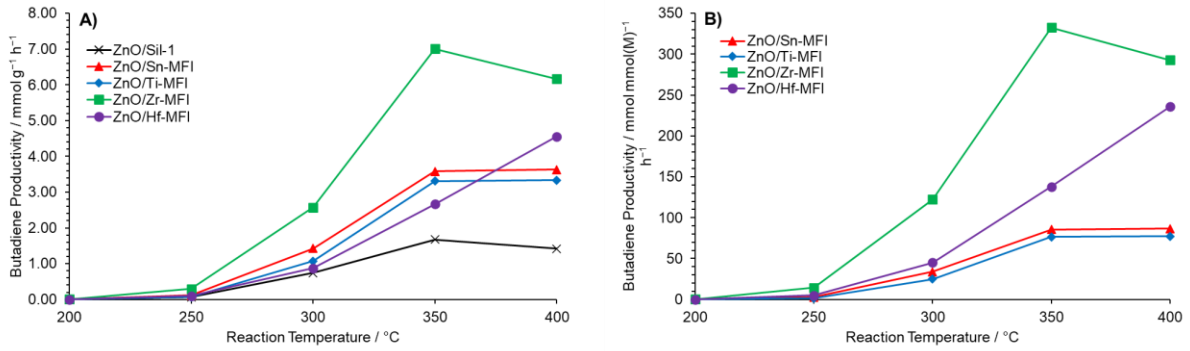

Figure S5.9: Butadiene productivities normalized by catalyst mass (A) and heteroatom content (B) for the reaction of ethanol at various temperatures over ZnO(3.15)/Si–MFI (×), ZnO(3.35)/Sn(108)–MFI (▲), ZnO(3.35)/Ti(113)–MFI (♦), ZnO(3.20)/Zr(231)–MFI (■) and ZnO(3.13)/Hf(249)–MFI (●). Ethanol feed rate = 0.197 mmol min^{-1}, catalyst mass = 0.300 g.

Chapter 6

Development of Multifunctional Zeolite Materials Containing Divalent Metal Atoms for the Cascade Conversion of Ethanol to 1,3–Butadiene.

6. Development of Multifunctional Zeolite Materials Containing Divalent Metal Atoms for the Cascade Conversion of Ethanol to 1,3–Butadiene.

Following the successful work presented in Chapter 5 focussing on the substitution of tetravalent metal atoms into an MFI framework as Lewis acidic centres for the cascade conversion of ethanol to 1,3–butadiene, an investigation into the use of divalent metals atoms, such as Mg^{II} and Zn^{II}, towards the same aim was undertaken.

Similar to tetravalent metal centres, divalent metal species are thought to be able to provide Lewis acidic centres when substituted into a zeolite framework.[1-3] In terms of their Lewis acidic behaviours desirable for this project, it is theorised that Zn–MFI should behave similarly to Sn–MFI owing to its d^{10} orbital configuration (see Chapter 5),[4] whereas Mg–MFI may behave more similarly to Ti–MFI, Zr–MFI and Hf–MFI owing to a d^0 electronic configuration allowing vacant d-orbitals, such as the d_{z^2}, to potentially partake in catalysis. However, it is unlikely that the d-orbitals of Mg will be energetically accessible and therefore reactivity may be mainly sourced through framework σ*(Mg–O) orbitals as for Sn–MFI (see Chapter 5).[4] One report from Yang *et al.* suggests that the Lewis acid strength of Mg is lesser than that of Sn when incorporated into the silanol vacancies of dealuminated BEA by virtue of FTIR spectroscopy of adsorbed pyridine and CD_3CN.[5]

An important feature of divalent centres, such as Zn^{2+} and Mg^{2+}, is that they are able to adopt multiple coordination configurations, namely open, partly open and closed configurations as shown in Figure 6.1.[1, 5, 6] As a result of partly open and closed configurations, an overall negative framework charge is obtained requiring the presence of counter-balancing cations to maintain overall charge neutrality, similar to that seen for aluminosilicate frameworks. Hence, the configuration of the tetrahedral metal atoms likely has large implications for the reactivity of M^{2+} substituted zeolites. Namely, due to the presence of counter-balancing cations and their potential for exchange, it is thought that the strength of Lewis acidic metal centres in divalent metal substituted zeolites may be highly tuneable. Potentially, the centres may take on a more Brønsted acidic nature if H^+ is present as the counter cation. Further, the presence of a formal T^{2-} tetrahedral centre in a closed configurations is thought to allow more facile ion-exchange of divalent cations, such as Co^{2+} and Ni^{2+}, than equivalent aluminosilicate materials.[6-13] Hence, introduction of extra-framework divalent

species such as Cu^{2+} and Zn^{2+} which are catalytically active for ethanol dehydrogenation could readily be combined with Lewis acidic framework sites.[7, 8, 14-17]

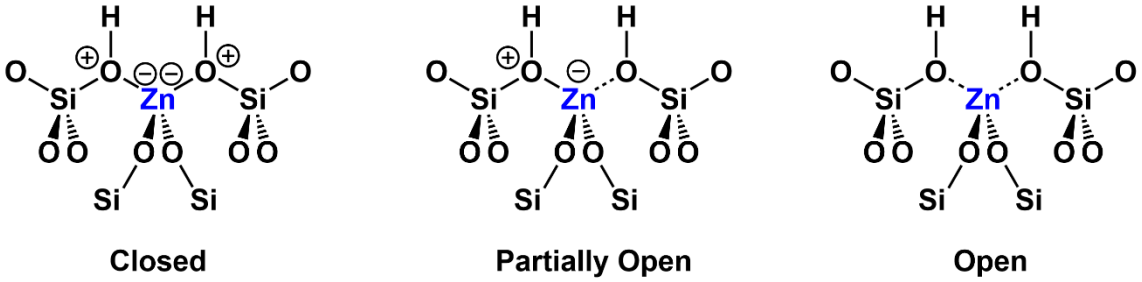

Figure 6.1: Potential configurations for M^{2+} ions when included into zeolite framework positions. Here, Zn^{II} is used as an example with H^+ as the counter-cation where required.

The variable Lewis acidic nature of Zn–MFI as a result of different tetrahedral configuration is aptly highlighted by Orazov *et al*. during the Diels–Alder cycloaddition–dehydration reactions of ethylene with methyl 5-(methoxymethyl)furan-2-carboxylate.[1] In this example, two disparate Zn sites are identified in Zn–BEA (CIT–6). One site contains Zn in a closed configuration, bearing a formal 2− framework charge which is balanced by two lithium monocations. The other site contains Zn in an open configuration which is bound to two framework atoms whilst maintaining dative bonds to surrounding silanols. The authors note that these dative bonds are insufficiently strong to generate a Brønsted acid site that is capable of protonating pyridine. These two types of site are characterised by FTIR spectroscopy of adsorbed CD_3CN with bands identified at 2290 cm^{-1} and 2312 cm^{-1} for closed and open sites respectively. Following catalytic analysis of their chosen Diels-Alder reaction, the authors report a difference in selectivity between Zn–BEA materials with varying concentrations of open and closed sites and state that: "*elimination of alkali-bearing sites is shown to significantly improve the selectivity of such reactions towards dimethyl terephthalate by lowering the extent of decarboxylation side-reactions that result in the formation of the notable by-products*."

The role of Lewis acidic Zn centres has also been highlighted in the work of Yan *et al.* in which Zn–MWW is employed in a range of dehydrogenation reactions.[2] In the oxidative dehydrogenation of 1-butene, Zn–MWW is seen to have a significantly higher selectivity to butadiene (40%) than either ZnO/ITQ-1 (22 %) or ZnO/MCM-22 (18 %), both of which do not contain Zn in framework positions. The authors claim that the resulting butadiene yield from reaction over Zn–MWW is the highest reported in literature at the time which they ascribe to "*generation of different active sites upon Zn insertion*". Within the same report, Zn–MWW is employed in the dehydrogenation of ethanol in which a 51% selectivity to acetaldehyde is

reported at 400 °C which they attribute to Lewis acidic Zn centres. Overall, the authors conclude that "*the catalytic performance is significantly affected by the successful insertion of Zn inside the MWW structure*", although they do not remark on the configuration of Zn in such sites.

Although reports are more limited, Mg^{2+} has also been shown to be active for Lewis acidic reactions when incorporated into tetrahedral positions of a zeolite framework. From the work of Yang *et al*, Mg–BEA is shown to be active for the conversion of glucose to methyl lactate and achieved a higher selectivity to the desired product than MgO.[5] The authors conclude that this results predominantly from framework Mg in Mg–BEA acting as a Lewis acid in comparison to the strongly basic MgO. Further, Mg–BEA is shown to achieve up to a 6.3% yield of fructose from glucose, although both its conversion and selectivity are considerably lower than that observed for Sn–BEA in the same study.[5] Additionally, Mg–MTW has been reported as an active Lewis acidic catalyst for the valorisation of glucose and furfural.[18] Therein it is reported that Mg–MTW is able to achieve up to a 76% yield of methyl lactate (MLA) from glucose with higher Lewis acid strengths favouring MLA formation. On the other hand, MgO and supported MgO are shown to favour glucose isomerisation to fructose, further highlighting the distinct nature of Mg^{II} when incorporated into a zeolite framework.

Within this chapter, the hydrothermal synthesis and characterization of divalently substituted Lewis acidic MFI type materials (M^{II}–MFI, where M = Mg, Zn) is reported and their inherent catalytic activity for ethanol conversion at various temperature points was explored. Subsequently, the dedicated dehydrogenation site, ZnO, identified in Chapter 4, was introduced into each catalyst material and the resulting materials were screened for their capability to affect the cascade conversion of ethanol to 1,3–butadiene by marriage of multiple disparate active sites. Zn–MFI was found to have particularly interesting reactivity and was explored more in-depth before being compared to bulk ZnO and the optimum material identified in Chapter 5, ZnO/Zr–MFI.

6.1. Synthesis and characterisation of Zn–MFI and Mg–MFI prepared by a hydrothermal method.

Following the successful substitution of an MFI framework with Sn, Si, Ti, Zr and Hf using the Sn–MFI synthesis method reported by Kolyagin *et al.* and Mal *et al* in Chapter 5, attempts to synthesise Zn–MFI and Mg–MFI were first undertaken in a similar fashion.[19, 20]

Briefly, synthesis gels containing TPA–OH, TEOS, the respective metal precursor ($ZnCl_2$ or $MgCl_2 \cdot 6H_2O$) and H_2O were produced and treated under static hydrothermal conditions for 72 h at 180 °C before washing and subsequent calcination; a more detailed method may be found in Section 9.3.7 and a schematic synthesis is shown in Figure 6.2.

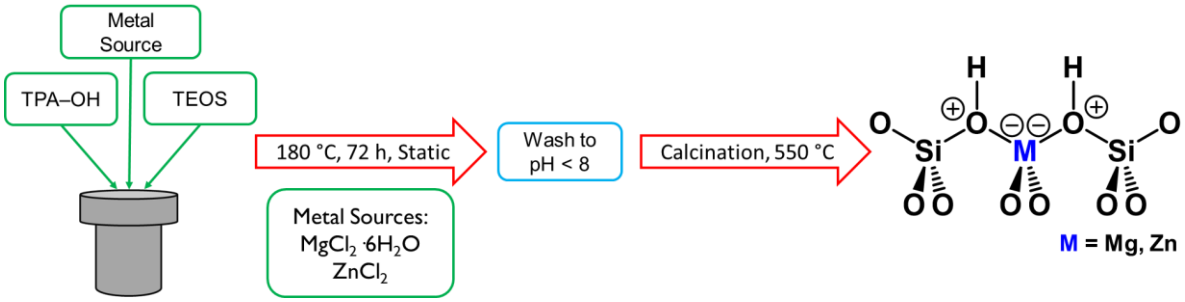

Figure 6.2: Schematic diagram of the hydrothermal synthesis procedure for synthesis of Zn–MFI and Mg–MFI materials adapted from Kolyagin *et al.* and Mal *et al.*.[19, 20]

Following successful crystallisation of both Zn–MFI and Mg–MFI materials, pXRD, ED-XRF, DR-UV-Vis spectroscopy and ^{31}P ssNMR spectroscopy were undertaken to assess framework phase purity, overall metal incorporation, degree of framework metal inclusion and acidity type. Initially, pXRD analysis was performed to assess if an MFI framework had formed for Zn–MFI and Mg–MFI materials following hydrothermal synthesis and if it was retained following calcination to remove the TPA^+ template. Figure 6.3 shows pXRD diffractograms of both Zn–MFI and Mg–MFI materials before and after calcination alongside an Al–MFI as a reference material. It is observed that both Zn–MFI and Mg–MFI exhibit typical features of an MFI framework and retain these features following high temperature calcination. Additionally, the patterns of Zn–MFI resemble those reported previously in literature.[1, 21-23] pXRD analysis was also undertaken in which LaB_6 was included as an internal reference for 2θ values to deduce whether framework contraction or expansion had occurred upon introduction of an M^{2+} species. Figure 6.3 (right) shows the pXRD traces of the calcined forms of Zn–MFI and Mg–MFI containing 10 wt% LaB_6 in the region of 2θ = 20–30 °. No peak shift is observed with respect to the Al–MFI reference, suggesting no significant framework expansion or contraction had resulted.[7] Notably, the single reflection at 2θ = 24.2° for Al–MFI is seen to be split into two reflections in the traces obtained for Zn–MFI and Mg–MFI, a phenomenon which is not previously observed for other reported zincosilicate materials.[7, 11]

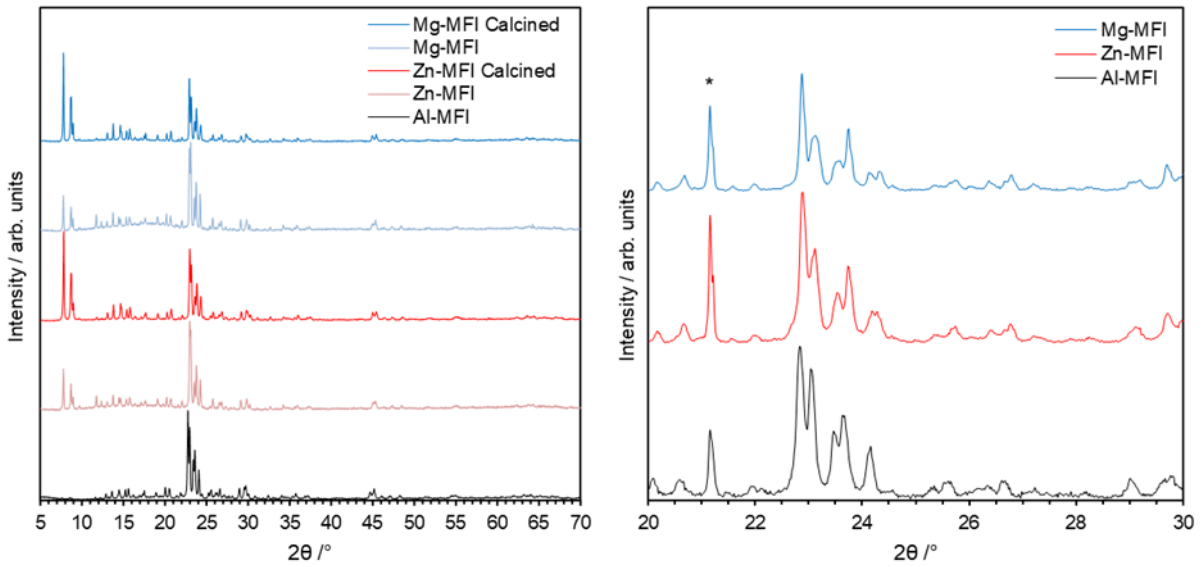

Figure 6.3: Left: pXRD patterns in the 2θ = 5–70 ° region of synthesized Zn–MFI and Mg–MFI materials both as-made and following calcination. The diffractogram of a commercial Al–MFI material is included as an MFI framework reference. Right: pXRD patterns in the 2θ = 20–30° range of synthesized Zn–MFI and Mg–MFI materials following calcination and containing 10 wt% LaB_6. The diffractogram of a commercial Al–MFI material is included as an MFI framework reference. Asterisks (*) denote peaks corresponding to LaB_6 which was used as an internal reference for 2θ values.

Elemental analysis of the calcined Zn–MFI and Mg–MFI obtained by ED-XRF spectroscopy is presented in Table 6.1 and displays relevant metal loadings alongside resultant Si/Zn and Si/Mg ratios. Additionally, the BET surface areas of Zn–MFI and Mg–MFI are shown in Table 6.1 with N_2 physisorption isotherms shown in Figure 6.4. As was seen for tetravalent M–MFI materials in Section 5.1.2, the metal incorporation of Mg and Zn resulted in unequal elemental ratios, despite equimolar concentrations of metal precursor present within the synthesis gel. This further suggests differing dynamics of metal incorporation for differing heteroatoms under identical crystallisation conditions. Additionally, both Zn–MFI and Mg–MFI possess a calculated BET surface area of around 420–430 $m^2\ g^{-1}$ similar to that seen for M–MFI materials in Chapter 5.1.2 and for the Al–MFI reference material (BET surface area = 447 ± 0.4 $m^2\ g^{-1}$).

Table 6.1: Elemental composition, elemental ratios and BET surface areas of synthesized Zn–MFI and Mg–MFI materials following calcination. Metal loadings were determined by ED–XRF analysis. ED–XRF values were averaged over three measurements and recorded as M wt%.

	Metal Loading / Wt%			Molar Ratios		BET Surface
Material	Si	Zn	Mg	Si/Zn	Si/Mg	**Area /$m^2\ g^{-1}$**
Zn–MFI	48.72	1.61	—	70.3	—	432 ± 1.8
Mg–MFI	40.35	—	0.27	—	131.8	418 ± 1.6

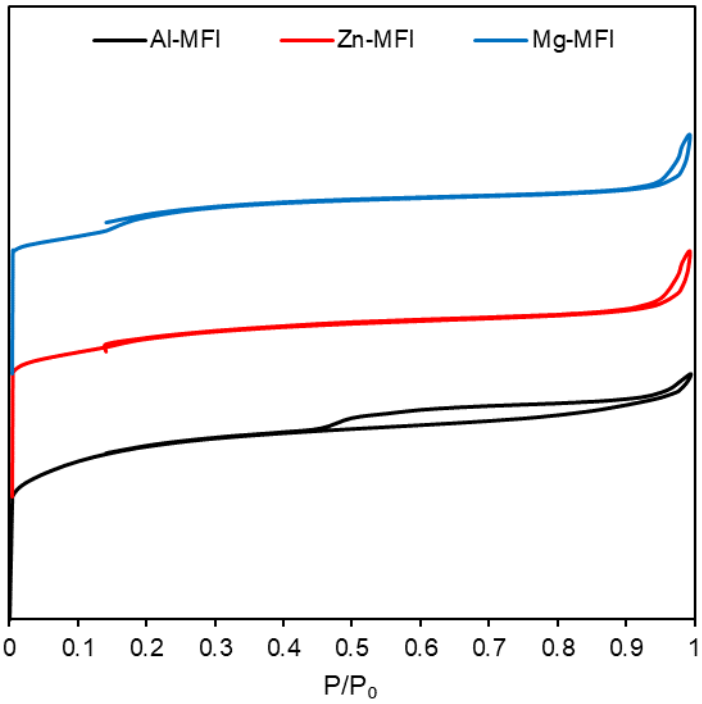

Figure 6.4: Normalised N_2 physisorption isotherm plots with vertical offset of synthesized Zn–MFI and Mg–MFI materials following calcination. A commercial Al–MFI material is included for reference. BET surface area of Al–MFI reference = 447 ± 0.4 m^2 g^{-1}.

Catalyst structure was further assessed by use of ^{29}Si direct excitation (Figure 6.5) and ^{1}H–^{29}Si cross-polarisation (Figure 6.6) solid-state NMR spectroscopy in order to probe the materials for silicon environments and silanol defects.[24, 25] As can be seen in Figure 6.5, the vast majority of silicon atoms likely reside in a Q_4 environment (δ_{Si} = −112 ppm), with the remainder residing in Q_3 environments (δ_{Si} = −103 ppm) for both Zn–MFI and Mg–MFI materials based upon typical ranges for MFI type zeolites reported by Iyoki *et al.* and Grosskreuz *et al.*.[24, 25] Enhancement of silanol group signals by use of a ^{1}H–^{29}Si cross-polarisation sequence confirms that the large majority of defects are Q_3 in nature (δ_{Si} = −103 ppm) for both materials. ^{29}Si direct excitation spectra of Zn–MFI resemble those reported previously in the literature by Kowalak *et al.*.[22]

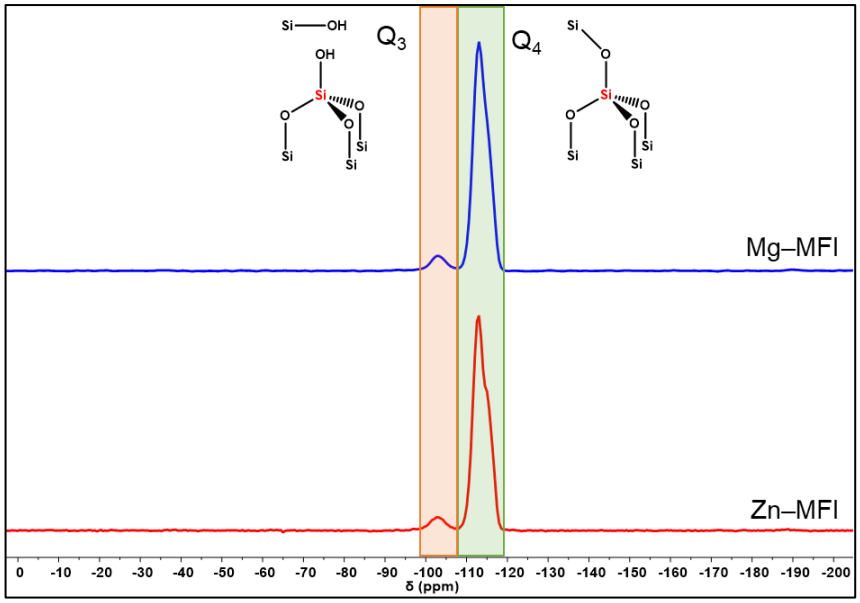

Figure 6.5: ^{29}Si direct excitation ssNMR spectra of Zn–MFI and Mg–MFI following calcination. CP spectra were averaged over 512 transients with a 30 s recycle delay. Spectra were acquired on a Varian VNMRS 400 MHz spectrometer using a 6 mm zirconia rotor. Spectrometer frequency: ^{29}Si = 79.44 MHz. MAS spin rate ≈ 6000 Hz.

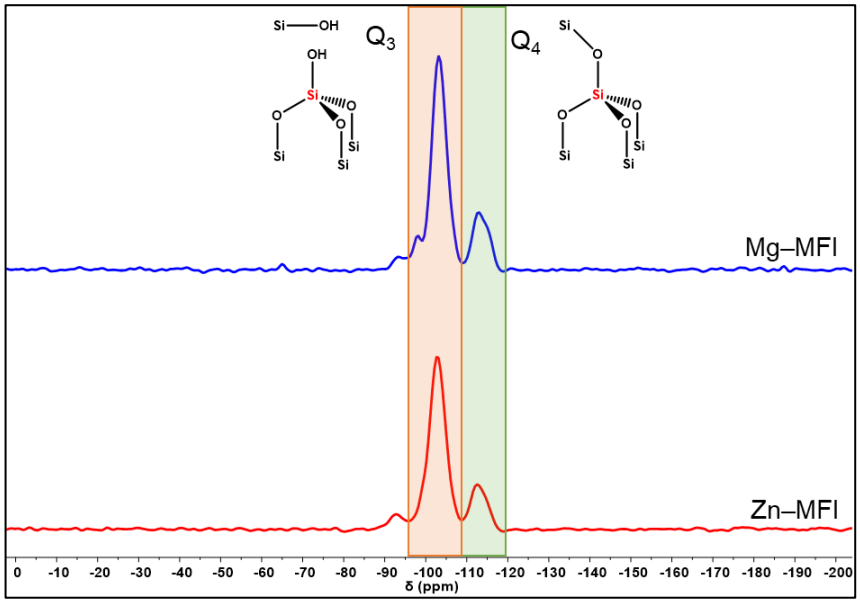

Figure 6.6: ^{1}H–^{29}Si cross polarisation ssNMR spectra of Si–MFI, Sn–MFI, Ti–MFI, Zr–MFI and Hf–MFI following calcination. CP spectra were averaged over 1800 transients with a 2 s recycle delay. Spectra were acquired on a Varian VNMRS 400 MHz spectrometer using a 6 mm zirconia rotor. Spectrometer frequency: ^{1}H = 399.88 MHz ^{29}Si = 79.44 MHz. MAS spin rate ≈ 6000 Hz.

Catalyst morphology was assessed by means of scanning electron microscopy (SEM) imaging with conventional SEM images of Zn–MFI and Mg–MFI shown in Figure 6.7. As for the tetravalent M–MFI materials (where M = Si, Sn, Ti, Zr, Hf) presented in Chapter 5.1.2, Zn–MFI and Mg–MFI exhibit a morphology predominantly composed of small tablet-like crystals with a diameter of around 300–400 nm with larger coffin-like crystals also observed. Again, the morphology of these materials are reminiscent of M–MFI materials reported in the literature that were synthesised in a fluoride-free environment,[26-30] although the crystals of Zn–MFI and

Mg–MFI appear more prismatic than the crystals seen for other M–MFI materials in Chapter 5. Zn–MFI crystals resemble those previously reported by Kowalak *et al.* following hydrothermal synthesis under similar conditions.[22, 23] Scanning electron microscopy-energy dispersive spectroscopy (SEM-EDS) mapping of Zn–MFI and Mg–MFI was also undertaken in order to assess homogeneity of metal distribution following hydrothermal synthesis and calcination. As for M–MFI materials in Chapter 5, Zn–MFI and Mg–MFI were mapped at two distinct locations and each exhibited a homogeneous distribution of heteroatomic metal atoms across the synthesized samples with no visible evidence of metal clustering (Figure 6.8 and Figure 6.9).

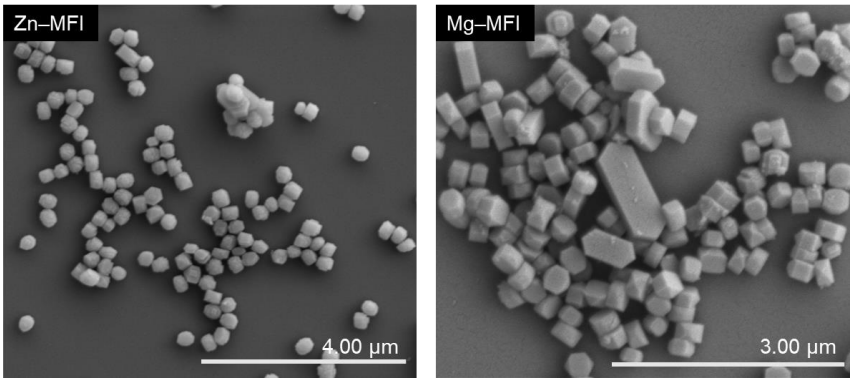

Figure 6.7: SEM images of Zn–MFI (left) and Mg–MFI (right) following calcination.

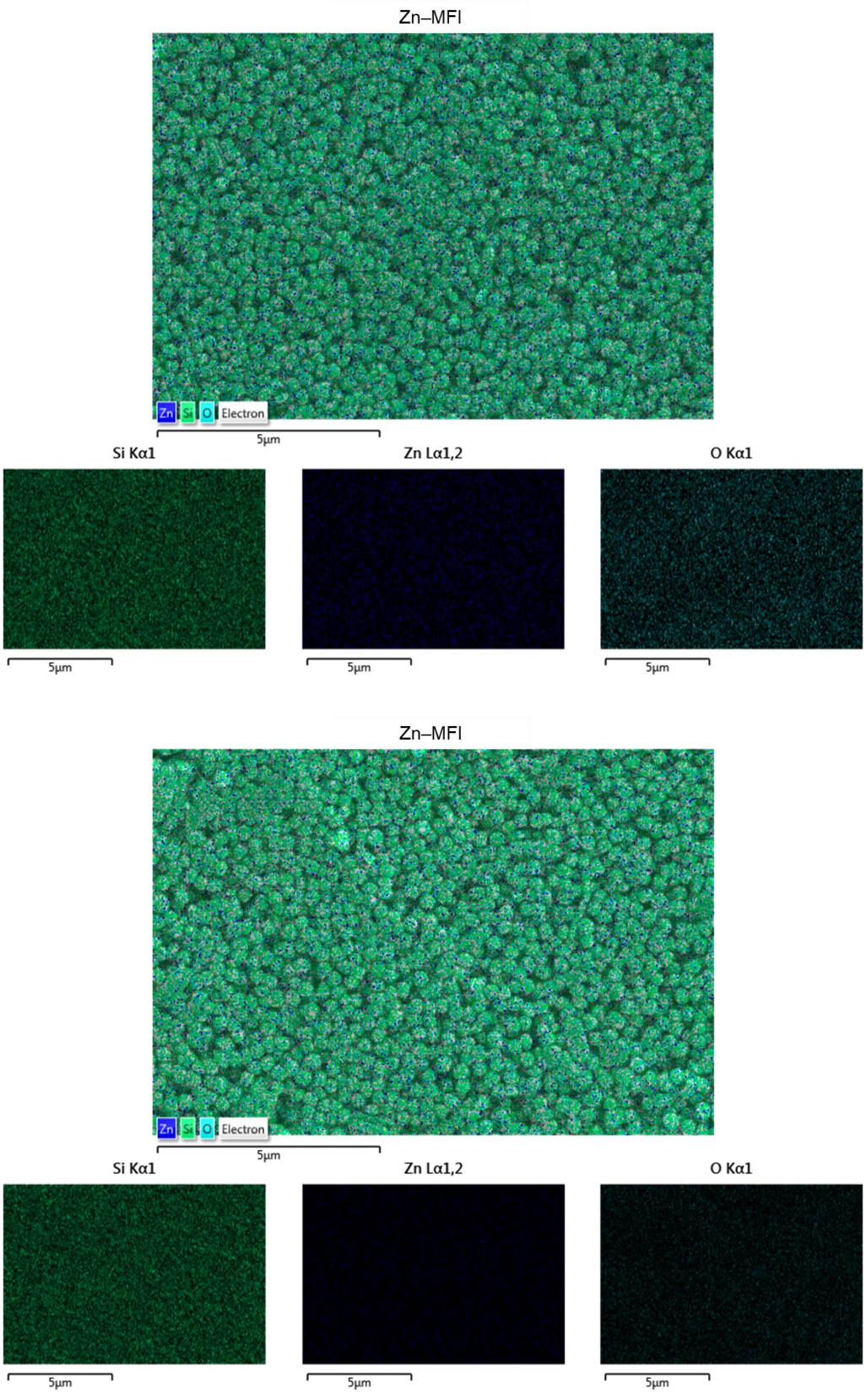

Figure 6.8: SEM-EDS mapping of Zn-MFI at Si Kα_1, Zn L$\alpha_{1,2}$ and O Kα_1.

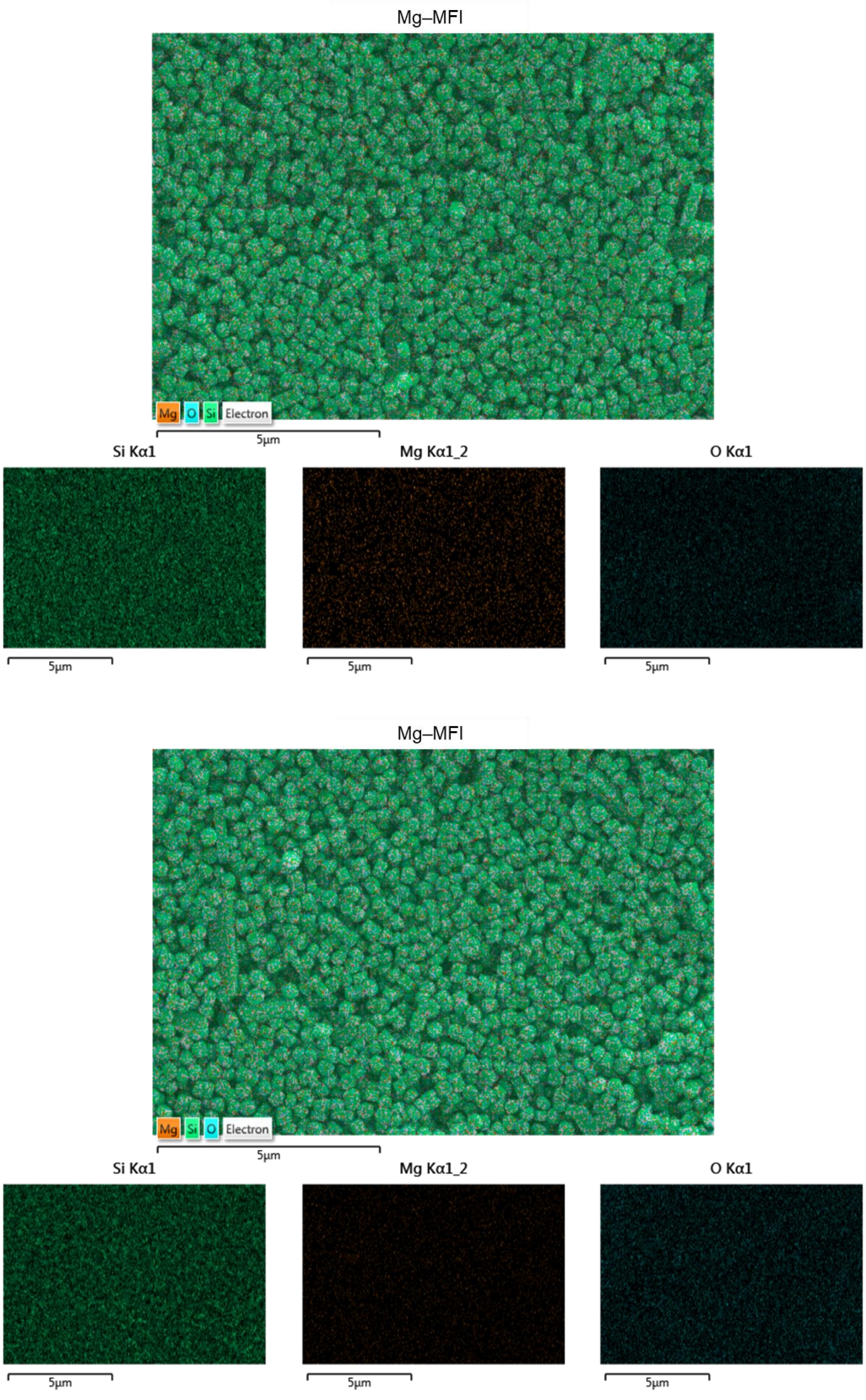

Figure 6.9: SEM-EDS mapping of Mg-MFI at Si Kα_1, Mg K$\alpha_{1,2}$ and O Kα_1.

In order to assess the degree of metal incorporation into the zeolite framework and to identify the presence of any extra-framework metal oxide phases, diffuse reflectance ultraviolet-visible (DR-UV-Vis) spectra were recorded for the calcined Zn–MFI and Mg–MFI samples (Figure 6.10). All samples exhibit a strong absorption band centred around 215 nm, similar to the band seen for M–MFI materials in Chapter 5.1.2 that was indicative of charge transfer transition between framework-bound metal atoms and surrounding oxygen atoms.[31-33] The DR-UV-Vis spectrum of Zn–MFI does not exhibit any substantial contributions from extra-framework ZnO type materials at absorption wavelengths > 250 nm, suggesting the non-presence of extra-framework ZnO.[7] The DR-UV-Vis spectrum of Mg–MFI does not exhibit any substantial shoulder associated with MgO at approximately 222 nm and therefore a lack of extra-framework MgO can be inferred.

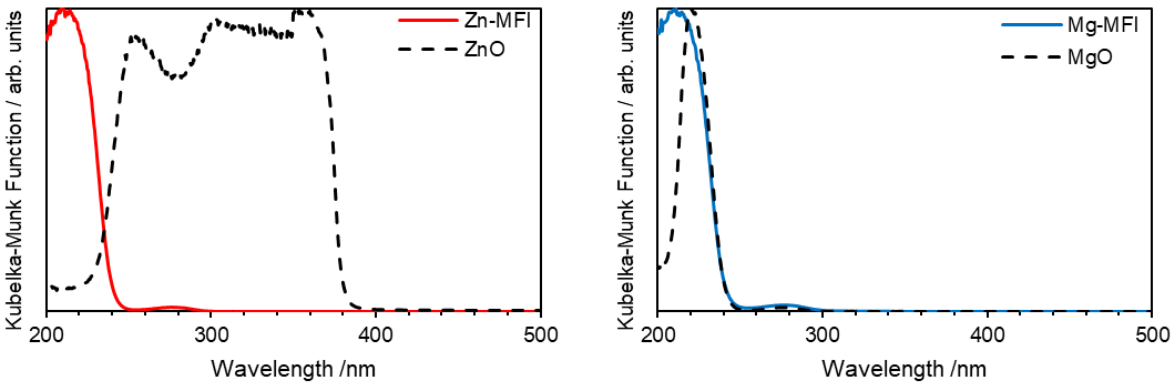

Figure 6.10: DR–UV–Vis spectra for synthesized Zn–MFI and Mg–MFI materials following calcination. Included for comparison are spectra of potential extra-framework oxide materials that could form during hydrothermal synthesis.

In addition to standard characterisation techniques described previously, ^{31}P ssNMR spectroscopy of adsorbed trimethylphosphine oxide (TMPO) was undertaken as described in Section 9.2.2 in an effort to predict the catalytic behaviour of Zn–MFI and Mg–MFI. As covered previously, it is plausible that Zn–MFI and Mg–MFI can adopt either an open or closed configuration that should result in either Brønsted or Lewis acidity, respectively as they are synthesised in the H–form. ^{31}P ssNMR spectroscopy of adsorbed TMPO allows predictions to be made as to the type and strength of acid sites by assessment of ^{31}P chemical shift as detailed in Section 2.1.3.3. The ^{31}P ssNMR spectra of Zn–MFI and Mg–MFI following TMPO absorption are shown in Figure 6.11, additionally a reference spectrum for a wholly Brønsted acidic MFI material (H–Al–MFI) is shown in the supplementary material located in Section 6.5 (Figure S6.1). Both spectra presented in Figure 6.11 exhibit resonances at δ_P = 42.1 and 30.6 ppm corresponding to crystalline TMPO resultant from the excess TMPO used within the sample preparation and adsorption into unstable silanol sites in MFI, respectively.[34-38] In Sn–

BEA, the $\delta_P \approx 41$ ppm resonance is reported to correspond to physisorbed TMPO at nonacidic Si–OH groups whilst the signal at $\delta_P \approx 30$ ppm may be assigned to "mobile" TMPO bound in the intercrystalline voids or near the windows of the pores of the zeolites.[36, 39, 40] In addition to these crystalline TMPO resonances, Mg–MFI exhibits a downfield resonance at $\delta_P = 49.3$ ppm, suggestive of a weak Lewis acidic centre. Further, no resonances are seen at $\delta_P > 60$ ppm, strongly suggesting a lack of zeolitic Brønsted acidity,[41] and allowing the prediction that the tetrahedral framework sites of Mg–MFI may act as weak Lewis acids. Zn–MFI exhibits a slightly further downfield resonance at $\delta_P = 56.6$ ppm than Mg–MFI, suggestive of stronger Lewis acidic framework sites.[39] As no resonances are observed at $\delta_P > 60$ ppm, it is predicted that Zn–MFI does not possess zeolitic Brønsted acidic sites and should also act solely as a Lewis acidic material.[41]

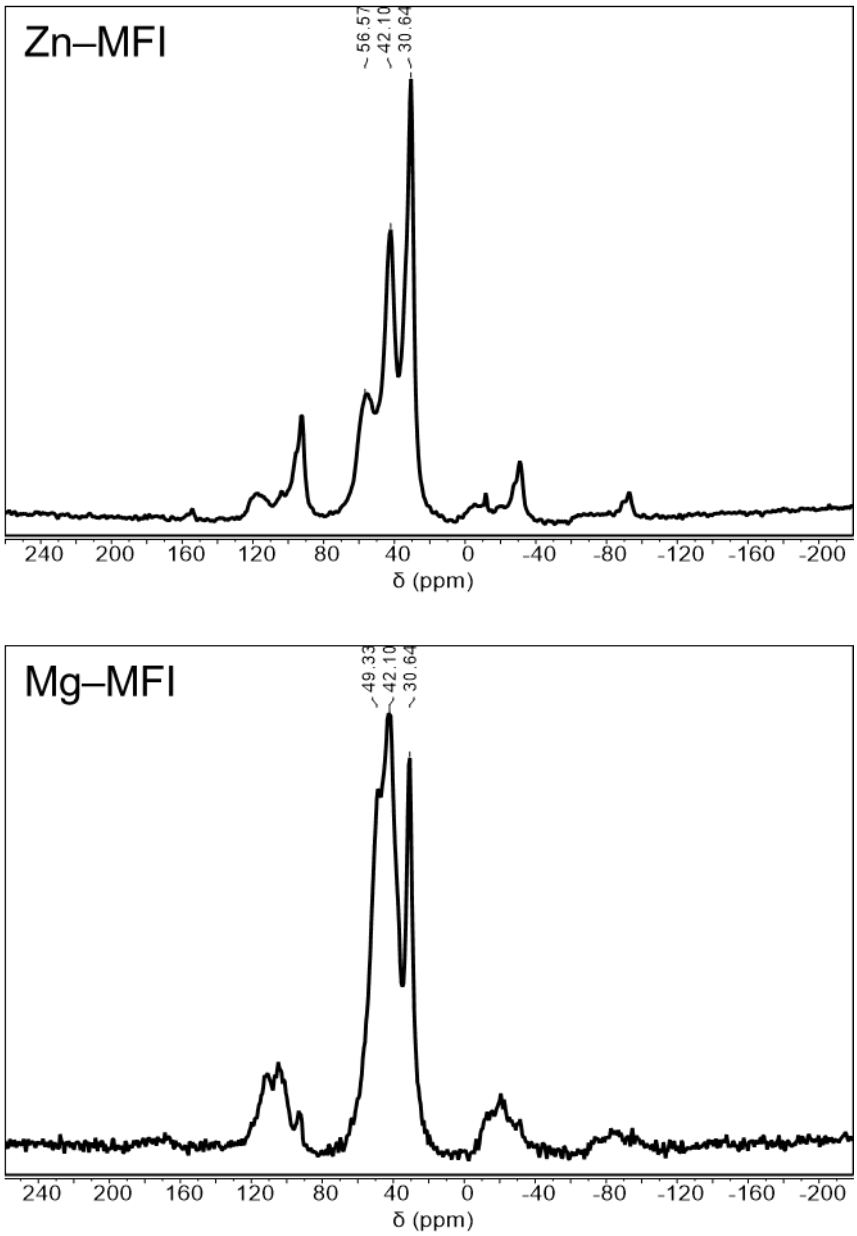

Figure 6.11: $^{31}P\{^{1}H\}$ High-power decoupling (hpdec) ssNMR spectra of TMPO adsorbed onto Zn–MFI (top) and Mg–MFI (bottom). Spectra were averaged over 100 and 360 transients respectively with a 10 s recycle delay. Spectra were acquired on a Bruker Avance III 400 MHz spectrometer using a 4 mm zirconia rotor. Spectrometer frequency: ^{31}P = 161.99 MHz. MAS spin rate ≈ 10000 Hz.

Thus, it can be concluded that MFI type materials containing Zn and Mg heteroatoms can be successfully synthesised using an adapted method for Sn–MFI synthesis reported by Kolyagin *et al.* and Mal *et al.*.[19, 20] pXRD analysis demonstrates that these materials adopt an MFI type framework with no additional metal oxide or silicate phases, further confirmed by DR-UV-Vis spectroscopy. Traditional SEM imaging shows that Zn–MFI and Mg–MFI possess similar crystal morphologies to M–MFI materials presented in Chapter 5.1.2 and reported in the literature. Heteroatom incorporation is seen to be relatively homogeneous by SEM-EDS mapping with a high degree of metal incorporation predicted by DR-UV-Vis spectroscopy.

Finally, ^{31}P ssNMR spectroscopy of adsorbed TMPO allows the prediction that both Zn–MFI and Mg–MFI should act solely as Lewis acidic materials.

6.2. Variable temperature screening of divalent Zn–MFI and Mg–MFI for ethanol to 1,3–butadiene cascade synthesis.

Following successful hydrothermal synthesis and characterisation of Zn–MFI and Mg–MFI, catalytic testing was undertaken to assess their performance for the transformation of ethanol.

6.2.1. Variable temperature screening of Zn–MFI and Mg–MFI materials.

Initially, catalytic reactions of ethanol over unmodified M^{II}–MFI materials (M^{II} = Mg, Zn) were performed to understand their inherent catalytic capacity and product distributions resulting from ethanol conversion under flow conditions. It was initially predicted that both Zn–MFI and Mg–MFI would yield similar product distributions to those seen for M^{IV}–MFI materials (M^{IV} = Si, Sn, Ti, Zr, Hf) in Chapter 5.2.1, yielding diethyl ether at reaction temperatures around 300 °C before transitioning to ethylene production at temperatures greater than 350 °C owing to their predicted Lewis acidic nature. This, however, was not the case, with both Zn–MFI and Mg–MFI exhibiting surprising reaction results.

Figure 6.12 shows the effluent composition following reaction of ethanol over calcined Zn–MFI over the temperature range of 200–400 °C. It is observed that production of diethyl ether is favourable at 300 °C, with production of ethylene increasing to a maximum at 400 °C, typical of Lewis acidic M–MFI seen in Chapter 5.2.1. Surprisingly, the major product detected at temperatures greater than 300 °C is acetaldehyde, a product of ethanol dehydrogenation rather than dehydration. Additionally, approximately 16% of the reaction effluent is composed of 1,3–butadiene, suggesting that this formed acetaldehyde can undergo subsequent aldol condensation over Lewis acidic Zn sites to affect the entire ethanol to butadiene cascade reaction. This behaviour is similar to that seen for ZnO impregnated M^{IV}–MFI materials reported in Chapter 5.2.2 which required the addition of impregnated ZnO to open the ethanol to butadiene cascade cycle. It is therefore proposed that $Zn^{\delta+}$–$O^{\delta-}$ framework bonds may act as a mimic for impregnated ZnO, allowing initial ethanol dehydrogenation before subsequent cascade conversion to butadiene over the Lewis acidic Zn framework sites (akin to M^{IV} such as Sn or Zr). During the course of this project, post-synthetic introduction of Zn^{II} species into framework sites have been reported to act as ethanol dehydrogenation sites within the literature.[15, 16, 42] In each example, Zn^{II} is introduced into the silanol nests of dealuminated BEA

zeolite. In their 2020 paper, Qi *et al.* use EXAFS analysis to demonstrate a lack of Zn–O–Zn backscattering pathways and rule out the presence of ZnO clusters in their system.[16] Further, they find a co-ordination number of 4 from EXAFS fitting and an average Zn–O bond distance of 1.97 Å which is remarkably similar to ZnO (C.N. = 4, distance = 1.98 Å). Hence, Qi *et al.* propose that the mechanism of ethanol dehydrogenation over framework bound Zn^{II} proceeds *via* an α–elimination from an adsorbed ethoxide intermediate on a single Zn centre as shown in Figure 4.2 (see Section 4).[16] It is therefore reasonable to envision that such a transformation could occur over $Zn^{\delta+}$–$O^{\delta-}$ bonds inherent to zeolite framework sites in hydrothermally synthesised Zn–MFI (Figure 6.13). One example of ethanol conversion to acetaldehyde by Zn in hydrothermally synthesised framework positions has been reported since this projects inception by Yan *et al.*.[2] In this contribution, Zn in the framework positions of Zn–MWW is seen to achieve up to a 51% selectivity to acetaldehyde following reaction at 400 °C for 20 h TOS. The authors conclude that "*Lewis acidity generated by the presence of Zn greatly enhances the formation of acetaldehyde*" but do not offer any further insight into mechanism. Interestingly, the phenomenon of total ethanol to butadiene transformation over framework Zn sites has been identified, but not reported in-depth by Dai *et al.* who observe a significant degree of butadiene production from a Zn impregnated dealuminated BEA zeolite.[42] Qi *et al.* also observe this phenomenon but proceed to introduce Y^{3+} as a dedicated C–C coupling site owing to their observation that "*the rates of 1,3-BD formation are nearly an order of magnitude lower than the rates of AcH formation*".[16] The structure and reactivity of Zn–MFI are explored further in Chapter 6.2.2.

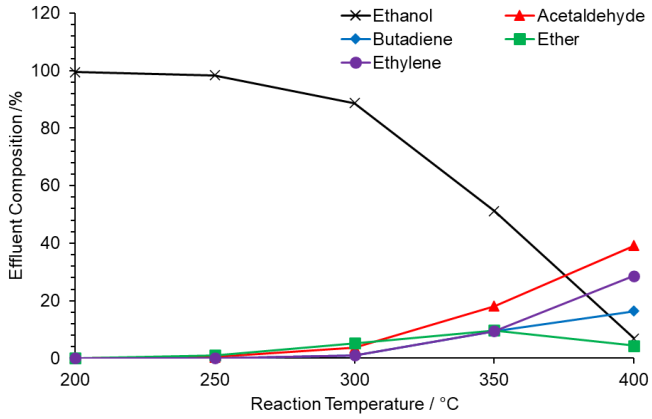

Figure 6.12: Effluent compositions resulting from reaction of ethanol at various temperatures over Zn–MFI. Ethanol feed rate = 0.197 mmol min^{-1}, catalyst mass = 0.300 g. Traces for ethanol (×), acetaldehyde (▲), butadiene (♦), diethyl ether (■) and ethylene (●) are shown. Additional trace amounts of other carbon containing products were detected and accounted for but omitted for clarity.

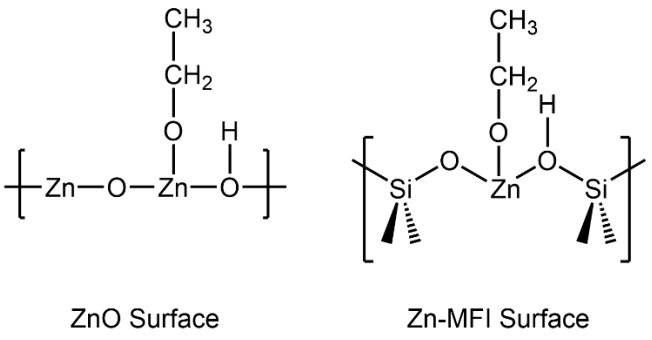

Figure 6.13: Proposed schematic comparison of adsorbed ethoxide species on ZnO (left) and Zn–MFI (right) surfaces.

In stark contrast to Zn–MFI, Mg–MFI is seen to possess little to no inherent activity for ethanol conversion, with the reactor effluent composed predominantly of unreacted ethanol (Figure 6.14A). Whilst traces of diethyl ether, ethylene and acetaldehyde are present in the reactor effluent, none of the components account for more than 3% of the effluent composition. This reactivity data suggests that Mg–MFI possesses very weak acidic sites, unable to catalyse ethanol dehydration to either diethyl ether or ethylene. This can be rationalised by the observation of a low shift in δ_P value of TMPO when doped onto Mg–MFI, resultant from weak association of TMPO with Mg–MFI framework sites as seen in the ^{31}P ssNMR spectrum presented in Figure 6.11 and indicative of weak Lewis acidic sites.

As for the M^{IV}–MFI materials showcased in Chapter 5.2.2, ZnO was loaded onto Mg–MFI by a wetness impregnation method to act as a dedicated dehydrogenation site in an attempt to open up the cascade ethanol to butadiene reaction. Figure 6.14B shows the effluent composition resulting from reaction of ethanol over ZnO/Mg–MFI at various temperature points. Herein, it is seen that the introduced ZnO acts as expected, producing acetaldehyde as a dedicated dehydrogenation product. Rather more unexpected is the observation of the cascade conversion product, butadiene, in the product effluent owing to the low apparent Lewis acidity of unmodified Mg–MFI. This observation may be rationalised by the predicted weakness of Lewis acidic tetrahedral sites in Mg–MFI potentially being insufficiently strong as not to affect ethanol dehydration reactions effectively, whilst being strong enough to affect the aldol condensation of acetaldehyde to crotonaldehyde and subsequent reactions. In order to validate this, DRIFTS of pyridine adsorbed materials should be undertaken. This observation may however suggest that application of very weak Lewis acidic sites, such as framework-bound Mg^{II}, in combination with a highly selective dehydrogenation site, such as ZnO, may allow increased selectivity to Lebedev products (acetaldehyde, butadiene) compared to ethanol dehydration products (ethylene, diethyl ether).

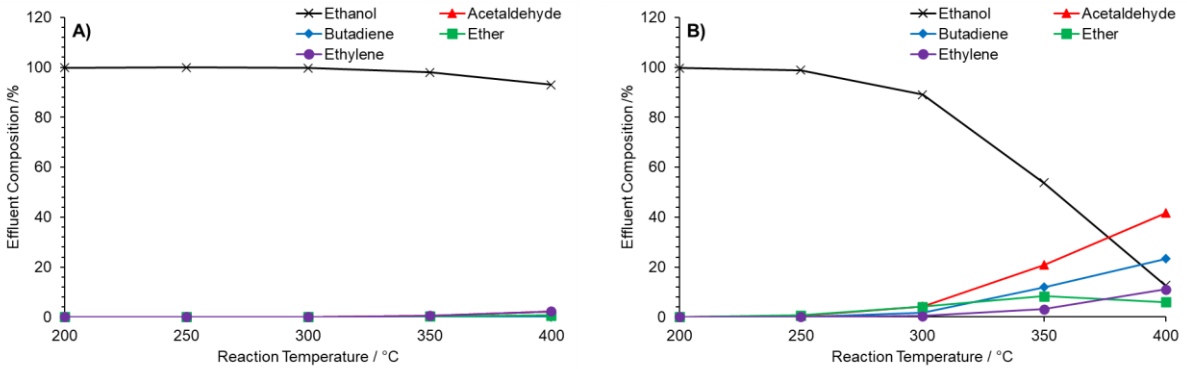

Figure 6.14: Effluent compositions resulting from reaction of ethanol at various temperatures over: Mg–MFI (A) and ZnO/Mg–MFI (B). Ethanol feed rate = 0.197 mmol min^{-1}, catalyst mass = 0.300 g. Traces for ethanol (×), acetaldehyde (▲), butadiene (♦), diethyl ether (■) and ethylene (●) are shown. Additional trace amounts of other carbon containing products were detected and accounted for but omitted for clarity.

6.2.2. Further investigation into the hydrothermal synthesis, structure, and reactivity of Zn–MFI.

Owing to the interesting properties of Zn–MFI, further investigation into its synthesis, structure and reactivity were undertaken. Initially, synthesis repeats were performed in order to assess the reproducibility of Zn–MFI hydrothermal synthesis. Table 6.2 shows the relevant elemental composition and ratios acquired by ED-XRF spectroscopy of three repeat Zn–MFI syntheses. Although individual metal loadings vary slightly, most likely resulting from varying zeolite hydration levels, an exceptional consistency of Si/Zn ratio is observed between all three synthesis attempts, implying excellent reproducibility of the Zn–MFI synthesis. Additionally, Figure 6.15 shows the pXRD diffractograms of the calcined materials, of which all adopt an MFI-type morphology with no extra reflections resulting from additional silicate or zinc oxide phases.

Table 6.2: Elemental analysis results acquired by ED-XRF spectroscopy and resultant molar ratios for synthesis repeats of Zn–MFI. ED-XRF results are averaged over three repeat measurements.

Material	Zn /Wt%	Si /Wt%	Si/Zn Ratio
Zn–MFI	1.61	48.73	70.3
Zn–MFI-rep	1.29	39.21	71.0
Zn–MFI-rep2	1.64	46.39	65.8

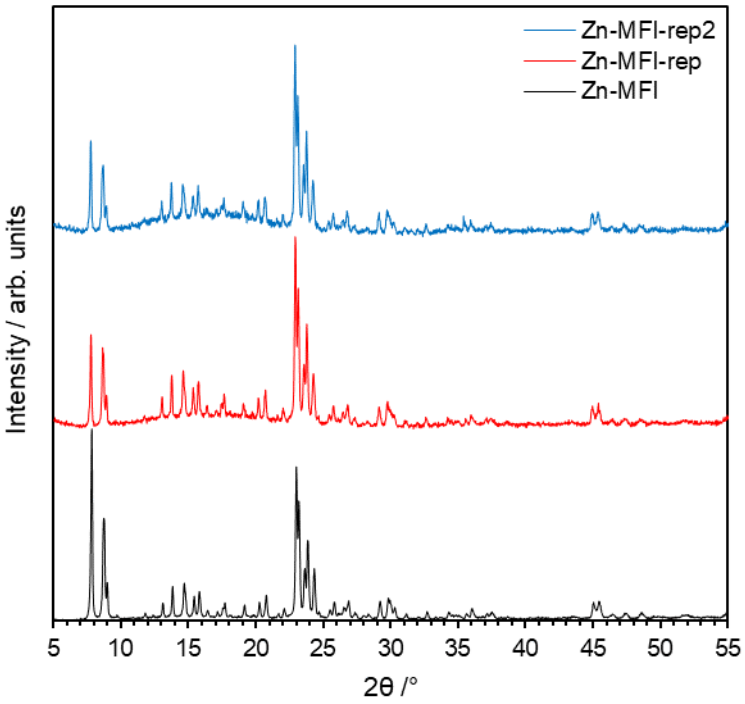

Figure 6.15: pXRD patterns of Zn–MFI synthesis repeats in the 2θ = 5–70 ° region following calcination. The diffractogram for Zn–MFI were acquired on a silicon pXRD slide. The diffractograms for Zn–MFI–rep and Zn–MFI–rep2 were acquired on glass pXRD slides.

Although possessing plentiful characterisation to suggest that Zn heteroatoms in Zn–MFI reside within framework tetrahedral sites, an XAS investigation was undertaken at Diamond Light Source Beamline B18 in order to further corroborate existing data and to provide solid comparison to existing literature. Figure 6.16 shows the XANES spectra of hydrated and dehydrated Zn–MFI materials collected at the Zn K-edge. When compared to the reported XAS data for Zn–MFI, Zn-exchanged Al–MFI and ZnO impregnated Al–MFI from Hagen *et al*. it is clear that the Zn–MFI material synthesised in this project most strongly resembles the framework included material (Figure 1 in reference 43).[43] Whilst changes in the XANES spectra are observed upon dehydration, no resemblance to ZnO is observed, suggesting that Zn is successfully retained within the zeolite framework. Further, the EXAFS plots for hydrated and dehydrated Zn–MFI as shown in Figure 6.17 do not exhibit a strong signal associated with either Zn–Zn or Zn–O–Zn pathways, strongly suggesting that Zn atoms in Zn–MFI occupy discrete single site framework positions.[16, 43, 44] Within Figure 6.17, the major feature observed at approximately 1.4 $Å^{-1}$ is proposed to be resultant from Zn–O as observed for both ZnO and Zn–MWW within the work reported by Yan *et al*..[2] Further, a feature centred around 2.7 $Å^{-1}$ is observed, likely indicative of Zn–O–Si pathways when compared to EXAFS data and fitting results of Zn–MWW. Modelling of both real and imaginary components of the EXAFS spectra would further aid this conclusion.

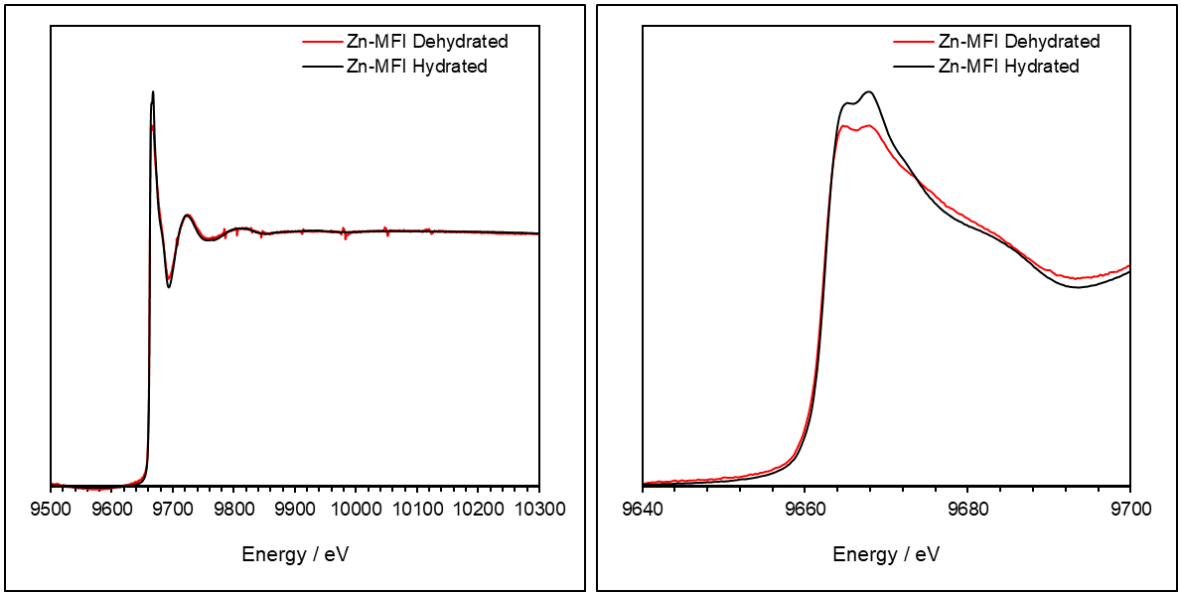

Figure 6.16: XANES spectra for hydrated and dehydrated Zn–MFI materials collected at the Zn K-edge.

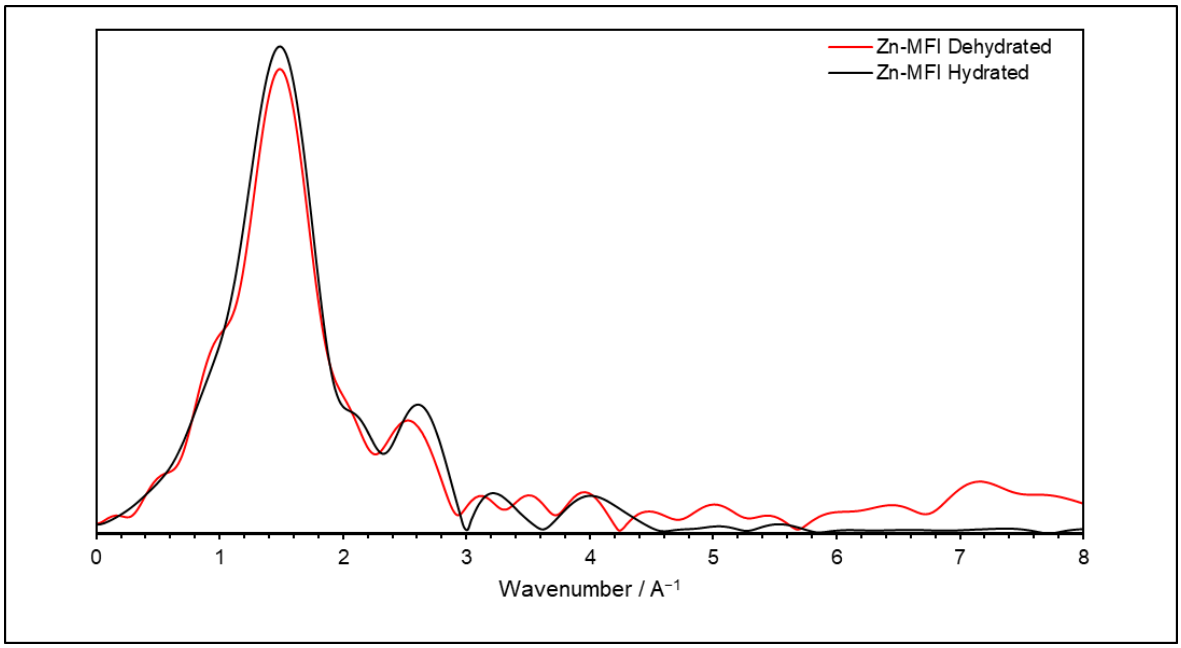

Figure 6.17: EXAFS spectra for hydrated and dehydrated Zn–MFI materials collected at the Zn K-edge.

The initial catalytic results presented in Figure 6.12 of Chapter 6.2.1 in combination with ^{31}P ssNMR spectroscopic data of adsorbed TMPO strongly suggest that Zn heteroatoms in the tetrahedral positions of Zn–MFI adopt a predominantly "open" configuration as shown in Figure 6.1. In order to further test this hypothesis, an ion-exchange study of Zn–MFI was undertaken with a variety of monovalent and divalent cations, namely Na^+, K^+, Mg^{2+} and Zn^{2+}. A standard ion-exchange procedure was undertaken in which a 500 mg sample of Zn–MFI was exchanged for 10 × 1 h intervals with 25 mL of a 0.3 M solution of the desired metal nitrate before being washed with a subsequent 10 × 25 mL of deionised water (see Section 9.3.2). The same Zn–MFI synthesis batch (Zn–MFI) was used for exchange with each cation and the

exchange procedures were undertaken in parallel to ensure identical conditions. It is predicted that a substantial degree of ion-exchange will only be observed if tetrahedral zinc sites are in a "closed" configuration with exchangeable charge balancing protons, as opposed to the "open" configuration in which the exchangeable protons are instead bound as part of a silanol group (Figure 6.). Table 6.3 shows the elemental composition of Zn–MFI materials acquired by ED-XRF spectroscopy before and after ion-exchange and the resulting exchange ratios. In all cases, no significant level of ion-exchange is observed regardless of cation choice, strongly corroborating with the prediction of Zn residing in "open" tetrahedral sites.

Table 6.3: Elemental analysis results acquired by ED-XRF spectroscopy and resultant exchange ratios following ion-exchange of H/Zn–MFI with Na^+, K^+, Mg^{2+} and Zn^{2+}.

Sample	Exchange Cation	Elemental Composition (M) / wt%				M/Zn Ratio
		Na	K	Mg	Zn	
Na/H/Zn–MFI	Na^+	0.00	—	—	1.19	0.00
K/H/Zn–MFI	K^+	—	0.02	—	1.10	0.03
Mg/H/Zn–MFI	Mg^{2+}	—	—	0.20	1.17	0.46
Zn/H/Zn–MFI	Zn^{2+}	—	—	—	1.13	—

6.2.3. Effect of ZnO doping on the catalytic activity of Zn–MFI for the cascade conversion of ethanol to butadiene.

Previously for heteroatomically substituted MFI materials, ZnO has been introduced by a wetness impregnation method to act as a dedicated catalytic site for ethanol dehydrogenation to form acetaldehyde which may then react over the Lewis acidic sites in M–MFI materials to form 1,3–butadiene. Zn–MFI, however, has exhibited the inherent ability to perform ethanol dehydrogenation over what is predicted to be a $Zn^{\delta+}$–$O^{\delta-}$ framework site acting as a ZnO mimic. Hence, in combination with framework Zn Lewis acidic sites, unmodified Zn–MFI was shown to possess the ability to catalyse the direct cascade transformation of ethanol to butadiene (Figure 6.12).

It was hypothesised that addition of ZnO to Zn–MFI by a wetness impregnation method may further promote acetaldehyde formation, potentially reducing ethylene and diethyl ether formation rates by providing further dehydrogenation sites and an increased rate of dehydrogenation. It was uncertain however, whether this would result in higher butadiene productivity. On one hand, the Lewis acidic sites responsible for aldol condensation may

already be operating at maximum capacity as excess acetaldehyde was observed in the product effluent following reaction of ethanol over unmodified Zn–MFI. On the other hand, a reduction of ethylene and diethyl productivity may result in the freeing up of Lewis acidic sites for increased aldol condensation capacity, resulting in higher butadiene productivity. Table 6.4 shows the relevant metal loadings and elemental ratios of Zn–MFI and ZnO/Zn–MFI used within this study.

Table 6.4: Elemental analysis results acquired by ED-XRF spectroscopy and resultant molar ratios for Zn–MFI and ZnO/Zn–MFI. ED-XRF results are averaged over three repeat measurements.

Material	Zn /Wt%	Si /Wt%	Si/Zn Ratio
Zn–MFI	1.39	44.95	55.4
ZnO/Zn–MFI	5.76	44.31	13.2

Figure 6.18 shows the reaction effluent composition resulting from reaction of ethanol at various temperatures over Zn–MFI and ZnO/Zn–MFI. Figure 6.19 shows the temperature dependant productivities of acetaldehyde, butadiene and ethylene resulting from the same reactions. It can be seen from both figures that the initial part of the hypothesis was confirmed as introduction of additional ZnO by a wetness impregnation method did indeed result in increased acetaldehyde productivity alongside reduced ethylene and diethyl ether productivities at all temperature points. The productivity of butadiene was also seen to increase by approximately 1 mmol g_{cat}^{-1} h^{-1} at temperatures above 350 °C, consistent with an increase of aldol condensation capacity aligning with a reduction in ethanol dehydration rate over Lewis acidic sites. Overall, reaction at 350 °C was concluded to be optimum for butadiene productivity whilst also minimising productivity of undesired by-products such as ethylene.

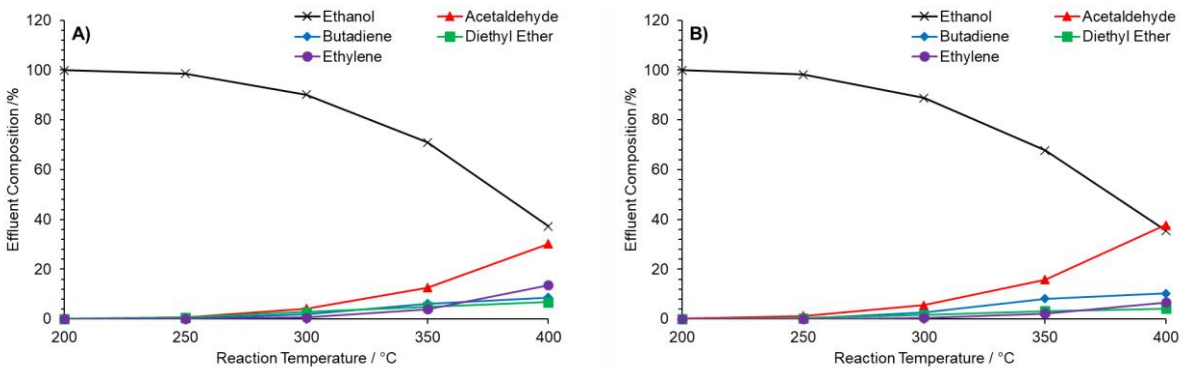

Figure 6.18: Effluent compositions resulting from reaction of ethanol at various temperatures over: Zn–MFI (A) and ZnO/Zn–MFI (B). Ethanol feed rate = 0.330 mmol min^{-1}, catalyst mass = 0.300 g. Traces for ethanol (×), acetaldehyde (▲), butadiene (♦), diethyl ether (■) and ethylene (●) are shown. Additional trace amounts of other carbon containing products were detected and accounted for but omitted for clarity.

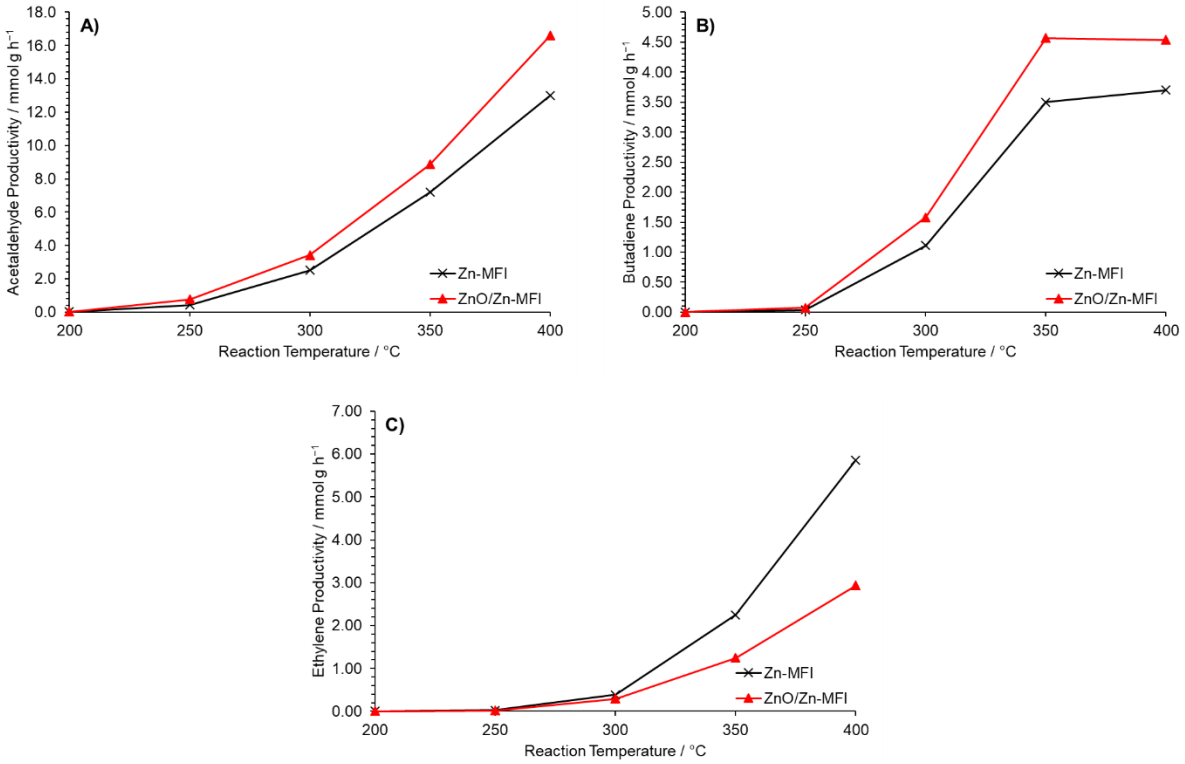

Figure 6.19: Acetaldehyde (A), butadiene (B) and ethylene (C) productivities from reaction of ethanol at various temperatures over: Zn–MFI (×) and ZnO/Zn–MFI (▲). Ethanol feed rate = 0.330 mmol min^{-1}, catalyst mass = 0.300 g.

Following variable temperature testing, both Zn–MFI and ZnO/Zn–MFI were tested for ethanol conversion to 1,3–butadiene at 350 °C over 4h TOS. Figure 6.20 shows the calculated acetaldehyde (A), butadiene (B) and ethylene (C) selectivites whilst Figure 6.20D shows the ethanol conversion values at each time point. As would be expected from the productivity data presented in Figure 6.19, the selectivity to butadiene is greater for ZnO/Zn–MFI than for Zn–MFI throughout the course of reaction, with values of 12% and 9% respectively after 4h TOS. Acetaldehyde selectivites are relatively similar for both materials at around 50%, whilst the ethylene selectivity for ZnO/Zn–MFI (5%) is substantially lower than for Zn–MFI (8%) after 4 h TOS. Other detected products include diethyl ether, ethyl acetate and isobutane with minor traces of linear butenes, isobutene, ethane, propylene, and propane. Full selectivity distributions of major contributions are presented in Figure S6.2. Ethanol conversion is also increased from 51% to 59% following introduction of excess ZnO to Zn–MFI (Figure 6.20D) whilst carbon balances for both reactions are maintained above 80% throughout (Figure S6.3). Unfortunately, an instability resulting from the MS filament reaching the end of its lifetime resulted in inaccurate data collection at TOS = 2.3 h and this is reflected across all MS dependant metrics (conversion, carbon balance, etc). Table 6.5 shows the catalyst coking resulting from reaction of ethanol over Zn–MFI and ZnO/Zn–MFI at 350 °C over 4h TOS.

Despite Zn–MFI possessing almost twice the selectivity to ethylene than ZnO/Zn–MFI their coking contents are remarkably similar, with Zn–MFI actually possessing a lower overall coking at 2.09 C wt% compared with 2.35 C wt% for ZnO/Zn–MFI. Under similar conditions, spent ZnO/Zr–MFI was found to possess a coking value of 3.21 C wt% (Table 5.6, Chapter 5). This may potentially imply that Lewis acidic Zn centres have a low propensity to aromatic coke formation regardless of ethylene formation rates. In comparison to existing literature, the acetaldehyde (50%) and butadiene (9%) selectivites of Zn–MFI presented in Figure 6.20 are similar to those observed by Qi *et al.* for reaction of ethanol over Zn–BEA zeolite at a reaction temperature of approximately 320 °C,[16] and also those observed by Yan *et al.* for reaction of ethanol over Zn–MWW at 400 °C.[2]

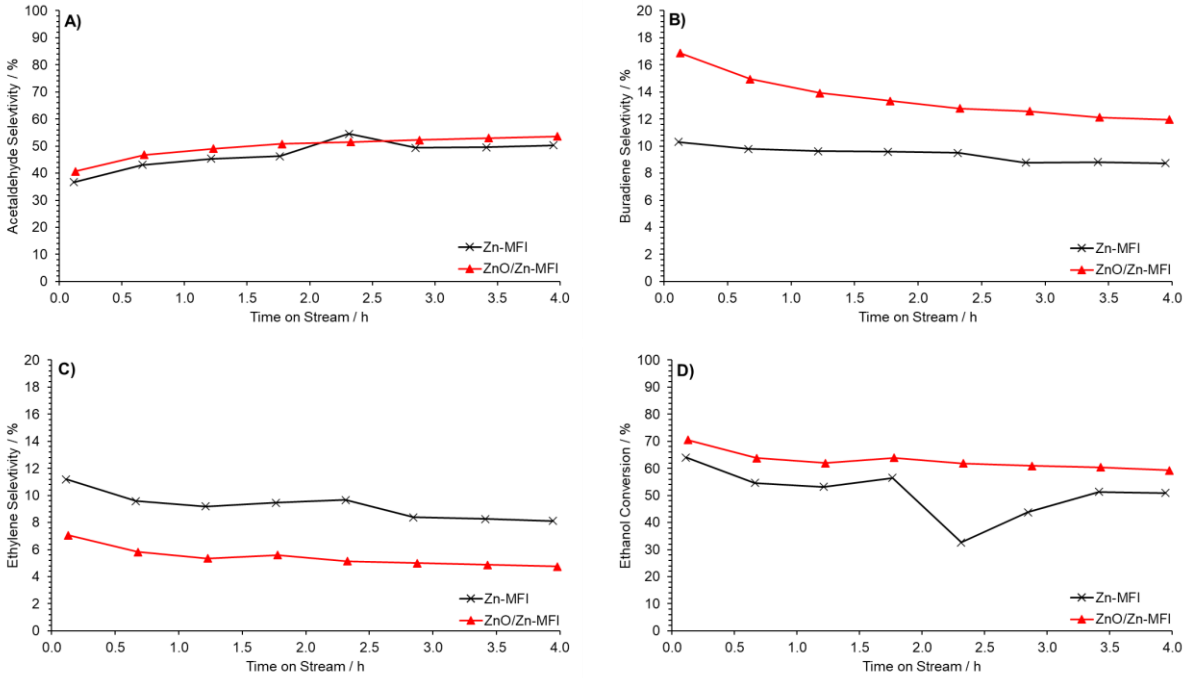

Figure 6.20: Acetaldehyde selectivity (A), butadiene selectivity (B), ethylene selectivity (C) and ethanol conversion (D) for Zn–MFI (×) and ZnO/Zn–MFI (▲) at 350 °C for 4 h TOS. Catalyst mass = 0.300 g. Ethanol feed rate = 0.390 mmol min^{-1}. Detection Columns: RTX-VMS + ShinCarbon ST.

Table 6.5: Catalyst coking (C wt%) of Zn–MFI and ZnO/Zn–MFI catalysts following ethanol reaction at 350 °C as determined by CHN microanalysis.

Sample	Catalyst Coking / C Wt%
Zn–MFI	2.09
ZnO/Zn–MFI	2.35

In order to put the selectivities of Zn–MFI and ZnO/Zn–MFI into perspective, their major product distributions at 4 h TOS were compared to those of ZnO/Zr–MFI and ZnO under their respective optimised reaction conditions as acquired in Chapters 4 and 5. Table 6.6 contains relevant reaction conditions for each material used within this comparison alongside Zn contents determined by ED-XRF spectroscopy. Figure 6.21 shows the selectivity distributions for ethanol conversion over Zn–MFI, ZnO/Zn–MFI and ZnO/Zr–MFI and ZnO at 4 h TOS under the respective conditions listed in Table 6.6. Although it is not ideal to compare selectivities at differing conversion values, the data for ZnO is included for general comparison. Notably, although Zn–MFI (50%) and ZnO/Zn–MFI (54%) both have a significantly higher acetaldehyde selectivity than ZnO/Zr–MFI (39%) neither Zn–MFI (9%) or ZnO/Zn–MFI (12%) achieve the same butadiene selectivity as ZnO/Zr–MFI (18%). Overall, both Zn–MFI and ZnO/Zn–MFI are seen to exhibit a higher total selectivity to Lebedev products (acetaldehyde, butadiene) than ZnO/Zr–MFI which exhibits a higher selectivity to ethanol dehydration products such as diethyl ether and ethylene.

Table 6.6: Reaction conditions used for comparison of Zn–MFI and ZnO/Zn–MFI with ZnO/Zr–MFI and ZnO. Catalyst coking values (C wt%) as determined by CHN microanalysis. n.d. = not detected. Zn contents were determined by ED-XRF spectroscopy

Catalyst	Catalyst Mass / mg	Reaction Temperature / °C	Ethanol Flow Rate / mmol min^{-1}	Zn Content / mmol
Zn–MFI	300	350	0.390	0.064
ZnO/Zn–MFI	300	350	0.390	0.264
ZnO/Zr–MFI	300	350	0.300	0.142
ZnO	12.6	400	0.399	0.157

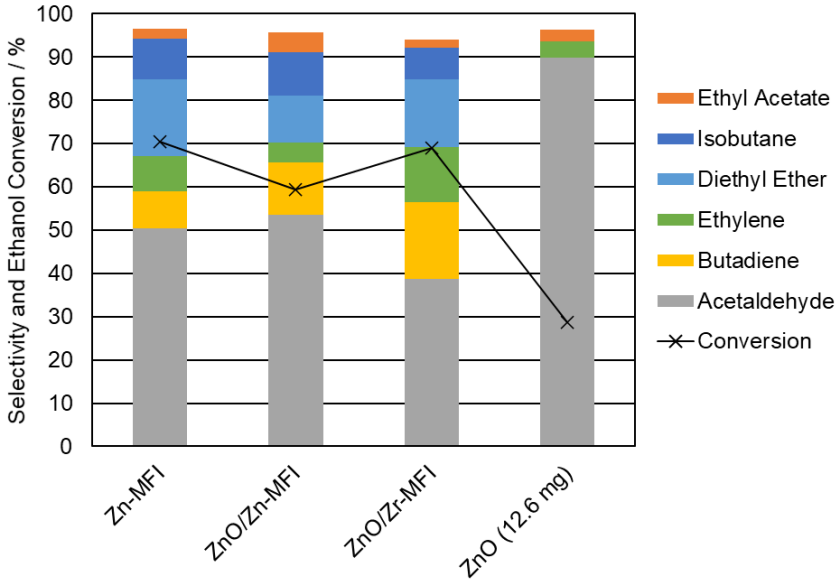

Figure 6.21: Selectivity distributions for ethanol conversion over Zn–MFI, ZnO/Zn–MFI and ZnO/Zr–MFI at 350 °C and ZnO at 400 °C at approx. 4 h TOS. Catalyst mass = 0.300 g. Ethanol feed rate: Zn–MFI and ZnO/Zn–MFI = 0.390 mmol min^{-1}; ZnO/Zr–MFI = 0.300 mmol min^{-1}; ZnO = 0.399 mmol min^{-1}. Detection Columns: RTX-VMS + ShinCarbon ST.

6.3. Conclusions.

Overall, divalently substituted MFI type materials containing Mg^{II} and Zn^{II} in tetrahedral positions have been successfully synthesised as evidenced by pXRD, BET, SEM, and ^{29}Si ssNMR spectroscopic analysis, with isolated framework sites confirmed by DR-UV-Vis spectroscopy and SEM-EDS mapping. Additionally, the acidities of both Mg–MFI and Zn–MFI were assessed by means of ^{31}P ssNMR spectroscopy of adsorbed TMPO. This investigation suggested that both materials contained predominantly Lewis acidic tetrahedral sites, with Zn–MFI possessing stronger Lewis acid sites than Mg–MFI.

Both Mg–MFI and Zn–MFI were assessed for their performance in the cascade reaction from ethanol to butadiene at varying temperature points. Pristine Mg–MFI was found to induce very low ethanol conversion, indicative of very weak acidity as concluded from ^{31}P ssNMR spectroscopy of adsorbed TMPO. Upon doping of Mg–MFI with ZnO to form ZnO/Mg–MFI, the material was observed to catalyse the total cascade reaction of ethanol to butadiene with low levels of additional dehydration products. It was concluded that the Lewis acid strength of the Mg^{II} tetrahedral sites is sufficient to promote C–C coupling reactions, but insufficient to catalyse the dehydration of ethanol, potentially leading to interesting selectivity effects when compared with M^{IV}–MFI systems from Chapter 5. Zn–MFI behaved in a remarkably interesting way, promoting both ethanol dehydrogenation and the total cascade reaction from ethanol to butadiene without the need for additional ZnO doping. Based upon literature surrounding

ethanol dehydrogenation over post-synthetic introduction of framework Zn^{II} species,[15, 16, 42] it was hypothesised that framework Zn–O bonds may act as a ZnO mimic promoting ethanol dehydrogenation to acetaldehyde which may then undergo aldol coupling by Lewis acidic Zn^{II} in framework positions.

In light of this hypothesis, the nature of framework Zn species was investigated further by means of XAS analysis and ion-exchange experiments. XANES spectra of Zn–MFI were found to match those of previous literature reports,[43] with EXAFS analysis allowing the conclusion that Zn atoms were present solely in framework positions by virtue of a lack of Zn–O–Zn backscattering.[16, 43, 44] Attempted ion-exchange of H–Zn–MFI with Na^{+}, K^{+}, Mg^{2+} and Zn^{2+} demonstrated minimal success, strongly suggesting that tetrahedral Zn is present in open framework positions.

In order to improve butadiene selectivity from ethanol, Zn–MFI was doped with ZnO to form ZnO/Zn–MFI and both pristine and doped materials were tested for ethanol conversion activity under variable temperature conditions. It was found that doping of ZnO increased both acetaldehyde and butadiene productivity at each temperature point alongside lowering ethylene productivity. From these observations, it was concluded that the additional ZnO allows ethanol to be dehydrogenated more rapidly and thus less ethanol is available to react over Lewis acidic framework Zn sites. Hence, less ethylene and diethyl ether are produced as dehydration products and Lewis acidic framework Zn sites are then more available to cataylse the aldol coupling and MPV reduction reactions necessary for butadiene formation. Subsequently, the reactions of ethanol over both Zn–MFI and ZnO/Zn–MFI were then assessed at 350 °C for 4h TOS. After 4 h TOS, butadiene selectivites of 9% and 12% were determined for Zn–MFI and ZnO/Zn–MFI. Acetaldehyde selectivites were relatively similar, around 50%, whilst the ethylene selectivity for ZnO/Zn–MFI (5%) was substantially lower than for Zn–MFI (8%) after 4 h TOS. Comparison to ZnO/Zr–MFI under similar conditions showed that, whilst ZnO/Zr–MFI possessed the highest butadiene selectivity (18%), Zn–MFI and ZnO/Zn–MFI were seen to exhibit a higher combined selectivity to Lebedev products (acetaldehyde, butadiene).

6.4. References.

1. M. Orazov and M. E. Davis, *Chem. Sci.*, 2016, **7**, 2264–2274.
2. W. Yan, S. Xi, Y. Du, M. K. Schreyer, S. X. Tan, Y. Liu and A. Borgna, *ChemCatChem*, 2018, **10**, 3078–3085.
3. J. Li, A. Corma and J. Yu, *Chem. Soc. Rev.*, 2015, **44**, 7112–7127.
4. M. Boronat, A. Corma and M. Renz, *J. Phys. Chem. B*, 2006, **110**, 21168–21174.
5. X. Yang, B. Lv, T. Lu, Y. Su and L. Zhou, *Catal. Sci. Technol.*, 2020, **10**, 700–709.
6. N. Koike, W. Chaikittisilp, K. Iyoki, Y. Yanaba, T. Yoshikawa, S. P. Elangovan, K. Itabashi and T. Okubo, *Dalton Trans.*, 2017, **46**, 10837–10846.
7. P. Hu, K. Iyoki, H. Yamada, Y. Yanaba, K. Ohara, N. Katada and T. Wakihara, *Micropor. Mesopor. Mater.*, 2019, **288**, 109594–109594.
8. M. A. Deimund, J. Labinger and M. E. Davis, *ACS Catal.*, 2014, **4**, 4189–4195.
9. N. Koike, K. Iyoki, S. H. Keoh, W. Chaikittisilp and T. Okubo, *Chem. Eur. J.*, 2018, **24**, 808–812.
10. B. Wang, N. Koike, K. Iyoki, W. Chaikittisilp, Y. Wang, T. Wakihara and T. Okubo, *Phys. Chem. Chem. Phys.*, 2019, **21**, 4015–4021.
11. N. Koike, K. Iyoki, B. Wang, Y. Yanaba, S. P. Elangovan, K. Itabashi, W. Chaikittisilp and T. Okubo, *Dalton Trans.*, 2018, **47**, 9546–9553.
12. *US Pat.*, US20160243531, 2016.
13. J. C. McKeen and M. E. Davis, *J. Phys. Chem. C*, 2009, **113**, 9870–9877.
14. H. Zhang, H.-R. Tan, S. Jaenicke and G.-K. Chuah, *J. Catal.*, 2020, **389**, 19–28.
15. T. Yan, W. Dai, G. Wu, S. Lang, M. Hunger, N. Guan and L. Li, *ACS Catal.*, 2018, **8**, 2760–2773.
16. L. Qi, Y. Zhang, M. A. Conrad, C. Russell, J. T. Miller and A. T. Bell, *J. Am. Chem. Soc.*, 2020, **142**, 14674–14687.
17. P. I. Kyriienko, O. V. Larina, S. O. Soloviev, S. M. Orlyk, C. Calers and S. Dzwigaj, *ACS Sustain. Chem. Eng.*, 2017, **5**, 2075–2083.
18. A. Kumar and R. Srivastava, *ChemCatChem*, 2020, **12**, 4807–4816.
19. Y. G. Kolyagin, A. V. Yakimov, S. Tolborg, P. N. R. Vennestrøm and I. I. Ivanova, *J. Phy. Chem. Lett.*, 2016, **7**, 1249–1253.
20. N. K. Mal, V. Ramaswamy, P. R. Rajamohanan and A. V. Ramaswamy, *Micropor. Mater.*, 1997, **12**, 331–340.
21. E. Yuan, W. Han, G. Zhang, K. Zhao, Z. Mo, G. Lu and Z. Tang, *Catal. Surv. Asia*, 2016, **20**, 41–52.
22. S. Kowalak, E. Janiszewska, M. Gierczyńska, V. Dolata, N. Evmiridis, T. Katranas, A. Vlessidis, V. Tsiatouras, F. Roessner and E. Schneider, *Stud. Surf. Sci. Catal.*, 2004, **154 C**, 2200–2207.
23. S. Kowalak, E. Szymkowiak, M. Gierczyńska and G. Giordano, *Stud. Surf. Sci. Catal.*, eds. R. Aiello, G. Giordano and F. Testa, Elsevier, 2002, vol. 142, pp. 351–358.
24. K. Iyoki, K. Kikumasa, T. Onishi, Y. Yonezawa, A. Chokkalingam, Y. Yanaba, T. Matsumoto, R. Osuga, S. P. Elangovan, J. N. Kondo, A. Endo, T. Okubo and T. Wakihara, *J. Am. Chem. Soc.*, 2020, **142**, 3931–3938.
25. I. Grosskreuz, H. Gies and B. Marler, *Micropor. Mesopor. Mater.*, 2020, **291**, 109683.
26. C. A. Fyfe, R. J. Darton, H. Mowatt and Z. S. Lin, *Micropor. Mesopor. Mater.*, 2011, **144**, 57–66.
27. P. Arudra, T. I. Bhuiyan, M. N. Akhtar, A. M. Aitani, S. S. Al-Khattaf and H. Hattori, *ACS Catal.*, 2014, **4**, 4205–4214.
28. A. Parulkar, R. Joshi, N. Deshpande and N. A. Brunelli, *Appl. Catal. A*, 2018, **566**, 25–32.

29. Z. Han, Y. Shen, F. Wang and X. Zhang, *J. Mater. Sci.*, 2018, **53**, 12837–12849.
30. Y. K. Hwang, T. Jin, J. M. Kim, Y. U. Kwon, S. E. Park and J. S. Chang, *J. Nanosci. Nanotechnol.*, 2006, **6**, 1786–1791.
31. N. K. Mal and A. V. Ramaswamy, *J. Mol. Catal. A*, 1996, **105**, 149–158.
32. W. Fan, R.-G. Duan, T. Yokoi, P. Wu, Y. Kubota and T. Tatsumi, *J. Am. Chem. Soc.*, 2008, **130**, 10150–10164.
33. Y. S. Ko and W. S. Ahn, *Korean J. Chem. Eng.*, 1998, **15**, 423–428.
34. A. Zheng, S.-J. Huang, W.-H. Chen, P.-H. Wu, H. Zhang, H.-K. Lee, L.-C. de Ménorval, F. Deng and S.-B. Liu, *J. Phys. Chem. A*, 2008, **112**, 7349–7356.
35. A. Zheng, S.-J. Huang, S.-B. Liu and F. Deng, *Phys. Chem. Chem. Phys.*, 2011, **13**, 14889–14901.
36. A. Zheng, S.-B. Liu and F. Deng, *Chem. Rev.*, 2017, **117**, 12475–12531.
37. S. Hayashi, *Anal. Sci.*, 2009, **25**, 133–136.
38. S. Hayashi, K. Jimura and N. Kojima, *Bull. Chem. Soc. Jpn.*, 2014, **87**, 69–75.
39. W. Dai, Q. Lei, G. Wu, N. Guan, M. Hunger and L. Li, *ACS Catal.*, 2020, **10**, 14135–14146.
40. Q. Zhao, W.-H. Chen, S.-J. Huang, Y.-C. Wu, H.-K. Lee and S.-B. Liu, *J. Phys. Chem. B*, 2002, **106**, 4462–4469.
41. C. Bornes, M. Sardo, Z. Lin, J. Amelse, A. Fernandes, M. F. Ribeiro, C. Geraldes, J. Rocha and L. Mafra, *Chem. Commun.*, 2019, **55**, 12635–12638.
42. W. Dai, S. Zhang, Z. Yu, T. Yan, G. Wu, N. Guan and L. Li, *ACS Catal.*, 2017, **7**, 3703–3706.
43. A. Hagen, K. H. Hallmeier, C. Hennig, R. Szargan, T. Inui and F. Roessner, *Stud. Surf. Sci. Catal.*, eds. H. K. Beyer, H. G. Karge, I. Kiricsi and J. B. Nagy, Elsevier, 1995, vol. 94, pp. 195–202.
44. A. A. Gabrienko, S. S. Arzumanov, A. V. Toktarev, I. G. Danilova, I. P. Prosvirin, V. V. Kriventsov, V. I. Zaikovskii, D. Freude and A. G. Stepanov, *ACS Catal.*, 2017, **7**, 1818–1830.

6.5. Supplementary Information.

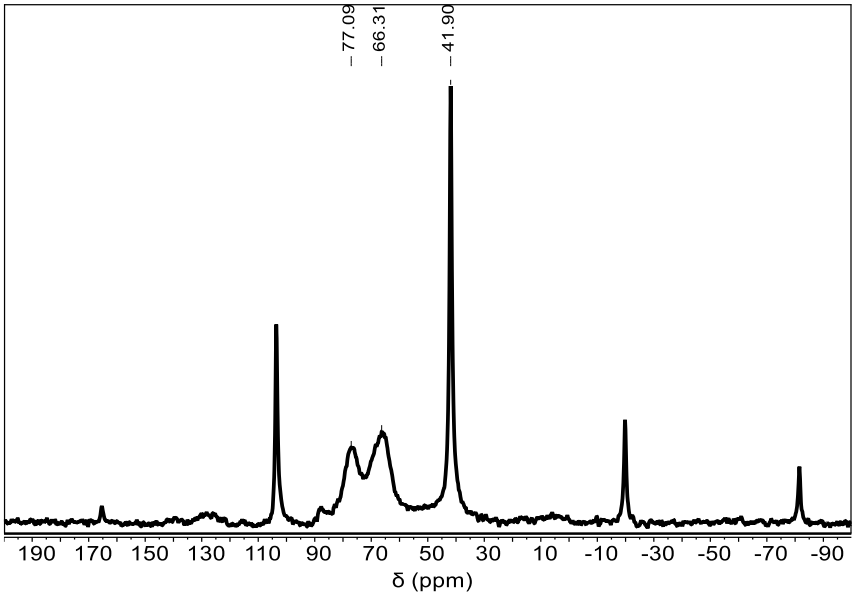

Figure S6.1: ^{31}P ssNMR spectra of TMPO adsorbed onto H–Al–MFI. Spectrum was averaged over 24 scans with a 300 s recycle delay. Spectrum was acquired on a Bruker Avance III 400 MHz spectrometer using a 4 mm zirconia rotor. Spectrometer frequency: ^{31}P = 161.99 MHz. MAS spin rate ≈ 10000 Hz.

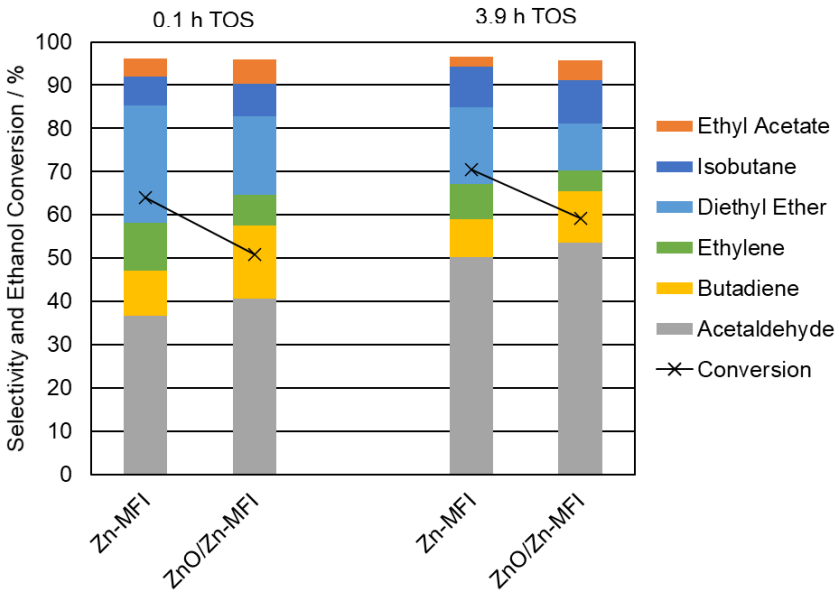

Figure S6.2: Selectivity distributions for ethanol conversion over Zn–MFI and ZnO/Zn–MFI at 350 °C for 0.1 and 3.9 h TOS. Catalyst mass = 0.300 g. Ethanol feed rate = 0.390 mmol min^{-1}. Detection Columns: RTX-VMS + ShinCarbon ST.

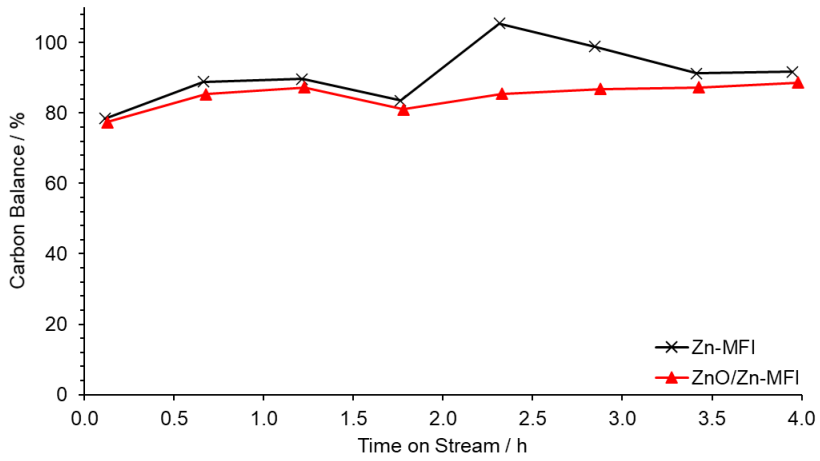

Figure S6.3: Carbon balance for ethanol conversion over Zn–MFI (×) and ZnO/Zn–MFI (▲) at 350 °C for 4 h TOS. Catalyst mass = 0.300 g. Ethanol feed rate = 0.390 mmol min^{-1}. Detection Columns: RTX-VMS + ShinCarbon ST.

Chapter 7

Investigations into the Role of Heteroatomic Framework Substitution Site in Mordenite on Lewis Acidity for the Direct Transformation of Ethanol to Butadiene.

7. Investigations into the Role of Heteroatomic Framework Substitution Site in Mordenite on Lewis Acidity for the Direct Transformation of Ethanol to Butadiene.

In Chapter 4, mordenite was presented as an ideal support material for the ZnO catalysed dehydrogenation of ethanol to acetaldehyde. In comparison to both MFI and BEA zeolites, MOR was shown to possess a narrower product distribution, forming predominantly acetaldehyde and ethylene, with insignificant amounts of large aromatic by-products. This was suggested to be resultant from a degree of product or transition-state selectivity inherent to the MOR framework, although at the expense of higher coking levels. Furthermore, variation of the zeolite counter cation to heavier alkali metals was seen to have a positive effect on dehydrogenation catalysis, with ZnO/Rb–MOR being identified as an optimum material in terms of acetaldehyde selectivity and productivity. Additionally, in Chapters 5 and 6, the substitution of an MFI framework with various divalent and tetravalent metal atoms was seen to introduce Lewis acidic framework sites, which in tandem with ZnO, could successfully affect the total cascade transformation of ethanol to 1,3–butadiene. From realisation of these two conclusions, it was deemed of interest to explore the heteroatomic substitution of MOR for the application of selective reaction of ethanol to 1,3–butadiene. In this case, the beneficial properties of the MOR framework may result in increased selectivity in the cascade transformation of ethanol to 1,3–butadiene. Additionally, an opportunity is also presented to investigate the reactivity of individual tetrahedral sites in MOR by targeted dealumination and remetallation.

In order to approach site selective modification and reactivity of mordenite, it is first essential to understand its framework structure, non-equivalent tetrahedral positions, and cation-exchange sites of importance. Mordenite is primarily characterised by its pseudo-1-dimensional channel systems comprising a linear 12 MR channel running parallel to a relatively non accessible and highly elliptical 8 MR channel. These parallel channels are linked by small cages, or side pockets, comprising 8 MR cage entrances (Figure 7.1). Distributed throughout these various confinement environments are four unique tetrahedral sites denoted T_1–T_4, each of which can be occupied by either silicon or aluminium atoms in the aluminosilicate material (Figure 7.1). T_1 and T_2 are located in the 12 MR main channel of mordenite whilst T_3 is located at the junction between the 8 MR channel and side pocket. T_4 is located at the border between the 12 MR channel and 8 MR side pocket.[1, 2]

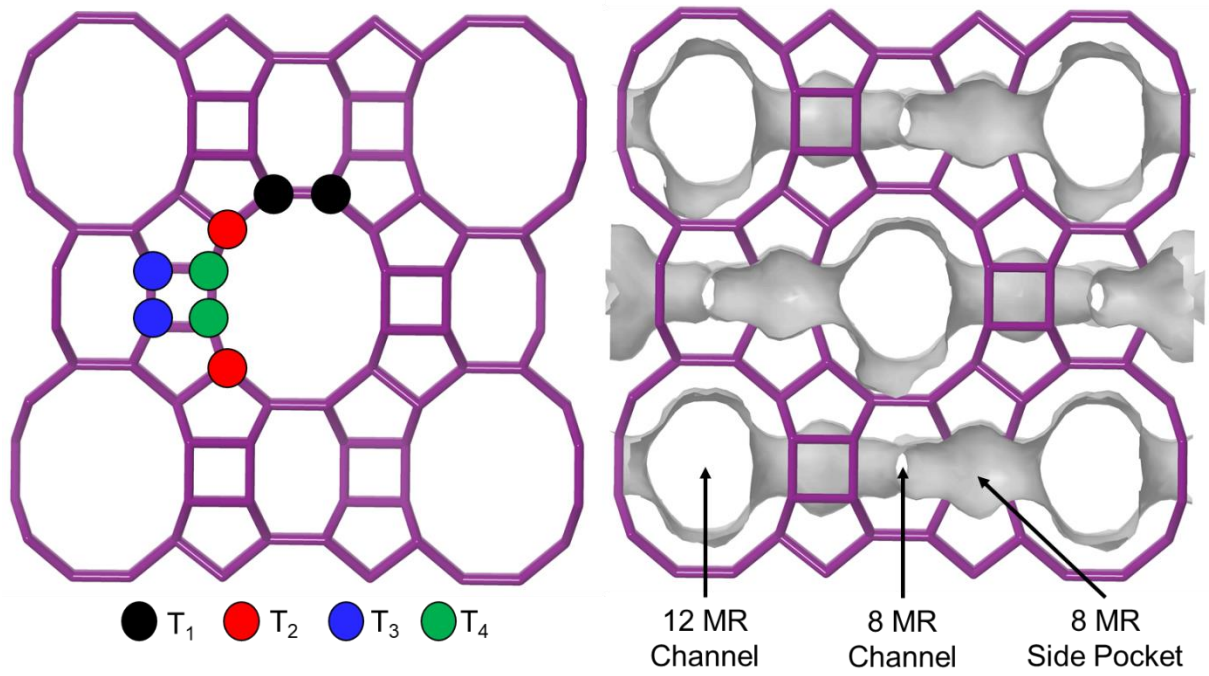

Figure 7.1: Schematic diagrams of the unique tetrahedral sites in MOR (left) alongside the channel and cage system (right). Zeolite structure and channel system generated using the IZA zeolite structure database.[2]

As a result of the various channel sizes and multiple Al tetrahedral positions, eight unique cation exchange sites are available in mordenite, however the occupation of such sites is not uniform and is heavily dependent upon the nature of the cation introduced. As an example that will be relevant later, Cs^+ cations within Cs–MOR can be located within one of three positions, Cs II, Cs IV, and Cs VI. Table 7.1 gives details of cation exchange positions for Cs^+ cations in MOR, with a diagram of each position presented in Figure 7.2.[3, 4] A detailed diagram of every available cation location alongside further examples of site occupancy can be found in W. J. Mortier's "*Compilation of Extra Framework Sites in Zeolites*", pp. 54–55.[4]

Table 7.1: Location and occupancy details for the three unique cation locations in Cs–MOR.[3, 4]

Cs^+ Cation Site	Channel Location	Coordination Ring Size	Coordination Number	Associated T Atoms	Site Occupancy
II	8 MR	8	6	T_1, T_3	3.8
IV	12 MR	8	6	T_2, T_4	1.9
VI	12 MR	6	4	T_1, T_2	1.8

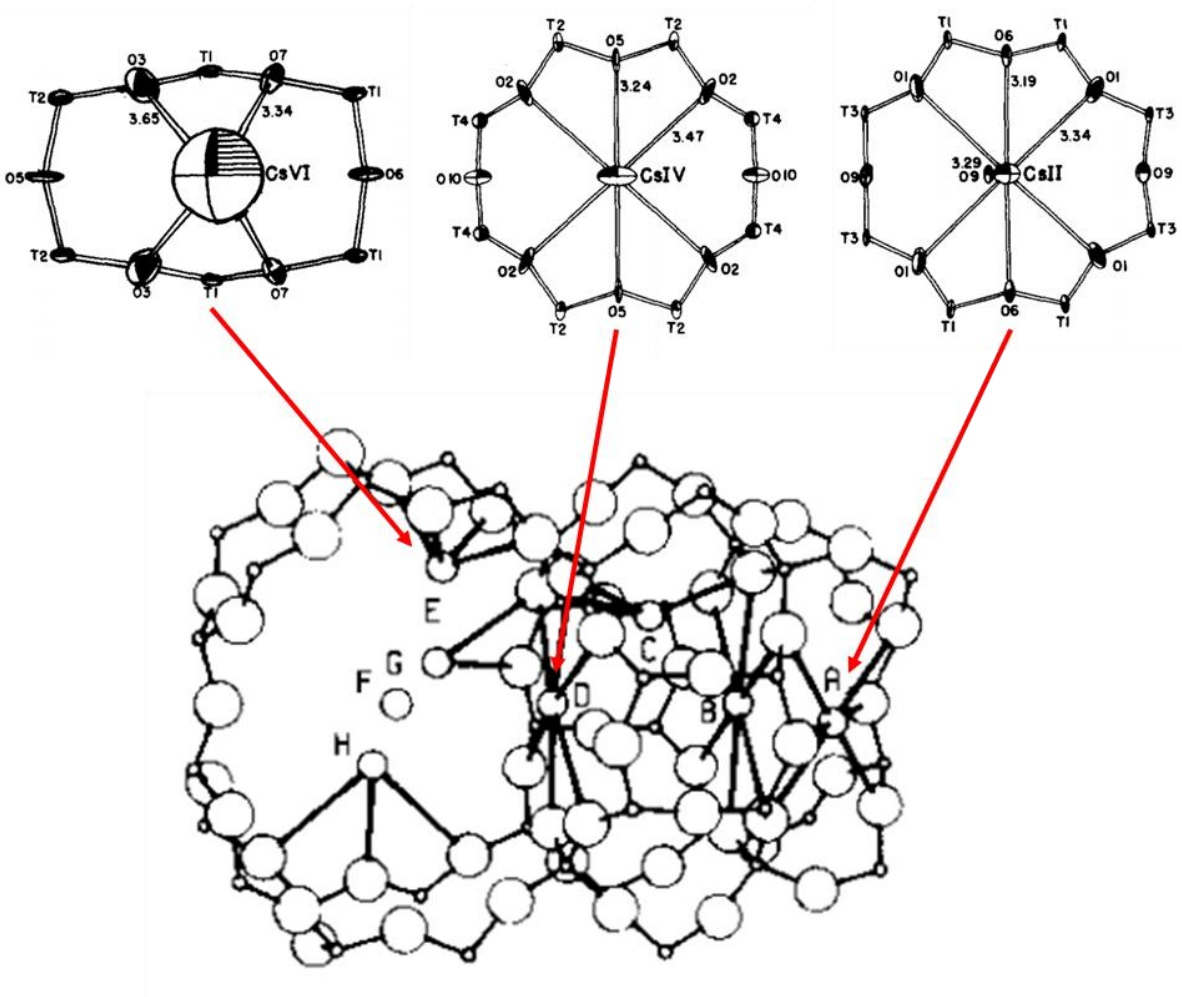

Figure 7.2: Cation location displacement ellipsoids for Cs^+ cations within mordenite alongside their location within the MOR framework. Adapted from references 3 and 4 with permission from Elsevier (reference 3). Copyright (1978) Elsevier.[3, 4]

Owing to the presence of various potential active sites within different confinement environments, research into the MOR framework frequently focusses into attempting to discern in which environment a given reaction takes place, i.e. the 12 MR channel or 8 MR side pocket, with a major set of contributions to this area related to the site selective carbonylation of dimethyl ether (DME).[1, 5-8] Advances in this field have managed to successfully elucidate the role that aluminium position plays in DME carbonylation, with Brønsted acid sites associated with T_3 aluminium located within the 8 MR side pockets of MOR being associated with higher activity and selectivity towards methyl acetate.[1, 5, 6] Computation of methoxy group stability, apparent activation energies and transition state geometries predicts high T_3 selectivity owing to the unique and well suited transition state at the T_3–O_{33} position.[5] Experimental work has sought to confirm these predictions by selective probing of the DME carbonylation reaction over Brønsted acid sites associated with various Al T_x positions.[1, 6] Reule *et al.* report selective dealumination of T_3 and T_4 positions of the 8 MR side pockets of MOR following nitric acid

treatment evidenced predominantly by DRIFTS of adsorbed pyridine in combination with NH_3–TPD.[1] Their reported dealumination results are in line with previous reports which suggests preferential dealumination of T_3 and T_4 sites from the strained 4 MR of MOR in a quasi-simultaneous manner.[9, 10] It is noted that, mathematically, T_1 and T_2 Al atoms may be removed in a similar manner, however this notion is discounted as "*there is no physical reason why the Al atoms should be taken out two by two from a chainlike structure*".[10] As catalytic evidence of their hypothesis, Reule *et al*. report a peak methyl acetate productivity decrease as more aluminium is removed from T_3 and T_4 sites.[1] As cross comparison, several groups have approached the matter by selective blocking or removing of Al residing within the 12 MR of MOR.[6, 11] Liu *et al.* report an almost unchanged selectivity to methyl acetate following saturation of Brønsted acid sites with pyridine within the 12 MR, effectively blocking them.[11] Xue *et al*. take the approach further by selective dealumination of the 12 MR of MOR by initial pyridine saturation of 12 MR sites, followed by selective Na^+ exchange into 8 MR cation sites in order to protect these sites from subsequent steam dealumination, hence resulting in selective dealumination of 12 MR sites.[6] This is possible as the ability for Na^+ to restrict access to the 8 MR side pockets of MOR has previously been reported, evidenced by both ^1H and ^{129}Xe ssNMR spectroscopy.[12] Following selective removal of the 12 MR sites as evidenced by deconvolution of FTIR spectra, Xue *et al*. observed a very similar methyl acetate formation rate to the pristine sample, hence further supporting the hypothesis that reaction over Al located within the 8 MR side pockets of MOR is selective for DME carbonylation. Crucially, between each of these reports, whilst it is predominantly concluded that Al within the 8 MR pockets of MOR is selective and active for DME carbonylation, sites responsible for catalyst deactivation, namely Al T_1 and T_2 located within the 12 MR channel in this case, are also identified.[1, 6] Knowledge and identification of sites that are responsible for side reactions and catalyst deactivation are equally as important as those that are active and selective in catalyst development, as targeted removal of such sites can afford further catalyst stability and performance improvement.

Hence, in order to combine the apparent selectivity of the MOR framework into the direct cascade transformation of ethanol to 1,3–butadiene, heteroatomic metal substituted mordenites were identified as target materials. So as to gain insight into which substituted tetrahedral sites of MOR are active for Lewis acid catalysed reactions, a synthetic method was devised in which aluminium containing mordenite would initially be dealuminated under conditions similar to those reported by Reule *et al*. before subsequent remetallation of the site,

ideally resulting in targeted introduction of Lewis acidic metal centres into the T_3 and T_4 positions of the 8 MR side pocket (Figure 7.3).[1] An extension to this work could include selective dealumination and metalation of solely the 12 MR sites of MOR (T_1 and T_2) *via* the method presented by Xue *et al.*.[6]

Although optimisation of the M–MFI system presented in Chapter 5 resulted in Zr–MFI being identified as the preferred analogue for cascade ethanol to butadiene transformation in terms of butadiene productivity, Sn was chosen as the heteroatom of choice for introduction into partially dealuminated MOR samples. Sn was chosen as it provides an excellent ssNMR spectroscopic handle for inclusion of ^{119}Sn into the zeolite framework by detection of the δ_{Sn} = −700 ppm signal in hydrated zeolite samples (see Section 2.1.3.4). Additionally, a wealth of characterisation of Sn active sites included into a zeolite framework is available within the literature alongside strong computational theory in order to distinguish specific reaction sites within Sn–containing materials.[13-23] Although many of these reports are with regard to the Sn–BEA system and are hence not *directly* transferrable, they provide an excellent point of reference for trends and interpretation of data. Additionally, remetallation of zeolite vacancies introduced by dealumination is well reported using reactive Sn compounds, such as $SnCl_4$.[24-26]

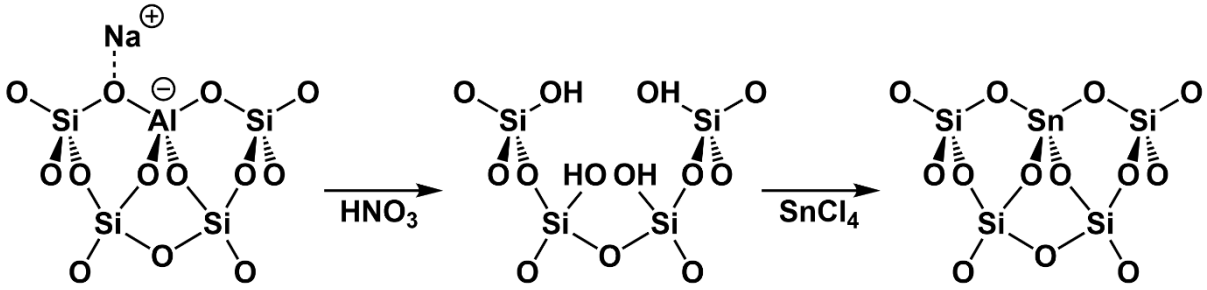

Figure 7.3: Schematic representation of the zeolite framework following dealumination and remetallation processes by HNO_3 and $SnCl_4$ respectively.

Unfortunately, synthesis of a wholly Sn^{4+} substituted MOR material for control reactions by either a bottom-up or top-down method is unlikely, as MOR seemingly requires a minimum amount of aluminium within the framework to retain crystallinity, manifesting in a maximum obtainable Si/Al ratio of approximately 30 after which a BEA phase begins to form under hydrothermal conditions.[27, 28] Hence, a wholly silica MOR is not known in the literature, nor are any other charge neutral analogues, and dealumination/remetallation strategies will likely result in mixed Sn/Al–MOR materials. Mixed bimetallic Sn/Al zeolite materials, however, have gained some research interest in the literature since the commencement of this project.[23, 26] Specifically, SnAl–BEA has been synthesised following partial dealumination of

Al–BEA and applied in the synthesis of ethyl lactate.[26] To the extent of this author's knowledge, few recent contributions report successful hydrothermal synthesis of bimetallic MOR materials. So far, a mixed Co/Al–MOR has been reported by a dry gel conversion method,[29] whilst Zn/Al–MOR[30, 31] and Sn/Al–MOR[23] have been reported to be prepared *via* a co-hydrolysis hydrothermal synthetic method with the Sn/Al–MOR analogue utilised for catalytic *tert*-butylation of toluene.[23]

7.1. Preparation and characterisation of a range of partially dealuminated MOR materials.

In order to prepare a library of partially dealuminated MOR samples, Na–MOR–(7) was dealuminated in a fashion similar to that reported by Reule *et al*..[1] Briefly, Na–MOR–(7) was added to a 0.55M solution of HNO_3 and stirred at 85 °C for varying time increments, namely 1 h, 6 h and 18 h. Following acid treatment, the resulting materials were washed to neutral pH with deionised water; further details are presented in Section 9.3.8.. Table 7.2 shows the elemental compositions and relevant elemental ratios for Na–MOR–(7) and its dealuminated products, denoted deAl–MOR–1h, deAl–MOR–6h and deAl–MOR–18h respectively. As is shown in Table 7.2, increased dealumination contact time leads to an increased Si/Al ratio, resulting from a decrease of aluminium content. Hence, a lower calculated T site occupancy was also obtained. When plotted, the increase of Si/Al ratio is almost linear following the first hour of dealumination and closely mirrors the change in aluminium content over time (Figure S7.1), implying no substantial loss of silicon from the zeolite framework. Additionally, each dealuminated material is seen to possess a very low sodium content, suggesting that exchange to the H–form of the materials was resultant from the acidic dealumination procedure. Whilst not corroborative with the work of Reule *et al*. where some sodium content is retained, the result is not entirely unexpected owing to the harsh acidic treatment and abundance of H^+ cations.[1] Reule *et al*., however, must have observed some significant Na^+–H^+ ion-exchange under similar conditions as the decrease in molar sodium loading observed for their samples dealuminated with 0.55 M HNO_3 is much greater than the observed molar Al loss.[1]

Table 7.2: Elemental composition and elemental ratios of Na–MOR–(7) and partially dealuminated MOR samples. ED–XRF values are averaged from three measurements and recorded as M wt%.

Sample	Elemental Loading / wt%			Elemental Ratios		Calculated T Site Occupancy / %
	Si	Al	Na	Si/Al	Na/Al	
Na–MOR–(7)	39.08	6.66	4.83	5.6	0.85	100
deAl–MOR–1h	41.22	4.64	0.00	8.5	0.00	60.8
deAl–MOR–6h	44.79	3.97	0.00	10.8	0.00	51.5
deAl–MOR–18h	46.15	2.77	0.00	16.0	0.00	37.9

Additionally, retention of zeolite structure was monitored by pXRD analysis as removal of aluminium from low silica zeolite materials has the potential to cause irreversible framework damage and disintegration. Figure 7.4A shows the pXRD patterns of Na–MOR–(7) and resultant dealuminated MOR samples; for each sample the major reflections associated with the MOR framework are retained, with no additional silicate or aluminate phases observed. Additionally, the relative crystallinity of each materials is predicted to be unaffected owing to a lack of substantive change in the relative signal intensity of the main MOR reflections or an increase in amorphous broadening. N_2 physisorption analysis of dealuminated mordenite shows a steady increase in BET surface area following extended dealumination times as would be expected (Figure 7.4B + Table 7.3). Unfortunately, the measurement for H–deAl–MOR–6h is inconsistent and a repeat would be desirable, however this was not able to be performed before the time of submission.

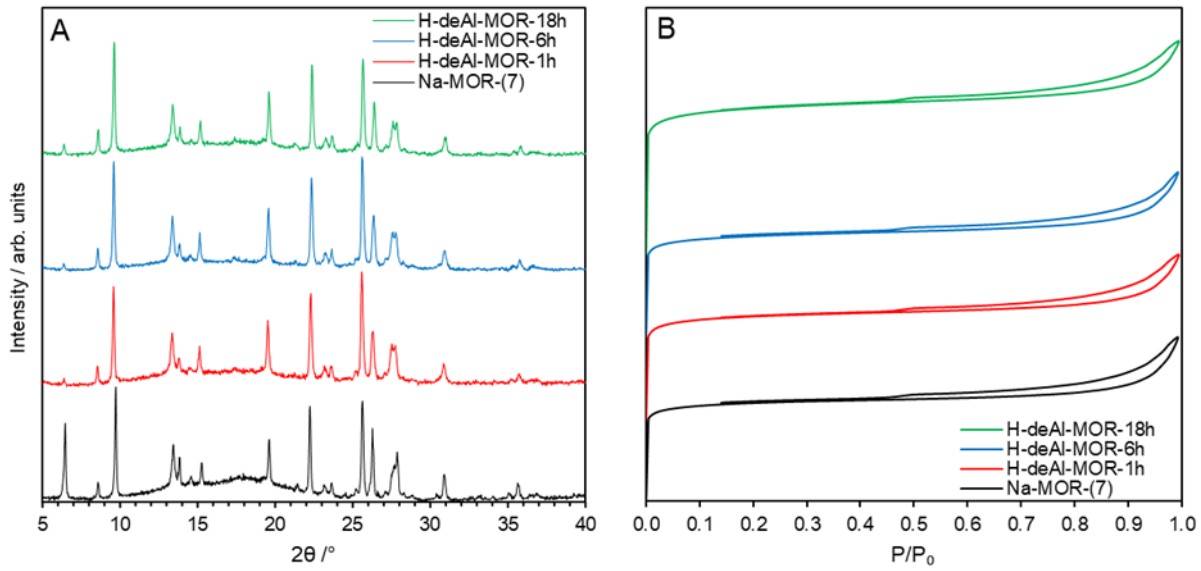

Figure 7.4: A) pXRD patterns in the 2θ = 5–40 ° region of Na–MOR–(7) and partially dealuminated MOR samples. B) Normalised N_2 physisorption isotherm plots of dealuminated MOR materials following calcination.

Table 7.3: BET surface area values for dealuminated MOR materials following calcination,

Material	BET Surface Area / $m^2 g^{-1}$
Na–MOR–(7)	404.7
H–deAl–MOR–1h	485.8
H–deAl–MOR–6h	391.7
H–deAl–MOR–18h	508.1

In addition to structural and surface area analysis assessed by pXRD and N_2 physisorption, location of residual Al was probed by the use of ^{27}Al ssNMR spectroscopy to discern whether the remaining aluminium was still bound within the tetrahedral zeolite framework sites or was instead ejected from the framework and retained as octahedral extra-framework alumina. Figure 7.5 (top) shows the ^{27}Al ssNMR spectra of Na–MOR–(7) and partially dealuminated MOR samples in the Na/H–form directly following preparation. Here it is seen that the parent material, Na–MOR–(7), exhibits a sole resonance at approximately δ_{Al} = 60 ppm indicative of tetrahedrally coordinated Al atoms, as would be expected for a pristine parent material.[32] The partially dealuminated materials, expected to be in the protic form from ED-XRF analysis, instead show two resonances at δ_{Al} = 60 ppm and 0 ppm indicative of tetrahedral and octahedral aluminium, respectively.[32] Octahedral aluminium characterised by a resonance at δ_{Al} = 0 ppm is typically regarded as being in the form of extra-framework alumina, however recent work by the Bokhoven group has suggested that this resonance may instead be resultant from hydrated framework aluminium which is still bound into the zeolite framework, but adopts an octahedral coordination geometry.[32, 33] In order to probe this, Na–MOR–(7) and partially dealuminated MOR samples were exchanged into their Cs^+ form and the ^{27}Al ssNMR spectroscopy study repeated. Figure 7.5 (bottom) shows the ^{27}Al ssNMR spectra of Na–MOR–(7) and partially dealuminated MOR samples in the Cs–form directly following preparation. Here it is observed that all four materials now exhibit a sole significant resonance at δ_{Al} = 60 ppm indicative of tetrahedrally coordinated Al atoms. It is therefore concluded that the dealumination process utilised does not result in formation of extra-framework alumina and that all aluminium atoms present in dealuminated samples are retained within the tetrahedral sites of the MOR framework. It is noted that the Si/Al ratios for Cs–deAl–MOR materials (Table 7.4) increase slightly following Cs^+ exchange in comparison to H–deAl–MOR materials (Table 7.2), potentially suggesting that some ex-FW alumina could

be washed out. However, it would be expected for this to happen during the washing stages following the dealumination procedure.

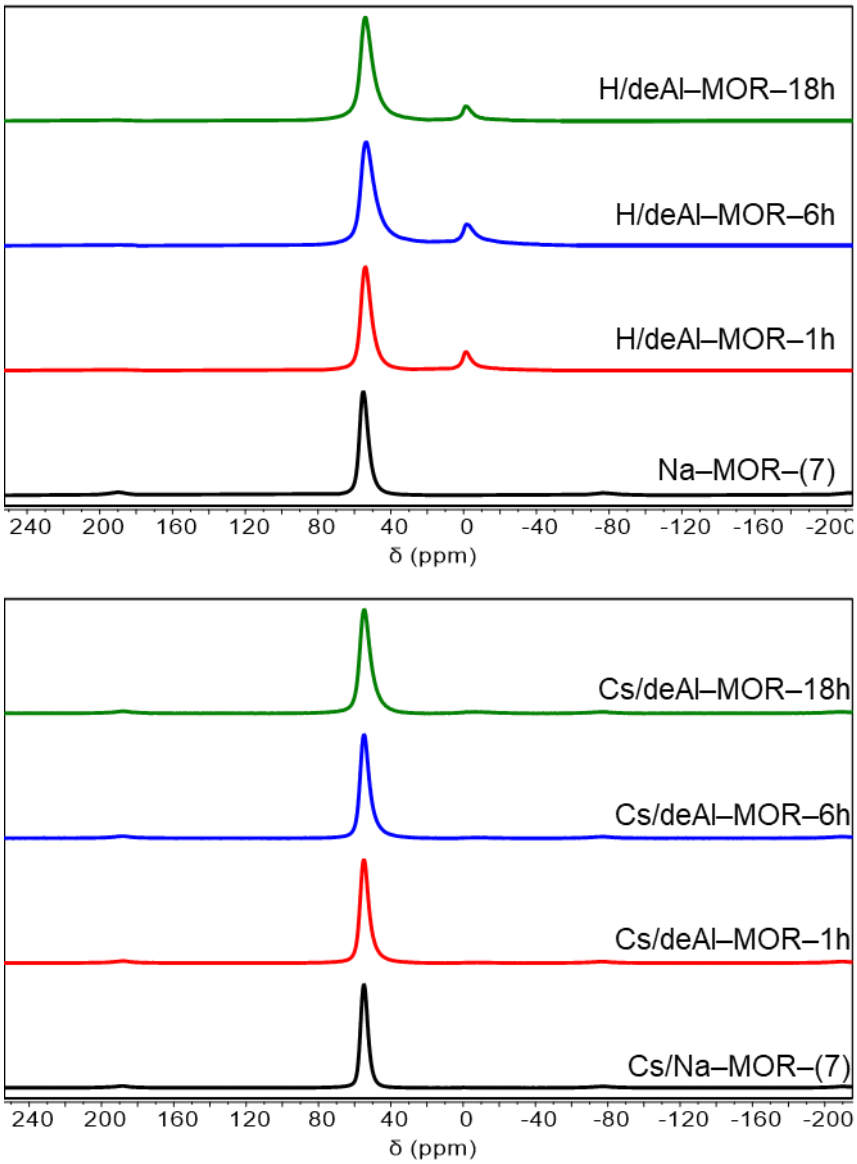

Figure 7.5: ^{27}Al ssNMR spectra of Na–MOR–(7) and partially dealuminated MOR samples in the Na/H–form (top) and Cs–form (bottom). Spectra were averaged over 10000 scans with a 0.2 s recycle delay. Spectra were acquired on a Varian VNMRS 400 MHz spectrometer using a 4 mm zirconia rotor. Spectrometer frequency: ^{27}Al = 104.20 MHz. MAS spin rate ≈ 14000 Hz.

Having the Na–MOR–(7) and partially dealuminated MOR materials in the Cs-form additionally allows use of ^{133}Cs ssNMR spectroscopy to discern the location of Cs^+ cations within the zeolite materials. As discussed in Section 2.1.3.5., the large and diffuse electron cloud of the Cs^+ cation can undergo perturbations due to confinement effects, allowing insight into the zeolite ring size housing Cs^+ from measurement of ^{133}Cs chemical shift. The elemental compositions and ratios resulting from Cs^+ exchange of Na–MOR–(7) and partially dealuminated MOR samples are shown in Table 7.4. It is observed that a maximum exchange

level of approximately 80% is observed for all MOR materials. It is noted that full exchange of other large pore zeolites (BEA and FAU) with Cs^+ cations is often not observed, with many literature examples showing a maximum Cs^+ exchange level of around 80%.[34-38] As the Cs-exchange level is similar for all samples, the assumption is made that all samples have undergone similar exchange processes, with any preferential site exchange occurring in the same order. Additionally, parent Na–MOR–(7) demonstrated a Na/Al ratio of only 0.85 (Table 7.2), potentially suggesting a maximum exchange level for this material.

Table 7.4: Elemental composition and maximum elemental ratios of Cs-exchanged Na–MOR–(7) and partially dealuminated MOR samples. ED–XRF values are averaged from three measurements and recorded as M wt%.

Sample	Elemental Loading / wt%			Elemental Ratios	
	Si	Al	Cs	Si/Al	Cs/Al
Cs/Na–MOR–(7)	28.08	4.80	18.18	5.6	0.77
Cs-deAl–MOR–1h	32.58	3.36	10.93	9.4	0.67
Cs-deAl–MOR–6h	34.71	2.88	9.60	11.6	0.68
Cs-deAl–MOR–18h	36.32	2.20	7.42	16.4	0.71

Figure 7.6 shows the stacked and normalised raw ^{133}Cs ssNMR spectra of Cs^+ exchanged Na–MOR–(7) and partially dealuminated MOR samples. As discussed in Section 2.1.3.5., the upfield resonance may be assigned to Cs^+ ions residing within the Cs II and Cs IV positions whilst the downfield resonance is associated with Cs^+ residing within the Cs VI positions (Figure 7.2).[3, 39, 40] Following dealumination, all samples exhibit a decrease in relative intensity of the downfield resonance ($\delta_{Cs} \approx 0$ ppm) associated with Cs^+ located within the Cs VI cation position and associated with the T_1 and T_2 tetrahedral positions of MOR.[v] Interestingly, this observation does not corroborate the report from Reule *et al*. who suggested selective removal of aluminium from T_3 and T_4 positions following treatment of MOR with 0.55 M HNO_3. Removal from T_3 and T_4 would instead be predicted to result in a reduction in the relative intensity of the upfield resonance ($\delta_{Cs} \approx -67$ ppm) associated with Cs II and Cs IV positions.[1]

[v] It is acknowledged that the lower intensity of the high frequency band could instead be resultant from a lower Cs/Al ratio for dealuminated samples than for the parent material if the ion-exchange dynamics dictate that the Cs VI site is the last to be populated. This is not thought to be the cause, however, as the amount of signal decrease is disproportionately large compared to the smaller differences in Cs/Al ratio.

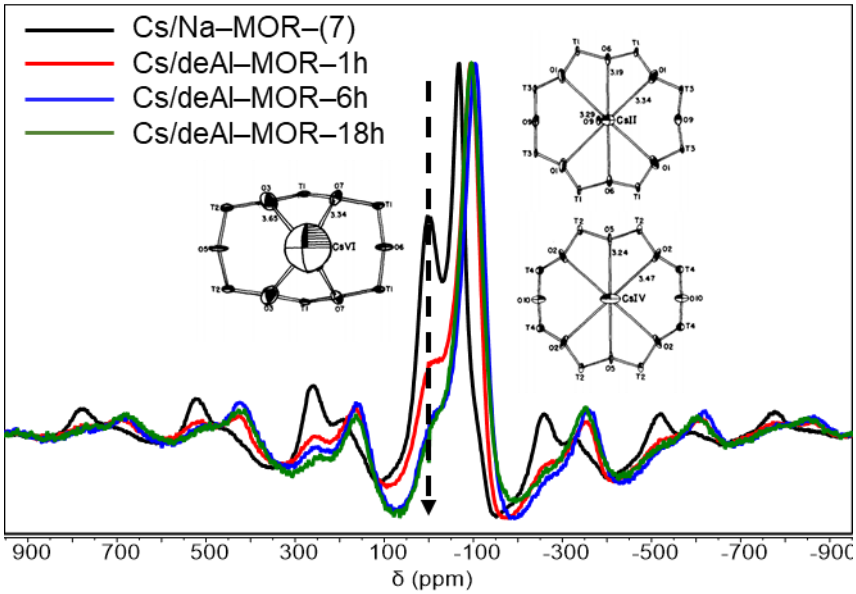

Figure 7.6: Stacked and baseline normalised raw ^{133}Cs ssNMR spectra of Cs^+ exchanged Na–MOR–(7) and partially dealuminated MOR samples. Spectra were averaged over 10000 scans with a 0.2 s recycle delay. Spectra were acquired on a Varian VNMRS 400 MHz spectrometer using a 4 mm zirconia rotor. Spectrometer frequency: ^{133}Cs = 52.45 MHz. MAS spin rate ≈ 10000 Hz. Catio locations adapted from references 3 with permission from Elsevier. Copyright (1978) Elsevier.[3]

Further information was obtained from the ^{133}Cs spectra by Dr. D. C. Apperley following mass-normalisation and deconvolution based upon the centre bands and first order side bands. Table 7.5 shows the sample mass used for ^{133}Cs ssNMR spectral acquisition alongside the mass-corrected absolute signal intensities for Cs-exchanged Na–MOR–(7) and partially dealuminated MOR samples based on the centre band and first order sideband signals. Figure 7.7 shows the stack of normalised ^{133}Cs ssNMR spectra of Cs^+ exchanged Na–MOR–(7) and partially dealuminated MOR samples that were based on deconvolution into six lines of the two centre bands plus first order side bands. Here it is observed that the relative intensities of the centre band resonances for dealuminated samples are not significantly different, suggesting similar population distribution of cation sites for each dealuminated material. When coupled with the absolute signal intensities presented in Table 7.5, it may be possible to suggest that, in the process of dealumination, Al is initially partially removed from framework sites associated with the Cs VI position (T_1, T_2 sites) before subsequent removal of Al from all remaining framework sites concurrently. This proposal is consistent with the data presented in Table 7.5 and Figure 7.7 as a decrease in downfield signal ($\delta_{Cs} \approx 0$ ppm) is observed for all dealuminated samples, but extended dealumination times do not result in further change to the relative signal intensities, rather just the overall signal intensity.

Additionally, a noticeable shift of the low frequency centre band resonance ($\Delta\delta_{Cs} \approx -30$ ppm) is observed for all dealuminated samples in comparison to the parent material, suggestive

of a change in ^{133}Cs speciation. At this point, it must be considered that the low frequency resonance is comprised of two resonances pertaining to ^{133}Cs residing within the Cs II and Cs IV cation positions.[3, 39] The ^{133}Cs ssNMR spectrum of the parent material shown in Figure 7.7 is observed to exhibit a low frequency shoulder ($\delta_{Cs} = -100$ ppm) on its centre band ($\delta_{Cs} = -67$ ppm) that aligns with the centre bands of the dealuminated materials ($\delta_{Cs} \approx -100$ ppm). This shoulder is calculated to account for approximately 10% of the spectral intensity. Following interpretation of the report by Chu *et al.*, the bands at $\delta_{Cs} \approx -67$ ppm and $\delta_{Cs} \approx -100$ ppm may be assigned to the Cs II and Cs IV cation positions respectively. Hence, it is suggested that Cs^+ is additionally lost from Cs II exchange positons (Al T_1 and T_3) whilst it is less affected in the Cs IV exchange positions (Al T_2 and T_4) following dealumination. As both the Cs II and Cs VI positions are associated with Al T_1, it is suggested that Al in this tetrahedral position is the first to be removed from MOR when dealumination is undertaken with nitric acid. Following initial dealumination of T_1, it is likely that aluminium may be removed from all tetrahedral poistions concurrrently resulting in overall signal intensity reduction and no major changes in relative intensities.

Alternatively, the observed shift in upfield resonance could be resultant from a change in pore diameters following dealumination. Potentially, as Al is removed, the channel structure may relax, resulting in expansion of the pores and lesser steric constraint of the Cs^+ electron cloud. In theory, this could manifest in a reduction of ^{133}Cs shielding and hence an upfield shift. This could be supported by N_2 physisorption analysis, especially with pore-size distribution analysis, as any increase in the pore size and volume would strongly support this hypothesis.

Table 7.5: Sample mass and absolute mass-normalised signal intensities of Cs-exchanged Na–MOR–(7) and partially dealuminated MOR samples based on the centre band and first order sideband signals.

Sample	Sample mass in rotor / mg	Absolute signal intensity (mass-corrected) / a.u.	Calculated T Site Occupancy / %
Cs/Na–MOR–(7)	46.2	100	100
Cs-deAl–MOR–1h	49.8	60	60
Cs-deAl–MOR–6h	47.3	47	49
Cs-deAl–MOR–18h	47.3	39	35

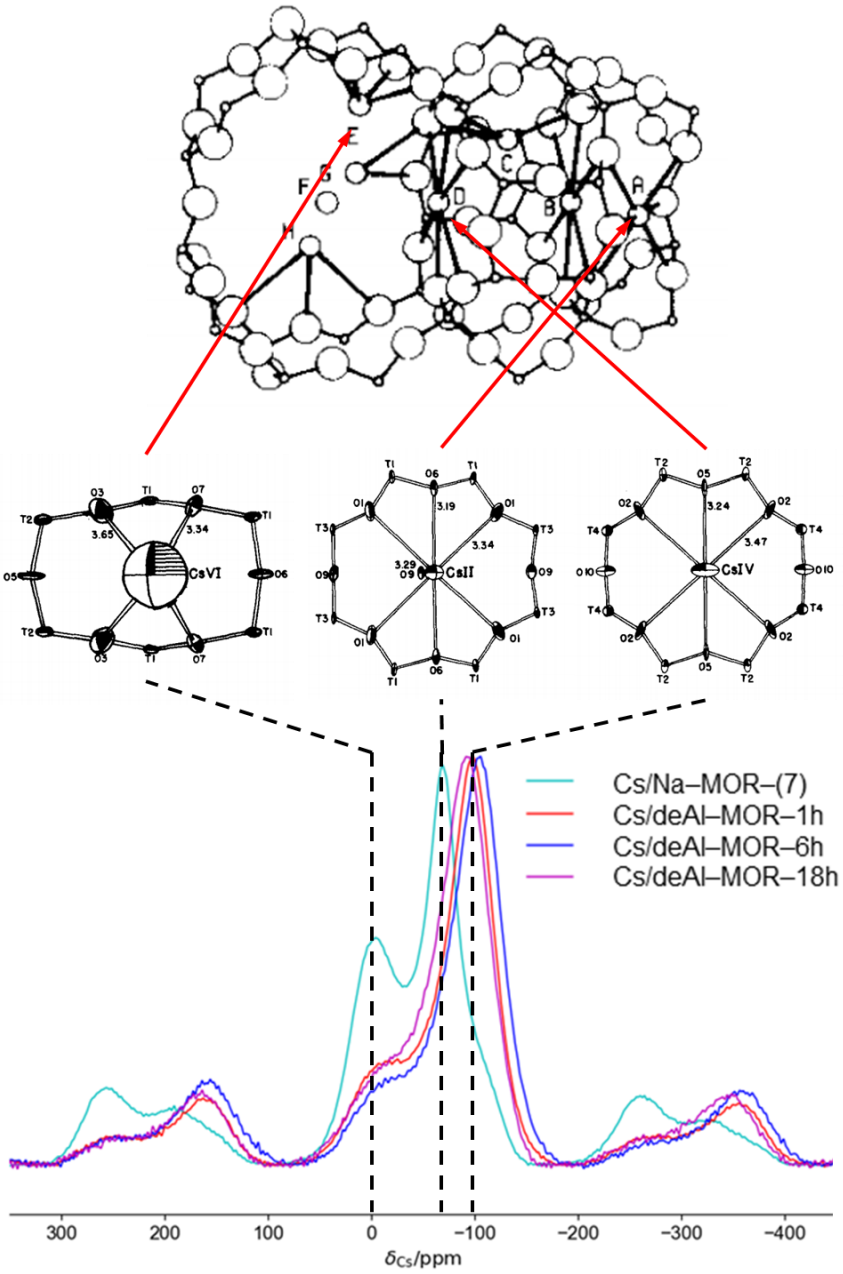

Figure 7.7: Stacked and deconvolution normalised ^{133}Cs ssNMR spectra of Cs^+ exchanged Na–MOR–(7) and partially dealuminated MOR samples. Spectra were averaged over 10000 scans with a 0.2 s recycle delay. Spectra were acquired on a Varian VNMRS 400 MHz spectrometer using a 4 mm zirconia rotor. Spectrometer frequency: ^{133}Cs = 52.45 MHz. MAS spin rate ≈ 10000 Hz. Cation locations adapted from references 3 and 4 with permission from Elsevier (reference 3). Copyright (1978) Elsevier.[3, 4]

Interestingly, the results and suggestions made hitherto in regard to ^{133}Cs ssNMR are in contradiction to the established zeolite literature regarding acidic dealumination of MOR.[1] Were the T_3 and T_4 sites removed selectively as suggested in previous literature, it would be expected that a relative decrease in ^{133}Cs ssNMR spectroscopy signals relating to the Cs II ($\delta_{Cs} \approx -67$ ppm) and Cs IV ($\delta_{Cs} \approx -100$ ppm) sites would be observed.[1, 10] In order to corroborate these potentially controversial findings, diffuse reflectance infrared Fourier transform

spectroscopy (DRIFTS) of adsorbed pyridine should be undertaken and compared to the results presented by Reule *et al*. and other contributors.[1, 6]

7.2. Preparation and characterisation of Sn-grafted MOR materials.

Following successful preparation of a library of dealuminated MOR materials containing various levels of tetrahedral site vacancies, a Sn grafting procedure utilising $SnCl_4$ under inert conditions was undertaken in order to introduce Sn atoms into the tetrahedral zeolite vacancy sites. The newly formed SnAl-MOR materials were characterised by ED-XRF spectroscopy, pXRD analysis, SEM imaging, ^{27}Al, ^{29}Si and ^{119}Sn ssNMR spectroscopy and DR-UV-Vis spectroscopy in order to assess Sn incorporation level and location alongside zeolite framework retention.

7.2.1. Test Sn grafting reaction on a wholly dealuminated BEA zeolite.

Before grafting of Sn was undertaken on prepared dealuminated MOR materials, a test grafting reaction on a wholly dealuminated BEA material was performed according to literature procedure and brief analysis undertaken to ensure the procedure was effective for Sn introduction and the resulting analysis of Sn–BEA closely resembled that previously reported by Vega-Vila *et al.* and van der Graaf *et al*..[24, 41] Briefly, a sample of zeolite Beta, H–BEA–(12.5), was subject to complete dealumination by overnight reaction with HNO_3 at 80 °C to yield H–BEA-deAl. Following dealumination, the sample was dried at 150 °C overnight under vacuum and subsequently treated with $SnCl_4$ in dry DCM at 60 °C overnight. The zeolite powder was separated by centrifugation and washed with methanol before being dried and calcined in order to yield Sn–BEA. Further experimental details are presented in Section 9.3.9.. The Sn grafting procedure was repeated on a separate sample of H–BEA-deAl in order to assess reproducibility of the grafting procedure, yielding Sn–BEA-rep. Table 7.6 shows the elemental compositions of H–BEA–(12.5), H–BEA-deAl, Sn–BEA and Sn–BEA-rep acquired by ED-XRF spectroscopy. Following the dealumination procedure, the aluminium content of H–BEA-deAl is seen to be reduced to effectively zero, implying successful total dealumination of the zeolite sample. Following Sn grafting, materials resulting from both repetitions are seen to possess a similar Sn loading, approximately 3.3 wt%, although with varying Si loadings, hence slightly differing Si/Sn ratios. Regardless, in both cases the Si/Sn ratio observed is much greater than the starting Si/Al ratio, suggesting that not all defect sites created during dealumination are filled by Sn following the grafting procedure. This is similar to literature reports in which Sn substitution efficiency is often seen to be incomplete.[24, 41] In order to ensure that the zeolite

framework structure was retained following dealumination and Sn grafting, pXRD analysis was undertaken and is presented in Figure 7.8. Here it is seen that the BEA framework reflections are successfully maintained following each synthetic step, implying no significant framework damage was caused by either dealumination or Sn grating procedures.

Table 7.6: Elemental composition and elemental ratios of H–BEA–(12.5), H–BEA-deAl, Sn–BEA and Sn–BEA-rep following calcination. ED–XRF values are averaged from three measurements and recorded as M wt%.

Sample	Metal Content / wt%			Molar Ratios	
	Si	Al	Sn	Si/Al	Si/Sn
H–BEA–(12.5)	50.53	4.15	—	11.7	—
H–BEA-deAl	55.61	< 0.1	—	>1000	—
Sn–BEA	54.20	0.44	3.32	118	69.1
Sn–BEA-rep	44.70	< 0.1	3.34	>1000	56.6

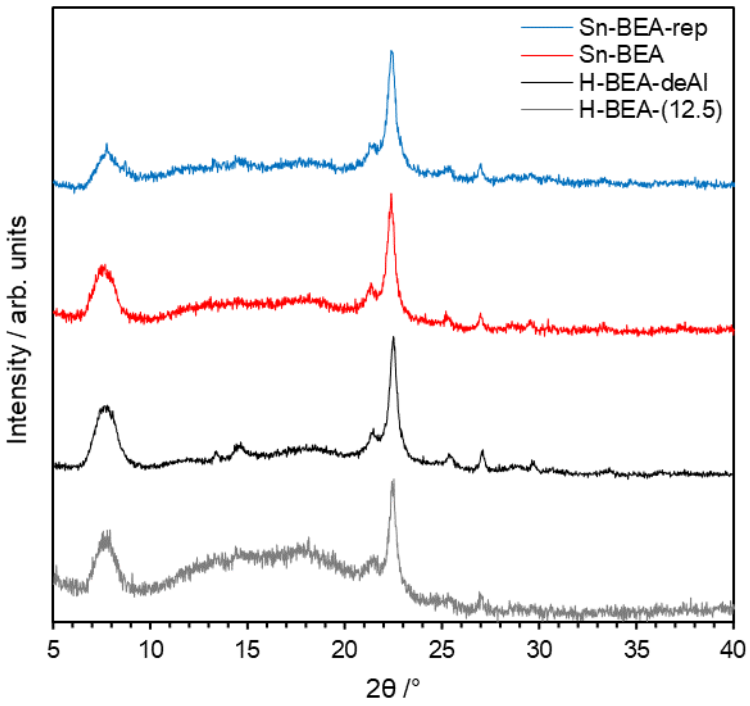

Figure 7.8: pXRD patterns in the 2θ = 5–40 ° region of H–BEA–(12.5), H–BEA-deAl, Sn–BEA and Sn–BEA-rep.

During the grafting procedure, the reactive $SnCl_4$/DCM/Zeolite suspension was decanted into centrifuge tubes and washed with methanol, hence atmospheric quenching of $SnCl_4$ could occur, resulting in the formation of extra-framework SnO_2. In order to assess whether Sn was successfully incorporated into the dealuminated BEA framework and if any extra-framework SnO_2 is present, ^{119}Sn ssNMR and DR-UV-Vis spectroscopies were undertaken. Figure 7.9 shows the DR–UV–Vis spectra for Sn–BEA, Sn–BEA-rep and common

oxides of tin that could be formed during the grafting or subsequent calcination procedure. Here it is seen that the both Sn–BEA spectra contain a single strong absorption band centred at 215–230 nm ascribed to the charge transfer transition between O^{2-} and Sn^{4+} which is indicative of framework coordinated metal atoms.[42-44] No major contributions matching those of either SnO_2 or SnO are observed, strongly suggesting that the Sn species within Sn–BEA reside predominantly in tetrahedral zeolite framework positions.

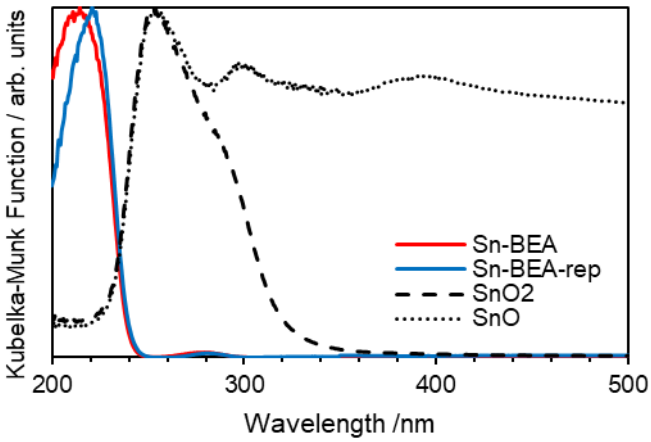

Figure 7.9: Normalised DR–UV–Vis spectra for Sn–BEA and Sn–BEA-rep following calcination. Included for comparison are spectra of potential extra-framework tin oxide materials that could form during Sn grafting or subsequent calcination.

Figure 7.10 shows the summed spikelet ^{1}H–^{119}Sn CP-CPMG ssNMR spectra of both calcined Sn–BEA materials. Spikelet spectra can be seen in Figure S7.2–3. Both materials exhibit a major resonance at approximately $\delta_{Sn} = -700$ ppm, typical of hydrated framework bound octahedral Sn species.[20, 45] Additionally, no major resonances at $\delta_{Sn} = -600$ ppm indicative of SnO_2 are identified, further suggesting the sole presence of framework Sn species. The spectra closely resemble those reported in the literature for framework bound Sn atoms in hydrated Sn–BEA materials.[20, 45]

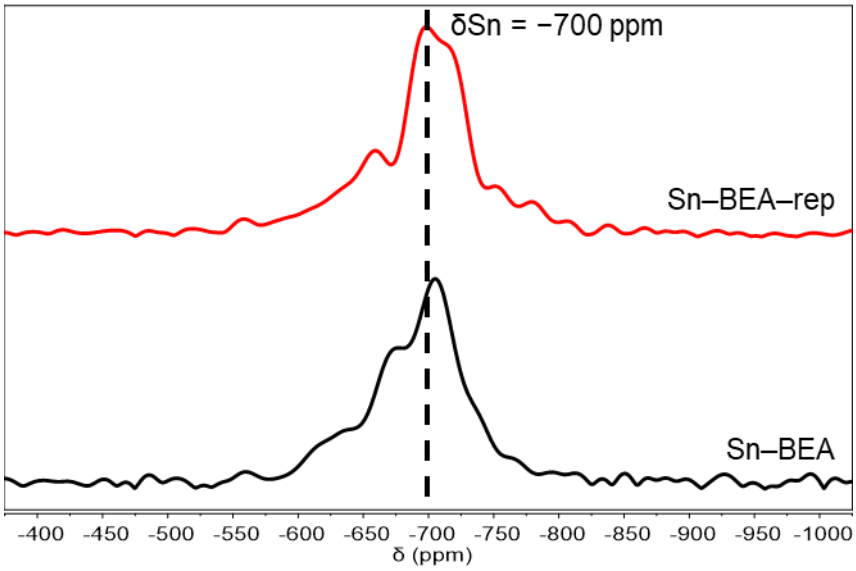

Figure 7.10: Spikelet sum ^{1}H–^{119}Sn CP-CPMG ssNMR spectra of Sn–BEA and Sn–BEA-rep averaged over 6400 and 25600 scans respectively with 2.0 s recycle delay and a 5 ms contact time. Spectrum acquired on a Bruker III Avance 400 MHz spectrometer using a 4 mm zirconia rotor. Spectrometer frequncies: ^{1}H = 400.17 MHz, ^{119}Sn = 149.12 MHz. MAS spin rate = 10000 Hz.

Additionally, the progress of Sn introduction was followed by ^{29}Si DE and ^{1}H–^{29}Si CP ssNMR spectroscopy. In both cases an enhancement of NMR signal intensity associated with Q_3 silanol groups (δ_{Si} = −102 ppm) would be expected following zeolite dealumination owing to introduction of larger numbers of silanol nests; the CP spectrum in particular should produce a large intensity increase owing to the increased presence of ^{1}H available for cross-polarisation. This enhancement should then be followed by a reduction in the Q_3 signal intensity when Sn is introduced into the newly formed vacancies (see Figure 7.3).[41] Figure 7.11 shows the overlaid ^{29}Si DE and ^{1}H–^{29}Si CP ssNMR spectra of H–BEA–(12.5), H–BEA-deAl and Sn–BEA. As expected, a large Q_3 intensity increase is observed following dealumination and a subsequent reduction is seen following Sn incorporation within the CP NMR spectra (Figure 7.11B). The ^{29}Si direct excitation NMR spectra of H–BEA–(12.5) appears to contain a large proportion of defects owing to its substantial Q_3 signal, although these span a broad range leading to convolution with the Q_4 signal and implying a wide range of defect type sites (Figure 7.11A). This may be a result of the zeolite being in the hydrated H–form, which could lead to the hydrolysis of Si–O–Al linkages and the apparent appearance of defect sites. The observed effect may be similar to that reported for ^{27}Al NMR spectra of hydrated H–form zeolites in which a resonance at δ_{Al} = 0 ppm is observed as previously described in Sections 7.1. and 2.1.3.1. Upon dealumination to H–BEA-deAl, the Q_3 and Q_4 signals become much more distinct implying that most silicon environments become discretely Q_3 or Q_4 owing to removal

of aluminium. Following remetallation with $SnCl_4$ to form Sn–BEA, the intensity of the Q_3 signal relative to the Q_4 decreases, implying defect filling by Sn atoms.[41]

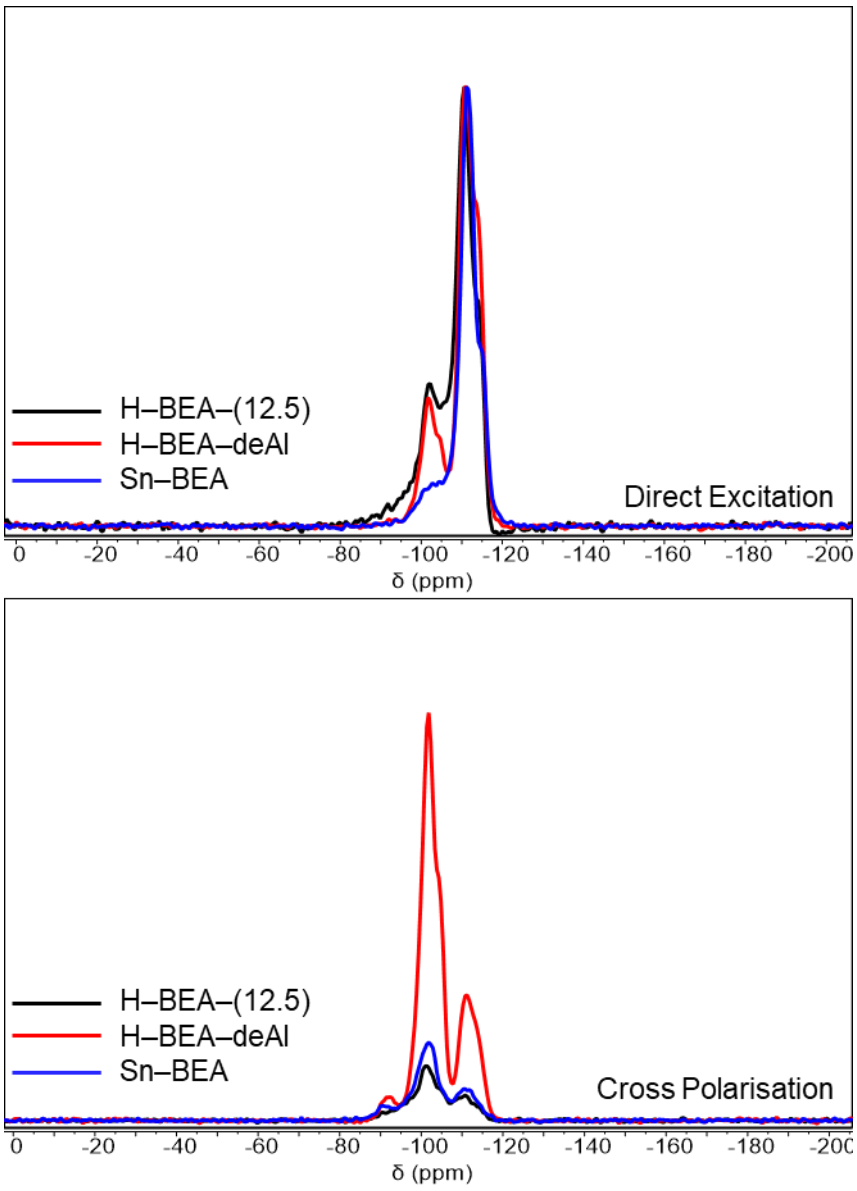

Figure 7.11: ^{29}Si direct excitation (top) and ^{1}H–^{29}Si cross polarisation (bottom) ssNMR spectra of H–BEA–(12.5), H–BEA-deAl and Sn–BEA. DE and CP spectra were averaged over 512 and 1800 transients respectively with a 60 s and 1.0 s recycle delay resepectively. Spectra were acquired on a Varian VNMRS 400 MHz spectrometer using a 6 mm zirconia rotor. Spectrometer frequency: ^{1}H = 399.88 MHz ^{29}Si = 79.44 MHz. MAS spin rate ≈ 6000 Hz.

7.2.2. Introduction of Sn heteroatoms into partially dealuminated MOR materials by a top-down grafting procedure.

Following successful Sn introduction into the tetrahedral vacancies of a wholly dealuminated BEA zeolite, the procedure was repeated with the partially dealuminated MOR samples from Section 7.1. As Sn grafting occurs on acidic sites, a set of control materials including Na–MOR–(7) and H–MOR–(7), were also subjected to the Sn grafting procedure to benchmark grafting onto surface silanol groups and zeolitic Brønsted acid sites respectively.

Briefly, the grafting procedure used was the same as that for Sn–BEA in Section 7.2.1. in which each sample was initially dried at 150 °C under vacuum overnight and subsequently treated with $SnCl_4$ in DCM at 60 °C overnight. Following washing with methanol, drying and calcination, Sn grafted materials were yielded. Further experimental details are presented in Section 9.3.9..

Table 7.7 contains elemental analysis data for materials resulting from Sn grafting on dealuminated MOR samples and control materials, Na–MOR–(7) and H–MOR–(7). Nomenclature is retained as including dealumination time for clarity. Herein it is observed that small amounts of Sn are present with the Sn grafted control materials, presumably either grafted to surface silanol groups or potentially existing as small portions of SnO_2 from atmospheric decantation during the grafting procedure (see Section 7.2.1). Each previously dealuminated MOR material shows a considerably higher Sn loading than the control materials following the grafting procedure, a trend which is reflected in a decrease of Si/Sn ratio. Additionally, a positive and expected trend is observed in that Sn loading is increased with increased dealumination. As was seen for Sn–BEA, not all vacancies formed during dealumination were filled by Sn following the grafting procedure, as the Si/(Al+Sn) ratio for each material does not reach that of the parent and the resulting T-site filling does not reach 100%.

Table 7.7: Elemental composition and elemental ratios of Na–MOR–(7), H–MOR–(7) and partially dealuminated MOR samples following Sn-grafting and subsequent calcination. ED–XRF values are averaged from three measurements and recorded as M wt%.

	Metal Content / wt%			Molar Ratios			
Sample	Si	Al	Sn	Si/Al	Si/Sn	Si/(Al+Sn)	**T-Site Filling**
Sn/Na–MOR–(7)	31.09	5.89	0.45	5.1	294.6	4.9	100%
Sn/H–MOR–(7)	36.54	6.59	0.16	5.3	961	5.3	100%
H–SnAl–MOR–1h	42.45	4.78	1.14	8.5	157.4	8.1	95%
H–SnAl–MOR–6h	38.42	3.60	1.20	10.2	135.6	9.5	93%
H–SnAl–MOR–18h	42.09	2.96	2.59	13.7	68.8	11.4	83%

In order to ensure zeolite framework retention and to assess for the presence of large deposits of tin oxides, pXRD analysis of the grafted samples was undertaken. Figure 7.12 shows the pXRD patterns of both control materials and dealuminated MOR samples following the Sn grafting procedure and subsequent calcination. All traces exhibit a good retention of the major reflections associated with the MOR framework, with no additional reflections owing to

formation of tin oxides, similar to the observations for Sn grafting of BEA materials in Section 7.2.1.. The intensity of reflections for Sn-grafted materials is substantially weaker than that seen for their dealuminated precursors, however this is predominantly attributed to reduction in particle size as opposed to a reduction in framework crystallinity. Each material produced was in the form of a very fine powder which, despite attempted pressing and sieving, did not retain large particulates. Additionally, the relative peak heights of each MOR associated reflection are very similar for all grafted materials, further implying retention of framework. On this basis it can be concluded that the Sn grafting procedure does not damage the zeolite framework, and no clusters of tin oxides sufficiently large to exhibit pXRD responses are formed. Additionally, Figure S7.4–7 show the pXRD transformation of each material throughout the total Sn substitution process, from parent and dealuminated states to Sn-grafted and calcined states. Herein it is observed that each material retains the major MOR framework reflections throughout the entire procedure.

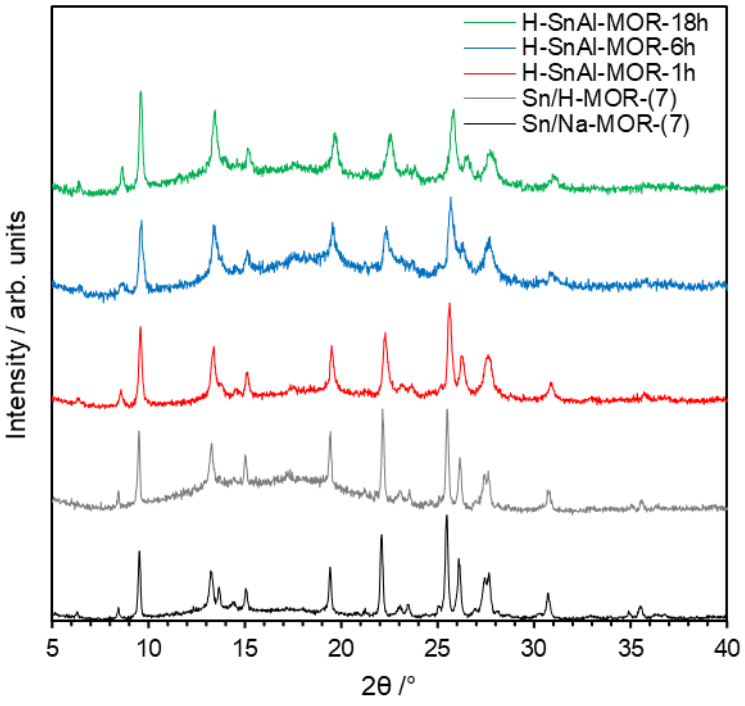

Figure 7.12: pXRD patterns in the 2θ = 5–40 ° region of Sn grafted Na–MOR–(7), H–MOR–(7) and partially dealuminated MOR samples following calcination. Where required, samples were pressed using a hand press before sieving in an attempt to produce particles of similar size to the parent materials.

Following confirmation of Sn inclusion and framework retention, DR-UV-Vis and ^{119}Sn ssNMR spectroscopic analyses were undertaken to assess the degree of Sn incorporation into the zeolite framework vacancies of dealuminated materials and to assess presence of extra-framework tin oxides for control and dealuminated materials. Figure 7.13 displays the

normalised DR-UV-Vis spectrum of H–SnAl–MOR–1h alongside common oxides of Sn.[vi] As for Sn–BEA in Section 7.2.1., framework Sn species are characterised in DR-UV-Vis spectroscopy by a strong absorption at approximately 220 nm pertaining to the strong charge transfer transition between O^{2-} and Sn^{4+} which is indicative of framework coordinated metal atoms.[42-44] As can be seen, H–SnAl–MOR–1h exhibits a sole major absorption at approximately 220 nm, highly suggestive of framework bound Sn^{4+} species. Small low-intensity adsorptions are seen at $\lambda > 300$ nm, but these are thought not to originate from any extra-framework tin oxide species.

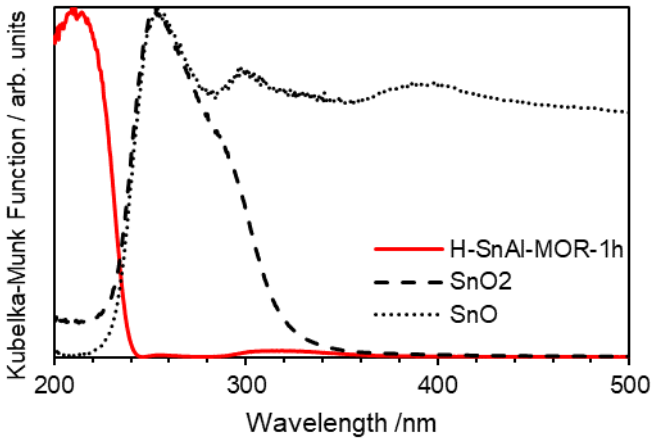

Figure 7.13: Normalised DR–UV–Vis spectrum for H-SnAl-MOR-1h following calcination. Included for comparison are spectra of potential extra-framework tin oxide materials that could form during Sn grafting or subsequent calcination

Additionally, ^{119}Sn ssNMR spectroscopic analysis was utilised to corroborate observations from DR-UV-Vis spectroscopy. As before for Sn–BEA in Section 7.2.1., hydrated framework Sn species are easily characterised by a resonance at $\delta_{Sn} = -700$ ppm, whilst extra-framework SnO_2 typically exhibits a resonance at approximately $\delta_{Sn} = -600$ ppm. Owing to ssNMR spectroscopy being highly sensitive to short-range local environment, the presence of small tin oxide clusters should be relatively easily detectable by a resonance at $\delta_{Sn} = -600$ ppm if present. Figure 7.14 shows the ^{1}H–^{119}Sn CP-CPMG ssNMR spectra for all Sn grafted materials following calcination and Figure S7.8 in this projects' supplementary information shows the same materials before calcination. Spikelet spectra for non-calcined and calcined materials may be found in Figure S7.9–11 and Figure S7.12–14 respectively. Due to the low Sn loadings, a spectrum of reasonable quality was not obtainable for Sn/Na–MOR–(7)

[vi] Unfortunately only data for H–SnAl–MOR–1h was able to be obtained. DR-UV-Vis spectra were acquired at Cardiff University and following the events of 2020/21, the remaining DR-UV-Vis spectra of Sn/H–MOR–(7), Sn/Na–MOR–(7), H–SnAl–MOR–6h and H–SnAl–MOR–18h were not able to be obtained before thesis submission.

or Sn/H–MOR–(7), despite employing extended experimental times and acquiring a higher number of transients. Generally, for all Sn-grafted dealuminated materials both as prepared and calcined, a strong resonance at approximately δ_{Sn} = −700 ppm is observed, with no significant SnO_2 character present. All non-calcined materials exhibit a slightly broader resonance, although it is still predominantly centred around δ_{Sn} = −700 ppm (Figure S7.8). This in tandem with DR-UV-Vis spectroscopy therefore allows conclusions that Sn is successfully introduced into the zeolite framework, most likely into the vacancies created by the previous dealumination process.

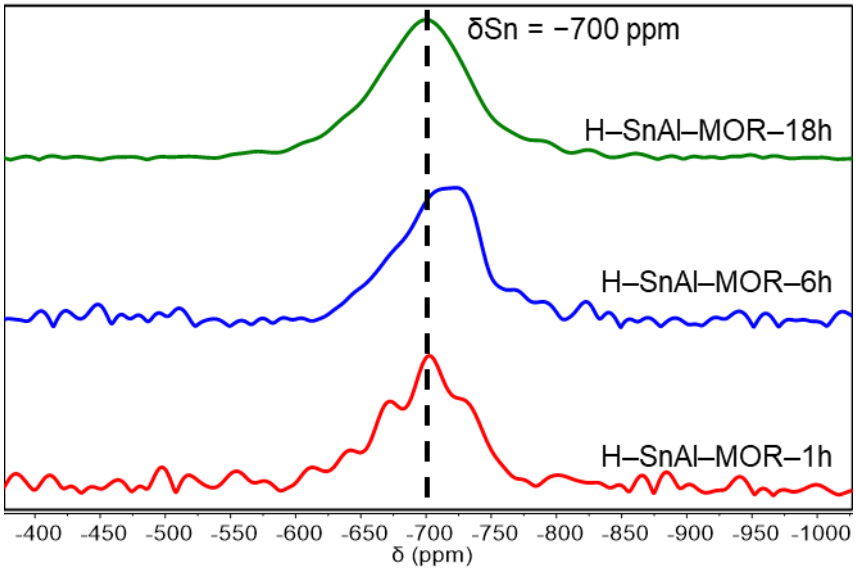

Figure 7.14: Spikelet sum ^{1}H–^{119}Sn CP-CPMG ssNMR spectra of H–SnAl–MOR–1h, H–SnAl–MOR–6h and H–SnAl–MOR–18h following calcination averaged over 40800, 33088 and 28800 scans with 2.0, 2.0 and 1.0 s recycle delays respectively and a 5 ms contact time. Spectra acquired on a Bruker III Avance 400 MHz spectrometer using a 4 mm zirconia rotor. Spectrometer frequencies: ^{1}H = 400.17 MHz, ^{119}Sn = 149.12 MHz. MAS spin rate = 10000 Hz.

In order to further confirm Sn speciation within SnAl–MOR materials, it would be desirable to undertake XAS analysis of the Sn K-edge (29210 eV).[46] Specifically, the use of EXAFS analysis would assist greatly in probing the local co-ordination of Sn atoms. Primarily, comparison of Sn–O–Si and Sn–O–Sn pathways would allow conclusions to be drawn as to whether Sn is framework-included or present in extra framework nanoclusters (SnO_2, SnO) too small to be detected by pXRD analysis or DR–UV–Vis and ^{119}Sn ssNMR spectroscopies. Additionally, the location of Sn atoms in specific tetrahedral sites (MOR-T_x) may be able to be discerned as was achieved for Sn–BEA by Bare *et al.*[46]

7.3. Catalytic activity of Sn/Al MOR containing Sn in various frameworks tetrahedral sites.

In order to prepare the H–deAl–MOR and H–SnAl–MOR materials for ethanol to butadiene catalysis, the H^+ cations were first exchanged to Rb^+ as it had previously been proven to be the optimal counter-cation in Chapter 4 with regard to exchangeability and acetaldehyde selectivity in MOR. The materials were exchanged five times with an aqueous 0.3 M $RbNO_3$ solution as described in Section 9.3.2. Table 7.8 shows the relevant elemental compositions and ratios of the Rb-exchanged materials. As can be seen, all dealuminated materials underwent full exchange with Rb, resulting in Rb/Al ratios of 1.07, 1.09 and 1.05 for samples dealuminated for 1 h, 6 h and 18 h respectively. The Sn remetallated materials, however, exhibited non-complete exchange of H^+ with Rb^+, potentially owing to pore blockage resulting from Sn insertion. Rb exchange levels of 73%, 73% and 84% were obtained for Rb-SnAl–MOR–1h, Rb-SnAl–MOR–6h and Rb-SnAl–MOR–18h respectively (Table 7.8).

Table 7.8: Elemental composition and elemental ratios of Rb-exchanged partially dealuminated and remetallated MOR samples. ED–XRF values are averaged from three measurements and recorded as M wt%.

Sample	Elemental Loading / wt%				Elemental Ratios		
	Si	Al	Sn	Rb	Si/Al	Si/Sn	Rb/Al
Rb-deAl–MOR–1h	36.56	3.40	0.00	11.53	10.3	–	1.07
Rb-deAl–MOR–6h	36.57	2.82	0.00	9.71	12.5	–	1.09
Rb-deAl–MOR–18h	40.25	2.31	0.00	7.70	16.7	–	1.05
Rb-SnAl–MOR–1h	33.68	3.27	1.13	7.55	9.9	126	0.73
Rb-SnAl–MOR–6h	33.43	2.66	1.24	6.12	12.1	114	0.73
Rb-SnAl–MOR–18h	34.52	1.99	2.43	5.28	16.6	60	0.84

Before introduction of 3.5 wt% Zn, ^{27}Al and ^{119}Sn ssNMR spectroscopies were undertaken for a final time on all samples to ensure that the T-site inclusion was retained following the Sn introduction and Rb-exchange processes. Figure 7.15 and Figure 7.16 show the ^{27}Al ssNMR spectra of Rb–deAl–MOR and Rb–SnAl–MOR samples respectively. For all Rb–deAl–MOR samples a lone resonance at δ_{Al} = 60 ppm is detected, indicative of aluminium in framework positions only (Figure 7.15). For all Rb–SnAl–MOR samples a major resonance at δ_{Al} = 60 ppm is detected which also comprises a high-field shoulder alongside a very minor resonance at δ_{Al} = 0 ppm (Figure 7.16). This observation is likely resultant from a small proportion of residual Brønsted acid sites likely in the form of octahedral Al within the material as opposed to extra-framework alumina species.[32] Figure 7.17 shows the spikelet summed ^{1}H–^{119}Sn CP-CPMG ssNMR spectra of Rb–SnAl–MOR–1h, Rb–SnAl–MOR–6h and Rb–SnAl–MOR–18h following calcination, spikelet spectra may be seen in Figure S7.15–17. A strong resonance at approximately δ_{Sn} = −700 ppm is observed for all materials with no significant SnO_2 character present (δ_{Sn} = −600 ppm), therefore allowing the conclusion that all Sn species are retained within the zeolite framework following Rb-exchange.

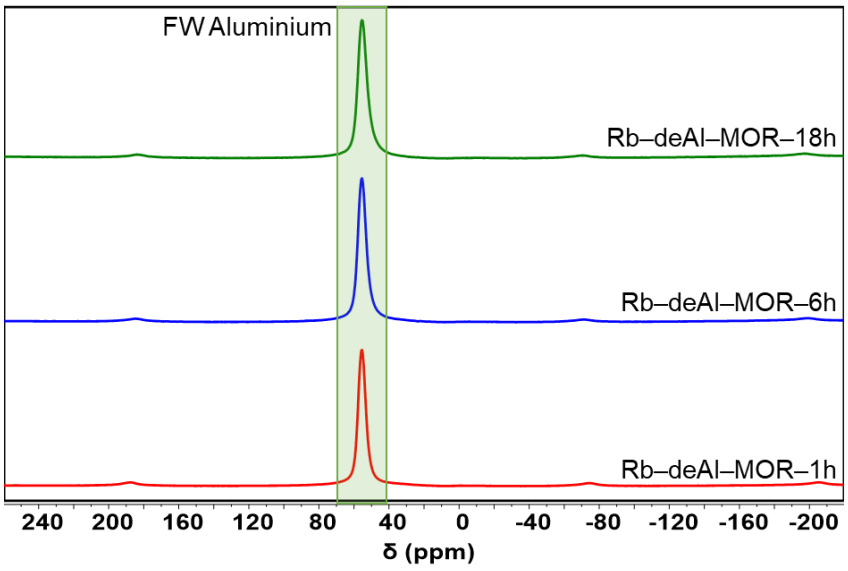

Figure 7.15: ^{27}Al ssNMR spectra of Rb–deAl–MOR–1h, Rb–deAl–MOR–6h and Rb–deAl–MOR–18h. Spectra were averaged over 10000 scans with a 0.2 s recycle delay. Spectra were acquired on a Varian VNMRS 400 MHz spectrometer using a 4 mm zirconia rotor. Spectrometer frequency: ^{27}Al = 104.20 MHz. MAS spin rate ≈ 14000 Hz.

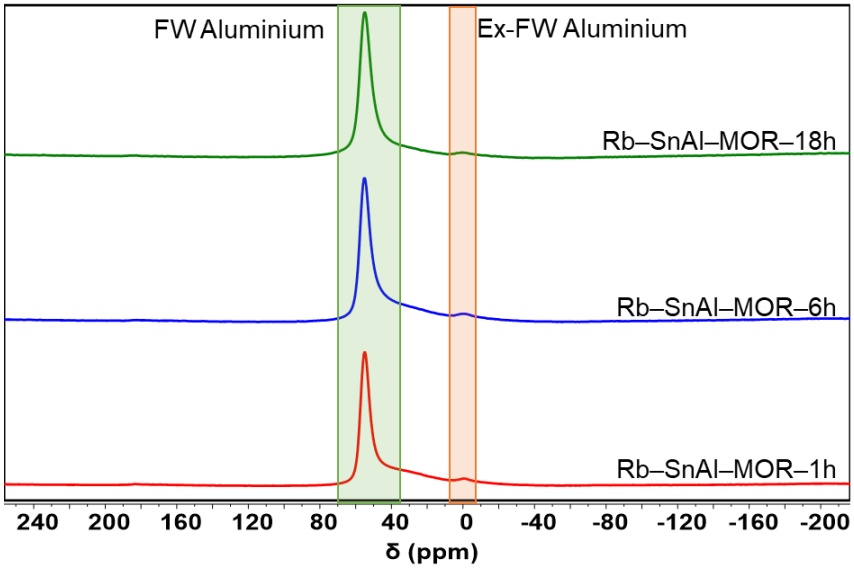

Figure 7.16: ^{27}Al ssNMR spectra of Rb–SnAl–MOR–1h, Rb–SnAl–MOR–6h and Rb–SnAl–MOR–18h. Spectra were averaged over 10000 scans with a 0.2 s recycle delay. Spectra were acquired on a Varian VNMRS 400 MHz spectrometer using a 4 mm zirconia rotor. Spectrometer frequency: ^{27}Al = 104.20 MHz. MAS spin rate ≈ 14000 Hz.

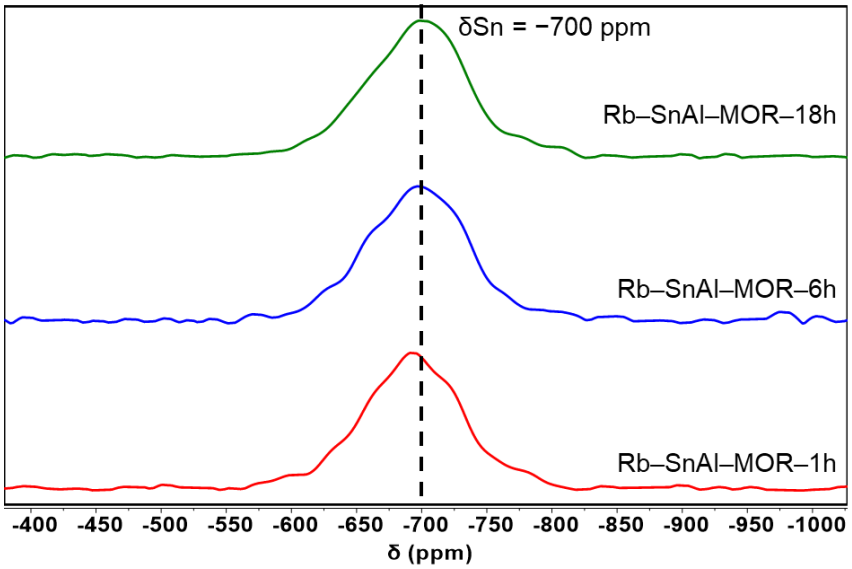

Figure 7.17: Spikelet sum ^{1}H–^{119}Sn CP-CPMG ssNMR spectra of Rb–SnAl–MOR–1h, Rb–SnAl–MOR–6h and Rb–SnAl–MOR–18h following calcination averaged over 65536, 32768 and 32768 scans respectively with a 1.0 s recycle delay and a 5 ms contact time. Spectra acquired on a Bruker III Avance 400 MHz spectrometer using a 4 mm zirconia rotor. Spectrometer frequncies: ^{1}H = 400.17 MHz, ^{119}Sn = 149.12 MHz. MAS spin rate = 10000 Hz.

Following confirmation of Sn and Al location, each Rb-exchanged dealuminated and Sn remetallated species was impregnated with a nominal 3.5 wt% Zn using a standard wetness impregnation technique as detailed in Section 9.3.3.. Table 7.9 details the relevant elemental loadings and elemental ratios as determined by ED-XRF analysis for all ZnO/Rb–deAl–MOR and ZnO/Rb–SnAl–MOR materials. Due to the small masses of ZnO/Rb-SnAl–MOR materials produced, analysis by ICP-OES was also undertaken in order to corroborate results and is

included in Table 7.9. Additionally, elemental analysis of ZnO/Rb–MOR–(7) is included to act as a standard and point of comparison for future catalysis reactions. For all ZnO/Rb-deAl–MOR materials a Rb/Al ratio of approximately 1 is retained following Zn impregnation and Si/Al ratios remain relatively unchanged from previous preparatory steps. Additionally, all dealuminated materials were successfully impregnated within an acceptable range of between 3–4 wt% Zn as targeted. Following ZnO impregnation, the Si/Sn ratios of ZnO/Rb-SnAl–MOR materials are relatively unaffected compared to Rb-SnAl–MOR materials, however both Si/Al and Rb/Al ratios are observed to decrease. This may suggest that some Al is being removed from the framework alongside potential exchange of Rb^{+} cations for Zn^{2+}. Alternatively, Zn^{2+} may begin to occupy vacant T-sites available from non-complete Sn incorporation, similar to that reported previously in the literature for Zn^{2+} incorporation into dealuminated BEA.[47-49] Analysis by DR-UV-Vis spectroscopy or XAS would likely be required to further investigate this suggestion.

Table 7.9: Elemental composition and relevant elemental ratios of Zn-impregnated and Rb-exchanged partially dealuminated and remetallated MOR samples. ED–XRF values are averaged from three measurements and recorded as M wt%. ICP-OES analysis of ZnO/Rb-SnAl–MOR was also undertaken due to the small masses of each materials produced.

Sample	Elemental Loading / wt%					Elemental Ratios		
	Si	Al	Sn	Rb	Zn	Si/Al	Si/Sn	Rb/Al
ZnO/Rb–MOR–(7)	27.05	4.21	0.00	17.56	3.39	6.4	–	1.31
ZnO/Rb-deAl–MOR–1h	31.48	2.98	0.00	9.67	3.34	10.6	–	1.02
ZnO/Rb-deAl–MOR–6h	27.09	2.17	0.00	6.91	3.14	12.5	–	1.00
ZnO/Rb-deAl–MOR–18h	32.71	1.93	0.00	6.34	3.73	16.9	–	1.03
ED-XRF Values								
ZnO/Rb-SnAl–MOR–1h	28.84	3.01	0.96	6.10	2.87	9.2	127	0.64
ZnO/Rb-SnAl–MOR–6h	30.39	2.87	1.11	5.04	3.06	10.2	116	0.56
ZnO/Rb-SnAl–MOR–18h	33.69	2.41	2.22	4.77	3.37	13.4	64	0.63
ICP-OES Values								
ZnO/Rb-SnAl–MOR–1h	27.96	3.49	0.86	6.04	3.41	7.7	137	0.55
ZnO/Rb-SnAl–MOR–6h	31.40	3.11	1.03	5.31	3.60	9.7	129	0.54
ZnO/Rb-SnAl–MOR–18h	29.92	2.24	1.96	4.49	3.52	12.8	65	0.63

Initially, the catalytic activity of ZnO/Rb-deAl–MOR materials was assessed and compared to ZnO/Rb–MOR in order to determine the effect of dealumination on the ethanol dehydrogenation reaction. Figure 7.18 shows selectivities for acetaldehyde (A), ethylene (B) and diethyl ether (C) alongside ethanol conversion (D) for ZnO/Rb-deAl–MOR materials at 350 °C for 4 h TOS. Despite similar acetaldehyde productivities across all tested materials (Figure S7.18), the selectivity to acetaldehyde is dramatically lower following dealumination of the MOR materials. Further, the selectivities to acid catalysed products (ethylene and diethyl ether) are considerably higher at similar conversion values for dealuminated materials (40% vs 3.5% for diethyl ether and 35% vs 1.2% for ethylene). It is therefore concluded that, the process of dealumination introduces acidic sites to the materials in the form of silanol nests. The new acidic sites are suggested to be Brønsted acidic in nature as supported by the absence of butadiene productivity, which should likely only be observed if a Lewis acidic site capable of performing the aldol condensation reaction is present. Further, it is concluded that Zn is not incorporated into silanol nest as reported by Qi *et al*. for dealuminated BEA owing to the lack of Lewis acidic reactivity, although further spectroscopic evidence, such as pyridine adsorption FTIR, would be required to further prove this hypothesis.[49] The initial ethanol conversion increase from around 40% to 70% for dealuminated materials when compared to ZnO/Rb–MOR likely results from the additional acid catalysed reactions forming ethylene and diethyl ether owing to the similar acetaldehyde productivity resulting from ZnO species. Table 7.10 shows the coking level of ZnO/Rb-deAl–MOR materials following reaction. Each ZnO/Rb-deAl–MOR material exhibits a carbon loading of around 4 wt% which is significantly higher than the 1.7 wt% recorded for ZnO/Rb–MOR–(7) under identical conditions. The increased carbon laydown is likely resultant from aromatisation of formed ethylene as carbon laydown and ethylene productivity would appear to be correlated as shown in Chapters 4 and 5.[50-52]

A further observation of interest is the similarity of activity between each dealuminated material despite their varying Si/Al ratios and variation in silanol nest density. It would not be unreasonable to assume that as dealumination progresses and more silanol nests are introduced, the selectivity to, and productivity of, acid catalysed products would increase further, particularly when operating below 100% conversion. This, however, is not observed as can be seen in Figure 7.18, Figure S7.18 and Figure S7.19. A hypothesis for this observation could relate to the location at which aluminium is removed from each material as determined by ^{133}Cs ssNMR spectroscopy in Section 7.1. If it is the case that T_1 aluminium is selectively removed followed by all other sites, it may be possible to suggest that silanol nests in the T_1 position are

particularly active for ethanol dehydration reactions. In this case it may be concluded that silanol nests in all other sites have a negligible effect on ethanol dehydration rates. Further evidence by analysis of Py- and CD_3CN-DRIFTS would be required to confirm the presence of silanol vacancy sites.[1]

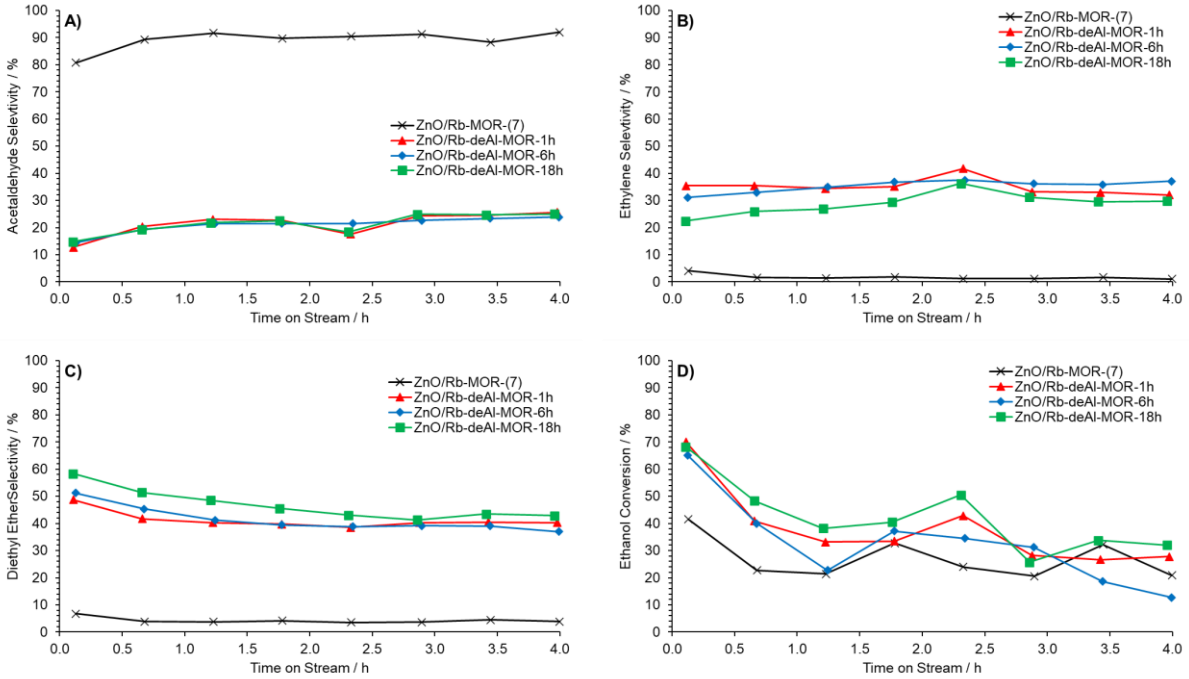

Figure 7.18: Acetaldehyde selectivity (A), ethylene selectivity (B), diethyl ether selectivity (C) and ethanol conversion (D) for ZnO/Rb–MOR–(7) (×), ZnO/Rb-deAl–MOR–1h (▲), ZnO/Rb-deAl–MOR–6h (♦) and ZnO/Rb-deAl–MOR–18h (■) at 350 °C for 4 h TOS. Catalyst mass = 0.150 g. Ethanol feed rate = 0.390 mmol min^{-1}. Detection Columns: RTX-VMS + ShinCarbon ST.

Table 7.10: Catalyst coking (C wt%) of ZnO/Rb-deAl–MOR catalysts following ethanol reaction at 350 °C as determined by CHN microanalysis.

Sample	Catalyst Coking (C Wt%)
ZnO/Rb–MOR–(7.0)	1.69
ZnO/Rb–deAl–MOR–1h	4.35
ZnO/Rb–deAl–MOR–6h	4.55
ZnO/Rb–deAl–MOR–18h	4.07

Subsequently, the potential for ZnO/Rb-SnAl–MOR to convert ethanol to butadiene was assessed under flow conditions. Figure 7.19 shows selectivities for acetaldehyde (A), butadiene (B), ethylene (C) and diethyl ether (D) alongside ethanol conversion (E) for ZnO/Rb-SnAl–MOR materials at 350 °C for 4 h TOS. Table 7.11 shows the catalyst coking levels

following reaction. Unfortunately, no considerable selectivity to butadiene is observed for any of the bimetallic materials, all of which exhibited a selectivity no greater than 0.30 % (Figure 7.19B). As may be expected, the overall selectivity to acetaldehyde for each material is relatively unchanged (approximately 30%) as it is not consumed within the cascade reaction. The selectivity to acetaldehyde is lower for ZnO/Rb-SnAl–MOR–18h at around 15%, although the acetaldehyde productivities of each material are similar (Figure S7.20). Further, the selectivity to ethylene for ZnO/Rb-SnAl–MOR–1h and ZnO/Rb-SnAl–MOR–6h is relatively unchanged following Sn introduction, although a short induction period of increased ethylene selectivity is observed for both materials. Overall, ZnO/Rb-SnAl–MOR–1h and ZnO/Rb-SnAl–MOR–6h do not perform too dissimilarly from their dealuminated analogues, with the exception of a small induction period of heightened ethylene productivity at low TOS. ZnO/Rb-SnAl–MOR–18h exhibits an overall greater selectivity to ethylene which is retained over 4h TOS. An explanation for the differing reactivity of ZnO/Rb-SnAl–MOR–18h may be that the MOR framework undergoes a structural reorganisation by recombination of silanol groups following significant dealumination, as suggested by Bodart *et al*., although such a framework change would also be expected to be reflected in the catalytic testing of ZnO/Rb-deAl–MOR–18h.[10] Alternatively, a greater number of open, hydrolysed Sn sites may be present in ZnO/Rb-deAl–MOR–18h, a feature that could be probed by infrared spectroscopy of adsorbed CD_3CN.[53]

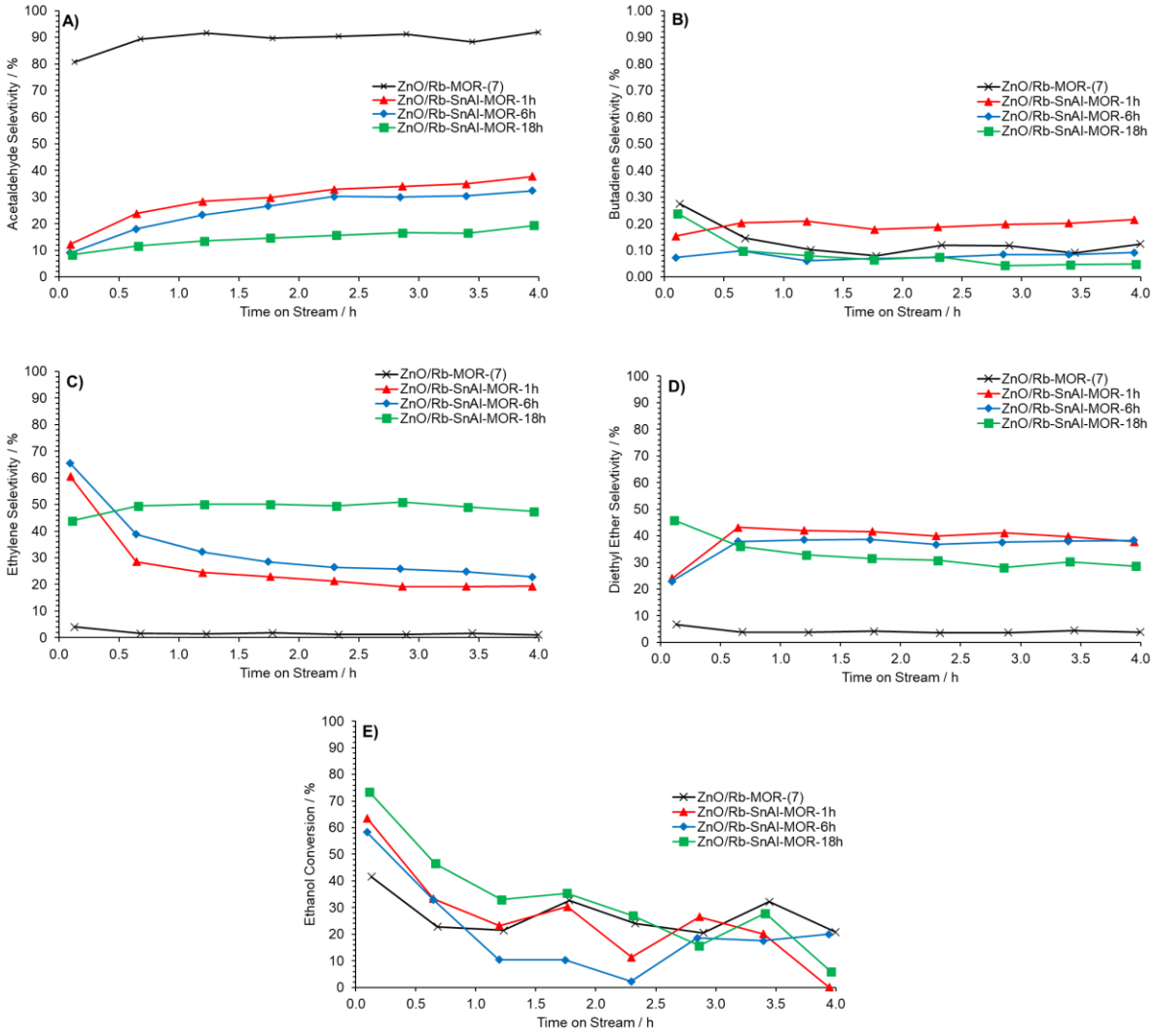

Figure 7.19: Acetaldehyde selectivity (A), butadiene selectivity (B), ethylene selectivity (C), diethyl ether selectivity (D) and ethanol conversion (E) for ZnO/Rb–MOR–(7) (×), ZnO/Rb-SnAl–MOR–1h (▲), ZnO/Rb-SnAl–MOR–6h (♦) and ZnO/Rb-SnAl–MOR–18h (■) at 350 °C for 4 h TOS. Catalyst mass = 0.150 g. Ethanol feed rate = 0.390 mmol min^{-1}. Detection Columns: RTX-VMS + ShinCarbon ST.

Table 7.11: Catalyst coking (C wt%) of ZnO/Rb-SnAl–MOR catalysts following ethanol reaction at 350 °C as determined by CHN microanalysis.

Sample	Catalyst Coking (C Wt%)
ZnO/Rb–MOR–(7.0)	1.69
ZnO/Rb–SnAl–MOR–1h	4.29
ZnO/Rb–SnAl–MOR–6h	2.96
ZnO/Rb–SnAl–MOR–18h	3.80

In order to probe the difference in reactivity between ZnO/Rb-SnAl–MOR materials, Al and Sn speciation were reassessed following reaction by means of ^{27}Al and ^{119}Sn ssNMR

spectroscopies. Figure 7.20 shows the ^{27}Al ssNMR spectra of each spent ZnO/Rb–SnAl–MOR material in which each exhibits a sole resonance centred at $\delta_{Al} \approx 60$ ppm with minor upfield broadening. This result suggests that the vast majority of aluminium is retained in tetrahedral framework positions with some minor contribution from five co-ordinate environments. Figure 7.21 shows the spikelet sum ^{1}H–^{119}Sn CP-CPMG ssNMR spectra of spent ZnO/Rb–SnAl–MOR materials, spikelet spectra may be seen in Figure S7.21–23. Whereas a standard hydrated sample containing Sn in framework positions would be expected to exhibit a sole resonance centred around $\delta_{Sn} \approx -700$ ppm, each spent material instead exhibits multiple convoluted bands. In each case, a contribution centered around $\delta_{Sn} = -700$ ppm is observed, implying some retention of hydrated framework Sn species. Specifically, the band centered at around $\delta_{Sn} = -689$ ppm may be ascribed to Sn centres which have dissociately adsorbed water, potentially resulting in Brønsted acidic sites which may be responsible for ethanol dehydration reactions.[20] The contribution centered at around $\delta_{Sn} = -650$ ppm is as yet unconfirmed although several possibilities have been wholly or partially ruled-out. Primarily, no sharp resonance at $\delta_{Sn} = -604$ ppm is detected, confirming the lack of SnO_2 species.[20] Adsorption of ethanol to Sn sites following catalysis is also unlikely as the work of Yakimov *et al*. would suggest that adsorption of alcohols to Sn sites cause a resonance shift to around $\delta_{Sn} = -580$ ppm.[20] Other potential solutions to the signal at $\delta_{Sn} = -650$ ppm could be adsorption of other intermediates or assocaition of carbonaceous depsits, both of which would require further ssNMR experiments to confirm.

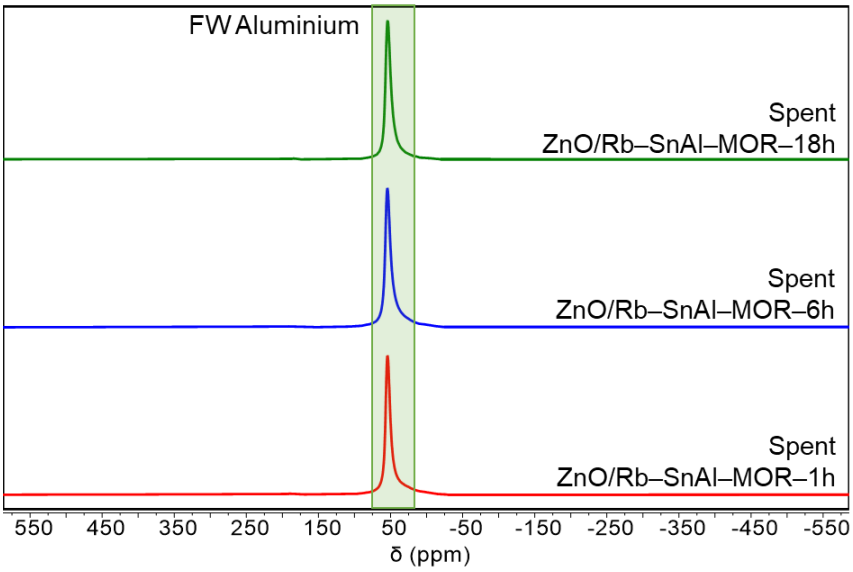

Figure 7.20: ^{27}Al ssNMR spectra of spent ZnO/Rb–SnAl–MOR–1h, ZnO/Rb–SnAl–MOR–6h and ZnO/Rb–SnAl–MOR–18h. Spectra were averaged over 10000 scans with a 0.2 s recycle delay. Spectra were acquired on a Varian VNMRS 400 MHz spectrometer using a 4 mm zirconia rotor. Spectrometer frequency: ^{27}Al = 104.20 MHz. MAS spin rate ≈ 14000 Hz.

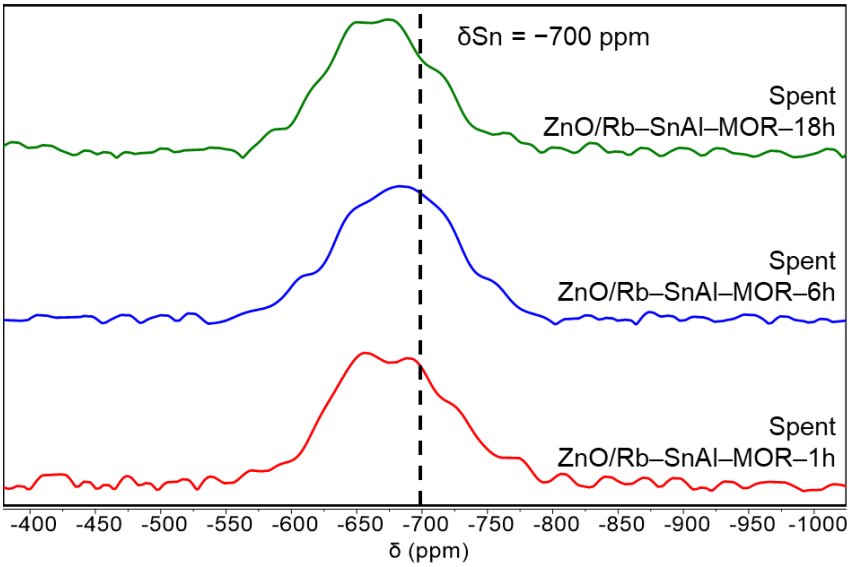

Figure 7.21: Spikelet sum ^{1}H–^{119}Sn CP-CPMG ssNMR spectra of spent ZnO/Rb–SnAl–MOR–1h, ZnO/Rb–SnAl–MOR–6h and ZnO/Rb–SnAl–MOR–18h following calcination averaged over 65536, 57344 and 25600 scans respectively with a 1.0 s recycle delay and a 5 ms contact time. Spectra acquired on a Bruker III Avance 400 MHz spectrometer using a 4 mm zirconia rotor. Spectrometer frequncies: ^{1}H = 400.17 MHz, ^{119}Sn = 149.12 MHz. MAS spin rate = 10000 Hz.

7.4. Conclusions.

Dealumination of Na–MOR–(7) to various extents was successfully achieved by treatment in HNO_3 as reported by Reule *et al.*[1] Partially dealuminated MOR materials (deAl–MOR) with Si/Al ratios of 8.5, 10.8 and 16.4 were achieved by treatments times of 1, 6 and 18 h respectively. pXRD analysis implied retention of a MOR framework whilst ^{27}Al ssNMR spectroscopy showed that all remaining Al was included in tetrahedral framework positions. Following Cs^+ exchange of deAl–MORs, ^{133}Cs ssNMR was undertaken in order to identify whether dealumination had been selective for T_3 and T_4 sites, as was initially targeted by the dealumination method. Evidence gathered following mass-normalisation and deconvolution of the ^{133}Cs ssNMR spectra based upon the centre bands and first order side bands suggested that, in this work, Al was initially removed from the T_1 site, followed by removal from all other sites equally. These observations do not corroborate with the existing literature, hence further analysis such as Py-DRIFTS would be required to strengthen the conclusions presented.[1]

Following exchange to the Rb^+ form and impregnation with ZnO to form ZnO/Rb–deAl–MOR, each material was tested for its catalytic conversion of ethanol at 350 °C under flow conditions. All ZnO/Rb–deAl–MOR materials produced product distributions consistent with Brønsted acidic ethanol dehydration which is anticipated to be resultant from acidic silanol nests present following dealumination, similar to that observed by Qi *et al.* over dealuminated BEA zeolite.[49] Whilst some acetaldehyde productivity from ethanol dehydrogenation over ZnO

was retained, the overall selectivity to and productivity of acetaldehyde was significantly lower for dealuminated materials compared to ZnO/Rb–MOR–(7), likely resulting from increased competition from ethanol dehydration pathways. Despite more extensive dealumination all ZnO/Rb–deAl–MOR materials behaved in a remarkably similar way with similar selectivites to major products at comparable conversion levels. Ethylene and diethyl ether productivities are observed to increase marginally with extended dealumination, although not in a manner proportional to silanol nest content. Paired with conclusions from ^{133}Cs ssNMR spectroscopic analysis, this may allow the conclusion that silanol nests in the T_1 position are particularly active for Brønsted acidic ethanol dehydration.

Following successful testing of the Sn–remetallation strategy for Sn–BEA, each of the H–deAl–MOR materials was successfully remetallated with $SnCl_4$ in DCM as evidenced by DR-UV-Vis and ^{119}Sn ssNMR spectroscopies confirming Sn presence solely in hydrated framework positions as reported for Sn–BEA.[24-26] Similar to the literature for Sn–BEA, remetallation efficiency was not 100% (see Table 7.7) which likely leads to the remaining presence of Brønsted acidic silanol nests in the grafted SnAl–MOR materials.[24, 41] Additionally, the remetallation efficacy of dealuminated materials is observed to decrease with greater extents of dealumination. Further analysis of Sn speciation could be achieved by means of XAS analysis of the Sn K-edge to identify tetrahedral site location (T_x) and better define local environments.[46] Additionally, dehydration of remetallated SnAl–MOR materials before adsorption of ethanol and acetaldehyde may allow further conclusions to be drawn regarding Sn acidity type and strength.[20]

Unfortunately, catalytic ethanol conversion over ZnO/Rb–SnAl–MOR materials at 350 °C revealed no significant production of butadiene, suggesting a lack of activity of Sn as a Lewis acidic centre in this application. In the cases of ZnO/Rb–SnAl–MOR-1h and ZnO/Rb–SnAl–MOR-6h, the materials predominantly behaved in a similar manner to their dealuminated counterparts, with the exception of an induction period of higher ethylene productivity at TOS < 2.0 h. ZnO/Rb–SnAl–MOR-18h behaved in a more dissimilar way, achieving an ethylene selectivity of around 50% compared to 25% for its dealuminated analogue, an observation likely resulting from a higher proportion of Brønsted acidic sites within the material, speculatively owing to introduction of hydrolysed Sn sites which could be probed by IR spectra of adsorbed CD_3CN.[53] Exact identification of T_x site distribution of Sn atoms by FTIR methods would aid the preceding conclusions further. For example, if it could be confirmed that Sn was present mainly in T_1 sites, efforts to selectively introduce Sn into T_3 sites may yield differing

reactivities and product selectivities. Alternatively, hydrothermal synthesis of a mixed SnAl–MOR materials with minimal defect vacancies and evenly distributed Sn atoms may yield a material better able to perform the aldol condensation of acetaldehyde.[23]

Overall, the dealumination-remetallation strategy attempted within this chapter to form mixed SnAl–MOR materials was successful, although the resulting materials application to the ethanol-to-butadiene cascade reaction were not. Additional confirmation as to site selectivity of dealumination and remetallation would be required by means of DRIFT spectroscopy of probe molecules, such as pyridine, to elicit further conclusions.[1, 10] The unsuccessful catalytic tests likely owe to excess Brønsted acidic sites resulting from a combination of residual silanol nests from dealumination and hydrolysed Sn species forming ethylene and diethyl ether from ethanol preferentially.

7.5. References.

1. A. A. C. Reule, J. A. Sawada and N. Semagina, *J. Catal.*, 2017, **349**, 98–109.
2. Database of Zeolite Structures, http://www.iza-structure.org/databases/, (accessed 25/04/2018).
3. J. L. Schlenker, J. J. Pluth and J. V. Smith, *Mater. Res. Bull.*, 1978, **13**, 901–905.
4. W. J. Mortier and I. Z. A. S. Commission, *Compilation of extra framework sites in zeolites*, Butterworth Scientific Limited on behalf of the Structure Commission of the International Zeolite Association, 1982.
5. M. Boronat, C. Martínez-Sánchez, D. Law and A. Corma, *J. Am. Chem. Soc.*, 2008, **130**, 16316–16323.
6. H. Xue, X. Huang, E. Zhan, M. Ma and W. Shen, *Catal. Commun.*, 2013, **37**, 75–79.
7. P. Cheung, A. Bhan, G. J. Sunley, D. J. Law and E. Iglesia, *J. Catal.*, 2007, **245**, 110–123.
8. A. Bhan, A. D. Allian, G. J. Sunley, D. J. Law and E. Iglesia, *J. Am. Chem. Soc.*, 2007, **129**, 4919–4924.
9. P. C. Van Geem, K. F. M. G. J. Scholle, G. P. M. Van der Velden and W. S. Veeman, *J. Phys. Chem.*, 1988, **92**, 1585–1589.
10. P. Bodart, J. B. Nagy, G. Debras, Z. Gabelica and P. A. Jacobs, *J. Phys. Chem.*, 1986, **90**, 5183–5190.
11. J. Liu, H. Xue, X. Huang, P.-H. Wu, S.-J. Huang, S.-B. Liu and W. Shen, *Chin. J. Catal.*, 2010, **31**, 729–738.
12. J. Nagano, T. Eguchi, T. Asanuma, H. Masui, H. Nakayama, N. Nakamura and E. G. Derouane, *Micropor. Mesopor. Mater.*, 1999, **33**, 249–256.
13. J. D. Lewis, M. Ha, H. Luo, A. Faucher, V. K. Michaelis and Y. Román-Leshkov, *ACS Catal.*, 2018, **8**, 3076–3086.
14. C. Hammond, S. Conrad and I. Hermans, *Angew. Chem.*, 2012, **51**, 11736–11739.
15. J. S. Bates, B. C. Bukowski, J. W. Harris, J. Greeley and R. Gounder, *ACS Catal.*, 2019, **9**, 6146-6168.
16. S. G. Elliot, I. Tosi, S. Meier, J. S. Martinez-Espin, S. Tolborg and E. Taarning, *Catal. Sci. Technol.*, 2019, **9**, 4339–4346.
17. C. Xia, Y. Liu, M. Lin, X. Peng, B. Zhu and X. Shu, *Catal. Today*, 2018, **316**, 193–198.
18. B. C. Bukowski, J. S. Bates, R. Gounder and J. Greeley, *J. Catal.*, 2018, **365**, 261–276.
19. V. L. Sushkevich, I. I. Ivanova and A. V. Yakimov, *J. Phys. Chem. C*, 2017, **121**, 11437–11447.
20. A. V. Yakimov, Y. G. Kolyagin, S. Tolborg, P. N. R. Vennestrøm and I. I. Ivanova, *J. Phys. Chem. C*, 2016, **120**, 28083–28092.
21. G. Yang, E. A. Pidko and E. J. M. Hensen, *J. Phys. Chem. C*, 2013, **117**, 3976–3986.
22. Y. G. Kolyagin, A. V. Yakimov, S. Tolborg, P. N. R. Vennestrøm and I. I. Ivanova, *J. Phys. Chem. Lett.*, 2018, **9**, 3738–3743.
23. F. Cheng, Z. Zhou, J. Qin, D. Li, J. Wang and W. Wu, *Russ. J. Phys. Chem. A*, 2018, **92**, 2640–2646.
24. J. C. Vega-Vila, J. W. Harris and R. Gounder, *J. Catal.*, 2016, **344**, 108–120.
25. J. Dijkmans, J. Demol, K. Houthoofd, S. Huang, Y. Pontikes and B. Sels, *J. Catal.*, 2015, **330**, 545–557.
26. J. Dijkmans, M. Dusselier, D. Gabriëls, K. Houthoofd, P. C. M. M. Magusin, S. Huang, Y. Pontikes, M. Trekels, A. Vantomme, L. Giebeler, S. Oswald and B. F. Sels, *ACS Catal.*, 2015, **5**, 928–940.

27. B. Lu, T. Tsuda, Y. Oumi, K. Itabashi and T. Sano, *Micropor. Mesopor. Mater.*, 2004, **76**, 1–7.
28. T. Tsuda, B. W. Lu, H. Sasaki, Y. Oumi, K. Itabashi, T. Teranishi and T. Sano, *Studies in Surface Science and Catalysis*, eds. E. van Steen, I. M. Claeys and L. H. Callanan, Elsevier, 2004, vol. 154, pp. 224–232.
29. Q. Wang, J. Wang, Y. Zhou and X. Lin, *J. Porous Mater.*, 2013, **20**, 1519–1523.
30. N. Koike, W. Chaikittisilp, K. Iyoki, Y. Yanaba, T. Yoshikawa, S. P. Elangovan, K. Itabashi and T. Okubo, *Dalton Trans.*, 2017, **46**, 10837–10846.
31. B. Wang, N. Koike, K. Iyoki, W. Chaikittisilp, Y. Wang, T. Wakihara and T. Okubo, *Phys. Chem. Chem. Phys.*, 2019, **21**, 4015–4021.
32. A. Omegna, J. A. van Bokhoven and R. Prins, *J. Phys. Chem. B*, 2003, **107**, 8854–8860.
33. M. Ravi, V. L. Sushkevich and J. A. van Bokhoven, *J. Phys. Chem. C*, 2019, **123**, 15139–15144.
34. P. Norby, F. I. Poshni, A. F. Gualtieri, J. C. Hanson and C. P. Grey, *J. Phys. Chem. B*, 1998, **102**, 839–856.
35. M. Hunger, U. Schenk, B. Burger and J. Weitkamp, *Angew. Chem.*, 1997, **36**, 2504–2506.
36. H. Liu and C. P. Grey, *Micropor. Mesopor. Mater.*, 2002, **53**, 109–120.
37. C. Bisio, P. Massiani, K. Fajerwerg, L. Sordelli, L. Stievano, E. R. Silva, S. Coluccia and G. Martra, *Micropor. Mesopor. Mater.*, 2006, **90**, 175–187.
38. H. L. Tidahy, S. Siffert, J. F. Lamonier, R. Cousin, E. A. Zhilinskaya, A. Aboukaïs, B. L. Su, X. Canet, G. De Weireld, M. Frère, J. M. Giraudon and G. Leclercq, *Appl. Catal. B*, 2007, **70**, 377–383.
39. P. J. Chu, B. C. Gerstein, J. Nunan and K. Klier, *J. Phys. Chem.*, 1987, **91**, 3588–3592.
40. M. Hunger and E. Brunner, in *Characterization I*, eds. H. G. Karge and J. Weitkamp, Springer Berlin Heidelberg, Berlin, Heidelberg, 2004, DOI: 10.1007/b94236, pp. 201–293.
41. W. N. P. van der Graaff, G. Li, B. Mezari, E. A. Pidko and E. J. M. Hensen, *Chemcatchem*, 2015, **7**, 1152–1160.
42. N. K. Mal and A. V. Ramaswamy, *J. Mol. Catal. A.*, 1996, **105**, 149–158.
43. W. Fan, R.-G. Duan, T. Yokoi, P. Wu, Y. Kubota and T. Tatsumi, *J. Am. Chem. Soc.*, 2008, **130**, 10150–10164.
44. Y. S. Ko and W. S. Ahn, *Korean J. Chem. Eng.*, 1998, **15**, 423–428.
45. Y. G. Kolyagin, A. V. Yakimov, S. Tolborg, P. N. R. Vennestrøm and I. I. Ivanova, *J. Phys. Chem. Lett.*, 2016, **7**, 1249–1253.
46. S. R. Bare, S. D. Kelly, W. Sinkler, J. J. Low, F. S. Modica, S. Valencia, A. Corma and L. T. Nemeth, *J. Am. Chem. Soc.*, 2005, **127**, 12924–12932.
47. W. Dai, S. Zhang, Z. Yu, T. Yan, G. Wu, N. Guan and L. Li, *ACS Catal.*, 2017, **7**, 3703–3706.
48. T. Yan, W. Dai, G. Wu, S. Lang, M. Hunger, N. Guan and L. Li, *ACS Catal.*, 2018, **8**, 2760–2773.
49. L. Qi, Y. Zhang, M. A. Conrad, C. Russell, J. T. Miller and A. T. Bell, *J. Am. Chem. Soc.*, 2020, **142**, 14674–14687.
50. V. R. Choudhary and S. D. Sansare, *Appl. Catal.*, 1984, **10**, 147–153.
51. E. A. Uslamin, H. Saito, N. Kosinov, E. Pidko, Y. Sekine and E. J. M. Hensen, *Catal. Sci. Technol.*, 2020, **10**, 2774–2785.
52. A. Devaraj, M. Vijayakumar, J. Bao, M. F. Guo, M. A. Derewinski, Z. Xu, M. J. Gray, S. Prodinger and K. K. Ramasamy, *Sci. Rep.*, 2016, **6**, 37586.
53. J. S. Bates and R. Gounder, *J. Catal.*, 2018, **365**, 213–226.

7.6 Supplementary Information.

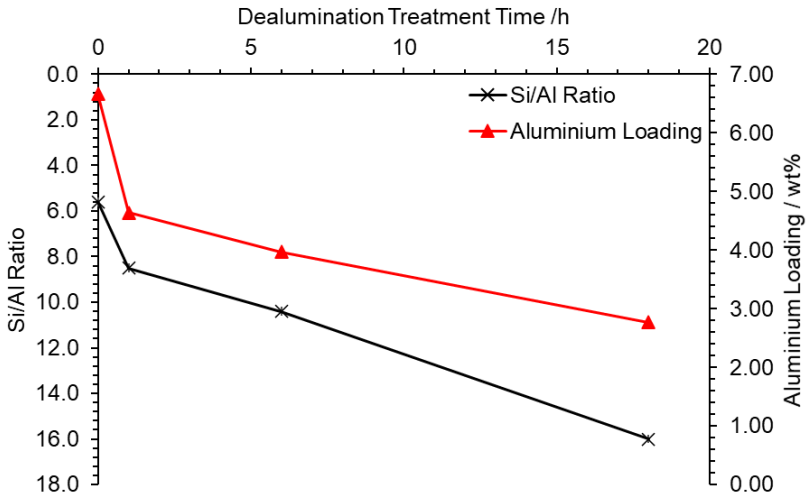

Figure S7.1: Plots of change in Si/Al ratio (×) and aluminium content (▲) with respect to dealumination contact time.

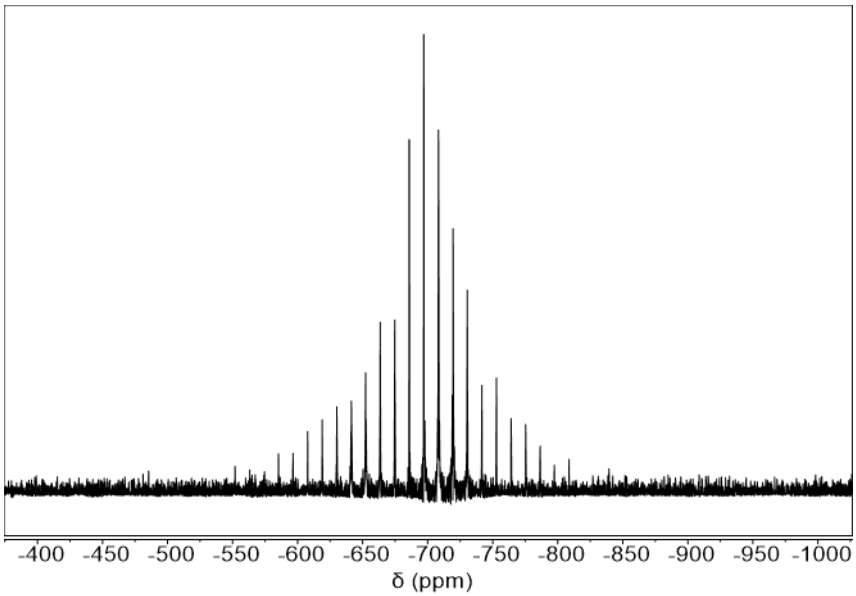

Figure S7.2: Spikelet ^{1}H–^{119}Sn CP-CPMG ssNMR spectrum of Sn–BEA averaged over 6400 scans with a 2.0 s recycle delay and a 5 ms contact time. Spectrum acquired on a Bruker III Avance 400 MHz spectrometer using a 4 mm zirconia rotor. Spectrometer frequncies: ^{1}H = 400.17 MHz, ^{119}Sn = 149.12 MHz. MAS spin rate = 10000 Hz.

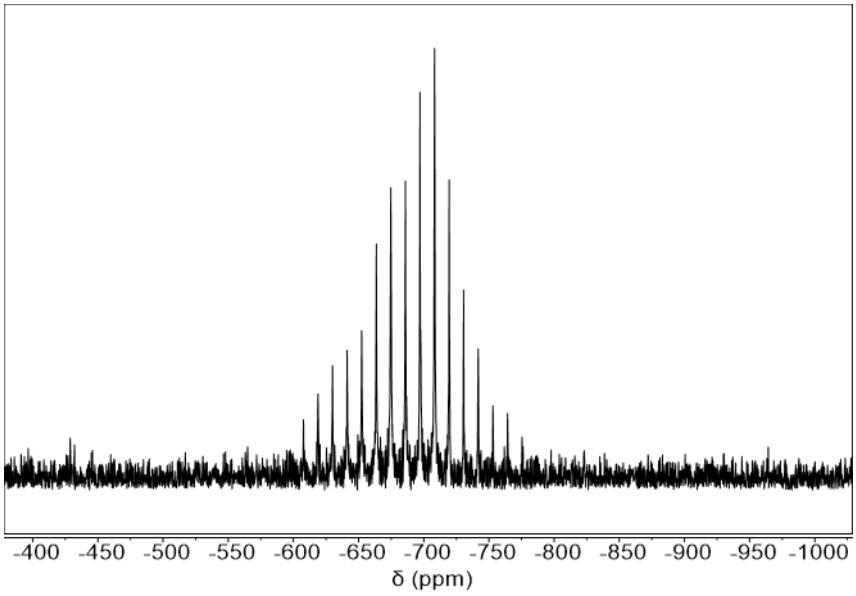

Figure S7.3: Spikelet ^{1}H–^{119}Sn CP-CPMG ssNMR spectrum of Sn–BEA-rep averaged over 25600 scans with a 2.0 s recycle delay and a 5 ms contact time. Spectrum acquired on a Bruker III Avance 400 MHz spectrometer using a 4 mm zirconia rotor. Spectrometer frequncies: ^{1}H = 400.17 MHz, ^{119}Sn = 149.12 MHz. MAS spin rate = 10000 Hz.

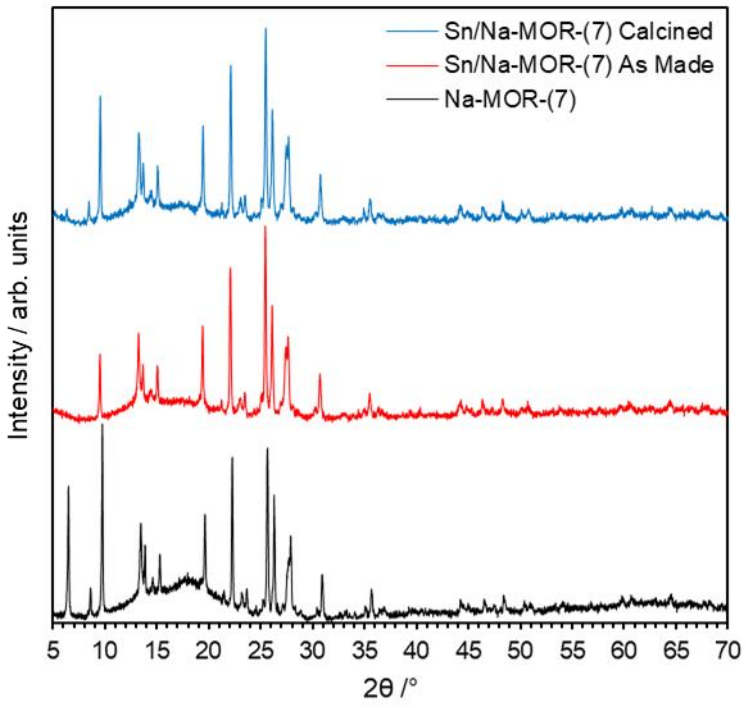

Figure S7.4: pXRD patterns in the 2θ = 5–70 ° region of Na–MOR–(7), Sn-grafted Na–MOR–(7) both as-made and following calcination.

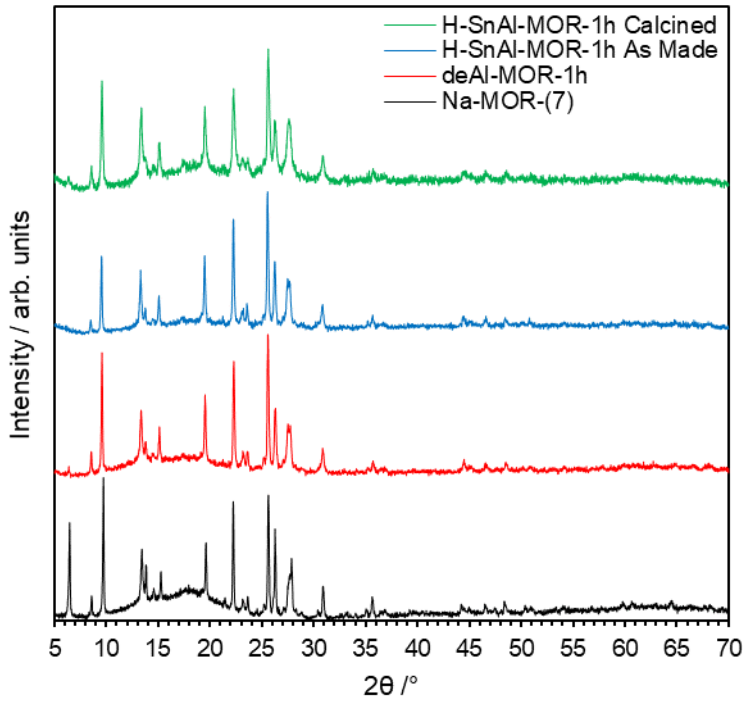

Figure S7.5: pXRD patterns in the 2θ = 5–70 ° region of Na–MOR–(7) and related materials following dealumination for 1h, subsequent Sn-grafting and final calcination. Some samples were pressed using a hand press before sieving in an attempt to produce particles of similar size to the parent materials.

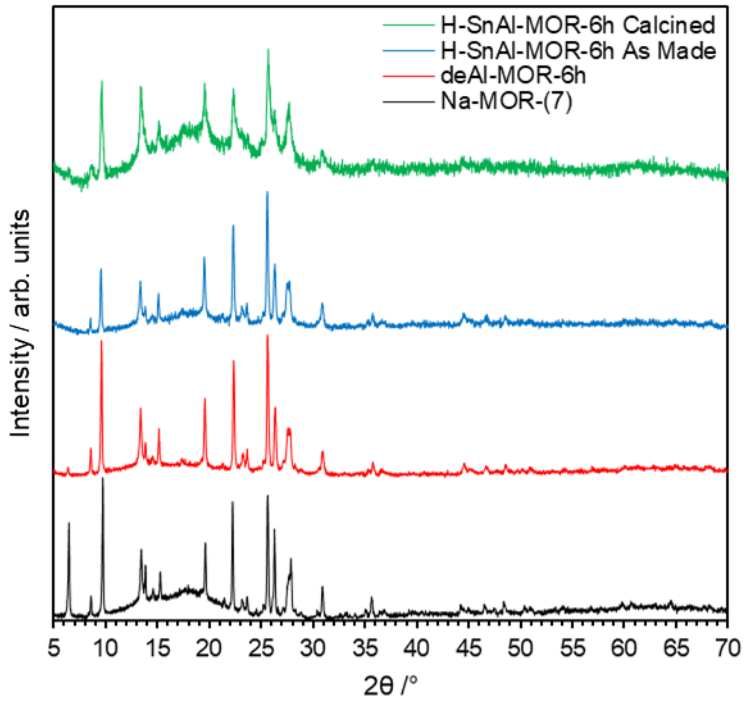

Figure S7.6: pXRD patterns in the 2θ = 5–70 ° region of Na–MOR–(7) and related materials following dealumination for 6h, subsequent Sn-grafting and final calcination. Some samples were pressed using a hand press before sieving in an attempt to produce particles of similar size to the parent materials.

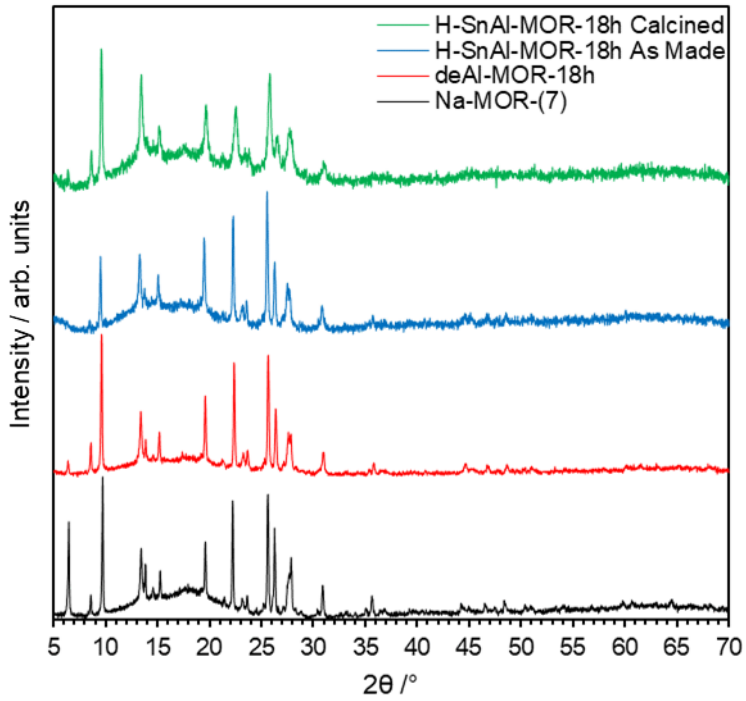

Figure S7.7: pXRD patterns in the 2θ = 5–70 ° region of Na–MOR–(7) and related materials following dealumination for 18h, subsequent Sn-grafting and final calcination. Some samples were pressed using a hand press before sieving in an attempt to produce particles of similar size to the parent materials.

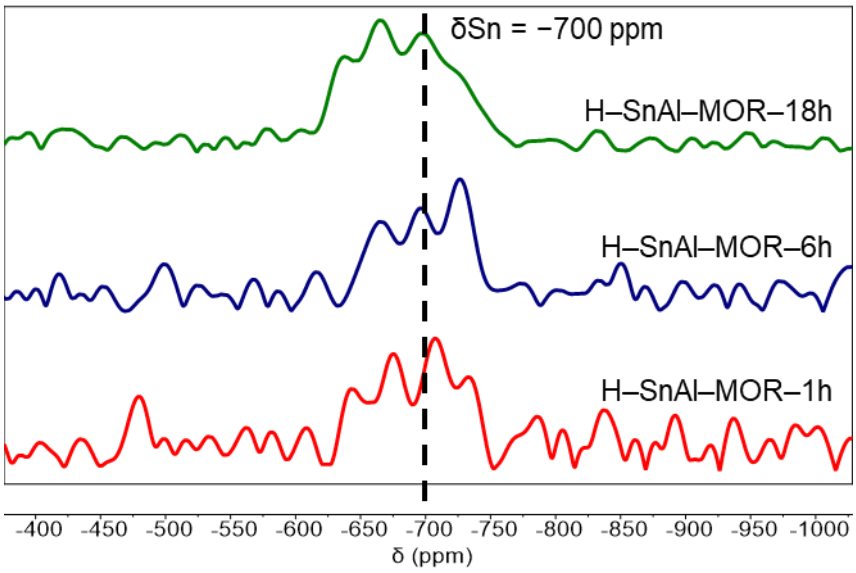

Figure S7.8: Spikelet sum ^{1}H–^{119}Sn CP-CPMG ssNMR spectra of H–SnAl–MOR–1h, H–SnAl–MOR–6h and H–SnAl–MOR–18h as prepared averaged over 25600, 28640 and 18096 scans with 2.0, 2.0 and 1.0 s recycle delays respectively and a 5 ms contact time. Spectra acquired on a Bruker III Avance 400 MHz spectrometer using a 4 mm zirconia rotor. Spectrometer frequncies: ^{1}H = 400.17 MHz, ^{119}Sn = 149.12 MHz. MAS spin rate = 10000 Hz.

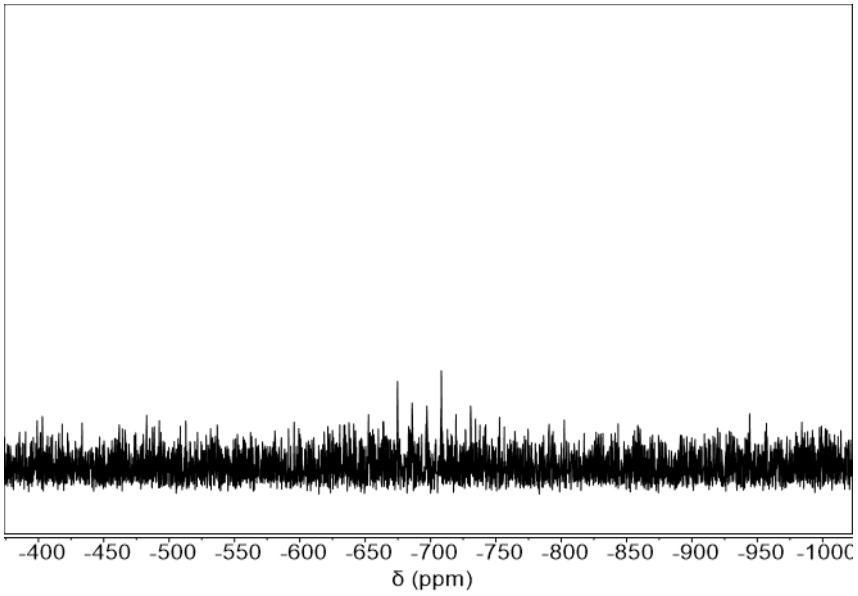

Figure S7.9: Spikelet $^{1}H–^{119}Sn$ CP-CPMG ssNMR spectrum of H–SnAl–MOR–1h as prepared averaged over 25600 scans with 2.0 s recycle delay and a 5 ms contact time. Spectrum acquired on a Bruker III Avance 400 MHz spectrometer using a 4 mm zirconia rotor. Spectrometer frequncies: ^{1}H = 400.17 MHz, ^{119}Sn = 149.12 MHz. MAS spin rate = 10000 Hz.

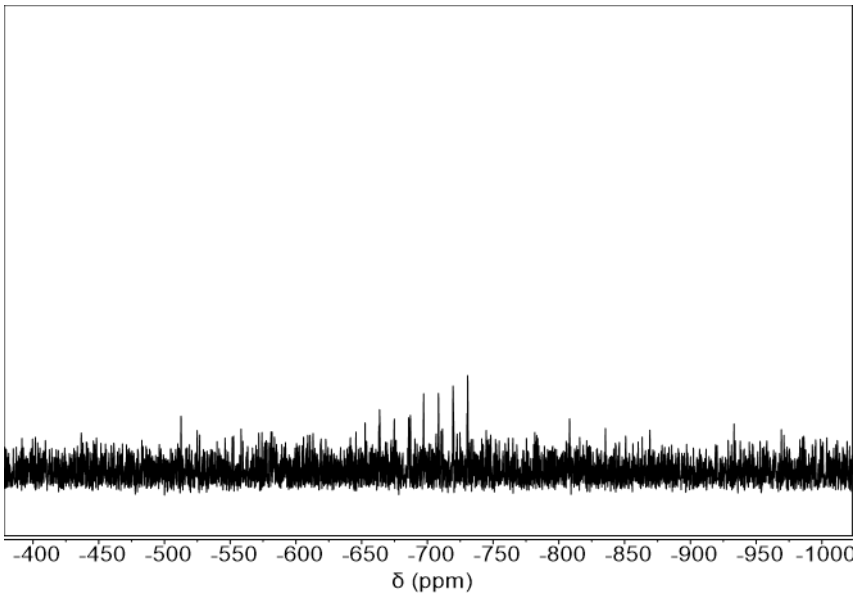

Figure S7.10: Spikelet $^{1}H–^{119}Sn$ CP-CPMG ssNMR spectrum of H–SnAl–MOR–6h as prepared averaged over 28640 scans with 2.0 s recycle delays and a 5 ms contact time. Spectrum acquired on a Bruker III Avance 400 MHz spectrometer using a 4 mm zirconia rotor. Spectrometer frequncies: ^{1}H = 400.17 MHz, ^{119}Sn = 149.12 MHz. MAS spin rate = 10000 Hz.

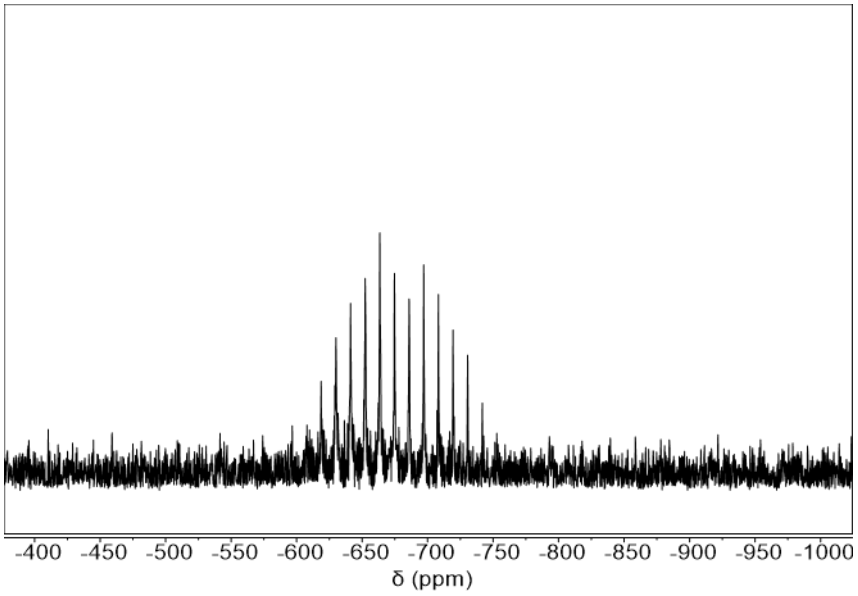

Figure S7.11: Spikelet $^{1}H–^{119}Sn$ CP-CPMG ssNMR spectrum of H–SnAl–MOR–18h as prepared averaged over 18096 scans with 1.0 s recycle delays respectively and a 5 ms contact time. Spectrum acquired on a Bruker III Avance 400 MHz spectrometer using a 4 mm zirconia rotor. Spectrometer frequncies: ^{1}H = 400.17 MHz, ^{119}Sn = 149.12 MHz. MAS spin rate = 10000 Hz.

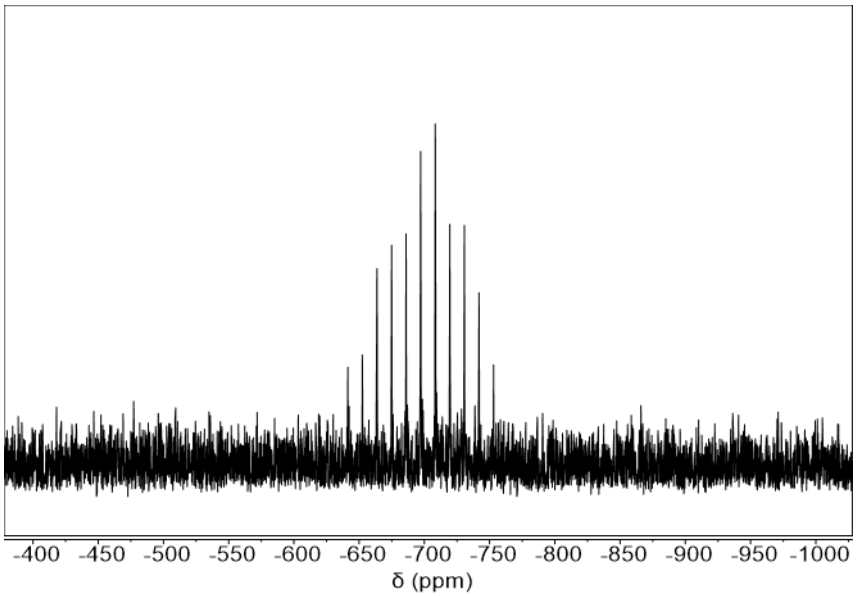

Figure S7.12: Spikelet $^{1}H–^{119}Sn$ CP-CPMG ssNMR spectrum of H–SnAl–MOR–1h following calcination averaged over 40800 scans with 2.0 s recycle delay and a 5 ms contact time. Spectrum acquired on a Bruker III Avance 400 MHz spectrometer using a 4 mm zirconia rotor. Spectrometer frequencies: ^{1}H = 400.17 MHz, ^{119}Sn = 149.12 MHz. MAS spin rate = 10000 Hz.

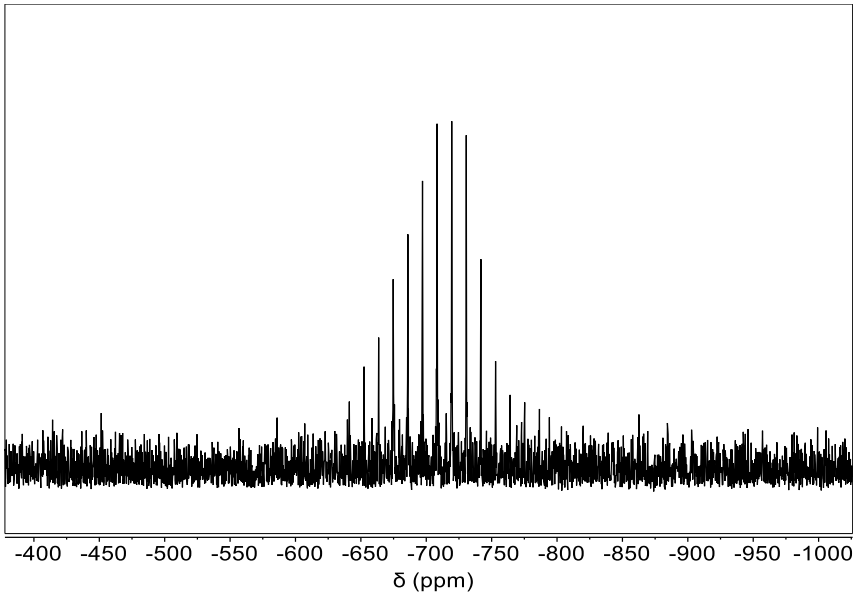

Figure S7.13: Spikelet $^{1}H–^{119}Sn$ CP-CPMG ssNMR spectrum of H–SnAl–MOR–6h following calcination averaged over 33088 scans with 2.0 s recycle delay and a 5 ms contact time. Spectrum acquired on a Bruker III Avance 400 MHz spectrometer using a 4 mm zirconia rotor. Spectrometer frequencies: ^{1}H = 400.17 MHz, ^{119}Sn = 149.12 MHz. MAS spin rate = 10000 Hz.

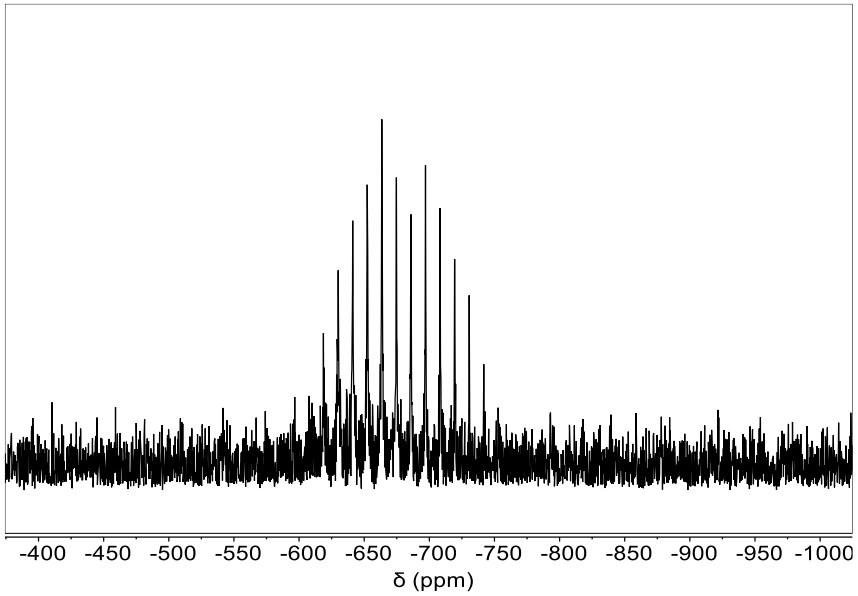

Figure S7.14: Spikelet $^{1}H–^{119}Sn$ CP-CPMG ssNMR spectrum of H–SnAl–MOR–18h following calcination averaged over 28800 scans with 1.0 s recycle delay and a 5 ms contact time. Spectrum acquired on a Bruker III Avance 400 MHz spectrometer using a 4 mm zirconia rotor. Spectrometer frequencies: ^{1}H = 400.17 MHz, ^{119}Sn = 149.12 MHz. MAS spin rate = 10000 Hz.

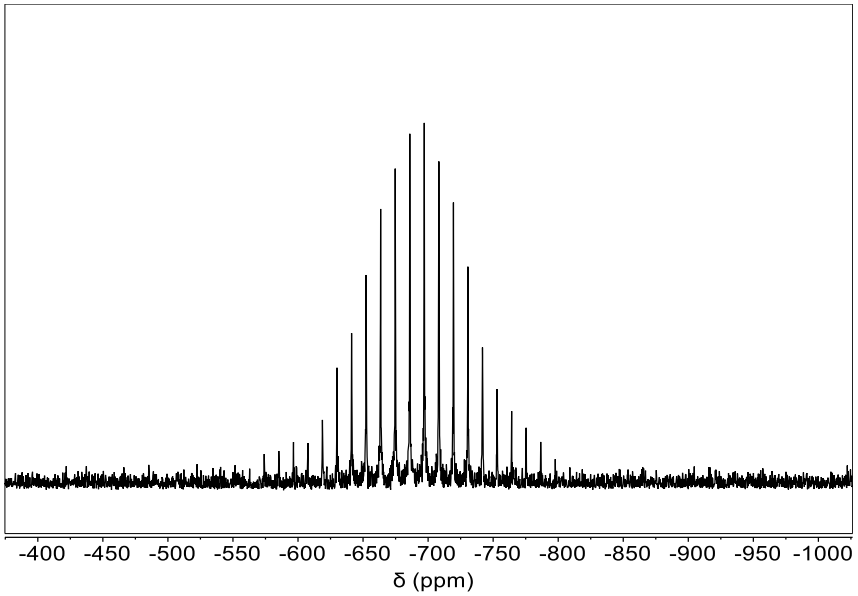

Figure S7.15: Spikelet ^{1}H–^{119}Sn CP-CPMG ssNMR spectrum of Rb–SnAl–MOR–1h following calcination averaged over 65536 scans with a 1.0 s recycle delay and a 5 ms contact time. Spectrum acquired on a Bruker III Avance 400 MHz spectrometer using a 4 mm zirconia rotor. Spectrometer frequncies: ^{1}H = 400.17 MHz, ^{119}Sn = 149.12 MHz. MAS spin rate = 10000 Hz.

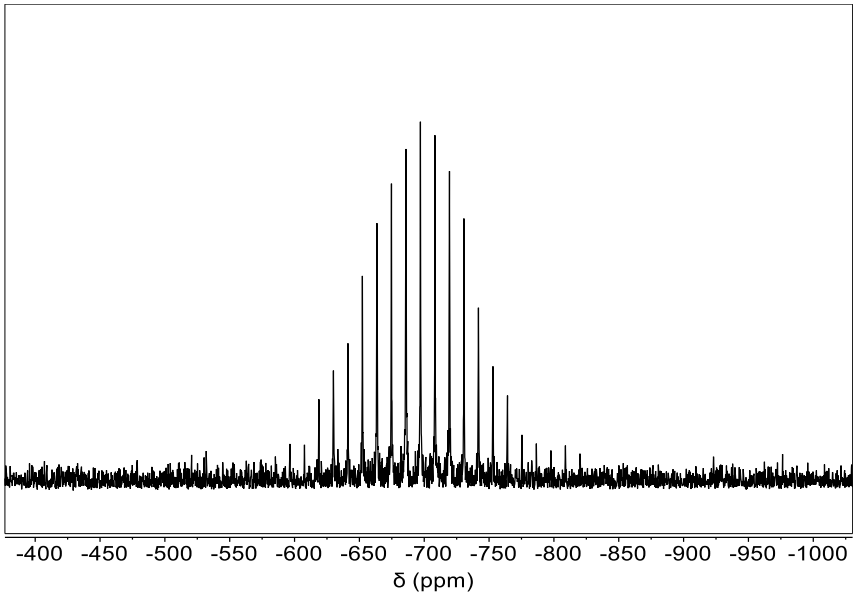

Figure S7.16: Spikelet ^{1}H–^{119}Sn CP-CPMG ssNMR spectrum of Rb–SnAl–MOR–6h following calcination averaged over 32768 scans with a 1.0 s recycle delay and a 5 ms contact time. Spectrum acquired on a Bruker III Avance 400 MHz spectrometer using a 4 mm zirconia rotor. Spectrometer frequncies: ^{1}H = 400.17 MHz, ^{119}Sn = 149.12 MHz. MAS spin rate = 10000 Hz.

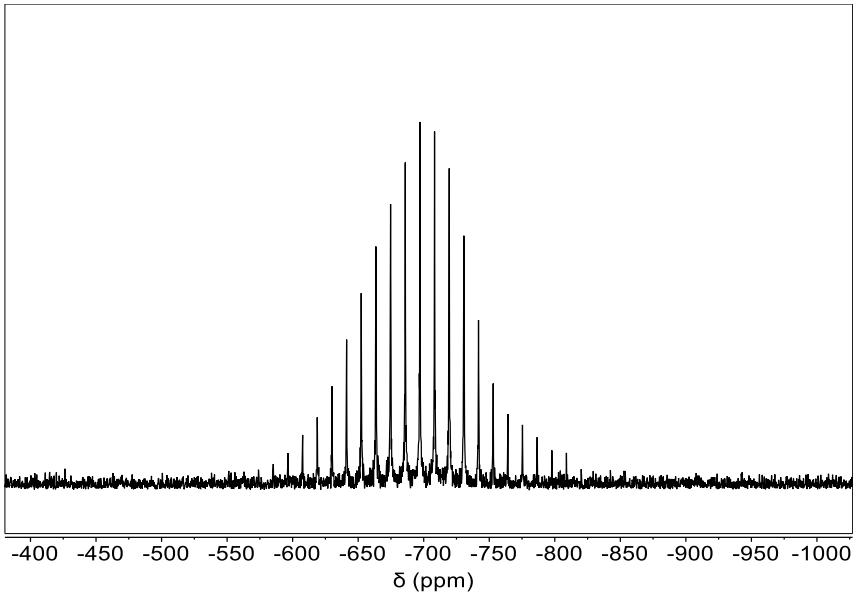

Figure S7.17: Spikelet ^{1}H–^{119}Sn CP-CPMG ssNMR spectrum of Rb–SnAl–MOR–18h following calcination averaged over 32768 scans with a 1.0 s recycle delay and a 5 ms contact time. Spectrum acquired on a Bruker III Avance 400 MHz spectrometer using a 4 mm zirconia rotor. Spectrometer frequncies: ^{1}H = 400.17 MHz, ^{119}Sn = 149.12 MHz. MAS spin rate = 10000 Hz.

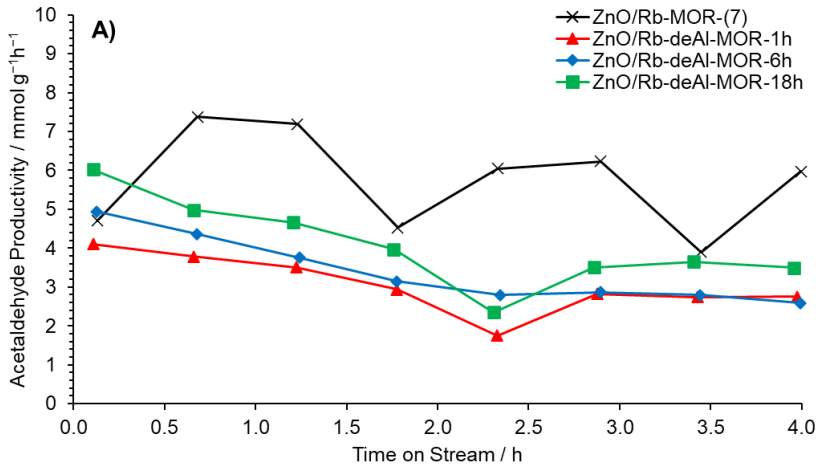

Figure S7.18: Acetaldehyde productivity per gram of catalyst for ZnO/Rb–MOR–(7) (×), ZnO/Rb-deAl–MOR–1h (▲), ZnO/Rb-deAl–MOR–6h (♦) and ZnO/Rb-deAl–MOR–18h (■) at 350 °C for 4 h TOS. Ethanol feed rate = 0.390 mmol min^{-1}. Detection Columns: RTX-VMS + ShinCarbon ST.

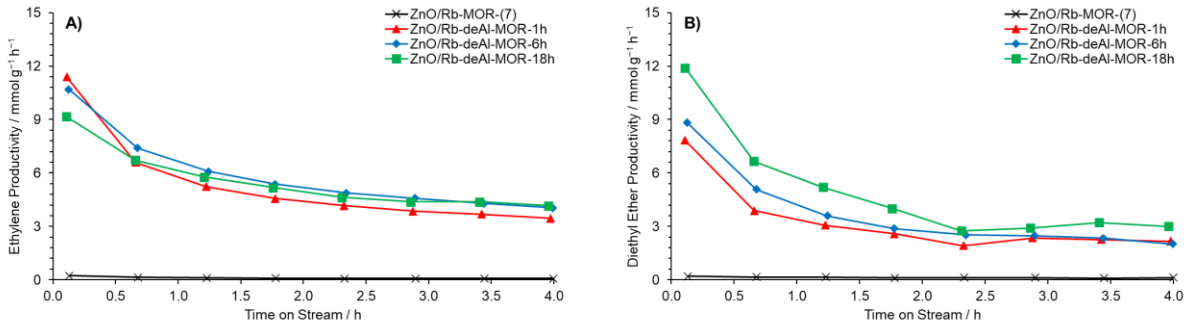

Figure S7.19: Ethylene (A) and diethyl ether (B) productivities per gram of catalyst for ZnO/Rb–MOR–(7) (×), ZnO/Rb-deAl–MOR–1h (▲), ZnO/Rb-deAl–MOR–6h (♦) and ZnO/Rb-deAl–MOR–18h (■) at 350 °C for 4 h TOS. Ethanol feed rate = 0.390 mmol min^{-1}. Detection Columns: RTX-VMS + ShinCarbon ST.

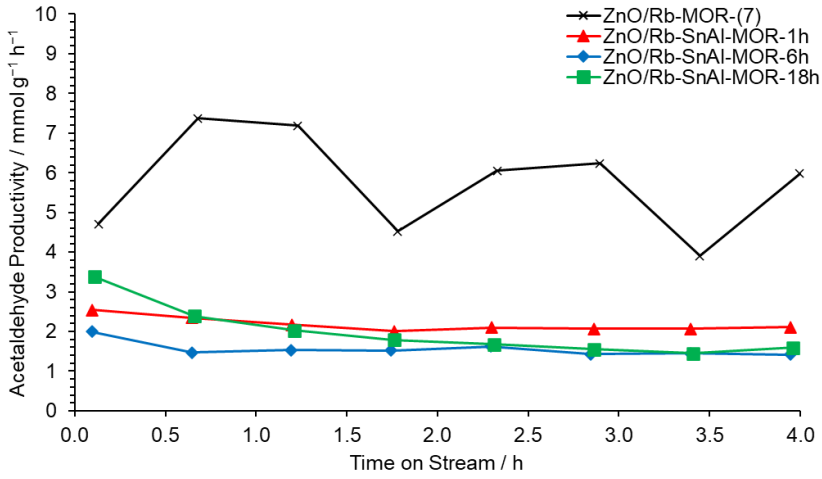

Figure S7.20: Acetaldehyde productivity per gram of catalyst for ZnO/Rb–MOR–(7) (×), ZnO/Rb-SnAl–MOR–1h (▲), ZnO/Rb-SnAl–MOR–6h (♦) and ZnO/Rb-SnAl–MOR–18h (■) at 350 °C for 4 h TOS. Ethanol feed rate = 0.390 mmol min^{-1}. Detection Columns: RTX-VMS + ShinCarbon ST.

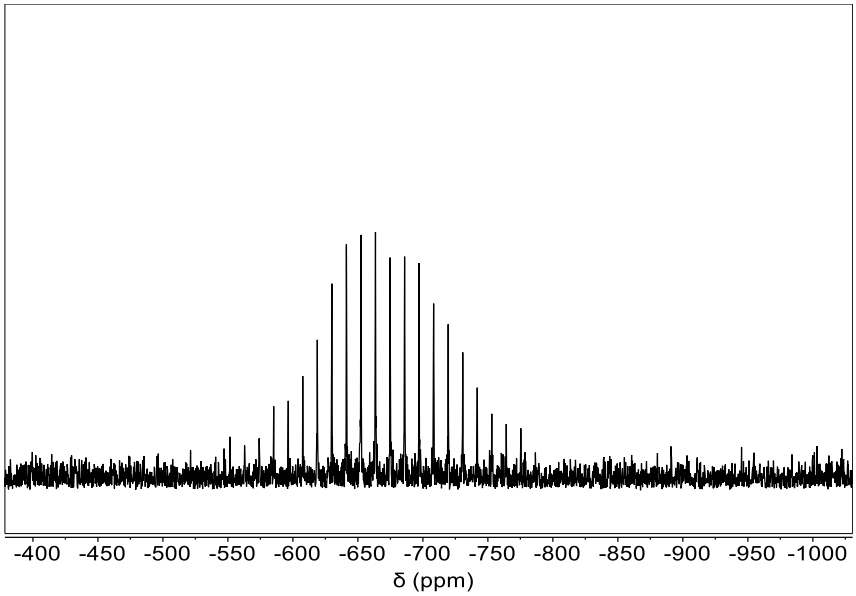

Figure S7.21: Spikelet ^{1}H–^{119}Sn CP-CPMG ssNMR spectrum of ZnO/Rb–SnAl–MOR–1h following reaction with ethanol at 350 °C over 4 h TOS averaged over 65536 scans with a 1.0 s recycle delay and a 5 ms contact time. Spectrum acquired on a Bruker III Avance 400 MHz spectrometer using a 4 mm zirconia rotor. Spectrometer frequncies: ^{1}H = 400.17 MHz, ^{119}Sn = 149.12 MHz. MAS spin rate = 10000 Hz.

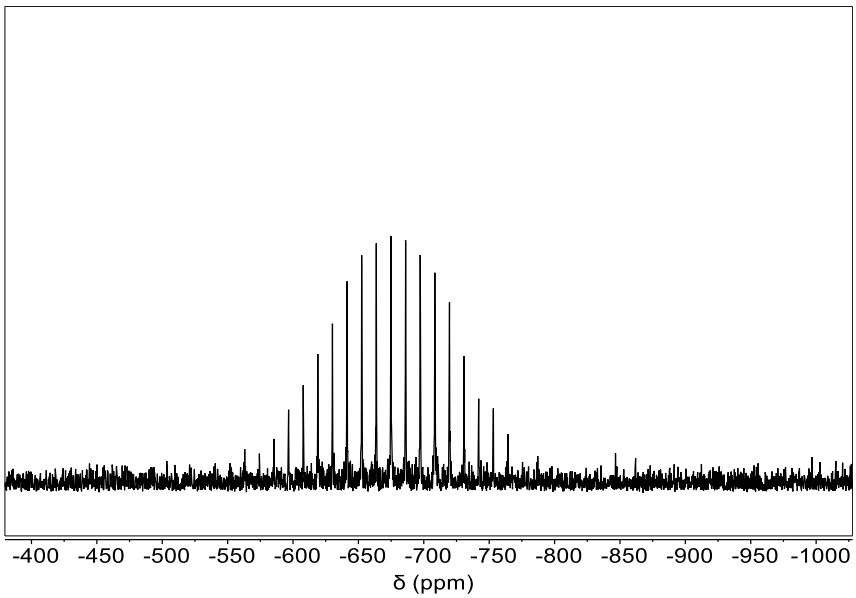

Figure S7.22: Spikelet ^{1}H–^{119}Sn CP-CPMG ssNMR spectrum of ZnO/Rb–SnAl–MOR–6h following reaction with ethanol at 350 °C over 4 h TOS averaged over 57344 scans with a 1.0 s recycle delay and a 5 ms contact time. Spectrum acquired on a Bruker III Avance 400 MHz spectrometer using a 4 mm zirconia rotor. Spectrometer frequncies: ^{1}H = 400.17 MHz, ^{119}Sn = 149.12 MHz. MAS spin rate = 10000 Hz.

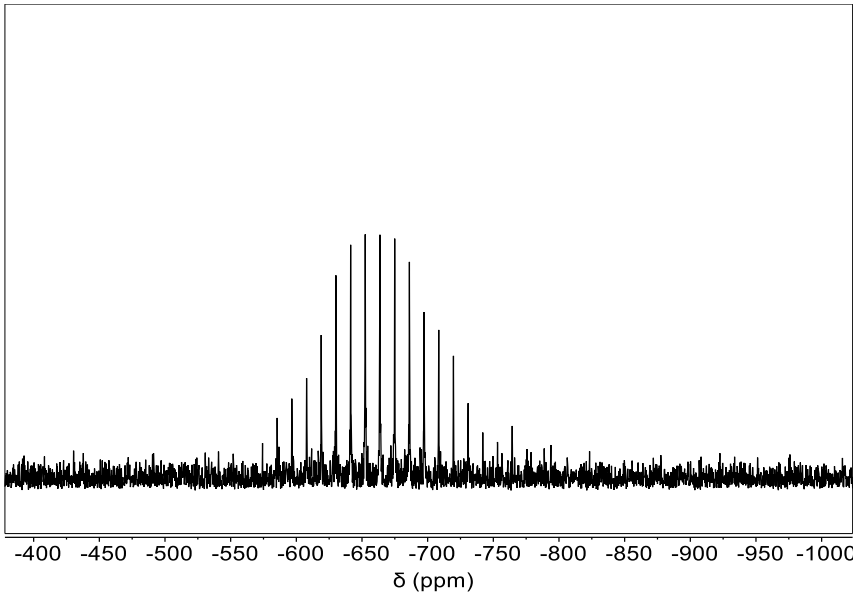

Figure S7.23: Spikelet ^{1}H–^{119}Sn CP-CPMG ssNMR spectrum of ZnO/Rb–SnAl–MOR–18h following reaction with ethanol at 350 °C over 4 h TOS averaged over 25600 scans with a 1.0 s recycle delay and a 5 ms contact time. Spectrum acquired on a Bruker III Avance 400 MHz spectrometer using a 4 mm zirconia rotor. Spectrometer frequncies: ^{1}H = 400.17 MHz, ^{119}Sn = 149.12 MHz. MAS spin rate = 10000 Hz.

Conclusions

8. Conclusions and Project Continuation.

8.1. Conclusions.

In Chapter 4, ZnO/Na–MOR was found to be an interesting candidate for ethanol dehydrogenation to acetaldehyde following an initial screening of several zeolite framework types, metal oxide species, and reaction conditions. ZnO/Na–MOR was found to possess a promising lifetime of over 24 h with no appreciable decrease in acetaldehyde yield (25%). Subsequently, ZnO/Na–MOR was optimised by both ZnO wt% variation and alkali metal cation exchange, with ZnO(3.5)/Rb–MOR–(7) being identified as the optimum materials of those tested, achieving an acetaldehyde selectivity of 95%. A long-term stability test showed that ZnO(3.5)/Rb–MOR–(7) exhibited remarkable stability following 120+ h TOS, maintaining a selectivity to acetaldehyde of over 90% at an ethanol conversion value of around 40%. It was found that, whilst mild coking occurred, the framework structure of the zeolite was retained with no observation of additional phases or extra-framework alumina as evidenced by pXRD analysis or ^{27}Al ssNMR spectroscopy respectively. It was also concluded that supporting ZnO onto Rb–MOR–(7) greatly benefitted the ethanol to acetaldehyde reaction, likely as a result of increased ZnO dispersion allowing a greater proportion of active sites to be available. Additionally, the productivity of ethylene was concluded to be the main cause of coke formation on ZnO/MOR materials.

In Chapter 5, several M^{IV} substituted MFI type materials containing Si, Sn, Ti, Zr and Hf in tetrahedral positions were successfully synthesised as evidenced by pXRD, BET, SEM, and ^{29}Si ssNMR spectroscopic analysis, with isolated framework sites in all materials confirmed by DR-UV-Vis spectroscopy and SEM-EDS mapping. Each M–MFI materials was assessed for its activity in ethanol conversion and, in each case, a product distribution composed predominantly of diethyl ether and ethylene was obtained, indicative of Lewis acidity. Following introduction of ZnO, the product distribution of each ZnO/M–MFI material shifted to include a large proportion of Lebedev products (acetaldehyde and butadiene), with maximum selectivites to Lebedev products observed at a reaction temperature of 350 °C. ZnO/Zr–MFI was identified as the optimum catalyst materials of those assessed but it exhibited deactivation *via* a loss of butadiene productivity at extended times on stream. This deactivation was investigated by both *in-situ* XAS analysis and coke analysis, following which coking was proposed to be the predominant cause of the observed deactivation. The synthesis conditions of Zr–MFI were optimised to maximise butadiene productivity of ZnO/Zr–MFI and it was

proposed that Zr may be zoned during synthesis, leading to improved butadiene yields for materials with higher Zr loadings and smaller particle diameters.

In Chapter 6, divalently substituted MFI type materials containing Mg^{II} and Zn^{II} in tetrahedral positions have been successfully synthesised as evidenced by pXRD, BET, SEM, and ^{29}Si ssNMR spectroscopic analysis, with isolated framework sites confirmed by DR-UV-Vis spectroscopy and SEM-EDS mapping. Catalytic testing of pristine Mg–MFI revealed very low ethanol conversion, however doping with ZnO resulted in observation of the total cascade reaction of ethanol to butadiene. Hence, it was concluded that the Lewis acid strength of the Mg^{II} tetrahedral sites is sufficient to promote C–C coupling reactions, but insufficient to catalyse the dehydration of ethanol, potentially leading to interesting selectivity effects when compared with M^{IV}–MFI systems. Zn–MFI behaved in a remarkably interesting way, promoting both ethanol dehydrogenation and the total cascade reaction from ethanol to butadiene without the need for additional ZnO doping. Based upon literature surrounding ethanol dehydrogenation over pseudo-framework Zn^{II} species,[1-3] it was hypothesised that framework Zn–O bonds may act as a ZnO mimic promoting ethanol dehydrogenation to acetaldehyde which may then undergo aldol coupling by Lewis acidic Zn^{II} in framework positions.

In Chapter 7, dealumination of Na–MOR–(7) to various extents was successfully achieved by treatment with HNO_3. Following Cs^+ exchange of deAl–MORs, ^{133}Cs ssNMR spectroscopy was undertaken which suggested that Al is initially removed from the T_1 site, followed by removal from all other sites concurrently. Catalytic testing of ZnO/Rb–deAl–MOR materials for ethanol conversion produced product distributions consistent with Brønsted acidic ethanol dehydration which is anticipated to be resultant from acidic silanol nests present following dealumination. Subsequently, H–deAl–MOR materials were successfully remetallated with $SnCl_4$ in DCM as evidenced by DR-UV-Vis and ^{119}Sn ssNMR spectroscopies, confirming Sn presence solely in hydrated framework positions, although 100% remetallation was not achieved. Unfortunately, catalytic ethanol conversion over ZnO/Rb–SnAl–MOR materials at 350 °C revealed no significant production of butadiene, suggesting a lack of activity of Sn as a Lewis acidic centre in this application. The unsuccessful catalytic tests likely owe to excess Brønsted acidic sites resulting from a combination of residual silanol nests from dealumination, non-exchanged aluminium based Brønsted acidic sites and hydrolysed Sn species forming ethylene and diethyl ether from ethanol preferentially.

Overall, through a series of optimisations, ZnO(3.5)/Rb–MOR–(7) was shown to be an efficient and selective catalysts for the direct dehydrogenation reaction of ethanol to form acetaldehyde at 400 °C under continuous flow conditions and ZnO was identified as a potential dedicated dehydrogenation site. Addition of ZnO in this role to Lewis acidic M^{IV} and M^{II} substituted zeolites resulted in observation of the total cascade reaction from ethanol to 1,3–butadiene, with ZnO/Zr–MFI being identified as the optimum materials within this study. The key metrics associated with catalytic ethanol conversion reactions over ZnO(3.5)/Rb–MOR–(7), ZnO/Zr–MFI, Zn–MFI and ZnO/Zn–MFI are shown in Table 8.1. In this regard, the aims of the project have been accomplished by successful realization of the cascade conversion of ethanol to 1,3–butadiene over multifunctional zeolitic materials housing disparate active sites.

Table 8.1: Summary table of key metrics associated with catalytic ethanol conversion reactions ZnO(3.5)/Rb–MOR–(7), ZnO/Zr–MFI, Zn–MFI and ZnO/Zn–MFI

Material	Reaction Temperature / °C	Conversion / %	Selectivity / %	
			Acetaldehyde	Butadiene
ZnO(3.5)/Rb–MOR–(7)	400	40	95	0
ZnO/Zr–MFI	350	70	40	18
Zn–MFI	350	70	50	9
ZnO/Zn–MFI	350	60	50	12

8.2. Project Continuation.

Following the completion of this project, several directions for future research are perceivable for continuation. First and foremost, identification of an ethanol dehydrogenation site with a lower temperature requirement in combination with the various M–MFI materials presented within this thesis may allow transition to products other than butadiene, particularly ^{n}butanol. Current literature would suggest that ^{n}butanol formation is favoured at lower temperatures (around 200 °C), hence reduction of the temperature requirement of dehydrogenation may aid access to this pathway. Ideally, a direct dehydrogenation mechanism should be retained in order to allow H_2 availability for the final stage of ^{n}butanol production. Potential candidates for this work may centre around reduced metal species, such as Cu, Au, Ni and Pd.

Quantification of the acidity of M–MFI materials presented within this thesis would aid greatly in their comparison alongside offering insight into their relative reactivities. In particular, DRIFTS and ssNMR spectroscopic analysis of M–MFI materials following

absorption of pyridine and acetonitrile-d3 would allow excellent insight into the strengths of their Brønsted and Lewis acidities, alongside their relative concentrations.[4] Additionally, further investigation into potential Zr zoning during the hydrothermal synthesis of Zr–MFI should be investigated. This could be achieved by undertaking SEM-EDS mapping of microtomed samples (as in Chapter 4) in order to identify Zr locations within the synthesised crystals.

In Chapter R3, it was hypothesised that Zn–O bonds within the framework of Zn–MFI could act as mimics to bulk ZnO. Further work could probe the mechanism behind ethanol dehydrogenation in order to confirm a similarity between the reaction over Zn–MFI and the known mechanism over ZnO.[3] This work could be undertaken by use of labelled ethanol (CH_3CH_2OD) and DRIFTS spectroscopy by identification of kinetic isotope effects and varying stretching frequency of oxygen bound hydrogen or deuterium atoms. Additionally, DFT calculations could be employed to rationalise similar free energy pathways and transition states between both systems if a similar mechanism was able to be suggested.

Further, continued research into the substitution of MOR materials with Lewis acidic metal centres is desirable owing to the improved product distribution of MOR when compared to MFI and BEA (see Chapter 4). Although MOR materials containing exclusively silicon or other M^{4+} atoms in tetrahedral positions are not known yet in the literature, further investigation into the hydrothermal synthesis of mixed metal MOR materials (Sn/Al, Zr/Al) may prove beneficial in comparison to the combined dealumination/remetallation approach taken within this thesis. In this case, full tetrahedral occupancy would be expected alongside likely more facile ion-exchange. Alternatively, as MOR type zeolites are typically synthesised in the presence of Na^+ cations, ion-exchange may not be required if H^+ cations and silanol nests were solely responsible for Brønsted acidic behaviour observed for ZnO/Rb–SnAl–MOR materials in Chapter 7. Additionally, a single step hydrothermal synthesis is likely more desirable to be performed on larger scale than a multistep dealumination/remetallation procedure requiring the use of hazardous chemicals such as $SnCl_4$. Considering this theory, several attempts to synthesise such a mixed Sn/Al MOR for this purpose were attempted during this project, but no success was achieved, and the results were not reported herein

8.3. References

1. W. Dai, S. Zhang, Z. Yu, T. Yan, G. Wu, N. Guan and L. Li, *ACS Catal.*, 2017, **7**, 3703–3706.
2. T. Yan, W. Dai, G. Wu, S. Lang, M. Hunger, N. Guan and L. Li, *ACS Catal.*, 2018, **8**, 2760–2773.
3. L. Qi, Y. Zhang, M. A. Conrad, C. Russell, J. T. Miller and A. T. Bell, *J. Am. Chem. Soc.*, 2020, **142**, 14674–14687.
4. G. Paul, C. Bisio, I. Braschi, M. Cossi, G. Gatti, E. Gianotti and L. Marchese, *Chem. Soc. Rev.*, 2018, **47**, 5684–5739.

Experimental

9. Experimental Procedures.

This chapter describes the general experimental procedures, equipment and materials used during this project. The synthesis and characterisation of all new compounds and materials presented in this project are described within the relevant chapters. The synthesis of several known compounds, which were used as precursors, is also presented alongside the characterisation data used to confirm their identity. All data was collected by the author unless otherwise stated.

9.1. Materials.

A list of chemicals used in this project may be found in Appendix 2 of this document. All commercial chemicals were used as received without further purification unless specifically stated.

Air sensitive materials were handled and stored in either a PureLab HE glove box under an argon atmosphere or on a Schlenk line with an N_2 purge that had been passed through a drying column containing Drierite™ with indicator (10–20 mesh). Schlenk line vacuum was provided by an Edwards RV8 rotary vacuum pump (typical vacuum $\approx 10^{-2}$ mbar).

Anhydrous ethereal and hydrocarbon solvents were dried over and distilled from metallic sodium, observing the sodium-benzophenone ketyl radical as an indicator. Anhydrous chlorinated solvents were dried over and distilled from phosphorus pentoxide. Small volumes of solvent (< 100 mL, such as those for NMR analysis of air-sensitive compounds) were dried over and distilled from phosphorus pentoxide. All distilled solvents were transferred into rigorously dried sealable ampules and stored under an atmosphere of N_2.

9.2. Characterisation of Materials.

9.2.1 General Instrumentation.

Centrifugation of samples was performed on a Heraeus™ Megafuge™ from Thermo Scientific. Pellets for catalysis were pelletized in a 32 mm evacuable pellet die from Apollo Scientific. Microvolume transfer was performed using Gilson Pipetman Classic P1000 and P200 pipettes. Zeolites were calcined in Carbolite CWF 11/13 (1100 °C), Carbolite HTC 16/3 (1600 °C) and Carbolite RHF14/3 (1400 °C) muffle furnaces. Vacuum calcinations were performed in a quartz tube attached to Schlenk line (vacuum provided by an Edwards RV8 rotary vacuum pump) using a Carbolite EVA 12/150B (1200 °C) tube furnace. Solution-state ^{1}H and ^{13}C NMR spectra were recorded across a pair of Bruker Avance III-HD-400

spectrometers operating at 399.95 or 400.07 MHz or a Bruker Neo-400 spectrometer operating at 400.13 MHz for ^{1}H using a standard 4 mm glass NMR tube. Chemical shifts are reported in ppm downfield of tetramethylsilane (TMS) using TMS or the residual solvent signal as an internal reference. All NMR spectra were processed using MestReNova software. Elemental (CHN) microanalyses were obtained on an Exeter Analytical Inc. E-440 elemental analyser. CHN data were kindly acquired by Dr. Emily Unsworth of Durham University. Service submitted electron ionisation (EI) tandem gas chromatography mass spectra (GC-MS) were recorded on a Shimadzu QP2010-Ultra quadrupole mass spectrometer. Samples (0.5 μL) were injected with a 25:1 He split ratio and chromatography performed over a Thames Restek Rxi-5Sil MS capillary column (length 10 m, I.D. 0.15 mm, film thickness 0.15 μm) at a carrier flow rate of 0.41 mL min^{-1}. Samples were introduced on to the column and held at 30 °C for 1 min before ramping at 50 °C min^{-1} to 300 °C at which they were held for 5 mins. Atmospheric Solids Analysis Probe mass spectrometry (ASAP-MS) was performed on a Waters LCT Premier XE QToF mass spectrometer equipped with Atmospheric Pressure Gas Chromatography (APGC) and Atmospheric Solids Analysis Probe (ASAP) ion sources. All service submitted MS data were kindly acquired by Dr. David Parker and Dr. Peter Stokes of Durham University. pXRD diffractograms were collected on a Bruker D8 avance X-ray diffractometer with Cu Kα radiation (λ = 1.54184 Å) using a step of 0.02 ° over a range of 2θ = 5–70 °. A knife edge was utilised for low angle scattering. Samples were mounted onto glass or silicon (9 1 1) slide holders and rotated during data acquisition. The surface area of materials was measured by means of nitrogen adsorption at 77 K on a Micromeritics ASAP 2020 gas adsorption analyser in a pressure range of P/P_0 = 0.005–1.00. Before the nitrogen adsorption, samples were degassed at 350 °C (623 K) for 4 hours. The total surface area was calculated *via* the Brunauer–Emmett–Teller (BET) equation within a pressure range of P/P_0 = 0.005–0.15. Diffuse reflectance UV-Vis (DR-UV-Vis) spectroscopy measurements were acquired at Cardiff University on an Agilent Cary 4000 UV-Vis spectrometer equipped with an extended sample compartment. All measurements were collected with an ordinate and abscissa mode of F(R) and wavelength (nm) respectively. Prior to the initial measurement, a fresh background measurement was collected with barium sulfate ($BaSO_4$) as the reference sample. The measurement range was from 800 to 200 nm at full slit height. Source change-over was set at 400 nm and a scan rate of 400 nm min^{-1} was used throughout the experiment. DR-UV-Vis spectra were kindly acquired at Cardiff University by Dr. Abdul-Lateef Adedigba of Durham University.

9.2.2 Solid-State NMR Spectroscopy.

Solid-state NMR spectra were acquired on either a Varian VNMRS 400 MHz or Bruker Avance III HD 400 MHz spectrometer. All solid-state NMR spectra were acquired in a 4 or 6 mm[7] magic-angle spinning probe using a zirconia rotor. All samples were analysed at ambient temperature (approx. 25 °C) with a recycle delay optimised depending upon the relaxation rates of the individual samples (between 1–10 s) unless otherwise stated. All NMR spectra were processed using MestReNova software. Spectra collected on the Varian spectrometer were generally collected by the author and spectra collected on the Bruker spectrometer were kindly acquired by Dr. David Apperley of Durham University

Solid-state ^{1}H NMR spectra were acquired on a Varian VNMRS spectrometer operating at 400.17 MHz with a spinning rate of approx. 12 KHz. Spectra were obtained using 64–128 scans utilising a DEPTH filter for background suppression. Spectra were referenced to an external standard of tetramethylsilane (TMS) by setting the high frequency signal from adamantane to 1.9 ppm.

Solid-state ^{13}C NMR spectra were acquired on a Varian VNMRS spectrometer operating at 100.57 MHz with a spinning rate of approx. 10 KHz. Spectra were obtained using 1000–14400 scans. Most ^{13}C spectra were obtained using a ^{1}H–^{13}C cross-polarization pulse sequence with a 5 ms contact time. Direct excitation ^{13}C spectra were obtained utilising a DEPTH filter for background suppression. In some cases, a non-quaternary suppression (NQS) sequence utilising a phase difference of 40 μs was applied to distinguish signals and assign spectra. Spectra were referenced to an external standard of TMS by setting the high frequency signal from adamantane to 38.5 ppm.

Solid-state ^{27}Al NMR spectra were acquired on a Varian VNMRS spectrometer operating at 104.198 MHz with a spinning rate of approx. 14 KHz. Spectra were obtained using direct excitation with a recycle delay of 0.2 s over 10000 scans. Spectra were referenced to an external standard of 1 M aq. $Al(NO_3)_3$ solution which was used as a primary reference ($\delta_{Al} = 0$ ppm).

Solid-state ^{29}Si NMR spectra were acquired on a Varian VNMRS spectrometer operating at 79.436 MHz with a spinning rate of approx. 8 KHz. Spectra were obtained using direct excitation with a recycle delay of 30–60 s over 512 scans. Silanol defect sites were

[7] Specified as the outer diameter of the zirconia rotor.

detected using a $^{1}H–^{29}Si$ cross-polarization pulse sequence with a 5 ms contact time and 1 s recycle delay over 1800 scans. Spectra were referenced to an external standard of TMS by setting the high frequency signal from neat tetrakis(tetramethylsilyl)silane to −9.9 ppm.

Solid-state ^{27}Al NMR spectra were acquired on a Bruker Avance III HD spectrometer operating at 161.992 MHz with a spinning rate of approx. 10 KHz. Spectra were obtained using direct excitation with ^{1}H high-powered decoupling. Spectra were obtained using a recycle delay of 10 s over 360 scans. Spectra were acquired by Dr. David Apperley of Durham University.

Solid-state ^{119}Sn NMR spectra were acquired on a Bruker Avance III HD spectrometer operating at 149.12 MHz with a spinning rate of approx. 10 KHz. Spectra were acquired using a $^{1}H–^{119}Sn$ CP-CPMG echo train pulse sequence as described by Kolyagin *et al*.[1] Cross-polarisation from protons (400.17 MHz) was acquired with a 5 ms contact time and 1–2 s recycle delay over a variable number of scans. Spectra were referenced to an external standard of tetramethyltin by setting the Sn signal from tetracyclohexyltin to −97.4 ppm. Spectra were acquired and spikelet patterns processed by Dr. David Apperley of Durham University.

Solid-state ^{133}Cs NMR spectra were acquired on a Varian VNMRS spectrometer operating at 52.45 MHz with a spinning rate of approx. 10 KHz. Spectra were obtained using direction excitation with a recycle delay of 0.2 s over 10000 scans. Spectra were referenced to an external standard of 1 M aq. CsCl solution which was used as a primary reference (δ_{Cs} = 0 ppm).

9.2.3 ICP-OES of Modified Zeolites.

Zeolite materials to be analysed by ICP-OES were prepared by one of two methods. Some were prepared in a traditional manner by digestion in concentrated hydrofluoric acid before being allowed to evaporate (150 °C) and subsequently being re-dispersed in a known volume of HNO_3. Some zeolite samples were prepared using Inorganic Ventures™ acid dissolution reagents following *Protocol A* for “elemental analysis of zeolites” at one quarter scale.[2] Briefly, 20–25 mg of zeolite materials was wetted with 2–3 drops of deionized water before addition of 2.5 mL UA–1 (Inorganic Ventures™ acid dissolution reagent) and 0.1 mL 70% HNO_3. The vessel was sealed and shaken for 1–3 minutes before addition of 10 mL UNS–1 (Inorganic Ventures™ stabilization reagent). The solution was adjusted to a final weight of 25–125 g with deionized water and thoroughly mixed. Additionally, solutions were diluted a further five-fold with deionized water before introduction into the spectrometer in order to

reduce viscosity and improve plasma stability. Both material dissolution methods and data collection were performed by Dr. Emily Unsworth of Durham University.

ICP-OES analysis was performed using a Jobin Yvon Horiba Ultima 2. Instrument setup: Radial torch, sequential monochromater, cyclonic spray chamber and concentric nebulizer. Sequential monochromator average wavelengths were 224.641 nm and 328.068 nm for Ag species, 394.401 nm and 396.152 nm for Al species, 413.380 nm and 418.660 nm for Ce species, 228.616 nm and 350.228 nm for Co species, 267.716 nm and 357.868 nm for Cr species, 455.531 nm for Cs species, 224.700 nm and 324.754 nm for Cu species, 238.204 nm and 259.940 nm for Fe species, 294.364 nm and 417.206 nm for Ga species, 766.490 nm and 769.896 nm for K species, 279.553 nm and 285.213 nm for Mg, 257.610 nm and 259.373 nm for Mn species, 221.647 nm and 231.604 nm for Ni species, 324.270 nm and 340.458 nm for Pd species, 780.023 nm for Rb species, 240.272 nm and 267.876 nm for Ru species, 410.238 nm for Y species, and 213.856 nm and 334.502 nm for Zn Species. Reported values for M wt% were determined from a mean average of all applicable wavelength values acquired.

9.2.4 X-Ray Fluorescence Analysis.

Wavelength dispersive X-ray fluorescence (WD-XRF) analyses were performed using a Panalytical Zeitium WD-XRF. The samples were provided as homogenized powders and weighed on a balance accurate to 0.1 mg. The sample weighing approximately 200 mg was placed directly into a Pt 95%/Au 5% crucible. To this, a Lithium Borate flux was added until the total weight of each sample and flux was 6.6 g. Claisse brand high purity flux was used containing 66.67% $Li_2B_4O_7$ – 32.83% $LiBO_2$ – and 0.50% LiI (releasing agent). The sample and flux were then mixed together using a vortex mixer, and the placed in a Claisse La Neo Fluxer using the ‘Refractory Materials’ fixed conditions method. The mixture was brought to a temperature of 1065 °C and rocked by the fluxer during fluxing. The total fluxing time was 15 minutes, and the cooling time was 6 minutes. Elemental analysis on the fused beads was conducted on a Panalytical Zeitium WD-XRF equipped with a 4 kW rhodium anode tube. The samples were analysed using the Panalytical’s proprietary ‘Wroxi’ calibration and corrections were made for the variable weight of each sample. The analysis time for each sample was 340 seconds. Samples for WD-XRF were prepared by the author and analysed by Dr. Kamal Badreshany of Durham University.

Energy dispersive X-ray fluorescence (ED-XRF) analyses were performed using a Panalytical Epsilon 1 ED-XRF equipped with a 50 kV silver anode tube. The samples (approx.

0.2–1 g) were provided as homogenized powders and were pressed into discs within a sample cup containing a polypropylene film. The run program featured collection of four spectra, one of which the X-rays were unfiltered and three of which utilised various metallic filters, details of each spectrum can be seen in Table 9.1. The total analysis time for each sample was around 20 minutes. The samples were analysed using the Malvern Panalytical's proprietary 'Omnian' calibration which had additional zeolite derived standards added to it to improve accuracy for specific elements, such as Si and Al.

Table 9.1: Conditions under which ED-XRF spectra were acquired.

Spectrum	Filter	Filter Thickness /μm	Voltage /kV	Analysis Time /s
1	Ag	100	50	99
2	Cu	500	50	282
3	Al	50	12	154
4	None	N/A	10	309

9.2.5. Scanning Electron Microscopy.

Scanning electron microscopy (SEM) was performed on a FEI Helios Nanolab electron microscope operated at 5 kV. The zeolite powders were suspended in isopropyl alcohol by ultrasonic treatment for 5 min. Samples were deposited onto a silicon (1 0 0) wafer (Agar Scientific, wafer thickness: 460-530 μm, polished) and coated with 20 nm of gold using a Cressington sputter coater 108 Auto. Scanning electron microscopy-energy dispersive X-ray spectroscopy (SEM-EDS) mapping was performed on samples that were pressed with a hand press into 8 mm pellets. Samples were prepared by the author and images collected by Dr. Meera Shah and Miss Irene Mazzei of Durham University.

SEM-EDS of microtomed samples was performed on a Zeiss Sigma 300 VP SEM operated at 15 kV. The zeolite powders were first set in epoxy resin before being mechanically ground down by several micrometres and the surfaces diamond polished. Care was taken to ensure that zeolite particles were not released from the resin during the polishing process and the absence of voids was verified by microscope analysis. As the particles were randomly suspended in the resin, the grinding and polishing steps revealed inner areas of the samples. Preparation of microtomed samples and data acquisition was performed by Dr. Diana-Alverez Ruiz of Durham University.

Particle size distributions were obtained by manual measurement of particle diameters using ImageJ software. The SEM images were loaded into ImageJ and their border contrast enhanced to aid clarity of measurement. For M–MFI materials, a sample of 100 particles was measured manually across the diameter of the small tablet-like crystals.

9.2.6. XAS Analysis.

XAS spectra were recorded in transmission and fluorescence modes at the Zn K-edge (9660 eV) and Zr K-edge (17998 eV), on beamline B18 at the Diamond Light Source operating with a ring energy of 3 GeV and at a current of 300 mA. XAS data was plotted and normalized using Athena software.

Pellets for *ex-situ* analysis were prepared by pressing in a 13 mm evacuable pellet die at approx. 1 ton for 30 s. Pellets weighed approximately 100 mg following preparation and were comprised of a calculated mass of sample and cellulose binder. The self-supporting pellets were transferred to an XAS plate and secured with Kapton tape before analysis. A minimum of three scans was performed for each sample in transmission (and optionally fluorescence) mode.

Air-sensitive pellets were prepared in an N_2 glovebox at Diamond Light Source by pressing in a 10 mm pellet die in a hand press. Pellets weighed approximately 40 mg following preparation and were comprised of approximately 25 mg sample and 15 mg cellulose binder. The self-supporting pellets were transferred to an XAS plate and secured with Kapton tape. The XAS plate was then loaded into an air-tight cell equipped with Kapton windows before being transferred out of the glovebox for analysis. A minimum of three scans was performed for each sample in transmission (and optionally fluorescence) mode.

In-situ samples were analysed under flowing He gas (40 mL min^{-1}) within a ceramic box furnace in order to best mimic catalysis experimental conditions. Samples were prepared by first pressing in a 32 mm evacuable pellet die from Apollo Scientific before being sieved to a size fraction of 40–60 mesh (420–250 μm). A recorded mass of sample was then transferred in to a glass capillary (o.d. 3 mm) and plugged at both ends with quartz wool. The capillary was then mounted into a custom holder comprising a mounting block with two Swagelok tube holders (see Figure 9.1 left) and secured with epoxy resin. Gas lines were then secured to the holder by use of Swagelok fittings and a thermocouple was inserted into the capillary bed before the apparatus was mounted into a box furnace on the beamline (see Figure 9.1 right). A second thermocouple was mounted into the box furnace to assess temperature consistency.

Following initiation and stabilisation of He flow, samples were heated to 400 °C at a ramp rate of 5 °C min^{-1} whilst scans were continually taken in transmission mode (scan rate = 30 h^{-1}).

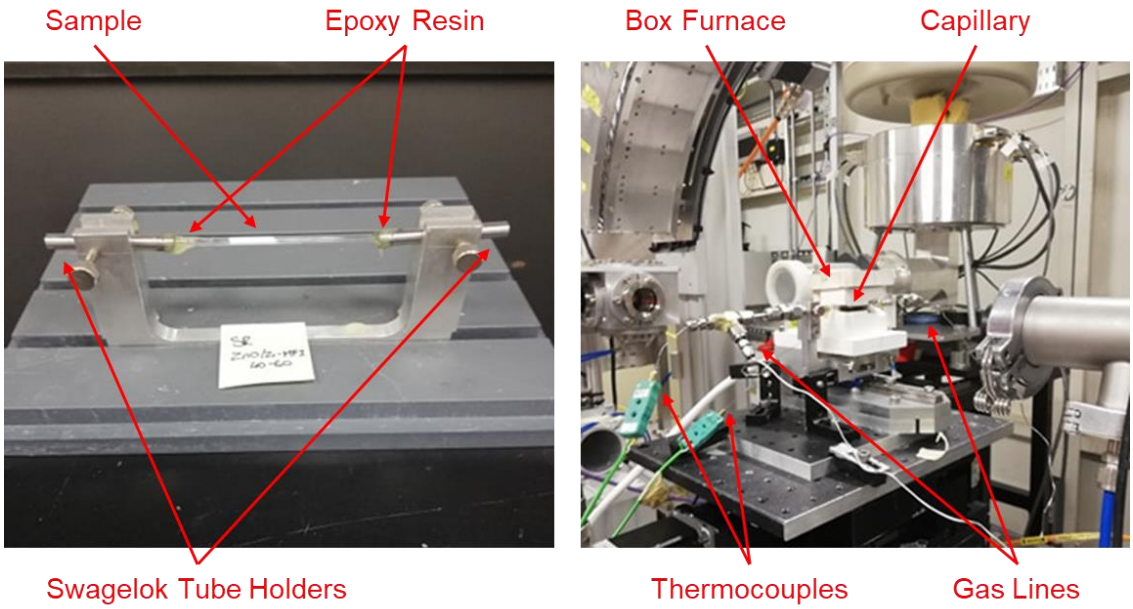

Figure 9.1: *In-situ* XAS apparatus at B18 beamline, Diamond Light Source. Left: Sample loaded into a glass capillary and mounted within a custom sample holder comprising Swagelok tube holders. Right: Sample holder loaded into a box furnace and affixed with gas lines and thermocouples on B18 beamline.

9.3. Experimental Procedures.

9.3.1 General Calcination Procedure for Zeolites.

Zeolites were calcined either in static air in a muffle furnace or *in vacuo* on a Schlenk line in a quartz tube mounted within a tubular furnace. The following temperature program was used in the appropriate furnace listed in Section 9.2.1: Ramp 5 °C min^{-1} to 150 °C > Hold for 1 h > Ramp 5 °C min^{-1} to 550 °C > Hold for 5 h > Cool to room temperature.

Conversion of an ammonium-form zeolite to a hydrogen-form zeolite was confirmed by use of solid-state ^{1}H NMR spectroscopy to observe the loss of the ammonium resonance at approx. 7.0 ppm alongside reduction in the measure nitrogen content by CHN microanalysis.

9.3.2 General Ion-Exchange Procedure.

To a centrifuge tube charged with zeolite (0.50–1.25 g) was added an aqueous solution of $M(NO_3)_x$ (25 mL, 0.3 M, where M is the desired metal cation to be exchanged into the zeolite, M^{x+}) which was then agitated constantly for 1 h using a mechanical tube roller. Following this, the tube was centrifuged at 4500 rpm for 5.5 min (330 s) and the resulting supernatant decanted off. The residual solid was then re-dispersed into a fresh measure of nitrate solution and the process repeated (×5–10). The solid samples were then washed with

deionised water and centrifuged to separate (×5–10) before being dried overnight at 80 °C and calcined (see Section 9.3.1) in preparation for usage and analysis.

9.3.3 General Wetness Impregnation Procedure.

Metal impregnated zeolites were prepared by a wetness impregnation method with the respective metal nitrate or metal chloride solution. A calculated amount of the metal precursor (1–10 wt% by metal) was dissolved in distilled water (4 mL) before the zeolite powder (1 g) was added. For differing masses of zeolite, the preparation was linearly scaled. The resulting suspension was then transferred into a 10 mL round bottom flask and mixed thoroughly overnight on a rotary evaporator. The sample was brought to dryness under reduced pressure and constant agitation, followed by further drying at 80 °C overnight and subsequent calcination (see Section 9.3.1) in preparation for usage and analysis.

9.3.4 Drying of Solvents over Metallic Sodium.

Under an atmosphere of nitrogen, a flask attached to a distillation setup was charged with 500 mL of the desired solvent to be dried. Benzophenone (10 g) was added and stirred to dissolve. Metallic sodium (5 g, approx. 1 mm^3 cubes) was added slowly and the mixture allowed to stir overnight until the blue colour of the sodium benzophenone ketyl radical was observed to indicate dryness. The dried solvent was then distilled into a clean flask and transferred *via* cannula to a rigorously dried ampule for storage.

9.3.5 Drying of Solvents over Phosphorus Pentoxide.

Under an atmosphere of nitrogen, a distillation setup was charged with the desired solvent to be dried. Phosphorous pentoxide (approx. 0.1 g per 10 mL solvent) was added and the mixture allowed to stir overnight. The dried solvent was then distilled directly into a rigorously dried ampule for storage. For larger volumes (~ 500 mL), the dried solvent was distilled into a clean flask and transferred *via* cannula to a rigorously dried ampule for storage.

9.3.6 Synthesis of M^{IV}–MFI materials where M^{IV} = Si, Sn, Ti, Zr, Hf.

M–MFI materials (where M = Si, Sn, Ti, Zr, Hf) were prepared under hydrothermal conditions with a method adapted from the synthesis of Sn–MFI reported by Kolyagin *et al.* and Mal *et al.*[1, 3] To a solution of tetrapropylammonium hydroxide (TPA–OH, 26.4 g, 25 % in H_2O, Acros Organics) was added distilled water (6.6 g) to form a 20% solution of TPA–OH (33 g). Under vigorous stirring, tetraethylorthosilicate (TEOS, 15.3 g, 98%, Fisher Scientific UK) was added and hydrolysis continued for 30 minutes. Subsequently, a solution of the desired metal precursor (1.084 mmol) in distilled water (10 g) was added and stirring continued

for 1 hour. Metal precursors were used as follows for Sn–MFI, Ti–MFI, Zr–MFI and Hf–MFI respectively: $SnCl_4 \cdot 5H_2O$ (0.380 g, 98%, Sigma Aldrich), $Ti(O^iPr)_4$ (0.114 g, 97%, Sigma Aldrich), $ZrOCl_2 \cdot 8H_2O$ (0.349 g, 98+%, Acros Organics), $HfOCl_2 \cdot 8H_2O$ (0.444 g, 98+%, Fisher Scientific UK). For Si–MFI, distilled water (10 g) was added instead. Gel preparation was completed by addition of further distilled water (9.0 g) and the resultant white to clear gel was stirred for 15 minutes. The gels were loaded into PTFE-lined stainless-steel autoclaves and crystallized in a preheated oven at 453 K for 72 hours under static conditions. Following hydrothermal treatment, the zeolite powders were centrifuged to separate the mother liquor and washed thoroughly with distilled water until the washings registered a pH value < 8. Samples were then dried overnight at 353 K before being calcined at 423 K for 1 hour and 823 K for 5 hours (5 K min^{-1} ramp rate).

9.3.7 Synthesis of M^{II}–MFI materials where M^{II} = Zn or Mg.

M–MFI materials (where M = Zn, Mg) were prepared under hydrothermal conditions with a method adapted from the synthesis of Sn–MFI reported by Kolyagin *et al.* and Mal *et al.*[1, 3] To a solution of tetrapropylammonium hydroxide (TPA–OH, 26.4 g, 25 % in H_2O, Acros Organics) was added distilled water (6.6 g) to form a 20% solution of TPA–OH (33 g). Under vigorous stirring, tetraethylorthosilicate (TEOS, 15.3 g, 98%, Fisher Scientific UK) was added and hydrolysis continued for 30 minutes. Subsequently, a solution of the desired metal precursor (1.084 mmol) in distilled water (10 g) was added and stirring continued for 1 hour. Metal precursors were used as follows for Zn–MFI and Mg–MFI respectively: $ZnCl_2$ (0.380 g, 98%, Sigma Aldrich), $MgCl_2$ (0.114 g, 97%, Sigma Aldrich). Gel preparation was completed by addition of further distilled water (9.0 g) and the resultant white to clear gel was stirred for 15 minutes. The gels were loaded into PTFE-lined stainless-steel autoclaves and crystallized in a preheated oven at 453 K for 72 hours under static conditions. Following hydrothermal treatment, the zeolite powders were centrifuged to separate the mother liquor and washed thoroughly with distilled water until the washings registered a pH value < 8. Samples were then dried overnight at 353 K before being calcined at 423 K for 1 hour and 823 K for 5 hours (5 K min^{-1} ramp rate).

9.3.8 Dealumination of Zeolites using Concentrated Nitric Acid.

A 500 mL round bottom flask was charged with the desired zeolite to be dealuminated (10 g) and an air condenser attached. Nitric acid (13 M, 200 mL) was added *via* the condenser and the resulting suspension stirred overnight whilst submerged in an oil bath set at 100 °C. Upon cooling, the suspension was decanted into 8 centrifuge tubes and centrifuged to separate.

The resulting solid in each tube was washed with 30 mL deionised water per tube (×4) until the washings were neutral and subsequently dried at 80 °C overnight.

Method adapted from van der Graaf *et al.*[4]

9.3.9 Remetallation of Dealuminated Zeolites using $SnCl_4$.

Zeolite that had been dealuminated according to procedure 9.3.8 (2 g) was dehydrated *in vacuo* at 150 °C overnight using a tube furnace and transferred to an inert atmosphere glovebox. Within the glovebox, 1 g of the zeolite was loaded into a three neck 250 mL round bottom flask and a reflux condenser, stopper, and gas tap attached before being transferred to a Schlenk line and evacuated and refilled with nitrogen gas (×3). Dry DCM (100 mL) was then added to the flask *via* cannula transfer and the resulting suspension dispersed by magnetic stirring. $SnCl_4$ solution (1 M in DCM, 40 mL, 40 mmol) was then added to the suspension and the system refluxed overnight under a blanket of N_2. Upon cooling, the suspension was decanted into 4 centrifuge tubes. Once fuming had subsided, the tubes were sealed and centrifuged to separate the remetallated solid, with the supernatant being quenched in MeOH and retained. The solid was then washed with 30 mL MeOH per tube (×3) and all supernatants combined and retained. The retained supernatants were treated with weak aqueous NaOH solution to precipitate $Sn(OH)_4$ which was filtered, dried and disposed of as SnO_2. The washed zeolite was dried at 80 °C overnight and calcined according to the following program under air in a muffle furnace: Ramp 3°C min^{-1} to 200 °C > Hold for 6 h > Ramp 3 °C min^{-1} to 550 °C > Hold for 6 h > Cool to room temperature.

Method adapted from Vega-Vila *et al.*[5]

9.4. Flow Reactor Designs and Setups.

9.4.1 Design, Operation and Limitations of the Quartz Tube Reactor.

In order to test the produced catalysts for their efficacy in the numerous desirable reaction steps within the Guerbet and Lebedev pathways, a home-designed flow reactor was constructed. The reactor (schematic view shown in Figure 9.) is based upon the classic ‘quartz tube’ model in which the catalytic reaction takes place inside a borosilicate glass or quartz tube (dependant on reaction temperature), supported within a tubular furnace.

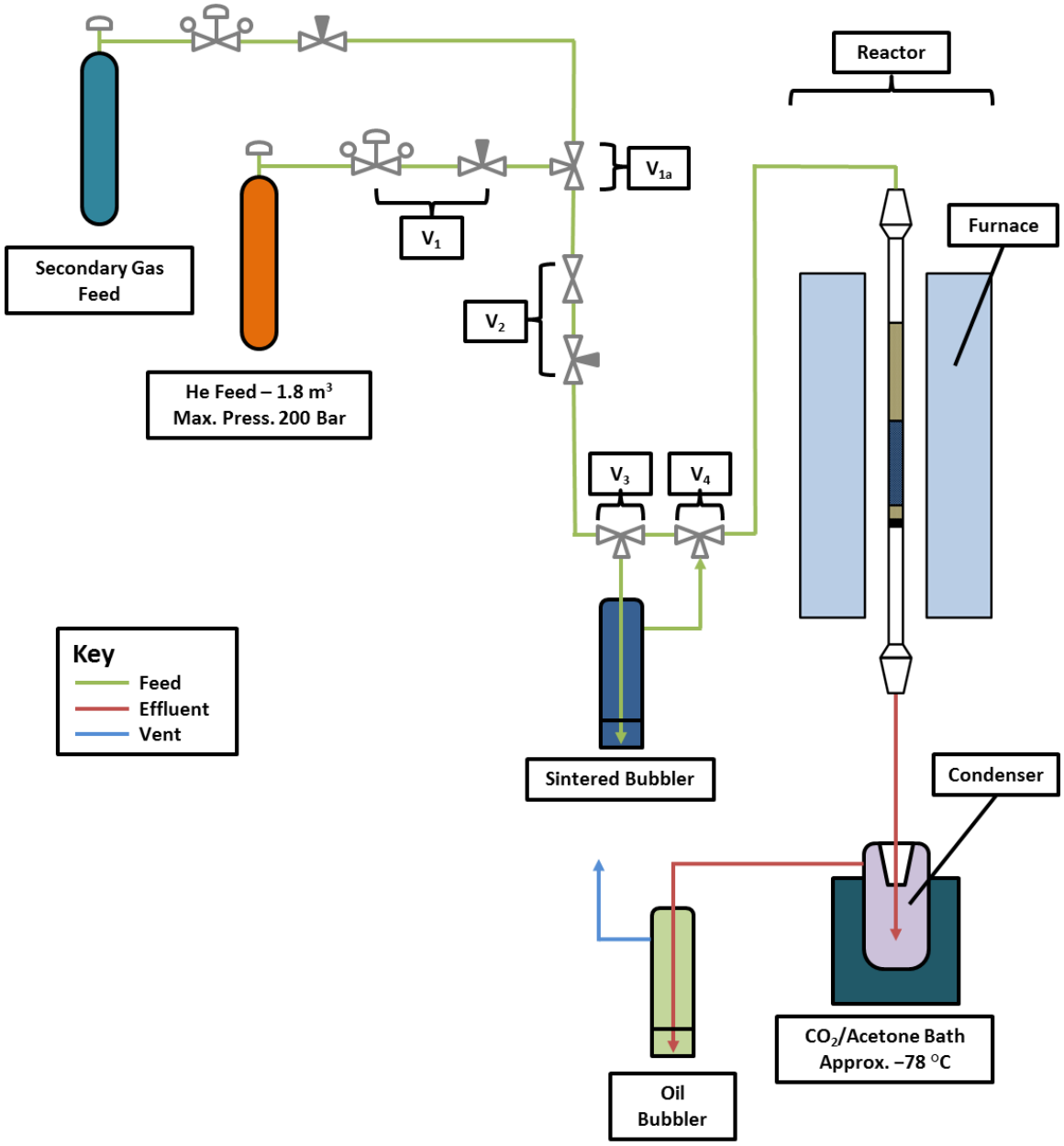

Figure 9.2: A schematic overview of the quartz tube catalytic testing set up: labelled are the helium cylinder, dual stage regulator (V_1), open/close valve and fine needle valve (V_2), three way taps (V_3 and V_4), sintered bubbler, tubular furnace with quartz reactor tube, condenser and oil bubbler. V_{1a} allows for the introduction of multiple gases in a sequential fashion.

Gases were supplied to the apparatus directly from cylinders *via* a dual stage regulator (V_1, IWS Gaffey) set at approximately 0.35 bar (5 psi) and equipped with a needle valve. Further control of flow rate was achieved by manipulation of a quarter turn shutoff valve and fine needle valve (V_2, Swagelok SS-43GS4 and OB-HV1013). Unless otherwise stated, V_1 and V_2 were not adjusted and, using a gas-liquid displacement method, the flow rate of gas was determined and a constant flow rate of approximately 40 mL min^{-1} was achieved. Owing to the nature of the apparatus, multiple gases may be utilised sequentially by installation and manipulation of one or more three-way taps, V_{1a}, between V_1 (one regulator per cylinder) and

V_2. Gases were used as received and not mixed. All gas lines were initially constructed out of Nalgene 180 PVC tubing (¼" internal diameter (I.D.), Thermo Scientific), although degradation was observed to occur upon exposure to certain reagents, e.g. ^{n}propylamine and acetaldehyde. As a result, this tubing was replaced after V_2 with PTFE tubing (8 mm I.D, Lab Unlimited). Similar observations were recorded with regard to degradation of the butyl rubber o-rings within the system, specifically those that were located at the connection of the sintered bubbler to the bypass (V_3 and V_4), and these were subsequently replaced with PTFE o-rings of the same dimensions.

Liquid reagents were introduced into the system by use of a sintered bubbler to saturate the gas flow. Two glass/PTFE three-way taps, V_3 and V_4, were used to control whether the gas saturator was on-line or allowed to be bypassed to supply a "dry" gas stream to the reactor bed. One disadvantage of this system is that the feed rate of liquid reagents is difficult to control, meaning that more volatile reagents were fed more quickly over the catalyst bed. However, due to the predominately qualitative nature of experiments performed on this setup, this was not particularly problematic.

Gas and liquid reagents were fed into a borosilicate or quartz glass tube supported inside of a vertically mounted Lenton LTF 12/25/250 single zone tube furnace with a maximum operating temperature of 1200 °C. The glass tubes were designed as such that a borosilicate or quartz glass frit was positioned at the base of the furnace's isothermal zone (see Figure 9.3) as dictated by the manufacturers' documents and temperatures cross-checked with a thermocouple (see Figure 9.5). This allowed the entire catalyst bed to be situated within the furnace's isothermal zone to ensure even heating throughout. Thermocouple measurements confirmed that the temperature inside the work tube was within an acceptable range of the set point ($\Delta T = < 1\%$). A glass or quartz wool plug was formed in the top of the work tube to improve thermal efficiency. Teflon sleeves were placed between the ground glass joints at the top and bottom of the reactor tube to attempt to minimise gas/vapour leakage. Joints were secured with glass clips.

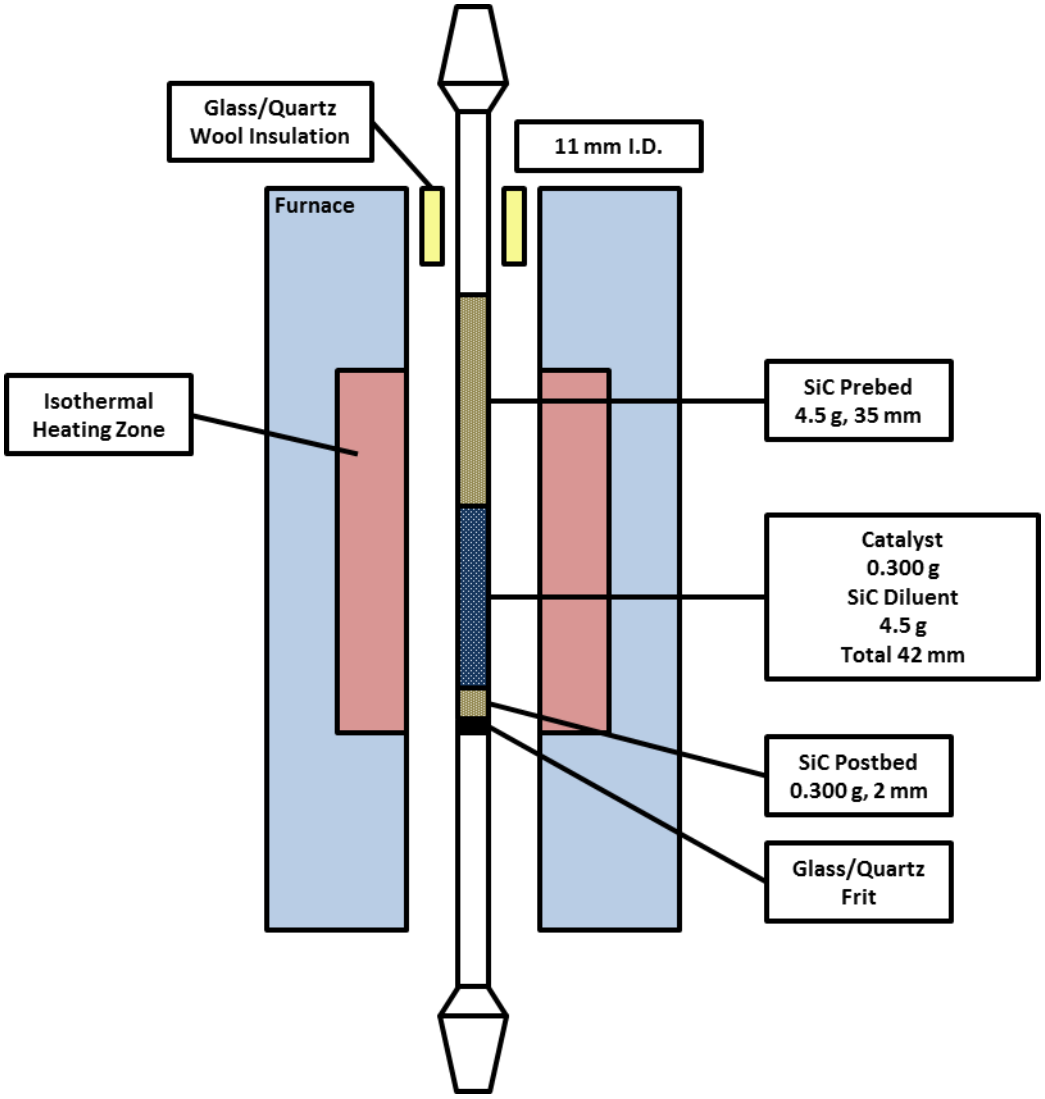

Figure 9.3: Tubular reactor design schematic and relevant dimensions.

Catalysts were pelletized by pressing at 10 tons for 30 s in an Apollo Scientific XRF die equipped with 32 mm KBX-320 pellets using a Specac hydraulic press. The pressed catalysts were then sieved between 40–60 mesh (420–250 μm). Three different reactor bed designs were used throughout this project and are shown in Figure 9.4, denoted as "bed type A, B and C". Bed type A consisted of a 0.300 g Silicon Carbide (SiC) pre-bed, followed by 0.300 g of prepared catalyst and a further 0.300g of SiC post-bed. Bed type B consisted of a 4.5 g SiC pre-bed, followed by 0.300 g of prepared catalyst and 0.300g of SiC post-bed. Bed type C consisted of a 4.5 g SiC pre-bed, followed by 0.300 g of prepared catalyst diluted in 4.5 g of SiC and a subsequent 0.300g of SiC post-bed.

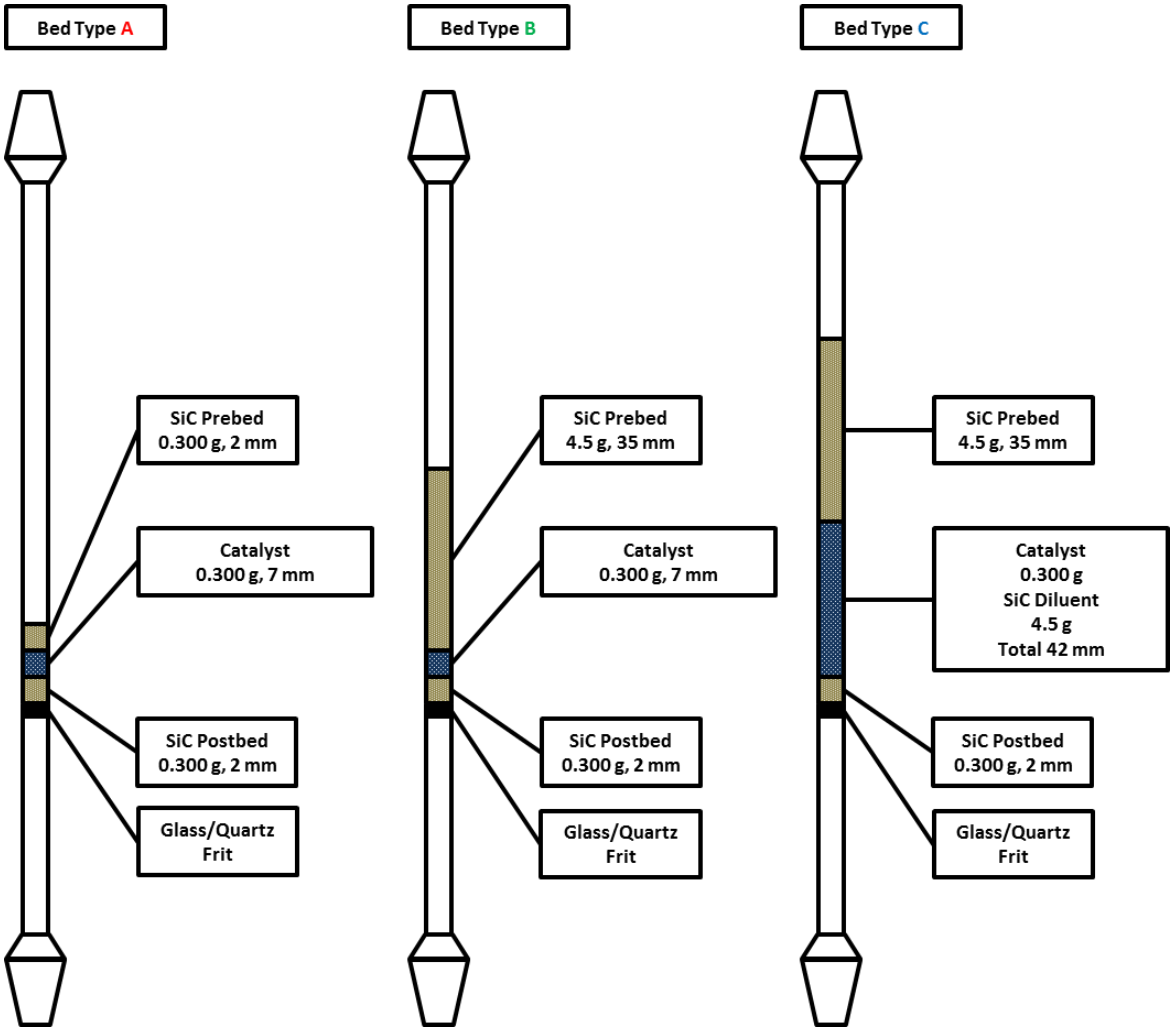

Figure 9.4: Various reactor bed designs (A, B and C) used within this project.

Bed type A was initially used, although following literature research on reactor bed design, bed types B and C were contrived in order to improve catalytic performance. The SiC pre-bed was extended in order to improve reagent heating before contact is made with the active catalyst. Additionally, the catalyst bed was diluted with further SiC to improve both thermal (minimisation of local heating or cooling, improved thermal homogeneity) and transport properties of the catalyst bed. In order to ensure that the catalyst bed of any design resides within the isothermal zone of the furnace, the temperature of the furnace was mapped *in situ* at 2 mm intervals whilst holding at 400 °C. The location of the catalyst Bed Type C (the longest and most likely to extend beyond the isothermal zone) with respect to the furnaces' isothermal zone is shown in Figure 9.5.

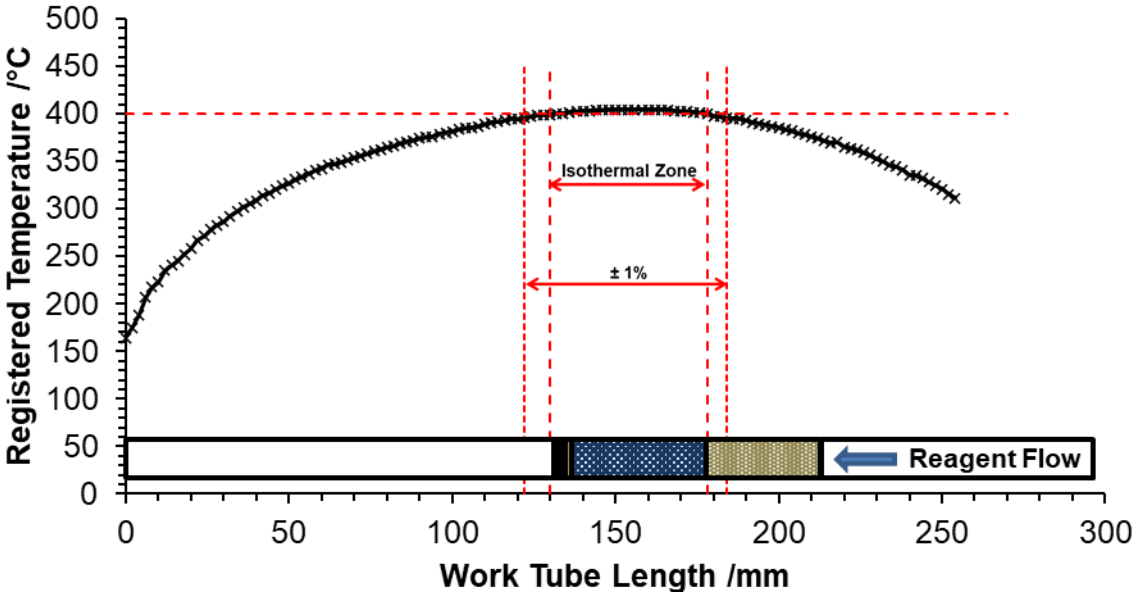

Figure 9.5: Single zone furnace temperature map with superimposed representation of where the quartz reactor tube (Bed Type C) sits within it, measured to an accuracy of ± 0.5 mm.

A comparison of the three bed types in the conversion of ethanol to acetaldehyde over a Zn-exchanged Na-MOR-(7.0) (5.49 wt% Zn, Zn/Al = 0.46) at 400 °C was performed to elucidate differences in acetaldehyde productivity over the various bed types; results are shown in Table 9.. Superimposed solution-state ^{1}H NMR spectra of the liquid effluent are shown in Figure 9.6. As can be seen, addition of a substantial SiC prebed (Bed Type B) results in a minor improvement in acetaldehyde productivity. Dilution of the catalyst bed in SiC (Bed Type C), however, provides a much greater improvement in acetaldehyde productivity. As such, Bed Type C was chosen as the design of choice for further reactions.

Table 9.2: Results of ethanol conversion to acetaldehyde over Zn-exchanged Na-MOR-(7.0) at 400 °C with various reactor bed designs. [a]Determined by solution-state ^{1}H NMR spectroscopy integrals

Reactor Bed Type	Ethanol Fed /g	Ratio of acetaldehyde to ethanol in liquid effluent[a].	Catalyst Coking (ΔC wt%)
A	1.219	1.18 : 1.00	6.11
B	1.214	1.25 : 1.00	6.30
C	1.205	2.72 : 1.00	6.89

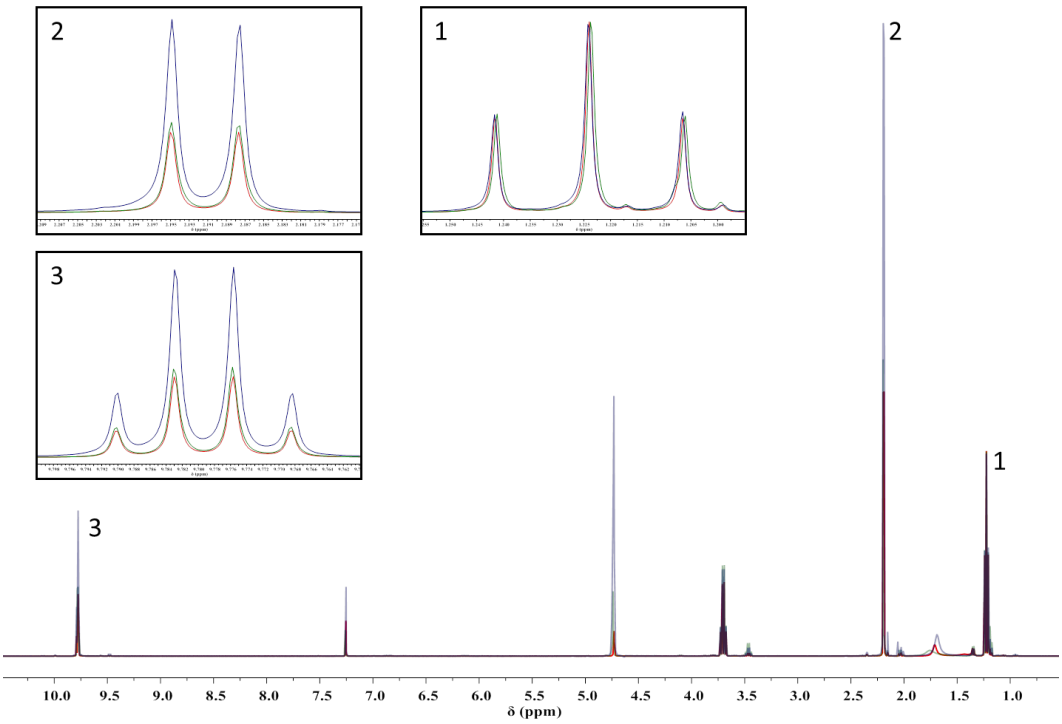

Figure 9.6: Stacked solution-state ^{1}H NMR spectra of product effluent from testing of Zn/Na-MOR-(7.0) over Bed Types A (red), B (green) and C (blue). Inset images and labelled peaks correspond to: 1) CH_3 peak of ethanol normalised to the same intensity, 2) CH_3 peak of acetaldehyde, 3) –COH peak of acetaldehyde.

A typical temperature ramp profile for catalysis in the quartz tube reactor is shown in Figure 9.7. Initially, the packed reactor bed and system are purged under flowing He at room temperature for a few minutes, the sintered bubbler is also briefly purged to replace the air atmosphere with an inert (He) although it is acknowledged that this will lead to a minor degree of reactant loss and a slight discrepancy with the reported reactant feed. The system is then ramped to 150 °C at a rate of 10 °C min^{-1} where it is held for 1 h in order to attempt to desorb water to prevent steaming of the zeolite (loss of Al from the framework *via* reaction with high temperature steam).[6] The system is then raised to the target reaction temperature (400 °C in the case of Figure 9.7) at a ramp rate of 10 °C min^{-1} where it is held for 30 min to complete desorption of any physisorbed atmosphere. Following this high temperature purge, V_3 and V_4 are opened and the gas stream is saturated with the reactant from the sintered bubbler for 2 h. Subsequently, the bubbler is bypassed, and the system allowed to purge for a further 30 min. The reactor tube is then cooled to approx. 200 °C at which point it is separated from the condenser and lifted from the furnace to cool completely.

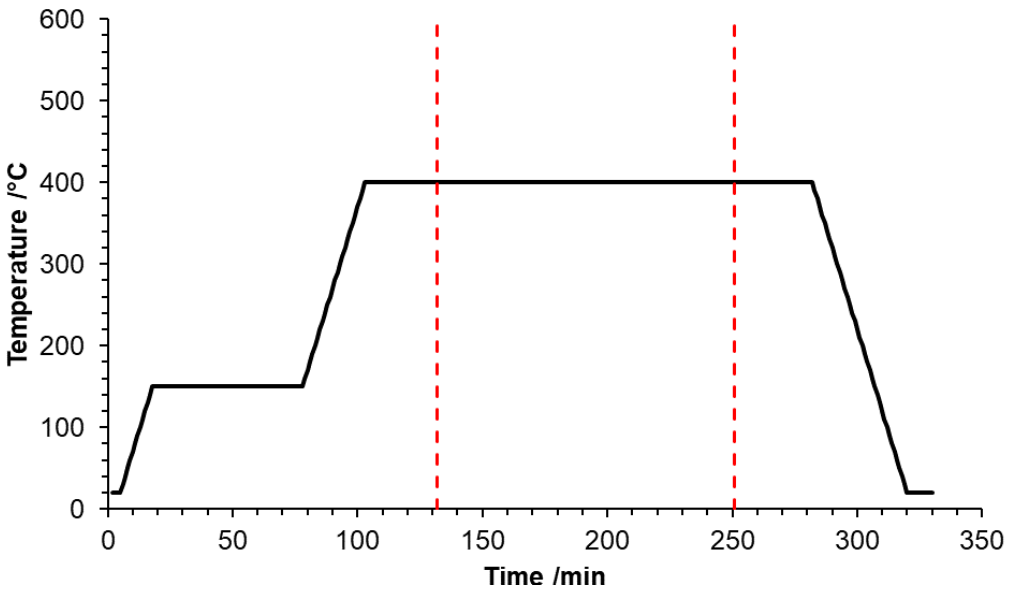

Figure 9.7: Typical temperature ramp graph in which the target reaction temperature was 400 °C. Red dashed lines indicate at which points the gas stream was opened and closed to the sintered bubbler respectively.

Following reaction in the vapour phase, liquid range effluent was condensed using a home designed condenser (see Figure 9.8) that was maintained at approx. −78 °C using a CO_2/acetone bath. The condenser was designed to attach directly and vertically to the reactor tube *via* a ground glass joint (Figure 9.8A) to minimise surfaces onto which liquid range effluent could condense before reaching the sampling point. One side arm was attached to exit tubing and an oil bubbler to allow monitored gas passage (Figure 9.8C) whilst another was stoppered with a suba-seal which allowed liquid to be removed by use of a needle to enable on-line sampling (Figure 9.8B). Unfortunately, the setup provided no consistent ability to accurately determine the mass of total liquid range products. This is resultant from a combination of factors: firstly, attempting to measure the mass of the condenser and liquid products (with view to subtract the original mass of the condenser) is impaired by condensation of atmospheric water across the glassware whilst cold adding superficial mass. Additionally, allowing the glassware to warm to ambient temperature may allow for substantial evaporation of low boiling products, such as acetaldehyde (b.p. ≈ 21 °C)[7]. Additionally, the total volume of condensate was typically low enough that any attempt to retrieve it in full in order to record a mass was detrimentally affected by that of which adhered to the glassware.

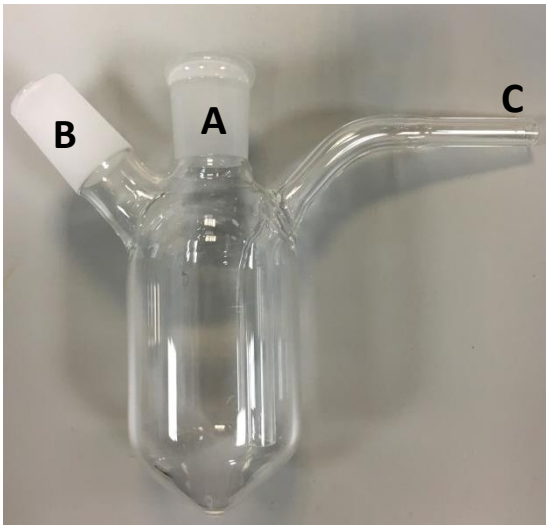

Figure 9.8: Photograph of the home designed condenser used for collection of liquid range effluent. Labelled are the joint that attaches the reactor tube to the condenser (A), the joint in which a septum is inserted to allow on-line sampling (B) and the gas outlet (C).

Following catalytic reaction, three samples were submitted for solution-state ^{1}H NMR spectroscopy for each catalytic run, one of the condensate diluted in $CDCl_3$ to analyse organic miscible products, one of the condensate diluted in D_2O to analyse more polar D_2O soluble products and one of $CDCl_3$ washed around the condenser following removal of the condensate to recover any residual condensate. Following separation from the SiC diluent and pre/postbed, the mass of the spent catalyst was recorded and a sample submitted for CHN elemental microanalysis to determine to level of coke formation during the reaction (ΔC wt%). Where appropriate, liquid phase samples were submitted for GC-MS to aid identification of any unknown species in the ^{1}H NMR spectrum. In later reactions, gas phase samples were collected using a gas bag and subsequently analysed by GC-MS-BID. The mass of the sintered bubbler and liquid reagent both before and after reaction were recorded to achieve the mass of liquid reagents fed into the system in order to calculate the weight hourly space velocity (WHSV), defined as the mass of reagents fed divided by the mass of catalyst used.

The major limitations within this system are firstly the inability to sample gaseous products (although later reactions equipping a gas bag and GC-MS-BID analysis aimed to circumvent this problem) and secondly the inability to accurately record the mass of liquid condensate as previously detailed. Hence it was decided that, in all reactions using this system, the metric of interest would solely be liquid range product selectivity. This metric is unaffected by the flaws detailed above as all samples were taken within the same time frame and under the same procedure. Hence, this system still gives valuable insight into the catalytic pathways of interest. Successful candidates that gave a high selectivity to the desired product were then

tested in a stainless-steel fixed bed reactor capable of online GC-MS-BID analysis (see Section 9.4.2).

9.4.2. HEL FlowCat Flow Reactor.

9.4.2.1. Reactor Setup and Operation.

With a focus on quantitation and catalytic reaction development, ethanol conversion was carried out using a HEL FlowCat flow reactor with on-line GC-MS-BID analysis. All reaction (temperature, flow rate, etc) and analysis parameters were controlled by external PCs.

Catalyst material was prepared as for the quartz reactor by pressing at 10 tons for 30 s in an Apollo Scientific XRF die equipped with 32 mm KBX-320 pellets using a Specac hydraulic press. The pressed catalysts were then sieved between 40–60 mesh (420–250 μm). In a typical reaction, 0.300 g of prepared catalyst was diluted with 1.4 SiC and packed into a stainless-steel reactor bed (I.D. 4 mm) with a 2.0 g SiC post bed and 1.6 g SiC pre-bed.

Unless stated, He or N_2 was used as the carrier gas and gas flow was maintained at 40 mL min^{-1} by an internal mass flow controller. Other gases were introduced in a sequential fashion *via* a Swagelok three-way tap positioned before the mass flow controller. Liquid reagents were delivered by an Eldex HPLC pump and were typically delivered at a rate of 0.010 or 0.025 mL min^{-1}. The stainless-steel reactor bed (4mm i.d.) was mounted in a vertical clamshell heater and reaction temperature was monitored with an internal thermocouple.

Figure 9.9 shows a typical isothermal reaction profile for ethanol conversion at 400 °C. Initially, the packed reactor bed and system are purged under flowing He or N_2 at room temperature for 30 minutes. The system is then ramped to 150 °C at a rate of 10 °C min^{-1} where it is held for 1 h in order to attempt to desorb water to prevent steaming of the zeolite (loss of Al from the framework *via* reaction with high temperature steam). The system is then raised to the target reaction temperature (400 °C in the case of Figure 9.9) at a ramp rate of 10 °C min^{-1} where it is held for 30 min to complete desorption of any physisorbed atmosphere. Following this high temperature purge, the HPLC pumped is engaged and liquid reagent is fed into the system for 2 h. Subsequently, the HPLC pump is disengaged and the system allowed to purge for a further 30 min. The reactor heater is then turned off and the system allowed to cool completely before removal of the reactor bed.

For variable temperature experiments, the packed reactor bed and system are purged under flowing He or N_2 at room temperature for 30 minutes. The system is then ramped to 150 °C at a rate of 10 °C min^{-1} where it is held for 1 h. The system is then raised to the target

reaction temperature (400 °C in the case of Figure 9.9) at a ramp rate of 10 °C min^{-1} where it is held for 30 min to complete desorption of any physisorbed atmosphere. Following this high temperature purge, the temperature of the reactor was ramped down to 200 °C at a rate of 10 °C min^{-1} where it is held for 0.5 h. Subsequently, the HPLC pumped is engaged and liquid reagent is fed into the system for 1 h. The HPLC pump is then disengaged and the system allowed to ramp to the next temperature point (250 °C) at a rate of 10 °C min^{-1}. The purge, reaction and ramping steps are then repeated at each desired temperature point (typically at increments of 50 °C) until the maximum desired temperature is reached (Figure 9.10). Following reaction, the system is allowed to purge for a further 30 min. The reactor heater is then turned off and the system allowed to cool completely before removal of the reactor bed.

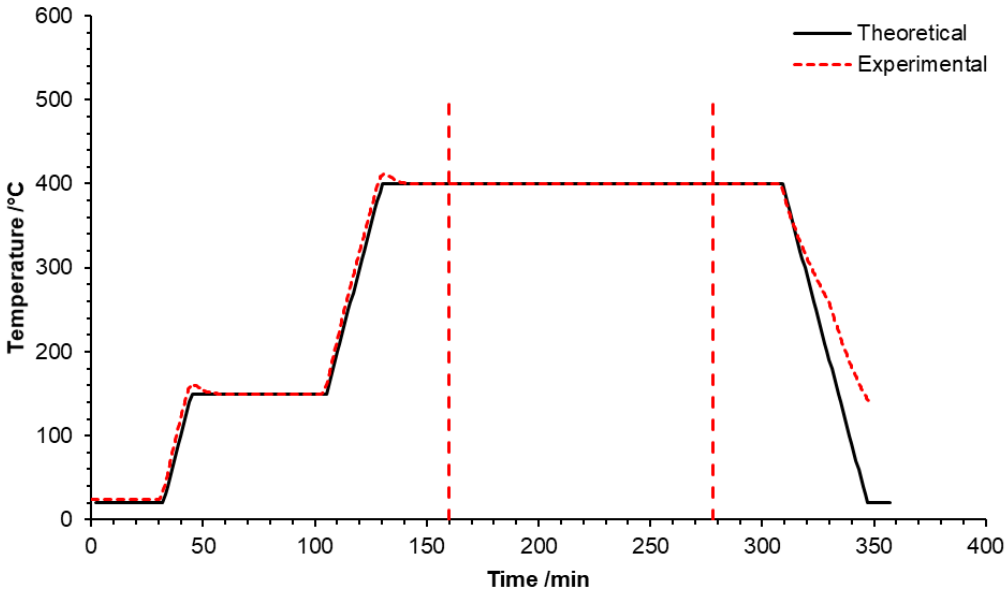

Figure 9.9: Typical temperature ramp graph in which the target reaction temperature was 400 °C. Red dashed lines indicated at which points the HPLC pump was engaged and disengaged respectively.

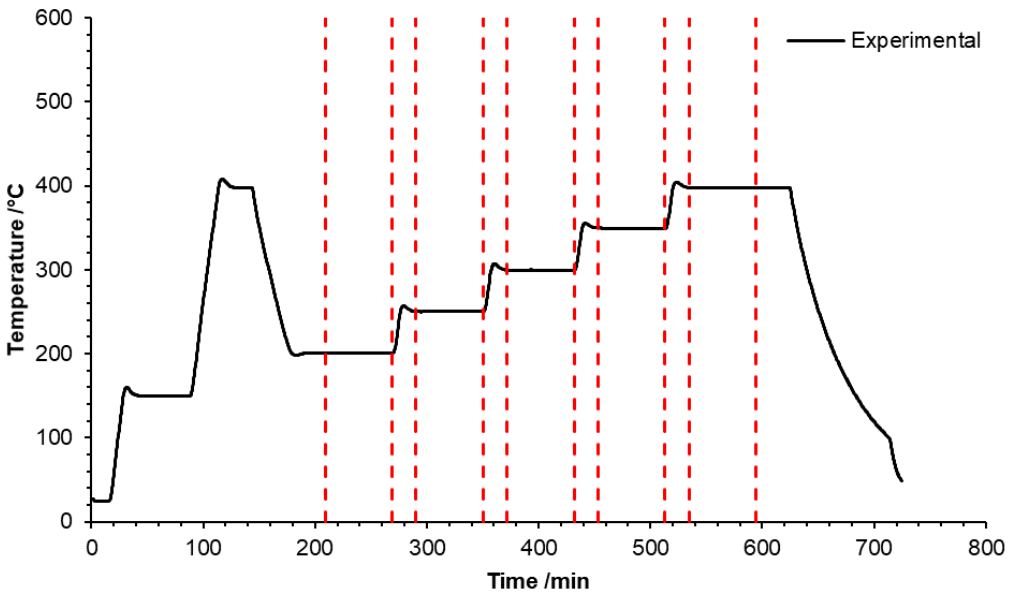

Figure 9.10: Typical temperature ramp graph in which the target reaction temperature was varied in increments of 50 °C from 200–400 °C. Red dashed lines indicated at which points the HPLC pump was engaged and disengaged respectively.

Product analysis was performed using on-line tandem GC-MS-BID analysis. The reactor effluent line was plumbed into a Shimadzu GC-2010 Plus gas chromatograph *via* 1/8-inch trace heated lines maintained at 170 °C. The reactor effluent passed through two 6 port Vici valves kept in a heated box (180 °C) through which two samples were automatically taken from the reactor effluent *via* a 0.5 mL sample loop on each Vici valve. The two samples were independently flushed to and injected through two separate split valves with the injection ports maintained at 220 °C (Sample 1) and 200 °C (Sample 2). Sample 1 was injected with a 250:1 He split ratio and chromatography performed over either a SGE Analytical BPX90 capillary column with a 90% cyanopropyl polysilphenylene-siloxane stationary phase (length 30 m, I.D. 0.25 mm, film thickness 0.25 μm) or a Thames Restek RTX-VMS fused silica capillary column (Length 30 m, I.D. 0.25 mm, film thickness 0.25 μm). Sample 2 was injected with a 10:1 He split ratio and chromatography performed over a Restek ShinCarbon ST packed column with a high surface area (~1,500 $m^2\ g^{-1}$) carbon molecular sieve stationary phase (length 2 m, I.D. 1.00 mm, O.D. 1/16", packed 100/120 mesh). Both columns were mounted in the same oven and hence underwent the same heating profile throughout the chromatography stage. A typical GC program used for analysis of ethanol conversion products involved injection onto the column at 80 °C at which it was held for 7.0 min before being ramped at 30 °C min^{-1} to 250 °C at which it was held for 8.0 min to give a total run time of approximately 20 min. For longer GC programs, the time at which the column oven was held at 250 °C was extended. Sample 1 was analysed using a Shimadzu GC-MS-QP2010 SE mass spectrometer maintaining interface

and ion source temperatures at 220 °C and 200 °C respectively. Mass spectrometry was performed over the entirety of the GC program with the first event occurring at 0.1 min and further events occurring every 0.3 s. Ions were detected in an m/z range of 10–200 with a scan speed of 666 ms. Sample 2 was analysed using a Shimadzu BID-2010 Plus detector maintaining the He plasma at 300 °C. Analysis was performed over the entirety of the GC program with a sampling rate of 40 ms. Figure 9.11 shows example MS and BID traces respectively for a standard ethanol to acetaldehyde reaction. Figure 9.12 shows example MS and BID traces respectively for a standard ethanol to butadiene reaction.

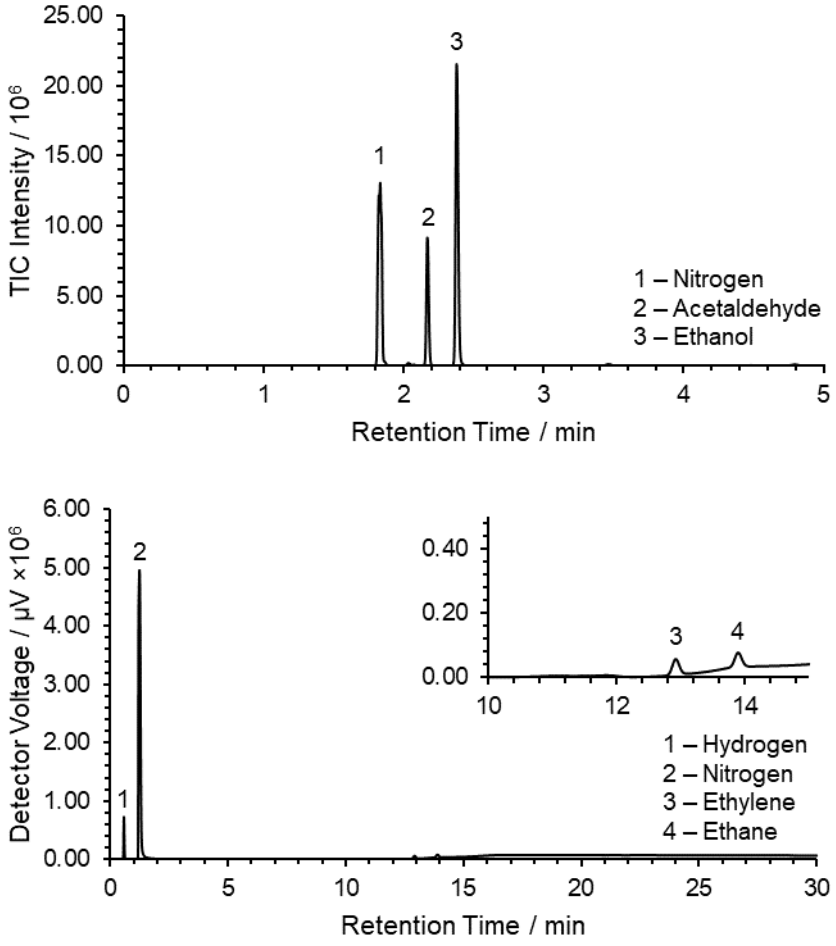

Figure 9.11: Example MS (top) and BID (bottom) traces from an ethanol to acetaldehyde reaction highlighting retention times of products of interest. Detection columns: RTX-VMS (MS), ShinCarbon ST (BID).

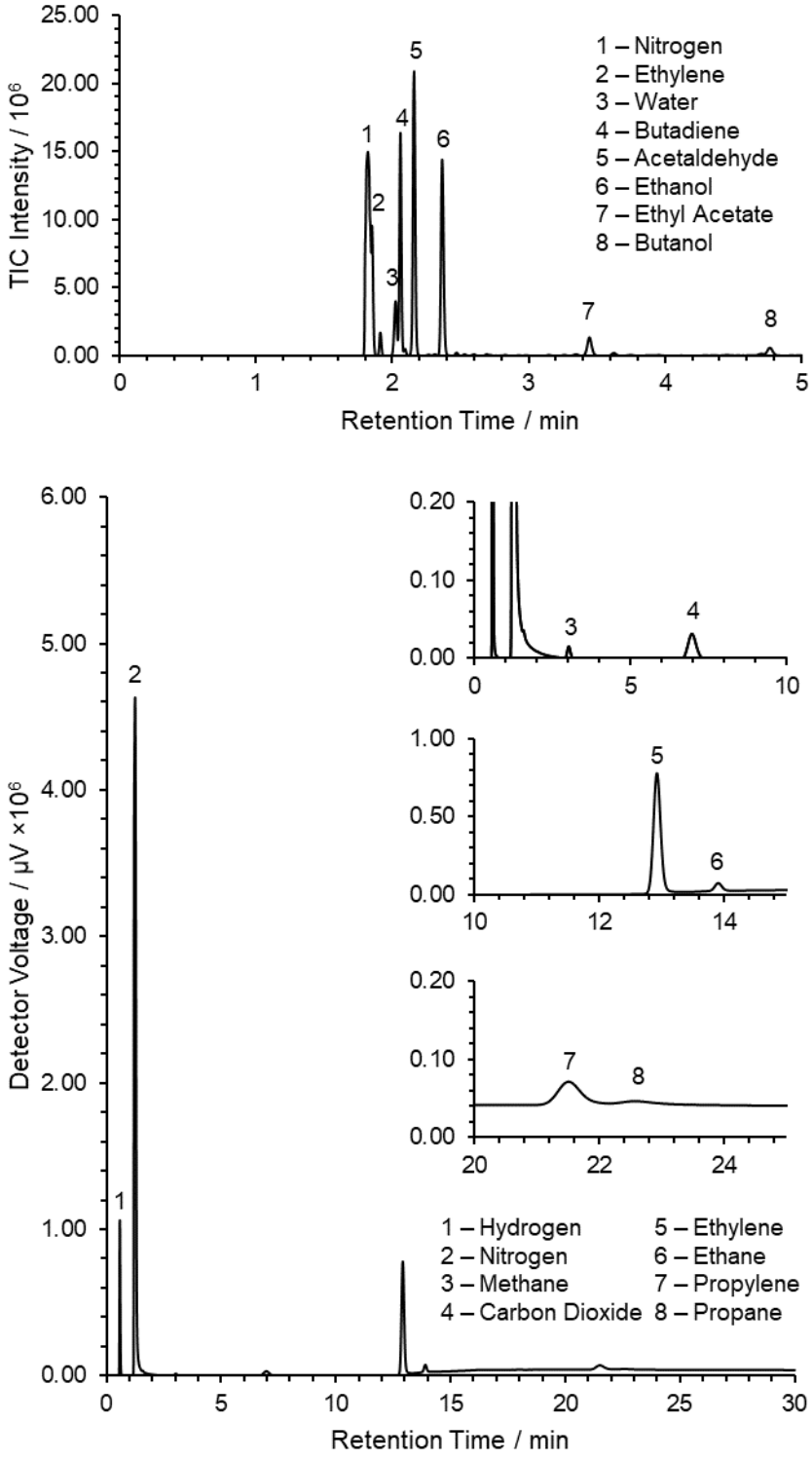

Figure 9.12: Example MS (top) and BID (bottom) traces from an ethanol to butadiene reaction highlighting retention times of products of interest. Detection columns: RTX-VMS (MS), ShinCarbon ST (BID).

9.4.2.2 Calibration of Liquid Range Products.

Mass spectrometry calibration for liquid range products was performed by pumping a known volume of the species to be calibrated through a SiC filled reactor bed maintained at

170 °C to match the maximum temperature of the trace heated lines and to minimise auto-reaction. Typically, each species was fed at 5–7 relevant flow rates and 5 data points were collected for each feed rate. A calibration curve was then plotted to allow transformation of mass spectrometry integrals to species productivity in mmol min^{-1} (see Appendix 3). Determination of conversions and selectivity values were then possible. Calibration curve data was collected in an isovolumetric and isobaric regime due to the nature of the GC-MS-BID system sampling in a known volume sample loop. To this effect, each species of interest was assumed to be act as an ideal gas. The volume of liquid reagent (mL min^{-1}) was converted first to a molar quantity (mmol min^{-1}) by application of the liquid's density (g mL^{-1}) and molar mass (g mol^{-1}). Following this, use of the molar volume of an ideal gas (22400 mL mol^{-1})[8] allowed conversion into a gas volume (mL min^{-1}). In a typical reaction in this project, He or N_2 gas was flowed at 40 mL min^{-1} and liquid ethanol was fed at 0.01 mL min^{-1} resulting in a total gaseous flow rate of 43.84 mL min^{-1}. For all other calibration data points where liquid ethanol was fed at different rates, the He gas flow was adjusted so that a total gas flow rate of 43.84 mL min^{-1} was attained (see Figure 9.13). In order to negate the effect of changing reaction temperature it is assumed that the gas expansion coefficient of all species obeys that of an ideal gas. Initially, for the BPX-90 column, only major species (acetaldehyde, ethylene, toluene and ethanol) were calibrated for in a molar regime as a change of MS column was planned. Subsequently, the RTX-VMS column was calibrated for a considerable range of plausible products as detailed in Appendix 3.

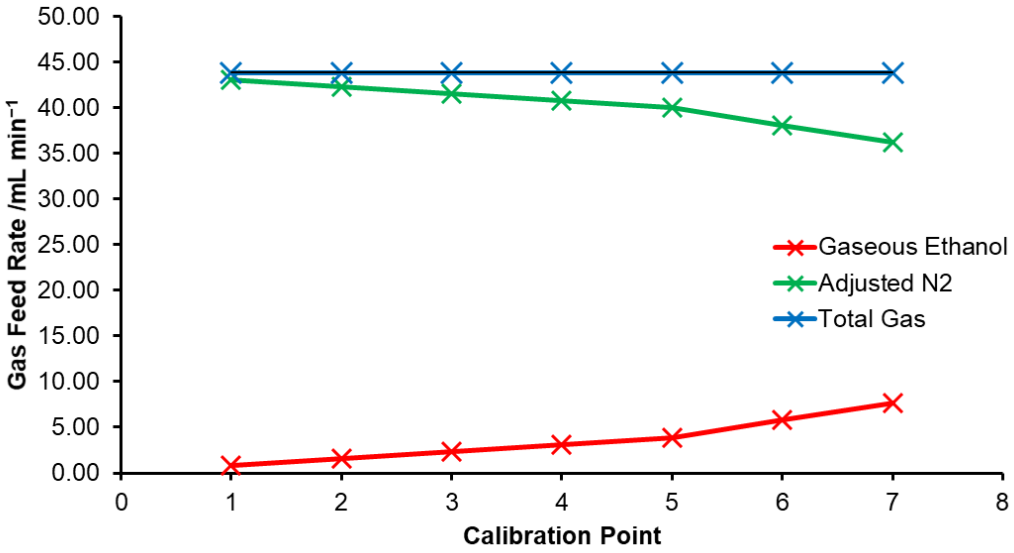

Figure 9.13: Gas feed rates of ethanol, helium and total gas flow used during ethanol calibration.

9.4.2.3 Calibration of Permanent Gas Products.

MS and BID calibration for permanent gases were performed by modulation of injection split values whilst maintaining a constant flow rate of a calibration gas mixture. A calibration gas mixture (supplied by BOC, pre-mixed, details in Table 9.3) was flowed through a SiC filled reactor bed maintained at 170 °C to match the maximum temperature of the trace heated lines and to minimise auto-reaction. The flow rate of calibration gas was maintained at 40 mL min^{-1}. In order to build a calibration curve, the injection split values into column 1 (MS) and column 2 (BID) were modulated as detailed in Appendix 3, effectively attaining a dilution effect. Typically, three data points were collected at each split value, and five various split values were used to build full calibration curves. All gases were assumed to act as ideal gases, hence relative gas expansions were not taken into consideration.

Table 9.3: Percentage composition of calibration gas mixture.

Gas	Volume %
Ethane	10.00
Ethylene	10.00
Propane	2.50
Propylene	2.50
Isobutylene	0.50
Isobutane	0.50
^{n}Butane	0.50
1-Butene	0.50
Cis-2-Butene	0.50
1,3-Butadiene	0.50
Helium (Balance)	72.00

9.4.2.4 Metrics of Interest.

Various metrics of interest such as ethanol conversion, product selectivites and carbon balance were calculated as shown below using mmol min^{-1} of carbon as input values. Conversion was calculated by observation of the quantity of ethanol detected in the mass spectrum and compared to the known quantity fed into the reactor as seen in Equation 9.1. The known quantity of ethanol fed into the reactor was determined by analysis of an ethanol feed over a blank SiC reactor bed at 170 °C.

$$Conversion = 100 \times \left(\frac{Ethanol\ Consumed\ (C\ mmol\ min^{-1})}{Ethanol\ Fed\ (C\ mmol\ min^{-1})} \right) \qquad (9.1)$$

Similarly, product selectivity to a given species was attained by division of the species productivity over that of all products of the reaction as seen in Equation 9.2. Yield of a given

product was attained by division of the species productivity by the quantity of ethanol fed into the reaction as seen in Equation 9.3. Effluent selectivity to a given product was attained by division of the species productivity by the quantity of all carbon detected in the effluent as seen in Equation 9.4. Carbon balance was calculated by division of the total moles of carbon detected by the theoretical number of moles of carbon fed into the reactor as shown in Equation 9.5.

$$Selectivity = 100 \times \left(\frac{Target\ Species\ Detected\ (C\ mmol\ min^{-1})}{All\ Species\ Detected\ (C\ mmol\ min^{-1})} \right) \tag{9.2}$$

$$Yield = 100 \times \left(\frac{Target\ Species\ Detected\ (C\ mmol\ min^{-1})}{Carbon\ Fed\ (C\ mmol\ min^{-1})} \right) \tag{9.3}$$

$$Effluent\ Composition = 100 \times \left(\frac{Target\ Species\ Detected\ (C\ mmol\ min^{-1})}{Total\ Carbon\ Detected\ (C\ mmol\ min^{-1})} \right) \tag{9.4}$$

$$Carbon\ Balance = 100 \times \left(\frac{Carbon\ Detected\ (C\ mmol\ min^{-1})}{Carbon\ Fed\ (C\ mmol\ min^{-1})} \right) \tag{9.5}$$

9.5. References.

1. Y. G. Kolyagin, A. V. Yakimov, S. Tolborg, P. N. R. Vennestrøm and I. I. Ivanova, *J. Phys. Chem. Lett.*, 2016, **7**, 1249–1253.
2. Elemental Analysis of Zeolites, https://www.inorganicventures.com/guides-and-papers/elemental-analysis-of-zeolites, (accessed 29/10/20).
3. N. K. Mal, V. Ramaswamy, P. R. Rajamohanan and A. V. Ramaswamy, *Micro. Mater.*, 1997, **12**, 331–340.
4. W. N. P. van der Graaff, G. Li, B. Mezari, E. A. Pidko and E. J. M. Hensen, *Chemcatchem*, 2015, **7**, 1152–1160.
5. J. C. Vega-Vila, J. W. Harris and R. Gounder, *J. Catal.*, 2016, **344**, 108–120.
6. A. de Lucas, P. Canizares, A. Durán and A. Carrero, *Appl. Catal. A*, 1997, **154**, 221–240.
7. Acetaldehyde, 99.5%, ACROS Organics™, https://www.fishersci.co.uk/shop/products/acetaldehyde-99-5-acros-organics-4/p-3777132, (accessed 05/03/2019).
8. I. Mills, *Quantities, units and symbols in physical chemistry/prepared for publication by Ian Mills...[et al.]*, Oxford; Boston: Blackwell Science; Boca Raton, Fla.: CRC Press [distributor], 1993.

Appendices

Appendix 1. Preliminary Qualitative Investigations into the Reaction Selectivity of Ethanol Dehydrogenation over Metal-modified Zeolite Catalysts.

A1.1 Qualitative Screening of Ethanol Dehydrogenation Catalysts.

In this section, a wide library of zeolites with varying framework type, counter-cation and extra-framework metal species are screened in a qualitative regime in order to assess their effectiveness for catalysis of the ethanol to acetaldehyde dehydrogenation reaction. All reactions are undertaken in a quartz fixed-bed flow reactor which was designed and operated in-house according to the description in Section 9.4.1. Briefly, the catalysts were pre-treated at 150 °C before being raised to the desired reaction temperature where ethanol was fed for a period of 2 hours. The effluent was fed *via* a −78 °C dry ice/acetone bath and the collected condensed liquid was analysed after the 2-hour TOS. Solution state ^{1}H NMR spectroscopy was used as the method of detection for liquid phase products and all NMR spectra can be seen in Appendix 1.3. It is noted that, despite ethylene not being directly detectable within the experimental set-up, the observation of water in the product effluent is strongly indicative of ethylene production from dehydration of ethanol. Another potential source of water, diethyl ether, is accounted for *via* ^{1}H NMR spectroscopy.

A1.1.1 The effect of framework morphology on product distribution resulting from ethanol conversion over H–form zeolites.

It is well-know that variations in zeolite topology, such as major channel sizes and presence of cages, may exhibit varying confinement effects and therefore have a large effect on reaction selectivities. Hence, in this section, ethanol dehydrogenation is explored over several different commercially available zeolite frameworks (MFI, BEA and MOR) in order to probe the effect of framework type on the selectivity of liquid range products. Key properties of these frameworks were previously detailed in Table 1.1 in Section 1.1.1..

The results of catalytic ethanol conversion over parent H–ZSM–5–(12.5), H–BEA–(12.5) and H–MOR–(10.0) at 400 °C and 300 °C alongside the results from the respective control reactions over SiC are displayed below in Table A1.1. As can be seen from Table A1.1, the control reactions over SiC, which is used in each test as a pre-bed, post-bed and diluent, are seen to produce small quantities of both acetaldehyde and water suggesting that a low-level auto-reaction occurs at 400 °C and 300 °C. In contrast to that observed for the control reactions, ethanol conversion over parent H–form zeolites produced no detectable amount of

acetaldehyde at either 400 °C or 300 °C. This is, however, in-line with expectation and most likely results from the dominance of the competing ethanol dehydration reaction owing to the strong Brønsted acidity of the H-form zeolite catalysts alongside the lack of a dedicated dehydrogenation site. Further to this, the observation of aromatics formed over H–ZSM–5 (and to a lesser extent H–BEA) further suggests that ethylene is formed as it is typically regarded as the initial step in the ethanol to aromatics reaction pathway (alternatively known as the hydrocarbon pool).[1-4]

Interestingly, H–MOR produced only a small trace of aromatic products, suggesting that the MOR framework may be favourable to induce transition state selectivity to more linear products. This could be a result of formed aromatic products bring too large to readily exit the channel system, resulting in product selectivity akin to that seen for xylene isomerisation over H–ZSM–5.[5, 6] Further, the 1-dimensional structure of MOR may further limit the rate of diffusion of aromatic products from the channel system. The latter suggestion is supported by the large increase in coking value seen for H–MOR (7.40 C%) compared to H–BEA (2.07 C%) and H–ZSM–5 (1.04 C%) following ethanol conversion at 400 °C (Table A1.1). High carbon contents are indicative of 'coking', the formation of large carbonaceous or aromatic species within the zeolite framework. Following reaction at 300 °C, it is observed that both H–BEA (4.72 C%) and H–ZSM–5 (4.76 C%) exhibit higher coking values than after reaction at 400 °C. This implies that the lower temperature of 300 °C is sufficient to form large aromatic products but is insufficient to allow them to diffuse out of the framework, most likely owing to their relatively low volatility or strong adsorption within the zeolite.[7] Further, 300 °C may be insufficient to allow any formed alkylated aromatics to be cracked into smaller products that are able to diffuse out of the channel system.

Table A1.1: Conversion of EtOH over SiC and H-form zeolite catalysts: summary of proposed extra-framework (FW) species, observed products and catalyst coking where applicable. $WHSV_{EtOH}$ = 2, TOS = 2 h, carrier gas flow (He) = 40 mL min^{-1}.. Catalyst bed type: A. Metal loadings and M/Al ratios were determined by ICP-OES, catalyst coking was determined by CHN analysis. AA = Acetaldehyde, CA = Crotonaldehyde, DEE = Diethyl ether, BTX = Benzene, toluene, xylene and other aromatics.

Sample	Reaction Temperature / °C	Proposed Extra-FW Species	Products observed in liquid effluent determined by ^1H NMR spectroscopy.					Catalyst Coking (ΔC wt%)
			AA	CA	DEE	BTX (Aromatics)	H_2O	
SiC Control	400	N/A	Minor	No	No	No	Minor	N/A
H–ZSM–5–(12.5)	400	H^+	No	No	No	Yes	Yes	1.04
H–BEA–(12.5)	400	H^+	No	No	No	Yes	Yes	2.07
H–MOR–(10.0)	400	H^+	No	No	No	Minor	Yes	7.40
SiC Control	300	N/A	Minor	No	No	No	Minor	N/A
H–ZSM–5–(12.5)	300	H^+	No	No	No	Yes	Yes	4.76
H–BEA–(12.5)	300	H^+	No	No	No	Yes	Yes	4.72
H–MOR–(10.0)	300	H^+	No	No	No	Minor	Yes	6.60

A1.1.2 The effect of framework morphology on product distribution resulting from ethanol conversion over Zn-modified zeolites.

In order to improve selectivity to the desired dehydrogenation product, zinc species were introduced into the zeolite frameworks by two methods: ion-exchange and wetness impregnation. It is thought that these methods will introduce predominantly Zn^{2+} cations at ion-exchange sites and ZnO clusters dispersed throughout the matrix, respectively. Zinc species were chosen as they are well known in the literature as promoters for the dehydrogenation of alcohols and alkanes both unsupported (as ZnO)[8-13] and on other heterogeneous supports such as ZrO_2.[14-16] Table A1.2 and

Table A1.3 show the liquid range products detected by ^{1}H NMR spectroscopy resulting from EtOH conversion over zinc-modified zeolite materials performed in a quartz tube reactor at both 400 °C and 300 °C, respectively. The Zn loadings and Zn/Al ratios of catalysts as determined by ICP-OES are also presented.

The starkest contrast in this series of experiments is the difference in acetaldehyde productivity over all three frameworks and across both types of catalytic site when the temperature is varied from 400 °C to 300 °C. For reaction at 400 °C, acetaldehyde is observed as a product across all systems. Reaction at 300 °C, however, only see acetaldehyde produced over Zn-modified H–BEA catalysts. This suggests that higher temperatures are more favourable for EtOH dehydrogenation over Zn-modified protic zeolite catalysts.

As observed previously for parent H-form catalysts, the framework type of the material also has a large effect on the liquid range product distribution. For reaction at 400 °C, both Zn-modified H–MOR and H–BEA are observed to produce significant quantities of acetaldehyde, whilst the major liquid product (by integration of ^{1}H NMR spectroscopy signals) of EtOH conversion over Zn-modified H–ZSM–5 is aromatics. Interestingly, Zn-modified H–MOR is seen to produce relatively low quantities of aromatics, suggesting that it may be a promising candidate for the selective conversion of EtOH to acetaldehyde owing to a reduced need to separate undesired liquid-range products. This observation is mirrored following reaction of ethanol at 300 °C. Whilst in this regime, very little acetaldehyde is produced. However, both Zn-modified H–BEA and H–ZSM–5 catalysts continue to produce large quantities of aromatic products. Additionally, Zn-modified H–MOR catalysts again produced a qualitatively small amount of aromatic products following reaction at 300 °C.

Within this regime and for each given framework type, the active Zn species does not confer any discernible reactivity differences between Zn-exchanged and impregnated samples as they produce similar product distributions, likely owing to the qualitative nature of the experiments. Although reaction of ethanol over Zn^{2+} cations may seem to produce visually more acetaldehyde in the ^{1}H NMR spectra relative to reaction over ZnO clusters, this cannot be accurately quantified in this regime.

In this respect, it can be concluded from this initial screening exercise that both Zn^{2+} cations and ZnO clusters are effective ethanol dehydrogenation promoters for H-form commercial zeolites. Further, whilst Zn-modified H–BEA and H–ZSM–5 produce a wide range of liquid products, Zn-modified H–MOR produces acetaldehyde as the predominant liquid product. As a result of these observations, MOR was chosen as the framework type to take forward into further optimisation.

Table A1.2: Conversion of EtOH over SiC and Zn-modified zeolite catalysts at 400 °C: summary of proposed extra-framework (FW) species, Zn loading, observed products and catalyst coking where applicable. $WHSV_{EtOH}$ = 2, TOS = 2 h, carrier gas flow (He) = 40 mL min^{-1}, reaction temperature = 400 °C. Catalyst bed type: A. Zinc loadings and Zn/Al ratios were determined by ICP-OES, catalyst coking was determined by CHN analysis. AA = Acetaldehyde, CA = Crotonaldehyde, DEE = Diethyl ether, BTX = Benzene, toluene, xylene and other aromatics.

Sample	Proposed Extra-FW Species	Zn Loading (Zn wt%)	Zn/Al Ratio	Products observed in liquid effluent determined by ^{1}H NMR spectroscopy.					Catalyst Coking (ΔC wt%)
				AA	CA	DEE	BTX (Aromatics)	H_2O	
SiC Control	N/A	N/A	N/A	Minor	No	No	No	Minor	N/A
Zn/H–ZSM–5–(12.5)	Zn^{2+}, H^+	2.84	0.44	Minor	No	No	Yes	Yes	2.42
Zn/H–BEA–(12.5)	Zn^{2+}, H^+	2.09	0.34	Yes	Minor	No	Yes	Yes	7.71
Zn/H–MOR–(10.0)	Zn^{2+}, H^+	2.51	0.33	Yes	Minor	No	Minor	Yes	7.25
ZnO/H–ZSM–5–(12.5)	ZnO, H^+	3.02	0.47	Minor	No	No	Yes	Yes	2.34
ZnO/H–BEA–(12.5)	ZnO, H^+	3.04	0.46	Yes	Minor	No	Yes	Yes	8.10
ZnO/H–MOR–(10.0)	ZnO, H^+	2.83	0.36	Yes	Minor	No	Minor	Yes	7.40

Table A1.3: Conversion of EtOH over SiC and Zn-modified zeolite catalysts at 300 °C: summary of proposed extra-framework (FW) species, Zn loading, observed products and catalyst coking where applicable. $WHSV_{EtOH}$ = 2, TOS = 2 h, carrier gas flow (He) = 40 mL min^{-1}, reaction temperature = 300 °C. Catalyst bed type: A. Zinc loadings and Zn/Al ratios were determined by ICP-OES, catalyst coking was determined by CHN analysis. AA = Acetaldehyde, CA = Crotonaldehyde, DEE = Diethyl ether, BTX = Benzene, toluene, xylene and other aromatics.

Sample	Proposed Extra-FW Species	Zinc Loading (Zn wt%)	M/Al Ratio	Products observed in liquid effluent determined by ^{1}H NMR spectroscopy.					Catalyst Coking (ΔC wt%)
				AA	CA	DEE	BTX (Aromatics)	H_2O	
SiC Control	N/A	N/A	N/A	Minor	No	No	No	Minor	N/A
Zn/H–ZSM–5–(12.5)	Zn^{2+}, H^+	2.84	0.44	No	No	No	Yes	Yes	4.46
Zn/H–BEA–(12.5)	Zn^{2+}, H^+	2.09	0.34	Minor	No	Minor	Minor	Yes	4.11
Zn/H–MOR–(10.0)	Zn^{2+}, H^+	2.51	0.33	No	No	No	Minor	Yes	4.08
ZnO/H–ZSM–5–(12.5)	ZnO, H^+	3.02	0.47	No	No	No	Yes	Yes	4.12
ZnO/H–BEA–(12.5)	ZnO, H^+	3.04	0.46	Yes	No	Minor	Yes	Yes	3.89
ZnO/H–MOR–(10.0)	ZnO, H^+	2.83	0.36	No	No	No	Minor	Yes	4.47

A1.1.3. Effect of zeolite counter-cation on product distribution resulting from ethanol conversion over Zn-modified mordenite.

Although acetaldehyde was observed to be produced from ethanol over Zn-modified H-MOR catalysts, it was hypothesised that the presence of H^+ at exchange positions was promoting the competing dehydration reaction by provision of strong Brønsted acid sites, as evidenced by the presence of substantial quantities of H_2O in the liquid effluent. Hence, in order to attempt to attenuate this competition, a commercial MOR parent containing Na^+ cations as opposed to H^+ was tested for the conversion of ethanol to acetaldehyde. Na–MOR was used both as received and as a support for the active zinc species highlighted in Section A1.1.2. Reaction conditions were identical to those used in the previous section and results may be seen in Table A1.4. In this situation, a new metric of comparison was determined as the ratio of acetaldehyde to water in the liquid effluent calculated by comparison of ^{1}H NMR spectroscopy integrals in the liquid effluent. This method of comparison should roughly indicate the relative productivity of the dehydrogenation and dehydration reactions, respectively.

As hypothesised and as can be seen throughout Table A1.4, with similar extra-framework species and under similar reaction conditions, the use of parent Na-form MOR catalysts result in a much larger acetaldehyde to water ratio in the liquid effluent than the equivalent parent H-form catalyst. This is most likely caused by a reduced dehydration rate owing to the lack of strong Brønsted acid sites that are able to catalytically dehydrate ethanol. Additionally, it is observed that carbon laydown, likely in the form of coke, is deposited to a lesser degree over the Na-form catalysts. As coke is normally thought to be built as bulky polyaromatic species from ethylene, this observation further suggests that the ethanol dehydration reaction has been curtailed.[7] An attempt to produce Na-exchanged forms of MFI and BEA was also undertaken, however total exchange was not achieved. As a result, the catalytic activity of Na/H–MFI and Na/H–BEA largely resembled that of the H-form catalysts wing to rapid ethanol dehydration.

This is further evidenced when the reactions of ethanol over Zn/H–MOR–(10.0) and Zn/Na–MOR–(7.0) are compared at 300 °C. In this regime no acetaldehyde is seen to be produced from the H-form system while a small amount is observed in the Na-form system. As the amount of acetaldehyde produced over Zn/Na–MOR–(7.0) is seen to be much lower at 300 °C than at 400 °C, it is further suggested that a reaction temperature of 400 °C is beneficial for ethanol dehydrogenation within this regime. Furthermore, in all reactions over Na–form

MOR catalysts, unreacted ethanol is observed in the liquid effluent, demonstrating that in these systems partial conversion is achieved, as opposed to the total ethanol conversion observed over the H-form analogues. Although reaction kinetics are not investigated in depth in this work, it may be suggested that the dehydrogenation reaction of ethanol is slower than that of the dehydration reaction as a result of the previous observations.

Critically speaking, there are several small discrepancies between the prepared Na-form and H-form MOR catalysts that must be also be considered before definitive conclusions of their different reactivities may be drawn. First and foremost, whilst Na^+ counter-cations may not be regarded as active in the dehydration of ethanol, they may be able to promote dehydrogenation to acetaldehyde owing to the Lewis basicity of the framework oxygen atom that they balance.[17] Although not strictly acting as zeolite framework counter-cations, Na^+ ions that have been grafted onto silanol groups at the surface of zeolite USY have previously been reported to provide basic sites capable of catalysing ethanol dehydrogenation.[17] In the current work it can be seen from Table A1.4 that whilst H–MOR–(10.0) produces no acetaldehyde at 400 °C, Na–MOR–(7.0) produces a non-negligible quantity. However, by comparison of the acetaldehyde to water ratio observed in the product effluent for both parent Na-form and Zn-modified catalysts it is clear that Zn species are still the major active species for ethanol dehydrogenation in these systems.

Additionally, the loading of Zn and Zn/Al ratio observed in the ion-exchanged H- and Na-form differs, most likely due to a more facile outward exchange of Na^+ cations than protons. Within the current hypothesis, an increase of Zn loading will improve acetaldehyde productivity. However, even if the ratio of acetaldehyde to water seen for Zn/Na–MOR–(7.0) is theoretically scaled down by a factor so that the Zn loading matches that of Zn/H–MOR–(10.0), the productivity of acetaldehyde is still much greater than that seen for Zn/H–MOR–(10.0) due to the rapid and out-competing dehydration reaction resulting from the presence of BAS.

It is therefore concluded that the presence of H^+ counter-cations acting as Brønsted acid sites are detrimental to the ethanol dehydrogenation reaction, resulting in increased formation of ethylene and aromatic side-products. Substitution with Na^+ cations was observed to increase the acetaldehyde to water ratio in the product effluent whilst also preventing formation of aromatic by-products, implying improved liquid range selectivity to acetaldehyde. As a result,

Na–MOR was chosen as the framework to take forward into further qualitative and quantitative work.

Table A1.4: Conversion of EtOH over SiC, Na-MOR and Zn-modified Na-MOR: summary of proposed extra-framework (FW) species, Zn loading, observed products and catalyst coking where applicable. $WHSV_{EtOH}$ = 2, TOS = 2 h, carrier gas flow (He) = 40 mL min^{-1}. Catalyst bed type: C. Zn loadings and Zn/Al ratios were determined by ICP-OES, catalyst coking was determined by CHN analysis. AA/H_2O ratio was calculated from the respective ^1H NMR spectroscopy integrals. N.d.*: No acetaldehyde (AA) was observable for these systems and hence a ratio is not able to be calculated. AA = Acetaldehyde, CA = Crotonaldehyde, BTX = Benzene, toluene, xylene and other aromatics.

Sample	Temperature / °C	Proposed Extra-FW Species	Zinc Loading (Zn wt%)	M/Al Ratio	Products observed in liquid effluent determined by ^1H NMR spectroscopy.				Ratio AA/H_2O in Liquid Effluent	Catalyst Coking (ΔC wt%)
					AA	CA	BTX (Aromatics)	H_2O		
SiC Control	400	N/A	N/A	N/A	Minor	No	No	Minor	0.02	N/A
H–MOR–(10.0)	400	H^+	N/A	N/A	No	No	Minor	Yes	n.d.*	7.40
Zn/H–MOR–(10.0)	400	Zn^{2+}, H^+	2.51	0.33	Yes	Minor	Minor	Yes	0.15	7.25
ZnO/H–MOR–(10.0)	400	ZnO, H^+	2.83	0.36	Yes	Minor	Minor	Yes	0.08	7.40
Na–MOR–(7.0)	400	Na^+	N/A	N/A	Yes	Minor	No	Yes	0.11	0.76
Zn/Na–MOR–(7.0)	400	Zn^{2+}, Na^+	5.49	0.47	Yes	Minor	No	Yes	1.08	6.11
Zn/Na–MOR–(7.0)	300	Zn^{2+}, Na^+	5.49	0.47	Yes	No	No	Yes	0.11	4.13
ZnO/Na–MOR–(7.0)	400	ZnO, Na^+	3.71	0.32	Yes	Minor	No	Yes	1.14	4.44

A1.1.4. Screening of metal oxide species supported on Na–MOR–7 for the conversion of ethanol to acetaldehyde.

Before quantitative testing, a wide library of metal oxide species supported on Na–MOR were screened for their ability to produce acetaldehyde from ethanol at 400 °C under flow conditions in the quartz tube reactor. The metals chosen were Ag, Cr, Co, Cu, Fe, Ga, Mn, Ni, Pd, Ru and Zn. Each metal oxide modified zeolite was prepared by a wetness impregnation method as described in Section 9.3.3 with the relevant metal chloride or metal nitrate at a target metal loading of 3.0 wt%. Following impregnation of the respective chloride or nitrate salt, the samples were calcined in static air according to the method in Section 9.3.1 (550 °C for 5 h) to afford the respective metal oxide impregnated zeolite material. Ag/Na–MOR–7 is an exception as the decomposition temperature of Ag_2O is lower than that of $AgNO_3$ and hence thermal decomposition of silver (I) nitrate likely results in production of elemental silver (Ag^0).[18, 19] As can be seen in Table A1.5, all metal oxide impregnated materials tested demonstrated conversion of ethanol to acetaldehyde at 400 °C as evidenced by ^{1}H NMR spectroscopy of the product effluent with many also exhibiting minor further conversion to crotonaldehyde. Additionally, the observation of H_2O in the product effluent for all materials indicates the presence of the ethanol dehydration reaction, although Ru_2O_3/Na–MOR–(7) was the only catalyst that produced aromatic products. Coking levels (C wt%) as determined by CHN microanalysis following reaction are similar for all materials, with values in the region of 3–5 wt%.

Table A1.5: Conversion of EtOH over SiC, Na-MOR and metal-modified Na-MOR: summary of proposed extra-framework (FW) species, metal loading, observed products and catalyst coking where applicable. $WHSV_{EtOH}$ = 2, TOS = 2 h, carrier gas flow (He) = 40 mL min^{-1}. Catalyst bed type: C. Zn loadings and Zn/Al ratios were determined by ICP-OES, catalyst coking was determined by CHN analysis. *These values were measured by ED-XRF as complete dissolution in HF in preparation for ICP-OES analysis could not be achieved. AA = Acetaldehyde, CA = Crotonaldehyde, DEE = Diethyl ether, BTX = Benzene, toluene, xylene and other aromatics.

Sample	Reaction Temperature / °C	Proposed Extra-FW Species	Metal Loading (M wt%)	Products observed in liquid effluent determined by ^{1}H NMR spectroscopy.					Catalyst Coking (ΔC wt%)
				AA	CA	DEE	BTX (Aromatics)	H_2O	
SiC Control	400	N/A	N/A	Minor	No	No	No	Minor	N/A
Na–MOR–(7.0)	400	Na^+	N/A	Yes	Minor	Minor	No	Yes	0.76
Ag/Na–MOR–(7)	400	Ag, Na^+	2.92	Yes	Minor	Yes	No	Minor	4.40
Cr_2O_3/Na–MOR–(7)	400	Cr_2O_3, Na^+	2.69	Yes	No	Minor	No	Yes	3.50
Co_3O_4/Na–MOR–(7)	400	Co_3O_4, Na^+	3.07	Yes	No	Minor	No	Yes	4.46
CuO/Na–MOR–(7)	400	CuO, Na^+	4.12	Yes	Minor	Yes	No	Yes	3.87
Fe_2O_3/Na–MOR–(7)	400	Fe_2O_3, Na^+	3.64	Yes	Minor	Minor	No	Yes	3.58
Ga_2O_3/Na–MOR–(7)	400	Ga_2O_3, Na^+	1.81	Yes	Minor	Yes	No	Yes	4.17
Mn_3O_4/Na–MOR–(7)	400	Mn_3O_4, Na^+	3.21	Yes	No	Minor	No	Yes	3.43

Sample	Reaction Temperature / °C	Proposed Extra-FW Species	Metal Loading (M wt%)	Products observed in liquid effluent determined by ^{1}H NMR spectroscopy.					Catalyst Coking (ΔC wt%)
				AA	CA	DEE	BTX (Aromatics)	H_2O	
NiO/Na–MOR–(7)	400	NiO, Na^+	2.91	Yes	No	Minor	No	Yes	4.80
PdO/Na–MOR–(7)	400	PdO, Na^+	3.13*	Minor	No	No	No	Yes	3.48
Ru_2O_3/Na–MOR–(7)	400	Ru_2O_3, Na^+	3.64*	Yes	Minor	Minor	Minor	Yes	3.09
ZnO/Na–MOR–(7.0)	400	ZnO, Na^+	3.71	Yes	Minor	Minor	No	Yes	4.44

A1.2. References.

1. Sudiyarmanto, A. Kristiani, L. N. H., Andreas and H. Abimanyu, *AIP Conference Proceedings*, 2016, **1755**, 080007.
2. Z. S. B. Sousa, C. O. Veloso, C. A. Henriques and V. Teixeira da Silva, *J. Mol. Catal. A*, 2016, **422**, 266–274.
3. E. A. Uslamin, H. Saito, N. Kosinov, E. Pidko, Y. Sekine and E. J. M. Hensen, *Catal. Sci. Technol.*, 2020, **10**, 2774–2785.
4. O. V. Bragin, T. V. Vasina and A. V. Preobrazhenskii, *Bulletin of the Academy of Sciences of the USSR, Division of chemical science*, 1984, **33**, 56–63.
5. S. Al-Khattaf, *Ind. Eng. Chem. Res.*, 2007, **46**, 59–69.
6. D. J. Collins, R. J. Medina and B. H. Davis, *Can. J. Chem. Eng.*, 1983, **61**, 29–35.
7. M. Guisnet and P. Magnoux, *Appl. Catal. A*, 2001, **212**, 83–96.
8. W. A. Lazier and H. Adkins, *J. Am. Chem. Soc.*, 1925, **47**, 1719–1722.
9. M. M. Rahman, S. D. Davidson, J. M. Sun and Y. Wang, *Top. Catal.*, 2016, **59**, 37–45.
10. C. Drouilly, J. M. Krafft, F. Averseng, H. Lauron-Pernot, D. Bazer-Bachi, C. Chizallet, V. Lecocq and G. Costentin, *Appl. Catal. A*, 2013, **453**, 121–129.
11. J. M. Vohs and M. A. Barteau, *Surf. Sci.*, 1989, **221**, 590–608.
12. M. V. Morales, E. Asedegbega-Nieto, A. Iglesias-Juez, I. Rodríguez-Ramos and A. Guerrero-Ruiz, *ChemSusChem*, 2015, **8**, 2223–2230.
13. T. De Baerdemaeker, M. Feyen, U. Müller, B. Yilmaz, F.-S. Xiao, W. Zhang, T. Yokoi, X. Bao, H. Gies and D. E. De Vos, *ACS Catal.*, 2015, **5**, 3393–3397.
14. J. M. Sun, R. A. L. Baylon, C. J. Liu, D. H. Mei, K. J. Martin, P. Venkitasubramanian and Y. Wang, *J. Am. Chem. Soc.*, 2016, **138**, 507–517.
15. J. M. Sun, K. K. Zhu, F. Gao, C. M. Wang, J. Liu, C. H. F. Peden and Y. Wang, *J. Am. Chem. Soc.*, 2011, **133**, 11096–11099.
16. J. Liu, N. He, W. Zhou, M. Shu, L. Lin, J. Wang, R. Si, G. Xiong, Q. Xin and H. Guo, *Catal. Sci. Technol.*, 2019, **9**, 1609–1620.
17. G. M. Lari, K. Desai, C. Mondelli and J. Pérez-Ramírez, *Catal. Sci. Technol.*, 2016, **6**, 2706–2714.
18. P. O. Dunstan, *Thermochim. Acta*, 1999, **333**, 5–11.
19. P. J. Herley and E. G. Prout, *J. Am. Chem. Soc.*, 1960, **82**, 1540–1543.

A1.3. Supplementary NMR spectra.

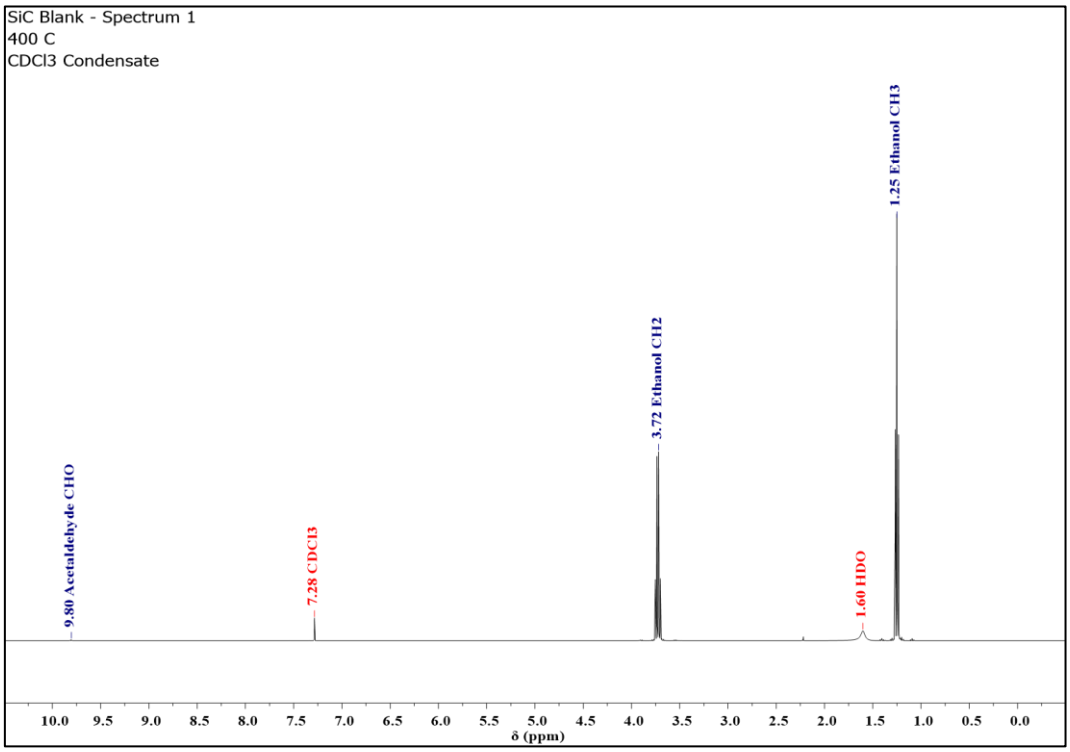

Figure A1.1: ^{1}H NMR spectrum of condensate from ethanol conversion over SiC at 400 °C averaged over 8 scans with a 1 s recycle delay. Spectrum was acquired on a Bruker Avance III-HD-400 spectrometer. Spectrometer frequency: ^{1}H = 399.95 MHz. NMR Solvent = $CDCl_3$.

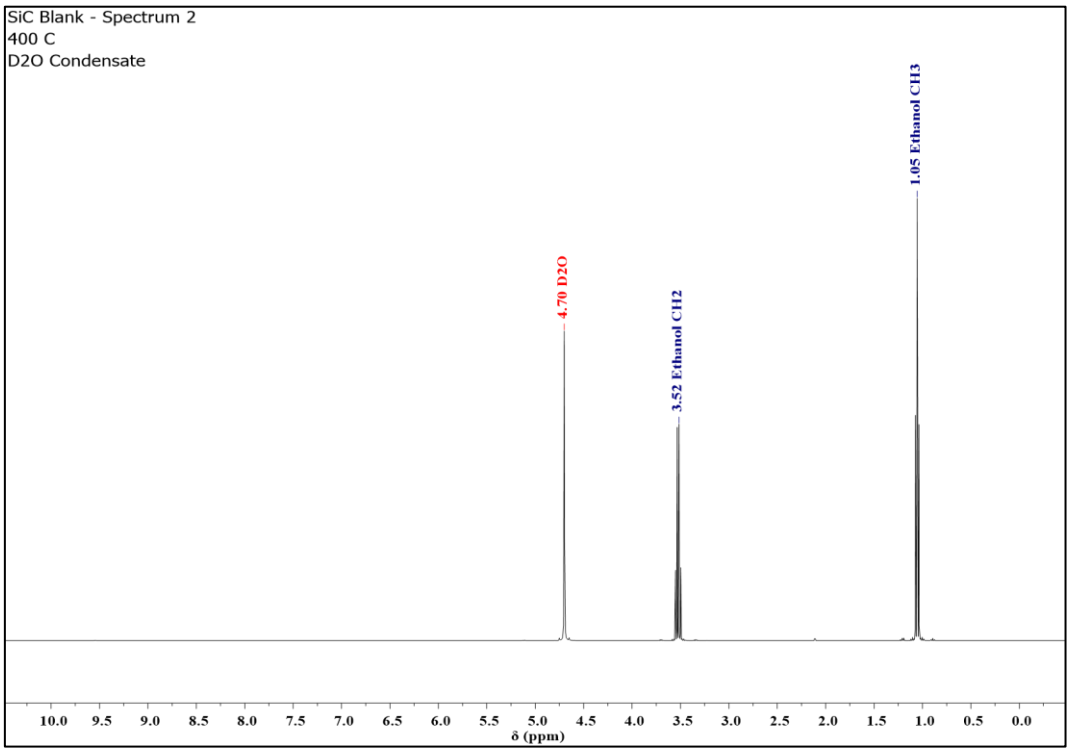

Figure A1.2: ^{1}H NMR spectrum of condensate from ethanol conversion over SiC at 400 °C averaged over 8 scans with a 1 s recycle delay. Spectrum was acquired on a Bruker Avance III-HD-400 spectrometer. Spectrometer frequency: ^{1}H = 399.95 MHz. NMR Solvent = D_2O.

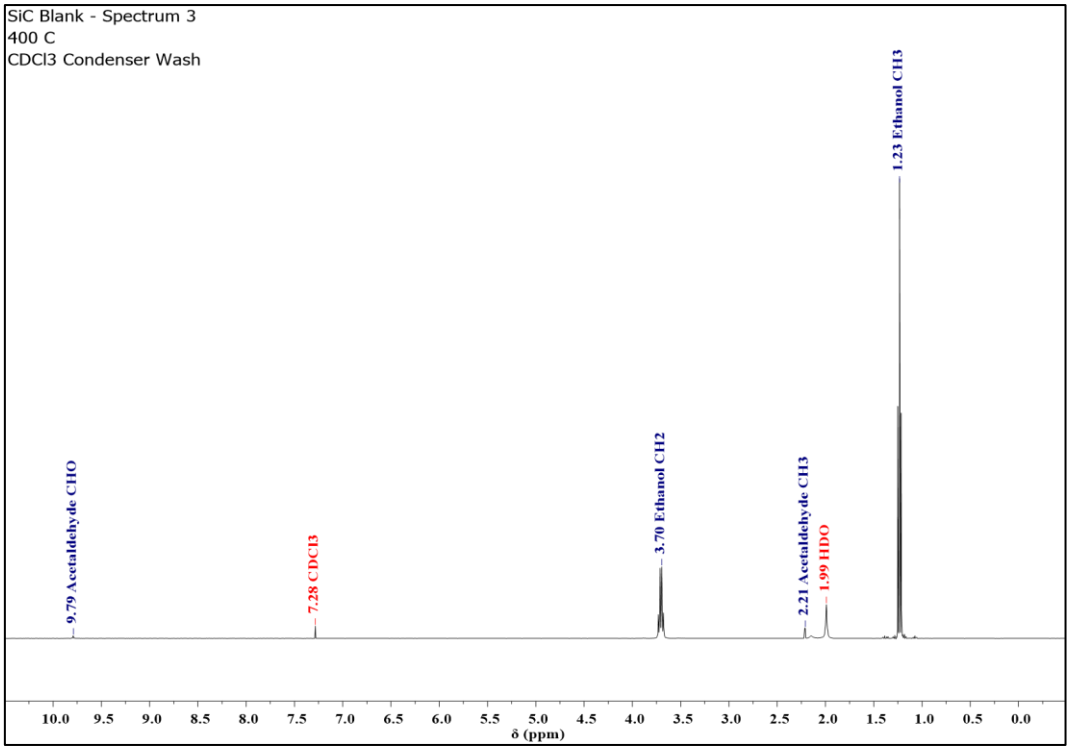

Figure A1.3: ^{1}H NMR spectrum of condenser washings from ethanol conversion over SiC at 400 °C averaged over 8 scans with a 1 s recycle delay. Spectrum was acquired on a Bruker Avance III-HD-400 spectrometer. Spectrometer frequency: ^{1}H = 399.95 MHz. NMR Solvent = $CDCl_3$.

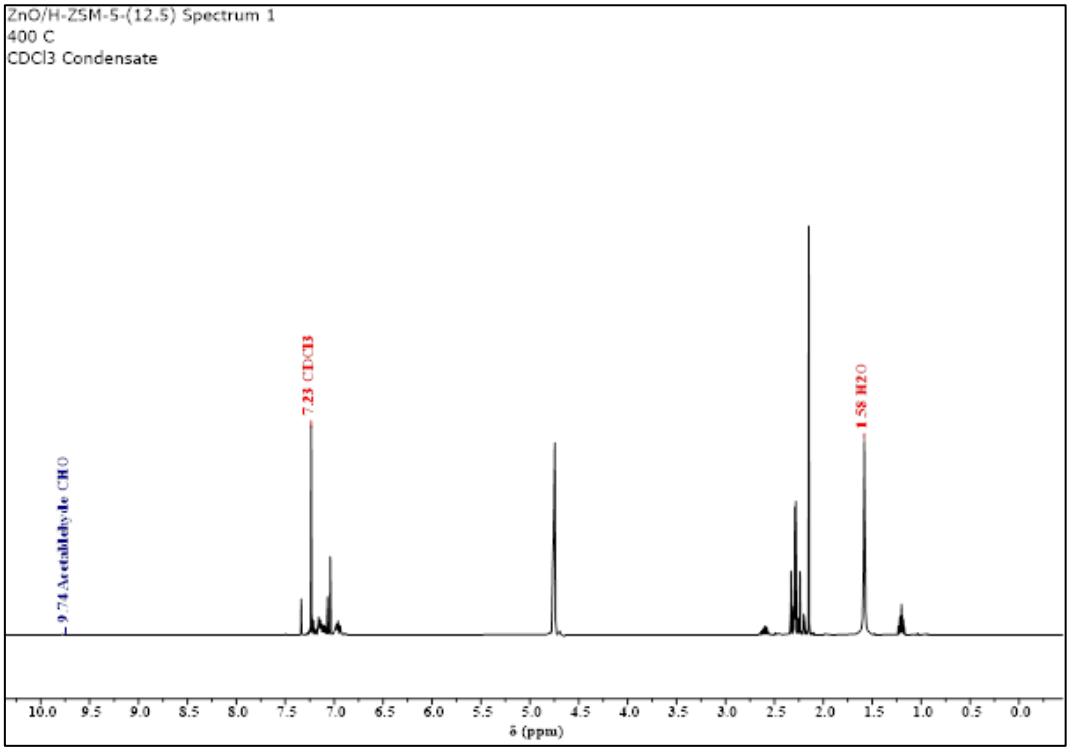

Figure A1.4: ^{1}H NMR spectrum of condensate from ethanol conversion over H–ZSM–5–(12.5) at 400 °C averaged over 8 scans with a 1 s recycle delay. Spectrum was acquired on a Bruker Avance III-HD-400 spectrometer. Spectrometer frequency: ^{1}H = 399.95 MHz. NMR Solvent = $CDCl_3$.

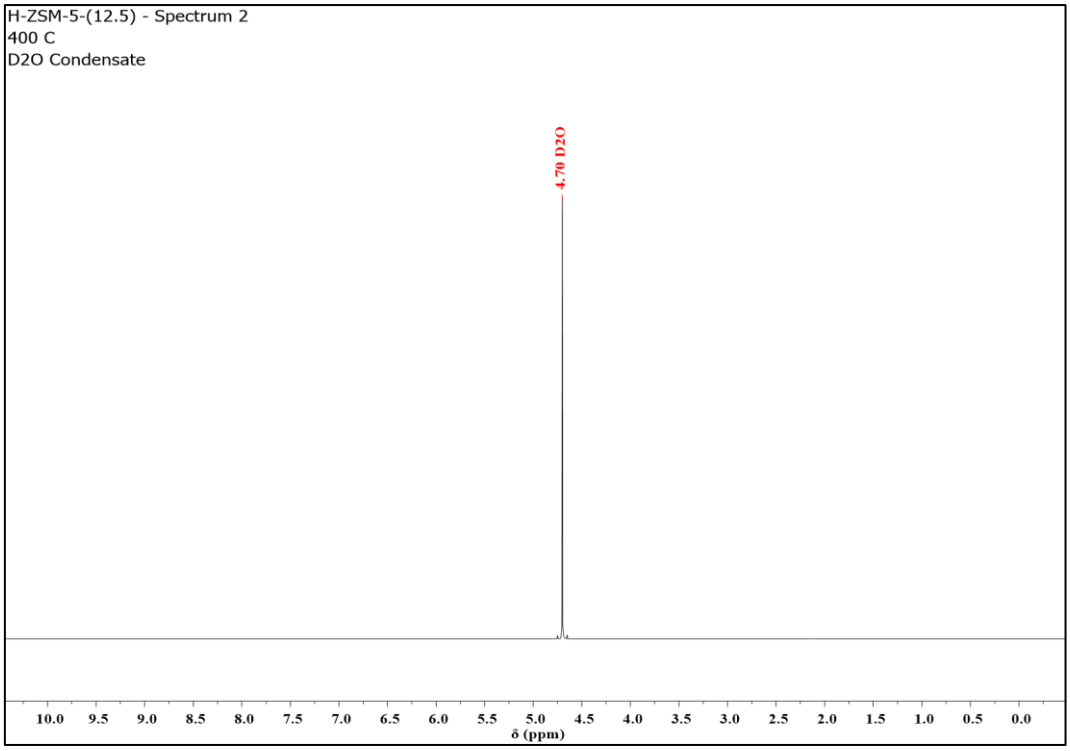

Figure A1.5: ^{1}H NMR spectrum of condensate from ethanol conversion over H–ZSM–5–(12.5) at 400 °C averaged over 8 scans with a 1 s recycle delay. Spectrum was acquired on a Bruker Avance III-HD-400 spectrometer. Spectrometer frequency: ^{1}H = 399.95 MHz. NMR Solvent = D_2O.

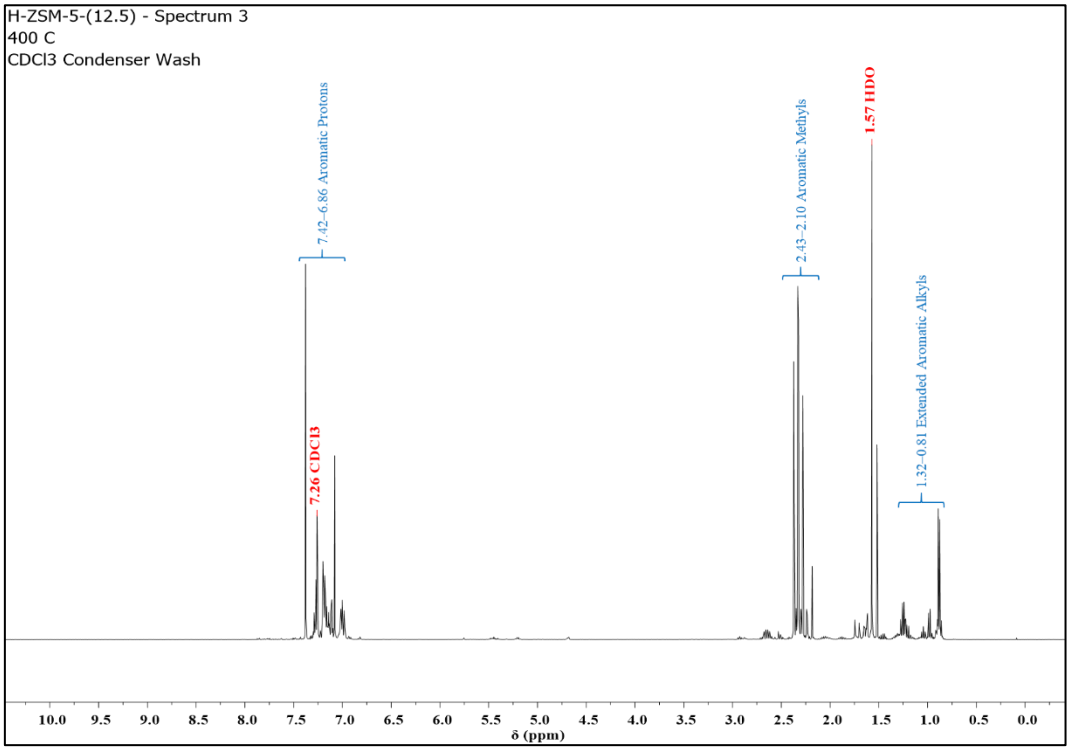

Figure A1.6: ^{1}H NMR spectrum of condenser washings from ethanol conversion over H–ZSM–5–(12.5) at 400 °C averaged over 8 scans with a 1 s recycle delay. Spectrum was acquired on a Bruker Avance III-HD-400 spectrometer. Spectrometer frequency: ^{1}H = 399.95 MHz. NMR Solvent = $CDCl_3$.

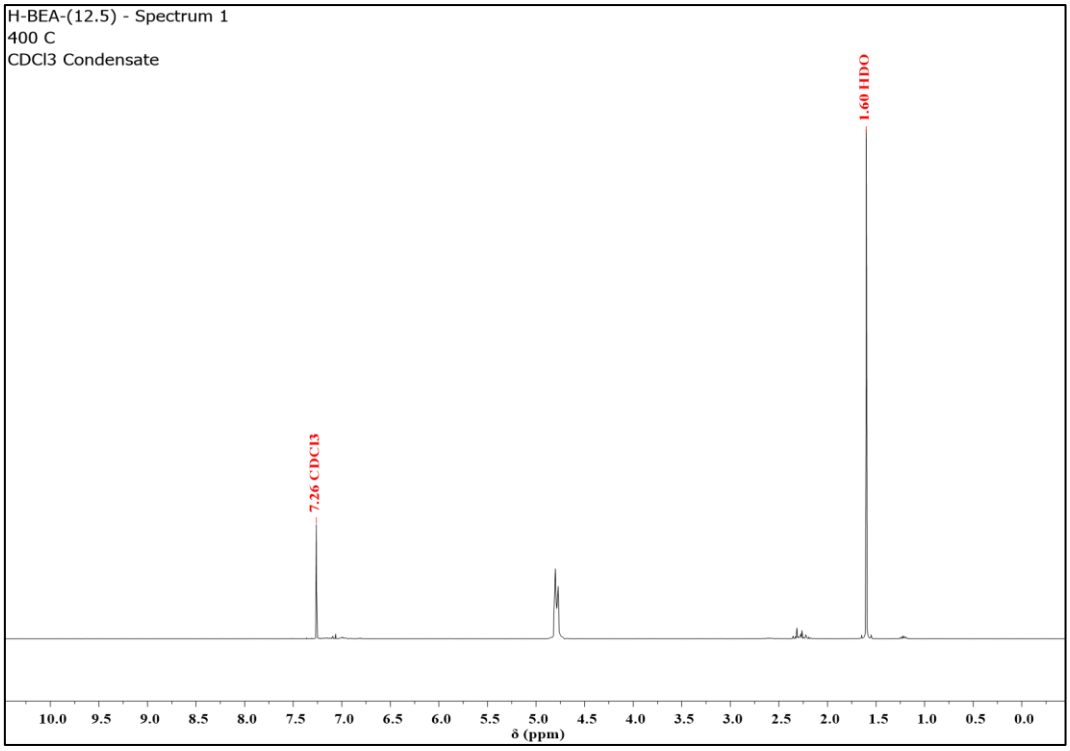

Figure A1.7: ^{1}H NMR spectrum of condensate from ethanol conversion over H–BEA–(12.5) at 400 °C averaged over 8 scans with a 1 s recycle delay. Spectrum was acquired on a Bruker Avance III-HD-400 spectrometer. Spectrometer frequency: ^{1}H = 399.95 MHz. NMR Solvent = $CDCl_3$.

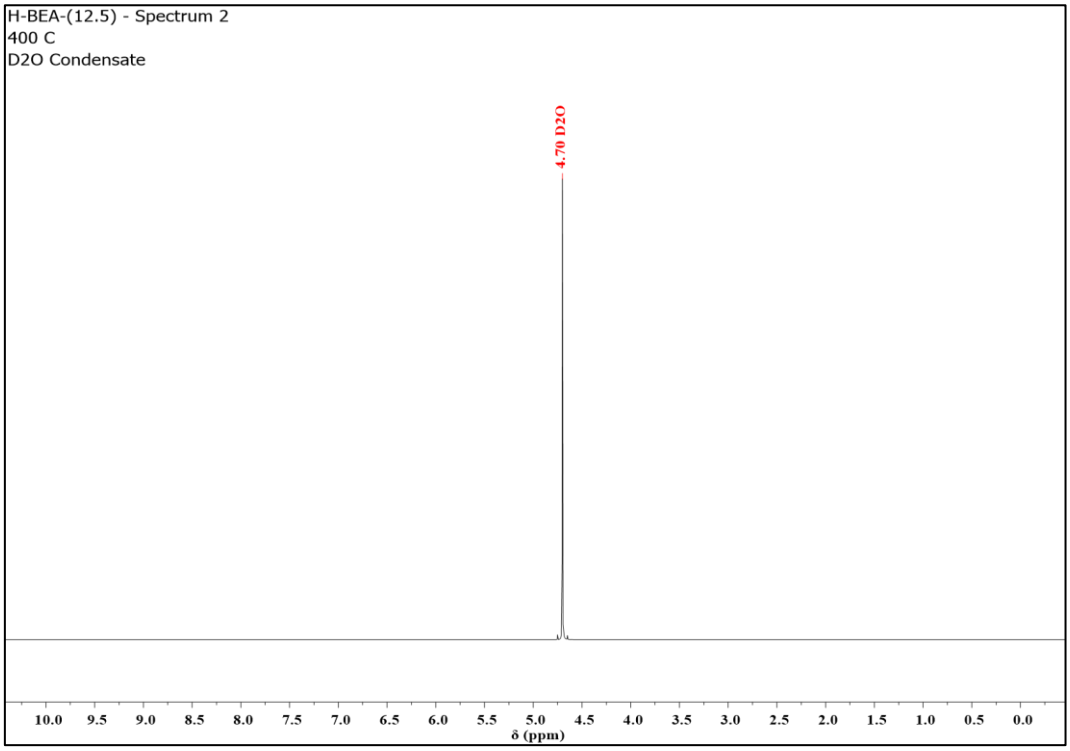

Figure A1.8: ^{1}H NMR spectrum of condensate from ethanol conversion over H–BEA–(12.5) at 400 °C averaged over 8 scans with a 1 s recycle delay. Spectrum was acquired on a Bruker Avance III-HD-400 spectrometer. Spectrometer frequency: ^{1}H = 399.95 MHz. NMR Solvent = D_2O.

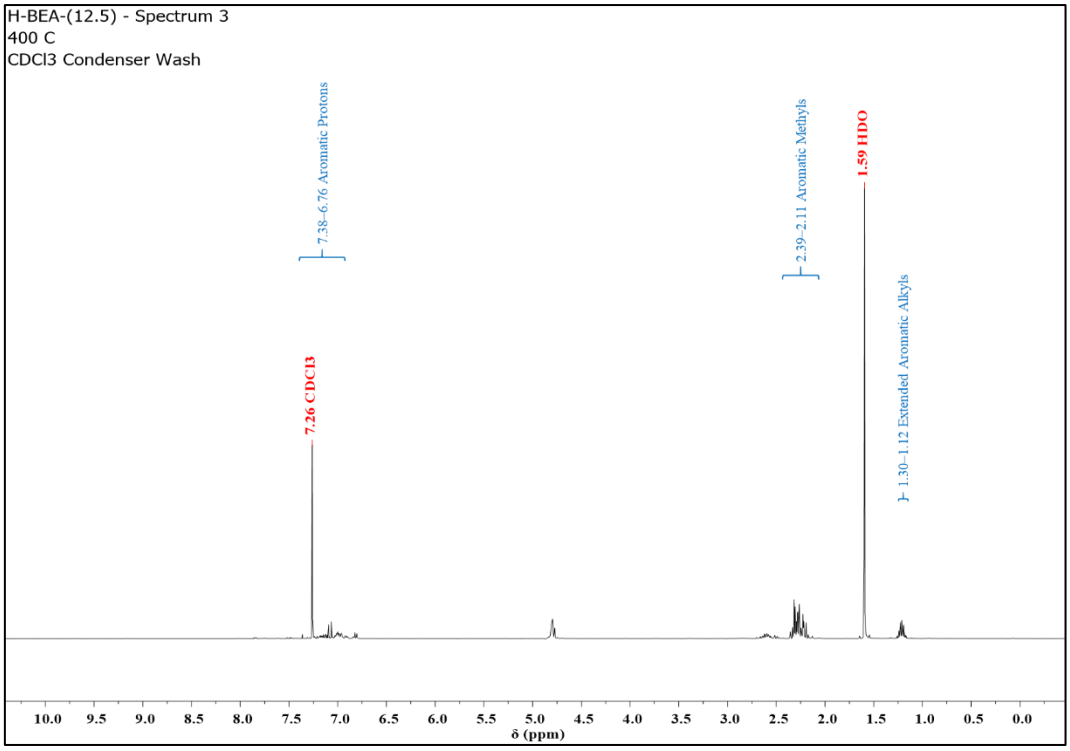

Figure A1.9: ^{1}H NMR spectrum of condenser washings from ethanol conversion over H–BEA–(12.5) at 400 °C averaged over 8 scans with a 1 s recycle delay. Spectrum was acquired on a Bruker Avance III-HD-400 spectrometer. Spectrometer frequency: ^{1}H = 399.95 MHz. NMR Solvent = $CDCl_3$.

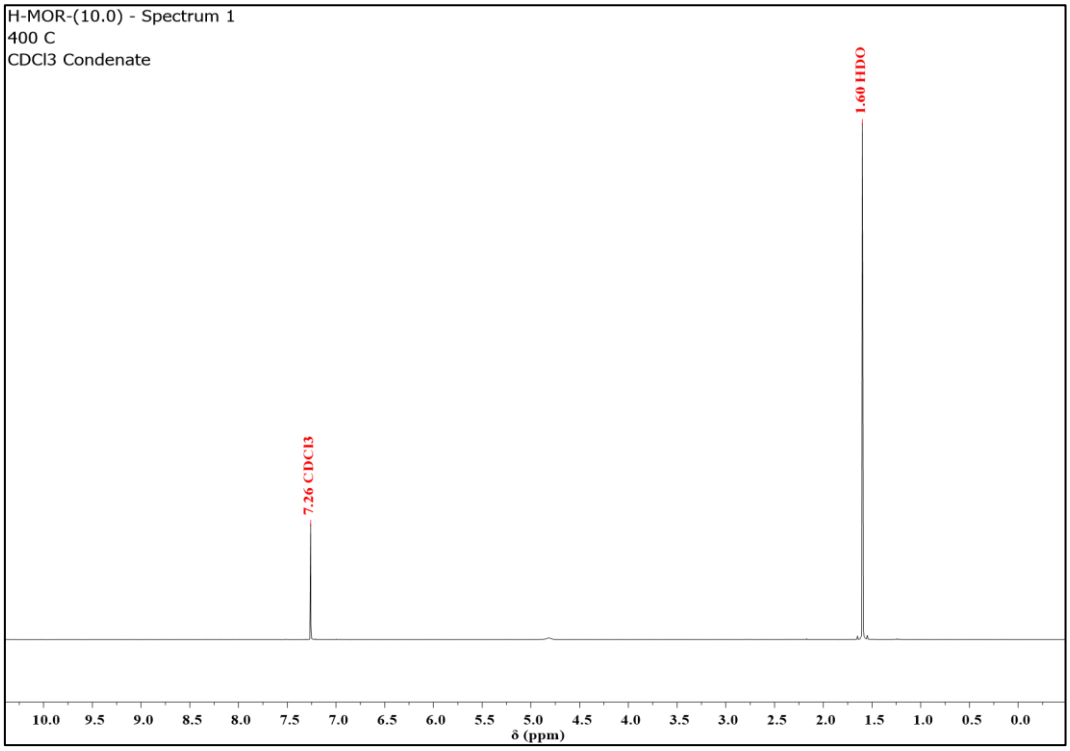

Figure A1.10: ^{1}H NMR spectrum of condensate from ethanol conversion over H–MOR–(10.0) at 400 °C averaged over 8 scans with a 1 s recycle delay. Spectrum was acquired on a Bruker Avance III-HD-400 spectrometer. Spectrometer frequency: ^{1}H = 399.95 MHz. NMR Solvent = $CDCl_3$.

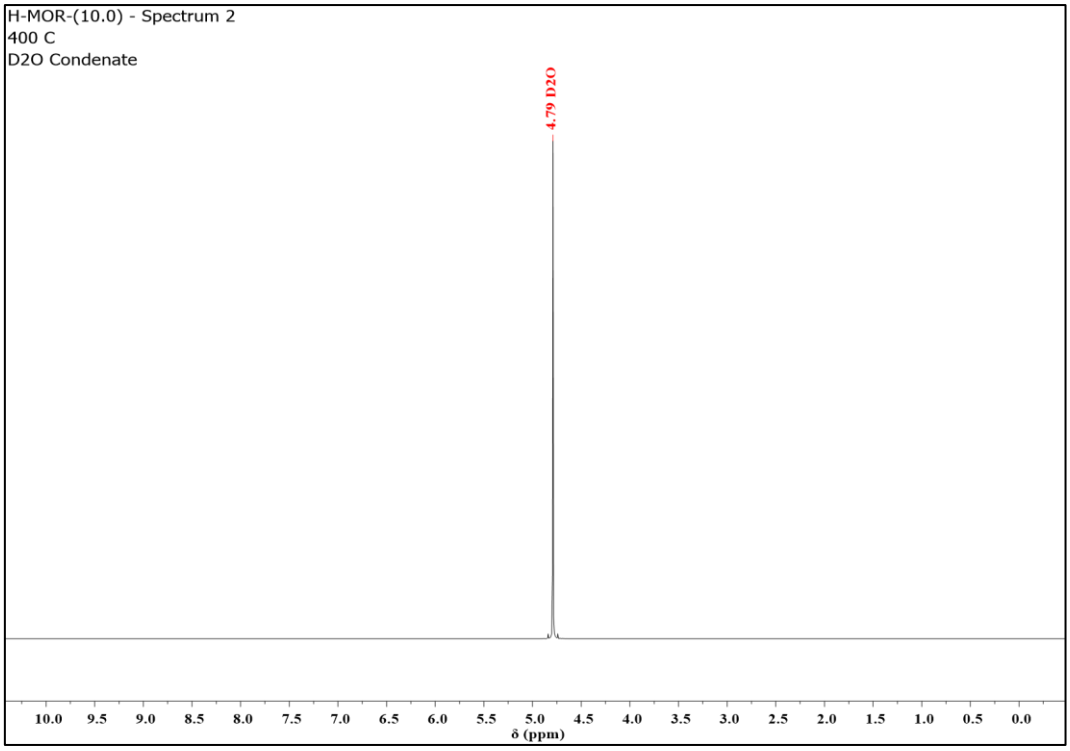

Figure A1.11: ^{1}H NMR spectrum of condensate from ethanol conversion over H–MOR–(10.0) at 400 °C averaged over 8 scans with a 1 s recycle delay. Spectrum was acquired on a Bruker Avance III-HD-400 spectrometer. Spectrometer frequency: ^{1}H = 399.95 MHz. NMR Solvent = D_2O.

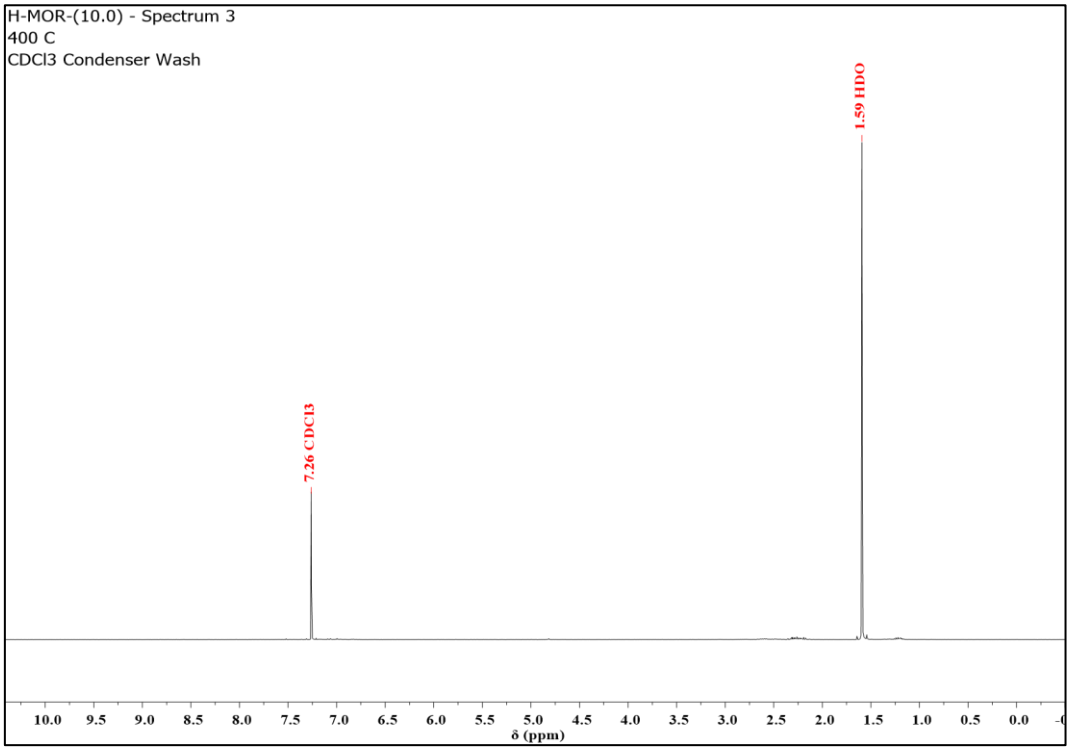

Figure A1.12: ^{1}H NMR spectrum of condenser washings from ethanol conversion over H–MOR–(10.0) at 400 °C averaged over 8 scans with a 1 s recycle delay. Spectrum was acquired on a Bruker Avance III-HD-400 spectrometer. Spectrometer frequency: ^{1}H = 399.95 MHz. NMR Solvent = $CDCl_3$.

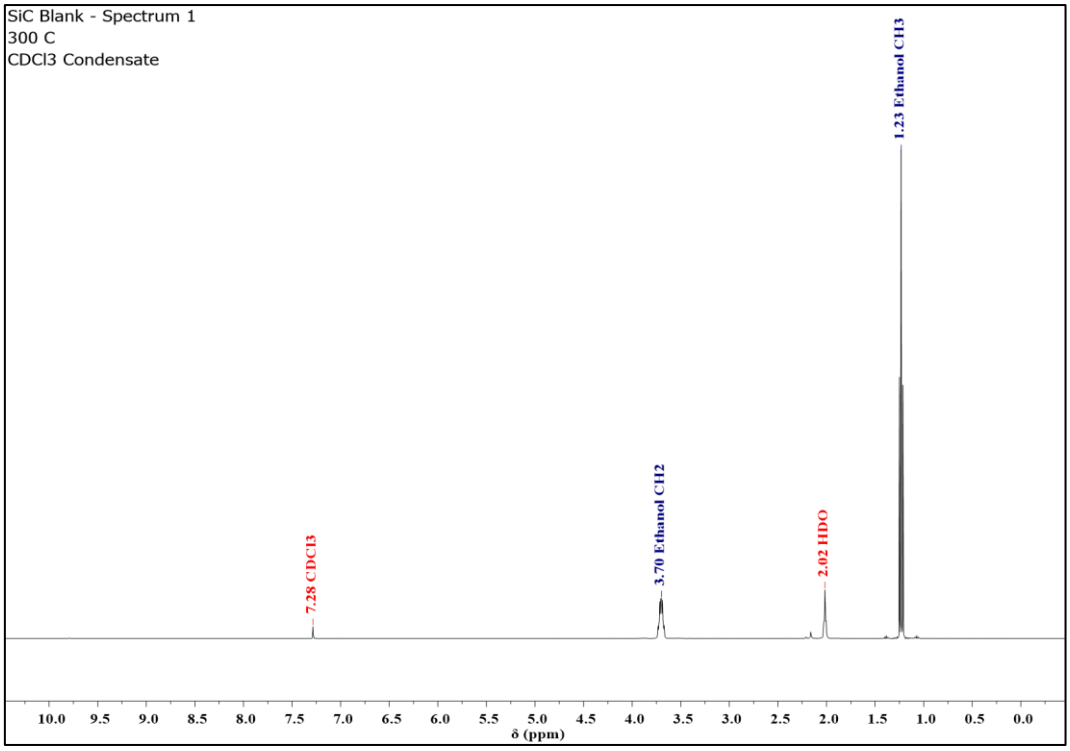

Figure A1.13: ^{1}H NMR spectrum of condensate from ethanol conversion over SiC at 300 °C averaged over 8 scans with a 1 s recycle delay. Spectrum was acquired on a Bruker Avance III-HD-400 spectrometer. Spectrometer frequency: ^{1}H = 400.07 MHz. NMR Solvent = $CDCl_3$.

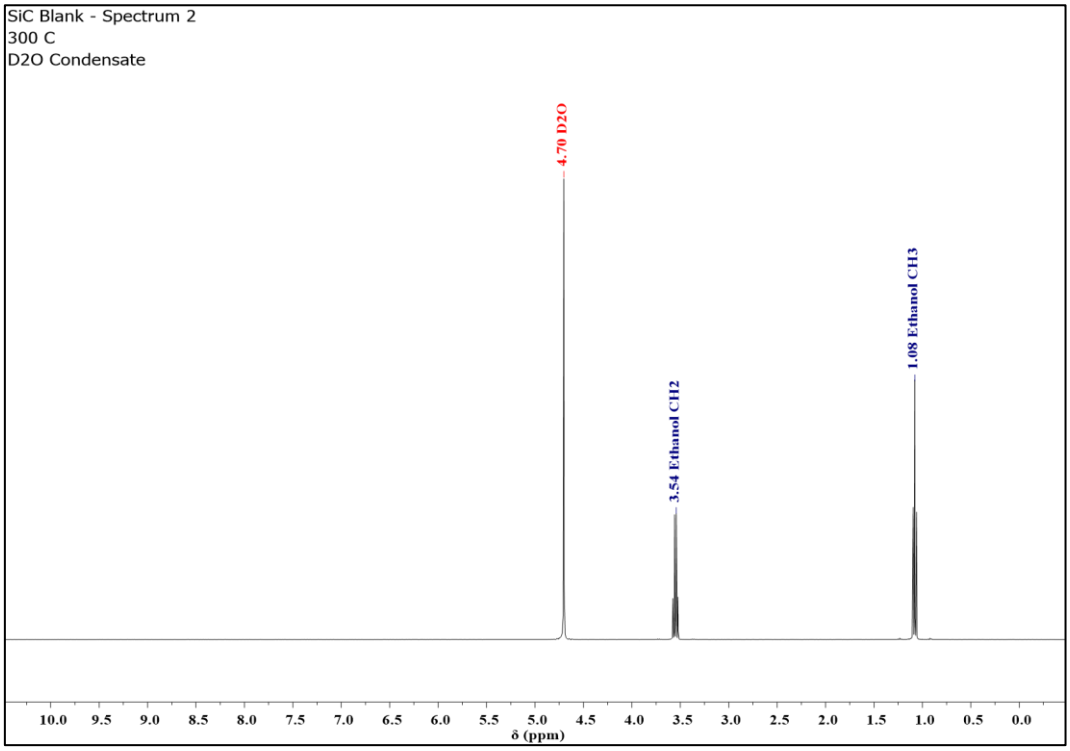

Figure A1.14: ^{1}H NMR spectrum of condensate from ethanol conversion over SiC at 300 °C averaged over 8 scans with a 1 s recycle delay. Spectrum was acquired on a Bruker Avance III-HD-400 spectrometer. Spectrometer frequency: ^{1}H = 400.07 MHz. NMR Solvent = D_2O.

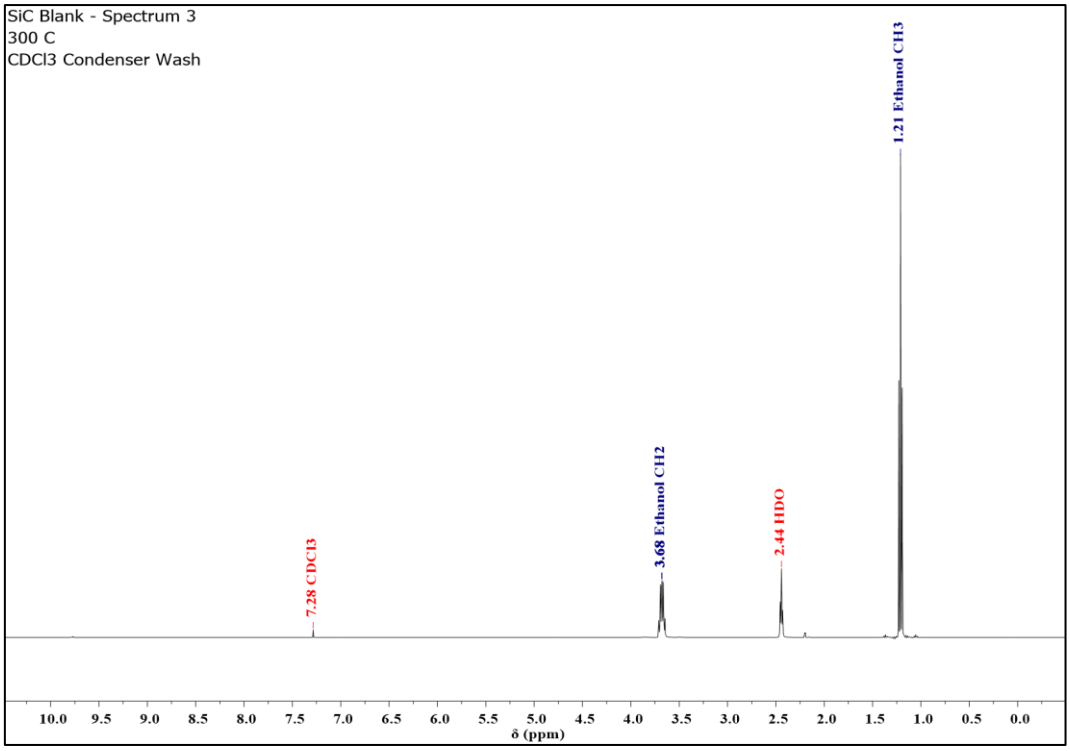

Figure A1.15: ^{1}H NMR spectrum of condenser wash from ethanol conversion over SiC at 300 °C averaged over 8 scans with a 1 s recycle delay. Spectrum was acquired on a Bruker Avance III-HD-400 spectrometer. Spectrometer frequency: ^{1}H = 400.07 MHz. NMR Solvent = $CDCl_3$.

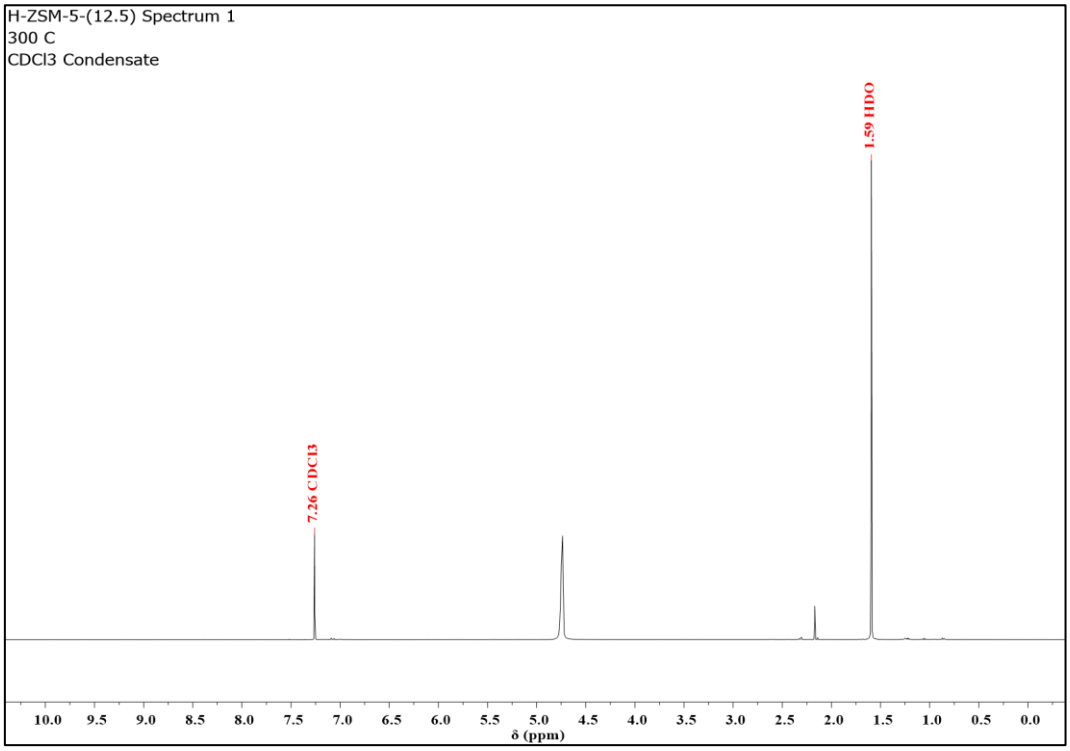

Figure A1.16: ^{1}H NMR spectrum of condensate from ethanol conversion over H–ZSM–5–(10.0) at 300 °C averaged over 8 scans with a 1 s recycle delay. Spectrum was acquired on a Bruker Avance III-HD-400 spectrometer. Spectrometer frequency: ^{1}H = 399.95 MHz. NMR Solvent = $CDCl_3$.

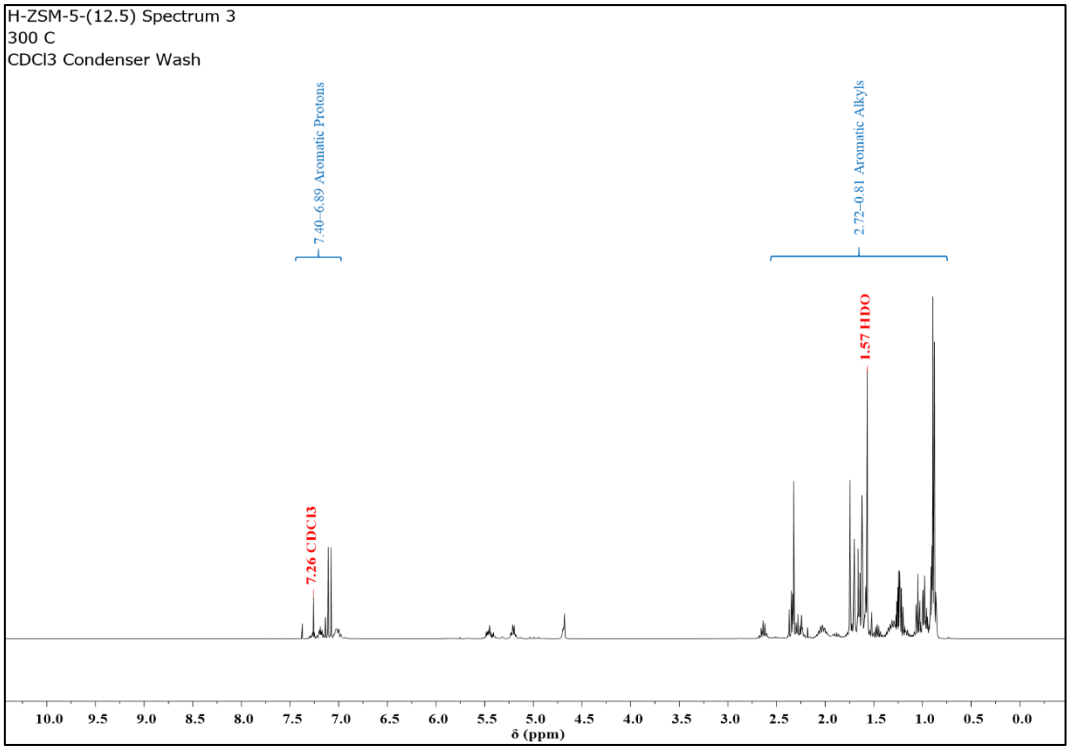

Figure A1.17: ^{1}H NMR spectrum of condenser washings from ethanol conversion over H–ZSM–5–(10.0) at 300 °C averaged over 8 scans with a 1 s recycle delay. Spectrum was acquired on a Bruker Avance III-HD-400 spectrometer. Spectrometer frequency: ^{1}H = 399.95 MHz. NMR Solvent = $CDCl_3$.

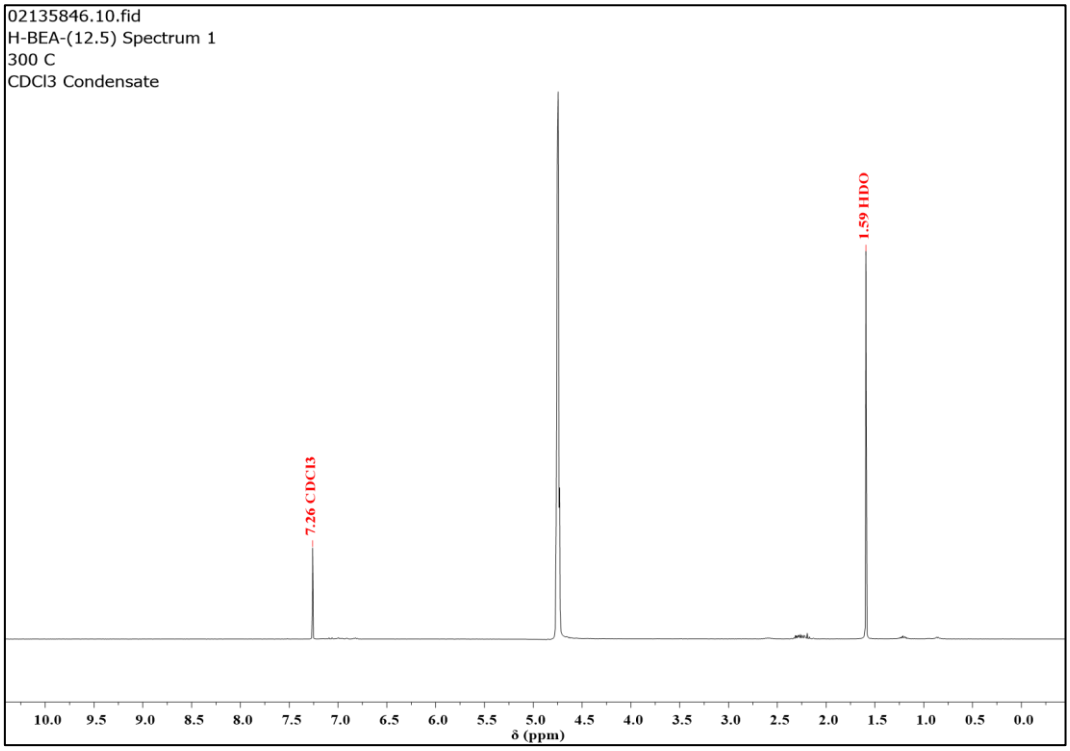

Figure A1.18: ^{1}H NMR spectrum of condensate from ethanol conversion over H–BEA–(12.5) at 300 °C averaged over 8 scans with a 1 s recycle delay. Spectrum was acquired on a Bruker Avance III-HD-400 spectrometer. Spectrometer frequency: ^{1}H = 399.95 MHz. NMR Solvent = $CDCl_3$.

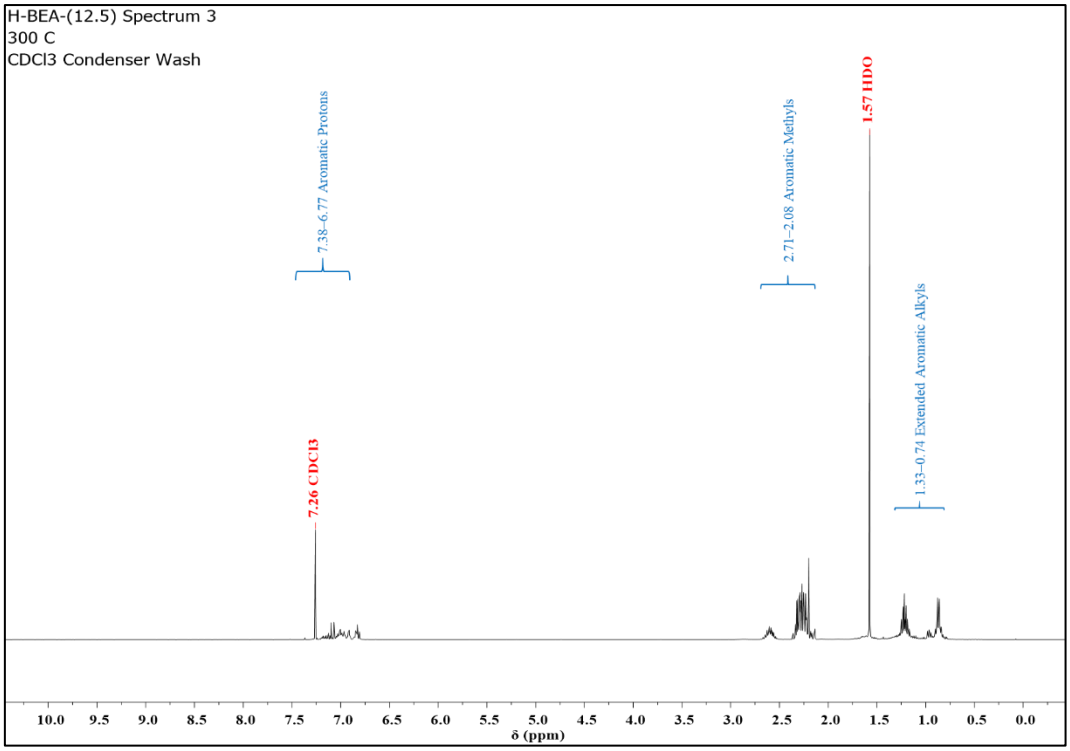

Figure A1.19: ^{1}H NMR spectrum of condenser washings from ethanol conversion over H–BEA–(12.5) at 300 °C averaged over 8 scans with a 1 s recycle delay. Spectrum was acquired on a Bruker Avance III-HD-400 spectrometer. Spectrometer frequency: ^{1}H = 399.95 MHz. NMR Solvent = $CDCl_3$.

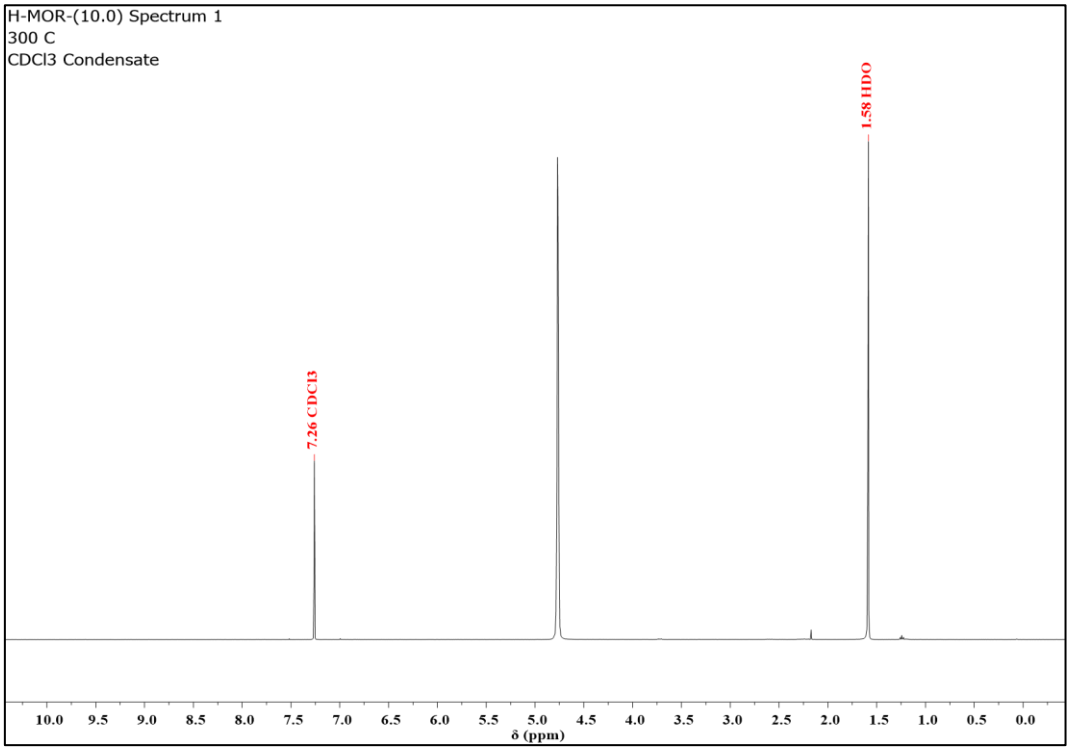

Figure A1.20: ^{1}H NMR spectrum of condensate from ethanol conversion over H–MOR–(10.0) at 300 °C averaged over 8 scans with a 1 s recycle delay. Spectrum was acquired on a Bruker Avance III-HD-400 spectrometer. Spectrometer frequency: ^{1}H = 399.95 MHz. NMR Solvent = $CDCl_3$.

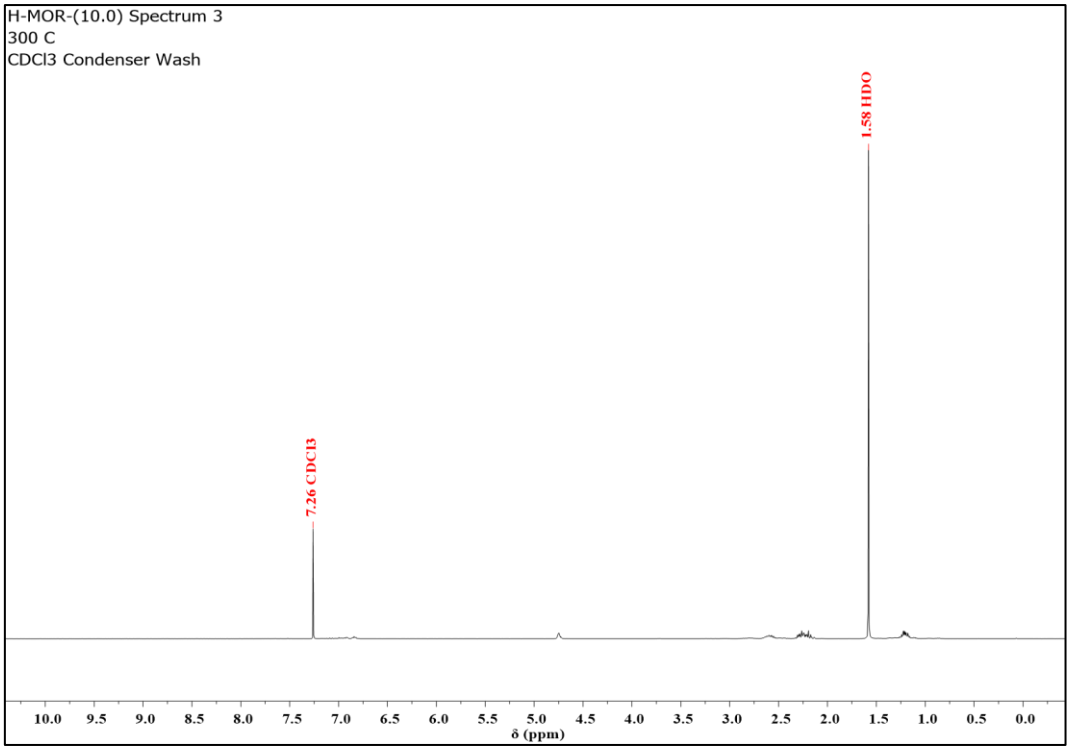

Figure A1.21: ^{1}H NMR spectrum of condenser washings from ethanol conversion over H–MOR–(10.0) at 300 °C averaged over 8 scans with a 1 s recycle delay. Spectrum was acquired on a Bruker Avance III-HD-400 spectrometer. Spectrometer frequency: ^{1}H = 399.95 MHz. NMR Solvent = $CDCl_3$.

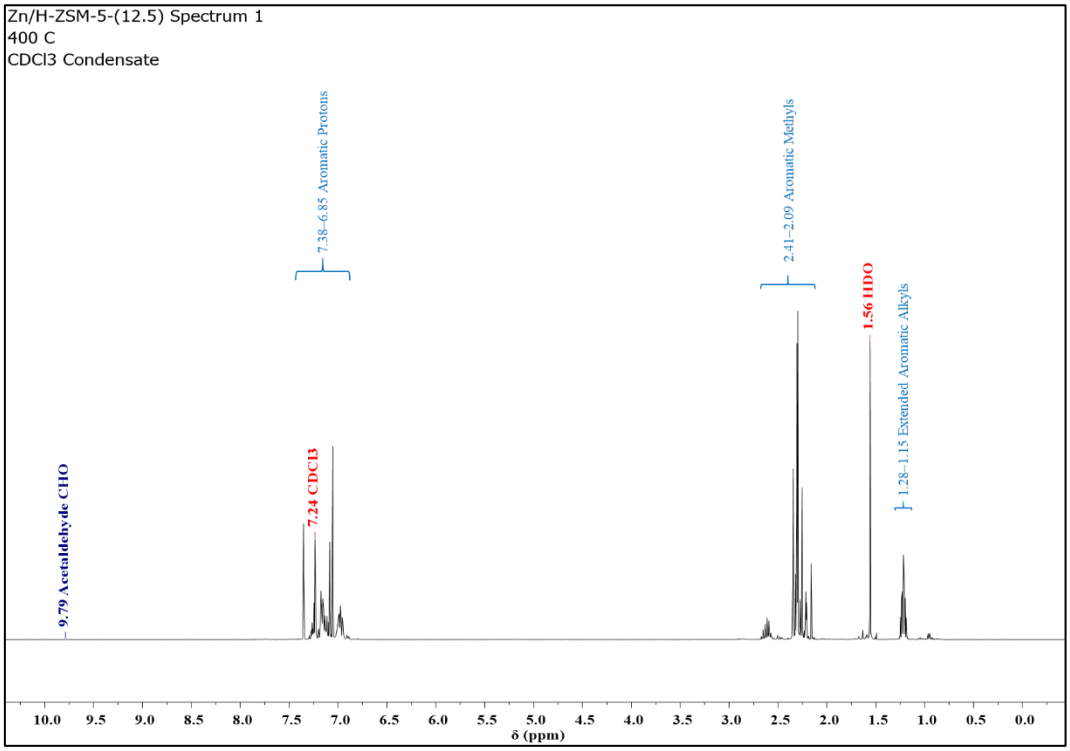

Figure A1.22: ^{1}H NMR spectrum of condensate from ethanol conversion over Zn/H–ZSM–5–(12.5) at 400 °C averaged over 8 scans with a 1 s recycle delay. Spectrum was acquired on a Bruker Avance III-HD-400 spectrometer. Spectrometer frequency: ^{1}H = 399.95 MHz. NMR Solvent = $CDCl_3$.

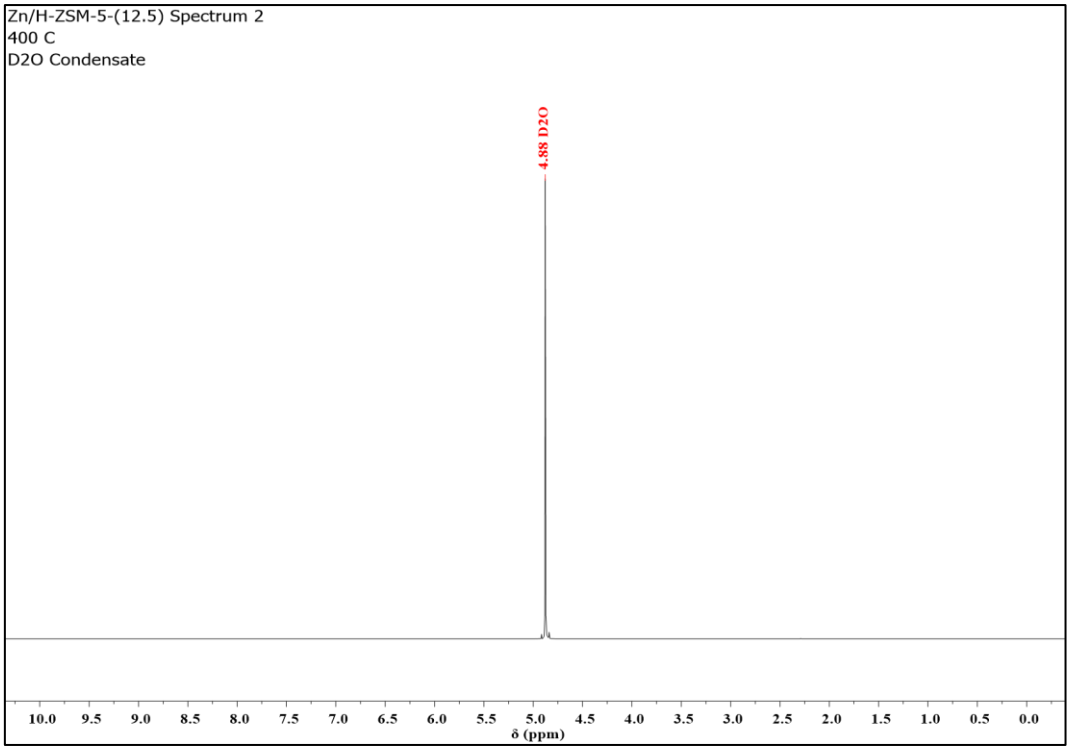

Figure A1.23: ^{1}H NMR spectrum of condensate from ethanol conversion over Zn/H–ZSM–5–(12.5) at 400 °C averaged over 8 scans with a 1 s recycle delay. Spectrum was acquired on a Bruker Avance III-HD-400 spectrometer. Spectrometer frequency: ^{1}H = 399.95 MHz. NMR Solvent = D_2O.

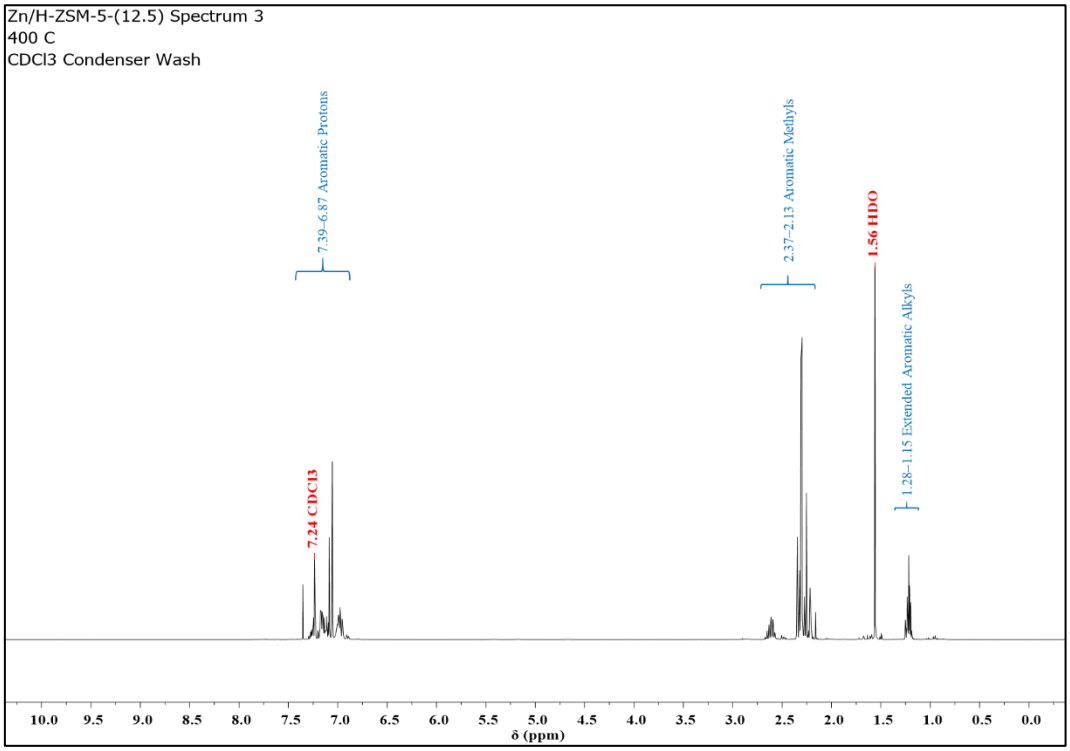

Figure A1.24: ^{1}H NMR spectrum of condenser washings from ethanol conversion over Zn/H–ZSM–5–(12.5) at 400 °C averaged over 8 scans with a 1 s recycle delay. Spectrum was acquired on a Bruker Avance III-HD-400 spectrometer. Spectrometer frequency: ^{1}H = 399.95 MHz. NMR Solvent = $CDCl_3$.

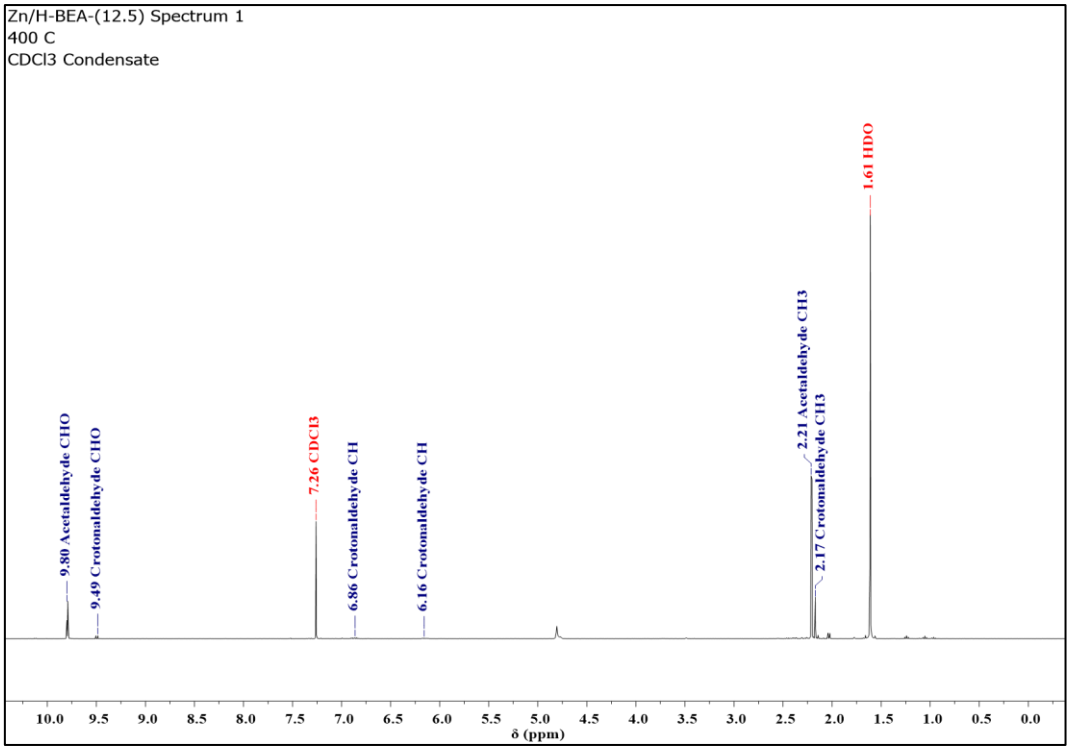

Figure A1.25: ^{1}H NMR spectrum of condensate from ethanol conversion over Zn/H–BEA–(12.5) at 400 °C averaged over 8 scans with a 1 s recycle delay. Spectrum was acquired on a Bruker Avance III-HD-400 spectrometer. Spectrometer frequency: ^{1}H = 399.95 MHz. NMR Solvent = $CDCl_3$.

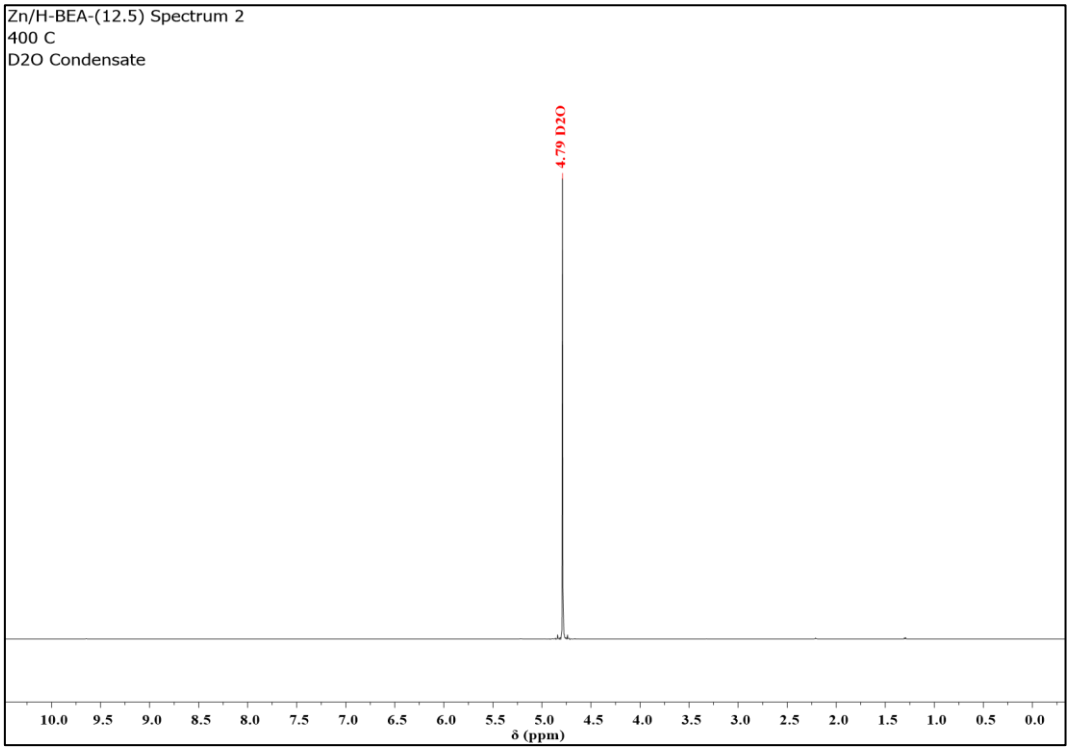

Figure A1.26: ^{1}H NMR spectrum of condensate from ethanol conversion over Zn/H–BEA–(12.5) at 400 °C averaged over 8 scans with a 1 s recycle delay. Spectrum was acquired on a Bruker Avance III-HD-400 spectrometer. Spectrometer frequency: ^{1}H = 399.95 MHz. NMR Solvent = D_2O.

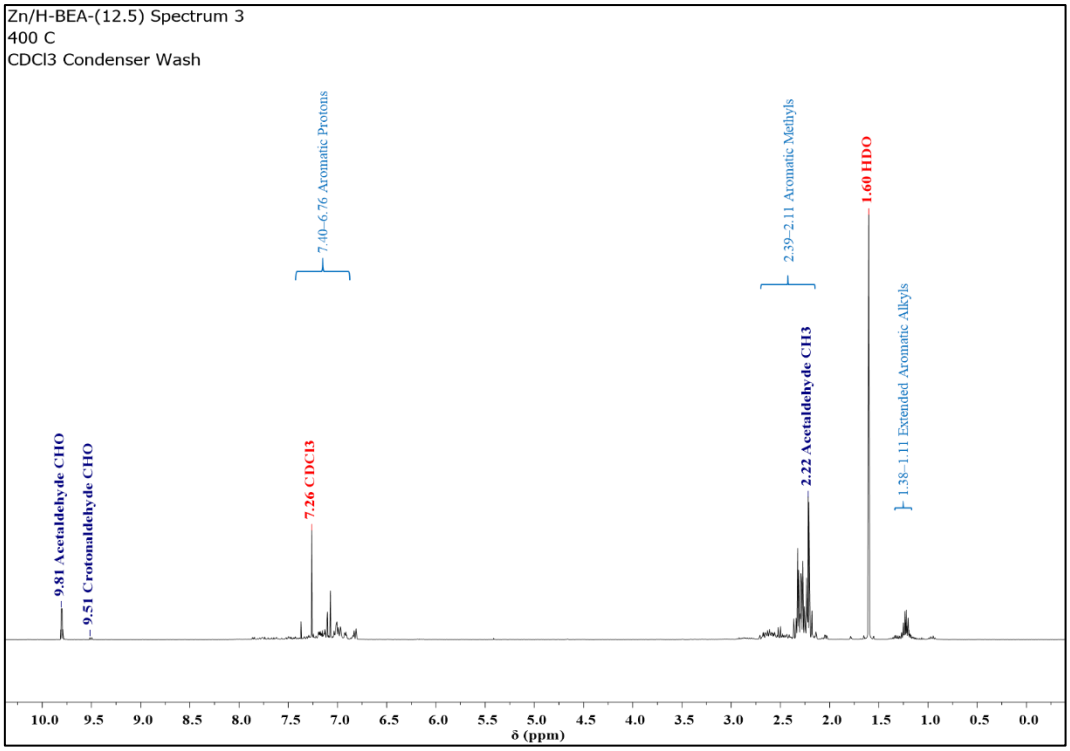

Figure A1.27: ^{1}H NMR spectrum of condenser washings from ethanol conversion over Zn/H–BEA–(12.5) at 400 °C averaged over 8 scans with a 1 s recycle delay. Spectrum was acquired on a Bruker Avance III-HD-400 spectrometer. Spectrometer frequency: ^{1}H = 399.95 MHz. NMR Solvent = $CDCl_3$.

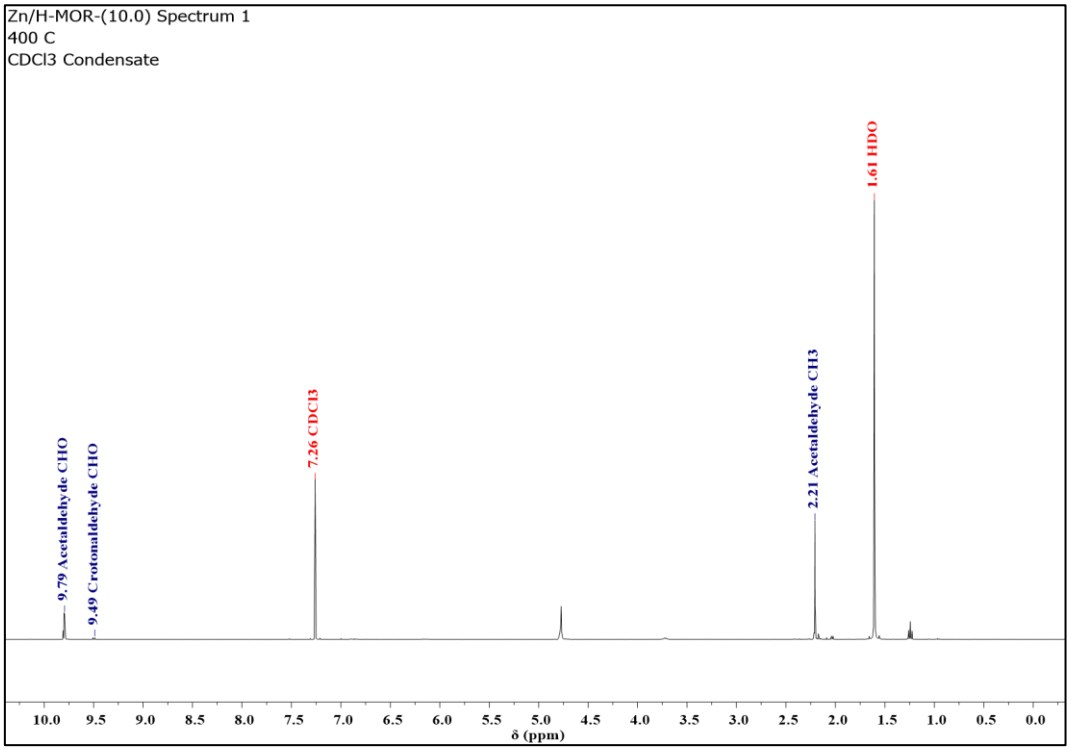

Figure A1.28: ^{1}H NMR spectrum of condensate from ethanol conversion over Zn/H–MOR–(10.0) at 400 °C averaged over 8 scans with a 1 s recycle delay. Spectrum was acquired on a Bruker Avance III-HD-400 spectrometer. Spectrometer frequency: ^{1}H = 399.95 MHz. NMR Solvent = $CDCl_3$.

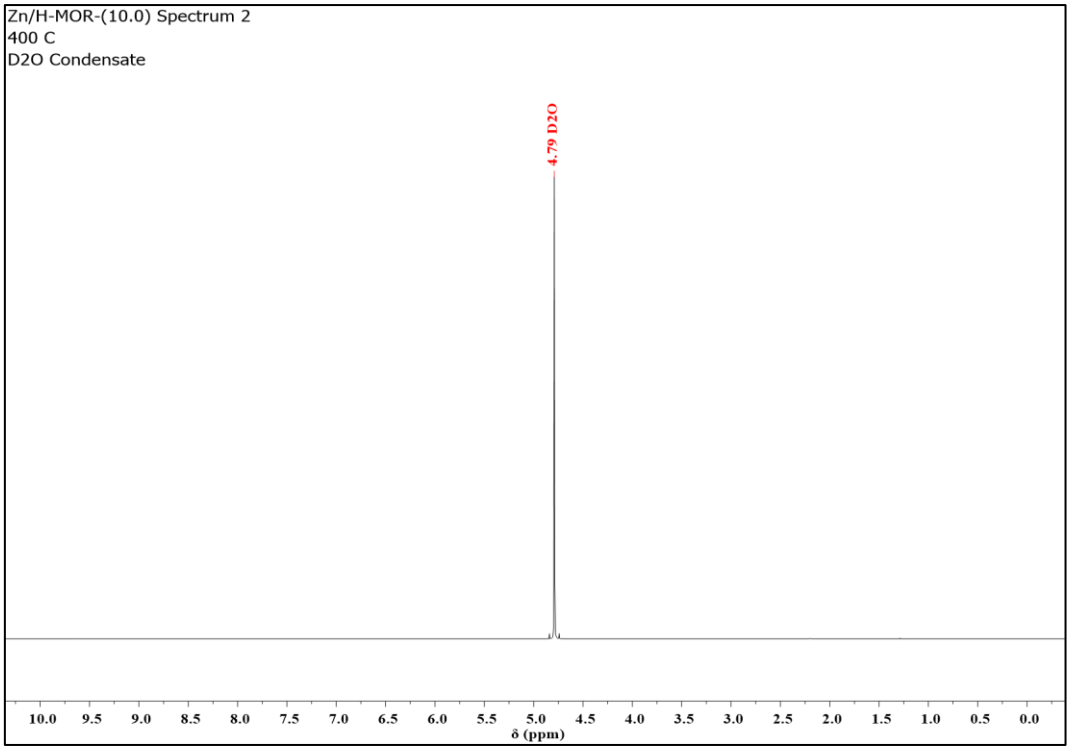

Figure A1.29: ^{1}H NMR spectrum of condensate from ethanol conversion over Zn/H–MOR–(10.0) at 400 °C averaged over 8 scans with a 1 s recycle delay. Spectrum was acquired on a Bruker Avance III-HD-400 spectrometer. Spectrometer frequency: ^{1}H = 399.95 MHz. NMR Solvent = D_2O.

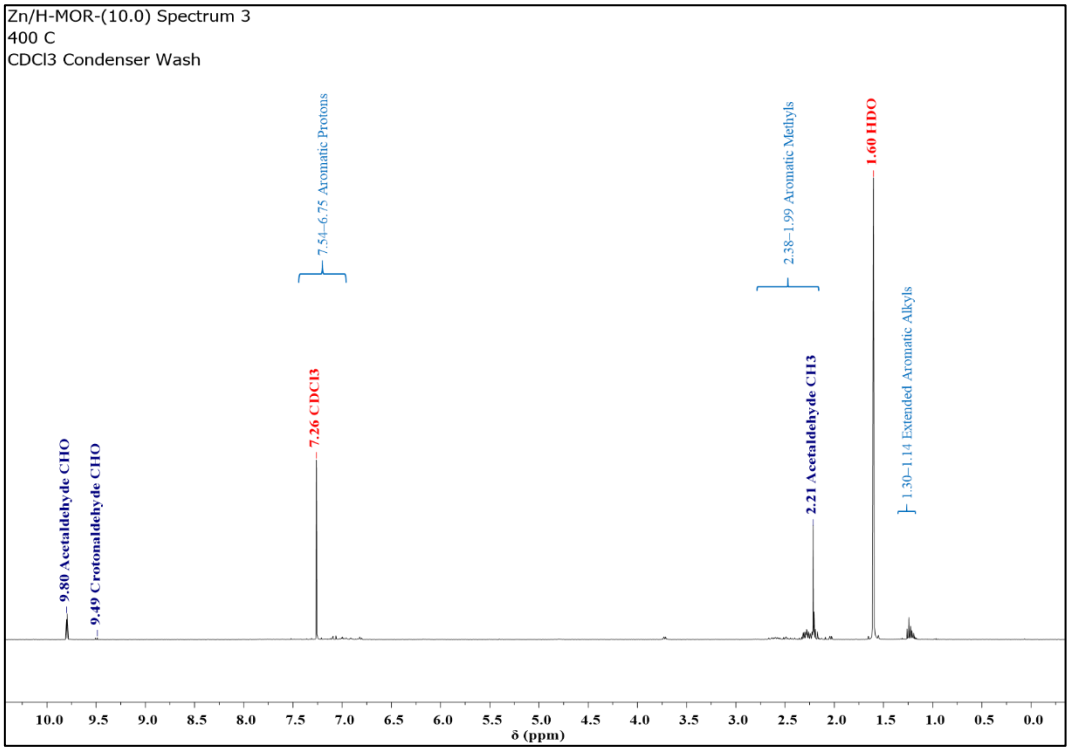

Figure A1.30: ^{1}H NMR spectrum of condenser washings from ethanol conversion over Zn/H–MOR–(10.0) at 400 °C averaged over 8 scans with a 1 s recycle delay. Spectrum was acquired on a Bruker Avance III-HD-400 spectrometer. Spectrometer frequency: ^{1}H = 399.95 MHz. NMR Solvent = $CDCl_3$.

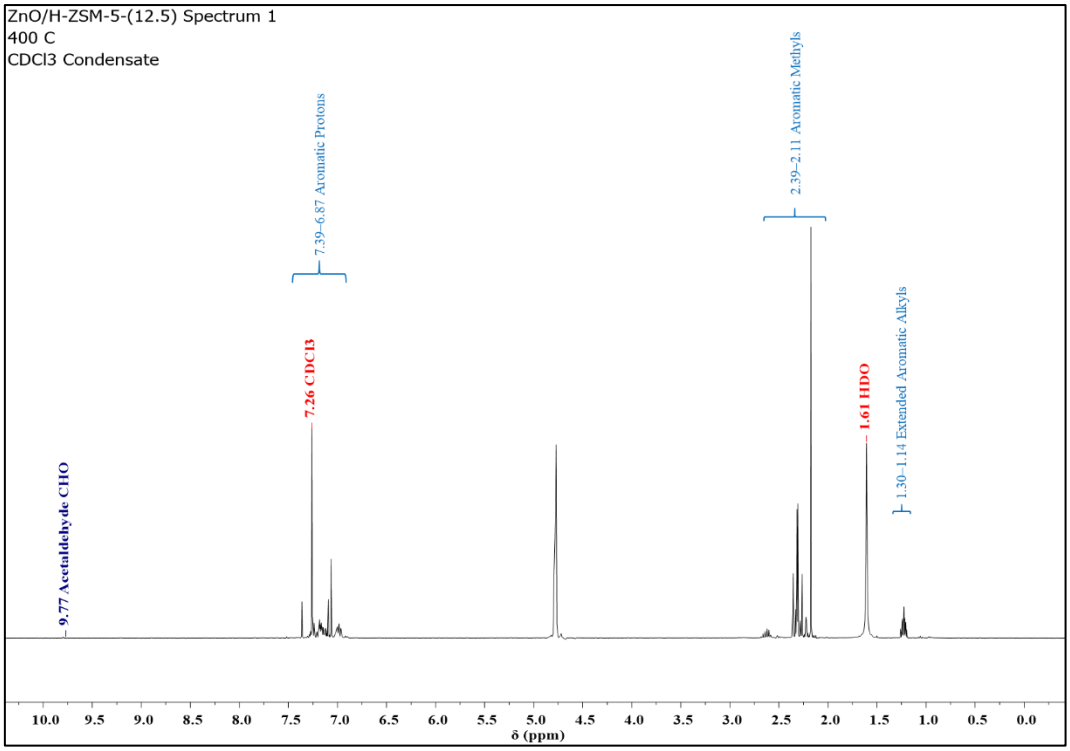

Figure A1.31: ^{1}H NMR spectrum of condensate from ethanol conversion over ZnO/H–ZSM–5–(12.5) at 400 °C averaged over 8 scans with a 1 s recycle delay. Spectrum was acquired on a Bruker Avance III-HD-400 spectrometer. Spectrometer frequency: ^{1}H = 399.95 MHz. NMR Solvent = $CDCl_3$.

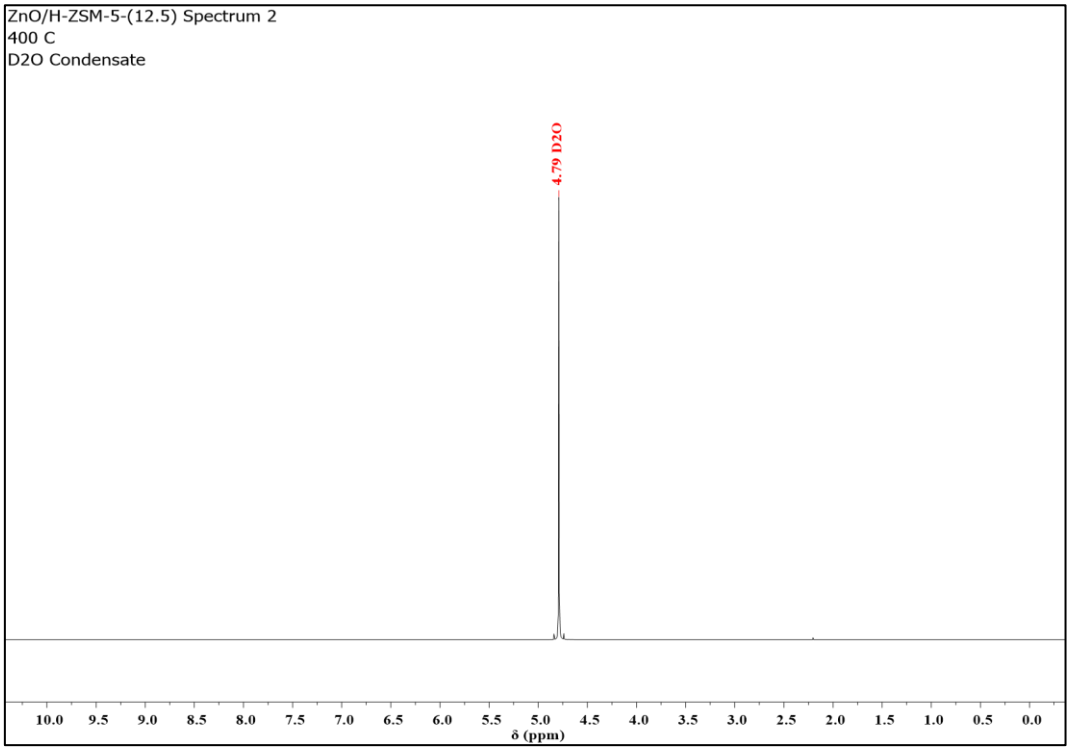

Figure A1.32: ^{1}H NMR spectrum of condensate from ethanol conversion over ZnO/H–ZSM–5–(12.5) at 400 °C averaged over 8 scans with a 1 s recycle delay. Spectrum was acquired on a Bruker Avance III-HD-400 spectrometer. Spectrometer frequency: ^{1}H = 399.95 MHz. NMR Solvent = D_2O.

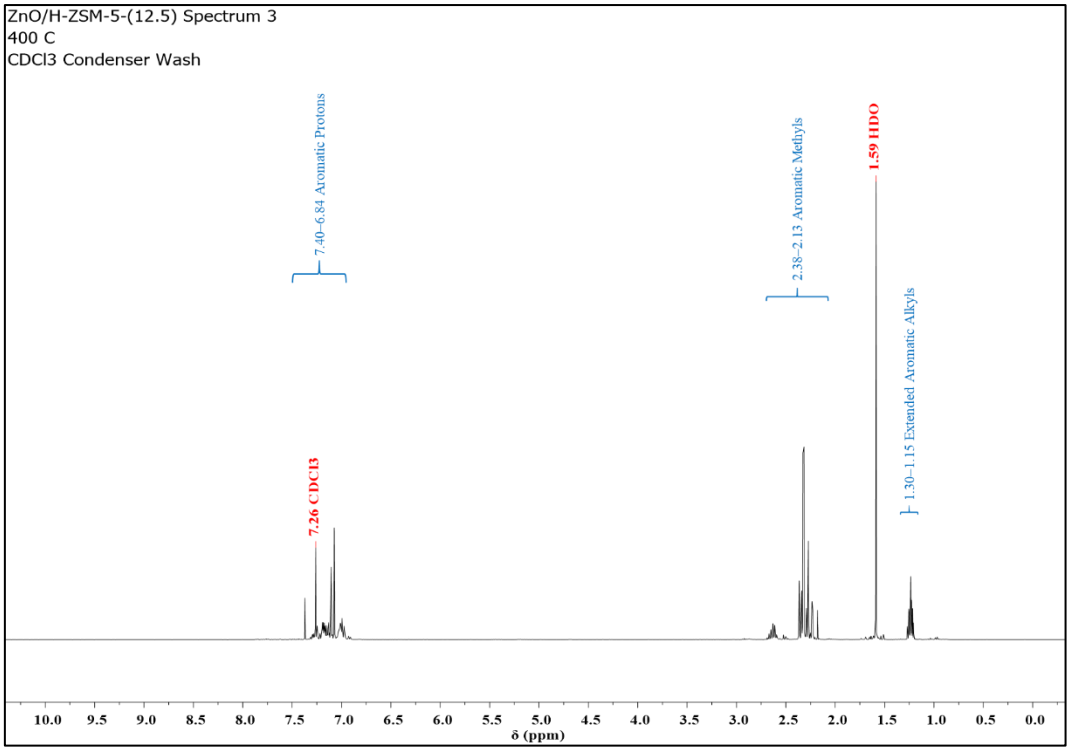

Figure A1.33: ^{1}H NMR spectrum of condenser washings from ethanol conversion over ZnO/H–ZSM–5–(12.5) at 400 °C averaged over 8 scans with a 1 s recycle delay. Spectrum was acquired on a Bruker Avance III-HD-400 spectrometer. Spectrometer frequency: ^{1}H = 399.95 MHz. NMR Solvent = $CDCl_3$.

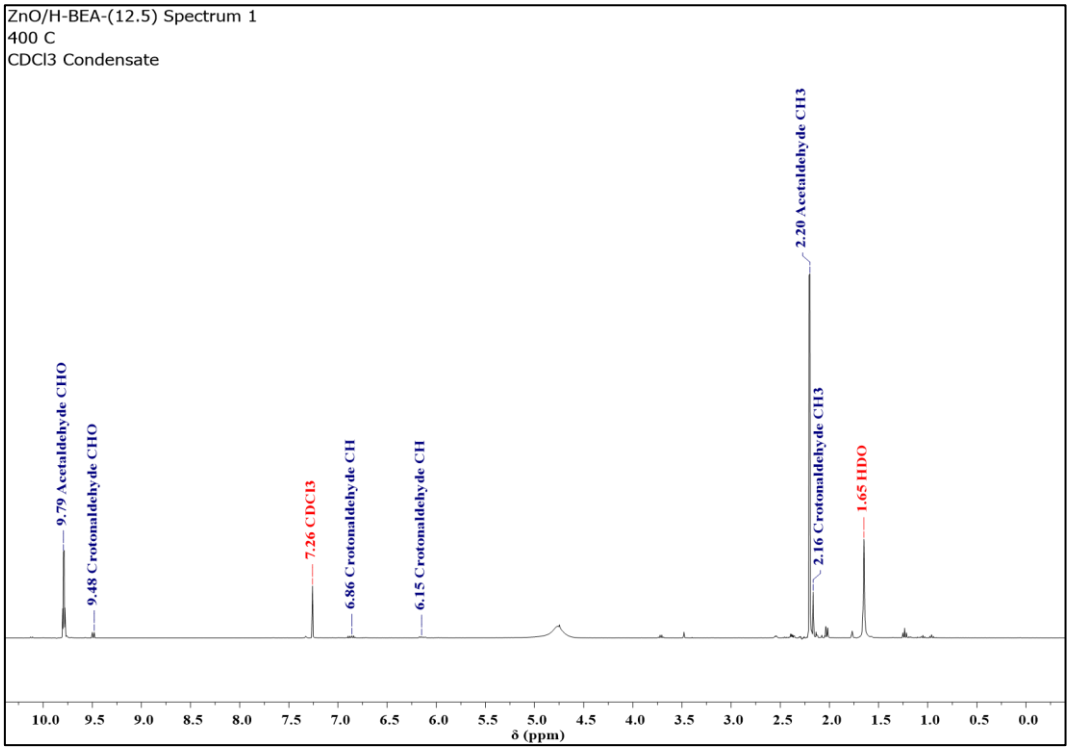

Figure A1.34: ^{1}H NMR spectrum of condensate from ethanol conversion over ZnO/H–BEA–(12.5) at 400 °C averaged over 8 scans with a 1 s recycle delay. Spectrum was acquired on a Bruker Avance III-HD-400 spectrometer. Spectrometer frequency: ^{1}H = 400.07 MHz. NMR Solvent = $CDCl_3$.

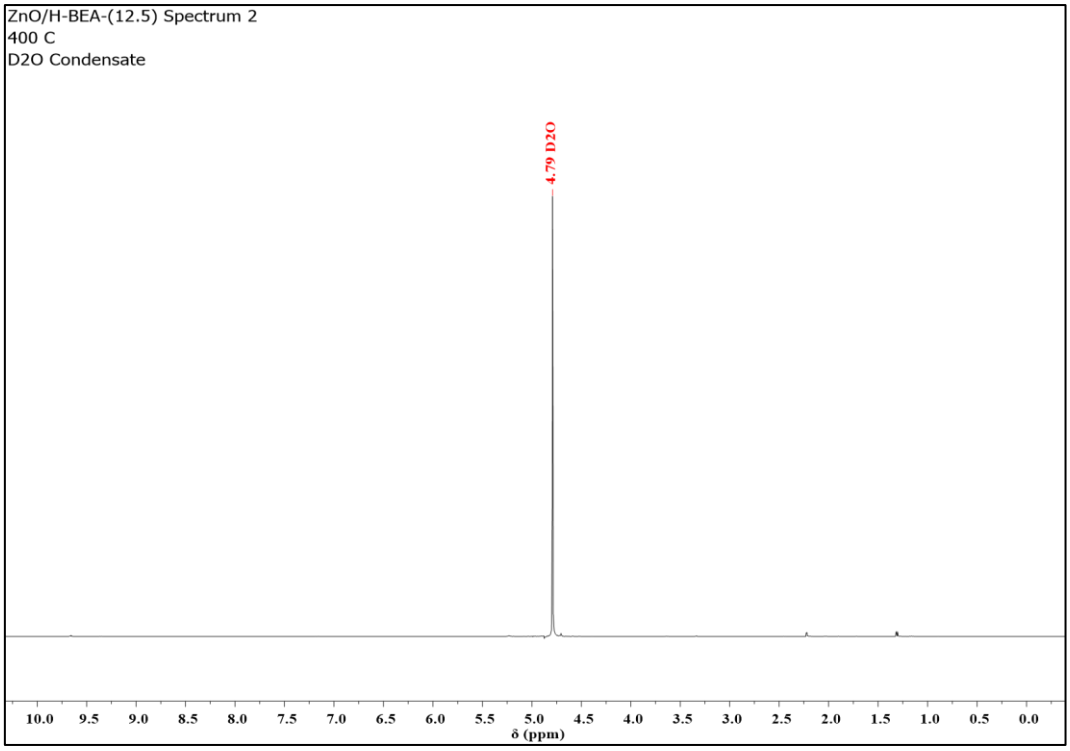

Figure A1.35: ^{1}H NMR spectrum of condensate from ethanol conversion over ZnO/H–BEA–(12.5) at 400 °C averaged over 8 scans with a 1 s recycle delay. Spectrum was acquired on a Bruker Avance III-HD-400 spectrometer. Spectrometer frequency: ^{1}H = 400.07 MHz. NMR Solvent = D_2O.

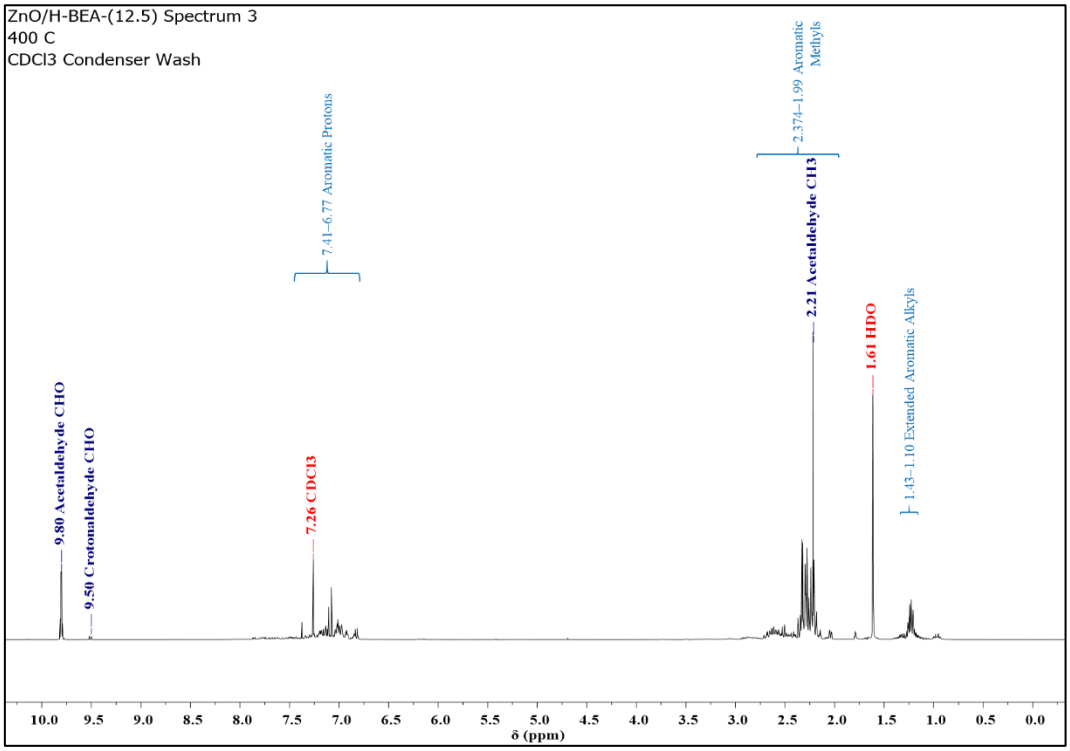

Figure A1.36: ^{1}H NMR spectrum of condenser washings from ethanol conversion over ZnO/H–BEA–(12.5) at 400 °C averaged over 8 scans with a 1 s recycle delay. Spectrum was acquired on a Bruker Avance III-HD-400 spectrometer. Spectrometer frequency: ^{1}H = 400.07 MHz. NMR Solvent = $CDCl_3$.

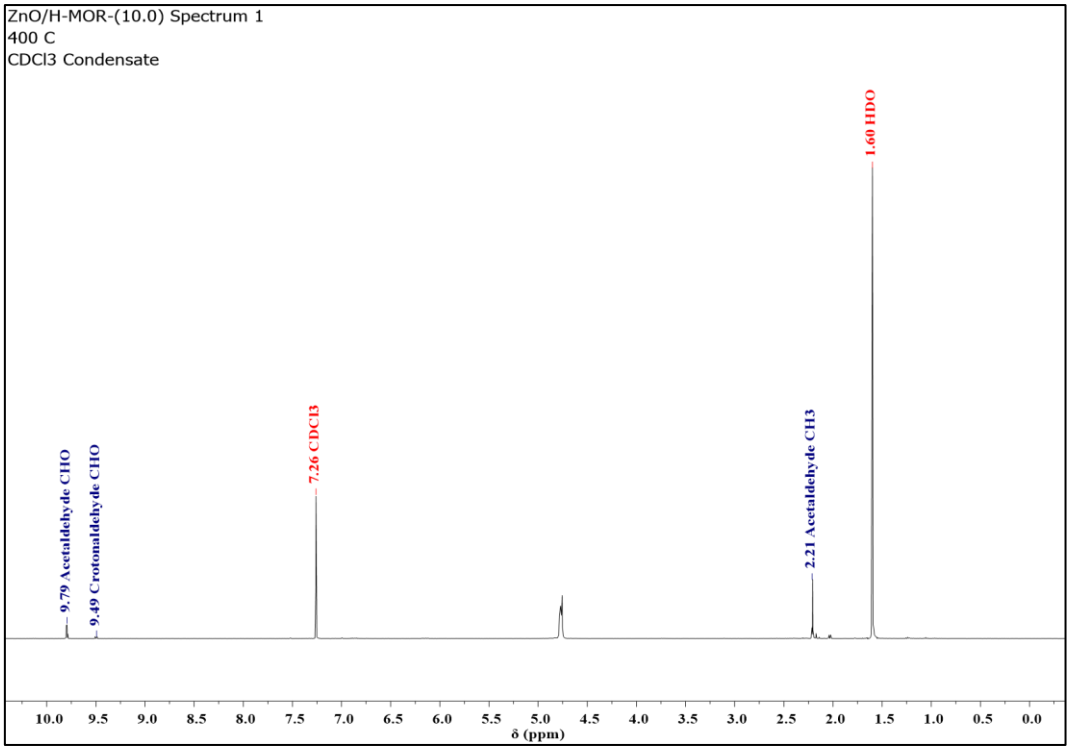

Figure A1.37: ^{1}H NMR spectrum of condensate from ethanol conversion over ZnO/H–MOR–(10.0) at 400 °C averaged over 8 scans with a 1 s recycle delay. Spectrum was acquired on a Bruker Avance III-HD-400 spectrometer. Spectrometer frequency: ^{1}H = 400.07 MHz. NMR Solvent = $CDCl_3$.

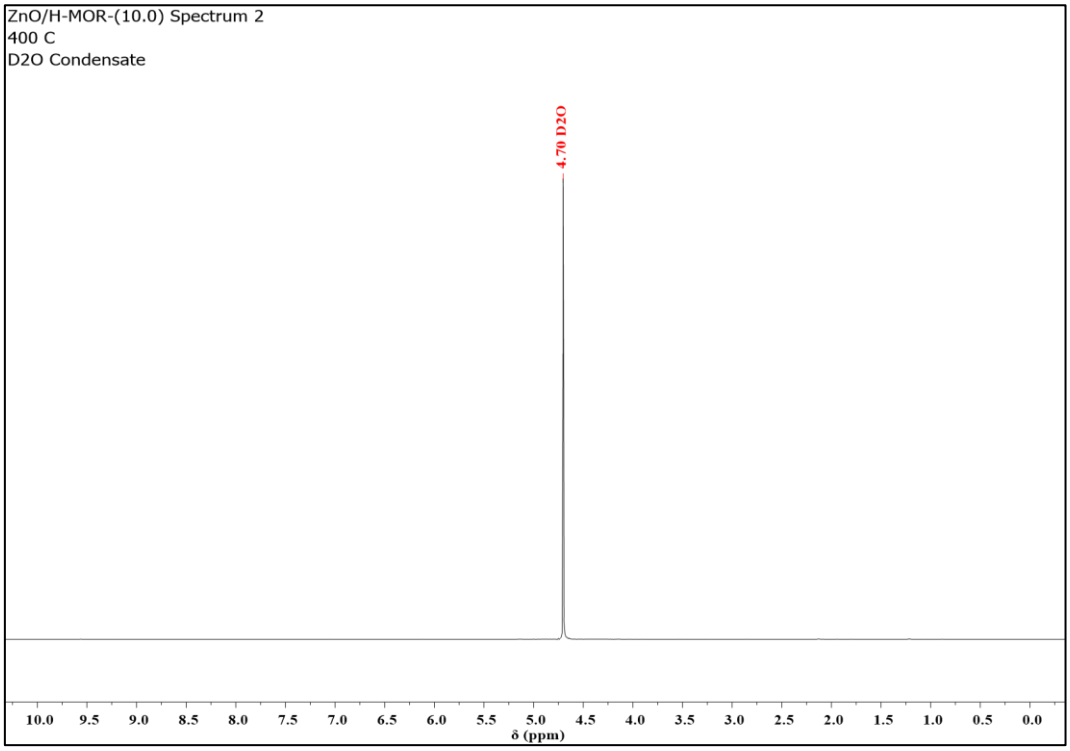

Figure A1.38: ^{1}H NMR spectrum of condensate from ethanol conversion over ZnO/H–MOR–(10.0) at 400 °C averaged over 8 scans with a 1 s recycle delay. Spectrum was acquired on a Bruker Avance III-HD-400 spectrometer. Spectrometer frequency: ^{1}H = 400.07 MHz. NMR Solvent = D_2O.

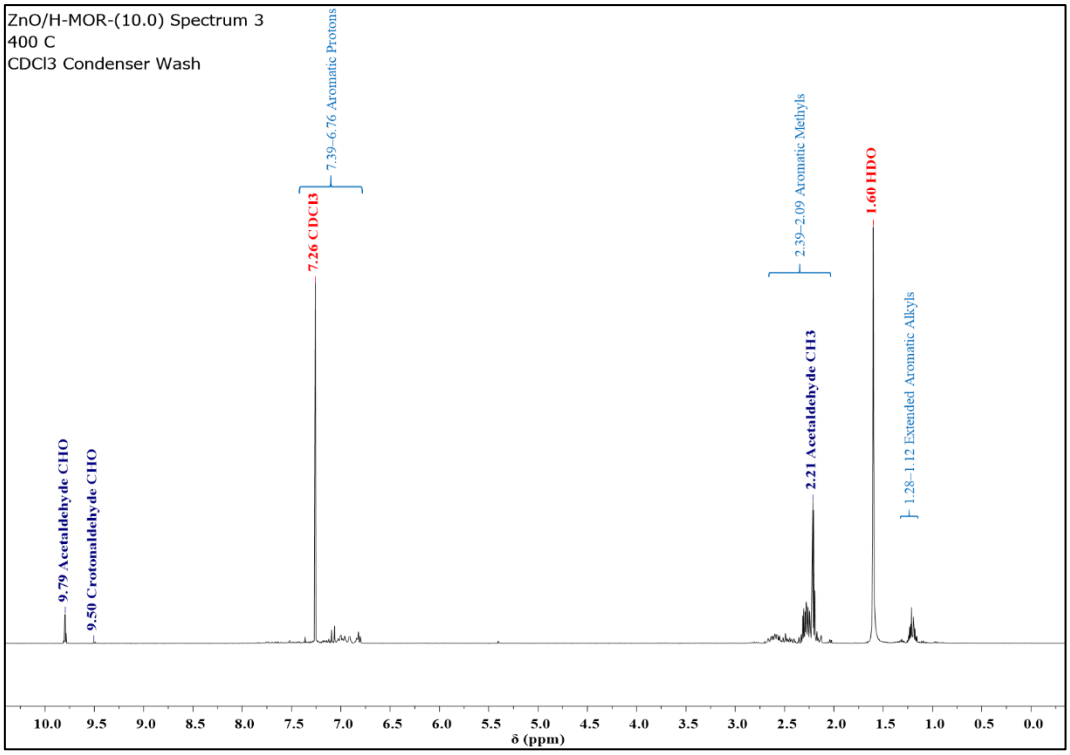

Figure A1.39: ^{1}H NMR spectrum of condenser washings from ethanol conversion over ZnO/H–MOR–(10.0) at 400 °C averaged over 8 scans with a 1 s recycle delay. Spectrum was acquired on a Bruker Avance III-HD-400 spectrometer. Spectrometer frequency: ^{1}H = 400.07 MHz. NMR Solvent = $CDCl_3$.

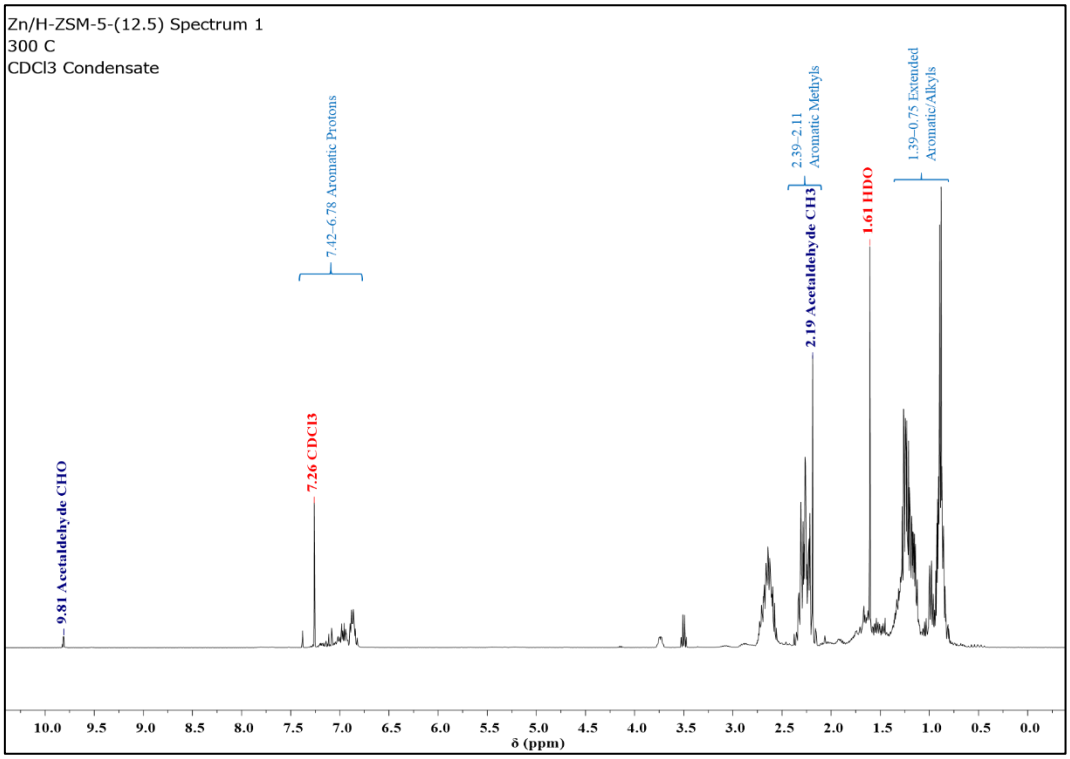

Figure A1.40: ^{1}H NMR spectrum of condensate from ethanol conversion over Zn/H–ZSM–5–(12.5) at 300 °C averaged over 8 scans with a 1 s recycle delay. Spectrum was acquired on a Bruker Avance III-HD-400 spectrometer. Spectrometer frequency: ^{1}H = 399.95 MHz. NMR Solvent = $CDCl_3$.

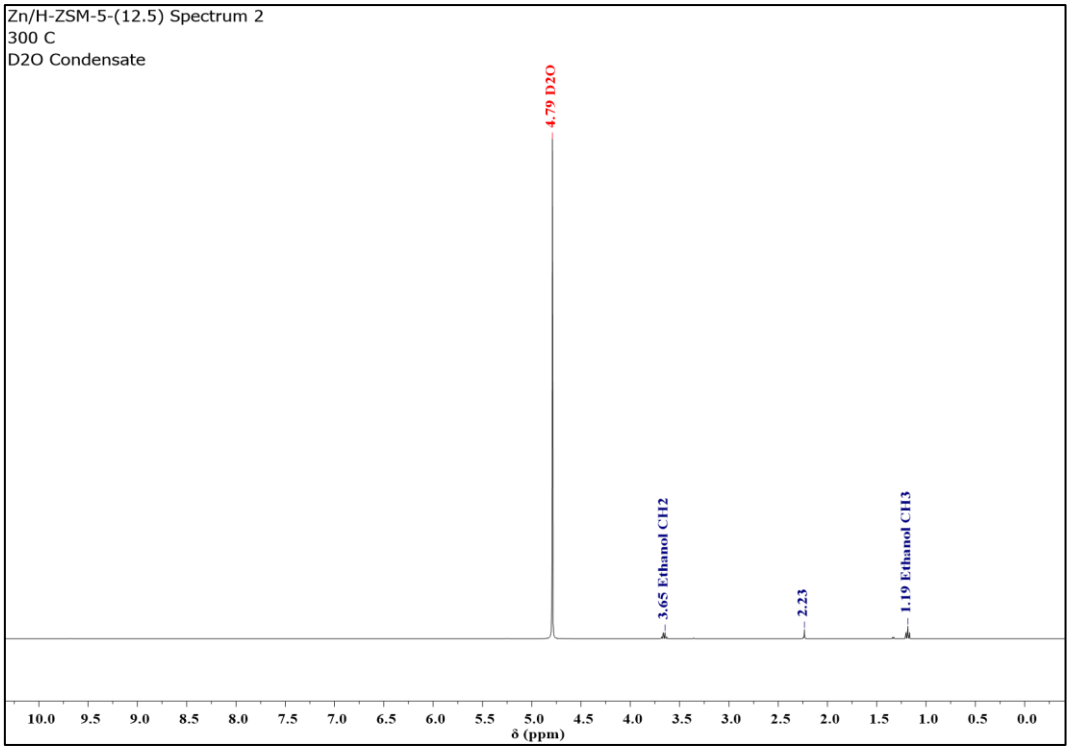

Figure A1.41: ^{1}H NMR spectrum of condensate from ethanol conversion over Zn/H–ZSM–5–((12.5) at 300 °C averaged over 8 scans with a 1 s recycle delay. Spectrum was acquired on a Bruker Avance III-HD-400 spectrometer. Spectrometer frequency: ^{1}H = 399.95 MHz. NMR Solvent = D_2O.

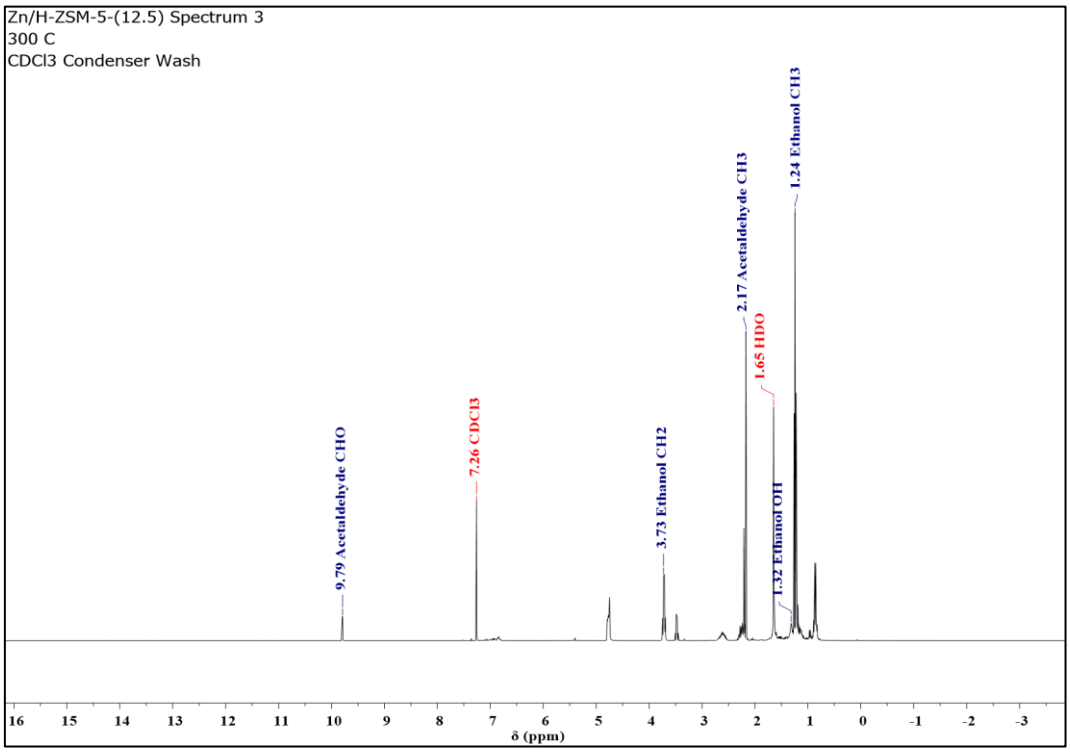

Figure A1.42: ^{1}H NMR spectrum of condenser washings from ethanol conversion over Zn/H–ZSM–5–((12.5) at 300 °C averaged over 8 scans with a 1 s recycle delay. Spectrum was acquired on a Bruker Avance III-HD-400 spectrometer. Spectrometer frequency: ^{1}H = 399.95 MHz. NMR Solvent = $CDCl_3$.

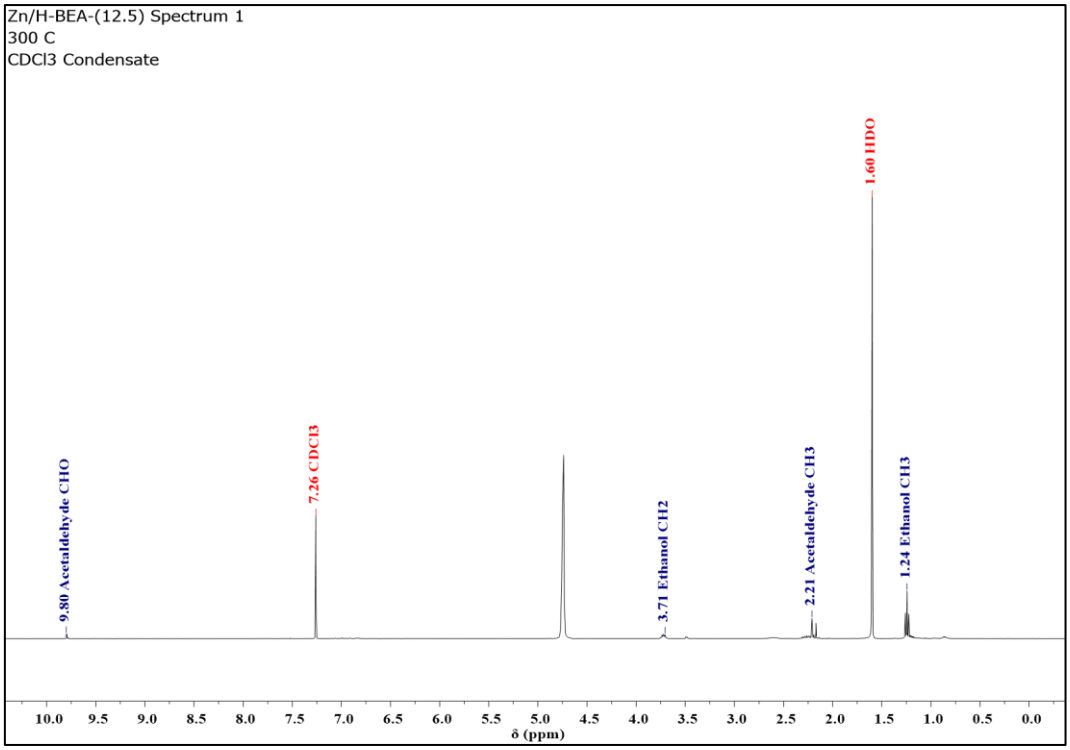

Figure A1.43: ^{1}H NMR spectrum of condensate from ethanol conversion over Zn/H–BEA–(12.5) at 300 °C averaged over 8 scans with a 1 s recycle delay. Spectrum was acquired on a Bruker Avance III-HD-400 spectrometer. Spectrometer frequency: ^{1}H = 399.95 MHz. NMR Solvent = $CDCl_3$.

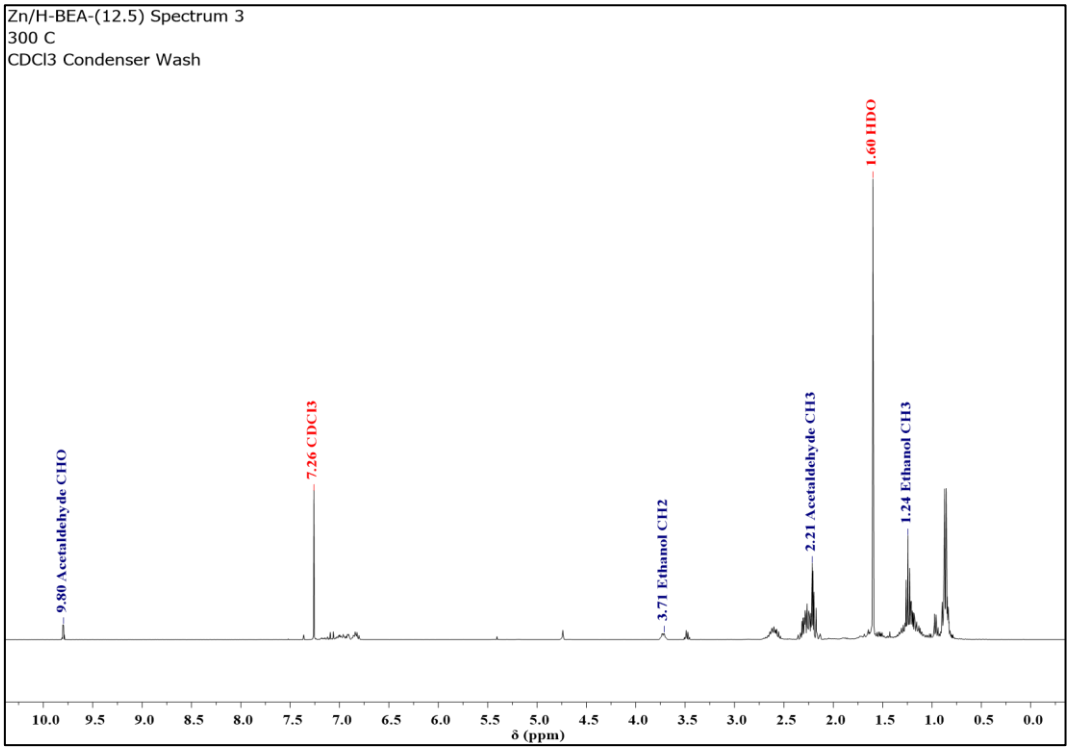

Figure A1.44: ^{1}H NMR spectrum of condenser washings from ethanol conversion over Zn/H–BEA–(12.5) at 300 °C averaged over 8 scans with a 1 s recycle delay. Spectrum was acquired on a Bruker Avance III-HD-400 spectrometer. Spectrometer frequency: ^{1}H = 399.95 MHz. NMR Solvent = $CDCl_3$.

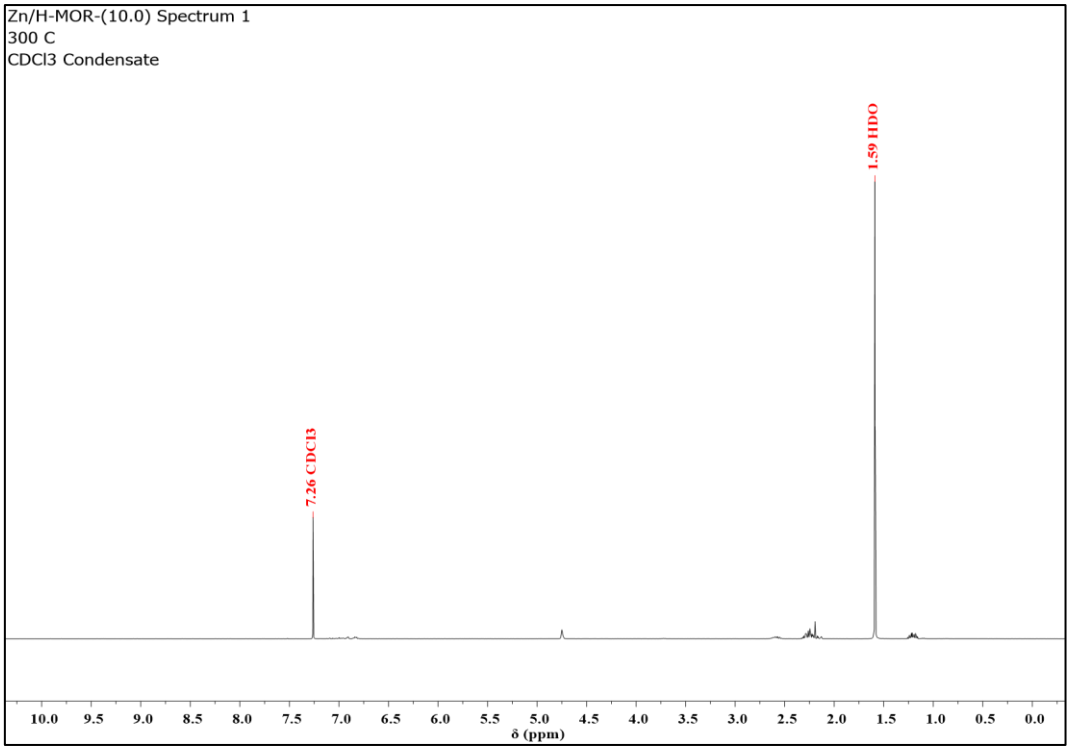

Figure A1.45: ^{1}H NMR spectrum of condensate from ethanol conversion over Zn/H–MOR–(10.0) at 300 °C averaged over 8 scans with a 1 s recycle delay. Spectrum was acquired on a Bruker Avance III-HD-400 spectrometer. Spectrometer frequency: ^{1}H = 399.95 MHz. NMR Solvent = $CDCl_3$.

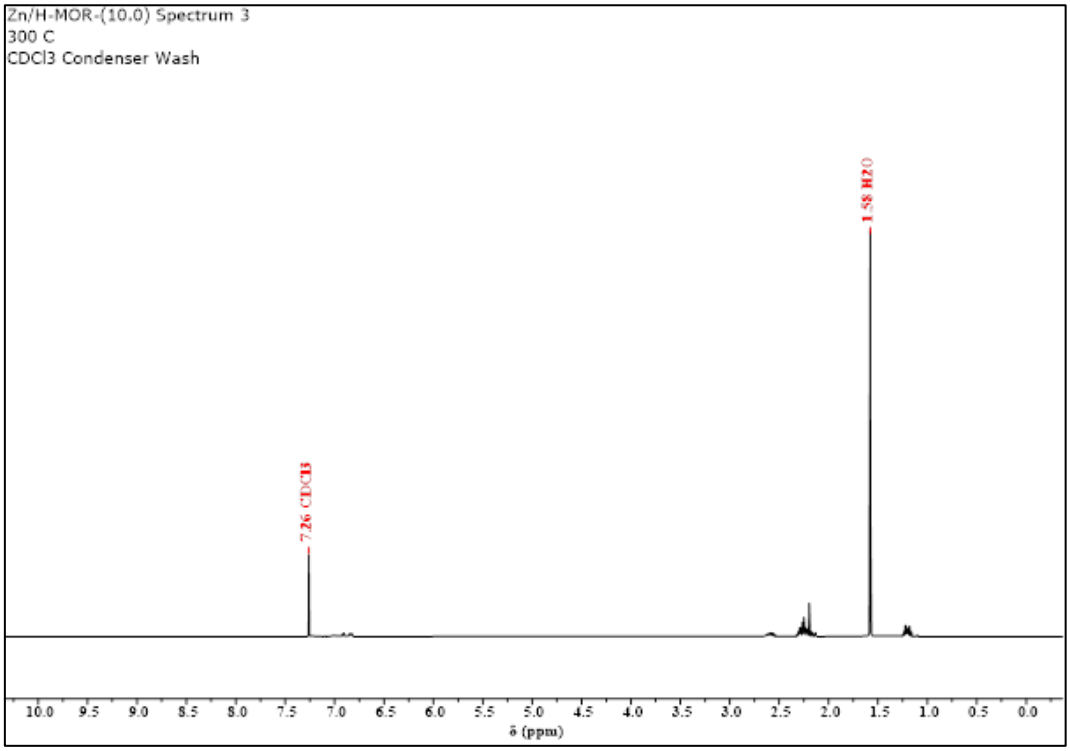

Figure A1.46: ^{1}H NMR spectrum of condenser wash from ethanol conversion over Zn/H–MOR–(10.0) at 300 °C averaged over 8 scans with a 1 s recycle delay. Spectrum was acquired on a Bruker Avance III-HD-400 spectrometer. Spectrometer frequency: ^{1}H = 399.95 MHz. NMR Solvent = $CDCl_3$.

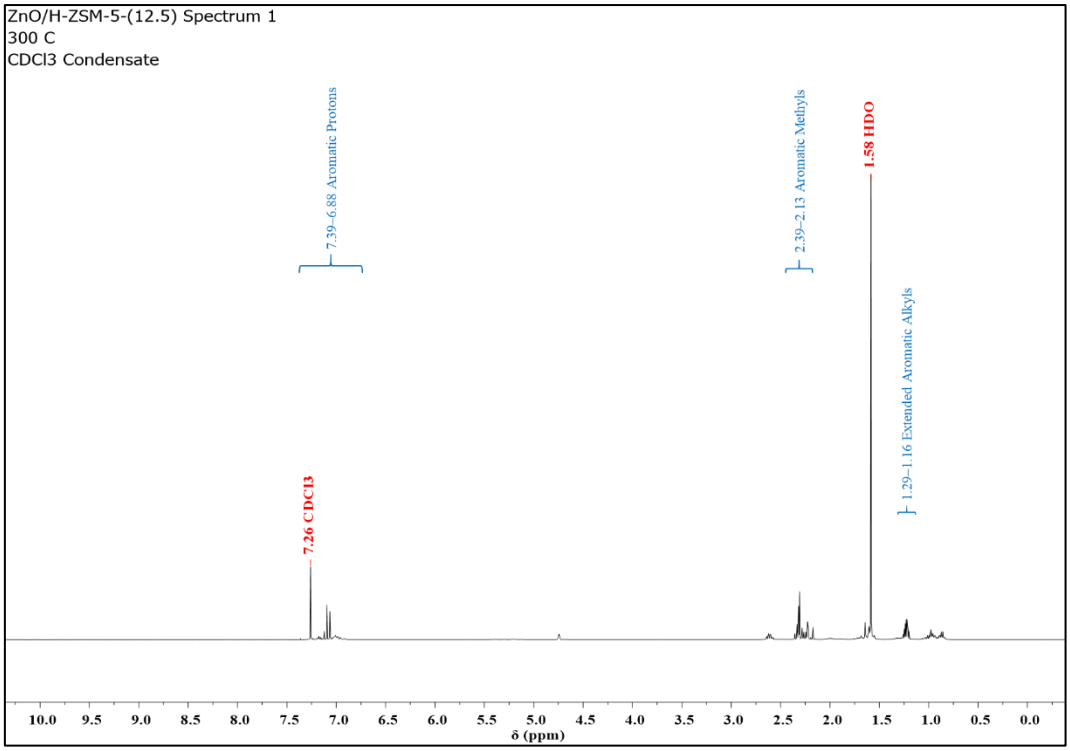

Figure A1.47: ^{1}H NMR spectrum of condensate from ethanol conversion over ZnO/H–ZSM–5–(12.5) at 300 °C averaged over 8 scans with a 1 s recycle delay. Spectrum was acquired on a Bruker Avance III-HD-400 spectrometer. Spectrometer frequency: ^{1}H = 399.95 MHz. NMR Solvent = $CDCl_3$.

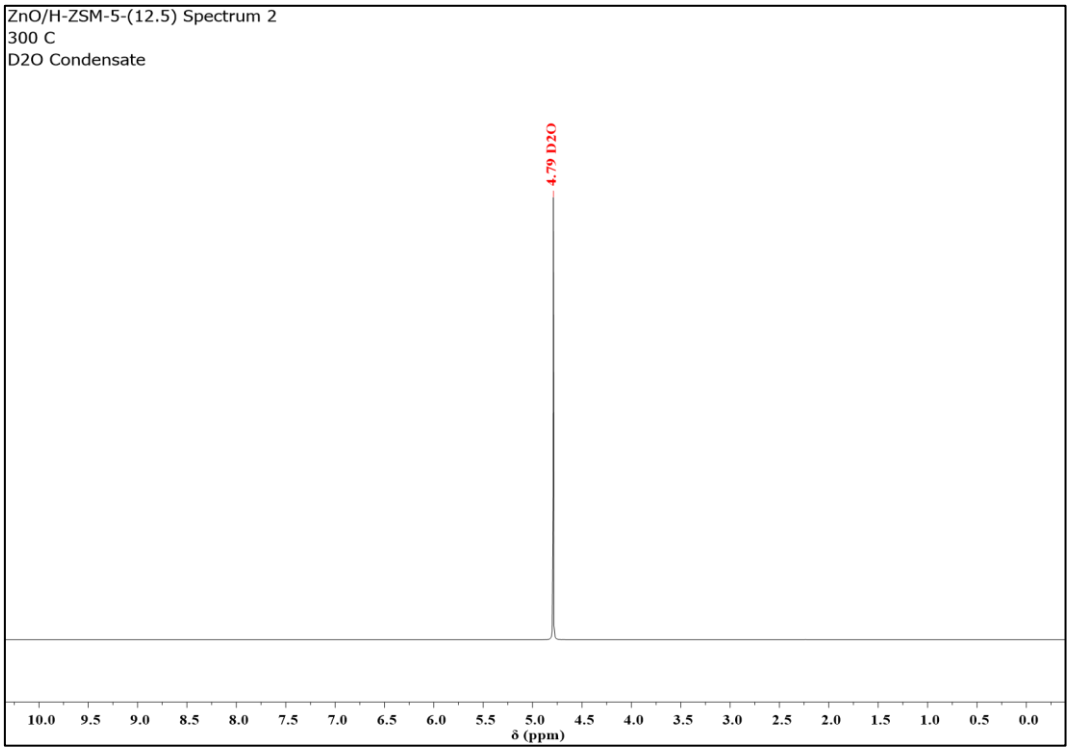

Figure A1.48: ^{1}H NMR spectrum of condensate from ethanol conversion over ZnO/H–ZSM–5–(12.5) at 300 °C averaged over 8 scans with a 1 s recycle delay. Spectrum was acquired on a Bruker Avance III-HD-400 spectrometer. Spectrometer frequency: ^{1}H = 399.95 MHz. NMR Solvent = D_2O.

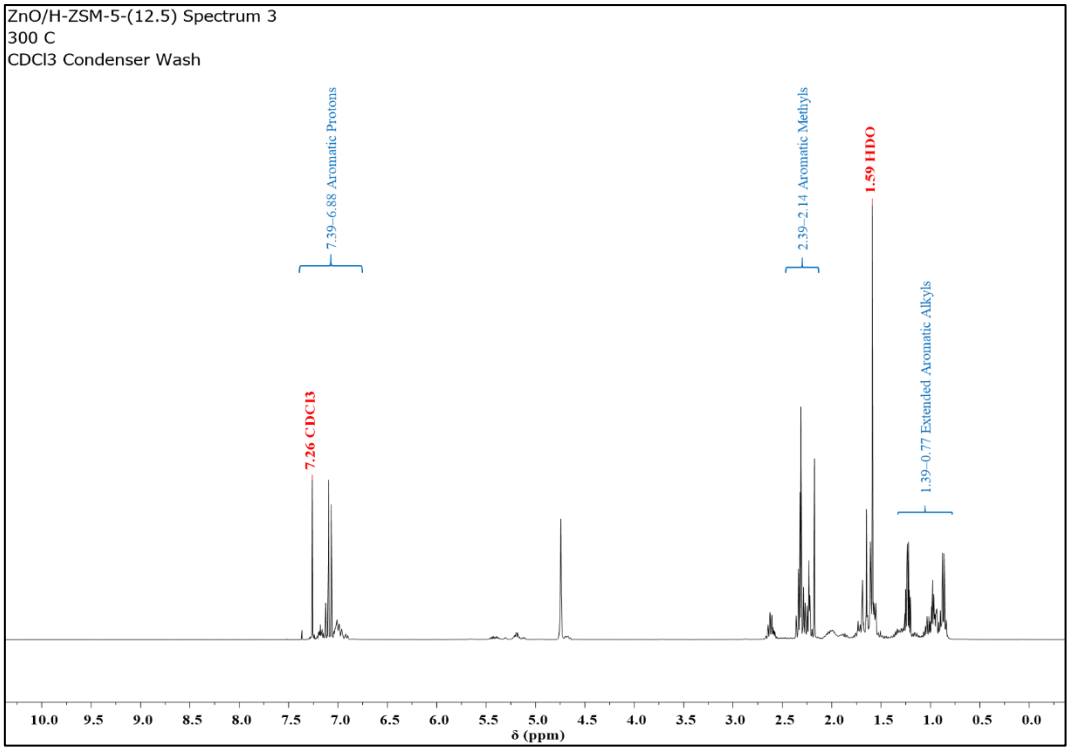

Figure A1.49: ^{1}H NMR spectrum of condenser washings from ethanol conversion over ZnO/H–ZSM–5–(12.5) at 300 °C averaged over 8 scans with a 1 s recycle delay. Spectrum was acquired on a Bruker Avance III-HD-400 spectrometer. Spectrometer frequency: ^{1}H = 399.95 MHz. NMR Solvent = $CDCl_3$.

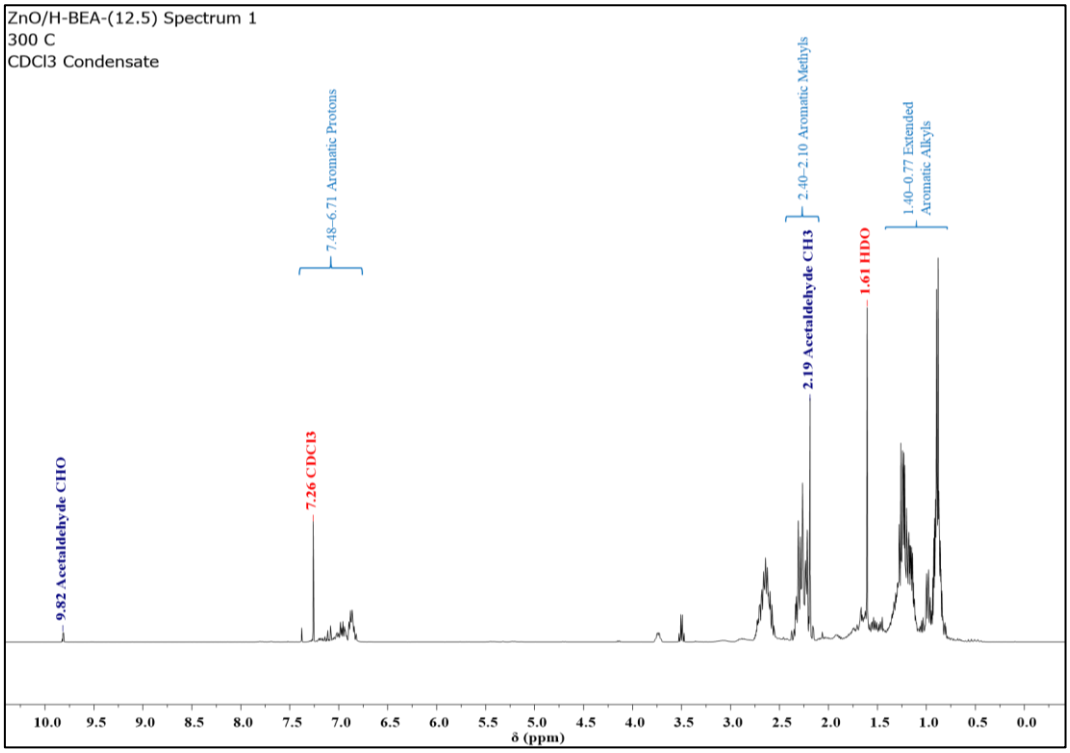

Figure A1.50: ^{1}H NMR spectrum of condensate from ethanol conversion over ZnO/H–BEA–(12.5) at 300 °C averaged over 8 scans with a 1 s recycle delay. Spectrum was acquired on a Bruker Avance III-HD-400 spectrometer. Spectrometer frequency: ^{1}H = 399.95 MHz. NMR Solvent = $CDCl_3$.

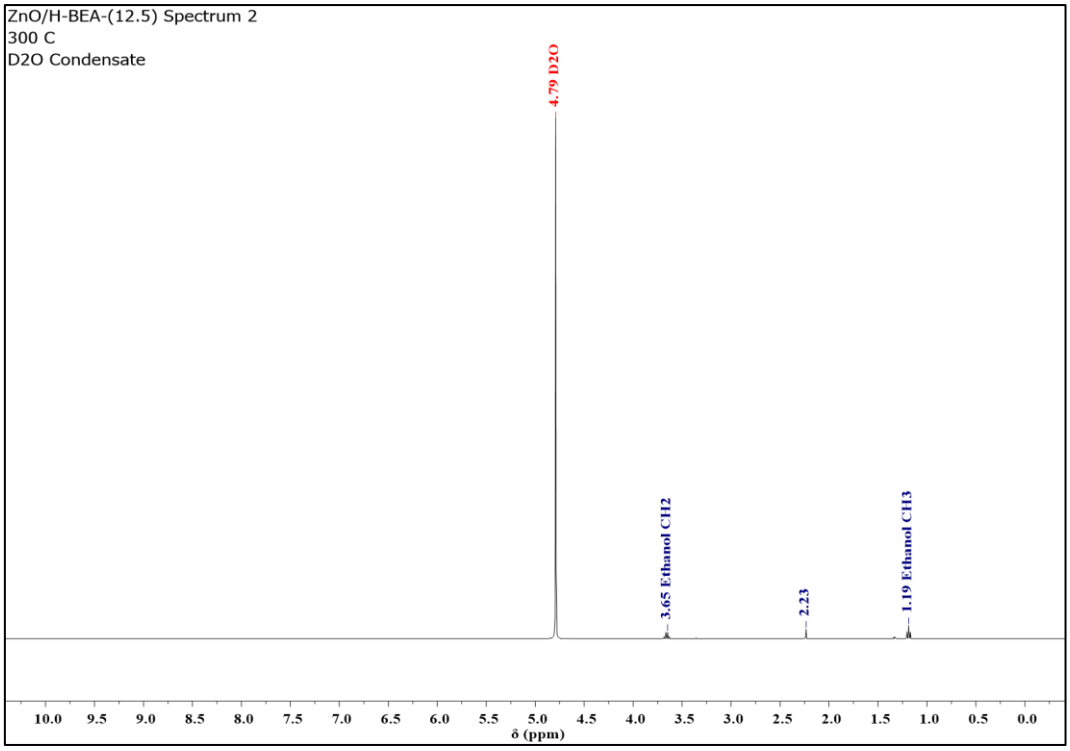

Figure A1.51: ^{1}H NMR spectrum of condensate from ethanol conversion over ZnO/H–BEA–(12.5) at 300 °C averaged over 8 scans with a 1 s recycle delay. Spectrum was acquired on a Bruker Avance III-HD-400 spectrometer. Spectrometer frequency: ^{1}H = 399.95 MHz. NMR Solvent = D_2O.

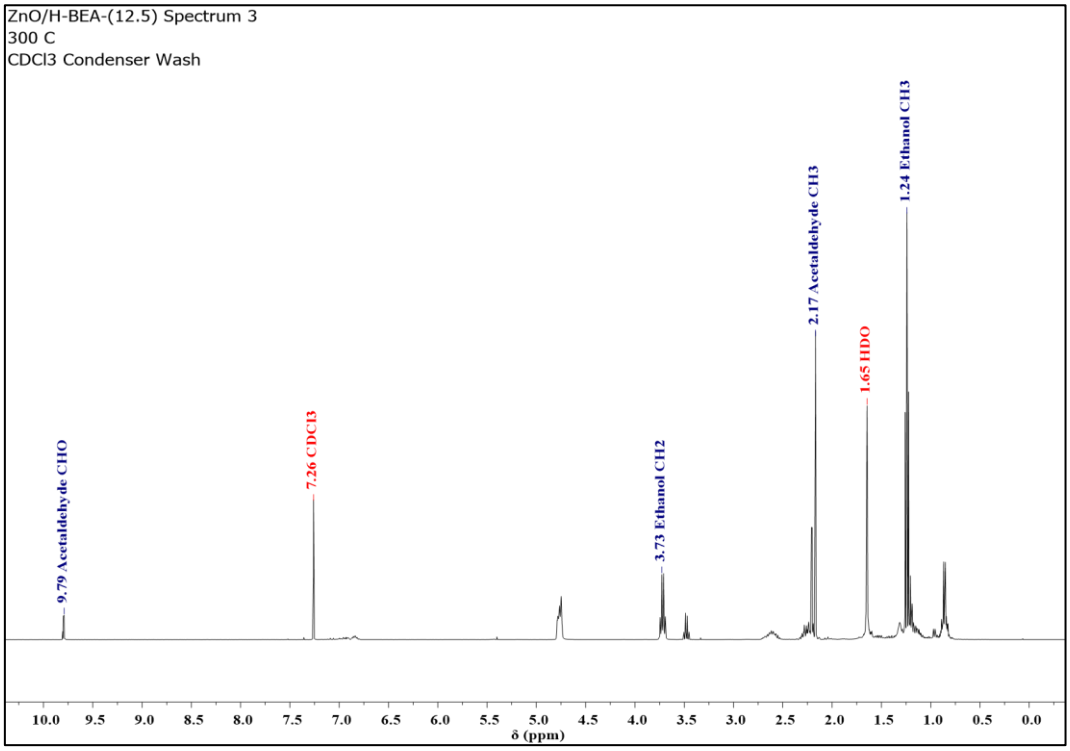

Figure A1.52: ^{1}H NMR spectrum of condenser washings from ethanol conversion over ZnO/H–BEA–(12.5) at 300 °C averaged over 8 scans with a 1 s recycle delay. Spectrum was acquired on a Bruker Avance III-HD-400 spectrometer. Spectrometer frequency: ^{1}H = 399.95 MHz. NMR Solvent = $CDCl_3$.

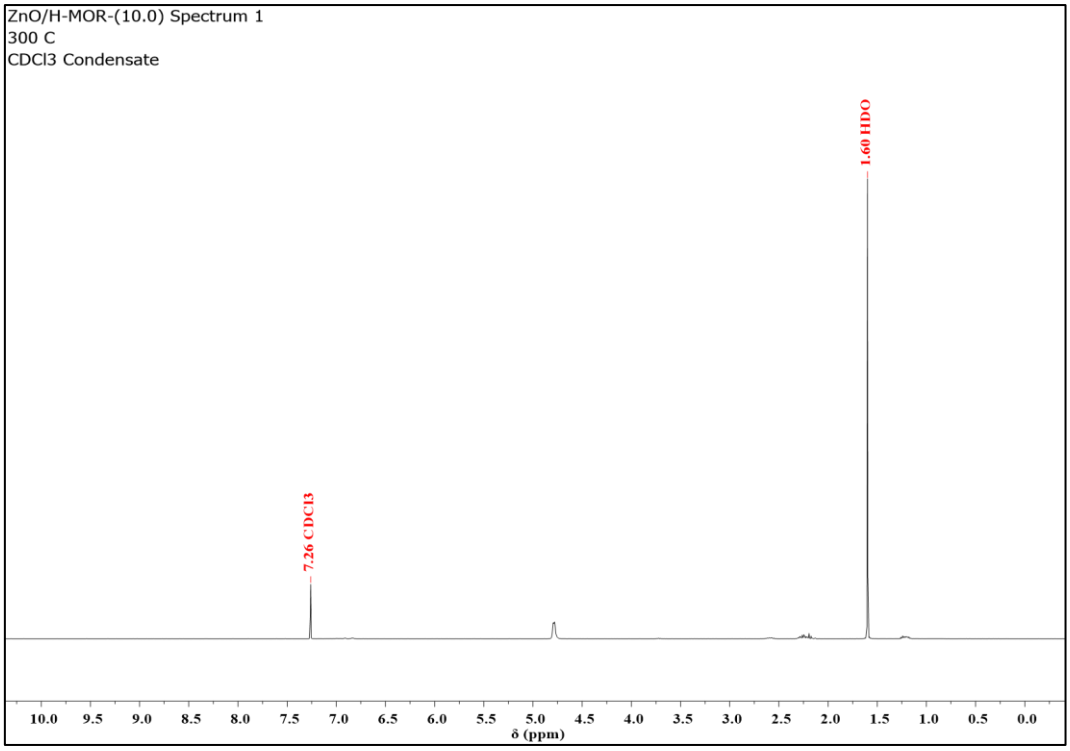

Figure A1.53: ^{1}H NMR spectrum of condensate from ethanol conversion over ZnO/H–MOR–(10.0) at 300 °C averaged over 8 scans with a 1 s recycle delay. Spectrum was acquired on a Bruker Neo-400 spectrometer. Spectrometer frequency: ^{1}H = 400.13 MHz. NMR Solvent = $CDCl_3$.

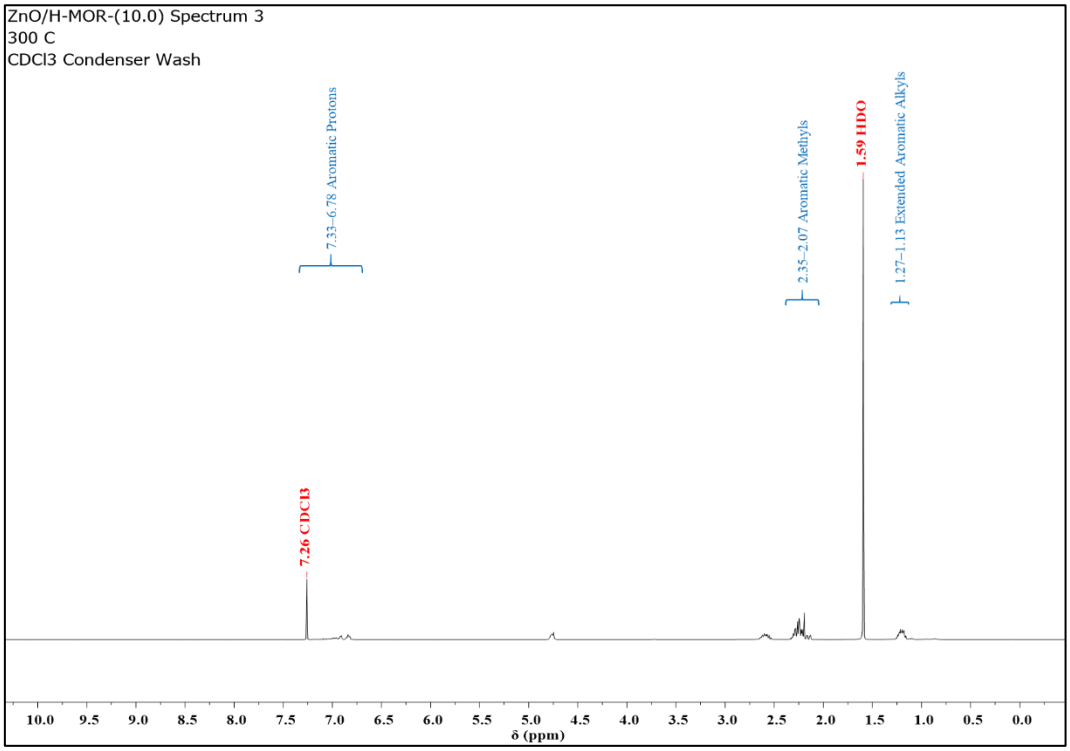

Figure A1.54: ^{1}H NMR spectrum of condenser washings from ethanol conversion over ZnO/H–MOR–(10.0) at 300 °C averaged over 8 scans with a 1 s recycle delay. Spectrum was acquired on a Bruker Neo-400 spectrometer. Spectrometer frequency: ^{1}H = 400.13 MHz. NMR Solvent = $CDCl_3$.

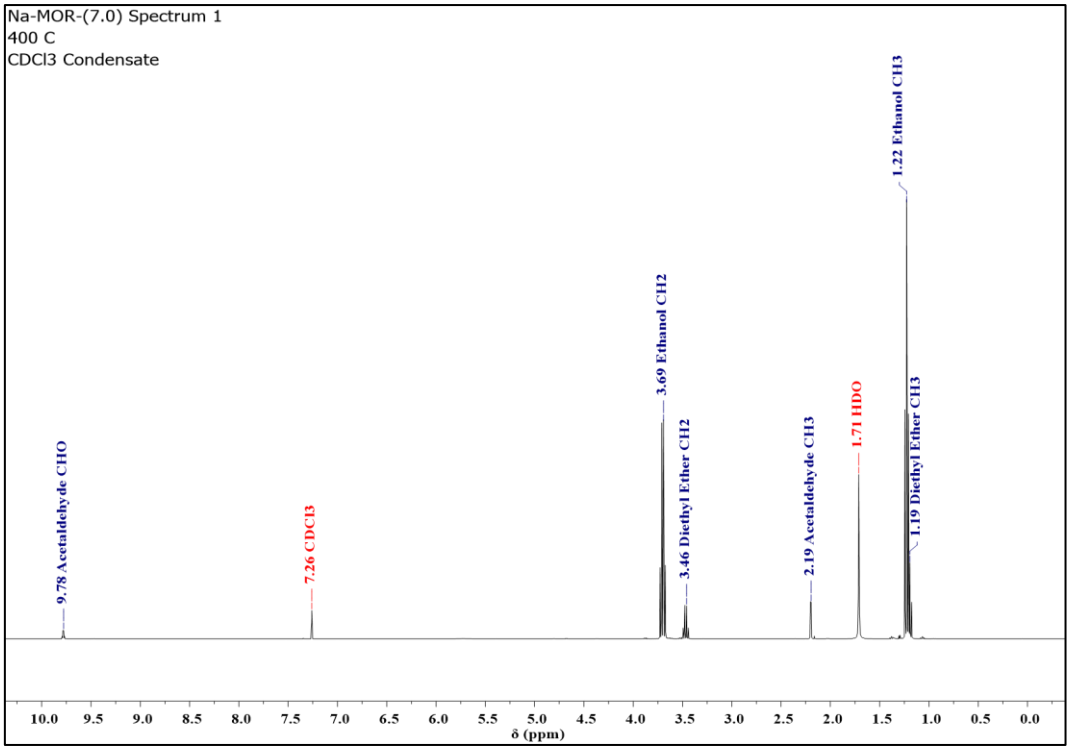

Figure A1.55: ^{1}H NMR spectrum of condensate from ethanol conversion over Na–MOR–(7.0) at 400 °C averaged over 8 scans with a 1 s recycle delay. Spectrum was acquired on a Bruker Avance III-HD-400 spectrometer. Spectrometer frequency: ^{1}H = 399.95 MHz. NMR Solvent = $CDCl_3$.

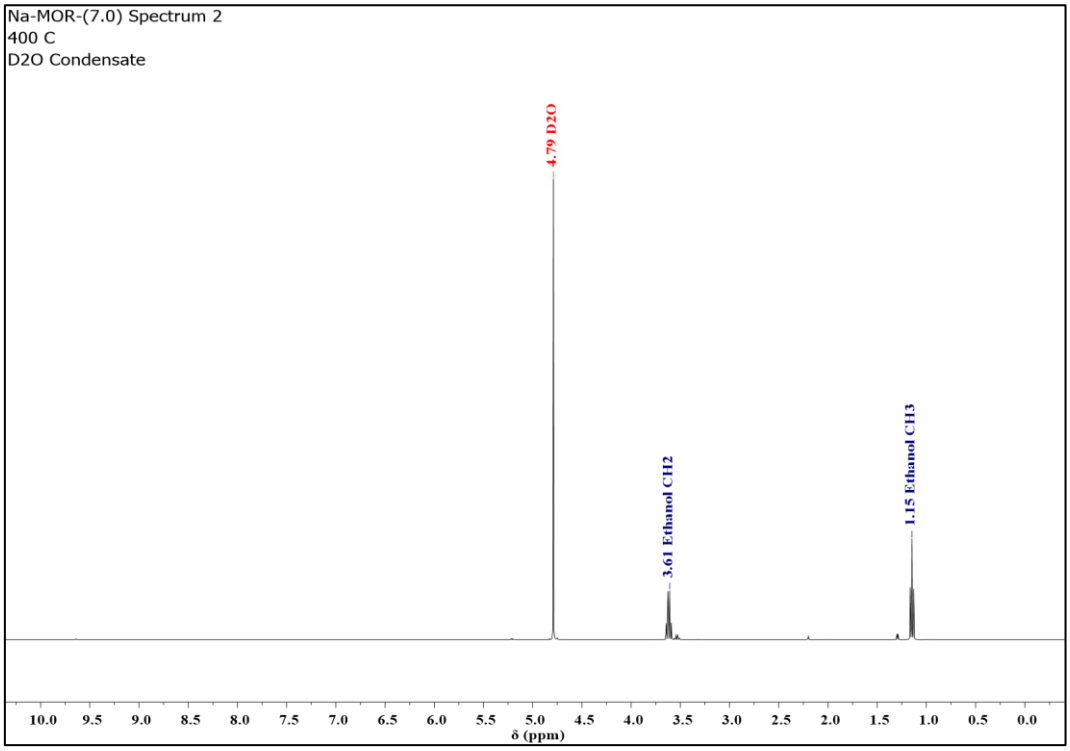

Figure A1.56: ^{1}H NMR spectrum of condensate from ethanol conversion over Na–MOR–(7.0) at 400 °C averaged over 8 scans with a 1 s recycle delay. Spectrum was acquired on a Bruker Avance III-HD-400 spectrometer. Spectrometer frequency: ^{1}H = 399.95 MHz. NMR Solvent = D_2O.

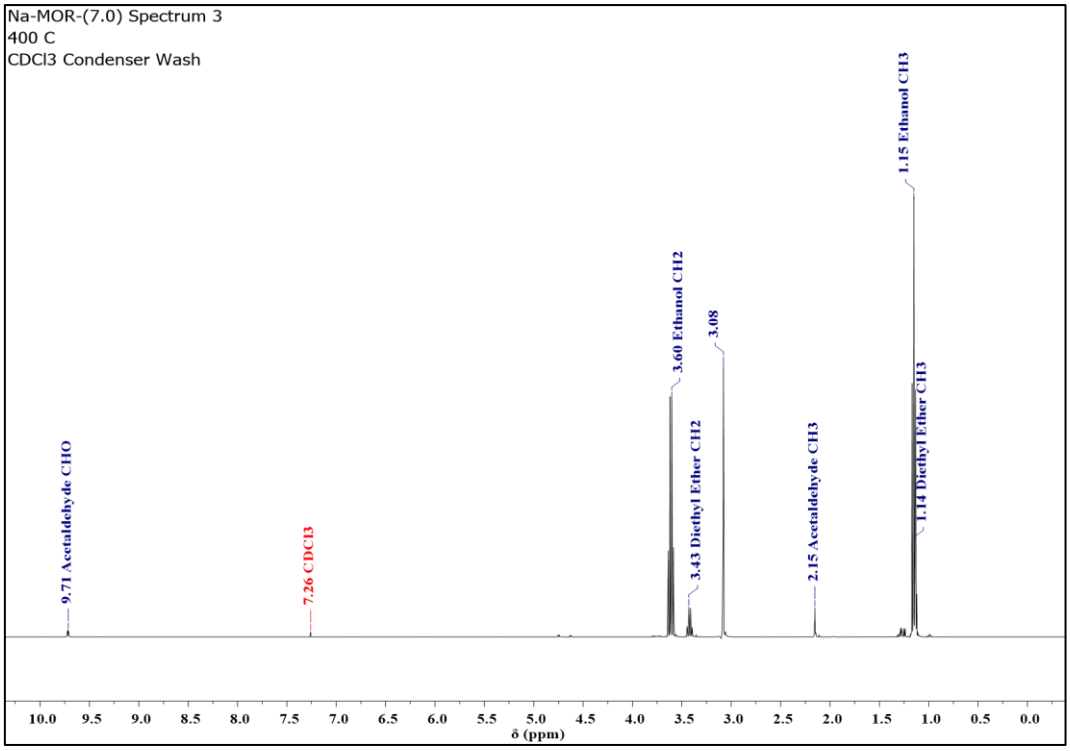

Figure A1.57: ^{1}H NMR spectrum of condenser washings from ethanol conversion over Na–MOR–(7.0) at 400 °C averaged over 8 scans with a 1 s recycle delay. Spectrum was acquired on a Bruker Avance III-HD-400 spectrometer. Spectrometer frequency: ^{1}H = 399.95 MHz. NMR Solvent = $CDCl_3$.

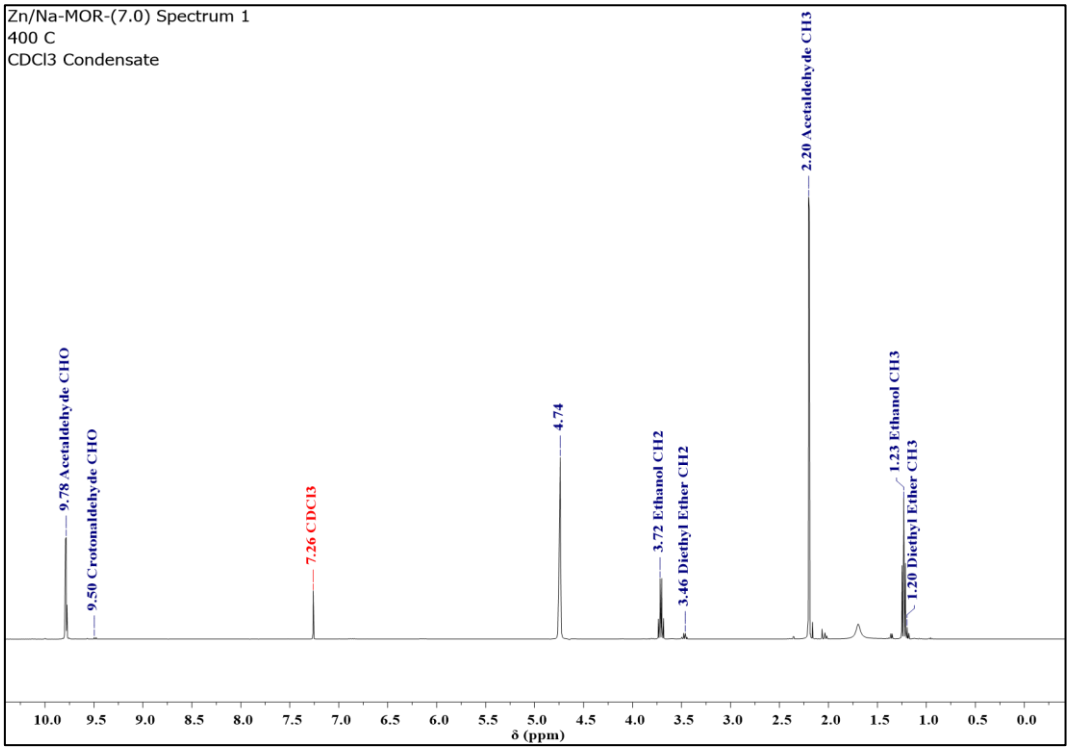

Figure A1.58: ^{1}H NMR spectrum of condensate from ethanol conversion over Zn/Na–MOR–(7.0) at 400 °C averaged over 8 scans with a 1 s recycle delay. Spectrum was acquired on a Bruker Avance III-HD-400 spectrometer. Spectrometer frequency: ^{1}H = 399.95 MHz. NMR Solvent = $CDCl_3$.

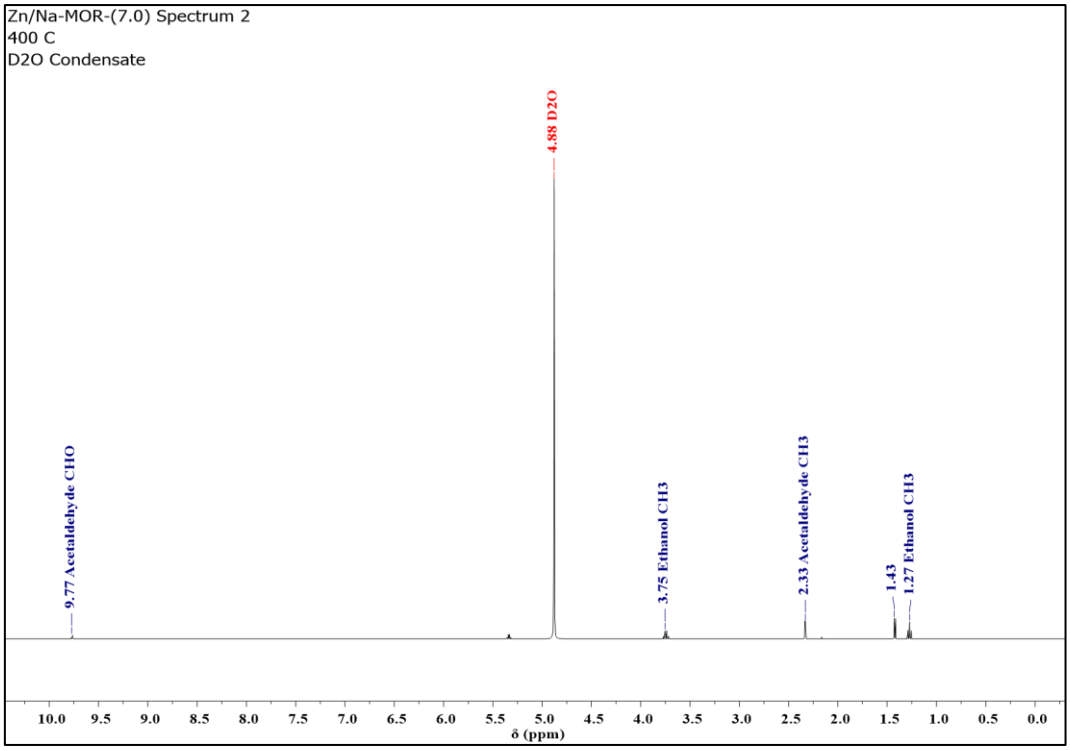

Figure A1.59: ^{1}H NMR spectrum of condensate from ethanol conversion over Zn/Na–MOR–(7.0) at 400 °C averaged over 8 scans with a 1 s recycle delay. Spectrum was acquired on a Bruker Avance III-HD-400 spectrometer. Spectrometer frequency: ^{1}H = 399.95 MHz. NMR Solvent = D_2O.

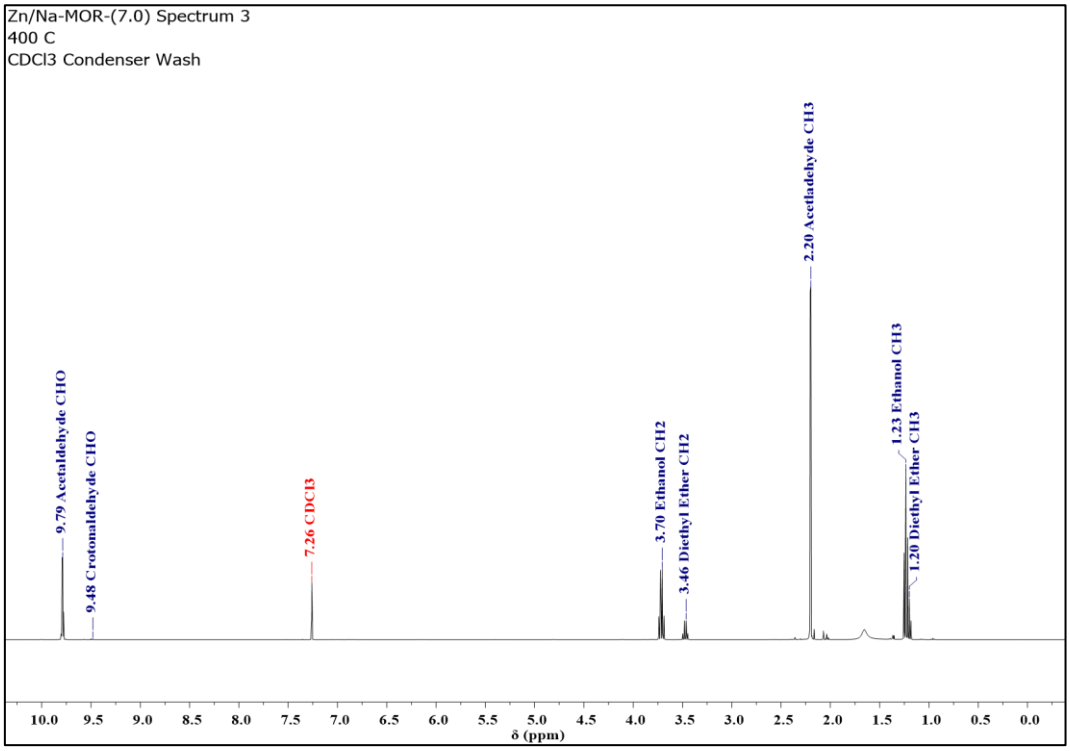

Figure A1.60: ^{1}H NMR spectrum of condenser washings from ethanol conversion over Zn/Na–MOR–(7.0) at 400 °C averaged over 8 scans with a 1 s recycle delay. Spectrum was acquired on a Bruker Avance III-HD-400 spectrometer. Spectrometer frequency: ^{1}H = 399.95 MHz. NMR Solvent = $CDCl_3$.

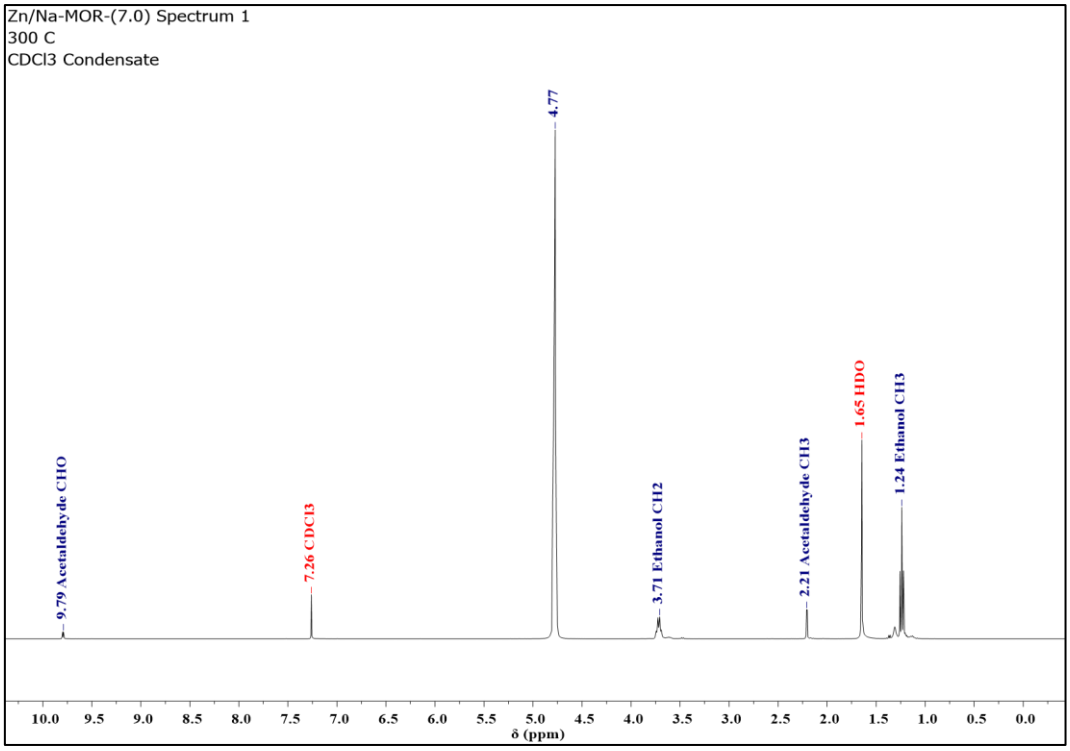

Figure A1.61: ^{1}H NMR spectrum of condensate from ethanol conversion over Zn/Na–MOR–(7.0) at 300 °C averaged over 8 scans with a 1 s recycle delay. Spectrum was acquired on a Bruker Neo-400 spectrometer. Spectrometer frequency: ^{1}H = 400.13 MHz. NMR Solvent = $CDCl_3$.

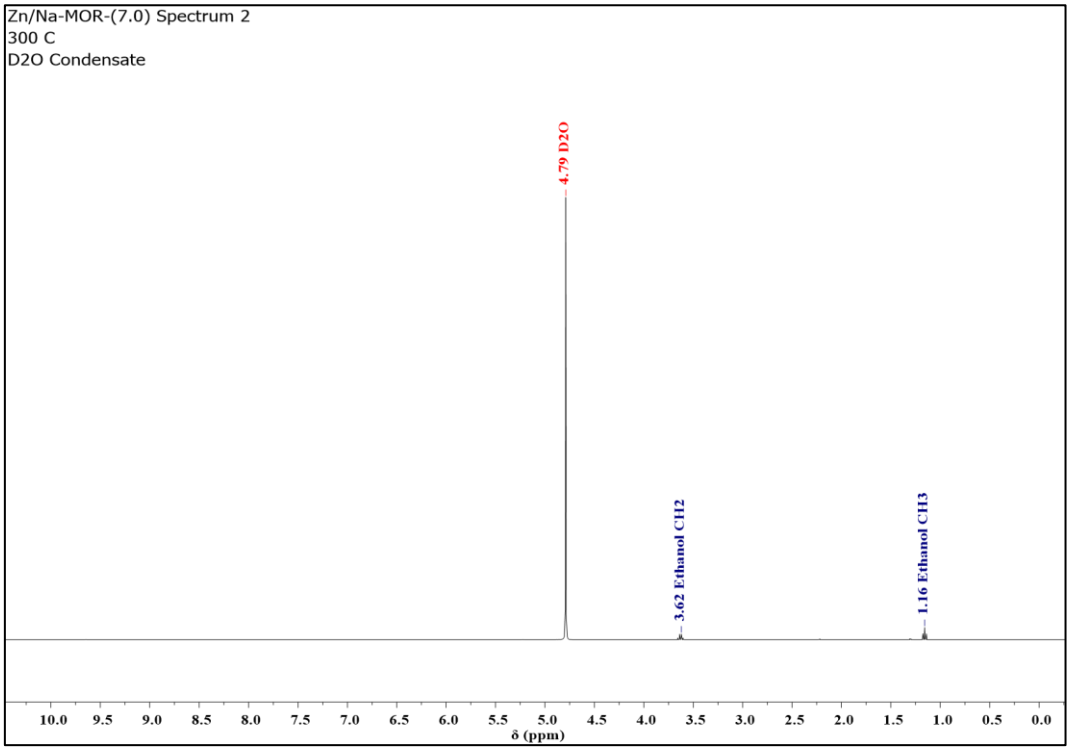

Figure A1.62: ^{1}H NMR spectrum of condensate from ethanol conversion over Zn/Na–MOR–(7.0) at 300 °C averaged over 8 scans with a 1 s recycle delay. Spectrum was acquired on a Bruker Neo-400 spectrometer. Spectrometer frequency: ^{1}H = 400.13 MHz. NMR Solvent = D_2O.

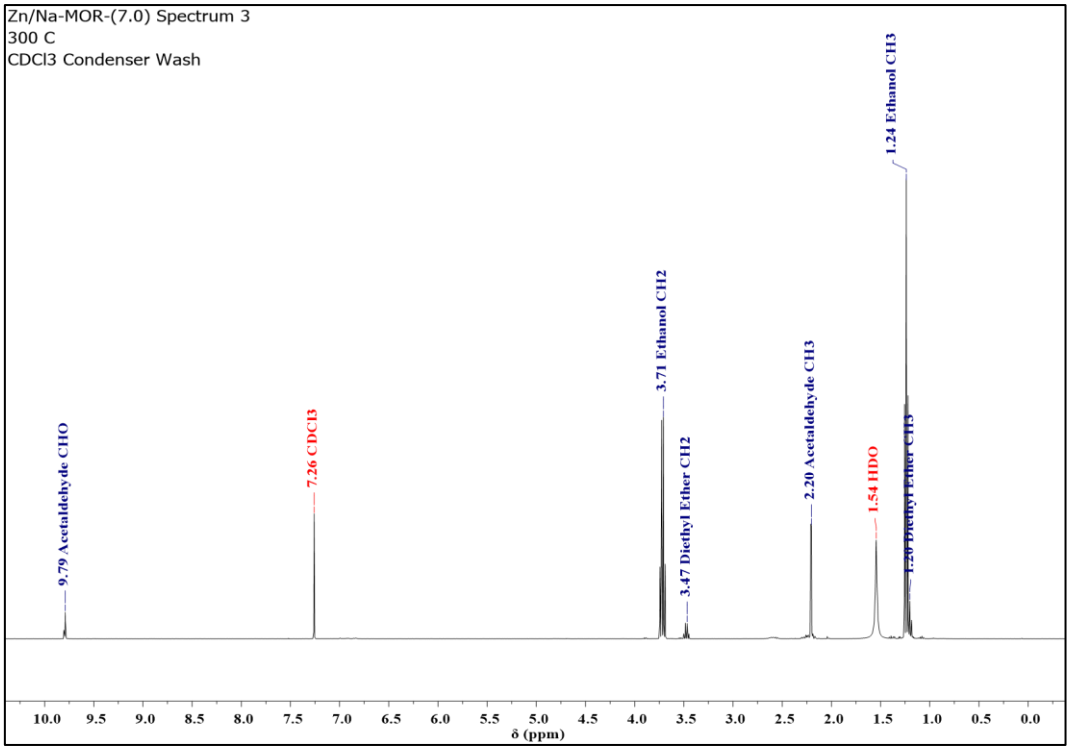

Figure A1.63: ^{1}H NMR spectrum of condenser washings from ethanol conversion over Zn/Na–MOR–(7.0) at 300 °C averaged over 8 scans with a 1 s recycle delay. Spectrum was acquired on a Bruker Neo-400 spectrometer. Spectrometer frequency: ^{1}H = 400.13 MHz. NMR Solvent = $CDCl_3$.

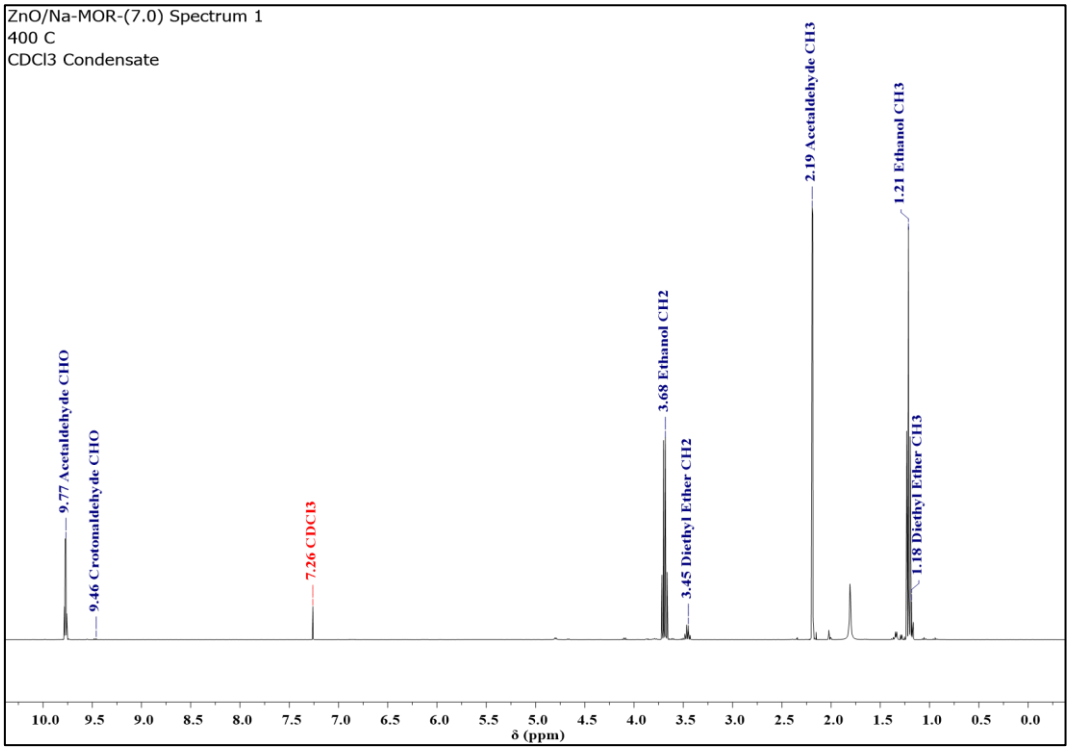

Figure A1.64: ^{1}H NMR spectrum of condensate from ethanol conversion over ZnO/Na–MOR–(7.0) at 400 °C averaged over 8 scans with a 1 s recycle delay. Spectrum was acquired on a Bruker Neo-400 spectrometer. Spectrometer frequency: ^{1}H = 400.13 MHz. NMR Solvent = $CDCl_3$.

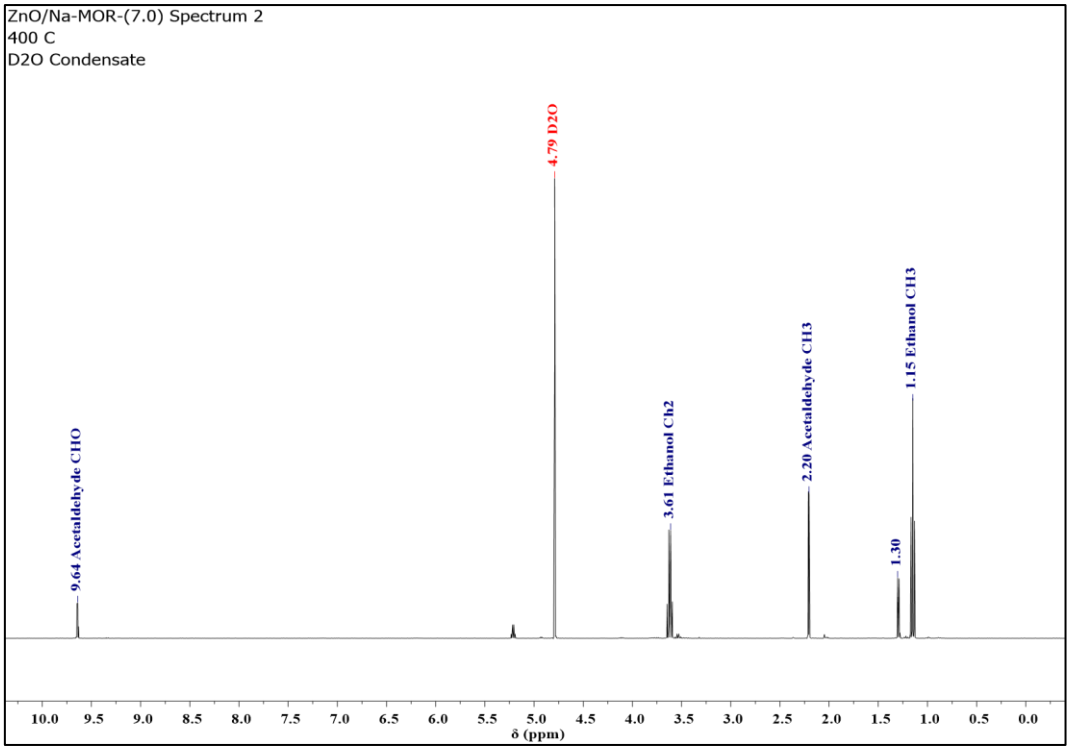

Figure A1.65: ^{1}H NMR spectrum of condensate from ethanol conversion over ZnO/Na–MOR–(7.0) at 400 °C averaged over 8 scans with a 1 s recycle delay. Spectrum was acquired on a Bruker Neo-400 spectrometer. Spectrometer frequency: ^{1}H = 400.13 MHz. NMR Solvent = D_2O.

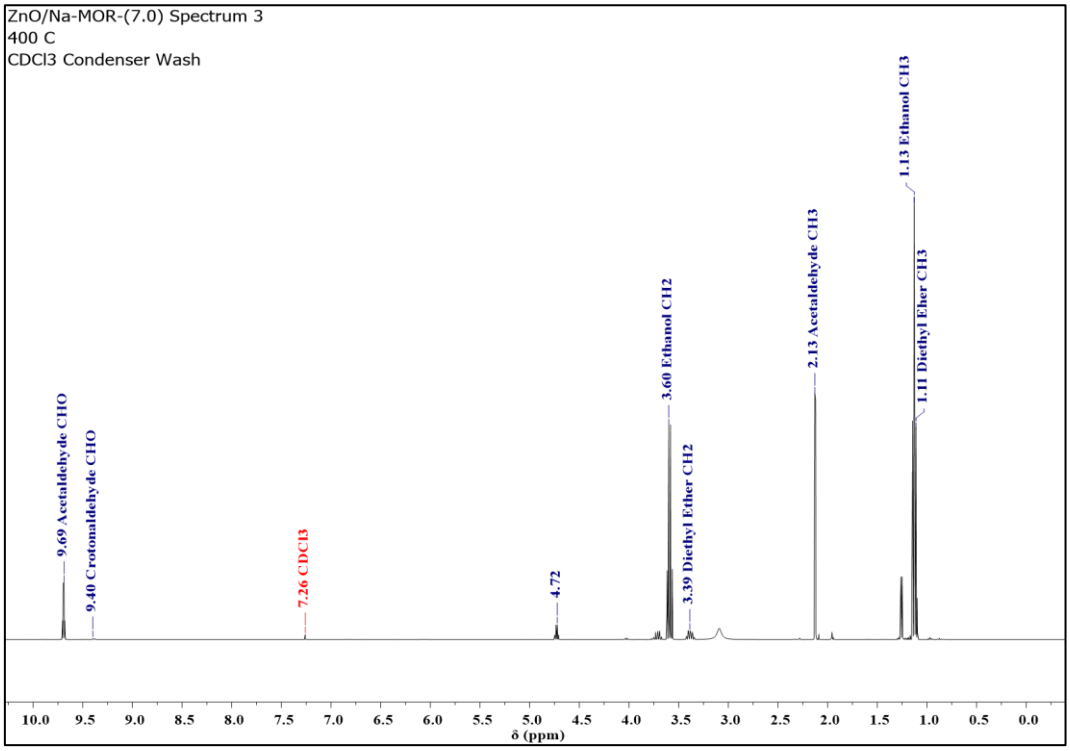

Figure A1.66: ^{1}H NMR spectrum of condenser washings from ethanol conversion over ZnO/Na–MOR–(7.0) at 400 °C averaged over 8 scans with a 1 s recycle delay. Spectrum was acquired on a Bruker Neo-400 spectrometer. Spectrometer frequency: ^{1}H = 400.13 MHz. NMR Solvent = $CDCl_3$.

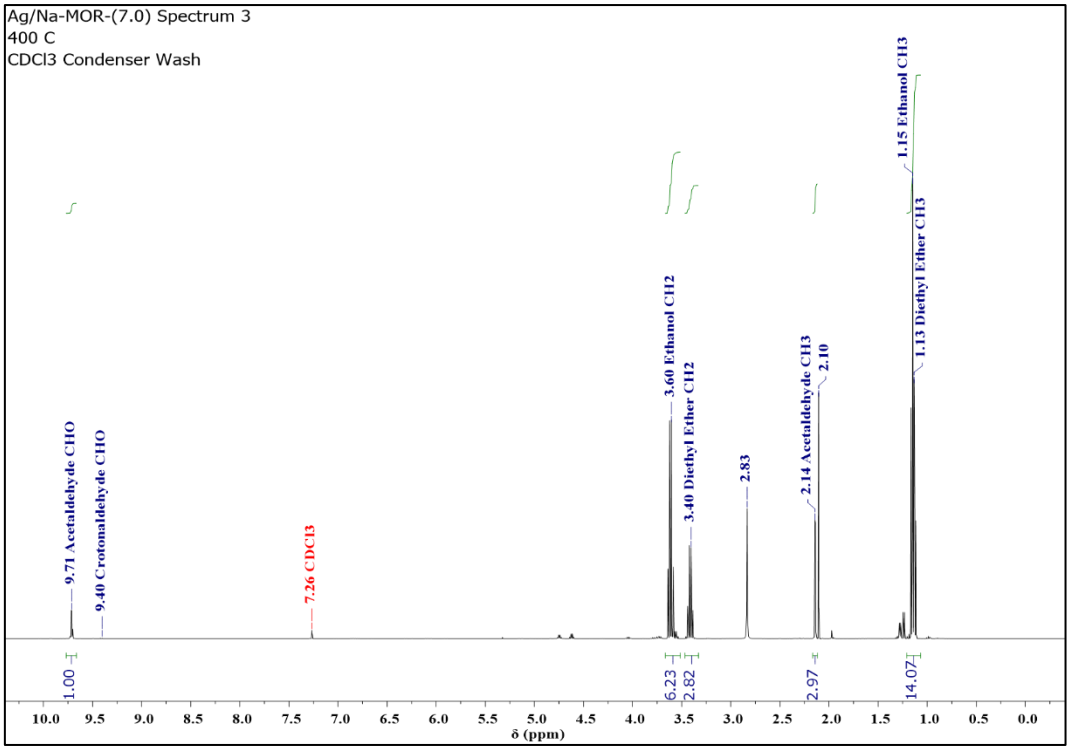

Figure A1.67: ^{1}H NMR spectrum of condensate from ethanol conversion over Ag/Na–MOR–(7.0) at 400 °C averaged over 8 scans with a 1 s recycle delay. Spectrum was acquired on a Bruker Neo-400 spectrometer. Spectrometer frequency: ^{1}H = 400.13 MHz. NMR Solvent = $CDCl_3$.

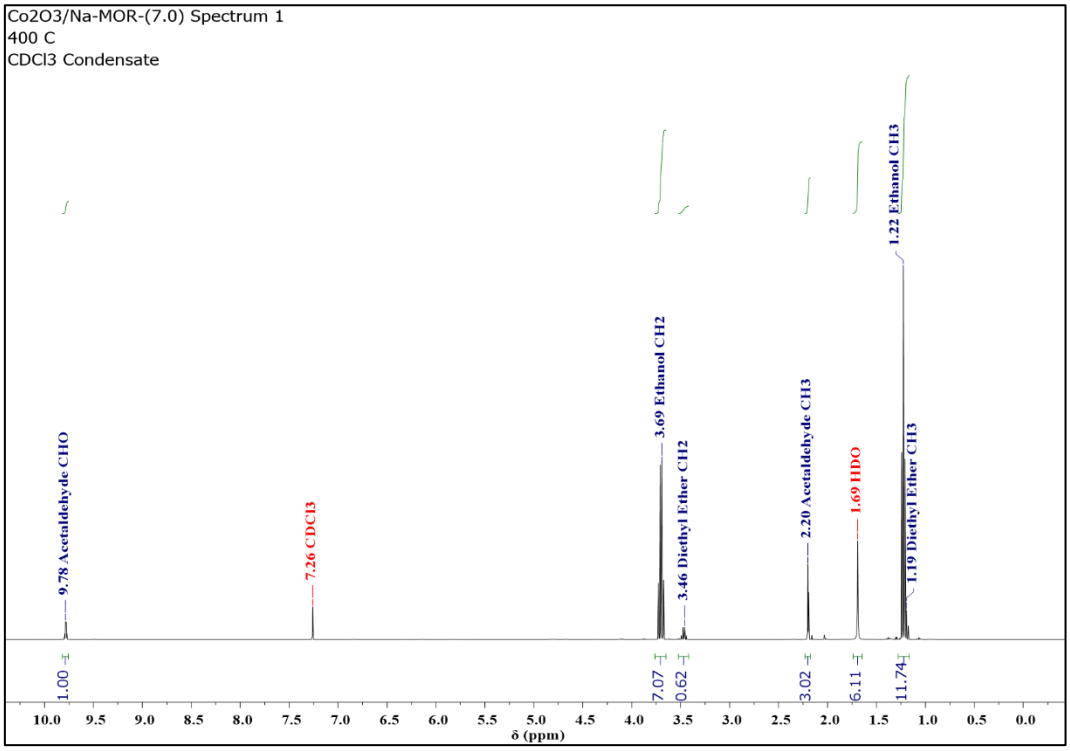

Figure A1.68: ^{1}H NMR spectrum of condensate from ethanol conversion over Co_2O_3/Na–MOR–(7.0) at 400 °C averaged over 8 scans with a 1 s recycle delay. Spectrum was acquired on a Bruker Neo-400 spectrometer. Spectrometer frequency: ^{1}H = 400.13 MHz. NMR Solvent = $CDCl_3$.

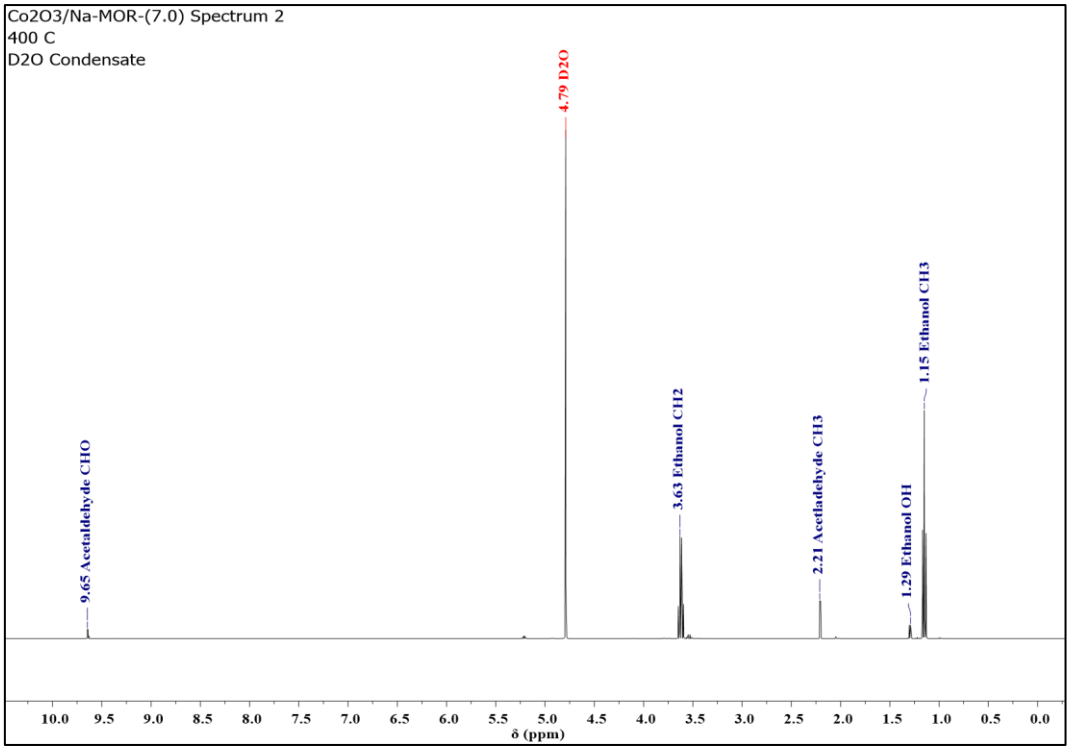

Figure A1.69: ^{1}H NMR spectrum of condensate from ethanol conversion over Cr_2O_3/Na–MOR–(7.0) at 400 °C averaged over 8 scans with a 1 s recycle delay. Spectrum was acquired on a Bruker Neo-400 spectrometer. Spectrometer frequency: ^{1}H = 400.13 MHz. NMR Solvent = D_2O.

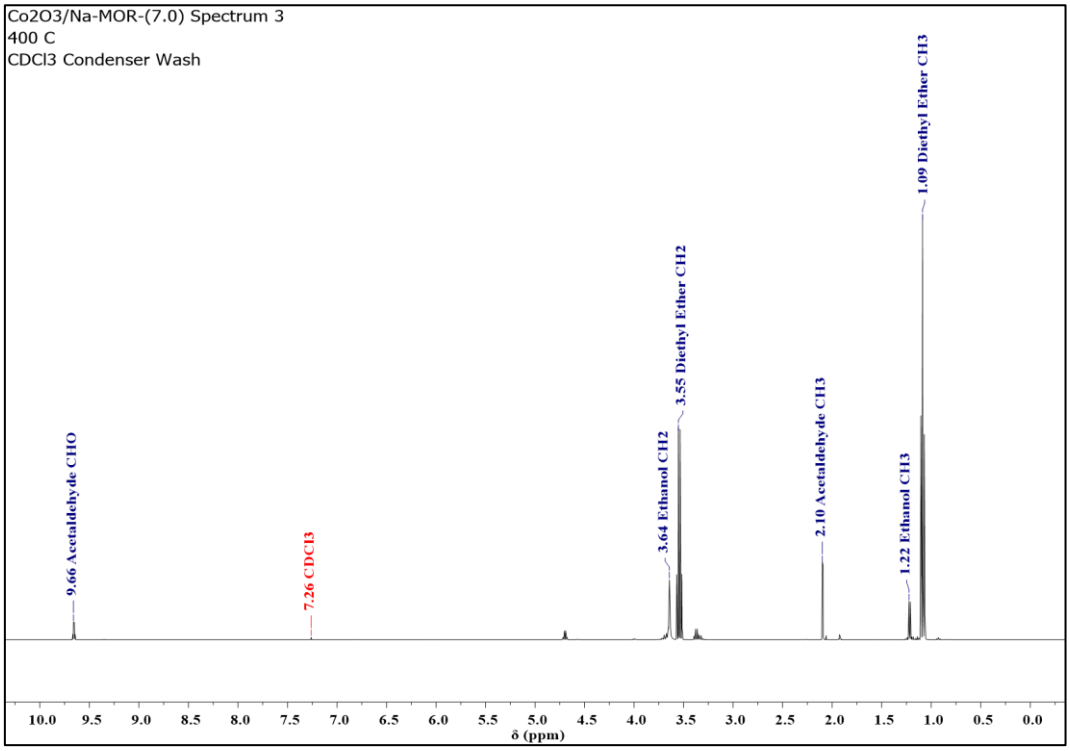

Figure A1.70: ^{1}H NMR spectrum of condenser washings from ethanol conversion over Cr_2O_3/Na–MOR–(7.0) at 400 °C averaged over 8 scans with a 1 s recycle delay. Spectrum was acquired on a Bruker Neo-400 spectrometer. Spectrometer frequency: ^{1}H = 400.13 MHz. NMR Solvent = $CDCl_3$.

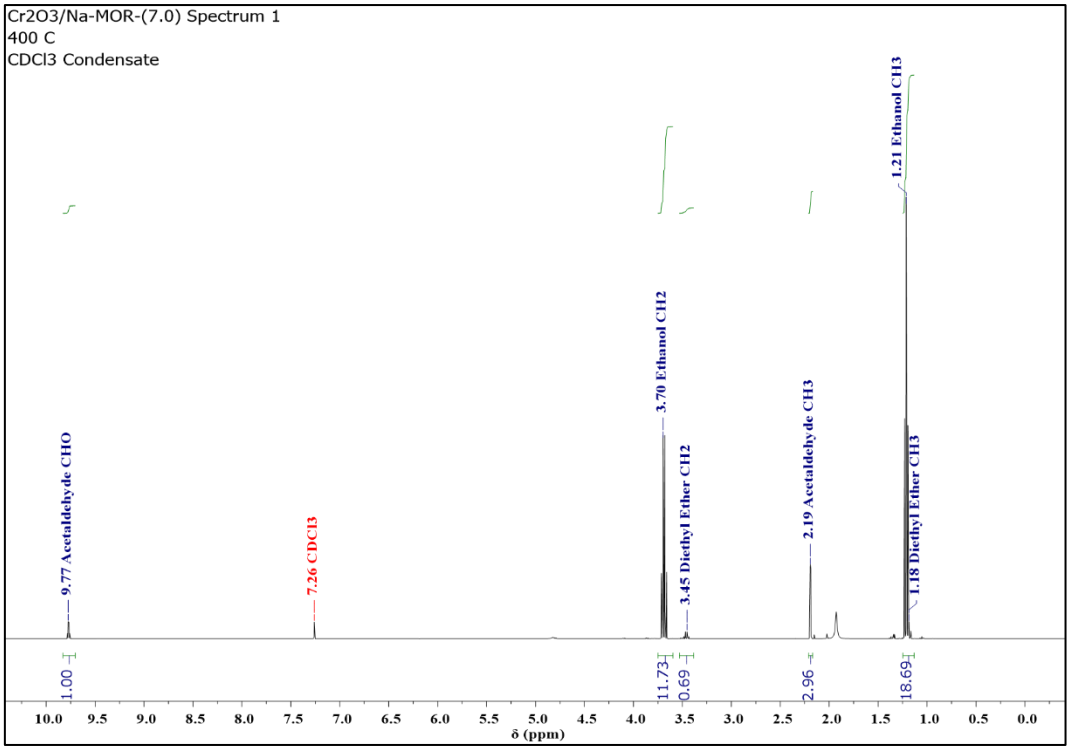

Figure A1.71: ^{1}H NMR spectrum of condensate from ethanol conversion over Cr_2O_3/Na–MOR–(7.0) at 400 °C averaged over 8 scans with a 1 s recycle delay. Spectrum was acquired on a Bruker Neo-400 spectrometer. Spectrometer frequency: ^{1}H = 400.13 MHz. NMR Solvent = $CDCl_3$.

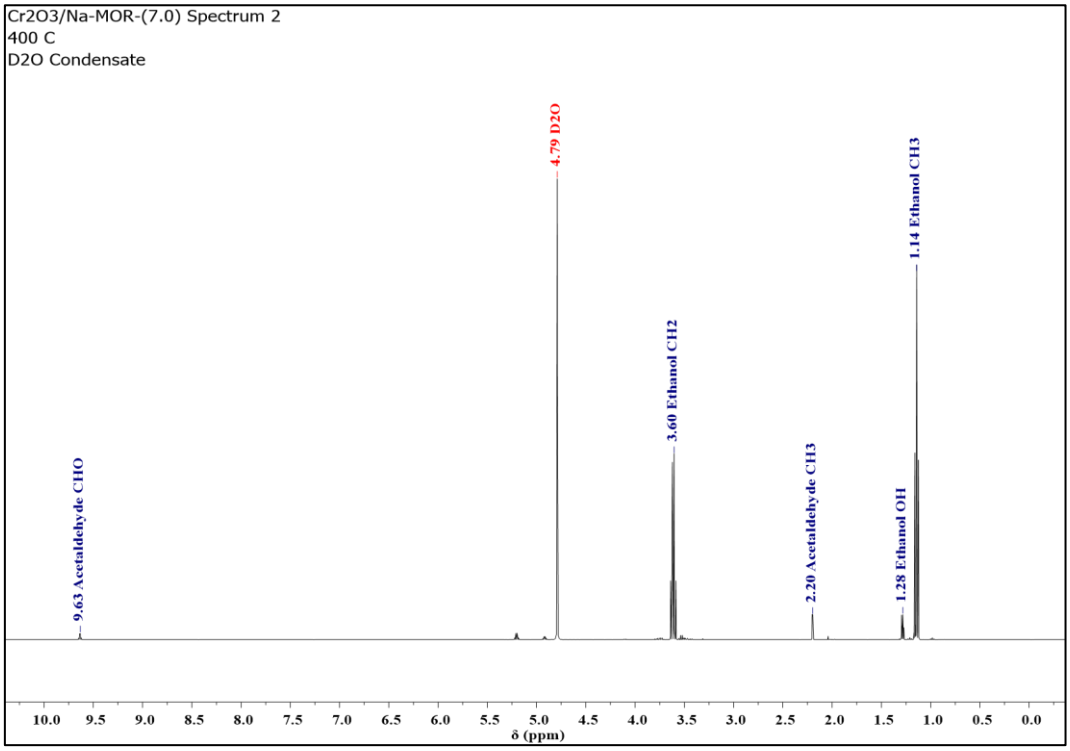

Figure A1.72: ^{1}H NMR spectrum of condensate from ethanol conversion over Cr_2O_3/Na–MOR–(7.0) at 400 °C averaged over 8 scans with a 1 s recycle delay. Spectrum was acquired on a Bruker Neo-400 spectrometer. Spectrometer frequency: ^{1}H = 400.13 MHz. NMR Solvent = D_2O.

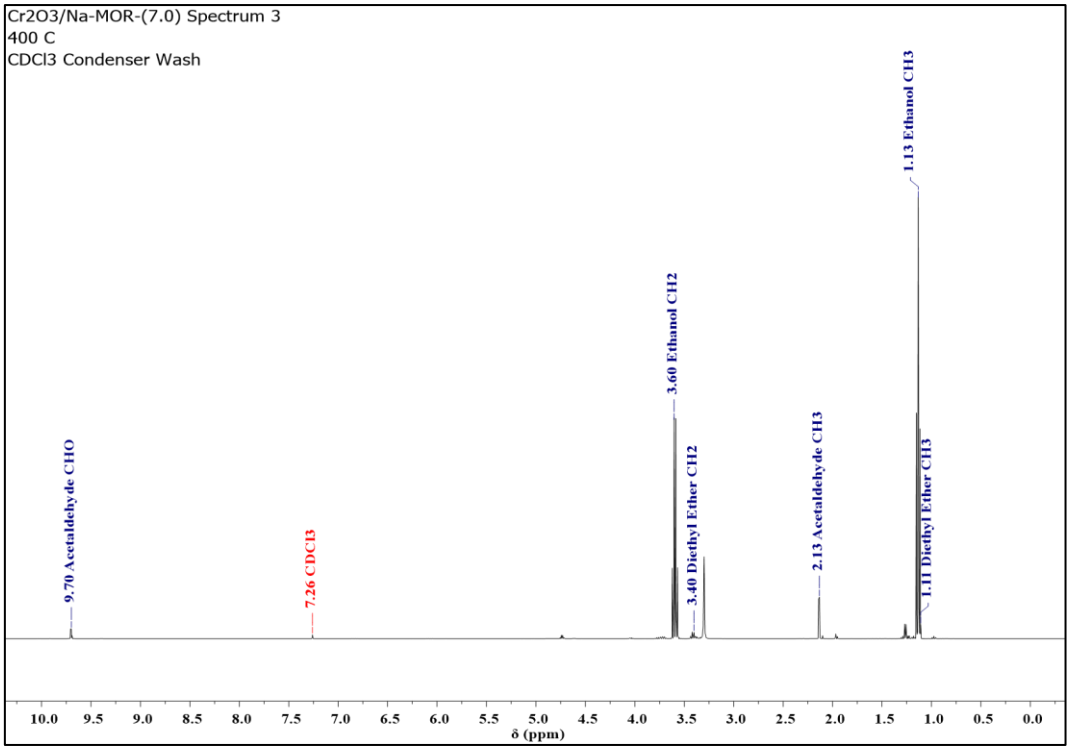

Figure A1.73: ^{1}H NMR spectrum of condenser washings from ethanol conversion over Cr_2O_3/Na–MOR–(7.0) at 400 °C averaged over 8 scans with a 1 s recycle delay. Spectrum was acquired on a Bruker Neo-400 spectrometer. Spectrometer frequency: ^{1}H = 400.13 MHz. NMR Solvent = $CDCl_3$.

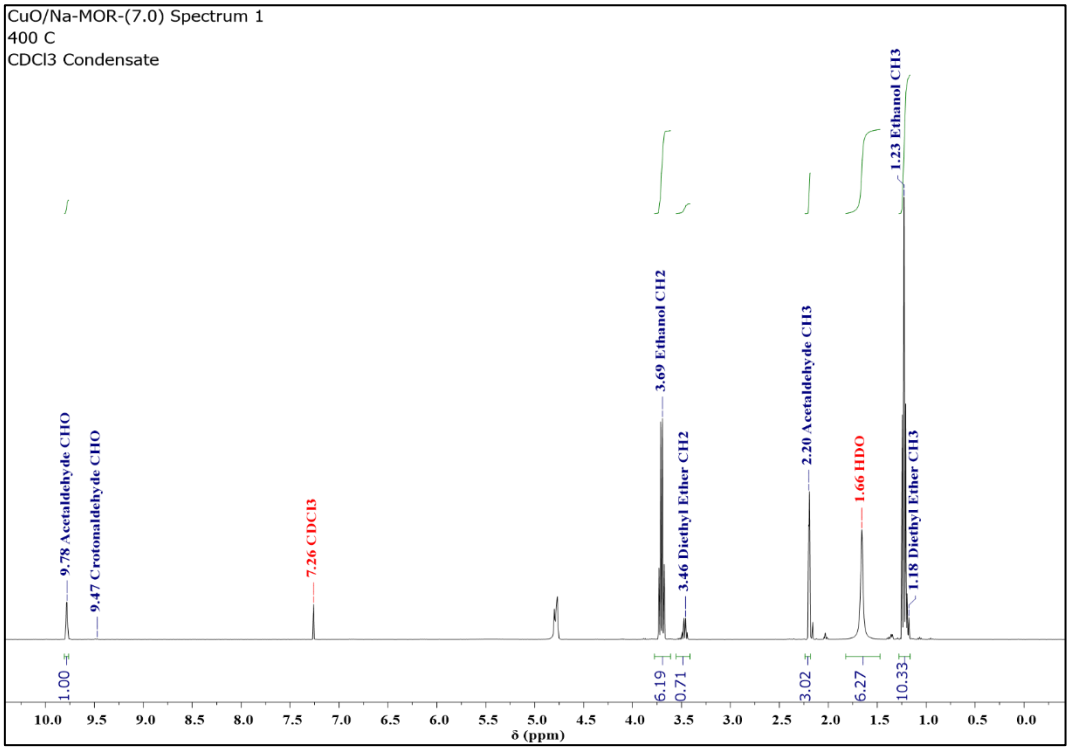

Figure A1.74: ^{1}H NMR spectrum of condensate from ethanol conversion over CuO/Na–MOR–(7.0) at 400 °C averaged over 8 scans with a 1 s recycle delay. Spectrum was acquired on a Bruker Neo-400 spectrometer. Spectrometer frequency: ^{1}H = 400.13 MHz. NMR Solvent = $CDCl_3$.

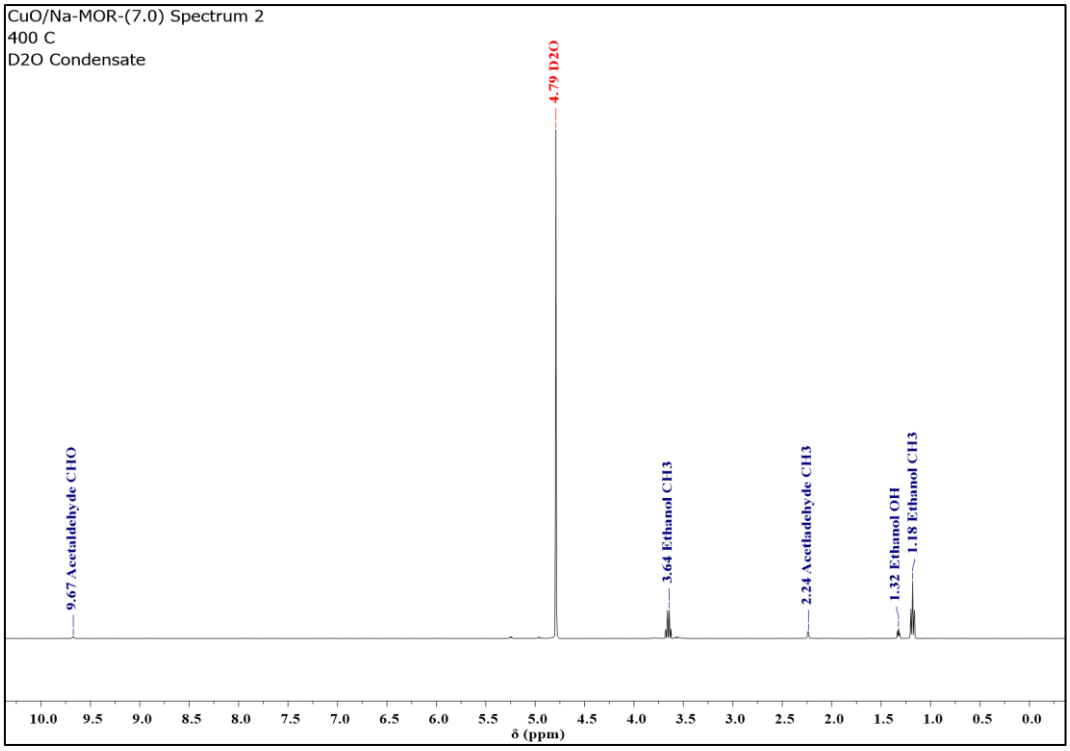

Figure A1.75: ^{1}H NMR spectrum of condensate from ethanol conversion over CuO/Na–MOR–(7.0) at 400 °C averaged over 8 scans with a 1 s recycle delay. Spectrum was acquired on a Bruker Neo-400 spectrometer. Spectrometer frequency: ^{1}H = 400.13 MHz. NMR Solvent = D_2O.

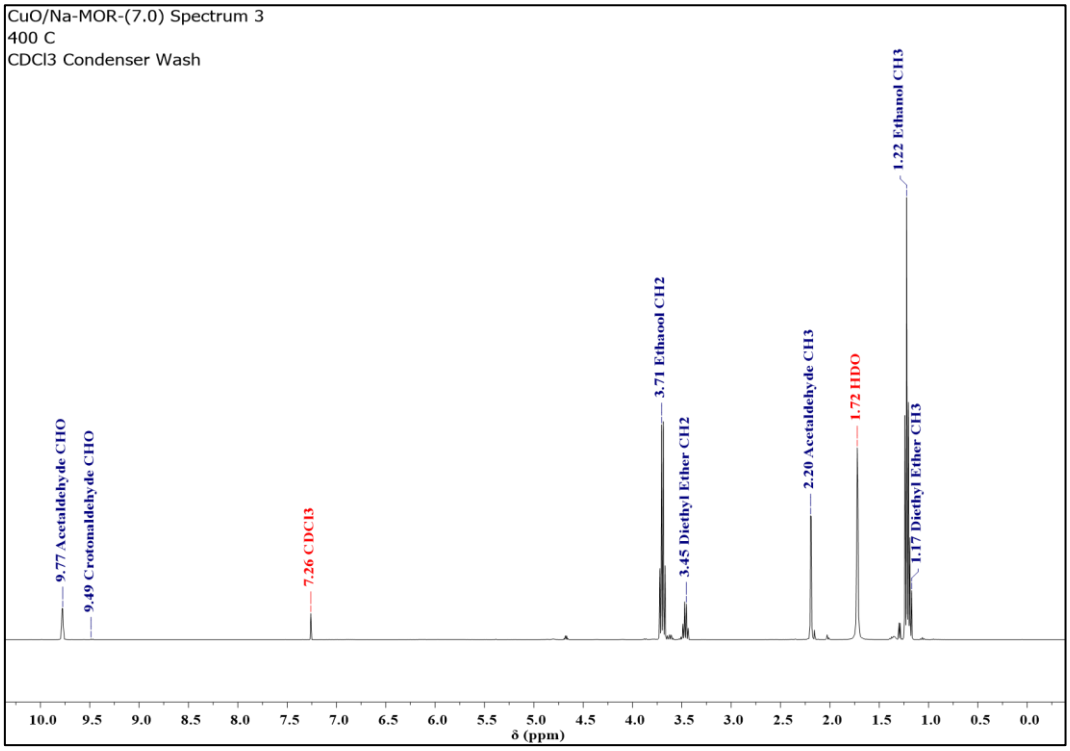

Figure A1.76: ^{1}H NMR spectrum of condenser washings from ethanol conversion over CuO/Na–MOR–(7.0) at 400 °C averaged over 8 scans with a 1 s recycle delay. Spectrum was acquired on a Bruker Neo-400 spectrometer. Spectrometer frequency: ^{1}H = 400.13 MHz. NMR Solvent = $CDCl_3$.

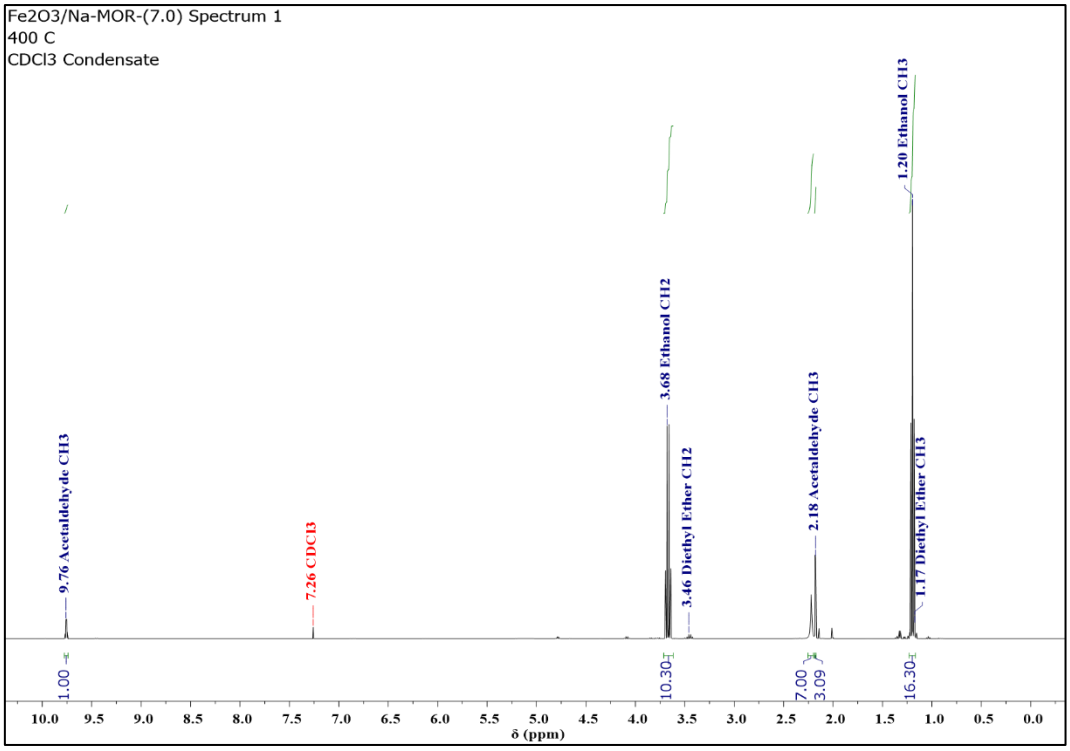

Figure A1.77: ^{1}H NMR spectrum of condensate from ethanol conversion over Fe_2O_3/Na–MOR–(7.0) at 400 °C averaged over 8 scans with a 1 s recycle delay. Spectrum was acquired on a Bruker Neo-400 spectrometer. Spectrometer frequency: ^{1}H = 400.13 MHz. NMR Solvent = $CDCl_3$.

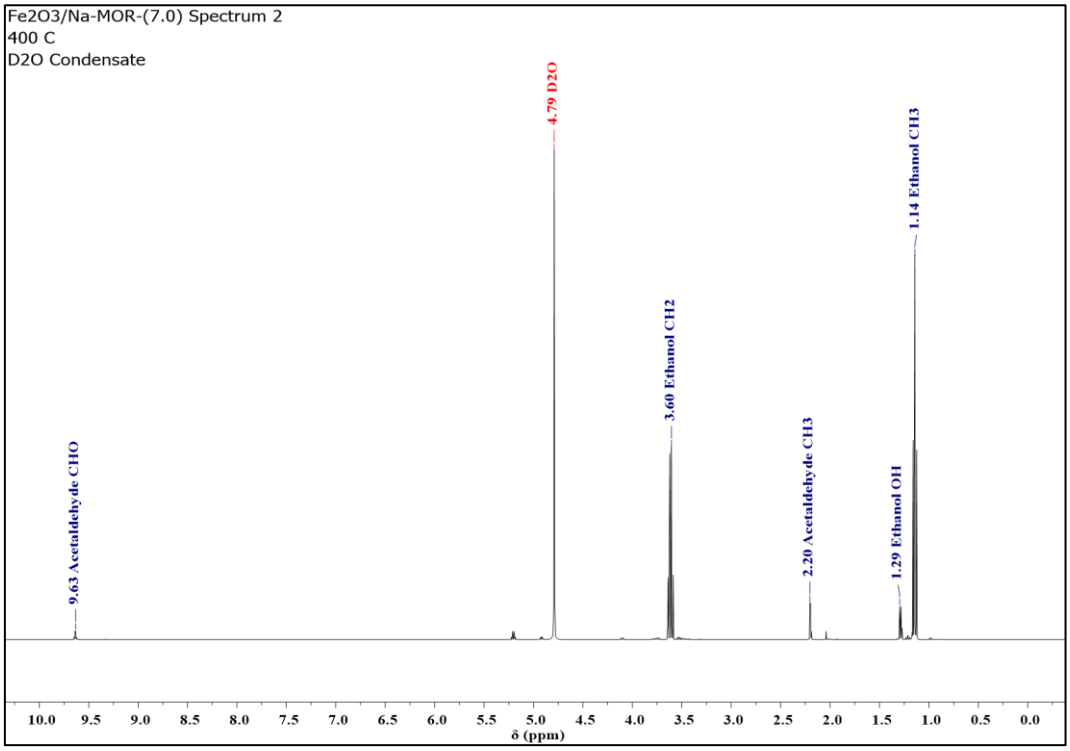

Figure A1.78: ^{1}H NMR spectrum of condensate from ethanol conversion over Fe_2O_3/Na–MOR–(7.0) at 400 °C averaged over 8 scans with a 1 s recycle delay. Spectrum was acquired on a Bruker Neo-400 spectrometer. Spectrometer frequency: ^{1}H = 400.13 MHz. NMR Solvent = D_2O

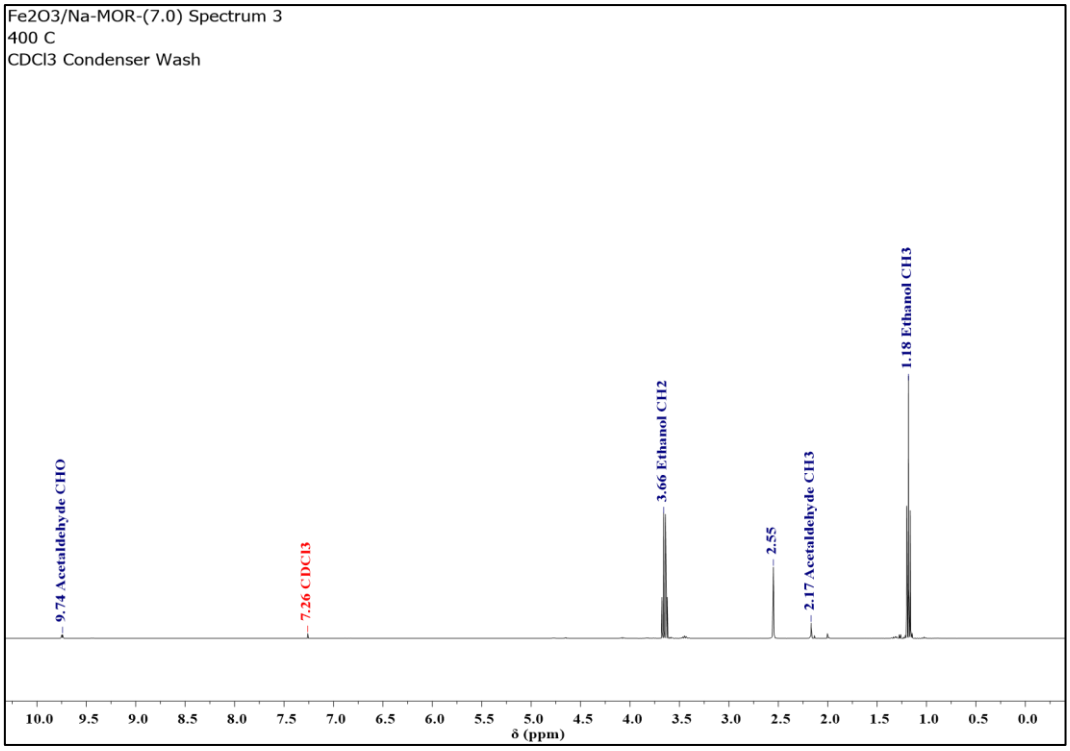

Figure A1.79: ^{1}H NMR spectrum of condenser washings from ethanol conversion over Fe_2O_3/Na–MOR–(7.0) at 400 °C averaged over 8 scans with a 1 s recycle delay. Spectrum was acquired on a Bruker Neo-400 spectrometer. Spectrometer frequency: ^{1}H = 400.13 MHz. NMR Solvent = $CDCl_3$.

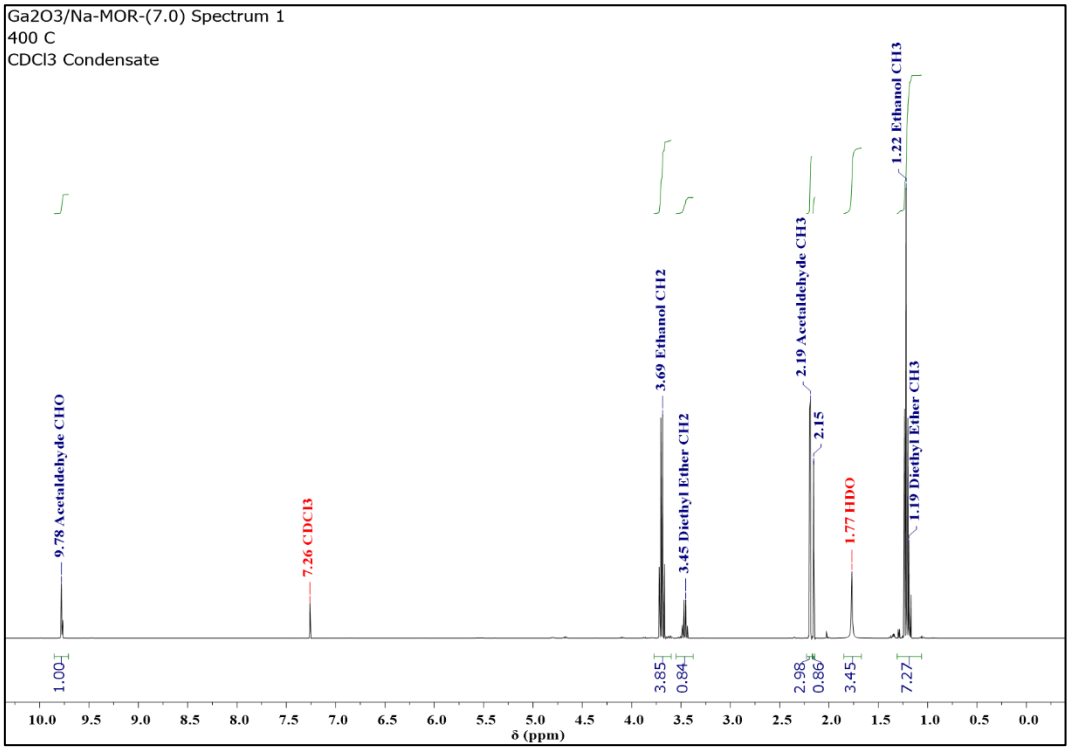

Figure A1.80: ^{1}H NMR spectrum of condensate from ethanol conversion over Ga_2O_3/Na–MOR–(7.0) at 400 °C averaged over 8 scans with a 1 s recycle delay. Spectrum was acquired on a Bruker Neo-400 spectrometer. Spectrometer frequency: ^{1}H = 400.13 MHz. NMR Solvent = $CDCl_3$.

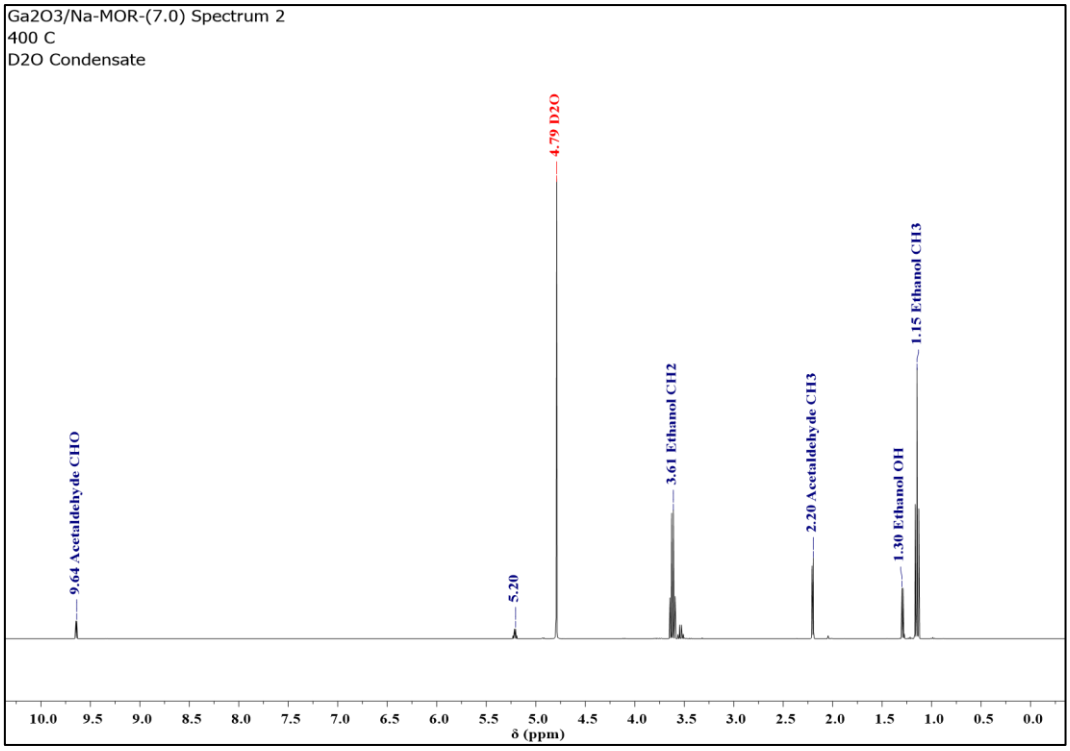

Figure A1.81: ^{1}H NMR spectrum of condensate from ethanol conversion over Ga_2O_3/Na–MOR–(7.0) at 400 °C averaged over 8 scans with a 1 s recycle delay. Spectrum was acquired on a Bruker Neo-400 spectrometer. Spectrometer frequency: ^{1}H = 400.13 MHz. NMR Solvent = D_2O.

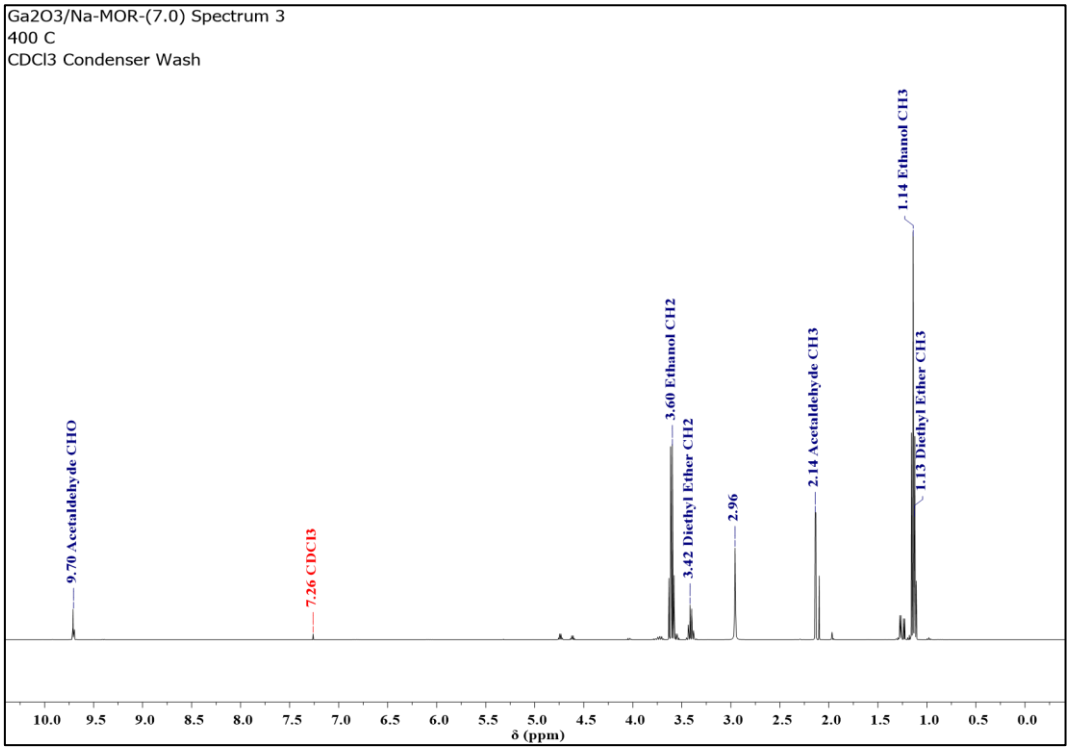

Figure A1.82: ^{1}H NMR spectrum of condenser washings from ethanol conversion over Ga_2O_3/Na–MOR–(7.0) at 400 °C averaged over 8 scans with a 1 s recycle delay. Spectrum was acquired on a Bruker Neo-400 spectrometer. Spectrometer frequency: ^{1}H = 400.13 MHz. NMR Solvent = $CDCl_3$.

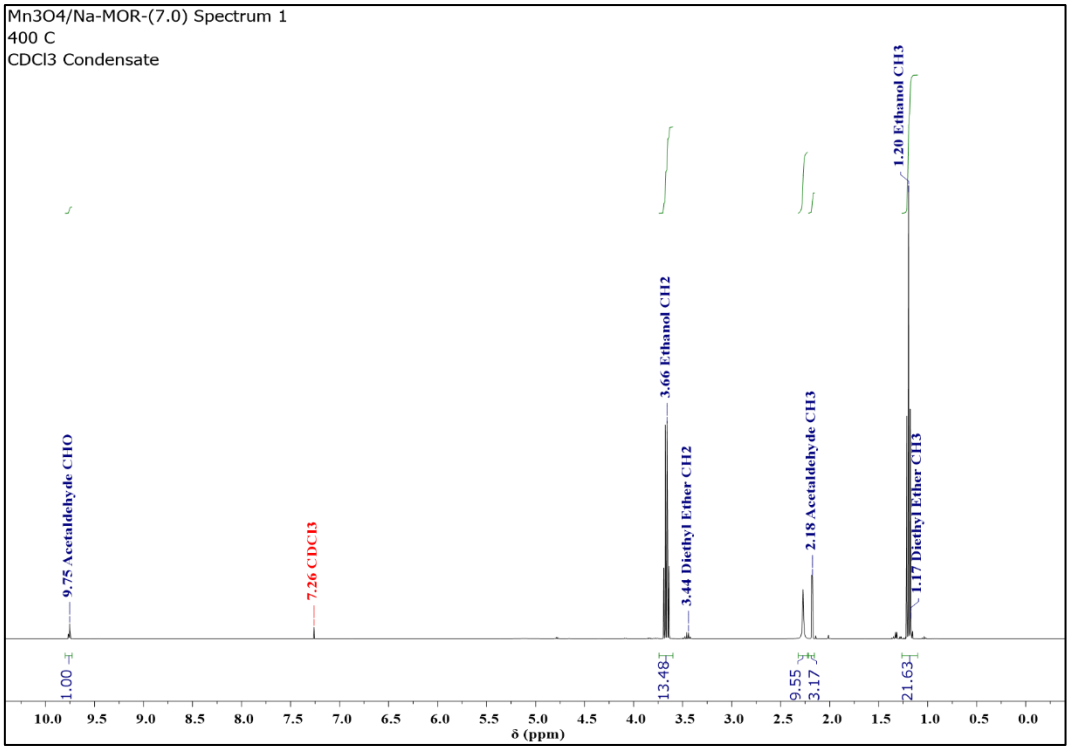

Figure A1.83: ^{1}H NMR spectrum of condensate from ethanol conversion over Mn_3O_4/Na–MOR–(7.0) at 400 °C averaged over 8 scans with a 1 s recycle delay. Spectrum was acquired on a Bruker Neo-400 spectrometer. Spectrometer frequency: ^{1}H = 400.13 MHz. NMR Solvent = $CDCl_3$.

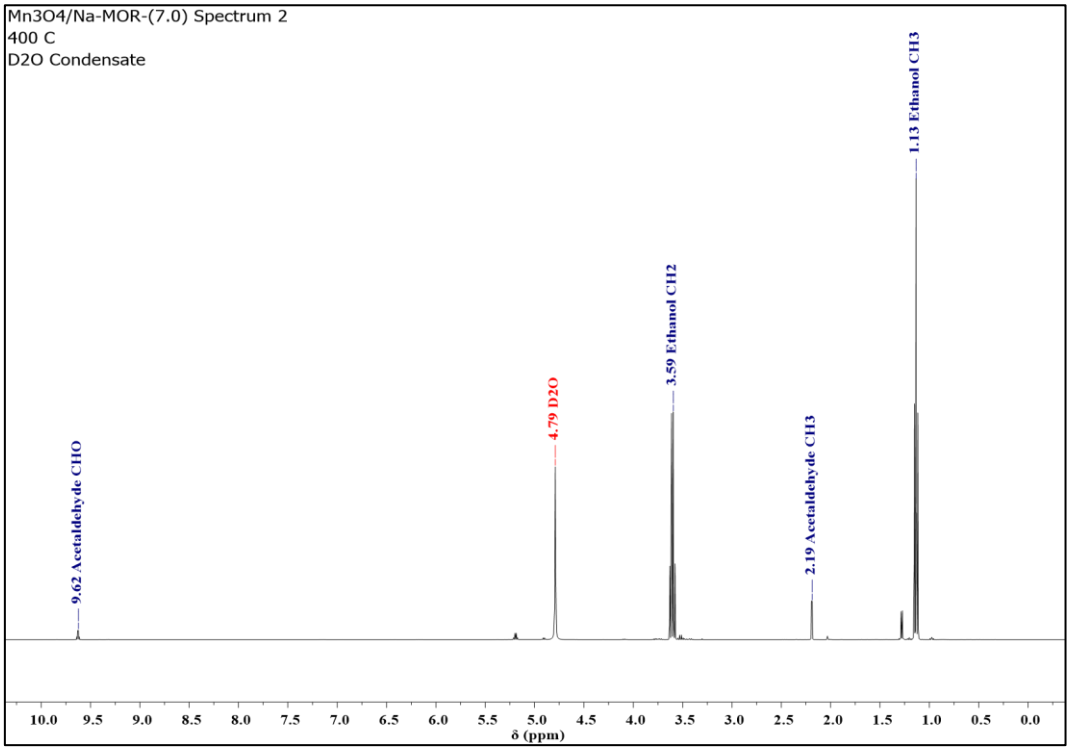

Figure A1.84: ^{1}H NMR spectrum of condensate from ethanol conversion over Mn_3O_4/Na–MOR–(7.0) at 400 °C averaged over 8 scans with a 1 s recycle delay. Spectrum was acquired on a Bruker Neo-400 spectrometer. Spectrometer frequency: ^{1}H = 400.13 MHz. NMR Solvent = D_2O.

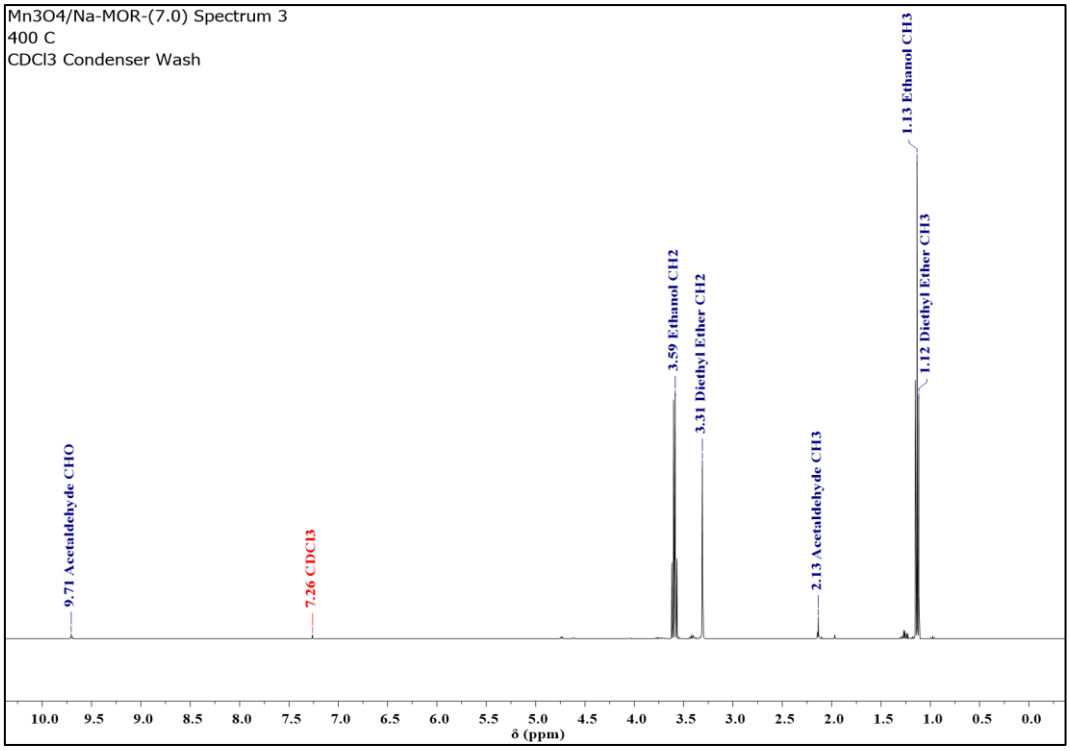

Figure A1.85: ^{1}H NMR spectrum of condenser washings from ethanol conversion over Mn_3O_4/Na–MOR–(7.0) at 400 °C averaged over 8 scans with a 1 s recycle delay. Spectrum was acquired on a Bruker Neo-400 spectrometer. Spectrometer frequency: ^{1}H = 400.13 MHz. NMR Solvent = $CDCl_3$.

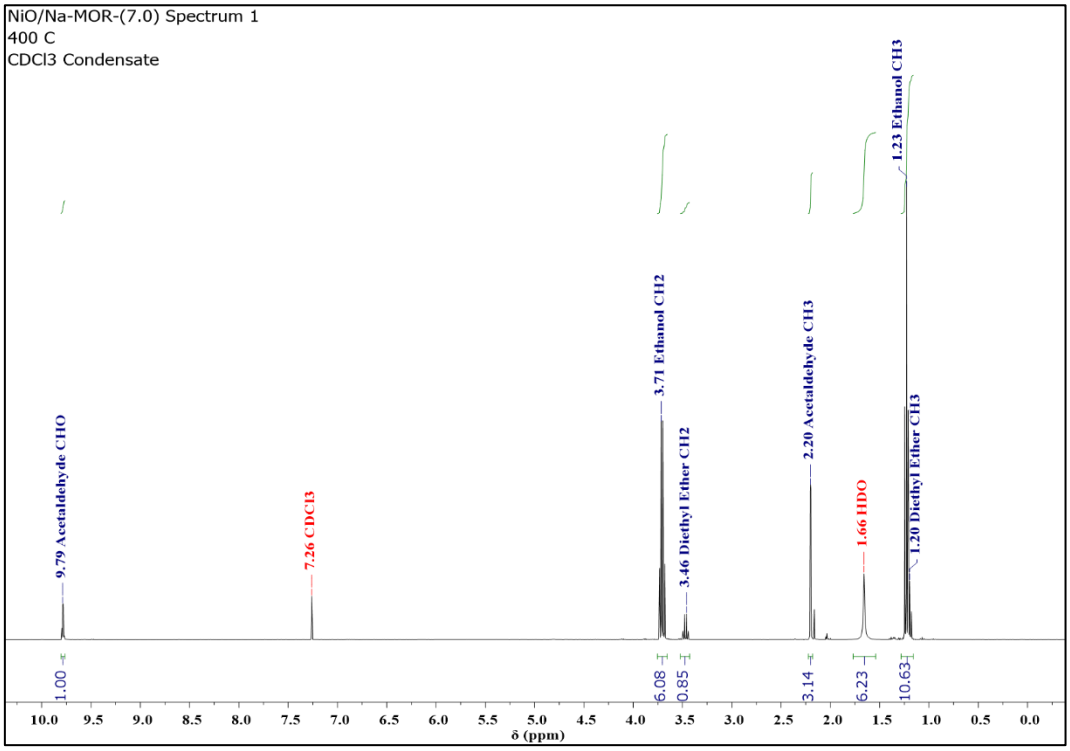

Figure A1.86: ^{1}H NMR spectrum of condensate from ethanol conversion over NiO/Na–MOR–(7.0) at 400 °C averaged over 8 scans with a 1 s recycle delay. Spectrum was acquired on a Bruker Avance III-HD-400 spectrometer. Spectrometer frequency: ^{1}H = 399.95 MHz. NMR Solvent = $CDCl_3$.

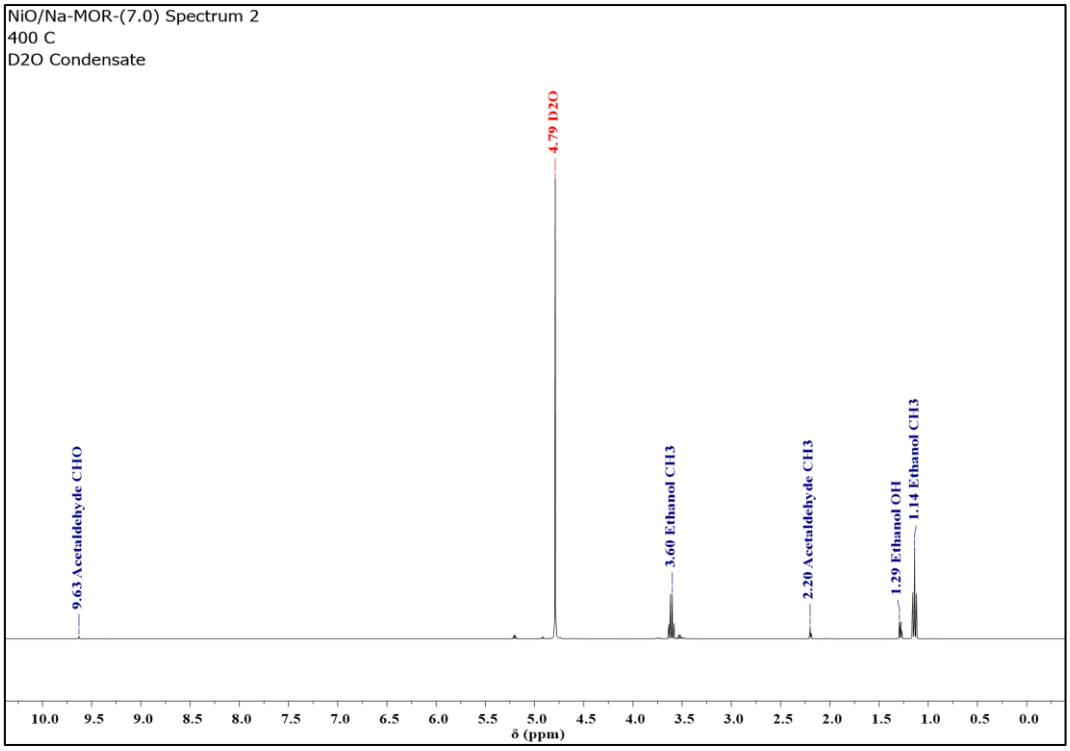

Figure A1.87: ^{1}H NMR spectrum of condensate from ethanol conversion over NiO/Na–MOR–(7.0) at 400 °C averaged over 8 scans with a 1 s recycle delay. Spectrum was acquired on a Bruker Avance III-HD-400 spectrometer. Spectrometer frequency: ^{1}H = 399.95 MHz. NMR Solvent = D_2O.

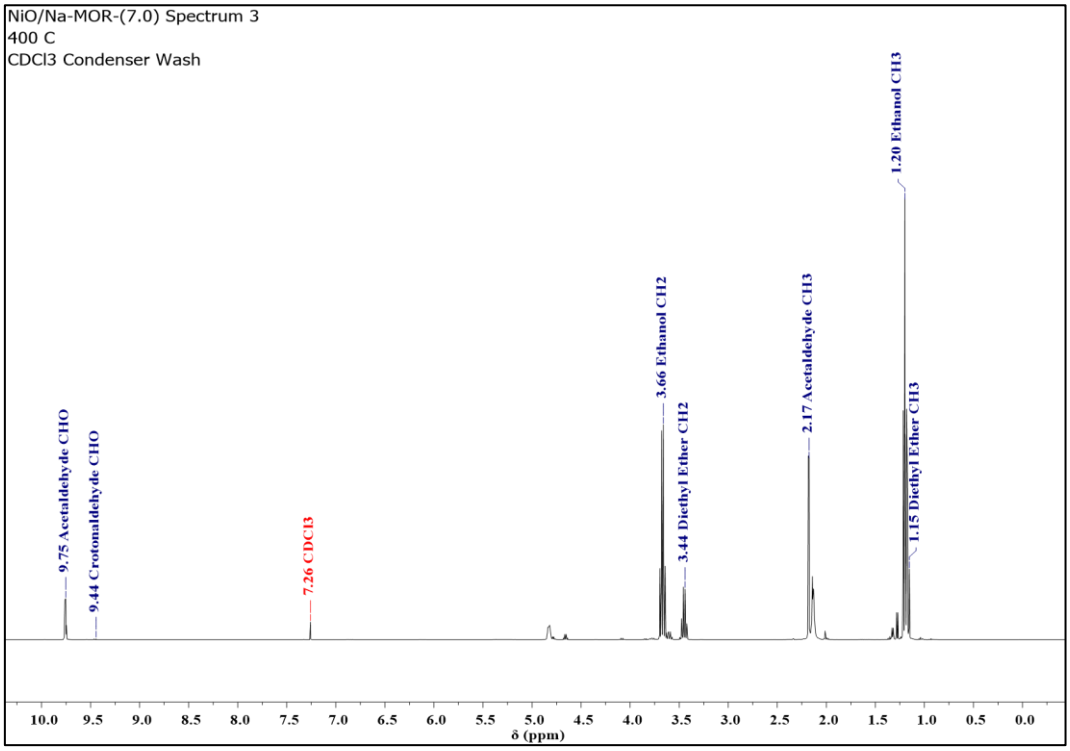

Figure A1.88: ^{1}H NMR spectrum of condenser washings from ethanol conversion over NiO/Na–MOR–(7.0) at 400 °C averaged over 8 scans with a 1 s recycle delay. Spectrum was acquired on a Bruker Avance III-HD-400 spectrometer. Spectrometer frequency: ^{1}H = 399.95 MHz. NMR Solvent = $CDCl_3$.

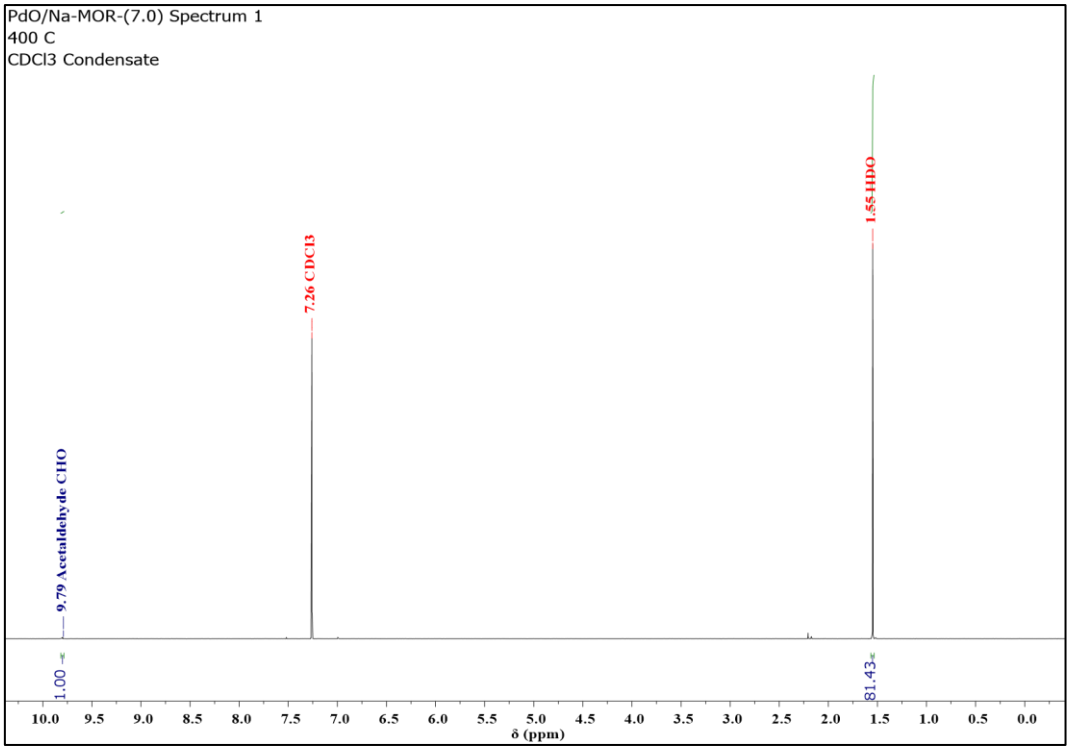

Figure A1.89: ^{1}H NMR spectrum of condensate from ethanol conversion over PdO/Na–MOR–(7.0) at 400 °C averaged over 8 scans with a 1 s recycle delay. Spectrum was acquired on a Bruker Neo-400 spectrometer. Spectrometer frequency: ^{1}H = 400.13 MHz. NMR Solvent = $CDCl_3$.

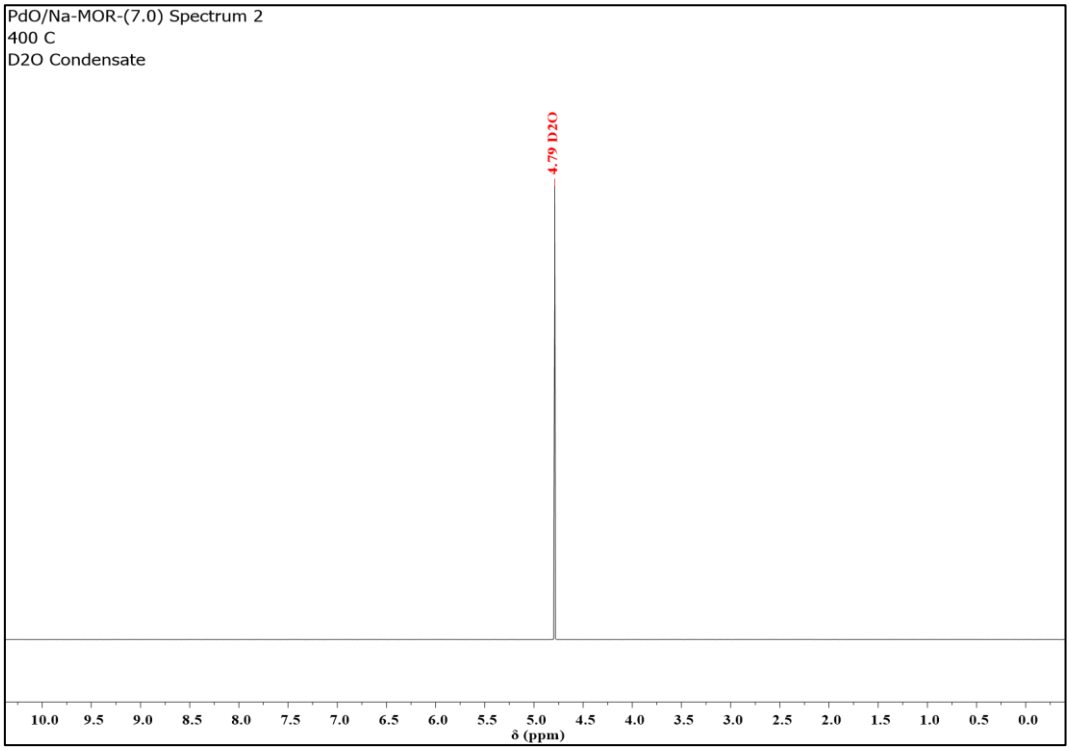

Figure A1.90: ^{1}H NMR spectrum of condensate from ethanol conversion over PdO/Na–MOR–(7.0) at 400 °C averaged over 8 scans with a 1 s recycle delay. Spectrum was acquired on a Bruker Neo-400 spectrometer. Spectrometer frequency: ^{1}H = 400.13 MHz. NMR Solvent = D_2O.

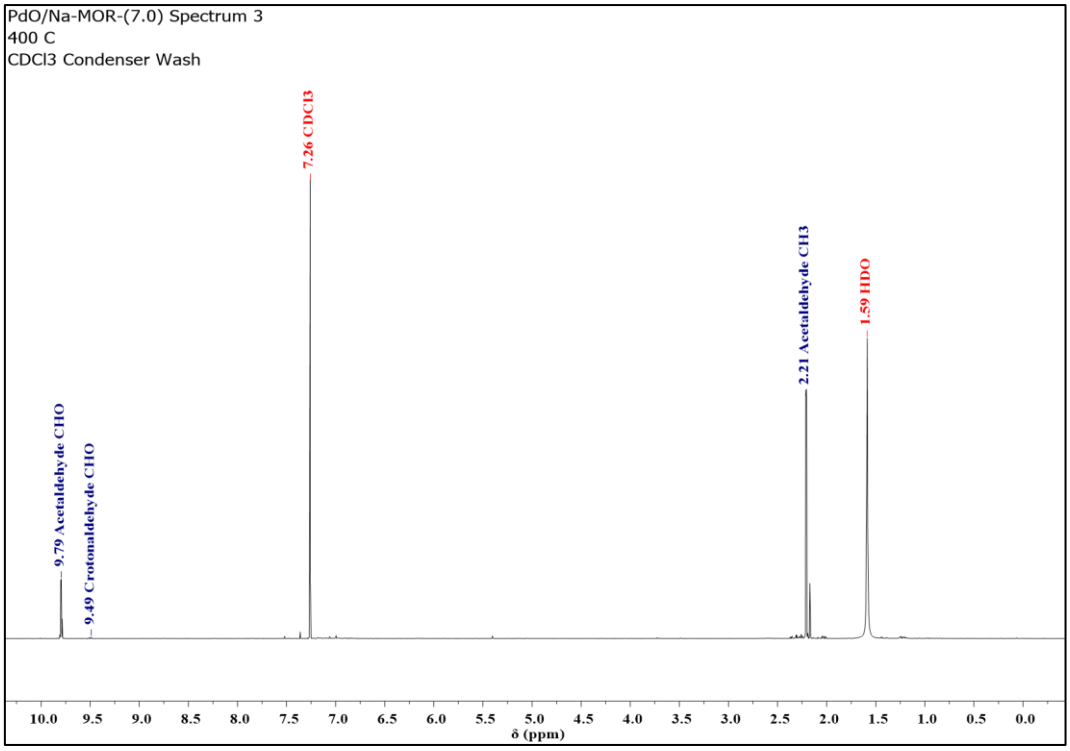

Figure A1.91: ^{1}H NMR spectrum of condenser washings from ethanol conversion over PdO/Na–MOR–(7.0) at 400 °C averaged over 8 scans with a 1 s recycle delay. Spectrum was acquired on a Bruker Neo-400 spectrometer. Spectrometer frequency: ^{1}H = 400.13 MHz. NMR Solvent = $CDCl_3$.

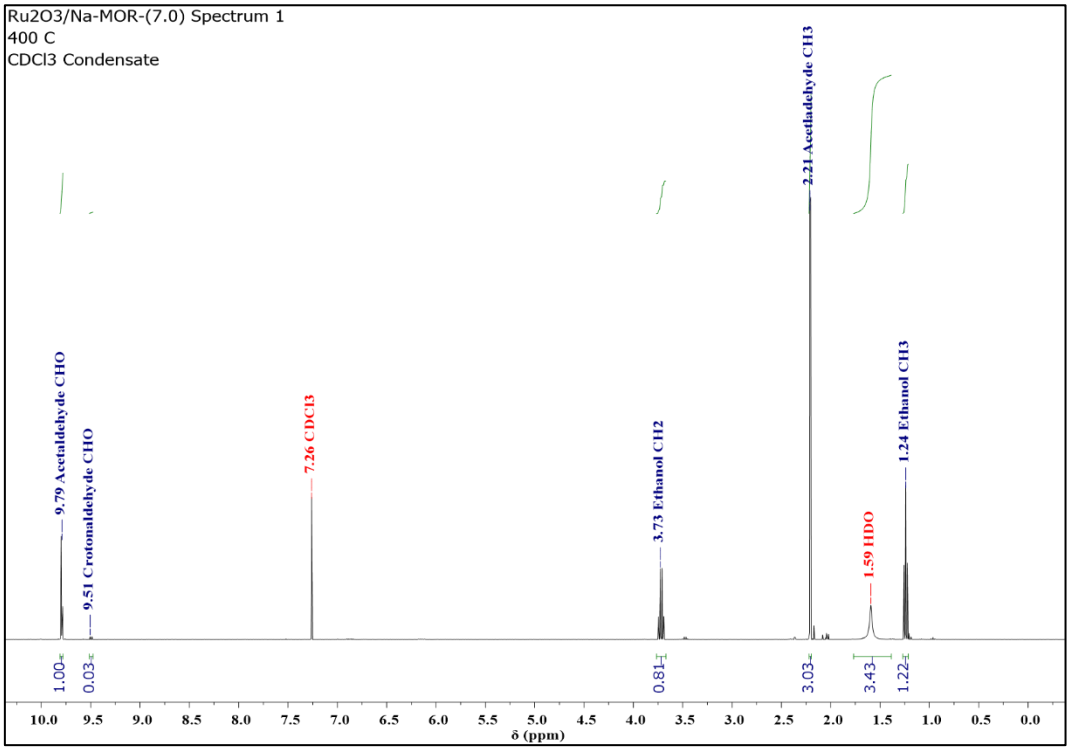

Figure A1.92: ^{1}H NMR spectrum of condensate from ethanol conversion over Ru_2O_3/Na–MOR–(7.0) at 400 °C averaged over 8 scans with a 1 s recycle delay. Spectrum was acquired on a Bruker Neo-400 spectrometer. Spectrometer frequency: ^{1}H = 400.13 MHz. NMR Solvent = $CDCl_3$.

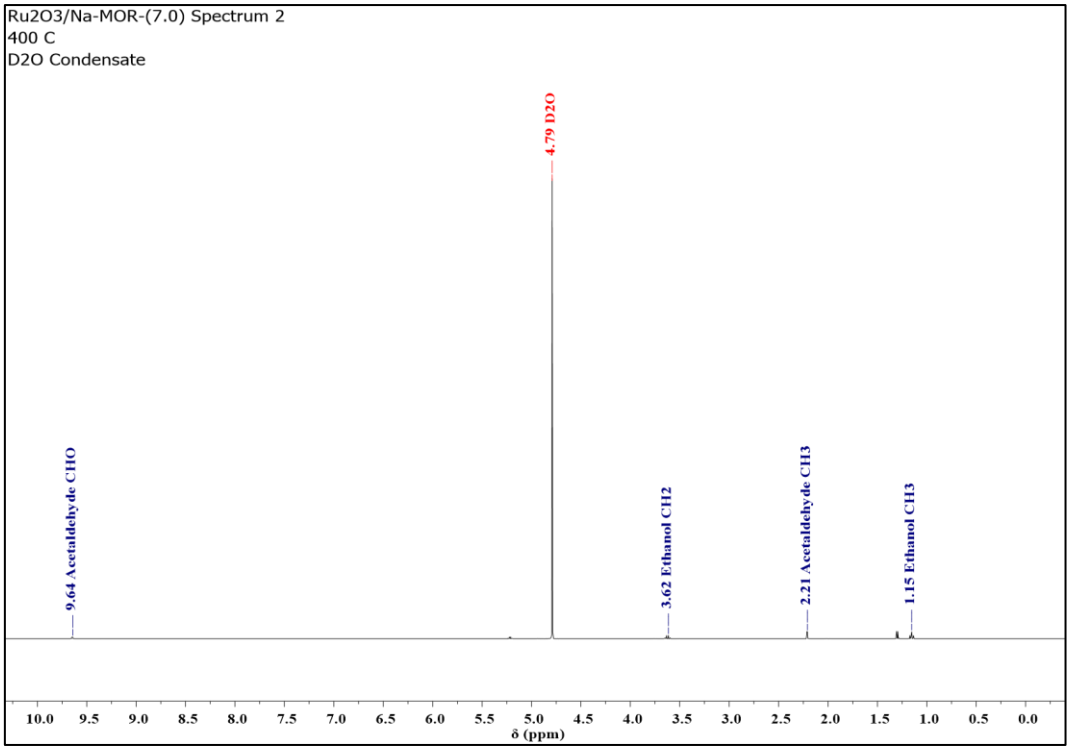

Figure A1.93: ^{1}H NMR spectrum of condensate from ethanol conversion over Ru_2O_3/Na–MOR–(7.0) at 400 °C averaged over 8 scans with a 1 s recycle delay. Spectrum was acquired on a Bruker Neo-400 spectrometer. Spectrometer frequency: ^{1}H = 400.13 MHz. NMR Solvent = D_2O.

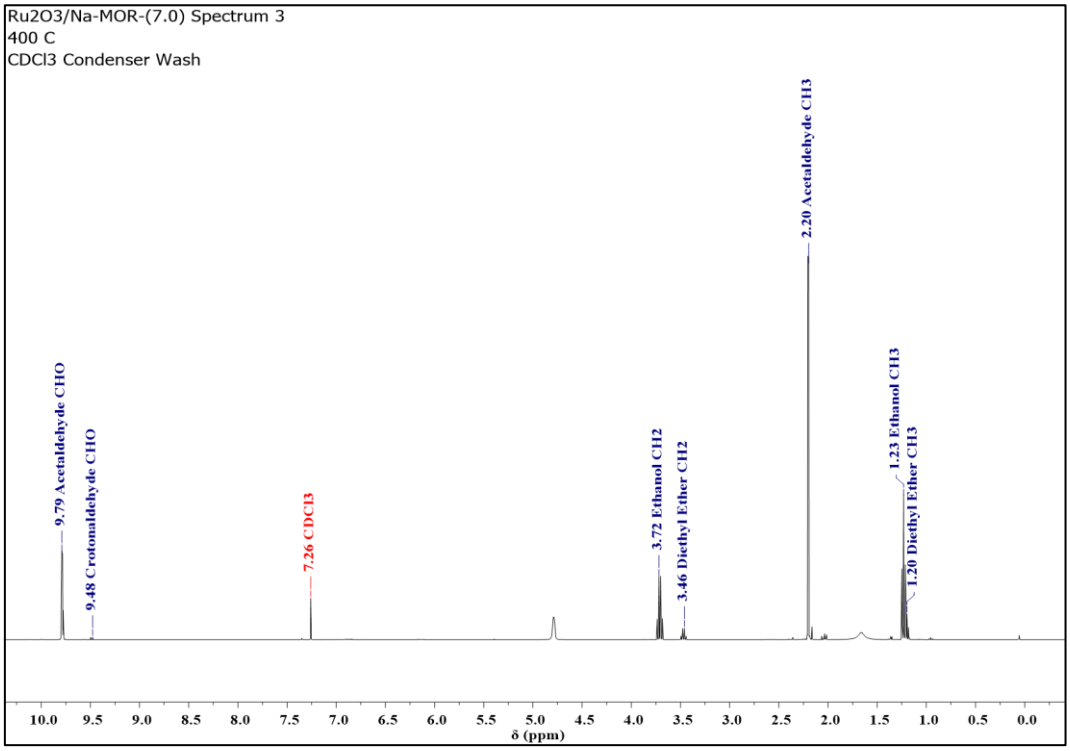

Figure A1.94: ^{1}H NMR spectrum of condenser washings from ethanol conversion over Ru_2O_3/Na–MOR–(7.0) at 400 °C averaged over 8 scans with a 1 s recycle delay. Spectrum was acquired on a Bruker Neo-400 spectrometer. Spectrometer frequency: ^{1}H = 400.13 MHz. NMR Solvent = $CDCl_3$.

Appendix 2. Table of Chemicals, Grades and Suppliers.

Chemical	Grade	Supplier
(3-Mercaptopropyl)trimethoxysilane	95%	Fisher Scientific UK
1,3-Butadiene (Part of calibration gas mix)	—	BOC
1,4–Dioxane	99.8%	Acros Organics
1,9-Diphenyl-1,3,6,8-nonatetraen-5-one	97%+	Fisher Scientific UK
1-Butanol	99%	Acros Organics
1-Butene (Part of calibration gas mix)	—	BOC
2-Mesitylmagnesium Bromide (1.0 M in diethyl ether)	—	Sigma-Aldrich
2-Mesitylmagnesium Bromide (1.0 M in THF)	—	Sigma-Aldrich
4-(Phenylazo)diphenylamine	97%	Fisher Scientific UK
Acetaldehyde	99.5%	Acros Organics
Acetic Acid – Glacial	99.5%+	Fisher Scientific UK
Acetone	AR	Fisher Scientific UK
Acetonitrile	HPLC	Fisher Scientific UK
Aluminium Nitrate Nonahydrate	98%+	Sigma Aldrich
Ammonium Hydroxide (35% in water)	—	Fisher Scientific UK
Argon (Pureshield)	99.998%	BOC
Benzophenone	99%	Sigma-Aldrich
Caesium Nitrate	99.8%	Alfa Aesar
Camphor-10-sulfonic acid	98%	Alfa Aesar
Celite® Hyflo Super-Cel®	—	Fluorochem
Cerium(III) Nitrate Hexahydrate	99.5%	Alfa Aesar
Cetyltrimethylammonium Bromide	99%+	Acros Organics
Chloroform–d	99.8%	Apollo Scientific
Chromium(III) Chloride Hexahydrate	96%	Aldrich
Cis-2-Butene	—	BOC

(Part of calibration gas mix)		
Cobalt(II) Chloride	97%	Aldrich
Cobalt(II) Nitrate Hexahydrate	99%	Acros Organics
Copper(I) Chloride	99%	Acros Organics
Copper(II) Nitrate Trihydrate	99%	Acros Organics
Crotonaldehyde	99%+	Acros Organics
Dichloromethane	99.8%	Fisher Scientific UK
Diethyl Ether (anhydrous)	LR	Fisher Scientific UK
Dimethyl Sulfoxide	AR	Fisher Scientific UK
Dimethylsulfoxide–d^6	99.8%	Apollo Scientific
Dimethylzinc (1.2M solution in toluene)	98%	Acros Organics
DL–Mandelic Acid	99%+	Acros Organics
Ethane (Part of calibration gas mix)	—	BOC
Ethanol (absolute)	AR	Fisher Scientific UK
Ethyl Acetate	AR	Fisher Scientific UK
Ethylene (Part of calibration gas mix)	—	BOC
Gallium	99.99%	Acros Organics
Gallium(III) Chloride	99.99%+	Acros Organics
Gallium(III) Nitrate Hydrate	99.9%	Alfa Aesar
Gallium(III) Oxide	99.99%	Acros Organics
Hafnium (IV) Oxide	99.9% Zr < 0.5%	Alfa Aesar
Hafnium (IV) Oxychloride Octahydrate	98%+	Alfa Aesar
Helium CP Grade	N5.0	BOC
Hexamethyldisilazane	99.9%	Sigma-Aldrich
Hexane	HPLC	Fisher Scientific UK
Hydrogen Peroxide 30%	Extra Pure SLR	Fisher Scientific UK
Hydrogen Tetrachloroaurate(III) Trihydrate	99.99% Au 49.5% min	Alfa Aesar
Iodomethane	99%	Acros Organics

Iron(III) Nitrate Nonahydrate	99%	Acros Organics
Isobutane (Part of calibration gas mix)	—	BOC
Isobutylene (Part of calibration gas mix)	—	BOC
Isopropanol	LR	Fisher Scientific UK
LUDOX® AS-30 Colloidal Silica	—	Sigma Aldrich
Magnesium Chloride Hexahydrate	98%+	Alfa Aesar
Magnesium Turnings	99.9%+	Acros Organics
Magnesium(II) Nitrate Hexahydrate	ACS	Alfa Aesar
Manganese(II) Chloride Tetrahydrate	98%	Sigma-Aldrich
Manganese(II) Nitrate Tetrahydrate	97.5%+	Acros Organics
Methanol	HPLC	Fisher Scientific UK
Methyl Yellow N,N-dimethyl-4-phenyldiazenylaniline	Indicator Grade	Fisher Scientific UK
N-Butane (Part of calibration gas mix)	—	BOC
Nickel(II) Chloride	98%	Aldrich
Nickel(II) Nitrate	97%+	Aldrich
Nitric Acid	70%	Fisher Scientific UK
Nitrogen (Oxygen Free)	OFN	BOC
Oxalic Acid	98%	Sigma-Aldrich
Palladium(II) Nitrate Hydrate	37.0–42.0% Pd	Fisher Scientific UK
Paraldehyde	97%+	Aldrich
Para-toluenesulfonic acid monohydrate	98%+	Sigma-Aldrich
Phosphorus Pentoxide	98%+	Fisher Scientific UK
Platinum (IV) Chloride	99%	Acros Organics
Platinum(IV) Chloride	99%	Acros Organics
Poly(4-styrenesulfonic acid) solution (18% in H_2O)	—	Sigma-Aldrich
Potassium Hydroxide	85.7%	Fisher Scientific UK

Potassium Nitrate	99%+	Acros Organics
Propane (Part of calibration gas mix)	—	BOC
Propylene (Part of calibration gas mix)	—	BOC
Pyridine, Extra Dry over Molecular Sieves	99.5%	Acros Organics
Rubidium Nitrate	99.5%	Sigma Aldrich
Ruthenium(III) Chloride Hydrate	95%+	Sigma-Aldrich
Silicon Carbide	Technical	Fisher Scientific UK
Silver Nitrate	GPR	BDH Chemicals (VWR)
Sodium	ACS	Sigma-Aldrich
Sodium Chloride	—	DU Chemistry Stores
Sodium Hydroxide	98.7%	Fisher Scientific UK
Sodium Nitrate	99%+	Alfa Aesar
Sulfuric Acid	95%	Fisher Scientific UK
tert-Butyllithium (1.7 M in pentane)	—	Sigma-Aldrich
Tetraethyl Orthosilicate	98%	Fisher Scientific UK
Tetrahydrofuran	LR	Fisher Scientific UK
Tetrapropylammonium Hydroxide (25% in H_2O)	—	Acros Organics
Tin(IV) Chloride Pentahydrate	98%	Sigma-Aldrich
Tin(IV) Chloride, 1M Solution in Dichloromethane	—	Acros Organics
Titanium (IV) Chloride, 1M Solution in Dichloromethane	—	Acros Organics
Titanium Isopropoxide	97%	Sigma Aldrich
Toluene	AR	Fisher Scientific UK
Toluene–d^8	99.6%	Goss Scientific Instruments
Xylenes (mixed)	AR	Fisher Scientific UK
Yttrium Nitrate	99.9%	Ventron
Zeolite H–BEA (Si/Al = 12.5)	—	Clariant
Zeolite H–MOR (Si/Al = 10.0)	—	Clariant

Zeolite H–Y (Si/Al = 2.55)	—	Alfa Aesar
Zeolite K–L (Si/Al = 3.0)	—	Clariant
Zeolite Na–MOR (Si/Al = 7.0)	—	Clariant
Zeolite NH_4–BEA (Si/Al = 12.5)	—	Johnson Matthey
Zeolite NH_4–FER (Si/Al = 10.0)	—	Johnson Matthey
Zeolite NH_4–MOR (Si/Al = 10.5)	—	Johnson Matthey
Zeolite NH_4–ZSM–5 (Si/Al = 12.5)	—	Johnson Matthey
Zeolite NH_4–ZSM–5 (Si/Al = 15.0)	—	Johnson Matthey
Zinc(II) Chloride	98%+	Acros Organics
Zinc(II) Nitrate Hexahydrate	98%	Acros Organics
Zinc(II) Oxide	99.99%	Sigma-Aldrich
Zirconium (IV) Oxide	99.7% Hf < 75 ppm	Alfa Aesar
Zirconium Silicate	—	Alfa Aesar
Zirconyl (IV) Chloride Octahydrate	98%+	Acros Organics

Appendix 3. GC-MS-BID Calibration.

A3.1. BPX-90 Calibration Calculations.

Ethanol was calibrated as a neat liquid.

Acetaldehyde and toluene were calibrated as a 1:1 volumetric mixture.

Ethylene was calibrated from the complete dehydration of ethanol.

Species	Retention Time /min	Calibrated Ion /m/z
Ethanol	1.840	31.00
Acetaldehyde	1.728	44.00
Toluene	2.190	91.00
Ethylene	1.610	28.00

Ethanol:

Calibration Point	Ethanol liquid feed rate / ml min^{-1}	Ethanol molar feed rate / mol min^{-1}	Ethanol gas feed rate / ml min^{-1}	Adjusted He Feed / ml min^{-1}	Total Gas Flow / ml min^{-1}
1	0.002	3.43E-05	0.767	43.07	43.84
2	0.004	6.85E-05	1.535	42.30	43.84
3	0.006	1.03E-04	2.302	41.54	43.84
4	0.008	1.37E-04	3.070	40.77	43.84
5	0.010	1.71E-04	3.837	40.00	43.84
6	0.015	2.57E-04	5.756	38.08	43.84
7	0.020	3.43E-04	7.674	36.16	43.84

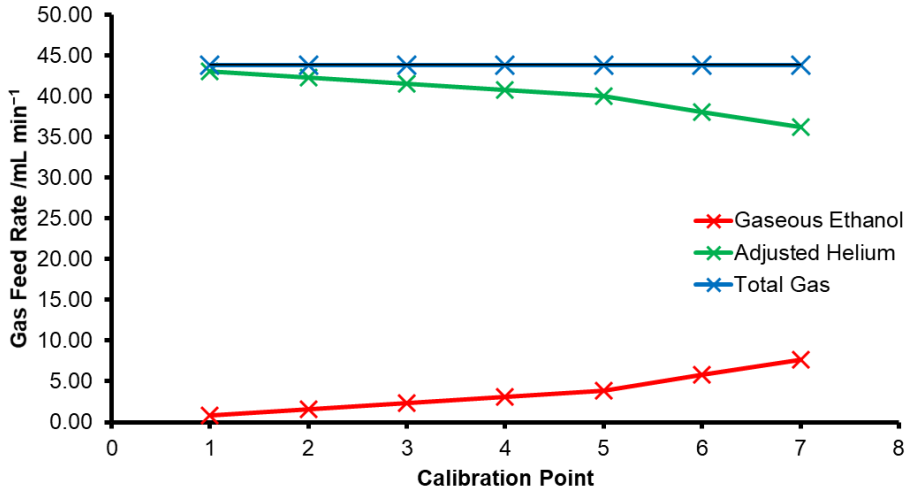

Acetaldehyde and toluene volumetric mixture:

Acetaldehyde density = 0.785 g mL^{-1}

Toluene density = 0.876 g mL^{-1}

Species	Volume / mL	Mass / g	Theoretical Density / g mL^{-1}	Experimental Density / g mL^{-1}	Percentage Error /%
Acetaldehyde	50	39.25	—	—	—
Toluene	50	43.80	—	—	—
Total	100	83.05	0.8305	0.8247	0.70

Calibration Point	Mix liquid feed rate / ml min^{-1}	Toluene liquid feed rate / ml min^{-1}	Toluene gas feed rate / ml min^{-1}	Toluene molar feed rate / mol min^{-1}
1	0.002	0.0010	0.213	9.51E-06
2	0.004	0.0020	0.426	1.90E-05
3	0.006	0.0030	0.639	2.85E-05
4	0.008	0.0040	0.852	3.80E-05
5	0.010	0.0050	1.065	4.75E-05
6	0.015	0.0075	1.597	7.13E-05
7	0.020	0.0100	2.130	9.51E-05
		Acetaldehyde liquid feed rate/ ml min^{-1}	**Acetaldehyde gas feed rate / ml min^{-1}**	**Acetaldehyde molar feed rate / mol min^{-1}**
1	0.002	0.0010	0.399	1.78E-05
2	0.004	0.0020	0.798	3.56E-05
3	0.006	0.0030	1.198	5.35E-05
4	0.008	0.0040	1.597	7.13E-05
5	0.010	0.0050	1.996	8.91E-05
6	0.015	0.0075	2.994	1.34E-04
7	0.020	0.0100	3.992	1.78E-04
		Total mixed gas feed rate / ml min^{-1}	**Adjusted He Feed / ml min^{-1}**	**Total Gas Flow / ml min^{-1}**
1	0.002	0.612	42.45	43.06
2	0.004	1.224	41.84	43.06
3	0.006	1.836	41.22	43.06
4	0.008	2.449	40.61	43.06
5	0.010	3.061	40.00	43.06
6	0.015	4.591	38.47	43.06
7	0.020	6.121	36.94	43.06

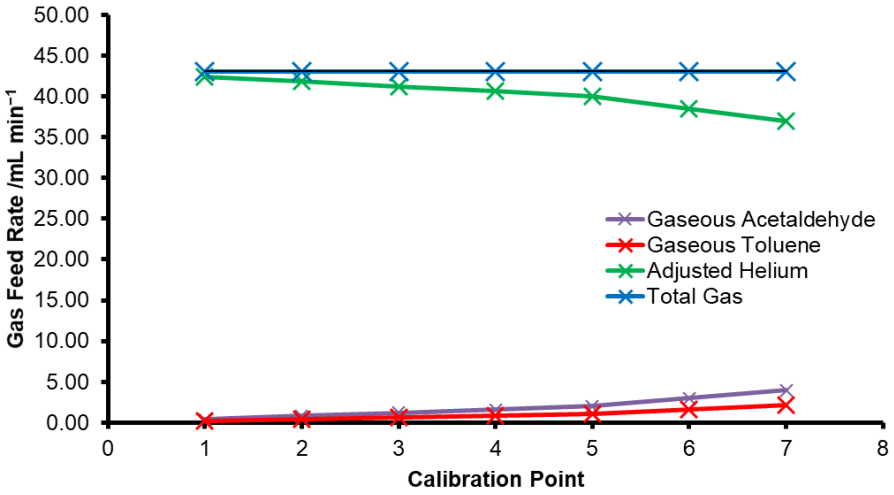
50.00
45.00
40.00
35.00
30.00
25.00
20.00
15.00
10.00
5.00
0.00
Gas Feed Rate /mL min⁻¹
0
1
2
3
4
5
6
7
8
Calibration Point
Gaseous Acetaldehyde
Gaseous Toluene
Adjusted Helium
Total Gas

A3.2. BPX-90 Calibration Curves (MS).

Compounds Calibrated: Ethanol, Acetaldehyde, Toluene, Ethylene.

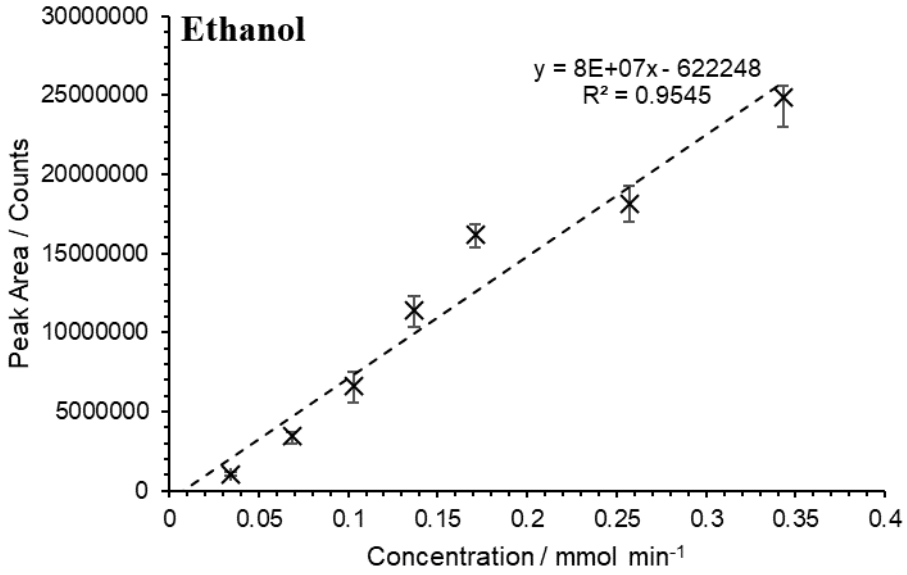

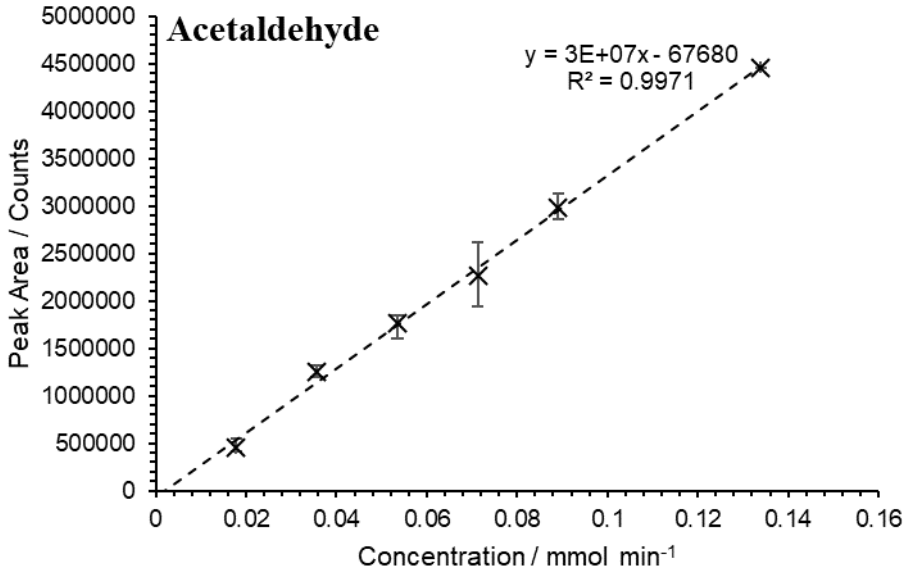

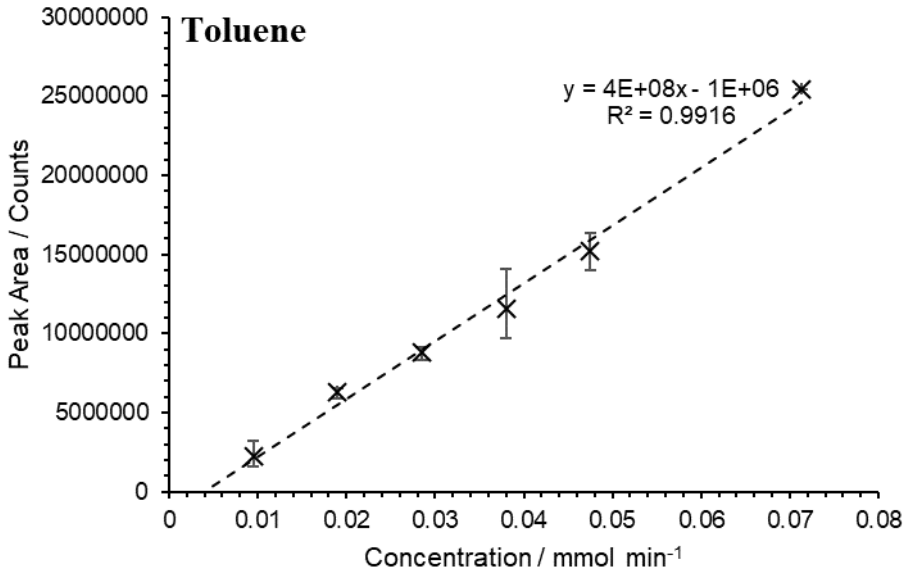
Toluene
y = 4E+08x - 1E+06
R² = 0.9916
Peak Area / Counts
Concentration / mmol min-1
30000000
25000000
20000000
15000000
10000000
5000000
0
0
0.01
0.02
0.03
0.04
0.05
0.06
0.07
0.08

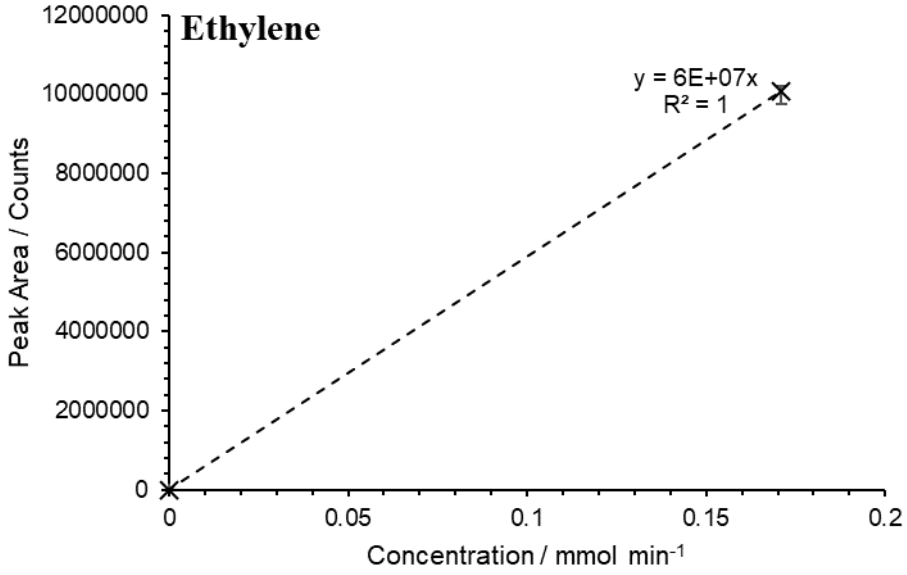
Ethylene
y = 6E+07x
R² = 1
Peak Area / Counts
Concentration / mmol min-1
12000000
10000000
8000000
6000000
4000000
2000000
0
0
0.05
0.1
0.15
0.2

Ethanol				
Concentration /mmol min^{-1}	Peak Area /Counts	Average	Standard Dev	%RSD
0.1710	16815544	16160521	523744.6	3.240889
0.1710	15410502			
0.1710	15704209			
0.1710	16535593			
0.1710	16336756			
0.1370	11395387	11410495	637071.7	5.583208
0.1370	12282992			
0.1370	11338679			
0.1370	11708399			
0.1370	10327020			
0.1030	7542368	6643780	692004.3	10.41582
0.1030	6728025			
0.1030	7145221			
0.1030	6238406			
0.1030	5564882			
0.0685	3656747	3415062	261546.8	7.658625
0.0685	3658079			
0.0685	3452676			
0.0685	2945646			
0.0685	3362161			
0.0343	949318	1018023	83394.46	8.191808
0.0343	988687			
0.0343	1150763			
0.0343	1074734			
0.0343	926611			
0.2570	18125869	18109561	791970.2	4.373216
0.2570	17618104			
0.2570	16957168			
0.2570	19271061			
0.2570	18575604			
0.3430	23000622	24886476	953861.9	3.832853
0.3430	25307960			
0.3430	25390464			
0.3430	25143059			
0.3430	25590273			

Acetaldehyde				
Concentration /mmol min^{-1}	Peak Area /Counts	Average	Standard Dev	%RSD
0.0891	2967122	2976863	100598.2	3.379337
0.0891	2854142			
0.0891	3045644			
0.0891	2888942			
0.0891	3128467			
0.0713	2460352	2259704	247100.3	10.93507
0.0713	2083926			
0.0713	1940938			
0.0713	2618000			
0.0713	2195303			
0.0535	1760641	1759522	80388.82	4.568787
0.0535	1843378			
0.0535	1607746			
0.0535	1795323			
0.0535	1790523			
0.0356	1318063	1254522	51516.97	4.106501
0.0356	1196958			
0.0356	1208310			
0.0356	1313201			
0.0356	1236079			
0.0178	417326	455298.2	47294.22	10.38753
0.0178	447572			
0.0178	429087			
0.0178	547864			
0.0178	434642			
0.1340	4460411	4460411	0	0

Toluene				
Concentration /mmol min^{-1}	Peak Area /Counts	Average	Standard Dev	%RSD
0.0475	13996395	15183381	766069.3	5.045446
0.0475	15060503			
0.0475	15492554			
0.0475	15007710			
0.0475	16359743			
0.0380	12163132	11543966	1520390	13.17043
0.0380	10345543			
0.0380	9680911			
0.0380	14046709			
0.0380	11483536			
0.0285	8807717	8800860	255505.4	2.903187
0.0285	8933314			
0.0285	8348673			
0.0285	9123739			
0.0285	8790855			
0.0190	6557191	6297477	234323.4	3.720909
0.0190	5894981			
0.0190	6330395			
0.0190	6490185			
0.0190	6214634			
0.0095	1606759	2266777	584819.1	25.79958
0.0095	1832937			
0.0095	2020217			
0.0095	2684924			
0.0095	3189050			
0.0713	25450181	25450181	0	0

Ethylene				
Concentration /mmol min^{-1}	Peak Area /Counts	Average	Standard Dev	%RSD
0.171	9738034	10079094	197505.8	1.959559
0.171	10191665			
0.171	10171703			
0.171	10214975			

A3.3. RTX-VMS Calibration Calculations (MS).

Ethanol was calibrated as a neat liquid.

Diethyl ether, ethyl acetate, isopropyl alcohol and acetone were calibrated as a 1:1:1:1 volumetric mixture.

Butanol was calibrated as a neat liquid.

Acetaldehyde was calibrated as 1:1 and 1:9 volumetric mixtures in acetone.

Butadiene, isobutene, linear butenes (1–butene, cis–2–butene) and isobutane were calibrated as part of a calibration gas mixture supplied by BOC.

Species	Retention Time /min	Calibrated Ion /m/z
Ethanol	2.334	46.05
Diethyl Ether	2.335	74.05
Ethyl Acetate	3.385	88.05
Isopropyl Alcohol	2.530	59.05
Acetone	2.650	58.05
Butanol	4.380	74.05
Acetaldehyde	2.130	44.05
Butadiene	2.050	54.05
Isobutene	1.965	43.05
Linear Butenes	2.015	56.05
Isobutane	2.080	56.05

Ethanol:

Calibration Point	Ethanol liquid feed rate / ml min^{-1}	Ethanol molar feed rate / mol min^{-1}	Ethanol gas feed rate / ml min^{-1}	Adjusted N_2 Feed / ml min^{-1}	Total Gas Flow / ml min^{-1}
1	0.002	3.43E-05	0.767	43.07	43.837
2	0.004	6.85E-05	1.535	42.30	43.837
3	0.006	1.03E-04	2.302	41.54	43.837
4	0.008	1.37E-04	3.070	40.77	43.837
5	0.010	1.71E-04	3.837	40.00	43.837
6	0.015	2.57E-04	5.756	38.08	43.837
7	0.020	3.43E-04	7.674	36.16	43.837

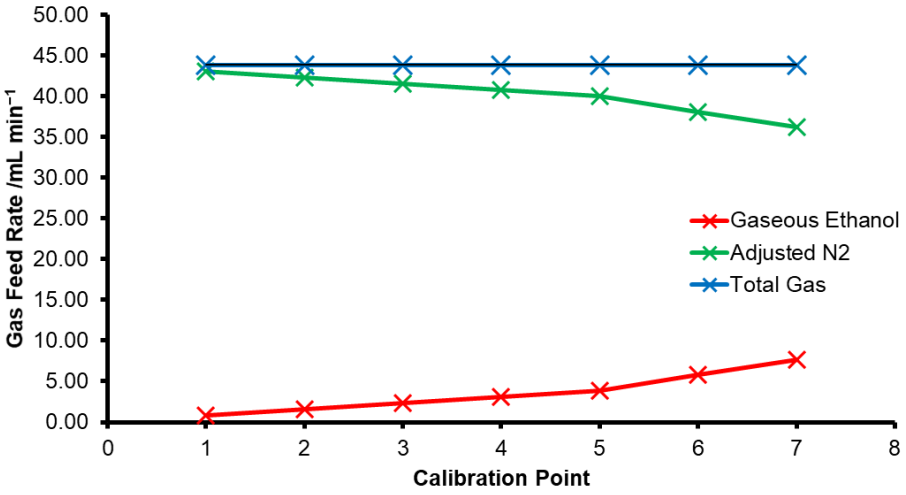
50.00
45.00
40.00
35.00
30.00
25.00
20.00
15.00
10.00
5.00
0.00
Gas Feed Rate /mL min⁻¹
0
1
2
3
4
5
6
7
8
Calibration Point
Gaseous Ethanol
Adjusted N2
Total Gas

Diethyl ether, ethyl acetate, isopropyl alcohol and acetone volumetric mixture:

Diethyl ether density = 0.785 g mL^{-1}

Ethyl acetate density = 0.876 g mL^{-1}

Isopropyl alcohol density = 0.785 g mL^{-1}

Acetone density = 0.784 g mL^{-1}

Species	Volume / mL	Mass / g	Theoretical Density / g mL^{-1}	Experimental Density / g mL^{-1}	Percentage Error /%
Diethyl Ether	25	17.825	—	—	—
Ethyl Acetate	25	22.550	—	—	—
Isopropyl Alcohol	25	19.650	—	—	—
Acetone	25	19.600	—	—	—
Total	100	79.625	0.796	0.793	0.35

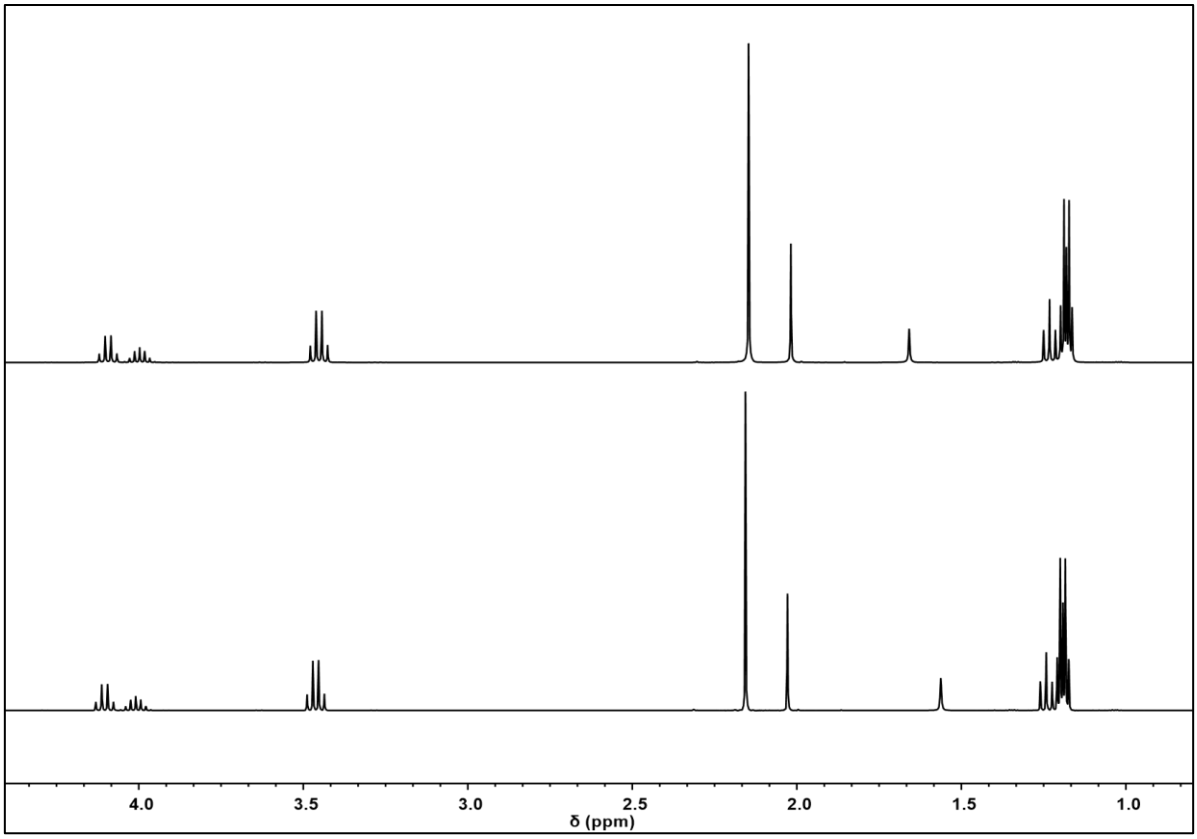

Figure X.95: Solution state ^{1}H NMR spectra of fresh (bottom) and overnight (top) sample mixtures of diethyl ether, ethyl acetate, isopropyl alcohol and acetone in $CDCl_3$. Following standing overnight no products resulting from internal reactions were observed. Spectra were acquired on a Bruker Avance III 400 MHz spectrometer using a 4 mm glass NMR tube. Spectrometer frequncy: ^{1}H = 399.95 MHz

Calibration Point	Mixed liquid feed rate / ml min^{-1}	Diethyl ether liquid feed rate / ml min^{-1}	Diethyl ether gas feed rate / ml min^{-1}	Diethyl ether molar feed rate / ml min^{-1}
1	0.002	0.0005	0.108	4.81E-06
2	0.004	0.0010	0.215	9.62E-06
3	0.006	0.0015	0.323	1.44E-05
4	0.008	0.0020	0.431	1.92E-05
5	0.010	0.0025	0.539	2.40E-05
6	0.015	0.00375	0.808	3.61E-05
7	0.020	0.0050	1.077	4.81E-05
		Ethyl acetate liquid feed rate / ml min^{-1}	**Ethyl acetate gas feed rate / ml min^{-1}**	**Ethyl acetate molar feed rate / ml min^{-1}**
1	0.002	0.0005	0.115	5.12E-06
2	0.004	0.0010	0.229	1.02E-05
3	0.006	0.0015	0.344	1.54E-05
4	0.008	0.0020	0.459	2.05E-05
5	0.010	0.0025	0.573	2.56E-05
6	0.015	0.00375	0.860	3.84E-05
7	0.020	0.0050	1.147	5.12E-05
		IPA liquid feed rate / ml min^{-1}	**IPA gas feed rate / ml min^{-1}**	**IPA molar feed rate / ml min^{-1}**
1	0.002	0.0005	0.146	6.54E-06
2	0.004	0.0010	0.293	1.31E-05
3	0.006	0.0015	0.439	1.96E-05
4	0.008	0.0020	0.586	2.62E-05
5	0.010	0.0025	0.732	3.27E-05
6	0.015	0.00375	1.099	4.90E-05
7	0.020	0.0050	1.465	6.54E-05
		Acetone liquid feed rate / ml min^{-1}	**Acetone gas feed rate / ml min^{-1}**	**Acetone molar feed rate / ml min^{-1}**
1	0.002	0.0005	0.151	6.75E-06
2	0.004	0.0010	0.302	1.35E-05
3	0.006	0.0015	0.454	2.02E-05
4	0.008	0.0020	0.605	2.7E-05
5	0.010	0.0025	0.756	3.37E-05
6	0.015	0.00375	1.134	5.06E-05
7	0.020	0.0050	1.512	6.75E-05

Calibration Point	Mixed liquid feed rate / ml min^{-1}	Total mixed gas feed rate / ml min^{-1}	Adjusted N_2 Feed / ml min^{-1}	Total Gas Flow / ml min^{-1}

1	0.002	0.520	42.08	42.60
2	0.004	1.040	41.56	42.60
3	0.006	1.560	41.04	42.60
4	0.008	2.080	40.52	42.60
5	0.010	2.600	40.00	42.60
6	0.015	3.900	38.70	42.60
7	0.020	5.200	37.40	42.60

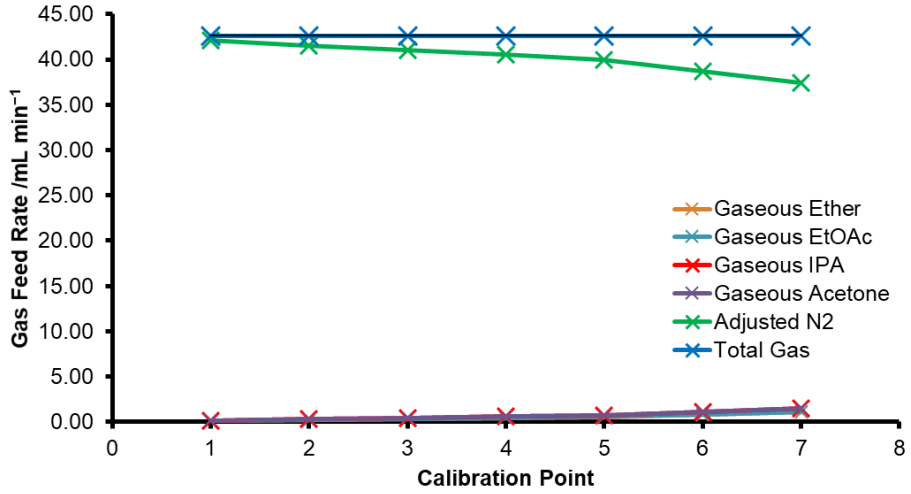

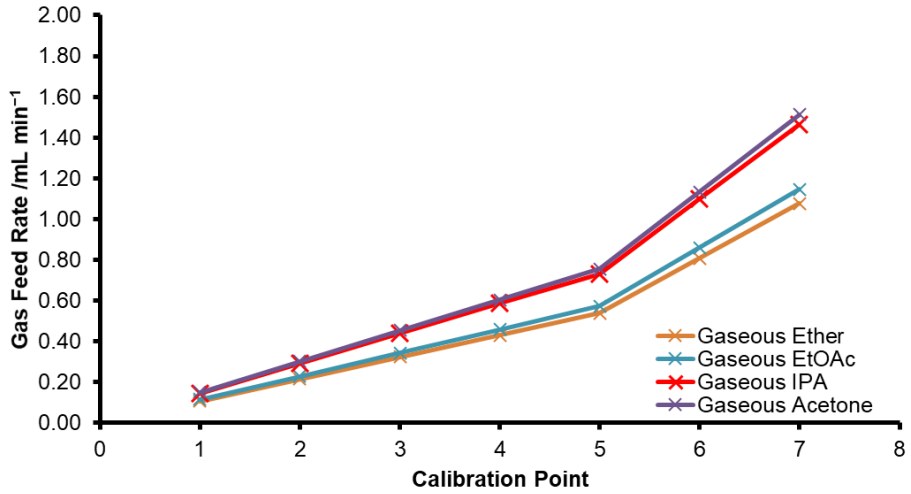

Butanol:

Calibration Point	Butanol liquid feed rate / ml min^{-1}	Butanol molar feed rate / mol min^{-1}	Butanol gas feed rate / ml min^{-1}	Adjusted N_2 Feed / ml min^{-1}	Total Gas Flow / ml min^{-1}
1	0.002	2.19E-05	0.490	41.96	42.45
2	0.004	4.37E-05	0.979	41.47	42.45
3	0.006	6.56E-05	1.469	40.98	42.45
4	0.008	8.74E-05	1.958	40.49	42.45
5	0.010	1.09E-04	2.448	40.00	42.45
6	0.015	1.64E-04	3.672	38.78	42.45
7	0.020	2.19E-04	4.896	37.55	42.45

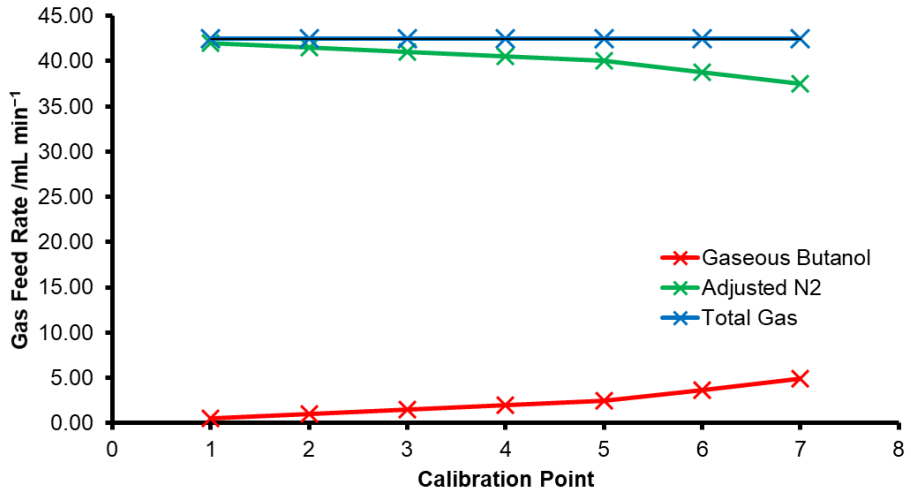

Acetaldehyde:

Acetaldehyde density = 0.788 g mL^{-1}

Acetone density = 0.784 g mL^{-1}

1:9 Volumetric Mixture:

Species	Volume / mL	Mass / g	Theoretical Density / g mL^{-1}	Experimental Density / g mL^{-1}	Percentage Error /%
Acetaldehyde	10	7.880	—	—	—
Acetone	90	70.560	—	—	—
Total	100	78.440	0.784	0.787	−0.364

Calibration Point	Mix liquid feed rate / ml min^{-1}	Acetaldehyde liquid feed rate / ml min^{-1}	Acetaldehyde gas feed rate / ml min^{-1}	Acetaldehyde molar feed rate / mol min^{-1}
1	0.025	0.0025	1.002	4.47E-05
2	0.030	0.003	1.202	5.37E-05
3	0.040	0.004	1.603	7.16E-05
4	0.050	0.005	2.004	8.94E-05
		Acetone liquid feed rate/ ml min^{-1}	**Acetone gas feed rate / ml min^{-1}**	**Acetone molar feed rate / mol min^{-1}**
1	0.025	0.0225	6.803	3.04E-04
2	0.030	0.027	8.164	3.64E-04
3	0.040	0.036	10.885	4.86E-04
4	0.050	0.045	13.607	6.07E-04
		Total mixed gas feed rate / ml min^{-1}	**Adjusted N_2 Feed / ml min^{-1}**	**Total Gas Flow / ml min^{-1}**
1	0.025	7.805	35.32	43.12
2	0.030	9.366	33.76	43.12
3	0.040	12.491	30.63	43.12
4	0.050	15.610	27.51	43.12

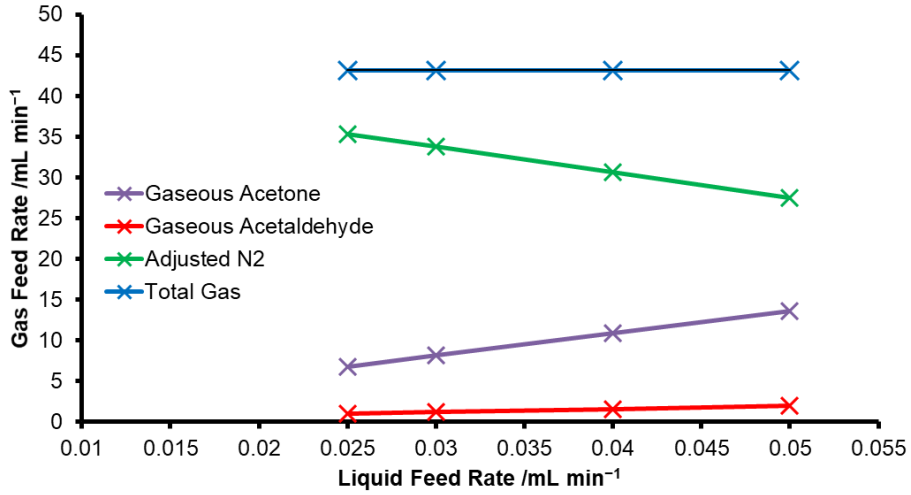

1:1Volumetric Mixture:

Species	Volume / mL	Mass / g	Theoretical Density / g mL^{-1}	Experimental Density / g mL^{-1}	Percentage Error /%
Acetaldehyde	50	39.400	—	—	—
Acetone	50	39.200	—	—	—
Total	100	78.600	0.786	0.784	0.214

Calibration Point	Mix liquid feed rate / ml min^{-1}	Acetaldehyde liquid feed rate / ml min^{-1}	Acetaldehyde gas feed rate / ml min^{-1}	Acetaldehyde molar feed rate / mol min^{-1}
1	0.020	0.010	4.007	1.79E-04
		Acetone liquid feed rate/ ml min^{-1}	**Acetone gas feed rate / ml min^{-1}**	**Acetone molar feed rate / mol min^{-1}**
1	0.020	0.010	3.024	1.35E-04
		Total mixed gas feed rate / ml min^{-1}	**Adjusted N_2 Feed / ml min^{-1}**	**Total Gas Flow / ml min^{-1}**
1	0.020	7.031	36.48	43.52

Calibration Gas:

Component	Volume / %	Flow Volume / ml min^{-1}	Molar Flow / ml min^{-1}	Molar Flow/ mmol min^{-1}
Ethane	10.00	4.00	1.79E-04	0.17857
Ethylene	10.00	4.00	1.79E-04	0.17857
Propane	2.50	1.00	4.46E-05	0.04464
Propylene	2.50	1.00	4.46E-05	0.04464
Isobutylene	0.50	0.20	8.93E-06	0.00893
Isobutane	0.50	0.20	8.93E-06	0.00893
N-Butane	0.50	0.20	8.93E-06	0.00893
1-Butene	0.50	0.20	8.93E-06	0.00893
Cis-2-Butene	0.50	0.20	8.93E-06	0.00893
1,3-Butadiene	0.50	0.20	8.93E-06	0.00893
Helium (Balance)	72.00	28.80	—	—
Total	100.00	40.00	—	—

Gas	Molar feed rate at given MS injection split ratio / mmol min^{-1}				
	125	200	250	350	500
Ethane	0.3571	0.2232	0.1786	0.1276	0.0893
Ethylene	0.3571	0.2232	0.1786	0.1276	0.0893
Propane	0.0893	0.0558	0.0446	0.0319	0.0223
Propylene	0.0893	0.0558	0.0446	0.0319	0.0223
Isobutylene	0.0179	0.0112	0.0089	0.0064	0.0045
Isobutane	0.0179	0.0112	0.0089	0.0064	0.0045
N-Butane	0.0179	0.0112	0.0089	0.0064	0.0045
1-Butene	0.0179	0.0112	0.0089	0.0064	0.0045
Cis-2-Butene	0.0179	0.0112	0.0089	0.0064	0.0045
1,3-Butadiene	0.0179	0.0112	0.0089	0.0064	0.0045

A3.4. RTX-VMS Calibration Curves (MS).

Compounds Calibrated: Ethanol, Diethyl ether, Ethyl acetate, Isopropyl alcohol, Acetone, Butanol, Acetaldehyde, Butadiene, Isobutene, Linear butenes (1–butene, cis–2–butene) and Isobutane.

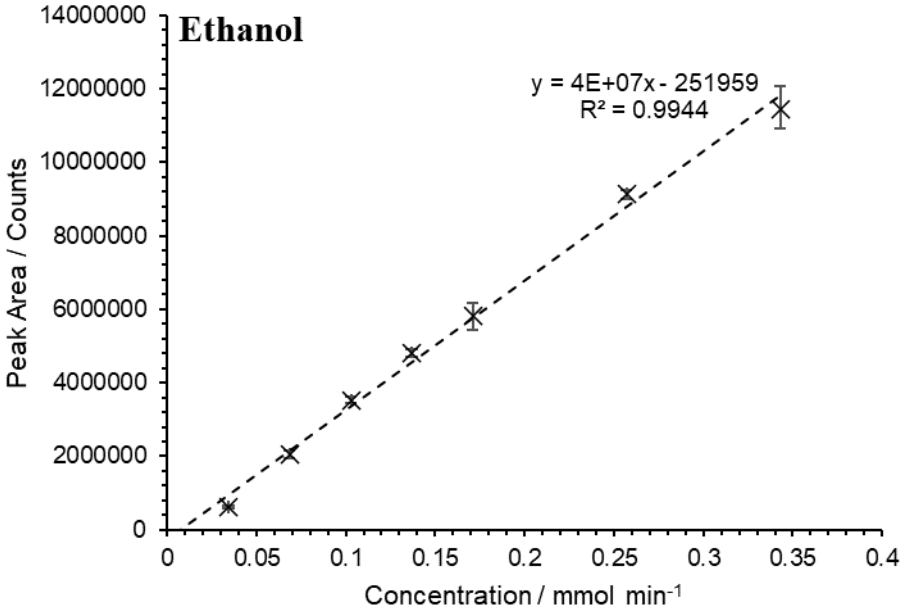

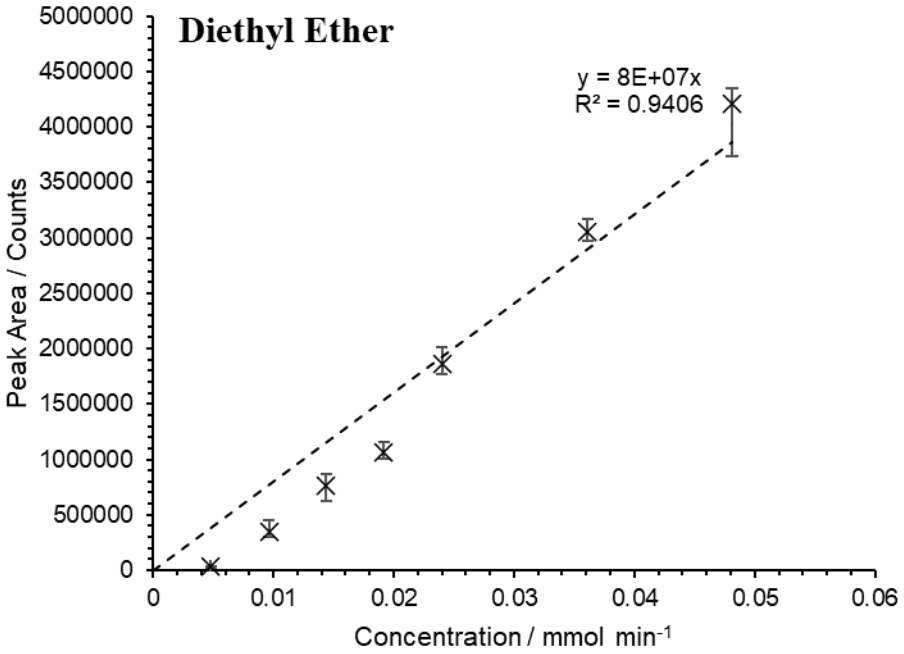

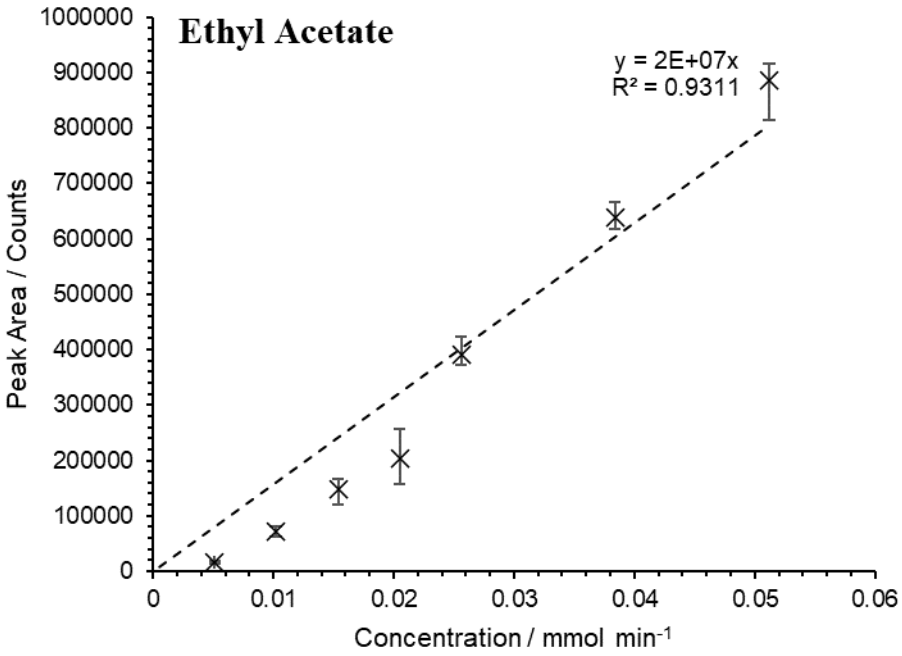
Ethyl Acetate
y = 2E+07x
R² = 0.9311
Peak Area / Counts
Concentration / mmol min-1
0
100000
200000
300000
400000
500000
600000
700000
800000
900000
1000000
0.01
0.02
0.03
0.04
0.05
0.06

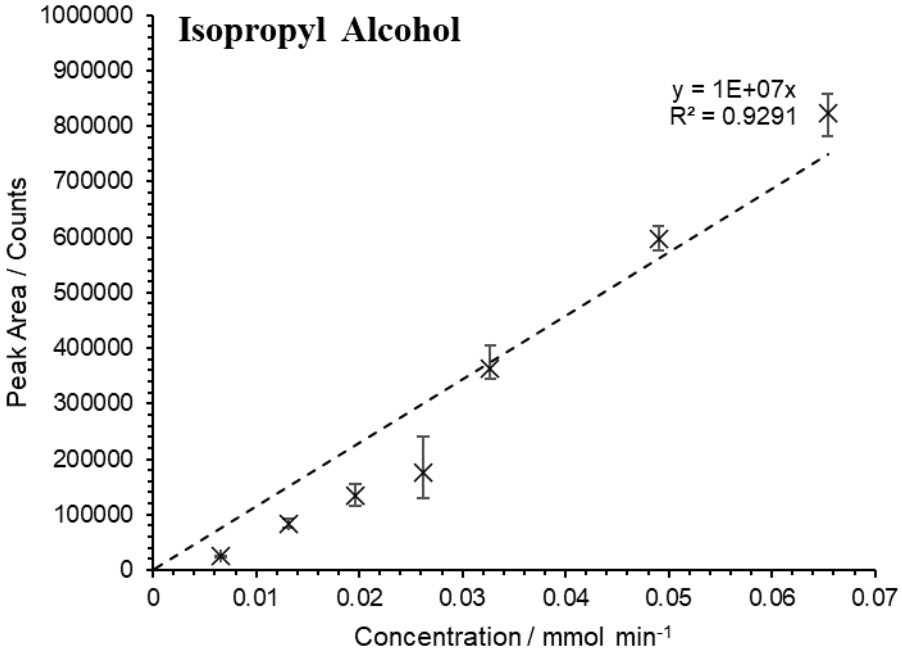
Isopropyl Alcohol
y = 1E+07x
R² = 0.9291
Peak Area / Counts
Concentration / mmol min-1
0
100000
200000
300000
400000
500000
600000
700000
800000
900000
1000000
0.01
0.02
0.03
0.04
0.05
0.06
0.07

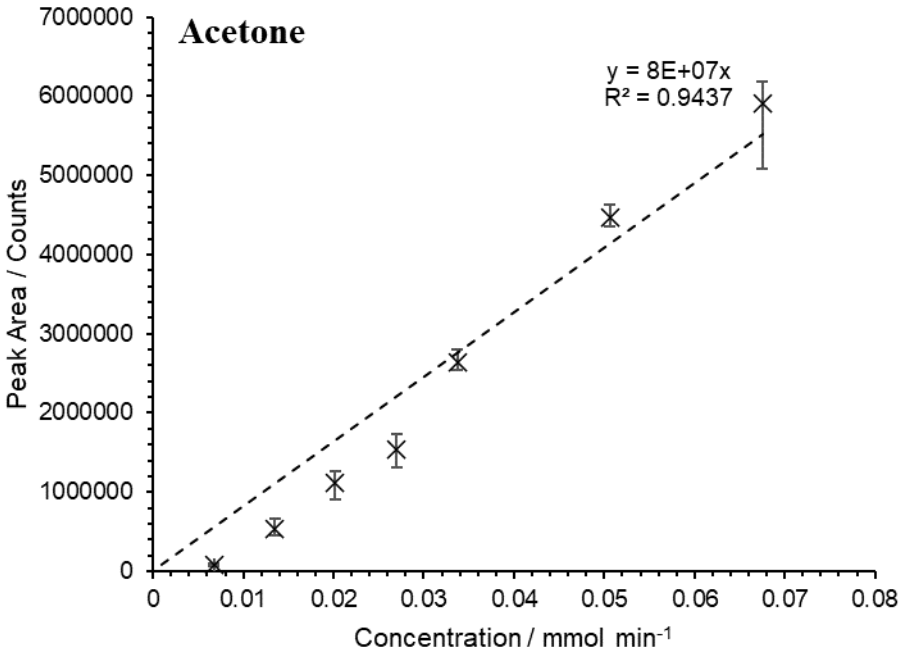
Acetone
y = 8E+07x
R² = 0.9437
Peak Area / Counts
Concentration / mmol min-1
0
1000000
2000000
3000000
4000000
5000000
6000000
7000000
0.01
0.02
0.03
0.04
0.05
0.06
0.07
0.08

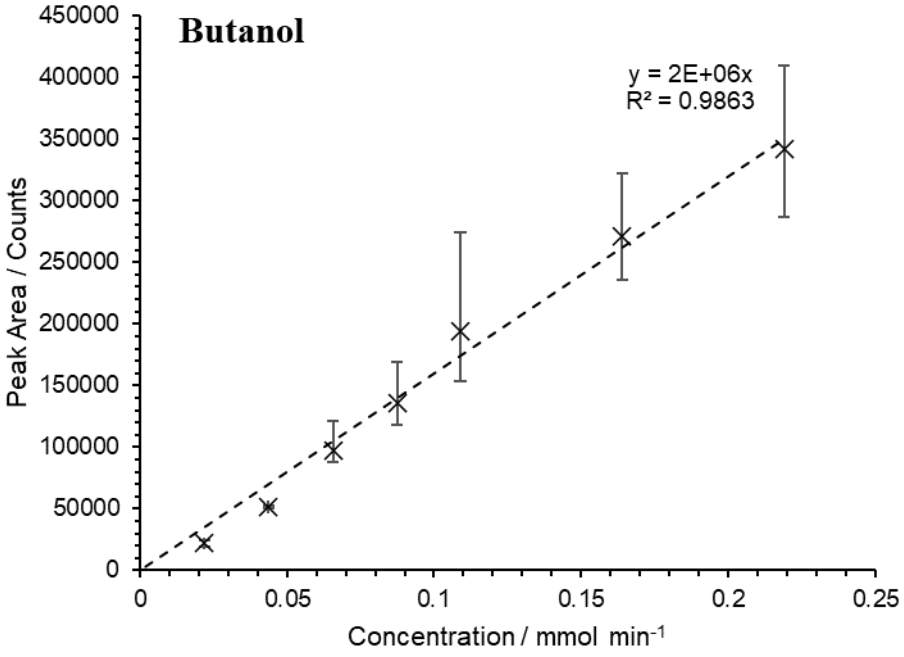
Butanol
y = 2E+06x
R² = 0.9863
Peak Area / Counts
Concentration / mmol min-1
0
50000
100000
150000
200000
250000
300000
350000
400000
450000
0.05
0.1
0.15
0.2
0.25

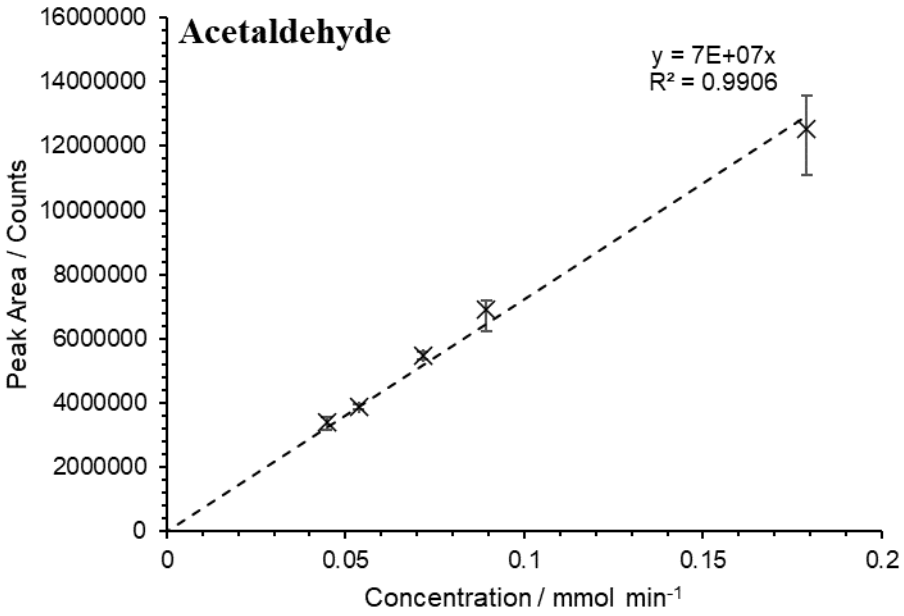
Acetaldehyde
y = 7E+07x
R² = 0.9906
Peak Area / Counts
Concentration / mmol min-1
16000000
14000000
12000000
10000000
8000000
6000000
4000000
2000000
0
0
0.05
0.1
0.15
0.2

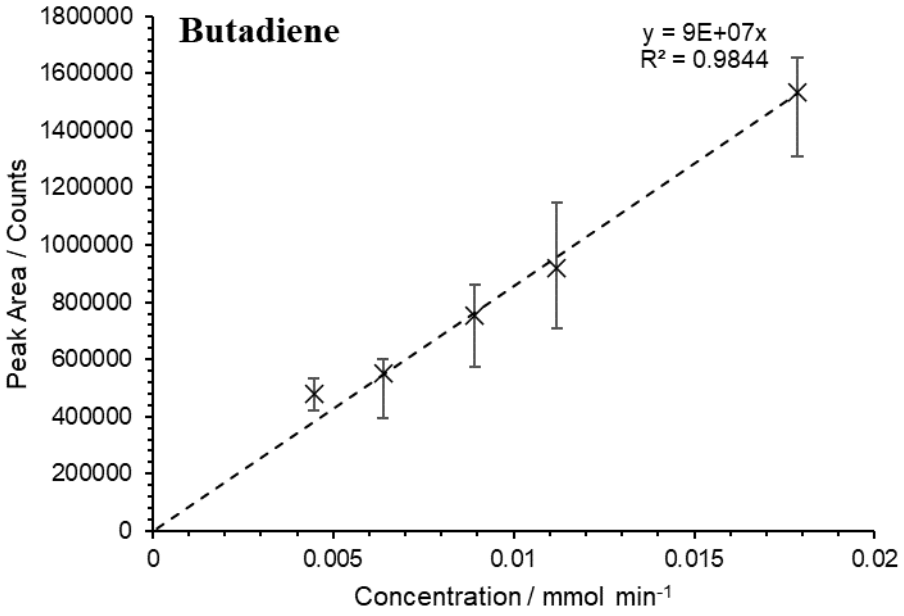
Butadiene
y = 9E+07x
R² = 0.9844
Peak Area / Counts
Concentration / mmol min-1
1800000
1600000
1400000
1200000
1000000
800000
600000
400000
200000
0
0
0.005
0.01
0.015
0.02

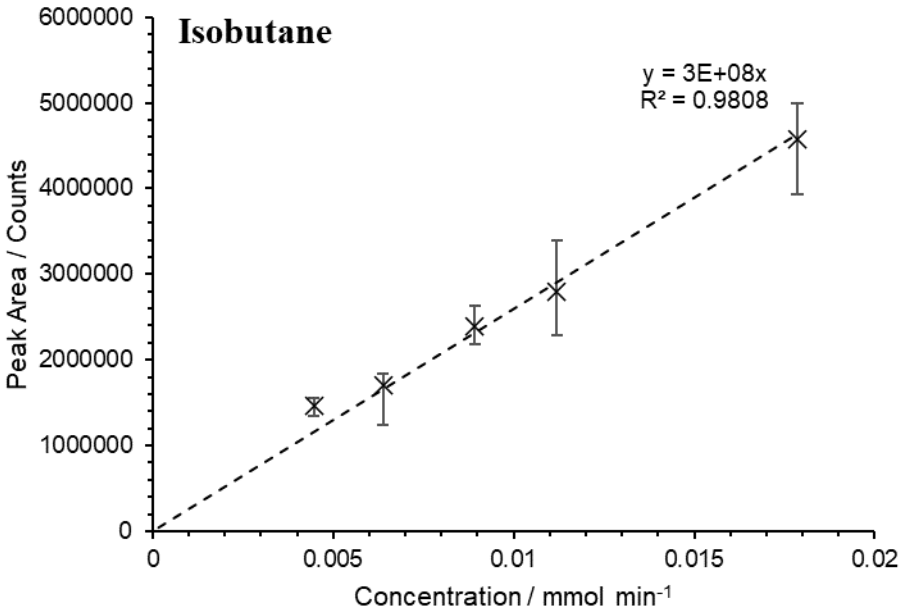
Isobutane
y = 3E+08x
R² = 0.9808
Peak Area / Counts
6000000
5000000
4000000
3000000
2000000
1000000
0
0
0.005
0.01
0.015
0.02
Concentration / mmol min-1

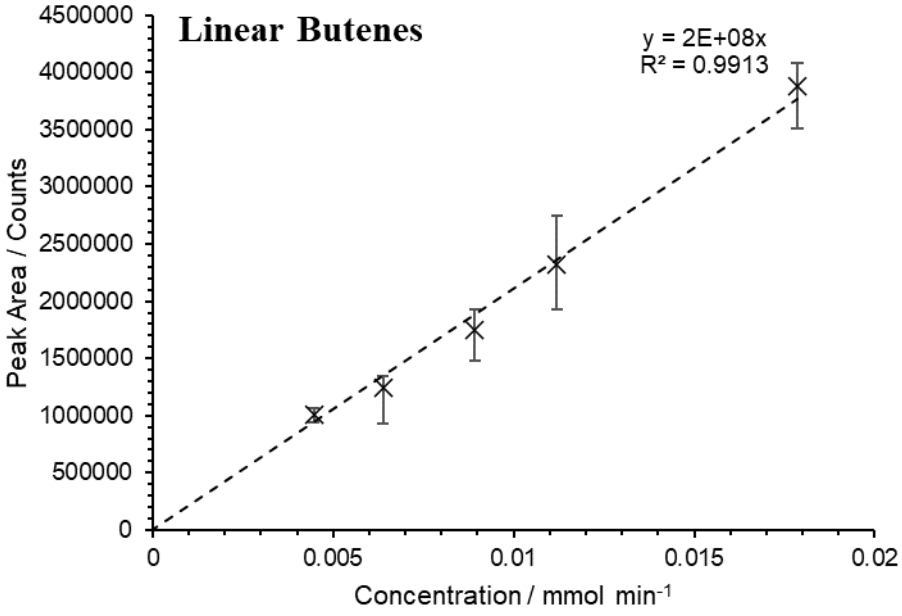
Linear Butenes
y = 2E+08x
R² = 0.9913
Peak Area / Counts
4500000
4000000
3500000
3000000
2500000
2000000
1500000
1000000
500000
0
0
0.005
0.01
0.015
0.02
Concentration / mmol min-1

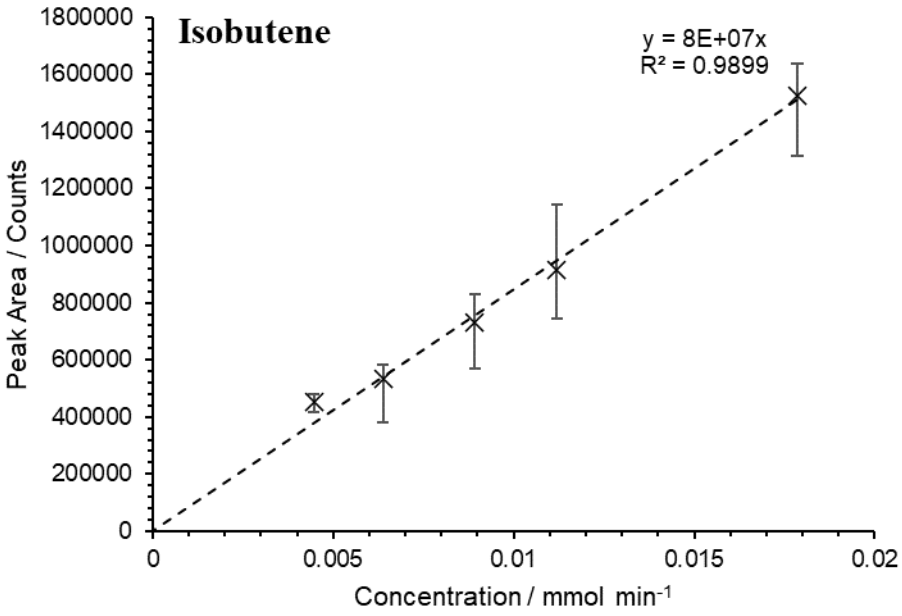

Ethanol				
Concentration /mmol min^{-1}	Peak Area /Counts	Average	Standard Dev	%RSD
0.343	11459265	11423148	397095.9	3.476239
0.343	11519223			
0.343	12084098			
0.343	11141679			
0.343	10911473			
0.257	8996981	9143672	83109.82	0.908933
0.257	9230604			
0.257	9084645			
0.257	9175566			
0.257	9232348			
0.257	9141889			
0.171	5463743	5829586	320925.2	5.505111
0.171	6064758			
0.171	6020927			
0.171	6178307			
0.171	5420196			
0.137	4836067	4818089	63504.3	1.318039
0.137	4829075			
0.137	4870034			
0.137	4755857			
0.137	4900967			
0.137	4716536			

0.103	3497476	3528908	55316.51	1.567525
0.103	3567303			
0.103	3480545			
0.103	3454902			
0.103	3559946			
0.103	3613277			
0.0685	1962391	2060923	86514.02	4.197828
0.0685	2134604			
0.0685	2166612			
0.0685	2083149			
0.0685	1957861			
0.0343	646657	616604.7	16488.77	2.674123
0.0343	630694			
0.0343	607747			
0.0343	602806			
0.0343	601992			
0.0343	609732			

Diethyl Ether				
Concentration /mmol min^{-1}	Peak Area /Counts	Average	Standard Dev	%RSD
0.0481	4318104	4212664	216076.8	5.129221
0.0481	4321453			
0.0481	4325954			
0.0481	4343098			
0.0481	4231151			
0.0481	3736226			
0.0361	2975342	3054152	84987	2.782671
0.0361	3015015			
0.0361	3163344			
0.0361	3149111			
0.0361	2967948			
0.0240	1843522	1862183	81929.47	4.399645
0.0240	1773062			
0.0240	1771018			
0.0240	1864967			
0.0240	1913230			
0.0240	2007301			
0.0192	1160682	1068306	47274.75	4.425206
0.0192	1054737			

0.0192	1070601			
0.0192	1073690			
0.0192	1003640			
0.0192	1046488			
0.0144	864133	762776	69439.94	9.103582
0.0144	759308			
0.0144	794975			
0.0144	765728			
0.0144	630109			
0.0144	762403			
0.00962	303101	347647.2	53434.97	15.37046
0.00962	453881			
0.00962	338225			
0.00962	310733			
0.00962	373828			
0.00962	306115			
0.00481	39028	39402.67	561.2589	1.424419
0.00481	38984			
0.00481	40196			

Ethyl Acetate				
Concentration /mmol min^{-1}	Peak Area /Counts	Average	Standard Dev	%RSD
0.0512	910342	885126.2	34790.43	3.930562
0.0512	904359			
0.0512	915465			
0.0512	896116			
0.0512	869954			
0.0512	814521			
0.0384	618431	638778.4	18368.03	2.875493
0.0384	623523			
0.0384	667294			
0.0384	652370			
0.0384	632274			
0.0256	378326	389972.8	18375.21	4.711922
0.0256	404579			
0.0256	373425			
0.0256	388314			
0.0256	372258			
0.0256	422935			

0.0205	257006	204191.5	31991.42	15.66736
0.0205	226396			
0.0205	209232			
0.0205	183220			
0.0205	156656			
0.0205	192639			
0.0154	167424	147635.8	16720.14	11.32526
0.0154	160690			
0.0154	157996			
0.0154	132167			
0.0154	119909			
0.0154	147629			
0.0102	63261	70860.33	5760.144	8.12887
0.0102	80956			
0.0102	70287			
0.0102	66921			
0.0102	75149			
0.0102	68588			
0.00512	14413	16225.67	1336.336	8.235937
0.00512	16669			
0.00512	17595			

Isopropyl Alcohol				
Concentration /mmol min^{-1}	Peak Area /Counts	Average	Standard Dev	%RSD
0.0654	844694	823628.3	27535.94	3.343249
0.0654	837393			
0.0654	859151			
0.0654	824871			
0.0654	794530			
0.0654	781131			
0.0490	578374	597450.6	17830.83	2.984485
0.0490	575700			
0.0490	619844			
0.0490	613044			
0.0490	600291			
0.0327	347604	363992.7	21118.15	5.801806
0.0327	379131			
0.0327	345113			
0.0327	353654			
0.0327	354221			

0.0327	404233			
0.0262	240351	174784.7	37454.24	21.42879
0.0262	203395			
0.0262	171376			
0.0262	143149			
0.0262	128807			
0.0262	161630			
0.0196	155738	134546.8	15020.76	11.16396
0.0196	144909			
0.0196	137552			
0.0196	115062			
0.0196	114865			
0.0196	139155			
0.0131	76722	83454	6186.896	7.41354
0.0131	80354			
0.0131	76743			
0.0131	84596			
0.0131	88941			
0.0131	93368			
0.00654	26075	25664.67	449.5185	1.751507
0.00654	25880			
0.00654	25039			

Acetone				
Concentration /mmol min^{-1}	Peak Area /Counts	Average	Standard Dev	%RSD
0.0675	6177547	5908164	380157.8	6.43445
0.0675	6115222			
0.0675	6177506			
0.0675	6001972			
0.0675	5887037			
0.0675	5089697			
0.0506	4352067	4468804	111256.1	2.489617
0.0506	4422055			
0.0506	4627165			
0.0506	4573800			
0.0506	4368933			
0.0337	2638512	2643921	81100.99	3.067451
0.0337	2617913			
0.0337	2538200			

0.0337	2684683			
0.0337	2588970			
0.0337	2795250			
0.0270	1737830	1534213	131543.8	8.574026
0.0270	1592537			
0.0270	1594789			
0.0270	1502909			
0.0270	1311441			
0.0270	1465771			
0.0202	1260368	1114274	108868.9	9.770389
0.0202	1149022			
0.0202	1190554			
0.0202	1067718			
0.0202	913052			
0.0202	1104929			
0.0135	473530	527173	70858.91	13.4413
0.0135	662391			
0.0135	531114			
0.0135	475509			
0.0135	563664			
0.0135	456830			
0.00675	70387	25664.67	449.5185	1.751507
0.00675	80230			
0.00675	89268			

Butanol				
Concentration /mmol min^{-1}	Peak Area /Counts	Average	Standard Dev	%RSD
0.219	286352	342150.5	36508.33	10.67025
0.219	352203			
0.219	336289			
0.219	327384			
0.219	409451			
0.219	341224			
0.164	322281	271247	31147.77	11.48318
0.164	248735			
0.164	281589			
0.164	235746			
0.164	243711			
0.164	295420			

0.109	274466	194493.4	41834.19	21.50931
0.109	175206			
0.109	153232			
0.109	178009			
0.109	191554			
0.0874	132159	136252.6	17135.47	12.57625
0.0874	118108			
0.0874	131508			
0.0874	168922			
0.0874	130566			
0.0656	87414	97375.6	12087.65	12.41343
0.0656	121034			
0.0656	90401			
0.0656	94441			
0.0656	93588			
0.0437	52662	51614.2	676.1421	1.309992
0.0437	51552			
0.0437	51094			
0.0437	50747			
0.0437	52016			
0.0219	24363	21927.83	1881.204	8.579068
0.0219	23815			
0.0219	22678			
0.0219	20656	25664.67	449.5185	1.751507
0.0219	18946			
0.0219	21109			

Acetaldehyde				
Concentration /mmol min^{-1}	Peak Area /Counts	Average	Standard Dev	%RSD
0.179	11102872	12533081	974984.9	7.779291
0.179	12936873			
0.179	13557668			
0.179	13398476			
0.179	11669516			
0.0894	6216595	6927917	324947	4.6904
0.0894	7116450			
0.0894	7176166			
0.0894	6962486			
0.0894	7062110			
0.0894	7033697			

0.0716	5594211	5474291	85398.51	1.559992
0.0716	5435615			
0.0716	5341611			
0.0716	5471189			
0.0716	5528828			
0.0537	3970356	3858824	74332.62	1.926303
0.0537	3831839			
0.0537	3920368			
0.0537	3785870			
0.0537	3785686			
0.0447	3544496	3417517	142012.4	4.155425
0.0447	3468785	97375.6	12087.65	12.41343
0.0447	3468863			
0.0447	3465650			
0.0447	3139790			

Butadiene				
Concentration /mmol min^{-1}	Peak Area /Counts	Average	Standard Dev	%RSD
0.0179	1653861	1536321	161295.9	10.49884
0.0179	1308250			
0.0179	1646852			
0.0112	848209	919289.3	147164.9	16.00855
0.0112	802258			
0.0112	1008909			
0.0112	996461			
0.0112	709743			
0.0112	1150156			
0.00892	768917	754827.8	106603.6	14.12291
0.00892	858990			
0.00892	710719			
0.00892	861073			
0.00892	574440			
0.00638	602988	549283.5	72568.45	13.21147
0.00638	535652			
0.00638	394063			
0.00638	584753			
0.00638	589930			
0.00638	588315			

0.00446	473875	478949.6	37462	7.8217
0.00446	499457	3417517	142012.4	4.155425
0.00446	465000	97375.6	12087.65	12.41343
0.00446	534666			
0.00446	421750			

Isobutane				
Concentration /mmol min^{-1}	Peak Area /Counts	Average	Standard Dev	%RSD
0.0179	4807946	4577207	459342.5	10.03543
0.0179	3935945			
0.0179	4987730			
0.0112	2615063	2791854	374790.4	13.42442
0.0112	2465720			
0.0112	3070564			
0.0112	2925079			
0.0112	2287068			
0.0112	3387632			
0.00892	2303884	2391219	171269.4	7.162432
0.00892	2634599			
0.00892	2296154			
0.00892	2546346			
0.00892	2175110			
0.00638	1838425	1697913	209796.4	12.35613
0.00638	1672166			
0.00638	1246140			
0.00638	1810714			
0.00638	1780666			
0.00638	1839369			
0.00446	1440648	1462159	69014.12	4.720016
0.00446	1554723	3417517	142012.4	4.155425
0.00446	1472700	97375.6	12087.65	12.41343
0.00446	1496674			
0.00446	1346049			

Linear Butenes				
Concentration /mmol min^{-1}	Peak Area /Counts	Average	Standard Dev	%RSD
0.0179	4037325	3876054	258477	6.668561
0.0179	3511325			
0.0179	4079513			

0.0112	2130524	2322557	322777	13.89748
0.0112	2012177			
0.0112	2702223			
0.0112	2415848			
0.0112	1925816			
0.0112	2748755			
0.00892	1741573	1744846	164511	9.428401
0.00892	1927345			
0.00892	1663880			
0.00892	1908576			
0.00892	1482854			
0.00638	1349634	1246461	148259.8	11.89446
0.00638	1230951			
0.00638	925918			
0.00638	1315385			
0.00638	1322912			
0.00638	1333968			
0.00446	993826	1003060	40827.04	4.07025
0.00446	1064935	3417517	142012.4	4.155425
0.00446	1004806	97375.6	12087.65	12.41343
0.00446	1014196			
0.00446	937536			

Isobutene				
Concentration /mmol min^{-1}	Peak Area /Counts	Average	Standard Dev	%RSD
0.0179	1632435	1526897	151269.9	9.907018
0.0179	1312975			
0.0179	1635280			
0.0112	835133	913804.5	138327.6	15.13755
0.0112	786668			
0.0112	990800			
0.0112	985789			
0.0112	742557			
0.0112	1141880			
0.00892	733205	730522.8	95678.71	13.09729
0.00892	829151			
0.00892	692253			
0.00892	826646			
0.00892	571359			

0.00638	582688	535376.8	72075.39	13.46255
0.00638	525109			
0.00638	380106			
0.00638	571031			
0.00638	572423			
0.00638	580904			
0.00446	449613	451094.8	22145.81	4.909347
0.00446	481397	3417517	142012.4	4.155425
0.00446	444261	97375.6	12087.65	12.41343
0.00446	465035			
0.00446	415168			

A3.5. RTX-VMS Calibration Curves (MS) - Recalibrated.

Following a repair to the GC-MS system, the mass spectrometer system was recalibrated to the same specifications as detailed in Section A3.3.

A3.4. RTX-VMS Calibration Curves (MS).

Compounds Calibrated: Ethanol, Diethyl ether, Ethyl acetate, Isopropyl alcohol, Acetone, Butanol, Acetaldehyde, Butadiene, Isobutene, Linear butenes (1–butene, cis–2–butene) and Isobutane.

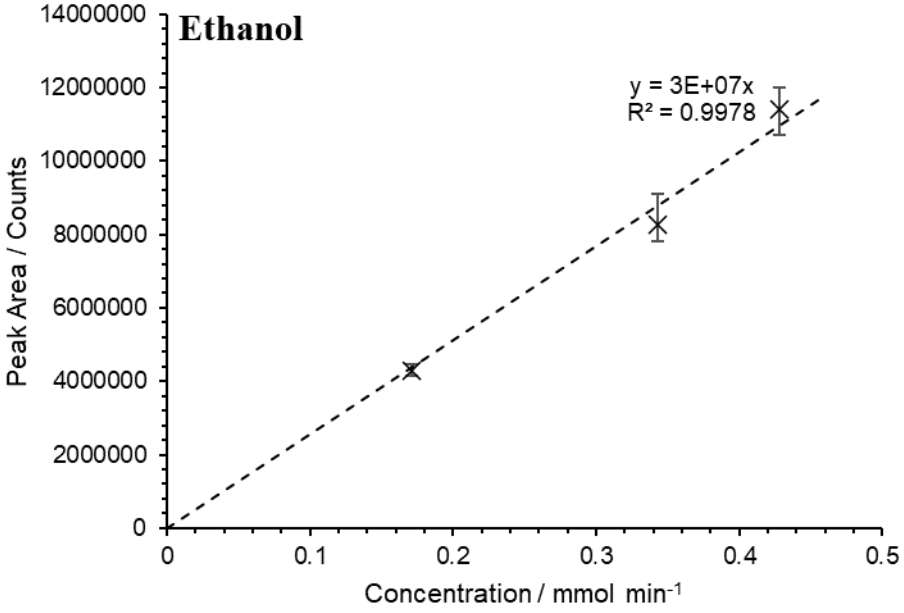

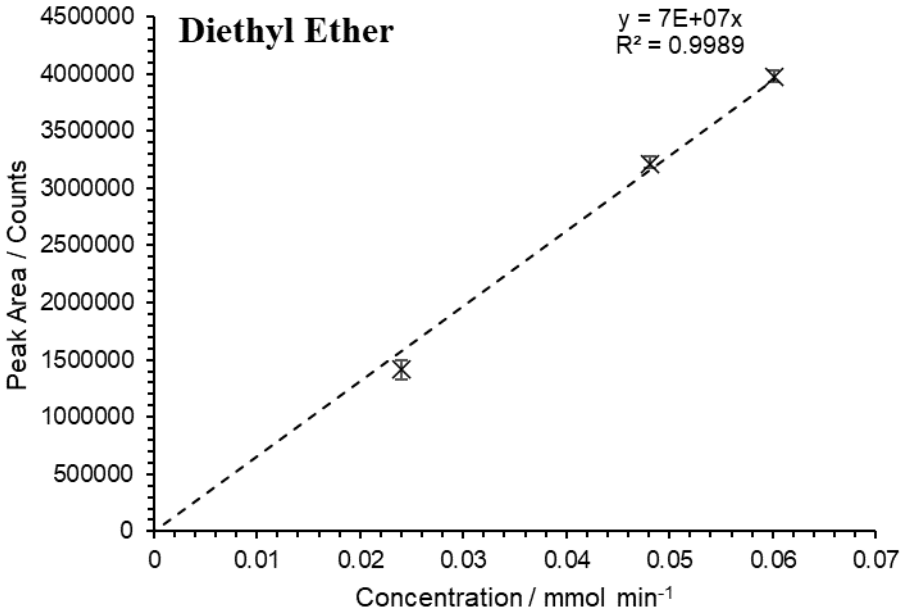

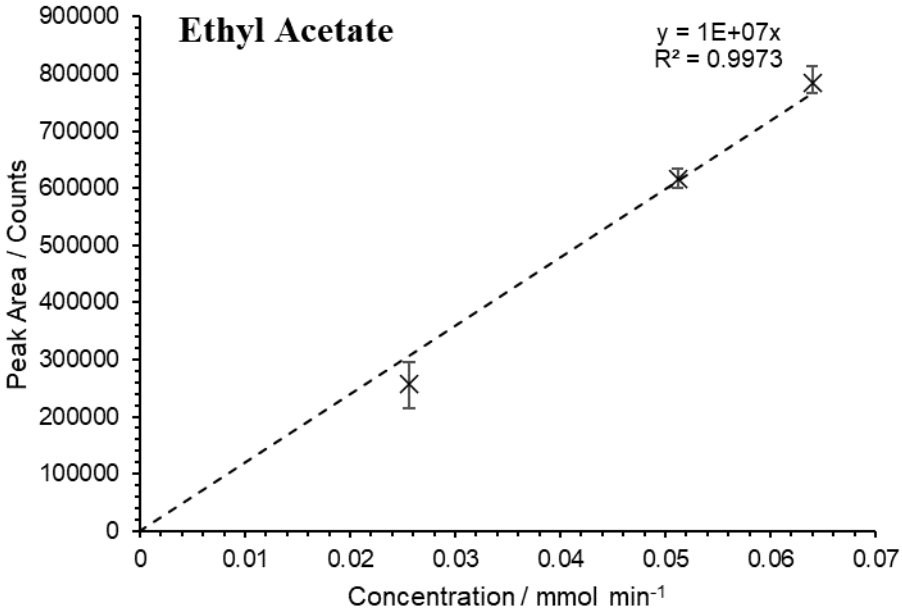
Ethyl Acetate
y = 1E+07x
R² = 0.9973
Peak Area / Counts
900000
800000
700000
600000
500000
400000
300000
200000
100000
0
0
0.01
0.02
0.03
0.04
0.05
0.06
0.07
Concentration / mmol min-1

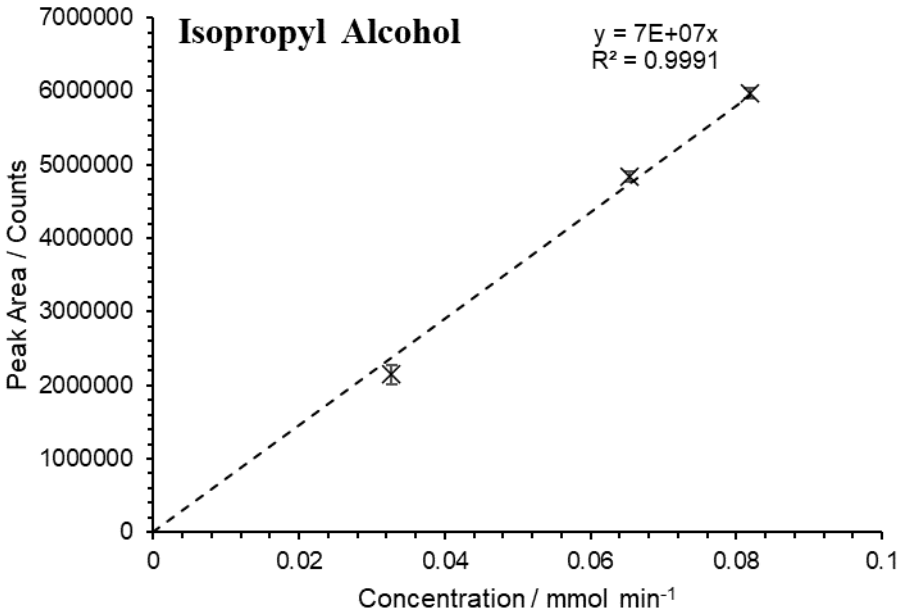
Isopropyl Alcohol
y = 7E+07x
R² = 0.9991
Peak Area / Counts
7000000
6000000
5000000
4000000
3000000
2000000
1000000
0
0
0.02
0.04
0.06
0.08
0.1
Concentration / mmol min-1

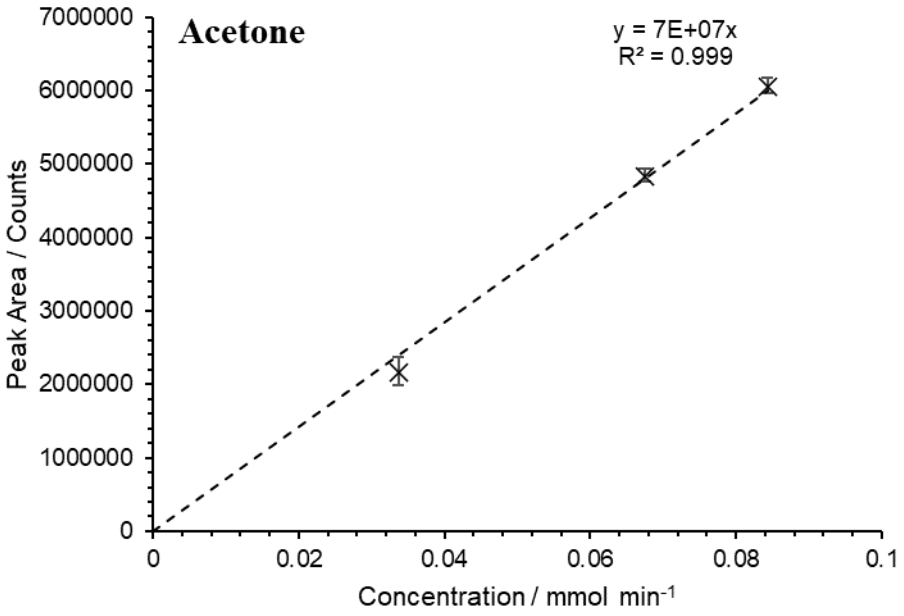
Acetone
y = 7E+07x
R² = 0.999
Peak Area / Counts
Concentration / mmol min-1
7000000
6000000
5000000
4000000
3000000
2000000
1000000
0
0
0.02
0.04
0.06
0.08
0.1

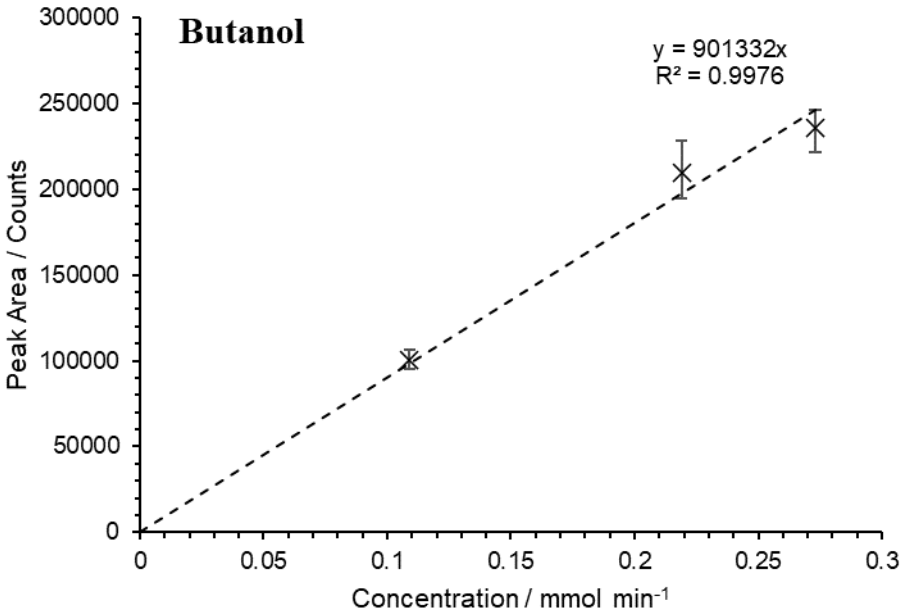
Butanol
y = 901332x
R² = 0.9976
Peak Area / Counts
Concentration / mmol min-1
300000
250000
200000
150000
100000
50000
0
0
0.05
0.1
0.15
0.2
0.25
0.3

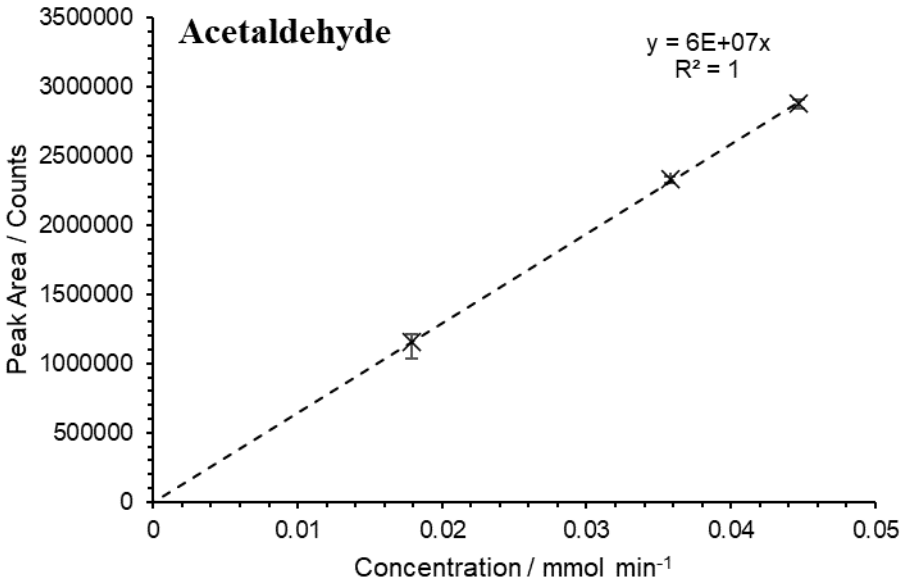
Acetaldehyde
y = 6E+07x
R² = 1
Peak Area / Counts
3500000
3000000
2500000
2000000
1500000
1000000
500000
0
0
0.01
0.02
0.03
0.04
0.05
Concentration / mmol min-1

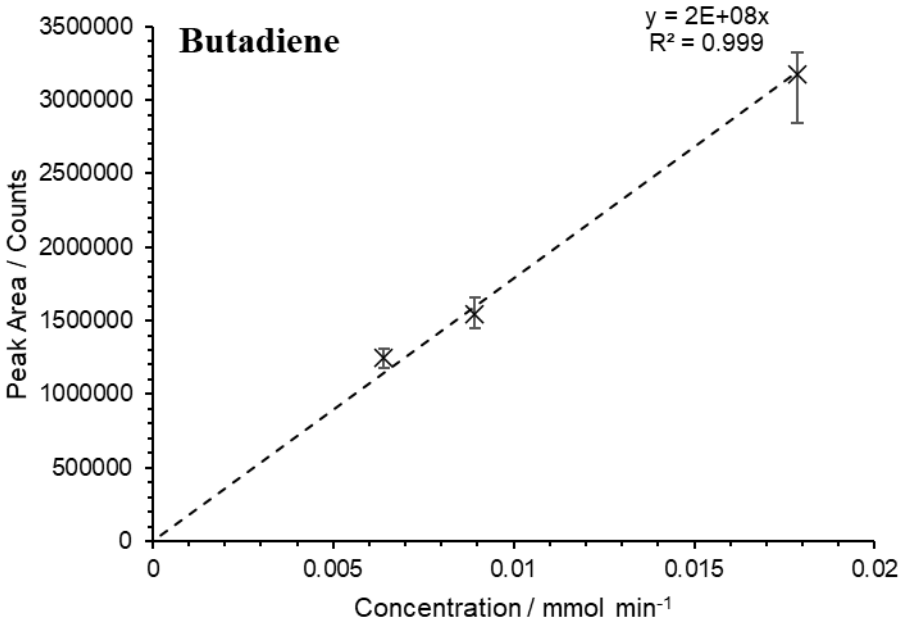
Butadiene
y = 2E+08x
R² = 0.999
Peak Area / Counts
3500000
3000000
2500000
2000000
1500000
1000000
500000
0
0
0.005
0.01
0.015
0.02
Concentration / mmol min-1

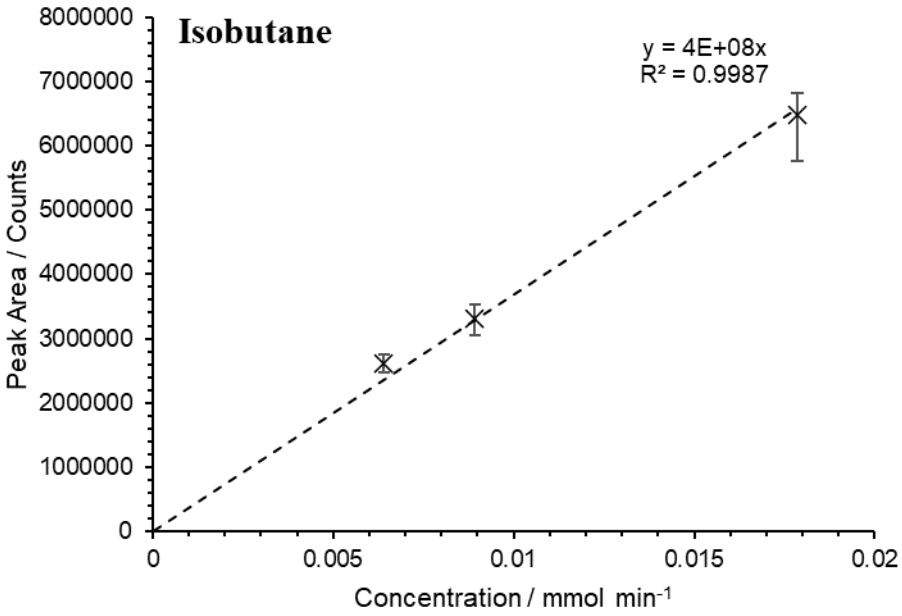
Isobutane
y = 4E+08x
R² = 0.9987
Peak Area / Counts
8000000
7000000
6000000
5000000
4000000
3000000
2000000
1000000
0
0
0.005
0.01
0.015
0.02
Concentration / mmol min-1

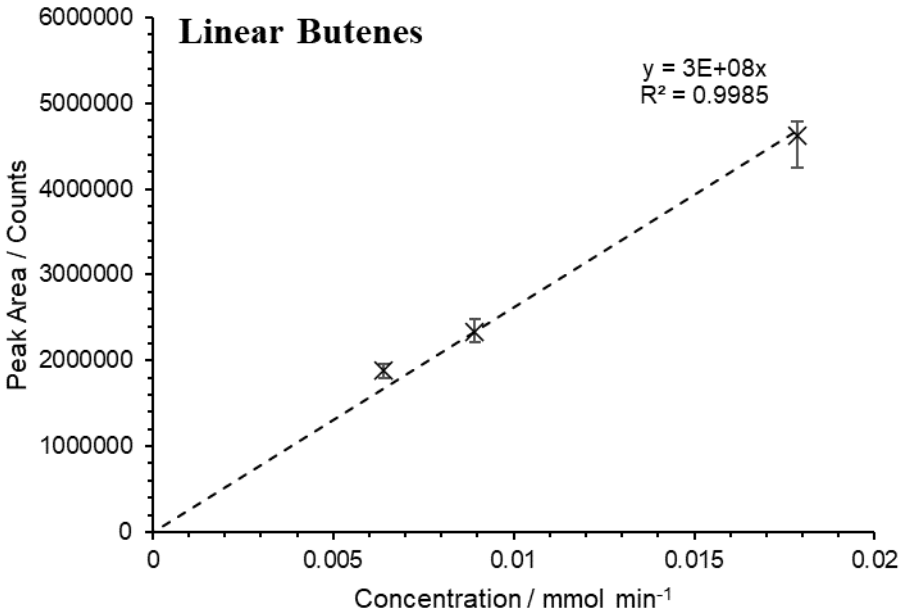
Linear Butenes
y = 3E+08x
R² = 0.9985
Peak Area / Counts
6000000
5000000
4000000
3000000
2000000
1000000
0
0
0.005
0.01
0.015
0.02
Concentration / mmol min-1

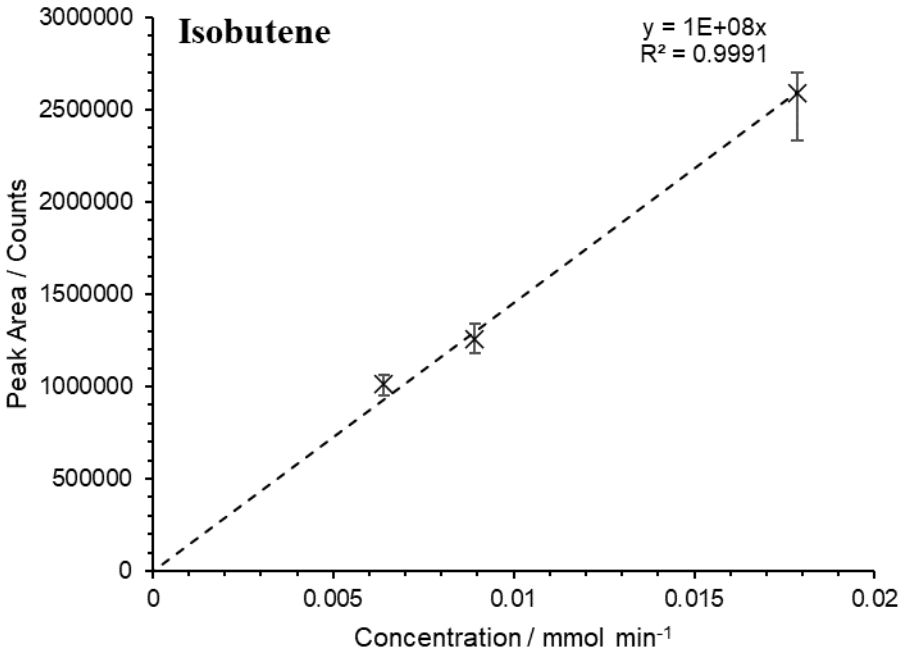

Ethanol				
Concentration /mmol min^{-1}	Peak Area /Counts	Average	Standard Dev	%RSD
0.171	4146365	4271594	114219.7	2.673935
0.171	4454784			
0.171	4347977			
0.171	4180639			
0.171	4228205			
0.343	9115946	8258114	473387	5.732387
0.343	8108450			
0.343	8380615			
0.343	7875866			
0.343	7809693			
0.428	10715307	11402322	547917	4.80531
0.428	10770436			
0.428	11696093			
0.428	12009878			
0.428	11819898			

Diethyl Ether				
Concentration /mmol min^{-1}	Peak Area /Counts	Average	Standard Dev	%RSD
0.024	1325863	1414210	57182.74	4.043442
0.024	1431824			
0.024	1497046			
0.024	1433641			
0.024	1382674			

0.0481	3229727	3215904	35152.3	1.093077
0.0481	3275351			
0.0481	3177074			
0.0481	3211959			
0.0481	3185407			
0.0601	3926005	3979166	39834.52	1.001077
0.0601	3979262			
0.0601	4011787			
0.0601	4033175			
0.0601	3945599			

Ethyl Acetate				
Concentration /mmol min^{-1}	Peak Area /Counts	Average	Standard Dev	%RSD
0.0256	254887	256131	33108.66	12.92646
0.0256	291159			
0.0256	295202			
0.0256	213706			
0.0256	225701			
0.0512	624099	616232	11372.52	1.845494
0.0512	633579			
0.0512	601350			
0.0512	613189			
0.0512	608943			
0.0640	766087	784504.8	15619.35	1.990982
0.0640	778861			
0.0640	782131			
0.0640	813434			
0.0640	782011			

Isopropyl Alcohol				
Concentration /mmol min^{-1}	Peak Area /Counts	Average	Standard Dev	%RSD
0.0327	2016399	2152873	85214.93	3.958195
0.0327	2190129			
0.0327	2266786			
0.0327	2185593			
0.0327	2105460			
0.0654	4858313	4831857	49134.39	1.016884
0.0654	4911929			
0.0654	4807157			

0.0654	4813319			
0.0654	4768566			
0.0818	5904884	5973293	45357.08	0.759331
0.0818	6002643			
0.0818	6034161			
0.0818	5982419			
0.0818	5942359			

Acetone				
Concentration /mmol min^{-1}	Peak Area /Counts	Average	Standard Dev	%RSD
0.0337	2079905	2157946	148426.6	6.878143
0.0337	2290686			
0.0337	2376618			
0.0337	2046354			
0.0337	1996169			
0.0675	4881429	4837375	63422.52	1.311094
0.0675	4934256			
0.0675	4761491			
0.0675	4826193			
0.0675	4783505			
0.0843	5962982	6058203	66031.94	1.089959
0.0843	6047542			
0.0843	6064306			
0.0843	6169758			
0.0843	6046429			

Butanol				
Concentration /mmol min^{-1}	Peak Area /Counts	Average	Standard Dev	%RSD
0.109	99011	100342	4670.237	4.65432
0.109	95405			
0.109	106610			
0.219	223294	209432.4	13748.04	6.56443
0.219	199594			
0.219	194448			
0.219	201284			
0.219	228542			
0.273	221718	235567.6	8751.942	3.715257
0.273	232821			
0.273	246466			

0.273	233486
0.273	243347

Acetaldehyde				
Concentration /mmol min^{-1}	Peak Area /Counts	Average	Standard Dev	%RSD
0.0179	1126563	1157850	69622.19	6.01306
0.0179	1034615			
0.0179	1215166			
0.0179	1200926			
0.0179	1211978			
0.0358	2335152	2335163	17617.99	0.754465
0.0358	2348218			
0.0358	2353888			
0.0358	2335501			
0.0358	2303057			
0.0447	2905382	2875435	22797.49	0.792836
0.0447	2874481			
0.0447	2894917			
0.0447	2859758			
0.0447	2842639			

Butadiene				
Concentration /mmol min^{-1}	Peak Area /Counts	Average	Standard Dev	%RSD
0.00892	1465099	1544904	79803.75	5.165611
0.00892	1605436			
0.00892	1553636			
0.00892	1446064			
0.00892	1654287			
0.00640	1180815	1250136	51740.21	4.138765
0.00640	1297503			
0.00640	1270503			
0.00640	1196524			
0.00640	1305337			
0.00179	2841889	3177106	176189.5	5.545598
0.00179	3326836			
0.00179	3309271			
0.00179	3231471			
0.00179	3176062			

Isobutane

Concentration /mmol min^{-1}	Peak Area /Counts	Average	Standard Dev	%RSD
0.00892	3314930	3305010	159420.2	4.823594
0.00892	3370817			
0.00892	3252338			
0.00892	3048937			
0.00892	3538028			
0.00640	2473223	2619561	111535.9	4.257807
0.00640	2714923			
0.00640	2654961			
0.00640	2504227			
0.00640	2750471			
0.00179	5770438	6479991	372240.7	5.744462
0.00179	6816713			
0.00179	6717025			
0.00179	6620563			
0.00179	6475218			

Linear Butenes				
Concentration /mmol min^{-1}	Peak Area /Counts	Average	Standard Dev	%RSD
0.00892	2252199	2335005	97576.9	4.178873
0.00892	2403336			
0.00892	2336578			
0.00892	2207302			
0.00892	2475610			
0.00640	1789817	1881598	67902.99	3.608793
0.00640	1928693			
0.00640	1911710			
0.00640	1813389			
0.00640	1964382			
0.00179	4245413	4617647	199025.8	4.310113
0.00179	4783935			
0.00179	4769825			
0.00179	4704709			
0.00179	4584352			

Isobutene				
Concentration /mmol min^{-1}	Peak Area /Counts	Average	Standard Dev	%RSD
0.00892	1190010	1256218	62611.71	4.984146
0.00892	1299811			
0.00892	1268205			

0.00892	1180546			
0.00892	1342516			
0.00640	949860	1012560	45283.17	4.472147
0.00640	1050137			
0.00640	1029831			
0.00640	968630			
0.00640	1064342			
0.00179	2330597	2589532	135721.2	5.241149
0.00179	2703561			
0.00179	2685197			
0.00179	2643197			
0.00179	2585107			

A3.6. ShinCarbon ST Calibration Calculations (BID).

Ethane, ethylene, propane and propylene were calibrated as part of a calibration gas mixture supplied by BOC.

Calibration Gas:

Component	Volume / %	Flow Volume / ml min^{-1}	Molar Flow / ml min^{-1}	Molar Flow/ mmol min^{-1}
Ethane	10.00	4.00	1.79E-04	0.17857
Ethylene	10.00	4.00	1.79E-04	0.17857
Propane	2.50	1.00	4.46E-05	0.04464
Propylene	2.50	1.00	4.46E-05	0.04464
Isobutylene	0.50	0.20	8.93E-06	0.00893
Isobutane	0.50	0.20	8.93E-06	0.00893
N-Butane	0.50	0.20	8.93E-06	0.00893
1-Butene	0.50	0.20	8.93E-06	0.00893
Cis-2-Butene	0.50	0.20	8.93E-06	0.00893
1,3-Butadiene	0.50	0.20	8.93E-06	0.00893
Helium (Balance)	72.00	28.80	—	—
Total	100.00	40.00	—	—

Gas	Molar feed rate at given BID injection split ratio / mmol min^{-1}				
	5	8	10	14	20
Ethane	0.3571	0.2232	0.1786	0.1276	0.0893
Ethylene	0.3571	0.2232	0.1786	0.1276	0.0893
Propane	0.0893	0.0558	0.0446	0.0319	0.0223
Propylene	0.0893	0.0558	0.0446	0.0319	0.0223
Isobutylene	0.0179	0.0112	0.0089	0.0064	0.0045
Isobutane	0.0179	0.0112	0.0089	0.0064	0.0045
N-Butane	0.0179	0.0112	0.0089	0.0064	0.0045
1-Butene	0.0179	0.0112	0.0089	0.0064	0.0045
Cis-2-Butene	0.0179	0.0112	0.0089	0.0064	0.0045
1,3-Butadiene	0.0179	0.0112	0.0089	0.0064	0.0045

Species	Retention Time /min
Ethylene	12.89
Ethane	13.87
Propylene	21.10
Propane	22.00

A3.7. ShinCarbon ST Calibration Curves (BID).

Compounds Calibrated: Ethylene, Ethane, Propylene, Propane.

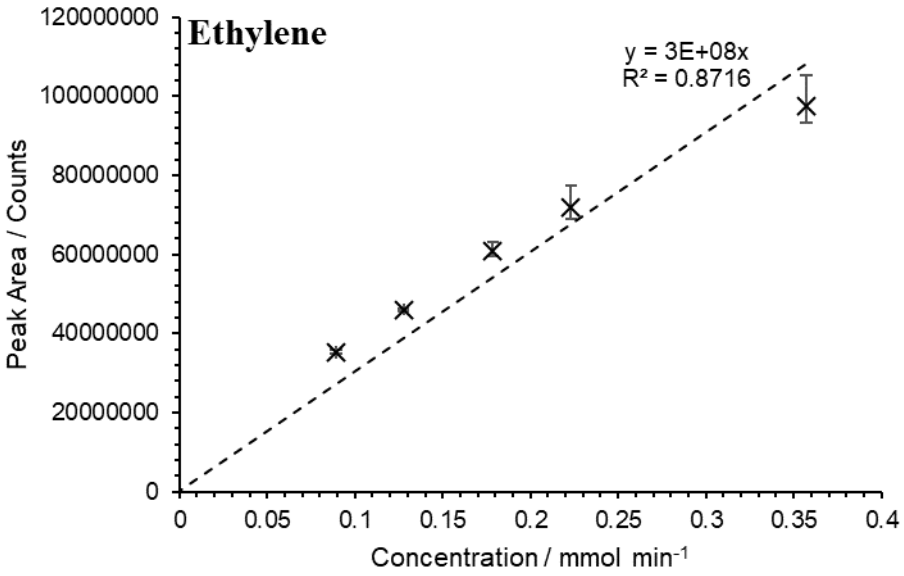

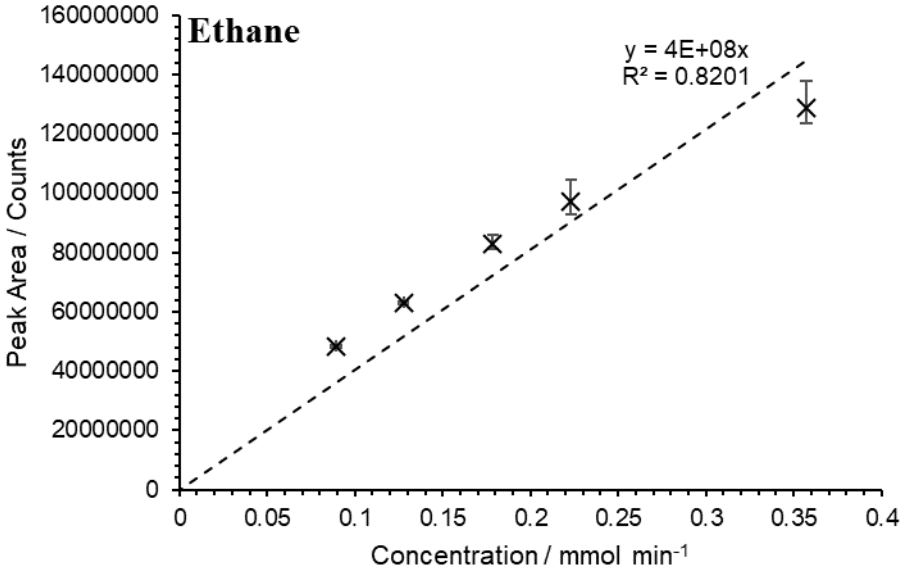

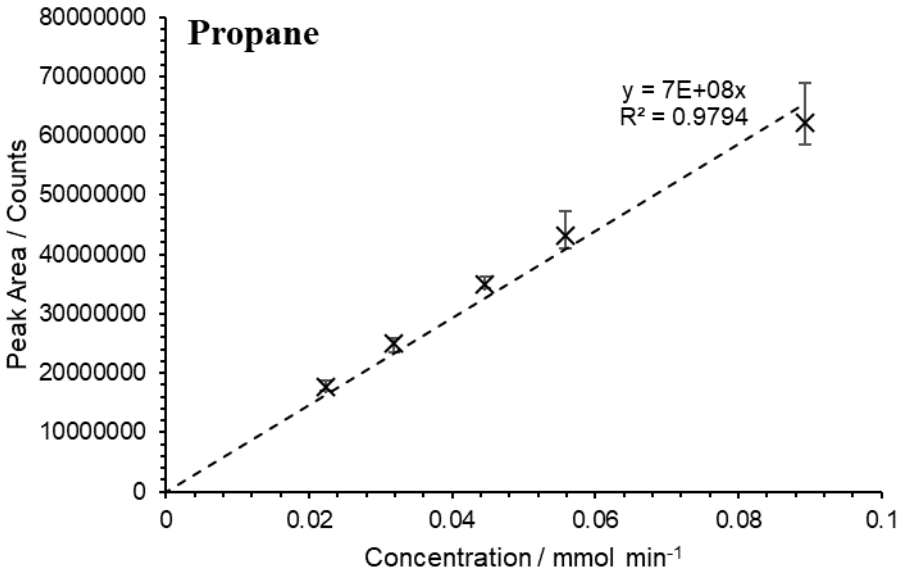
Propane
y = 7E+08x
R² = 0.9794
Peak Area / Counts
Concentration / mmol min-1
80000000
70000000
60000000
50000000
40000000
30000000
20000000
10000000
0
0
0.02
0.04
0.06
0.08
0.1

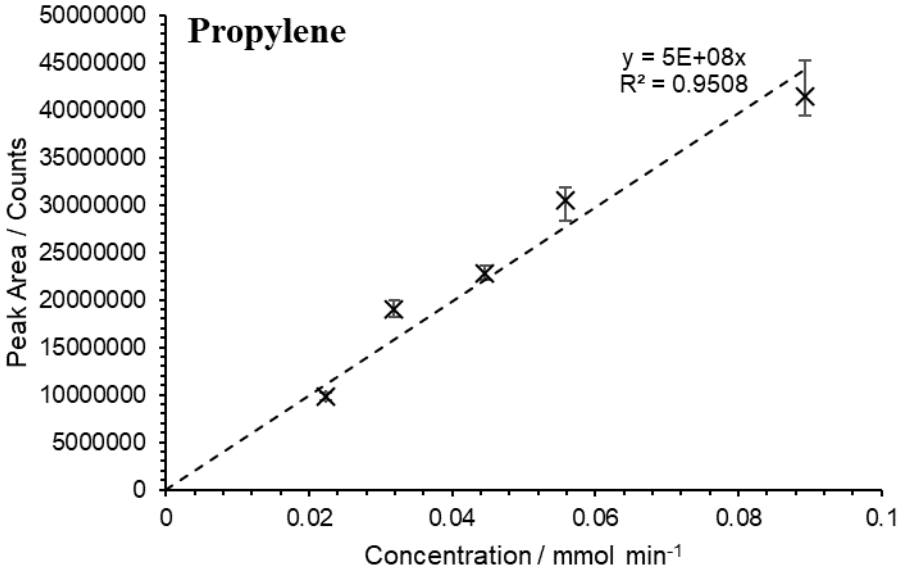
Propylene
y = 5E+08x
R² = 0.9508
Peak Area / Counts
Concentration / mmol min-1
50000000
45000000
40000000
35000000
30000000
25000000
20000000
15000000
10000000
5000000
0
0
0.02
0.04
0.06
0.08
0.1

Ethylene				
Concentration /mmol min^{-1}	Peak Area /Counts	Average	Standard Dev	%RSD
0.3571	93816780	97425600	5568266	5.715403
0.3571	105291420			
0.3571	93168600			
0.2232	69226745	71933579	3962465	5.508506
0.2232	77536288			
0.2232	69037703			
0.1786	59607305	60836611	1528714	2.512818
0.1786	62991411			
0.1786	59911117			
0.1276	45689341	46001137	277722.2	0.603729
0.1276	45950198			
0.1276	46363873			
0.0893	34783164	35158182	502558.2	1.42942
0.0893	35868537			
0.0893	34822844			

Ethane				
Concentration /mmol min^{-1}	Peak Area /Counts	Average	Standard Dev	%RSD
0.3571	124228987	1.29E+08	6568862	5.111275
0.3571	137797952			
0.3571	123524333			
0.2232	93690135	96975031	5304306	5.469765
0.2232	104457906			
0.2232	92777052			
0.1786	81157878	82883484	1983401	2.392999
0.1786	85661368			
0.1786	81831207			
0.1276	63253673	63067679	240281	0.380989
0.1276	62728395			
0.1276	63220968			
0.0893	48647077	48415772	412656.1	0.852318
0.0893	48764125			
0.0893	47836114			

Propylene				
Concentration /mmol min^{-1}	Peak Area /Counts	Average	Standard Dev	%RSD
0.0893	39536100	41395091	2702369	6.528235
0.0893	45216352			
0.0893	39432820			
0.0558	28272787	30458571	1556964	5.111744
0.0558	31781610			
0.0558	31321315			
0.0446	22041505	22719486	630223.9	2.773936
0.0446	23559505			
0.0446	22557448			
0.0319	18212620	18981253	737062.1	3.883105
0.0319	19975318			
0.0319	18755821			
0.0223	10158244	9805276	290725.3	2.964989
0.0223	9811389			
0.0223	9446194			

Propane				
Concentration /mmol min^{-1}	Peak Area /Counts	Average	Standard Dev	%RSD
0.0893	58977178	62149298	4818743	7.753496
0.0893	68958735			
0.0893	58511980			
0.0558	41038623	43110013	2862377	6.639705
0.0558	47157653			
0.0558	41133762			
0.0446	34180164	34927973	952932	2.728277
0.0446	36272808			
0.0446	34330948			
0.0319	25470858	24882016	1061955	4.267961
0.0319	23391112			
0.0319	25784077			
0.0223	18722071	17594783	797246.3	4.531152
0.0223	17013282			
0.0223	17048996			

Appendix 4. Publication: Direct conversion of methane to methanol with zeolites: towards understanding the role of extra-framework d-block metal and zeolite framework type.

This appendix contains the following publication resulting from the work in this thesis:

S. Raynes, M. A. Shah, and R. A. Taylor, Direct conversion of methane to methanol with zeolites: towards understanding the role of extra-framework d-block metal and zeolite framework type, *Dalton Transactions*, 2019, **48**, 10364-10384.

This appendix is supplied as an additional pdf document.

Appendix 5. Publication: Zinc oxide-modified mordenite as an effective catalyst for the dehydrogenation of (bio)ethanol to acetaldehyde.

This appendix contains the following publication resulting from the work in this thesis:

S. Raynes and R Taylor, Zinc oxide-modified mordenite as an effective catalyst for the dehydrogenation of (bio)ethanol to acetaldehyde, *Sustainable Energy Fuels*, 2021, **5**, 2136–2148.

This appendix is supplied as an additional pdf document.